Université de Montréal

Systèmes catalytiques pour la photosynthèse artificielle: Optimisation par l'application des concepts du design moléculaire en chimie de coordination

par Thomas Auvray

Département de Chimie
Faculté des Arts et Sciences

Thèse présentée
en vue de l'obtention du grade de
Philosophae Doctor (Ph.D.) en Chimie

Juillet 2019

Université de Montréal
Faculté des Arts et Sciences, Département de Chimie

Cette thèse intitulée

Systèmes catalytiques pour la photosynthèse artificielle: Optimisation par l'application des concepts du design moléculaire en chimie de coordination

Présentée par

Thomas Auvray

A été évaluée par un jury composé des personnes suivantes

Prof. Frank Schaper
Président-rapporteur

Prof. Garry S. Hanan
Directeur de recherche

Prof. James D. Wuest
Membre du jury

Prof. Marek B. Majewski
Examinateur externe

Résumé

Dans le contexte éco-environnemental actuel, l'Humanité est à la recherche d'alternatives pour remplacer les carburants fossiles responsables du changement climatique affectant le quotidien un peu plus chaque année. Inspiré par la Nature et le processus de la photosynthèse, un nouveau domaine à l'interface entre chimie, physique et ingénierie émergea dans les années 70 : la photosynthèse artificielle. Depuis, de nombreux systèmes catalytiques ont été rapportés mais leur intégration à l'échelle commerciale n'est pas encore d'actualité. De nombreux défis demeurent afin d'améliorer les performances, coupler les différentes réactions et s'assurer de la stabilité à long terme des dispositifs.

Dans le cadre de cette thèse de doctorat, nous nous sommes attachés à explorer la chimie de coordination de complexes de ruthénium et de rhénium, omniprésents dans la littérature mais dont les propriétés peuvent être encore largement modulées par le design de nouveaux ligands. Dans un deuxième temps, les polyoxométallates, composés inorganiques à mi-chemin entre oxydes et molécules aux propriétés fascinantes, ont été recrutés pour développer des dyades covalentes, stratégie permettant de stabiliser un chromophore dans les conditions photocatalytiques.

Mots-clés : photosynthèse, photocatalyse, chimie de coordination, polyoxométallate

Abstract

In the current ecological and environmental context, Mankind needs to find alternative energy sources to replace fossil fuels, as their combustion is a major cause of the current global climate change affecting our daily life a bit more each year. Inspired by Nature and the photosynthetic process, a new area at the interface between chemistry, physics and engineering has emerged in the 70s: artificial photosynthesis. Since then, many catalytic systems have been reported but their integration at commercial scale has not yet been achieved. Several challenges remain to improve their performances, ensure efficient coupling between the different reactions and enhance the long-term stability of these devices.

Within this doctoral thesis, we have focused on exploring the coordination chemistry of ruthenium and rhenium complexes, ubiquitous in the literature though their properties can still be vastly tuned by designing new ligands. In a different approach, polyoxometalates, which are inorganic compounds half-way between oxides and molecules with fascinating properties, were recruited to develop covalent dyads, a strategy enabling stabilization of the dye under photocatalytic conditions.

Keywords: photosynthesis, photocatalysis, coordination chemistry, polyoxometalate

Table des matières

Liste des tableaux

Liste des figures

Liste des abréviations

ΔG énergie libre / free energy

Å Angström

a.u. arbitrary unit

BINAP 2,2'-bis(diphénylphosphino)-1,1'-binaphthyl

bpy 2,2'-bipyridine

Calc. Calculated

Calcd Calculated

CFC Chlorofluorocarbure

CIF Crystallographic information file

CH_4 méthane / methane

CO_2 dioxyde de carbone / carbon dioxide

COF covalent organic framework

CPCM conductor-like polarizable continuum model

δ déplacement chimique

Δ chaleur

d doublet

dd doublet de doublet / doublet of doublet

DFT density functional theory

DCM dichloromethane

DMAc N,N'-Diméthylacetamide

DMF N,N'-Diméthylformamide

DMSO diméthylsulfoxide

E potentiel

E énergie

e^- électron

ECS électrode au calomel saturé

equiv. équivalent

eq. cf. equiv.

ESI-MS Electrospray ionization mass spectrometry

Et éthyle

EtOH éthanol / ethanol

etc. et cætera

f force d'oscillateur

fac- facial

Fc ferrocène

g gramme

GES gaz à effet de serre

GooF goodness of fit

GS ground state

H_2 dihydrogène

H_2O eau

H-hpp 1,3,4,6,7,8-hexahydro-2H-pyrimido[1,2-α]pyrimidine

HOMO highest occupied molecular orbital

HR-MS high-resolution mass spectrometry

ILCT intra-ligand charge transfer

IR infrarouge

ISC intersystem crossing

J joule

J constante de couplage

kJ kilojoule

λ_{exc} longueur d'onde d'excitation

λ_{em} longueur d'onde d'émission

λ_{max} longueur d'onde d'absorption/d'émission maximale

LANL2DZ Los Alamos National Laboratory 2 double ζ

LC ligand-centered

LF ligand field state

LLCT ligand-to-ligand charge transfer

LMCT ligand-to-metal charge transfer

LUMO lowest unoccupied molecular orbital

m multiplet

M metal

mg milligramme

MC metal-centered

Me méthyle

MeCN acétonitrile

mer- méridional

MLCT transfert de charge metal-ligand / metal-to-ligand charge transfer

MLLCT transfert de charge metal/ligand-ligand / metal-ligand-to-ligand charge transfer

MO molecular orbital

MOF polymère de coordination / metal organic framework

m/z ratio masse sur charge / ratio of mass to charge

NIR near infrared

nm nanomètre

ns nanoseconde

NMR nuclear magnetic resonance

O_2 dioxygène

Obs. Observed

ORTEP Oak Ridge thermal ellipsoid program

ox. oxidation

PBE Perdew-Burke-Ernzerhof

Ph phényle

phen 1,10-phénanthroline

ppm partie par million / part per million

POM polyoxométallate / polyoxometalate

PS photosensibilisateur / photosensitizer

PSI photosystème I

PSII photosystème II

py pyridine / pyridyl

quint quintuplet

red. réduction

r.t. room temperature

RT room temperature

s singulet ou seconde

SCE standard calomel electrode

t triplet

tbu *tert*-butyle

tt triplet de triplet / triplet of triplet

TBAP tetrabutylammonium hexafluorophosphate

TD-DFT time-dependent density functional theory

tpy 2,2':6',2"-terpyridine

UV ultraviolet

Vis visible

Wh watt-heure

XRD X-ray diffraction

Z nombre de molécules dans la maille élémentaire

À mon grand-père,
Qui m'enseigna une qualité indispensable :
La persévérance.

Remerciements

Je tiens premièrement à remercier mon directeur de thèse, Prof. Garry S. Hanan, de m'avoir accueilli au sein de son laboratoire pour effectuer ce travail. Je suis en particulier reconnaissant pour la confiance qu'il m'a accordé pour conduire mes travaux avec une très large autonomie et la possibilité d'explorer mes idées, ainsi que son soutien pour le développement de compétences au-delà du travail de laboratoire, en particulier dans le cadre des tâches d'auxiliaire d'enseignement et la supervision d'étudiants.

La réalisation de ce travail n'a pu se faire sans le support des organismes de financements et les programmes de bourse du Département de Chimie. Je suis ainsi extrêmement reconnaissant au Conseil de recherches en sciences naturelles et en génie (CRSNG), la Fondation Canadienne pour l'Innovation (FCI) et Calcul Canada qui ont supporté le groupe de recherche durant mon doctorat. J'ai également eu l'honneur de recevoir des bourses reconnaissants les efforts fournis de la part de l'Université de Montréal, notamment via la Faculté des études supérieures et postdoctorales (FESP), la Faculté des Arts et Sciences (FAS), le Département de Chimie et la Direction des Affaires Internationales (DAI), qui m'ont permis de subvenir à mes besoins au cours de la thèse mais également de participer à des conférences.

Bien que le doctorat soit souvent un travail solitaire, je n'aurais jamais accompli celui-ci sans le support de mes collègues du groupe Hanan, ainsi que des différents groupes de recherches de l'Université de Montréal. Je dois en particulier beaucoup à Mihaela, Daniel et Baptiste qui m'ont formé à mon arrivée. Je remercie également les membres du groupe durant ces cinq années, en particulier Jessica, Élodie, André, Mathieu, Mira et Rosana. Une pensée particulière à mes stagiaires : Jacqueline, Mélanie, Amélie, Georges et Rakesh. J'aimerais aussi remercier chaleureusement les groupes de recherche des professeurs Reber, Schaper, Wuest, Skene et Zargarian (Nicolas, Stéphanie, Loïc, J.P, Alice, Sophie, Pargol). Des remerciements supplémentaires sont dus à Profs. Schaper et Wuest, mon comité, qui m'ont offert de précieux conseils au fil du temps et des rencontres stressantes mais enrichissantes.

Je souhaite remercier le personnel des plateformes techniques de l'Université de Montréal pour leur formation, conseils et soutien : Thierry Maris (rayons X), Elena Nadezhina (analyse élémentaire), Antoine Hamel et Cédric Malveau (RMN), Denis Deschênes et Medgine Lindor-Ménard (laboratoires d'enseignement). Un grand merci à mes collaborateurs internationaux des équipes de Prof. Nelsi Zaccheroni (Bologne) Prof. Mirco Natali (Ferrara) et Prof. Benjamin Elias (Louvain).

Finalement, cette thèse n'aurait jamais été possible sans le soutien de ma famille et en particulier de ma conjointe Olga. Merci d'avoir été présente pour moi durant tout ce temps et dans nos projets à venir.

Chapitre I. Introduction

I.1 De la nécessité de convertir l'énergie solaire.

Notre planète est actuellement le théâtre de changements sans pareil malgré 4,6 milliards d'années d'histoire. Ce n'est pas tant leur amplitude que la vitesse à laquelle ils ont pris place qui les rends uniques. On sait par ailleurs que l'humanité en est la principale responsable.[1] Notre développement social, économique et technologique fulgurant au cours du XX^{ème} siècle s'est accompagné d'une dramatique augmentation de la concentration atmosphérique de gaz responsables du réchauffement climatique, en particulier le dioxyde de carbone (CO_2), principal gaz à effet de serre (GES), ou encore les chlorofluorocarbures (CFC), responsables du trou dans la couche d'ozone.[2] L'augmentation des températures terrestres et océaniques a de nombreuses répercussions sur la faune et la flore de notre planète et nécessite des changements immédiats et réfléchis de notre mode de vie et surtout de notre gestion des ressources naturelles.[3] Dans cet optique, de nombreuses initiatives existent à différentes échelles. Chacun peut adapter son mode de vie afin de réduire son empreinte environnementale. Pour faciliter cette transition à l'échelle individuelle, des initiatives de sensibilisations, couplées à des décisions politiques guidées par la science, sont indispensables. En parallèle, un vaste effort de développement technologique est en cours afin d'améliorer l'efficacité énergétique des procédés industriels et des produits de consommation, mais également de favoriser la réutilisation des ressources via l'utilisation de matériaux recyclables et/ou plus durables afin de réduire la quantité de déchet. Enfin, il faut modifier la nature de l'énergie utilisée au quotidien dans nos foyers, nos véhicules ou notre industrie.[4]

Avec une population proche de sept milliards et demi, et en constante croissance, la demande énergétique annuelle mondiale ne cesse d'augmenter. Elle est actuellement estimée à 13 000 Mtep (mégatonnes d'équivalent pétrole) soit 150 PWh, contre 5 000 Mtep dans les années 70. Selon l'Agence internationale pour l'énergie, cette demande est répartie comme présenté sur la Figure I.1.[5] Avec respectivement 37, 22 et 29 % de la demande, les secteurs industriel, résidentiel et du transport sont les principaux consommateurs. Au-delà de la quantité d'énergie en demande, c'est son origine qui est problématique. En effet, à l'échelle mondiale, la part des carburants fossiles (pétrole, gaz naturel et charbon) dépasse les 80%. L'extraction et la

combustion de ces ressources génèrent de larges quantités de GES. Elles sont par ailleurs disponibles en quantité finie du fait de leur processus de génération sur plusieurs siècles. Il est donc crucial de réduire leur part dans le mélange énergétique mondial. Pour ce faire, une transition vers des sources alternatives d'énergie est indispensable.

Si on s'intéresse à la situation au Canada[6] et en France[7] (Figure I.2), pays représentant chacun

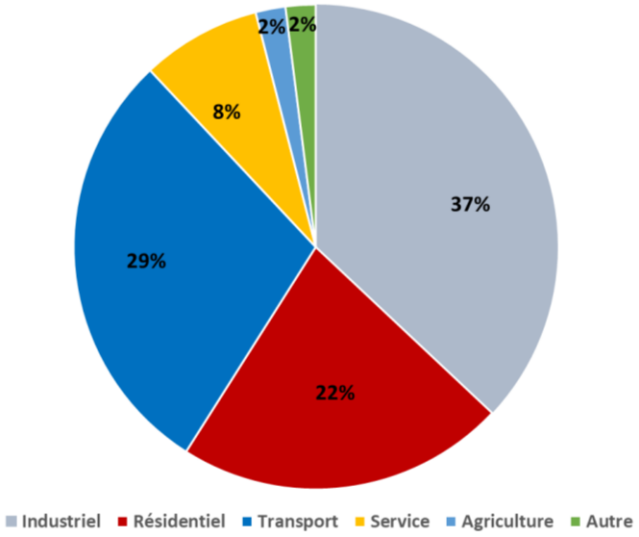

Figure I.1. Répartition par secteurs de la consommation mondiale d'énergie en 2016. (Adapté du rapport de l'Agence internationale pour l'énergie World Energy Balances: Overview, 2018)[5]

environ 2 % de la demande mondiale, on peut voir l'impact de ces sources alternatives. Au Canada, et plus particulièrement au Québec, la part des carburants fossiles est abaissée par l'utilisation massive de l'hydroélectricité. En France, c'est l'utilisation de l'énergie nucléaire qui réduit drastiquement l'impact des carburants fossiles. Ces deux exemples démontrent la possibilité d'adapter la production d'énergie pour diminuer la part des carburants fossiles tout en répondant à la demande. Il existe cependant une limite à l'implantation massive de ces technologies : les centrales nucléaires et hydroélectriques sont des infrastructures lourdes, coûteuses et ayant elles-mêmes un impact environnemental non négligeable. Par ailleurs, suite aux catastrophes de Tchernobyl et de Fukushima, l'opinion publique est négative vis-à-vis du nucléaire. Le nucléaire génère également des inquiétudes concernant le devenir des combustibles épuisés qui demeurent fortement radioactifs. Aucune solution de gestion à long terme de ces déchets, à part l'enfouissement, ne semble exister.[8]

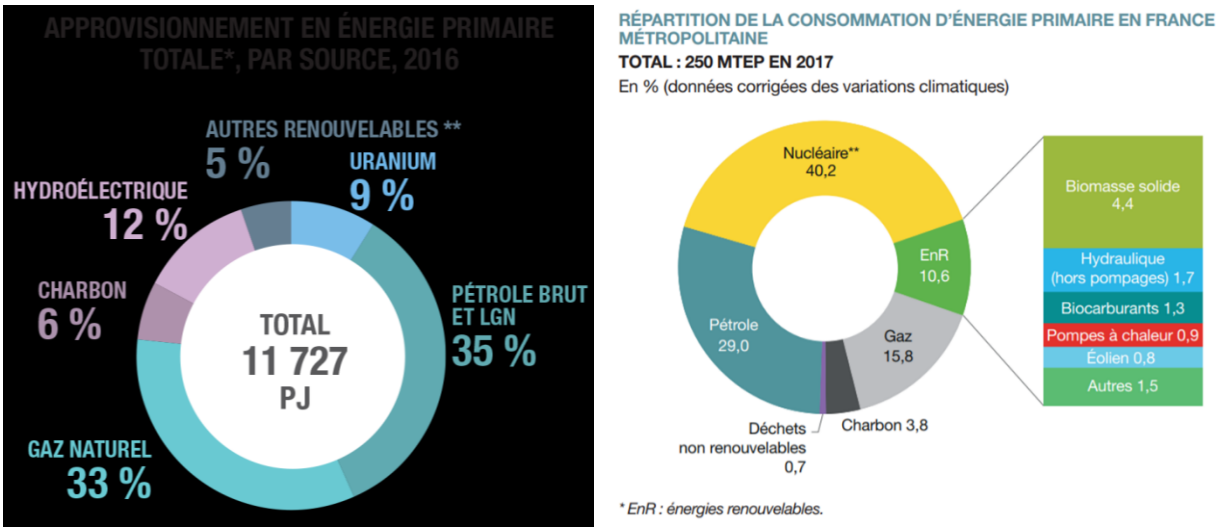

Figure I.2. Constitution des mélanges énergétiques du Canada en 2016 (gauche) et de la France en 2017 (droite). (Sources : https://www.rncan.gc.ca/energie/faits/energie-ges/20074 et rapport du SDES, Chiffres clés de l'énergie 2018)

La solution se trouve plus vraisemblablement dans les énergies renouvelables. Celles-ci sont basées sur l'utilisation de ressources pérennes ou dont la gestion permet d'équilibrer production et consommation, telles que le bois et les biocarburants. Néanmoins, ces derniers constituent une alternative aux carburants fossiles sans régler la question du CO_2. Dans le cas de l'éolien ou de l'hydroélectricité, les besoins techniques des installations demeurent importants et limitent l'implantation à grande échelle. Finalement, l'énergie solaire, non explicitée dans la Figure I.2, est l'énergie renouvelable la plus prometteuse. En effet, celle-ci est infiniment disponible à l'échelle humaine et extrêmement abondante puisque l'énergie reçue par la Terre sous forme de rayonnement lumineux représente 885 000 PWh par an, soit 6 000 fois la demande annuelle mondiale.[9] Dit autrement : en une heure, nous recevons la quantité d'énergie nécessaire pour alimenter la planète pour une année entière, en supposant que l'on soit capables de la collecter et de la stocker. Cependant, la conversion de l'énergie solaire en électricité, bien que compatible avec la grille d'alimentation actuelle, souffre de sa disponibilité cyclique. La nuit ou lors de journées pluvieuses, l'énergie solaire n'est que peu ou pas accessible alors que la demande demeure. Cela implique l'utilisation de batteries, une technologie certes en développement rapide, mais vraisemblablement incapable de stocker les quantités d'énergies nécessaires. Prenons l'exemple d'une solution domestique commerciale actuelle, la batterie *Powerwall* de la compagnie Tesla. Celle-ci est annoncée avec une capacité utile de 13,5 kWh

pour un poids de 114 kg et un coût d'environ 10 000 $CAD.[10] Si on voulait stocker la consommation quotidienne en énergie (150 PWh pour 365 jours soit 411 TWh/d) dans ce genre de batterie, il en faudrait 30 milliards… Bien que le stockage d'énergie à une telle échelle se fera très probablement en utilisant d'autres types de batteries, les quantités de matières nécessaires pour la fabrication de ces produits, notamment le lithium et le cobalt, font actuellement l'objet d'inquiétudes au vu du rythme de consommation et l'absence de récupération efficace.[11]

Face à ce défi, nous trouvons une fois de plus l'inspiration dans la Nature. En effet, le monde biologique, y compris l'Homme, est alimenté à l'énergie solaire. Celle-ci est collectée par phytoplanctons et plantes qui l'utilisent pour convertir minéraux et CO_2 en dioxygène (O_2) et matières organiques. Et comme ces organismes sont à la base de la chaine alimentaire, ultimement, nous nous nourrissons de l'énergie solaire qu'ils ont convertie en composés organiques. La photosynthèse apparait alors comme un procédé idéal pour la conversion de l'énergie solaire et son stockage via sa conversion en énergie chimique.

I.2 La photosynthèse et ses milliards d'années d'expérience

La photosynthèse est un processus biologique ayant impacté de façon majeure notre planète. Les experts de diverses disciplines s'accordent sur le fait qu'il y a environ 2,4 milliards d'années, durant un événement appelée «la grande oxygénation», la concentration atmosphérique en dioxygène a augmenté de façon drastique.[12] Cette transformation causa l'oxydation du méthane atmosphérique en CO_2, menant à une longue période de glaciation. En effet, le méthane est un gaz à effet de serre plus fort que le CO_2 et sa disparition de l'atmosphère causa une rapide diminution de la température du globe. L'augmentation du caractère oxydant de l'atmosphère eut bien d'autres conséquences, visibles encore aujourd'hui, notamment au niveau minéral.[13] Bien que le point d'origine exact de cette augmentation soit encore débattu, le lien avec le développement des cyanobactéries est communément accepté. Aussi appelées algues bleu-vertes, ces organismes unicellulaires réalisent la photosynthèse oxygénique et sont parmi les plus anciens êtres vivants identifiés. Du point de vue biologique, l'acquisition par ces organismes de la capacité à convertir l'énergie solaire en composés organiques est une étape évolutive unique. L'ensemble du processus a lieu dans le thylakoïde, une sorte de poche

délimitée par une bicouche lipidique ; l'intérieur de cette poche est appelé lumen. Dans les cyanobactéries, les thylakoïdes sont directement en contact avec le cytoplasme. Chez les plantes, on retrouve un organite dédié à l'activité photosynthétique : le chloroplaste. Celui-ci contient les thylakoïdes et les isole du cytoplasme de la cellule. Il résulterait, selon la théorie endosymbiotique, de l'incorporation d'une cyanobactérie par une cellule qui bénéficia alors des capacités photosynthétiques de la bactérie en échange de nutriments pour celle-ci.

La collecte d'énergie et la cascade de transferts électroniques qui l'accompagne prennent place directement dans la membrane du thylakoïde (Figure I.3)[14]. Différentes protéines sont impliquées dans la cascade d'électrons partant du complexe d'oxydation de l'eau (COE) produisant du dioxygène et finissant par une enzyme, la ferrédoxine-$NADP^+$ reductase (FNR). Celle-ci convertit le $NADP^+$ en NADPH (NADP : nicotinamide adénine dinucléotide phosphate). Le NADPH est consommé par la suite pour la fixation du CO_2 dans le cycle de Calvin conduisant, après plusieurs étapes, à la formation de glucose.

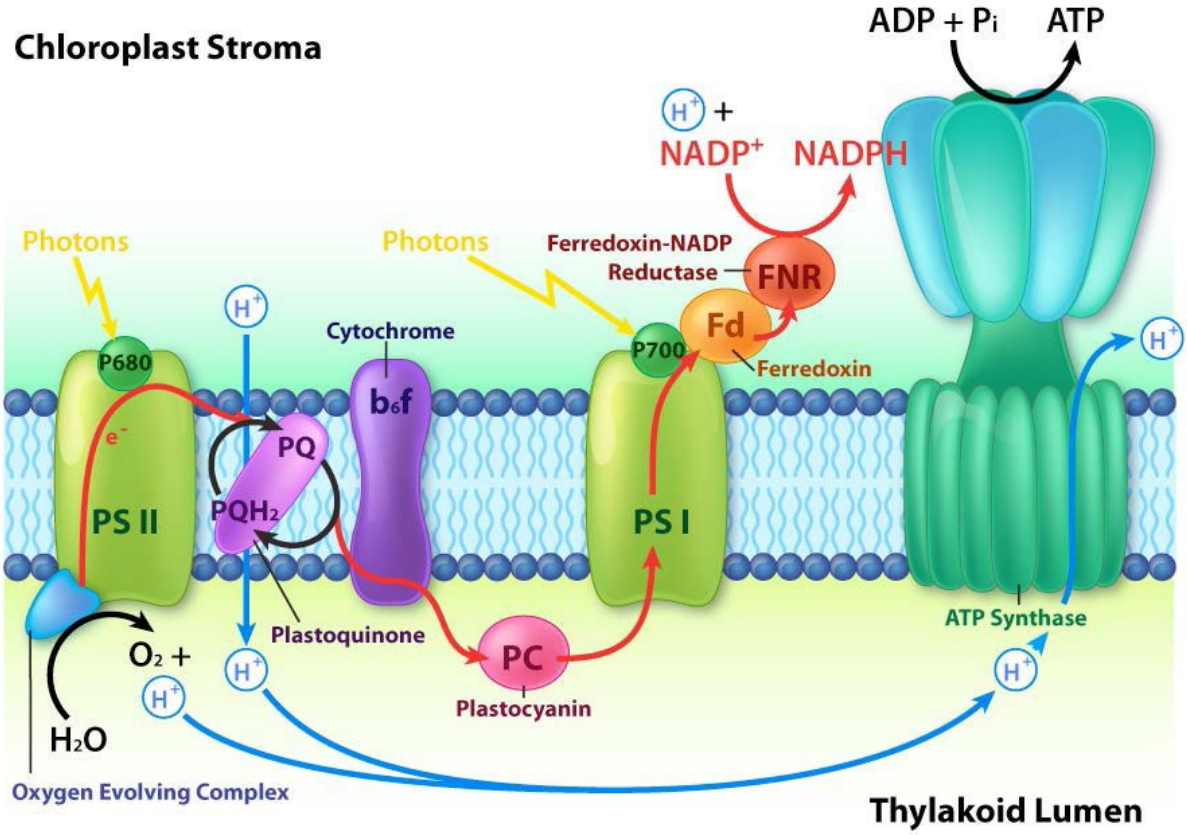

Figure I.3. Mouvement des électrons et protons au travers de la membrane du thylakoïde contenant les différentes unités actives du système photosynthétique d'une plante.[14]

L'enzyme clé du cycle de Calvin est appelée RubisCO (Ribulose-1,5-bisphosphate carboxylase/oxygenase) et implique un cation Mg^{2+} dans l'activation du CO_2. Le bilan de la photosynthèse est donc :

$$6\,H_2O + 6\,CO_2 + h\nu \rightarrow C_6H_{12}O_6 + 6\,O_2$$

Les deux unités en charge de la collecte de l'énergie solaire sont les photosystèmes (PS) I et II. L'élucidation de la structure tridimensionnelle de ces protéines, en particulier du centre de réaction, fut récompensée par le Prix Nobel de Chimie en 1988.[15] Les pigments P680 et P700, mis en évidence dans la Figure I.3, se trouvent dans le centre de réaction. Ce sont des chlorophylles de type *a* dont le nom renvoie à la longueur d'absorption maximale (680 et 700 nm, respectivement). Ils correspondent au point d'arrivée des transferts d'énergie prenant place au sein d'un arrangement complexe de chlorophylles et de bêta-carotènes (Figure I.4) agissant comme antenne pour l'absorption de l'énergie solaire et la transfère au centre de réaction. Dans les cyanobactéries, le complexe antenne est appelée phycobilisome car il contient des phycobilines, pigments basés sur un motif tetra-pyrrole non cyclique contrairement à celui des chlorophylles (Figure I.4).[16] Leurs spectres d'absorptions sont visibles sur la Figure I.5.

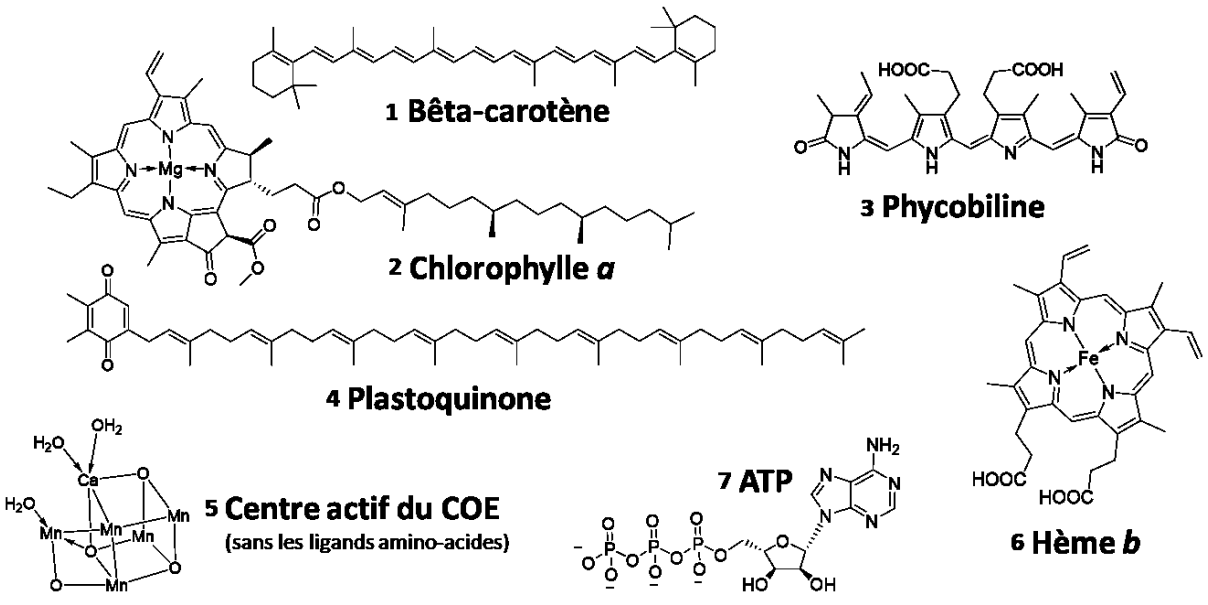

Figure I.4. Structure des molécules impliquées dans l'activité photosynthétique, jouant le rôle de pigments (1-3), de centres rédox (4-6) ou de source d'énergie cellulaire (7).

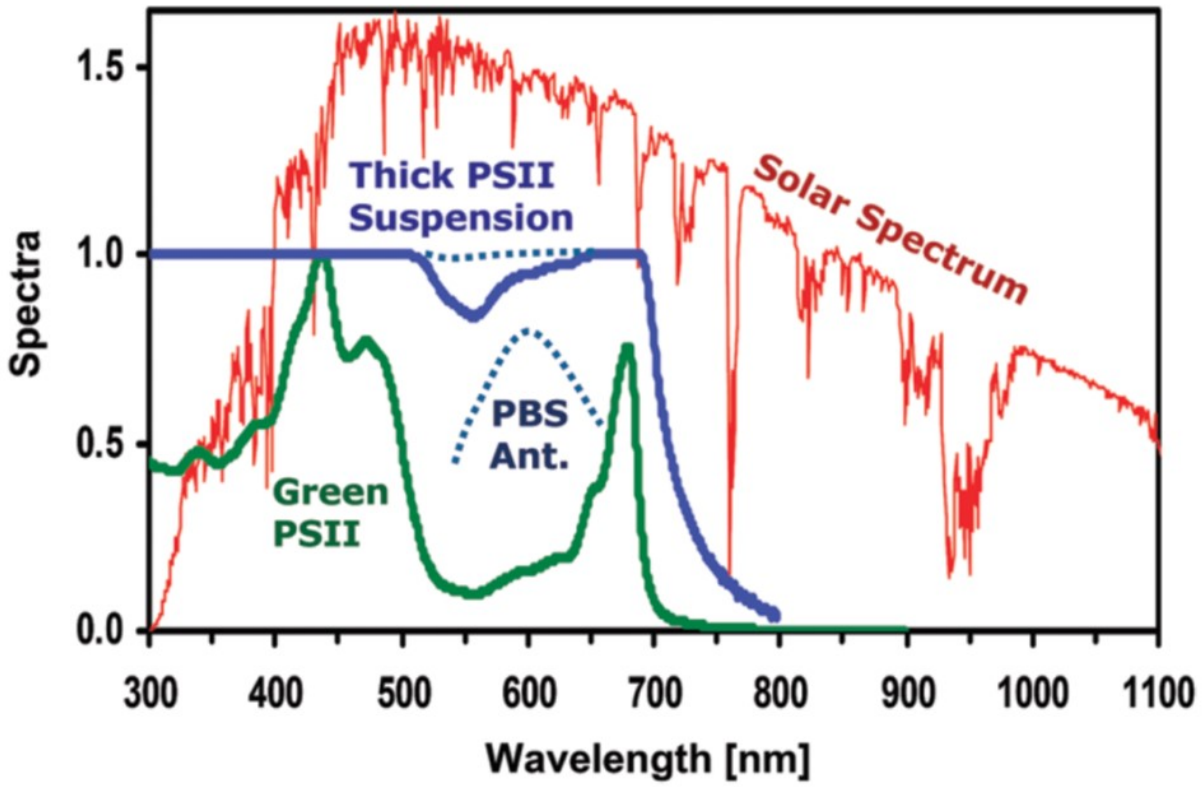

Figure I.5. Superposition du spectre solaire (en $W.m^{-2}.nm^{-1}$, en rouge), des spectres d'absorption de particules de PS II extraites d'épinards (unités arbitraires, en vert) et d'un phycobilisome de cyanobactérie (unité arbitraire, en pointillé bleu) ainsi que de la fraction de photons incidents absorbés par une suspension opaque de PS II, typiquement observée dans une feuille (en bleu). (Adapté avec permission de Dau, H.; Zaharieva, I., *Acc. Chem. Res.* 2009, ***42*** (12), 1861-70. Copyright 2009 American Chemical Society)

La combinaison de carotènes et chlorophylles du PS II donnent le spectre d'absorption en vert sur la Figure I.5. Dans les conditions naturelles, la concentration en pigments est telle que la quasi-totalité de la lumière entre 300 et 700 nm est absorbée (en bleu). On peut y voir un creux d'absorbance entre 500 et 650 nm, expliquant la couleur verte des plantes. Certaines bactéries absorbent à plus basses longueurs d'ondes, i.e. jusqu'à 850 nm dans le cas des bactéries pourpres, grâce à des modifications de la structure des chlorophylles dans les antennes collectrices. Au-delà de la structure et des propriétés mêmes des pigments utilisés, leur arrangement au sein des antennes collectrices est un chef d'œuvre de design moléculaire.[17] La Figure I.6 présente l'arrangements des pigments en unités collectrices (*light harvesting units* LH) cycliques. Ces unités sont positionnées dans la membrane thylakoïde de façon concentrique : LH-I entoure le centre de réaction (*reaction center* RC) et est elle-même entourée

d'unités LH-II. Les transferts d'énergie sont tous dirigés vers le centre de réaction grâce à l'ajustement fin des maxima d'absorption de chaque pigment ; les carotènes absorbants à 500 nm transfèrent leur énergie aux différentes bactériochlorophylles (B800, B820, B850 et B875) dont le nom est associé au maximum d'absorbance propre à chacune.

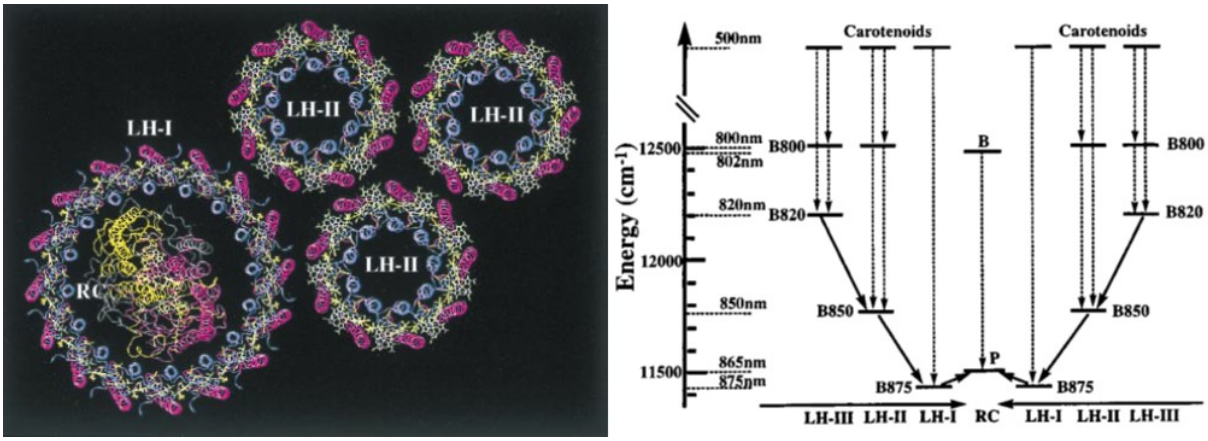

Figure I.6. Arrangements des antennes collectrices autour du centre de réaction dans une bactérie pourpre (Gauche). Transferts d'énergie entre les différents pigments concentrant l'énergie vers le centre de réaction. (Droite) (Adapté avec permission de Hu, X.; Damjanović, A.; Ritz, T.; Schulten, K., *Proc. Natl. Acad. Sci. U.S.A.* 1998**, *95*** (11), 5935. Copyright 1998 National Academy of Sciences)

Cette optimisation de la collecte d'énergie vers le centre de réaction assure la mise en place efficace de la cascade de transferts d'électrons reliant oxydation de l'eau et réduction du NADPH, illustrée dans la Figure I.7.[18] Ainsi, le PS II, via l'excitation de P680, transfère un électron à la phéophytine (Pheo), dont la structure correspond à celle d'une chlorophylle sans le cation Mg^{2+}. Il est régénéré en collectant les électrons libérés par l'oxydation de l'eau au niveau du COE. Une quinone (Q) régénère la phéophytine et transfert les électrons à la plastoquinone (PQ, structure présentée Figure I.4) qui sert ainsi de médiateur au sein de la membrane du thylakoïde entre le PS II et le cytochrome b6f. Ce dernier transfère les électrons de la plastoquinone réduite (plastoquinol) à la plastocyanine (PC), une protéine avec un centre Cu^{2+} alors réduit en Cu^{+}. La réoxydation du plastoquinol s'accompagne de la libération de deux protons qui sont transférés du stroma du chloroplaste au lumen du thylakoïde, ce qui participe à créer le gradient de protons nécessaires au fonctionnement de l'ATP synthase (ATP = adénosine triphosphate), protéine présente dans la membrane du thylakoïde générant l'ATP, source universelle d'énergie dans les cellules vivantes.[19]

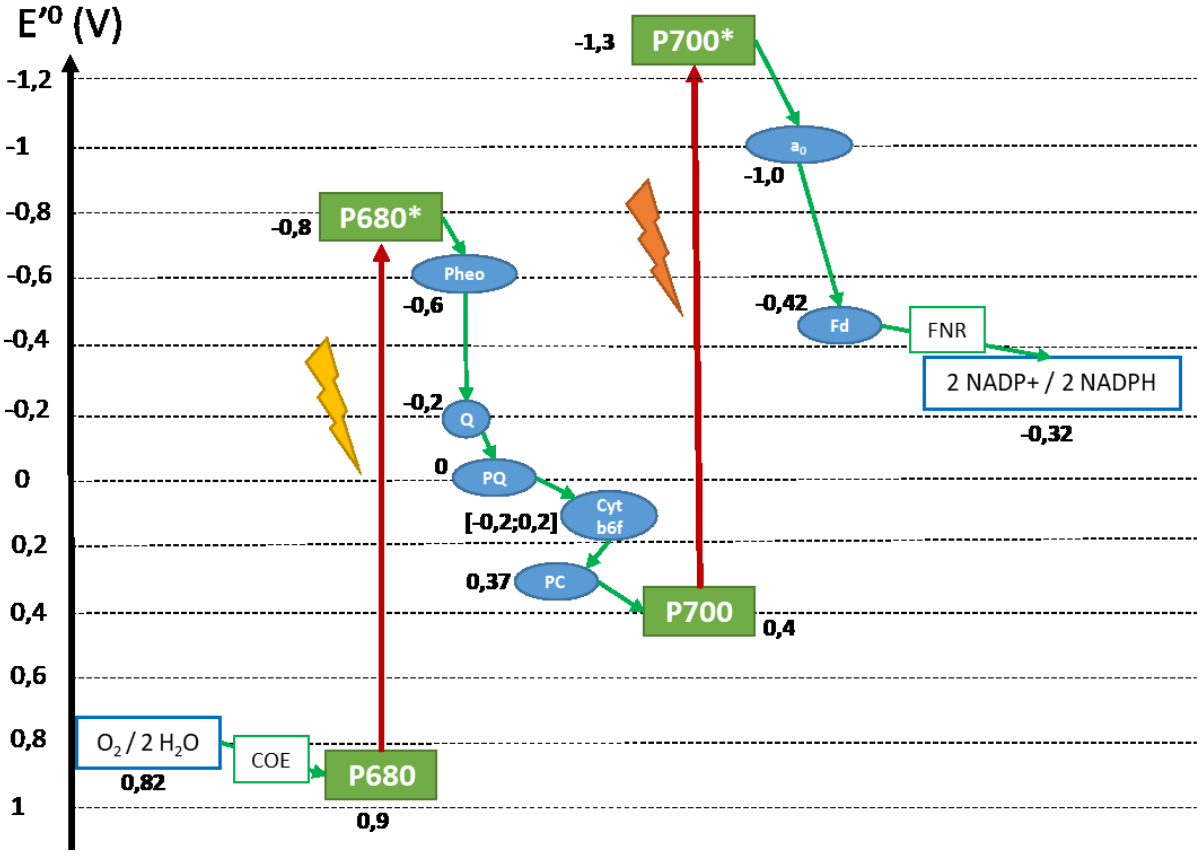

Figure I.7. Schéma en Z des transferts d'électrons impliqués dans la photosynthèse. Les potentiels rédox des différentes unités sont indiqués. (Adapté de https://rnbio.upmc.fr, Ressources numérique pour l'enseignement en biologie de Sorbonne-Université)[18]

Finalement, la plastocyanine régénère le pigment P700 ayant été oxydé par a_0 ; a_0 étant une chlorophylle modifiée qui constitue l'accepteur final du PS I. Finalement, les électrons sont transférés à la ferrédoxine dont le centre actif est un cluster $[Fe_xS_y]$ de stœchiométrie variable (x,y = 2,2 ou 4,4). Celui-ci interagit avec les cystéines présentes dans la séquence d'amino-acides de la protéine. La ferrédoxine réduite sert finalement de donneur d'électrons pour la ferrédoxine-$NADP^+$ reductase (FNR), générant du NADPH. Cette séquence complexe de transferts électroniques couvre l'intégrale de la fenêtre de potentiel accessible dans l'eau. Elle est rendue possible par l'adaptation de structure de chaque unité pour ajuster son potentiel de réduction ainsi que de l'arrangement de ces unités dans la membrane thylakoïde.

Si l'on ne peut que s'émerveiller devant cette machinerie biologique de précision, il faut reconnaitre que la photosynthèse naturelle possède certaines limitations pour être considérée

comme source d'énergie alternative à long terme. Elle est premièrement peu efficace ; on trouve dans la littérature des valeurs généralement inférieures à 1%, mais allant jusqu'à 3% pour des microalgues cultivées en bioréacteurs et même 5 à 7% lors de la période de croissance de l'organisme.[20-21] Cette efficacité réduite n'est cependant pas liée à un défaut dans la conception. La Nature a optimisé ce système sur plusieurs milliards d'années, assurant l'absorption optimale de la lumière mais également la dissipation de l'énergie excédentaire qui pourrait lui être dommageable. Il existe de nombreux mécanismes de régulation de l'activité photosynthétique selon les variations dans son environnement. Deuxièmement, la nature biologique du processus lui permet de ne pas être stable dans le temps. Si une des protéines est dégradée, elle peut facilement être recyclée et resynthétisée par la machinerie cellulaire. Si une cellule meurt, une autre va la remplacer. Ces cycles de vie sont courts. Les protéines constituant le PS II ont une durée de demi-vie estimée entre 1 et 11 heures, celles du PS I étant plus stables avec une demi-vie de 30 à 75 heures.[22] Enfin, comme vu plus haut, la photosynthèse naturelle est optimisée uniquement pour la lumière visible (400-800 nm), laissant passer jusqu'à 40% du rayonnement solaire, sous forme de rayonnement infra-rouge.

L'étude de ce phénomène naturel unique se poursuit encore aujourd'hui. Du point de vue ingénierie, les modes de cultures sont optimisés pour maximiser l'exposition lumineuse de cultures de microalgues ; celles-ci étant d'intérêt pour l'industrie agroalimentaire, cosmétique et des bio-carburants.[23] D'intenses efforts de recherche visent à améliorer les performances d'enzymes naturelles.[24] On peut mentionner ici l'évolution dirigée, thème du Prix Nobel de chimie 2018, qui vise également l'introduction de fonctions catalytiques absentes dans la Nature.[25] Enfin, diverses approches biomimétiques ont conduit à l'obtention de systèmes capables d'accomplir des tâches similaires au photosystème, mais en utilisant des composés synthétiques.

I.3 La photosynthèse artificielle moléculaire

> *" On the arid lands there will spring up industrial colonies without smoke and without smokestacks; forest of glass tubes will extend over the plains and glass buildings will rise everywhere; inside of these will take place the photochemical processes that hitherto have been the guarded secret of the plants, but that will have been mastered by human industry which will know how to make them bear even more abundant fruit than nature, for nature is not in a hurry and mankind is. And if in a distant future the supply of coal becomes completely exhausted, civilization will not be checked by that, for life and civilization will continue as long as the sun shines. "*
>
> G. Ciamician, 1912.[26]

Giacomo Luigi Ciamician, l'un des pionniers de la photochimie, publia en 1912 un plaidoyer pour une société agro-industrielle se détachant de sa dépendance au charbon *via* l'intégration de processus photochimiques. Plus d'un siècle plus tard, l'Humanité tente toujours d'atteindre cet objectif, avec un incitatif très pressant qu'est le changement climatique ; l'étendue des travaux de recherche dans les domaines de la photophysique et de la photochimie en témoigne. Comme discuté dans la section précédente, la compréhension du fonctionnement du photosystème naturel est encore incomplète malgré de nombreuses avancées. Au-delà de la photosynthèse, l'idée d'utiliser l'énergie solaire pour conduire diverses réactions chimiques classiquement activées thermiquement a mené au développement de nombreuses méthodes synthétiques.[27-28] Le développement des connaissances et méthodes de caractérisations, notamment spectroscopiques, a également permis de mieux comprendre les interactions lumière-matière. Les premiers spectrophotomètres UV-visible commerciaux, par exemple, ne furent développés que dans les années 40.[29] L'idée d'une industrie photochimique capable de convertir, à l'instar de la Nature, les éléments nous entourant en carburants, mena au développement du domaine de la photosynthèse artificielle.

Lors du processus photosynthétique, le dioxyde de carbone et l'eau sont transformés en dioxygène et glucose. Ces composés sont cependant peu intéressants si l'on souhaite obtenir un carburant remplaçant le charbon. Or, on trouve dans la Nature des organismes utilisant les électrons extraits de l'eau pour produire du dihydrogène. Les électrons sont transférés à une

enzyme appelée hydrogénase, au lieu de la réductase présentée précédemment, qui comme son nom l'indique catalyse la formation de dihydrogène. Le dihydrogène représente une source d'énergie avantageuse. En effet, elle est potentiellement carbone neutre puisque sa combustion libère uniquement de l'eau et possède une densité massique unique, 3 à 7 fois plus élevée que les carburants fossiles (Figure I.8).[30]

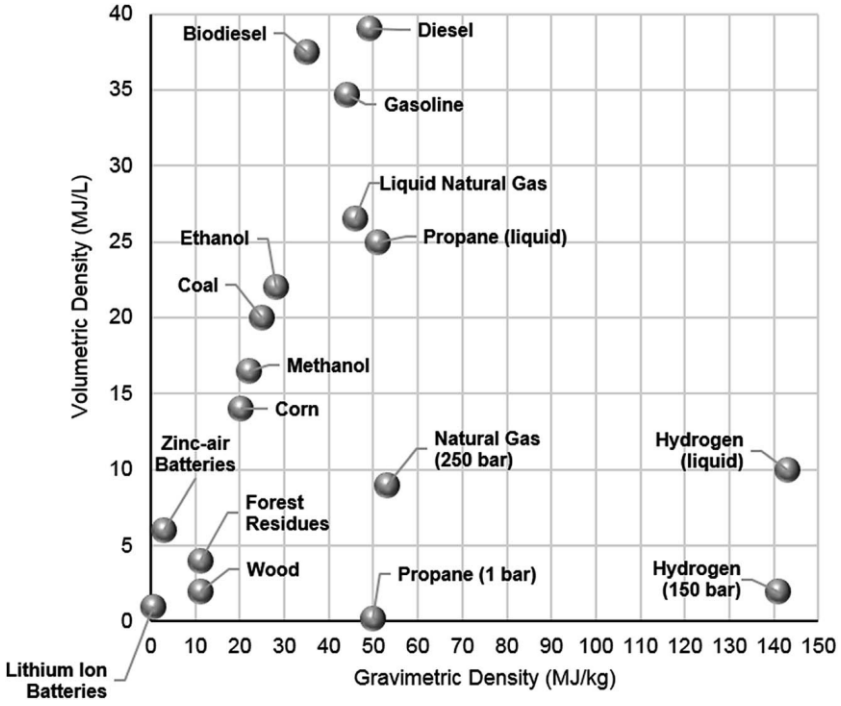

Figure I.8. Densité d'énergie par unité de poids ou de volumes pour différentes sources d'énergie. (Reproduit de C. Bozal-Ginesta and J. R. Durrant, *Faraday Discuss.*, 2019, 10.1039/c1039fd00076c. avec permission, Copyright 2019 The Royal Society of Chemistry)

Cependant, le dihydrogène est majoritairement produit par vaporeformage du gaz naturel, un procédé couteux car réalisé à hautes température et pression.[31] L'électrolyse de l'eau est une méthode alternative connue depuis bien longtemps, mais là encore coûteuse en raison des matériaux impliqués et des besoins en électricité pour réaliser cette réaction de façon efficace. En effet, au-delà des potentiels théoriques (Tableau I.1), il faut appliquer une tension supplémentaire (surtension) afin de dépasser les barrières d'activation des différentes réactions.

Tableau I.1. Potentiels thermodynamiques des réactions d'intérêt pour la photosynthèse artificielle (en V *vs.* ECS à pH 7)

Oxydation de l'eau et réduction de H^+		Réduction du CO_2	
Réaction	$E^{0\prime}$	Réaction	$E^{0\prime}$
$H_2O \rightarrow HO^{\bullet -} + H^+ + e^-$	2.15	$CO_2 + e^- \rightarrow CO_2^{\bullet -}$	-2.14
$2H_2O \rightarrow HOOH + 2H^+ + 2e^-$	1.13	$CO_2 + 2\,H^+ + 2e^- \rightarrow HCO_2H$	-0.85
$2H_2O \rightarrow HOO^{\bullet -} + 3H^+ + 3e^-$	1.02	$CO_2 + 2H^+ + 2e^- \rightarrow CO + H_2O$	-0.77
$2H_2O \rightarrow O_2 + 4H^+ + 4e^-$	0.58	$2CO_2 + 2H^+ + 2e^- \rightarrow H_2C_2O_4$	-0.73
		$CO_2 + 4H^+ + 4e^- \rightarrow HC(O)H + H_2O$	-0.72
$2H^+ + 2\,e^- \rightarrow H_2$	-0.65	$CO_2 + 6H^+ + 6e^- \rightarrow H_3COH + H_2O$	-0.62
		$CO_2 + 8H^+ + 8e^- \rightarrow CH_4 + H_2O$	-0.48

En 1967, Fujishima et Honda firent une découverte majeure, publiée en 1972 : le dioxyde de titane est capable, sous irradiation lumineuse, de conduire le craquage de l'eau de façon électrochimique lorsqu'il est couplé à une électrode de platine, et ce, à un plus faible voltage que dans les électrolyseurs classiques. La différence d'énergie provient de la lumière absorbée.[32] Depuis, la compréhension du mécanisme associé a fortement évolué et son champ d'application s'est largement étendu, notamment pour la dégradation de contaminants permettant la dépollution de l'air.[33] Cependant, le spectre d'absorption du TiO_2 est limité à l'UV, représentant moins de 10% de l'énergie disponible dans le spectre solaire. En quelques années, de multiples semiconducteurs furent considérés pour le remplacer ou le compléter.[34] En 1979, Fujishima et Honda démontrèrent que plusieurs de ces semiconducteurs sont également capables de réduire photo-électrochimiquement le dioxyde de carbone.[35] Nous ne discuterons pas plus en détails des avancées dans le domaine des semiconducteurs et autres matériaux pour la photocatalyse hétérogène car ceux-ci dépassent le cadre des travaux présentés dans cette thèse. Pour de plus amples informations, le lecteur peut se référer aux récentes revues de littérature.[36-37]

C'est le travail de Jean-Marie Lehn et Jean-Pierre Sauvage en 1977 qui propulsa le domaine du craquage de l'eau dans une nouvelle ère : celui de la photosynthèse artificielle moléculaire.[38-39]

S'appuyant sur les travaux émergents concernant les propriétés photophysiques du complexe de ruthénium tris(2,2'-bipyridine=bpy) $[Ru(bpy)_3]^{2+}$ (*vide infra*),[40] ils proposèrent un système catalytique moléculaire permettant la génération de dihydrogène en continu sous irradiation lumineuse. En 1979, Grätzel *et al.* proposèrent un système au fonctionnement similaire, bénéficiant notamment des propriétés d'absorption améliorée de $[Ru(bpy)_3]^{2+}$ pour activer le dioxyde de titane, puis étendent ce système en introduisant un second catalyseur attaché à la surface du semiconducteur.[41-43] Ces travaux furent vraisemblablement précurseurs au développement des cellules solaires à colorant, un dispositif de conversion de l'énergie solaire en électricité, par ce même groupe de recherche.[44-45]

Le diagramme général de la photosynthèse artificielle (Figure I.9) rappelle celui de la photosynthèse naturelle (Figure I.3). L'entité centrale est un assemblage de chromophores, appelée antenne collectrice, concentrant l'énergie collectée par transferts d'énergie jusqu'au photosensibilisateur final (P), à l'image de l'assemblage observé dans les photosystèmes naturels. Celui va alors réagir avec les médiateurs rédox afin de transférer les électrons générés par l'oxydation (Cat-Ox) vers le site de réduction (Cat-Red). Ce transfert d'électron(s) peut se faire directement avec les catalyseurs ou par l'intermédiaire de médiateurs rédox (D et A).

Les étapes clés du processus sont donc :

- L'absorption de l'énergie solaire sous forme de rayonnement électromagnétique par le photosensibilisateur et l'antenne collectrice, accompagnée de transferts d'énergie pour faire converger l'énergie vers P,
- Les transferts d'électrons entre les différentes unités, notamment entre le photosensibilisateur terminal P et les médiateurs rédox,
- Les réactions d'intérêt sont poly-électroniques et requièrent donc des catalyseurs capables de moduler leur état d'oxydation pour accommoder les électrons impliqués.

Dans la suite de cette section, nous détaillerons les différents mécanismes impliqués dans la cascade d'absorption de la lumière et de transferts d'énergie ou d'électron(s) nécessaires à la conversion de l'eau et du dioxyde de carbone. Nous discuterons également la structure et les

propriétés des composés moléculaires classiquement utilisés dans les photosystèmes catalytiques moléculaires.

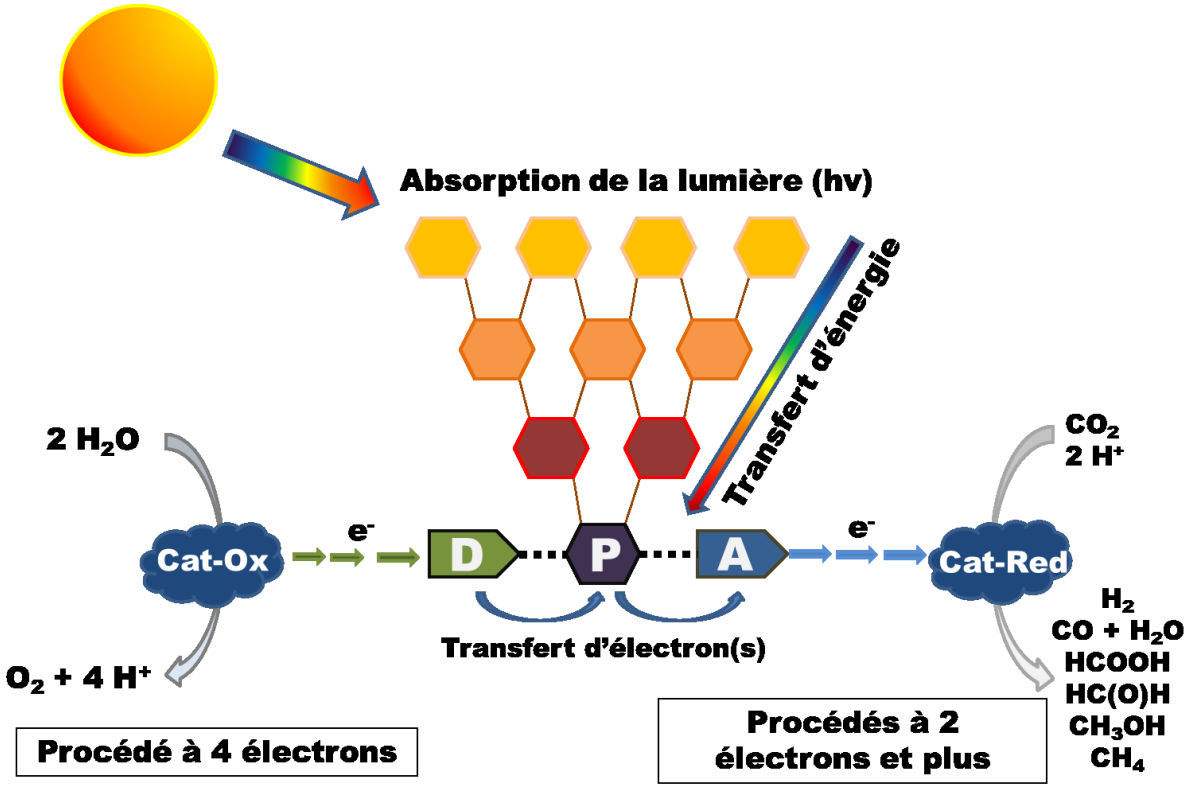

Cat-Ox : catalyseur pour l'oxydation de l'eau

P : photosensibilisateur

D : médiateur rédox donnant un électron au photosensibilisateur

A : médiateur rédox acceptant un électron du photosensibilisateur

Cat-Red : catalyseur pour la réduction des protons ou du dioxyde de carbone

I.3.1 Absorption de l'énergie lumineuse et transferts d'énergie

La lumière ultraviolette proche, visible et proche infra-rouge a une longueur d'onde comprise entre 200 et 1600 nm, soit une énergie de 0.8 à 6.2 eV soit 6500 à 50000 cm^{-1}. Celle-ci correspond aux écarts en énergie entre orbitales moléculaires occupées et vacantes. Ainsi la majorité des composés moléculaires connus absorbent dans cette région du spectre électromagnétique et l'absorption d'un photon permet la promotion d'un électron vers cette orbitale vacante. Comme présenté dans le diagramme de Jablonski (Figure I.10), la molécule à son état fondamental (ÉF) peut être excitée par absorption d'un photon de différentes énergies

(ici $h\nu_1$ et $h\nu_2$) et atteint alors les états excités ($ÉE_n$) correspondants.[46] L'état fondamental possède une multiplicité de spin dépendant de ses constituants. Les molécules organiques ont généralement un état fondamental singulet (n= 2(S+1) = 1) car elles ne possèdent normalement pas de spins non appariés (sauf radicaux). Les complexes de coordination peuvent avoir une plus grande variété de spin en raison de la présence d'électrons dans les orbitales d. Lorsque la molécule atteint son état excité de plus haute énergie ($ÉE_2$), elle peut se relaxer pour atteindre le niveau excité de plus basse énergie $ÉE_1$, par désactivation vibrationnelle notamment. On parle alors de conversion interne (CI). Elle peut ensuite retrouver son état fondamental par émission d'un photon ayant une énergie hν' quasi identique à celle nécessaire pour l'excitation, $h\nu_1$. On parle alors de fluorescence. Les temps caractéristiques de cette émission sont généralement de l'ordre des nano ou microsecondes pour les molécules organiques. Dans certains composés, un changement de spin de l'état excité peut avoir lieu. Il y a alors croisement inter-système (CIS). Les transitions $^{n}ÉF \rightarrow {}^{n+2}ÉE_x$ sont interdites par la règle de conservation du spin et n'apparaissent pas dans le spectre d'absorption de la molécule (sauf exception). Cela conduit à des états excités de plus longue durée de vie, généralement de l'ordre de la milliseconde ou même de la seconde. Les métaux de transition, en particulier ceux des deuxièmes et troisièmes rangées, favorisent le

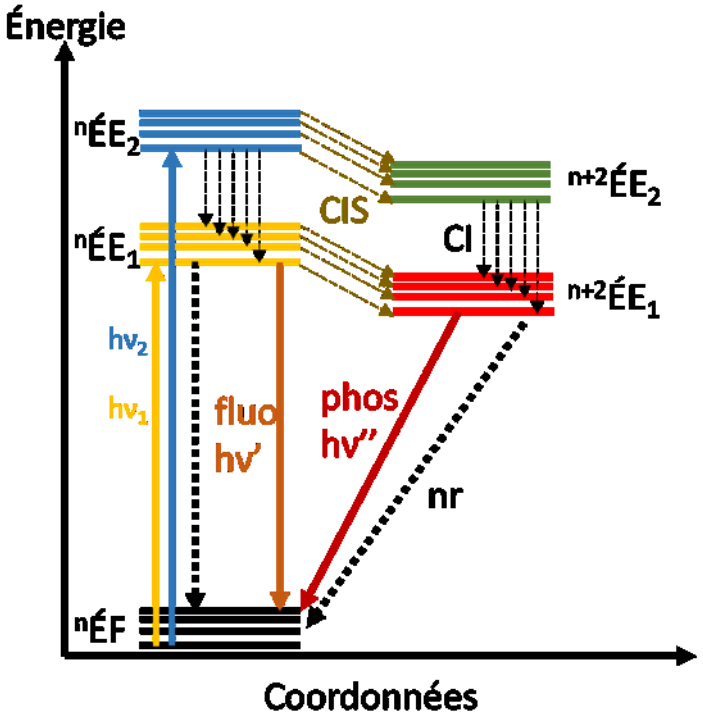

Figure 1.10. Diagramme de Jablonski

CIS (le rendement quantique pour le CIS est de 100% pour $[Ru(bpy)_3]^{2+}$) en raison de leur fort couplage spin-orbite. La désactivation radiative à partir du niveau excité $^{n+2}ÉE_1$ se fait à une énergie $hν_2$ plus faible que la longueur d'excitation ou de fluorescence (si elle existe). Dans tous les cas, il peut également y avoir désactivation par voie non-radiative, liée à des modes de vibrations du composé ou des collisions avec le solvant ou une autre molécule. Concernant les temps de vie indiqués ici, on notera que les complexes de métaux de transition présentent classiquement des temps de vie amoindris, dans l'ordre de la nano ou la microseconde pour de la phosphorescence.[47]

Le transfert de l'énergie absorbée par une molécule vers une molécule à l'état fondamental est d'intérêt dans le contexte de la collection de l'énergie solaire. Ce transfert d'énergie se fait selon deux mécanismes (Figure I.11), appelés transfert de type Förster ou résonnant[48] et transfert de type Dexter ou d'échange[49]. Le mécanisme Förster est un transfert d'énergie à longue distance basé sur les interactions dipôle-dipôle, menant à une dépendance de la constante de vitesse inverse à la distance à la puissance 6 ($\alpha\ 1/r^6$) et un caractère directionnel du transfert. Il est favorisé lorsque la gamme d'énergie absorbée par l'accepteur se superpose à celle de l'émission du donneur. À l'inverse, le mécanisme Dexter est un mécanisme au-travers de liaison(s) ; un recouvrement orbital, via un groupement pontant parfois, est nécessaire. Cela conduit à une décroissance exponentielle de la constante de vitesse de transfert ($\alpha\ e^{-r}$). On le considère parfois comme correspondant à un transfert simultané de deux électrons. Par ailleurs, la règle de

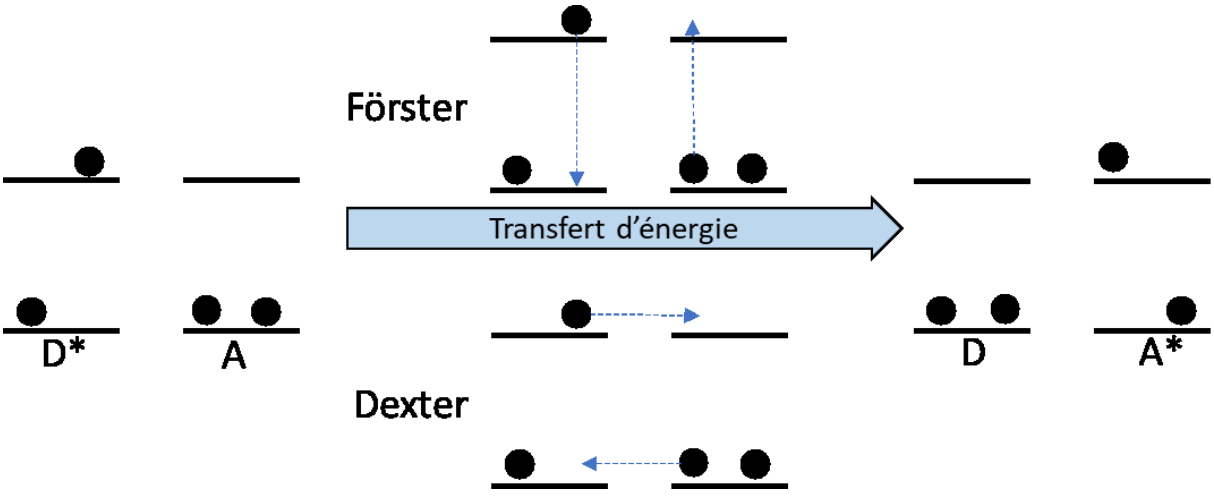

Figure I.11. Schéma du transfert d'énergie entre deux molécules via différents mécanismes.

conservation du spin implique que si le donneur est à un état excité triplet, l'accepteur aura également un état triplet après transfert.

I.3.2 Transferts d'électron

Après collection de l'énergie solaire, le système photocatalytique effectue de nombreux transferts d'électrons entre ses différents constituants afin de déplacer les électrons de l'oxydation de l'eau vers la réduction de protons ou du dioxyde de carbone. L'étude des transferts d'électrons, en particulier en chimie de coordination, fut l'objet de deux prix Nobel décernés à des chercheurs canadiens (1983, Henry Taube[50] et 1992, Rudolph A. Marcus[51]). Le transfert d'électron entre deux espèces peut se faire selon un mécanisme de sphère interne, impliquant l'existence d'un lien entre les deux centres rédox au moins au cours du transfert, ou de sphère externe, les deux composés devant se trouver physiquement proches; on parle d'un complexe de rencontre, induisant une barrière d'activation liée aux répulsions s'opposant à ce rapprochement. La théorie de Marcus permet d'exprimer la constante de vitesse de transfert électronique comme une fonction de cette barrière d'activation. Celle-ci est alors :

$$k_i = \nu \exp(^{-\Delta G^{\ddagger}}/_{RT}) \quad \text{avec} \quad \nu = \frac{2H_{AB}^2}{h}\sqrt{^{\pi^3}/_{\lambda RT}} \quad \text{et } \Delta G^{\ddagger} = \frac{(\lambda+\Delta G^0)^2}{4\lambda}$$

où H_{AB} est le recouvrement entre les fonctions d'ondes du donneur et de l'accepteur, $\Delta G^{\ddagger}$ est l'énergie libre d'activation, dépendant de l'énergie libre de la réaction ΔG^0 et de λ, l'énergie de réorganisation prenant en compte la réorganisation liée aux variations de distances et angles dans les partenaires de réactions et la réorientation du solvant. Cela conduit à la définition de trois zones : la zone normale où la constante de vitesse augmente avec une augmentation de la force motrice, une zone sans activation et une zone inverse où la constante de vitesse diminue avec l'augmentation de la force motrice.[52]

I.3.3 Potentiels d'oxydo-réduction et états excités

L'absorption de lumière par les unités collectrices dans les plantes ou par les photosensibilisateurs permet de conduire des réactions rédox non accessibles ($\Delta G > 0$) en passant par l'état excité. Afin d'illustrer ce phénomène, nous utiliserons l'exemple de $[Ru(bpy)_3]^{2+}$, introduit précédemment comme l'archétype du photosensibilisateur.[53] Son

diagramme d'orbitales moléculaires simplifié, pour l'état fondamental et l'état excité, est présenté Fig I.12. En utilisant un diagramme de Latimer (Figure I.13), il est possible de calculer les potentiels à l'état excité en connaissant l'énergie de l'état excité, estimée à partir de la longueur d'onde d'émission du complexe, le complexe émettant à 585 nm soit une énergie de 2.12 eV lorsqu'il est excité dans sa transition de transfert de charge du métal vers le ligand.

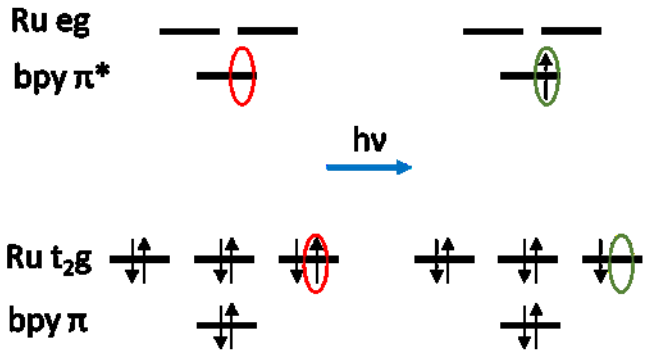

Figure I.12. Diagramme orbitalaire simplifié de $[Ru(bpy)_3]^{2+}$ (gauche) et $\{[Ru(bpy)_3]^{2+}\}^*$ (droite).

Les valeurs ainsi obtenues démontrent que l'état excité du complexe est un meilleur oxydant et un meilleur réducteur que l'état fondamental. Ainsi, l'énergie solaire collectée permet d'activer le photosensibilisateur de sorte qu'il puisse accomplir des réactions inaccessibles dans son état fondamental. Pour que ce changement de réactivité soit utilisable, il faut cependant que l'état excité ait une durée de vie suffisante pour permettre à la réaction d'avoir lieu. Par ailleurs, en modulant la structure du composé, il est possible de concevoir des photosensibilisateurs plus oxydants ou plus réducteurs, selon les cibles envisagées.

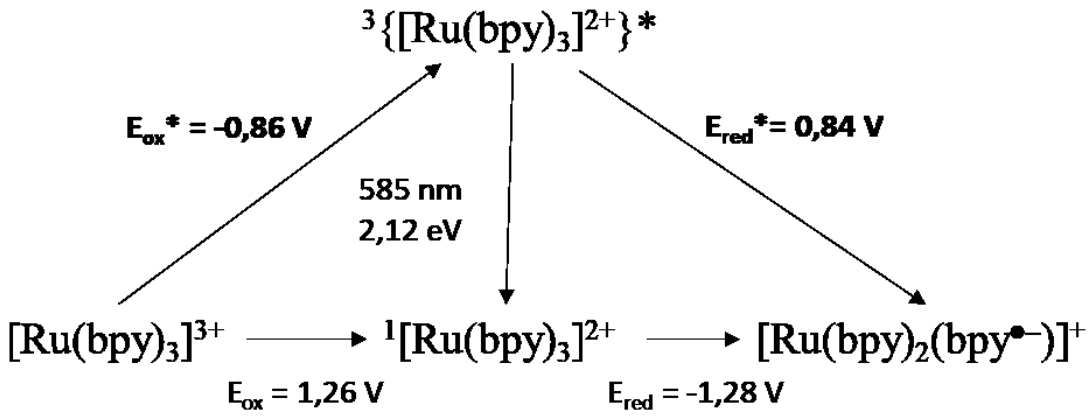

Figure I.13. Diagramme de Latimer pour $[Ru(bpy)_3]^{2+}$

$E_{ox}^* = E_{ox} - E_{h\nu} = -0,86$ V $E_{red}^* = E_{red} + E_{h\nu} = 0,84$ V

I.3.4 Photosensibilisateurs pour la photosynthèse artificielle

Dans leur étude initiale, Lehn et Sauvage avaient recours à $[Ru(bpy)_3]^{2+}$,[38-39] un photosensibilisateur aujourd'hui devenu composé de référence, notamment en photophysique (rendement quantique de référence 9.4% dans l'acétonitrile dégazé pour le sel d'hexafluorophosphate).[54] Le nombre de dérivés de ces complexes, 40 ans après le travail séminal de Lehn et Sauvage, est gigantesque. D'autres métaux sont également étudiés, notamment l'iridium (III)[55] et le rhenium (I)[56], ayant la même configuration électronique d^6 (Figure I.14).[57] Ces photosensibilisateurs sont principalement basés sur des ligands de type polypyridines.

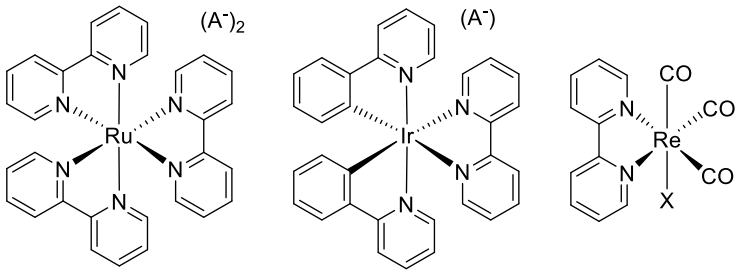

Figure I.14. Complexes de coordination utilisés comme photosensibilisateur, basés sur des métaux d^6 et des ligands polypyridines (A^- est un anion).

Dans la section précédente, le diagramme orbitalaire simplifié d'un complexe de Ru(II) était présenté (Figure I.12). Celui-ci permet d'apprécier les différentes possibilités de modulation des propriétés électroniques et photophysiques du complexe en variant la nature du ligand. L'orbitale vacante de plus basse énergie (LUMO pour *lowest unoccupied molecular orbital*) est une orbitale π anti-liante centrée sur les ligands, aussi une variation de la densité électronique du ligand permet de moduler l'énergie de cette orbitale et donc le potentiel de réduction ainsi que les longueurs d'onde d'absorption et d'émission. Ces modifications auront cependant également un effet sur l'orbitale occupée de plus haute énergie (HOMO pour *highest occupied molecular orbital*), celle-ci ayant un caractère π liant lié au recouvrement orbitalaire avec les niveaux π vacant du ligand.

L'utilisation d'Ir(III) et de Re(I) fut motivée par l'observation de la photodégradation des complexes tris(bidentés) de Ru(II). Ils peuvent en effet perdre un ligand sous irradiation.[53] Les composés d'Ir(III) possèdent par ailleurs de meilleures propriétés photophysiques (rendement

quantique, temps de vie améliorés) mais en contrepartie, leur absorption est un peu moins étendue dans le visible.[58] Les composés de Re(I) sont eux assez marginaux comme photosensibilisateur, leur absorption étant également peu étendue dans le visible. Ils sont en revanche activement étudiés du fait de leur capacité à réduire sélectivement le CO_2 (*vide infra*).[59] D'autres métaux ont également été considérés, mais demeurent marginaux.[57] On retrouve également des chromophores organiques comme l'éosine, ainsi que des chromophores inspirés de la Nature et discutés plus haut : les métalloporphyrines et leurs nombreux dérivés.[60]

Quel que soit le photosensibilisateur utilisé, celui-ci joue toujours le même rôle : transférer les électrons entre les deux catalyseurs. Cela se fait par réaction de l'état excité du chromophore avec les médiateurs rédox.

I.3.5 Piégeage oxydatif ou réductif - donneurs et accepteurs sacrificiels

Dans les premières études de craquage de l'eau par un système moléculaire, Lehn *et al.* ainsi que Grätzel *et al.* utilisaient un médiateur rédox susceptible d'être réduit par le chromophore par piégeage oxydatif pour ensuite transporter les électrons vers le catalyseur de réduction : un complexe de rhodium Rh(III) ($[Rh(bpy)_3]^{3+}$) dans le cas de Lehn[38] et le paraquat dans le cas de Grätzel.[41] Comme mentionné précédemment, à l'état excité, le photosensibilisateur devient à la fois plus facile à oxyder et à réduire. Il peut alors prendre part à deux procédés conceptuellement identiques : le piégeage réductif ou oxydatif (Figure I.15).

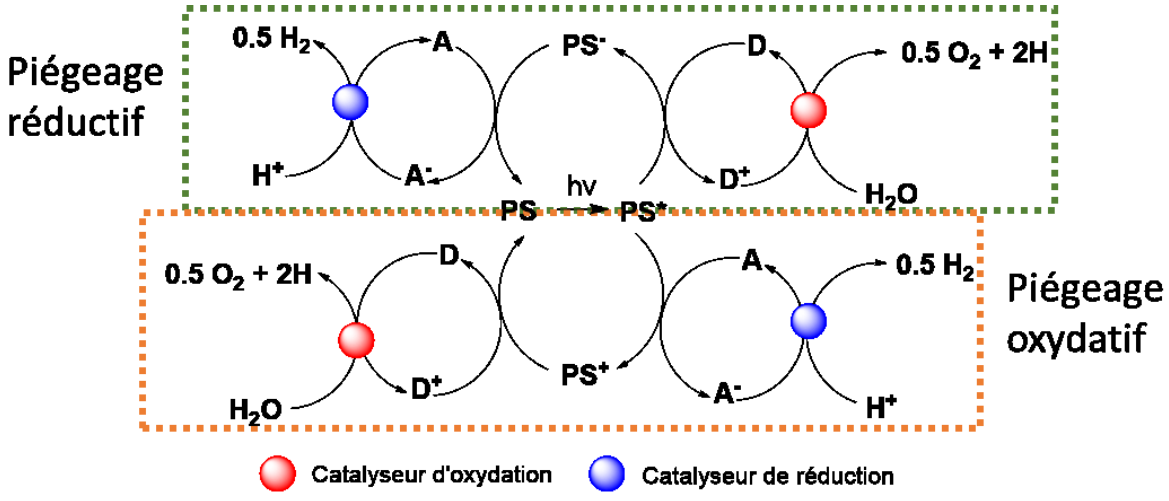

Figure I.15. Schéma des piégeages oxydatif et réductif pour le craquage de l'eau.

Le bilan de la réaction est identique dans les deux cas et le donneur (D) et l'accepteur (A) réagissent avec le photosensibilisateur (PS) pour modifier son état d'oxydation puis le régénérer. Ils sont à leur tour régénérés lorsqu'ils réagissent avec le catalyseur correspondant.

Cependant, au cours de leur étude complémentaire, Sauvage *et al.* ont réalisés que le complexe de Rh(III) pouvait lui-même agir comme catalyseur, supprimant la nécessité d'avoir un accepteur d'électron intermédiaire.[39] Ils introduisirent également une amine tertiaire comme donneur sacrificiel d'électrons pour remplacer la réaction d'oxydation de l'eau. L'utilisation de donneurs ou accepteurs sacrificiels devint rapidement pratique courante, car cette approche, bien que s'éloignant de l'application souhaitée, permet d'étudier plus facilement la demi-équation d'intérêt. En effet, l'oxydation de l'eau est notoirement plus lente que sa réduction, ce qui rend difficile l'étude de la cinétique de réduction prenant place en parallèle. Par ailleurs, la nécessité d'extraire 4 électrons pour l'oxydation de l'eau alors que 2 électrons suffisent pour promouvoir la formation de dihydrogène ou la réduction du CO_2 en CO font que pour un cycle catalytique d'oxydation, deux cycles de réduction prennent place.

À ce jour, les amines tertiaires demeurent majoritairement utilisées comme donneurs sacrificiels en milieu organique, principalement la triéhylamine et la triéthanolamine, tandis qu'en milieux aqueux, on retrouve principalement l'acide ascorbique ou l'acide éthylènediaminetétraacétique (EDTA).[61] Le nitrate d'ammonium et de cérium $(NH_4)_2Ce(NO_3)_6$ et l'anion peroxodisulfate $S_2O_8^{2-}$ sont quant à eux des accepteurs sacrificiels courants dans l'étude de l'oxydation de l'eau.

Un point important est à noter ici. Chaque cycle de piégeage ne permet de transférer qu'un seul électron. Aussi pour que la réaction indiquée pour le catalyseur d'oxydation sur la Figure I.15 ait lieu, il faut actuellement deux cycles du couple photosensibilisateur – donneur, soit deux photons. Cela impose une contrainte pour le choix d'espèce capable d'agir comme catalyseur : ces composés doivent être capables d'accommoder plusieurs électrons de façon stable et sur une étroite gamme de potentiels pour favoriser la réaction. Ce prérequis est facilement accessible par l'utilisation de métaux de transition comme centre actif, ces derniers pouvant exister à divers états d'oxydation, stabilisés par les ligands constituant leur sphère de coordination.

I.3.6 Catalyseurs pour l'oxydation de l'eau

Bien que non considérée dans le cadre de ce travail de recherche, la quête pour l'obtention de catalyseurs moléculaires efficaces pour l'oxydation de l'eau reste malheureusement sans réponse évidente. L'oxydation de l'eau est vue comme le col d'étranglement de la photosynthèse artificielle.[60,62-63] Le premier catalyseur rapporté est le 'dimère bleu' de T.J. Meyer, un complexe dinucléaire de Ru(III) équipé de ligand bpy et possédant un ligand oxo O^{2-} pontant (Figure I.16).[64] De nombreux dérivés de ce composé ont été développés, menant à une amélioration progressive des propriétés. On retrouve également des complexes d'iridium, de manganèse, de cobalt ou de fer.[63,65] Une famille d'intérêt dans le cadre de cette thèse est celle des complexes de type sandwich où un cœur tetra-nucléaire de ruthénium ou de cobalt est stabilisé par deux polyoxométallates vacants.[66] Les polyoxométallates sont une famille d'oxydes moléculaires aux propriétés fascinantes, robustes et facilement réductibles.[67] Nous reviendrons à ces composés plus loin dans la thèse.

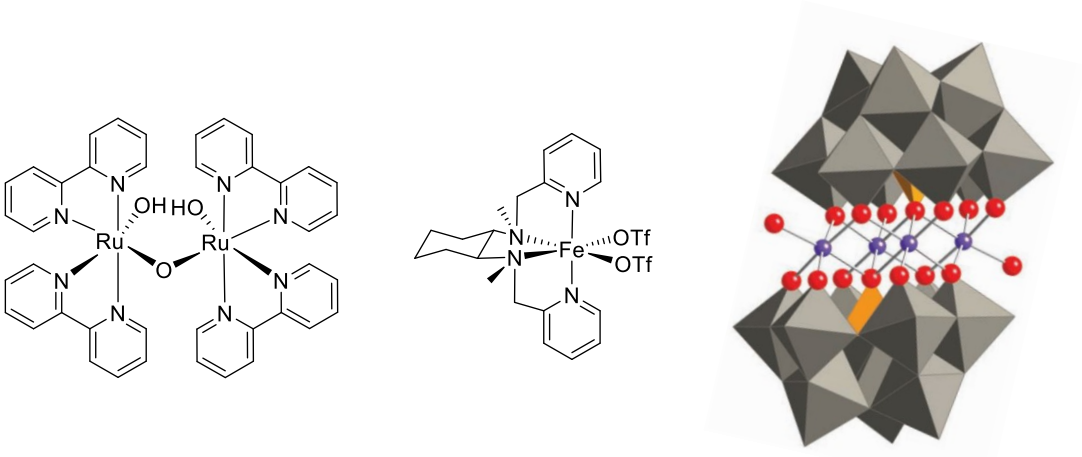

Figure I.16. Exemples choisis de catalyseurs pour l'oxydation de l'eau.

Du point de vue du design moléculaire, ces composés nécessitent la présence de sites de coordination accessibles pour une molécule d'eau, combinés à un ligand polydenté robuste. On retrouve de nombreux composés multi-métalliques, ceux-ci favorisant la formation de la liaison O-O par mécanisme concerté. Ces composés sont également pertinents pour des études fondamentales de la cinétique des transferts d'électrons en raison de l'importance du couplage entre transfert électronique et transfert de proton.[68-69] Enfin, les protons relâchés causent une diminution majeure du pH localement, avant de diffuser vers le catalyseur de réduction.

I.3.7 Catalyseurs pour la production d'hydrogène

Le platine métallique est connu depuis le début du XX^{ème} siècle comme étant capable d'agir comme catalyseur pour la réduction des protons en dihydrogène.[39] Bien qu'efficace, il demeure dispendieux et ne permet pas de modification afin d'optimiser le système catalytique. Aussi en 1983, Lehn *et al.* remplacèrent les particules colloïdales de Pt par un complexe de coordination de cobalt appartenant à la famille des cobaloximes (Figure I.17).[70-71] Ces complexes sont encore aujourd'hui considérés comme catalyseurs de référence, malgré leur inhérente instabilité. Ils sont en effet utilisés par défaut avec un excès de ligands pour remplacer les ligands se dégradant au cours de la réaction.[72] De nombreux autres complexes de cobalt, principalement basés sur des ligands de la famille des polypyridines, ont été rapportés ces dix dernières années, avec une stabilité accrue dans les conditions catalytiques. On retrouve également des complexes de nickel, de fer ou de molybdène.[73-75] Les composés de fer sont principalement des dimères avec un ligand dithiolate pontant, préparés dans l'esprit de l'approche biomimétique car ils correspondent au centre actif de certaines hydrogénases.[76]

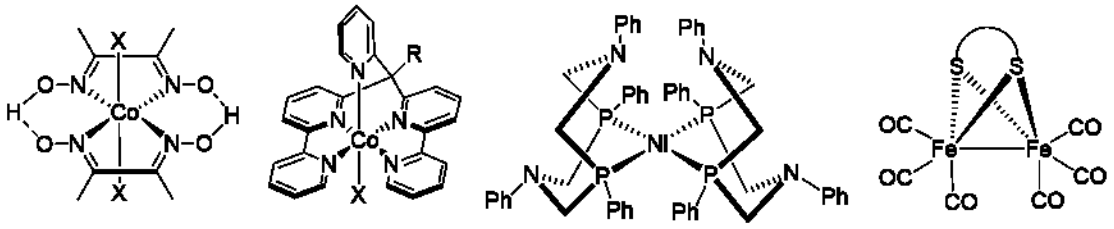

Figure I.17. Exemples choisis de catalyseurs pour la production de dihydrogène.

Bien que l'application soit différente, on retrouve des critères de design communs avec les catalyseurs d'oxydation de l'eau. Un site de coordination accessible est nécessaire pour la formation cette fois d'un hydrure métallique. La présence de sites basiques pouvant servir de relai pour l'approche d'un second proton est également bénéfique. Dans certains cas, il n'est pas clair si la seconde réduction implique le centre métallique seul ou possède également une contribution du ligand, la plupart des ligands utilisés appartenant à la famille étendue des ligands dit 'non-innocents'.[73,77]

I.3.8 Catalyseurs pour la réduction du CO_2

Tout comme Honda *et al.* avaient rapidement appliqué leur système photocatalytique pour la production de dihydrogène à la réduction du dioxyde de carbone, Lehn *et al.* ont publié en 1982 qu'un système basé sur $[Ru(bpy)_3]^{2+}$, triethanolamine et $CoCl_2$, en présence de quantités variables de 2,2'-bipyridine, est capable de générer du monoxyde de carbone et du dihydrogène sous irradiation lumineuse.[78] Ce résultat pointe vers le défi majeur de la réduction du CO_2 : la sélectivité. Comme présenté dans le Tableau I.1, une large gamme de produits de réduction est accessible dans une étroite gamme de potentiel [-0.85 ; -0.48] V *vs* ECS, comprenant le potentiel de réduction des protons (-0.65 V vs ECS à pH 7).

C'est face à ce défi que le complexe de Re(I) introduit précédemment comme photosensibilisateur, $[Re(bpy)(CO)_3X]$ (où X est un halogénure), joue un rôle important. En effet, en 1983, Lehn et al. démontrèrent que, combiné à $[Ru(bpy)_3]^{2+}$ et en présence de triéthanolamine, ce complexe catalyse la réduction sélective de CO_2 en CO.[79] De plus, ce complexe est véritablement un photocatalyseur puisqu'il est capable d'assumer à la fois le rôle de photosensibilisateur et celui de catalyseur.[80] Depuis, d'autres catalyseurs ont été rapportés, plusieurs ayant été dans un premier temps rapportés comme électrocatalyseurs (Figure I.18).

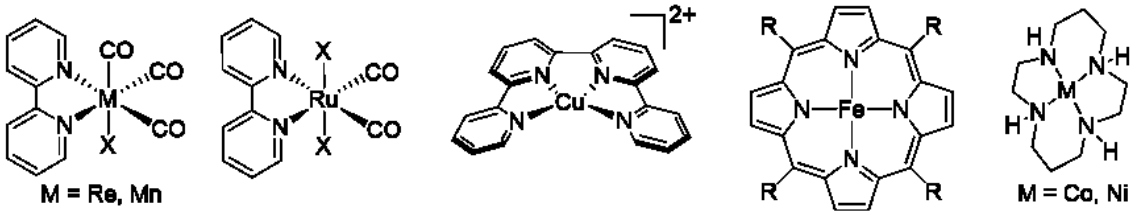

Figure I.18. Exemples choisis de catalyseurs pour la réduction photocatalytique du CO_2.

Les complexes de manganèse Mn(I) dérivés du complexe de Re(I) initialement rapporté sont également actifs en photoréduction, avec cependant une sélectivité inférieure.[81] Divers complexes polypyridines de ruthenium, d'iridium, de cuivre ou de cobalt notamment ont été rapportés.[82-83] Les macrocycles de cobalt et de nickel ont également été étudiés, dérivés du motif cyclam.[84] Enfin, les porphyrines de fer sont également intensément étudiées. Leur étude démontra la possibilité de modifier la sélectivité de conversion en modifiant le pouvoir réducteur du photosensibilisateur. En effet, en utilisant $[Ir(ppy)_3]$ comme photosensibilisateur, Robert *et*

al. sont parvenus à convertir le CO_2 en méthane alors que le même catalyseur en présence de $[Ru(bpy)_3]^{2+}$ donne uniquement du CO.[85]

En raison de la variété de produits accessibles, une attention particulière est accordée aux mécanismes de réactions. Les mécanismes d'actions des catalyseurs de Re(I) et de Ru(II) ont été activement explorés et l'identification du mécanisme pour d'autres catalyseurs est un champ d'étude actif.[86] Bien que de nombreux catalyseurs ont été développés lors de la récente décennie, c'est principalement par le développement de composés supramoléculaires combinant photosensibilisateur et catalyseur que la réduction du dioxyde de carbone a progressé.

I.3.9 Systèmes supramoléculaires

Comme démontré dans les sections précédentes, les chercheurs du domaine de la photosynthèse artificielle moléculaire disposent d'une large gamme de composés pour constituer des photosystèmes catalytiques ayant différentes cibles ou fonctionnant dans différentes conditions.[87] Cette librairie de composés s'est vastement enrichie, et ce à un rythme soutenu au cours de la dernière décennie après une période de dormance, comme le montre la Figure I.19.[30]

Figure I.19. Évolution du nombre de publications ayant comme sujet central la photosynthèse artificielle publiées par année depuis 1970. (Reproduit, avec permission, de C. Bozal-Ginesta and J. R. Durrant, *Faraday Discuss.*, 2019, 10.1039/c1039fd00076c, Copyright 2019 The Royal Society of Chemistry)

Au-delà du développement de composés, c'est leur utilisation synergique qui contrôle l'efficacité des systèmes photocatalytiques. Aussi, afin d'optimiser les transferts d'énergie ou d'électron, de nombreux travaux de recherches se sont attachés à préparer des entités supramoléculaires, combinant les différents rôles au sein d'une 'supermolécule' dont les propriétés finales dépassent la somme des propriétés individuelles de chaque unité constitutive. Le contrôle des interactions entre sous-unités et de leur organisation dans l'espace est pré-programmable par le design soigné de ces sous-unités.[88] Les exemples suivants sont choisis parmi ceux rapportés dans la littérature pour illustrer les différentes approches existantes.

Une illustration des stratégies de synthèse pour la construction d'antennes collectrices est fournie par le travail de Balzani *et coll.* en 1992. Ces auteurs ont préparé le composé présenté dans la Figure I.20 en s'appuyant sur la complémentarité entre les différentes unités, dans une approche de 'complexe utilisé comme ligand'.[89] En contrôlant l'accessibilité du site de coordination, ils purent contrôler la croissance excentrique de cet assemblage dendrimérique contenant 22 centres métalliques capables d'absorber le rayonnement solaire.

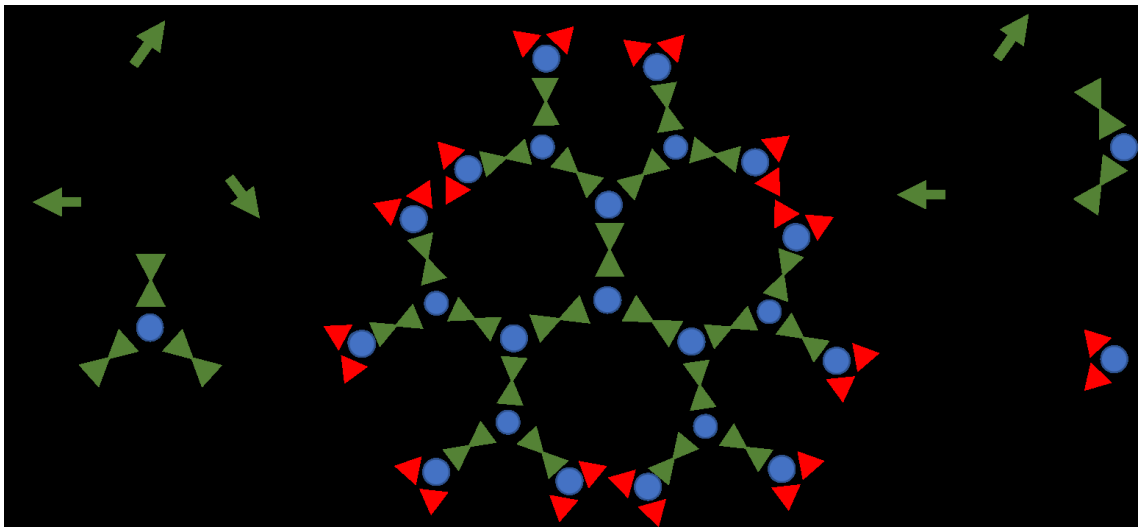

Figure I.20. Schéma de l'assemblage dendrimérique de 22 complexes de Ru(II) comme antenne collectrice préparé par Balzani. *et coll.*

De nombreux autres complexes polynucléaires de Ru(II) ont par la suite été rapportés, bénéficiant notamment de la communication entre chromophores pour abaisser l'énergie de la LUMO afin d'absorber dans le domaine du visible et du proche infra-rouge.[90-91] On trouve

également des exemples de systèmes polynucléaires de Re(I) cycliques développés par Ishitani *et al.* (Figure I.21), bénéficiant d'une stabilité accrue sous conditions photocatalytiques lorsqu'ils sont utilisés comme photosensibilisateur pour la réduction du dioxyde de carbone.[92]

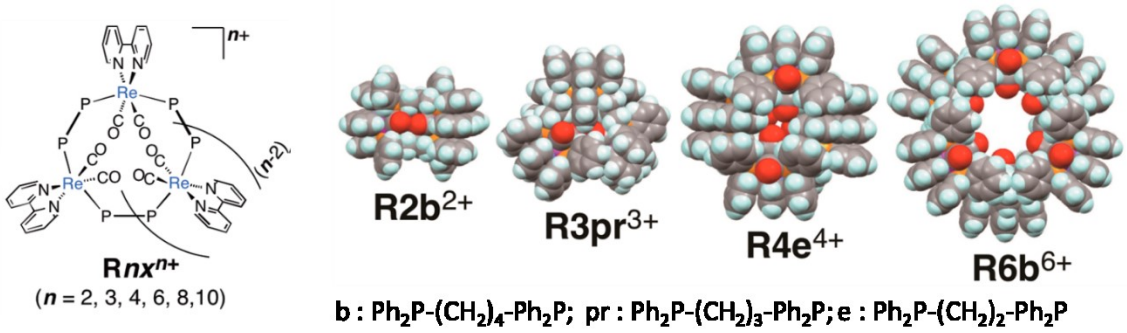

Figure I.21. Structures de photosensibilisateurs de Re(I) cycliques. (Adapté, avec permission, de O. Ishitani *et al.*, *J. Am. Chem. Soc.*, 2013, **135**, 13266-13269. Copyright 2013 American Chemical Society)

Au-delà des chromophores polynucléaires, de multiples dyades combinant chromophores et catalyseurs ont été rapportés.[93] La Figure I.22 contient différents exemples pertinents pour la réduction des protons (gauche),[94-95] l'oxydation de l'eau (haut, droite)[96] et la réduction du CO_2 (bas, droite).[97]

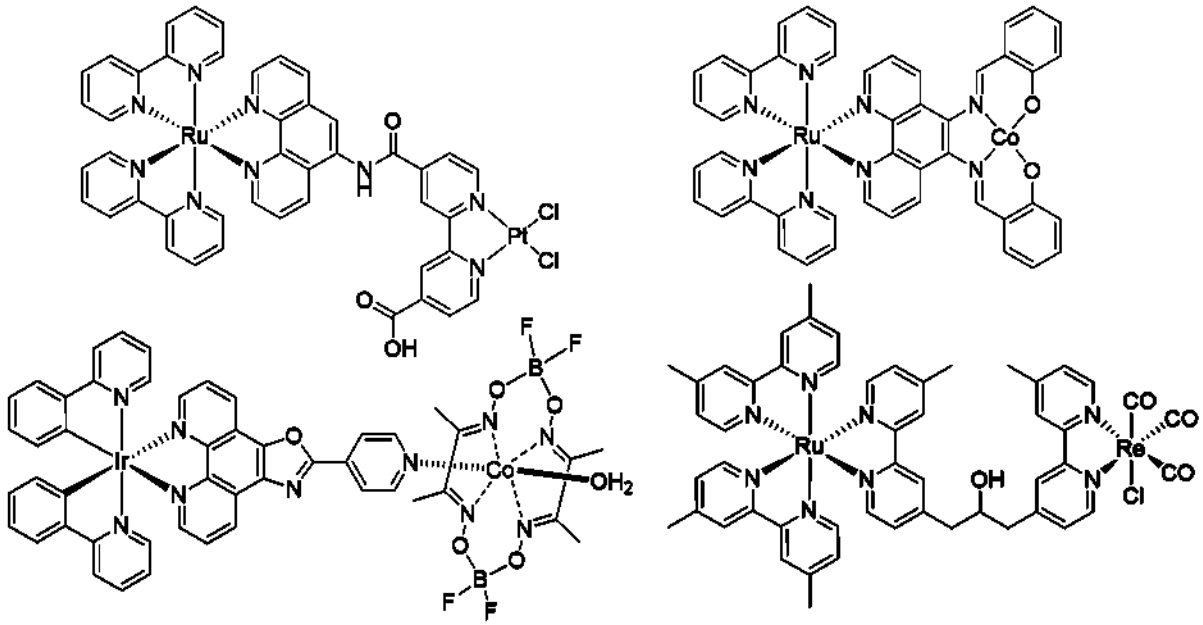

Figure I.22. Exemples choisis de dyades pour la photosynthèse artificielle.

Cette approche d'attache covalente ou par lien de coordination entre catalyseur et chromophore permet généralement d'obtenir de meilleures performances catalytiques que le système bimoléculaire correspondant. Cependant, l'ajustement fin des niveaux d'énergie de chaque unité est important et rend cette stratégie parfois infructueuse, comme dans le cas de la dyade Ru-Co Figure I.22 en haut à droite, qui au lieu d'extraire les électrons du cobalt, censé être le site d'oxydation de l'eau, présente un piégeage oxydatif du chromophore par le centre Co. Les constantes de vitesse des transferts d'électron dans ces systèmes sont fortement augmentées du fait de la proximité dans l'espace, mais cette accélération affecte le transfert dans les deux directions. Cela s'avère bénéfique à condition que l'espèce catalytique soit très efficace, afin que la constante de vitesse du transfert électronique en retour soit plus faible que la constante de vitesse de la réaction étudiée.

Enfin, afin de répondre à la problématique de combiner réactions multiélectroniques et transfert monoélectronique depuis l'état excité du chromophore, de nombreuses études s'attachent à modifier les ligands afin d'introduire des sites pouvant servir de réservoirs d'électrons.[98-99] Dans cette optique, l'approche proposée par Sakai *et al.* parait prometteuse (Figure I.23).[100] En effet, chaque paraquat peut stocker jusqu'à deux électrons en périphérie du chromophore, attendant d'être transféré au catalyseur de réduction des protons.

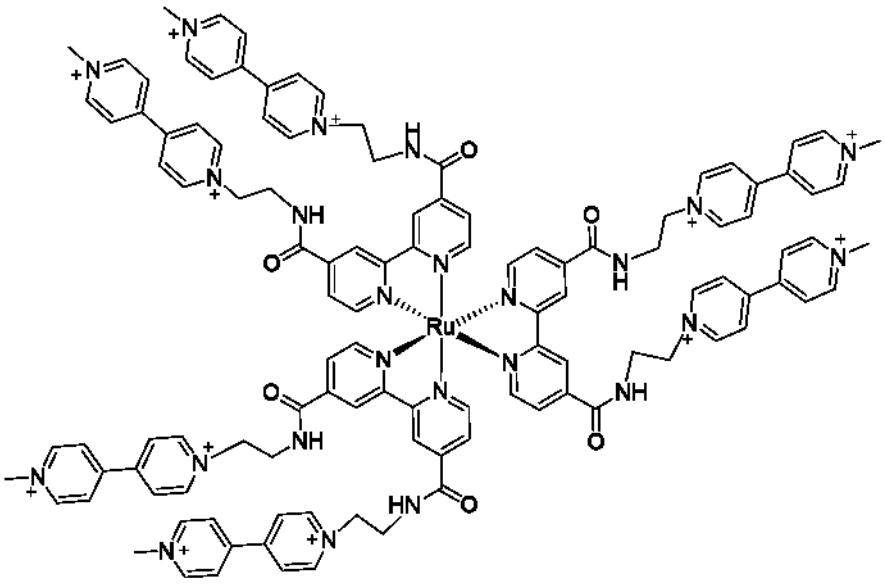

Figure I.23 Photosensibilisateur de Ru(II) équipé de multiples accepteurs d'électrons préparés par Sakai *et al.*

I.4 Objectifs de la thèse

Les sections précédentes ont permis d'introduire les concepts clés pour l'étude de systèmes photocatalytiques pour la photosynthèse artificielle moléculaire, ainsi que les enjeux et outils de design accessibles pour y répondre. Les efforts de recherche dans le domaine permettent à la fois des avancées dans la connaissance des mécanismes fondamentaux sous-jacents mais également vers le développement de systèmes potentiellement applicables pour répondre aux enjeux de société actuels. De nombreux défis demeurent néanmoins avant de pouvoir transférer ces technologies émergentes à l'échelle industrielle / commerciale. Le principal problème des systèmes moléculaires réside probablement dans leur pauvre stabilité à long terme. Comparés au photosystème naturel, les composés synthétiques présentent de meilleures performances en termes d'activité mais conservent une stabilité similaire. Pour rappel, le photosystème I survit de 1 à 11 heures, contre 30 à 75 heures pour le photosystème II.

Dans le cadre de cette thèse, nous nous sommes attachés à exploiter dans un premier temps l'expertise en chimie des polypyridines du groupe Hanan pour valoriser des composés auparavant inactifs (Chapitre II) et développer les connaissances concernant la chimie de coordination des composés de Re(I) (Chapitre III et Chapitre IV). Ainsi, les chapitres II, III et IV illustrent les possibilités offertes par le design moléculaire, que ce soit la synthèse de nouveaux ligands ou l'ajustement de la sphère de coordination, pour moduler les propriétés de photosensibilisateurs organométalliques d'intérêt pour la photosynthèse artificielle.

Chapitre II Le design de complexes bis(terpyridines) de Ru(II) portant des ligands de densité électronique opposée - l'un des ligands étant équipé d'un donneur interne d'électron, l'autre étant électro-déficient et portant des sites de coordinations périphériques pour le catalyseur - est mis en application pour la préparation de nouveaux complexes capables de conduire l'évolution photocatalytique de dihydrogène avec un taux de production stable sur plusieurs jours.

Chapitre III Des complexes de Re(I) basés sur une famille de ligands comportant des fragments guanidyles bicycliques (i.e. hpp pour hexahydro-pyrimidopyrimidine) ont été préparés et analysés via une combinaison de techniques spectroscopiques, diffraction des rayons sur monocristaux et modélisés par DFT/TD-DFT. L'impact de l'introduction d'un groupe

coordonnant fortement donneur est ainsi discuté et l'analyse des données spectroscopiques démontrent que les propriétés des complexes sont fortement influencées par celles des ligands.

Chapitre IV Cette étude illustre la versatilité des ligands polydentés. Une série de complexes de Re(I) portant des ligands 2,2';6',2''-terpyridine est caractérisée. Dans ces composés, la terpyridine est coordonnée par deux ou trois de ses pyridines selon les conditions synthétiques employées. Les changements de propriétés induits par ces variations de mode de coordination sont étudiés par une combinaison de spectroscopies, électrochimie et modèle théorique.

Avec pour objectif d'améliorer la stabilité à long terme d'un photocatalyseur connu, nous nous sommes ensuite intéressés à la combinaison de complexes de Re(I) et de polyoxométallates. Ainsi, le **Chapitre V**, présentant brièvement la chimie des polyoxométallates (POMs) et la place particulière que ces composés inorganiques aux propriétés fascinantes occupent dans le domaine de la photosynthèse artificielle, permet d'introduire les dyades hybrides étudiées par une combinaison de techniques de caractérisations aux chapitres VI et VII.

Chapitre VI La synthèse optimisée de dyades covalentes basées sur un POM de type Dawson fonctionnalisé par des ligands polypyridines et leur utilisation comme ligand pour la préparation de complexes de Re(I). Les propriétés électroniques et photophysiques des dyads sont présentées, indiquant l'existence d'un piégeage oxydatif de l'état excité des complexes de Re(I) par le polyoxométallate dont l'efficacité est améliorée suite au greffage.

Chapitre VII La série de composés décrite au chapitre VI est étendue et le phénomène de piégeage oxydatif analysé plus en profondeur, notamment par spectroscopie d'absorption transitoire. La possibilité de recruter ce transfert d'électron afin d'accumuler des équivalents réducteurs sur le POM est mise en évidence par des tests de photoproduction de dihydrogène, mettant également en évidence l'impact bénéfique de la stratégie de greffage sur la stabilité à long terme des complexes de Re(I) sous conditions catalytiques.

Enfin, le **Chapitre VIII** constitue une brève conclusion aux études présentées et leurs apports aux domaines de la chimie de coordination, la photophysique et la photosynthèse artificielle moléculaire, suivi d'une ouverture présentant les approches les plus prometteuses, selon l'auteur, pour le développement du domaine de la photosynthèse artificielle dans les prochaines années.

I.5 Références

1. E. Bush, D. S. Lemmen and (editors), *Canada's Changing Climate Report*, 2019, **Government of Canada, Ottawa, ON.**

2. https://www.nobelprize.org/prizes/chemistry/1995/press-release/, Communiqué de presse - Prix Nobel de Chimie 1995, (accessed 2019/05/22).

3. O. Hoegh-Guldberg, D. Jacob, M. Taylor, M. Bindi, S. Brown, I. Camilloni, A. Diedhiou, R. Djalante, K. L. Ebi, F. Engelbrecht, J. Guiot, Y. Hijioka, S. Mehrotra, A. Payne, S. I. Seneviratne, A. Thomas, R. Warren and G. Zhou, *In: Global Warming of 1.5°C. An IPCC Special Report on the impacts of global warming of 1.5°C above pre-industrial levels and related global greenhouse gas emission pathways, in the context of strengthening the global response to the threat of climate change, sustainable development, and efforts to eradicate poverty*, 2018, [Masson-Delmotte, V., P. Zhai, H.-O. Pörtner, D. Roberts, J. Skea, P.R. Shukla, A. Pirani, W. Moufouma-Okia, C. Péan, R. Pidcock, S. Connors, J.B.R. Matthews, Y. Chen, X. Zhou, M.I. Gomis, E. Lonnoy, T. Maycock, M. Tignor, and T. Waterfield (eds.)].

4. J. Rogelj, D. Shindell, K. Jiang, S. Fifita, P. Forster, V. Ginzburg, C. Handa, H. Kheshgi, S. Kobayashi, E. Kriegler, L. Mundaca, R. Séférian and M. V. Vilariño, *In: Global Warming of 1.5°C. An IPCC Special Report on the impacts of global warming of 1.5°C above pre-industrial levels and related global greenhouse gas emission pathways, in the context of strengthening the global response to the threat of climate change, sustainable development, and efforts to eradicate poverty*, 2018, [Masson-Delmotte, V., P. Zhai, H.-O. Pörtner, D. Roberts, J. Skea, P.R. Shukla, A. Pirani, W. Moufouma-Okia, C. Péan, R. Pidcock, S. Connors, J.B.R. Matthews, Y. Chen, X. Zhou, M.I. Gomis, E. Lonnoy, T. Maycock, M. Tignor, and T. Waterfield (eds.)].

5. A. Jager-Waldau, C. Bucher, K. H. B. Frederiksen, R. Guerro-Lemus, G. Mason, B. Mather, C. Mayr, D. Moneta, J. Nikoletatos, M. B. Roberts and I. P. T. 14, *2018 Ieee 7th World Conference on Photovoltaic Energy Conversion (Wcpec) (a Joint Conference of 45th Ieee Pvsc, 28th Pvsec & 34th Eu Pvsec)*, 2018, **OECD/IEA, Paris**, 1424-1430.

6. https://www.rncan.gc.ca/energie/faits/energie-ges/20074, Énergie et les émissions de gaz à effet de serre (GES), Ressources naturelles Canada, (accessed 2019/05/16).

7. SDES, 2018, **Service de la donnée et des études statistiques (SDES), dépendant du Ministère de la transition écologique et solidaire, France**.

8. http://www.cea.fr/comprendre/Pages/radioactivite/essentiel-sur-dechets-radioactifs.aspx, Commissariat à l'énergie atomique et aux énergies alternatives, (accessed 2019-05-18).

9. IEA, *Solar Energy Perspective*, 2011, **OECD/IEA, Paris**.

10. https://www.tesla.com/fr_CA/powerwall, Tesla Inc. Spécifications du Powerwall, (accessed 2019-05-16).

11. *BP Statistical Review of World Energy 2018.*, Data compiled by the Centre for Energy Economics Research and Policy, Heriot-Watt University, ceerp.hw.ac.uk.

12. R. Buick, *Philos Trans R Soc Lond B Biol Sci*, 2008, **363**, 2731-2743.

13. D. E. Canfield, L. Ngombi-Pemba, E. U. Hammarlund, S. Bengtson, M. Chaussidon, F. Gauthier-Lafaye, A. Meunier, A. Riboulleau, C. Rollion-Bard, O. Rouxel, D. Asael, A. C. Pierson-Wickmann and A. El Albani, *Proc. Natl. Acad. Sci. U.S.A.*, 2013, **110**, 16736-16741.

14. K. Ahern, I. Rajagopal and T. Tan, *Biochemistry Free For All*, https://bio.libretexts.org/Bookshelves/Biochemistry/Book%3A_Biochemistry_Free_For_All_(Ahern%2C_Rajagopal%2C_and_Tan), 2019.

15. https://www.nobelprize.org/prizes/chemistry/1988/press-release/, Communiqué de presse - Prix Nobel de Chimie 1988, (accessed 2019/05/23).

16. A. R. Grossman, M. R. Schaefer, G. G. Chiang and J. L. Collier, *Microbiol Rev*, 1993, **57**, 725-749.

17. X. Hu, A. Damjanovic, T. Ritz and K. Schulten, *Proc. Natl. Acad. Sci. U.S.A.*, 1998, **95**, 5935-5941.

18. https://rnbio.upmc.fr, Ressources numérique pour l'enseignement en biologie de Sorbonne-Université, (accessed 2019/05/17).

19. https://www.nobelprize.org/prizes/chemistry/1978/press-release/, Communiqué de presse - Prix Nobel de Chimie 1978, (accessed 2019/05/22).

20. R. E. Blankenship, D. M. Tiede, J. Barber, G. W. Brudvig, G. Fleming, M. Ghirardi, M. R. Gunner, W. Junge, D. M. Kramer, A. Melis, T. A. Moore, C. C. Moser, D. G. Nocera, A. J. Nozik, D. R. Ort, W. W. Parson, R. C. Prince and R. T. Sayre, *Science*, 2011, **332**, 805-809.

21. H. Dau and I. Zaharieva, *Acc. Chem. Res.*, 2009, **42**, 1861-1870.

22. D. C. Yao, D. C. Brune and W. F. Vermaas, *FEBS Lett.*, 2012, **586**, 169-173.

23. https://www.energy.gov/eere/bioenergy/algal-biofuels, Algal biofuels, Office of energy efficiency and renewable energy, Department of Energy, USA, (accessed 2019-05-23).

24. P. F. South, A. P. Cavanagh, H. W. Liu and D. R. Ort, *Science*, 2019, **363**, eaat9077.

25. https://www.nobelprize.org/prizes/chemistry/2018/press-release/, Communiqué de presse - Prix Nobel de Chimie 2018, (accessed 2019/05/22).

26. G. Ciamician, *Science*, 1912, **36**, 385-394.

27. I. Ninomiya and T. Naito, in *Photochemical Synthesis*, eds. I. Ninomiya and T. Naito, Academic Press, London, 1989.

28. M. H. Shaw, J. Twilton and D. W. MacMillan, *J. Org. Chem.*, 2016, **81**, 6898-6926.

29. *Varian Cary 50 Series Spectrophotometer (1999)*, https://www.ncnr.nist.gov/userlab/pdf/E136uvvis.pdf (accessed 2019/06/25).

30. C. Bozal-Ginesta and J. R. Durrant, *Faraday Discuss.*, 2019, **215**, 439-451.

31. *The Future of Hydrogen*, Report from the International Energy Agency, OECD/IEA, Paris, 2019.

32. A. Fujishima and K. Honda, *Nature*, 1972, **238**, 37-38.

33. J. Schneider, M. Matsuoka, M. Takeuchi, J. Zhang, Y. Horiuchi, M. Anpo and D. W. Bahnemann, *Chem. Rev.*, 2014, **114**, 9919-9986.

34. A. J. Nozik, *Annu. Rev. Phys. Chem.*, 1978, **29**, 189-222.

35. T. Inoue, A. Fujishima, S. Konishi and K. Honda, *Nature*, 1979, **277**, 637-638.

36. Z. Wang, C. Li and K. Domen, *Chem. Soc. Rev.*, 2019, **48**, 2109-2125.

37. J. L. White, M. F. Baruch, J. E. Pander Iii, Y. Hu, I. C. Fortmeyer, J. E. Park, T. Zhang, K. Liao, J. Gu, Y. Yan, T. W. Shaw, E. Abelev and A. B. Bocarsly, *Chem. Rev.*, 2015, **115**, 12888-12935.

38. J. M. Lehn and J. P. Sauvage, *Nouv. J. Chim.*, 1977, **1**, 449.

39. M. Kirch, J.-M. Lehn and J.-P. Sauvage, *Helv. Chim. Acta*, 1979, **62**, 1345-1384.

40. V. Balzani, L. Moggi, M. F. Manfrin, F. Bolletta and G. S. Laurence, *Coord. Chem. Rev.*, 1975, **15**, 321-433.

41. J. Kiwi and M. Grätzel, *Nature*, 1979, **281**, 657-658.

42. E. Borgarello, J. Kiwi, E. Pelizzetti, M. Visca and M. Grätzel, *Nature*, 1981, **289**, 158-160.

43. M. Graetzel, *Acc. Chem. Res.*, 2002, **14**, 376-384.

44. B. O'Regan and M. Grätzel, *Nature*, 1991, **353**, 737-740.

45. A. Hagfeldt, G. Boschloo, L. Sun, L. Kloo and H. Pettersson, *Chem. Rev.*, 2010, **110**, 6595-6663.

46. J. R. Lakowicz, *Principles of Fluorescence Spectroscopy*, Springer US, Boston, MA, 2006.

47. V. Balzani, G. Bergamini, S. Campagna and F. Puntoriero, in *Photochemistry and Photophysics of Coordination Compounds I*, eds. V. Balzani and S. Campagna, Springer Berlin Heidelberg, Berlin, Heidelberg, 2007, ch. Chapter 132, pp. 1-36.

48. T. Főrster, *Discuss. Faraday Soc.*, 1959, **27**, 7-17.

49. D. L. Dexter, *J. Chem. Phys.*, 1953, **21**, 836-850.

50. https://www.nobelprize.org/prizes/chemistry/1983/press-release/, Communiqué de presse - Prix Nobel de Chimie 1983, (accessed 2019/06/26).

51. https://www.nobelprize.org/prizes/chemistry/1992/press-release/, Communiqué de presse - Prix Nobel de Chimie 1992, (accessed 2019/06/26).

52. M. Kuss-Petermann and O. S. Wenger, *Angew. Chem. Int. Ed.*, 2016, **55**, 815-819.

53. B. Durham, J. V. Caspar, J. K. Nagle and T. J. Meyer, *J. Am. Chem. Soc.*, 1982, **104**, 4803-4810.

54. K. Suzuki, A. Kobayashi, S. Kaneko, K. Takehira, T. Yoshihara, H. Ishida, Y. Shiina, S. Oishi and S. Tobita, *Phys. Chem. Chem. Phys.*, 2009, **11**, 9850-9860.

55. J. I. Goldsmith, W. R. Hudson, M. S. Lowry, T. H. Anderson and S. Bernhard, *J. Am. Chem. Soc.*, 2005, **127**, 7502-7510.

56. A. Zarkadoulas, E. Koutsouri, C. Kefalidi and C. A. Mitsopoulou, *Coord. Chem. Rev.*, 2015, **304**, 55-72.

57. Y. J. Yuan, Z. T. Yu, D. Q. Chen and Z. G. Zou, *Chem. Soc. Rev.*, 2017, **46**, 603-631.

58. I. N. Mills, J. A. Porras and S. Bernhard, *Acc. Chem. Res.*, 2018, **51**, 352-364.

59. P. Kurz, B. Probst, B. Spingler and R. Alberto, *Eur. J. Inorg. Chem.*, 2006, **2006**, 2966-2974.

60. S. Berardi, S. Drouet, L. Francas, C. Gimbert-Surinach, M. Guttentag, C. Richmond, T. Stoll and A. Llobet, *Chem. Soc. Rev.*, 2014, **43**, 7501-7519.

61. Y. Pellegrin and F. Odobel, *C. R. Chim.*, 2017, **20**, 283-295.

62. Q. Zhang and J. Guan, *ChemSusChem*, 2019, **12**, 3209-3235.

63. B. Zhang and L. Sun, *Chem. Soc. Rev.*, 2019, **48**, 2216-2264.

64. S. W. Gersten, G. J. Samuels and T. J. Meyer, *J. Am. Chem. Soc.*, 1982, **104**, 4029-4030.

65. J. L. Fillol, Z. Codola, I. Garcia-Bosch, L. Gomez, J. J. Pla and M. Costas, *Nat. Chem.*, 2011, **3**, 807-813.

66. Q. Yin, J. M. Tan, C. Besson, Y. V. Geletii, D. G. Musaev, A. E. Kuznetsov, Z. Luo, K. I. Hardcastle and C. L. Hill, *Science*, 2010, **328**, 342-345.

67. M. T. Pope, *Heteropoly and Isopoly Oxometalates*, Springer-Verlag Berlin Heidelberg GmbH, 1983.

68. M. Natali, F. Nastasi, F. Puntoriero and A. Sartorel, *Eur. J. Inorg. Chem.*, 2019, **2019**, 2027-2039.

69. G. A. Parada, Z. K. Goldsmith, S. Kolmar, B. Pettersson Rimgard, B. Q. Mercado, L. Hammarstrom, S. Hammes-Schiffer and J. M. Mayer, *Science*, 2019, **364**, 471-475.

70. J. Hawecker, J. M. Lehn and R. Ziessel, *Nouv. J. Chim.*, 1983, **7**, 271.

71. M. Razavet, V. Artero and M. Fontecave, *Inorg. Chem.*, 2005, **44**, 4786-4795.

72. N. Queyriaux, R. T. Jane, J. Massin, V. Artero and M. Chavarot-Kerlidou, *Coord. Chem. Rev.*, 2015, **304-305**, 3-19.

73. W. T. Eckenhoff, *Coord. Chem. Rev.*, 2018, **373**, 295-316.

74. S. Fukuzumi, Y. M. Lee and W. Nam, *Coord. Chem. Rev.*, 2018, **355**, 54-73.

75. M. L. Helm, M. P. Stewart, R. M. Bullock, M. R. DuBois and D. L. DuBois, *Science*, 2011, **333**, 863-866.

76. R. Lomoth and S. Ott, *Dalton Trans.*, 2009, 9952-9959.

77. V. Lyaskovskyy and B. de Bruin, *ACS Catal.*, 2012, **2**, 270-279.

78. J. M. Lehn and R. Ziessel, *Proc. Natl. Acad. Sci. U.S.A.*, 1982, **79**, 701-704.

79. J. Hawecker, J.-M. Lehn and R. Ziessel, *J. Chem. Soc., Chem. Commun.*, 1983, 536-538.

80. J. Hawecker, J.-M. Lehn and R. Ziessel, *Helv. Chim. Acta*, 1986, **69**, 1990-2012.

81. H. Takeda, H. Koizumi, K. Okamoto and O. Ishitani, *Chem. Commun.*, 2014, **50**, 1491-1493.

82. Y. H. Luo, L. Z. Dong, J. Liu, S. L. Li and Y. Q. Lan, *Coord. Chem. Rev.*, 2019, **390**, 86-126.

83. Z. Guo, F. Yu, Y. Yang, C. F. Leung, S. M. Ng, C. C. Ko, C. Cometto, T. C. Lau and M. Robert, *ChemSusChem*, 2017, **10**, 4009-4013.

84. J. L. Grant, K. Goswami, L. O. Spreer, J. W. Otvos and M. Calvin, *J. Chem. Soc., Dalton Trans.*, 1987, 2105-2109.

85. H. Rao, L. C. Schmidt, J. Bonin and M. Robert, *Nature*, 2017, **548**, 74-77.

86. Y. Kuramochi, O. Ishitani and H. Ishida, *Coord. Chem. Rev.*, 2018, **373**, 333-356.

87. D. M. Arias-Rotondo and J. K. McCusker, *Chem. Soc. Rev.*, 2016, **45**, 5803-5820.

88. J. M. Lehn, *Supramolecular Chemistry, Concepts and Perspectives*, VCH Verlagsgesellschaft mbH, 1995.

89. S. Serroni, G. Denti, S. Campagna, A. Juris, M. Ciano and V. Balzani, *Angewandte Chemie-International Edition in English*, 1992, **31**, 1493-1495.

90. S. Campagna, F. Puntoriero, F. Nastasi, G. Bergamini and V. Balzani, in *Photochemistry and Photophysics of Coordination Compounds I*, eds. V. Balzani and S. Campagna, Springer Berlin Heidelberg, Berlin, Heidelberg, 2007, pp. 117-214.

91. Y. Tsuji, K. Yamamoto, K. Yamauchi and K. Sakai, *Angew. Chem. Int. Ed.*, 2018, **57**, 208-212.

92. T. Morimoto, C. Nishiura, M. Tanaka, J. Rohacova, Y. Nakagawa, Y. Funada, K. Koike, Y. Yamamoto, S. Shishido, T. Kojima, T. Saeki, T. Ozeki and O. Ishitani, *J. Am. Chem. Soc.*, 2013, **135**, 13266-13269.

93. J. Huo, Y.-B. Zhang, W.-Y. Zou, X. Hu, Q. Deng and D. Chen, *Catal. Sci. Technol.*, 2019, **9**, 2716-2727.

94. H. Ozawa, M. A. Haga and K. Sakai, *J. Am. Chem. Soc.*, 2006, **128**, 4926-4927.

95. A. Fihri, V. Artero, A. Pereira and M. Fontecave, *Dalton Trans.*, 2008, 5567-5569.

96. A. M. Lopez, M. Natali, E. Pizzolato, C. Chiorboli, M. Bonchio, A. Sartorel and F. Scandola, *Phys. Chem. Chem. Phys.*, 2014, **16**, 12000-12007.

97. B. Gholamkhass, H. Mametsuka, K. Koike, T. Tanabe, M. Furue and O. Ishitani, *Inorg. Chem.*, 2005, **44**, 2326-2336.

98. J. F. Lefebvre, J. Schindler, P. Traber, Y. Zhang, S. Kupfer, S. Grafe, I. Baussanne, M. Demeunynck, J. M. Mouesca, S. Gambarelli, V. Artero, B. Dietzek and M. Chavarot-Kerlidou, *Chem. Sci.*, 2018, **9**, 4152-4159.

99. J. Nomrowski and O. S. Wenger, *J. Am. Chem. Soc.*, 2018, **140**, 5343-5346.

100. K. Yamamoto, A. Call and K. Sakai, *Chem. Eur. J.*, 2018, **24**, 16620-16629.

Chapitre II. Heteroleptic ruthenium bis-terpyridine complexes bearing a 4-(dimethylamino)phenyl donor and free coordination sites for hydrogen photo-evolution

II.1 Contexte et résumé

Contrairement aux complexes dérivés de $[Ru(bpy)_3]^{2+}$ présentés dans le chapitre d'introduction, les complexes équivalents basés sur des ligands polypyridines tridentés tel que 2,2';6',2''-terpyridine (tpy), $[Ru(tpy)3]^{2+}$, n'avaient jamais été rapportés comme photosensibilisateur dans une réaction photocatalytique. En effet, ces composés possèdent des propriétés photophysiques intéressantes (absorption plus forte et à plus basse énergie) mais un rendement quantique et un temps de vie très faible, dû en particulier à la présence d'un état excité non radiatif facilement accessible à température de la pièce. Cependant, dans le cadre d'un des projets de doctorat de Mira Rupp, une étudiante en cotutelle sous la supervision de Prof. Hanan et Prof. Kurth (Uni. Würzburg), nous avons récemment rapporté le premier exemple de système photocatalytique basé sur un complexe bis(terpyridine) de Ru(II). Le complexe en question, $[Ru(toltpy)(bipytpy)](PF_6)_2$ (toltpy: 4'-(tolyl)-2,2':6',2''-terpyridine ; bipytpy: 4'-(4-bromophenyl)-4,4''':4'',4''''-di-pyridinyl-2,2':6',2''-terpyridine), est capable de conduire la photoréduction de protons en conservant son activité pour au moins 12 jours [Ref. 21].[a]

En s'appuyant sur cette preuve de concept, nous avons préparé, caractérisé et utilisé comme photosensibilisateur trois nouveaux complexes Ru(II) bis(terpyridine) basés sur un design 'donneur-accepteur'. Ces complexes possèdent des propriétés physiques légèrement améliorées comparées à celles de complexes précédemment rapportés et conduisent à la production de 18 à 52 moles de H_2 par mole de photosensibilisateur sous irradiation de lumière bleue (450 nm), et de 14 à 47 sous lumière verte (525 nm), tout en maintenant leur activité pour au moins 48 h.

---

[a] Contribution à la ref. 21 : étude cristallographique, modélisation théorique (DFT/TD-DFT), analyses photocatalytiques complémentaires pour proposition d'un modèle de réactivité et co-rédaction de l'article.

Heteroleptic ruthenium bis-terpyridine complexes bearing 4-(dimethylamino)phenyl donor and free coordination sites for hydrogen photo-evolution

Thomas Auvray, Rakesh Sahoo, Denis Deschênes, Garry S. Hanan

Département de Chimie, Université de Montréal, Montréal, Canada, H3T-1J4

Full paper

Published online on 13 September 2019

Reproduced with permission of The Royal Society of Chemistry from *Dalton Trans.*, **2019**, **48**, 15136-15143

Contributions :

Thomas Auvray : Conception du projet. Synthèse et caractérisation des ligands et complexes (RMN, ESI-MS, EA). Analyse des propriétés optiques et électroniques par spectroscopies d'absorption et d'émission et mesures électrochimiques. Analyse des performances photocatalytiques. Modèle théorique (DFT / TD-DFT). Rédaction de l'article.

Rakesh Sahoo : Synthèse et caractérisation partielle de deux complexes.

Denis Deschênes : Optimisation de la synthèse du précurseur 2-acetyl-4-(*tert*-butyl)pyridine

Garry S. Hanan : Supervision, révision de l'article.

II.2 Abstract

Motivated by the recent report of a heteroleptic ruthenium bis-terpyridine complex **[Ru(toltpy)(bipytpy)](PF$_6$)$_2$** (toltpy: 4'-(tolyl)-2,2':6',2''-terpyridine ; bipytpy: 4'-(4-bromophenyl)-4,4''':4'',4''''-di-pyridinyl-2,2':6',2''-terpyridine) capable of driving hydrogen photo-evolution with a constant rate of activity for 12 days [M. Rupp *et al.*, *Inorg. Chem.*, 2019, **58**, 9127–9134], we investigated the impact of an internal electron donor on the photoactivity of three new ruthenium bis-terpyridine photosensitizers. We used 4'-(N,N-dimethylaminophenyl)-4,4"-di-*tert*-butyl-2,2':6',2"-terpyridine (**Dtpy**) as donor ligand. These complexes also bear peripheral coordination sites at various positions on the terpyridine backbone, allowing for photosensitizer–catalyst interactions. Their performances in photocatalysis under blue and green light (450 and 525 nm, respectively) were measured, in the presence of triethanolamine, using a cobaloxime catalyst **[Co(dmgH)$_2$(H$_2$O)$_2$](BF$_4$)$_2$**. Complexes **II-C1 [Ru(Dtpy)(pytpy)](PF$_6$)$_2$** (**pytpy**: 4'-(pyridin-4-yl)-2,2':6',2"-terpyridine) and **II-C3 [Ru(toltpy)(bipytpy)](PF$_6$)$_2$** appeared to have a photostability similar to that of **[Ru(toltpy)(bipytpy)](PF$_6$)$_2$** but with lower activity rates, while **II-C2 [Ru(Dtpy)(pz$_2$bpy)](PF$_6$)$_2$** (**pz$_2$bpy**: 2,6-di(pyrazin-2-yl)-4,4'-bipyridine) displayed a better peak activity, however, followed by a progressive decay. After 24 hours, complexes **II-C1**, **II-C2** and **II-C3** had reached TONs of 18, 35 and 52 under blue light and 14, 20 and 47 under green light, and were still found to be active. Their photophysical and electronic properties are discussed to rationalize the photocatalytic trends.

II.3 Introduction

Light driven hydrogen evolution is a promising approach to ensure economically viable use of H_2 as a renewable, carbon free, energy source.[1-2] Since the report from Lehn *et al.* in 1979,[3] the study of the proton reduction reaction of the overall water splitting has been the focus of many studies involving various photosensitisers (PSs) and catalysts.[4] While the initial report involved colloidal platinum as catalyst, it has been successfully replaced by more abundant metal ions.[5] Among them, the most common are cobalt catalysts, based either on dimethylglyoxime or polypyridyl ligands.[6] That same family of ligands has been used to prepare many ruthenium, iridium and rhenium complexes with suitable photophysical properties, such as lifetime and

quantum yield.[7] Once excited, these complexes become both better oxidant and reductant, thus enabling reactions not possible in the ground state. However, being based on expensive second and third row transition metals, alternatives based on first row transition metal or even metal free PS have become more abundant in the literature.[8-13]

Irrespective of the nature of the PS used, one of the main limitations of the current systems is their photostability. **[Ru(bpy)$_3$](PF$_6$)$_2$** is used as a reference system in both photocatalytic water reduction and water oxidation.[14-17] However, typical photoactivity profiles consist of a peak activity minutes after the irradiation begins, followed by an exponential-like decay, leading to loss of activity within hours.[9,14,18-20] Recently we showed that a substantial increase in stability can be obtained by using a bis-terpyridine ruthenium complex instead.[21] These complexes were disregarded for application in photocatalysis due to their poor photophysical properties, despite their more extended absorption over the visible region.[22-24] However, intrigued by the report of Mulfort and Tiede on a dyad combining a ruthenium bis-terpyridine PS and a cobaloxime catalyst showing efficient charge transfer towards the catalyst,[25] we and others investigated a heteroleptic complex bearing free coordination site on the 4 and 4'' positions of the terpyridine backbone (see Figure II.1). This complex has enhanced photophysical properties compared to

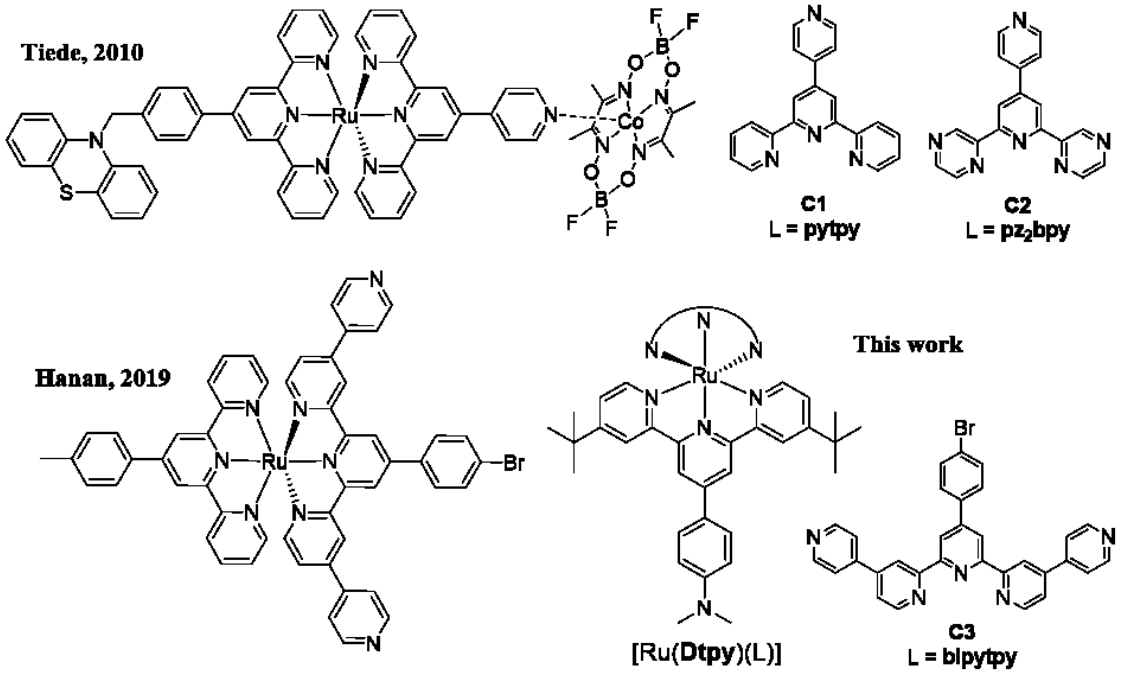

Figure II.1. Structures of selected ruthenium bis-terpyridine complexes used as photosensitizers in the literature.

the homoleptic **[Ru(toltpy)$_2$](PF$_6$)$_2$** complex (toltpy : 4'-(tolyl)- 2,2':6',2''-terpyridine) and drives the photo-evolution of H_2 with a constant rate of activity for 12 days.[21]

In this study, we chose to introduce a more electron rich ligand with an internal electron donor group to replace the **toltpy** ligand. We used **Dtpy** (4'-(N,N-dimethylaminophenyl)-4,4''-di-*tert*-butyl-2,2':6',2''-terpyridine) as shown in Figure II.1. The dimethylaniline fragment should be the first oxidation site and could change the nature of the lower energy excited state. The peripheral position of this substituent should favour charge separation in the excited state where the electron is transferred to the electron poor ligand. As acceptor ligand, we chose **pytpy** (4'-(pyridin-4-yl)-2,2':6',2''-terpyridine), **pz$_2$bpy** (2,6-di(pyrazin-2-yl)-4,4'-bipyridine) and **bipytpy** to study the variation induced in the electronic properties of the complexes and their impact on the photocatalytic activity in H_2 evolution.

II.4 Experimental section

II.4.1 Materials

Solvents (ACS grade) and precursor chemicals were obtained from commercial sources (Fisher Scientific, Millipore-Sigma) and used as received. Ruthenium trichloride trihydrate was obtained from Pressure Chem. **Dtpy** (4-(4,4''-di-*tert*-butyl-[2,2':6',2''-terpyridin]-4'-yl)-N,N-dimethylaniline),[26] **pytpy** (4'-(pyridin-4-yl)-2,2':6',2''-terpyridine),[27] **pz2bpy** (2,6-di(pyrazin-2-yl)-4,4'-bipyridine)[28] and **bipytpy** (4'-(4-bromophenyl)-4,4''':4'',4''''-di-pyridinyl-2,2':6',2''-terpyridine)[21] were prepared following published procedures.

II.4.2 Physical measurements

^{1}H and ^{13}C NMR spectra were recorded using a Bruker AV400 (400MHz). Chemical shifts are reported in parts per million (ppm) relative to the residual solvent protons (7.26 ppm for $CDCl_3$, 1.94 ppm for CD_3CN) or carbon resonances (77.16 ppm for $CDCl_3$, 1.32 and 118.26 ppm for CD_3CN) of the solvent. All photophysical measurements were carried out in deaerated solutions (acetonitrile). Absorption spectra were measured using an Agilent Cary6000i UV-Vis-NIR spectrophotometer and luminescence spectra using a PerkinElmer LS55 fluorescence spectrometer. Luminescence lifetimes were measured using an Edinburg Instrument FL900 using a 405 nm centred Hamamatsu diode laser. Quantum yield were calculated relative to

$[Ru(bpy)_3]^{2+}$ and $[Ru(ptpy)_2)]^{2+}$ using a dilution method.[23,29-30] Electrochemical measurements involved a three-electrode set-up with a glassy carbon disk (d = 3 mm) working electrode, a platinum coil as counter electrode and a platinum wire as pseudo-reference. Measurements were made using a SP-50 BioLogic potentiostat interfaced to a computer equipped with the EC-lab software V11.21. The potentials were measured using the ferrocenium/ferrocene couple in acetonitrile (0.40 V *vs* ECS) as the reference.[31] The concentration of the analyte was 1 mM and that of the electrolyte (tetrabutylammonium hexafluorophosphate TBAP) was 0.1 M.

II.4.3 Computational studies

The geometries of the three complexes were optimized for both the di-cationic and one electron reduced species by DFT with the PBE0 hybrid functional[32] without symmetry constraints using Gaussian16 Rev. B01.[33] All elements were assigned using the LANL2DZ basis set.[34-37] Frequency calculations were performed to ensure that local minima had been reached. The absorption and emission properties of the di-cationic species were modelled by time dependent DFT (TD-DFT). All calculations were performed in acetonitrile solution using a conductor-like polarizable continuum model (CPCM).[38] The results were visualized and tabulated using Gaussview6.0, GaussSum3.0[39] and Chemissian4.53[40]. Natural transition orbital (NTO) analysis was performed to attribute the nature of the calculated transitions.[41]

II.4.4 Synthesis

[Ru(Dtpy)Cl$_3$] In a 250 mL round-bottomed flask, the ligand **Dtpy** (465 mg, 1 mmol) was dissolved in DCM (95 mL). To this yellow solution was then added $RuCl_3 \cdot 3H_2O$ (262 mg, 1 mmol) and ethanol (5 mL). The dark solution was then refluxed for 3 h. Solvents were then removed under reduced pressure. The solid was suspended in water and isolated by filtration then air dried. Yield: 88%, 590 mg. This compound was used as obtained to prepare the heteroleptic complexes.

II-C1 [Ru(Dtpy)(pytpy)](PF$_6$)$_2$ In a 50 mL round-bottomed flask, **[Ru(Dtpy)Cl$_3$]** (50 mg, 74 µmol) and **pytpy** (23 mg, 74 µmol) were suspended in ethylene glycol (20 mL). $AgNO_3$ (38 mg, 3 eq.) was then added and the flask covered with aluminium foil. The suspension was then heated to 150 °C for 16 h under N_2. Once back to room temperature, water (25 mL) was added

to the red slurry, followed by 2 mL of saturated aqueous KPF_6. The suspension was filtered through Celite and washed thoroughly with water. The dark red solid was washed away from the Celite with acetonitrile. The solvent was then removed under reduced pressure and the residue purified on a silica column using acetonitrile/saturated aqueous KNO_3 (7/1). The first band was the homoleptic **[Ru(Dtpy)$_2$](PF$_6$)$_2$** complex, and the second band was the targeted complex. A third band was sometimes observed, corresponding to the homoleptic **[Ru(pytpy)$_2$](PF$_6$)$_2$** complex. The fractions containing the complex were combined and freed of solvent under reduced pressure. The residue was added to water and 1 mL of saturated aqueous KPF_6 was added. The product was then extracted twice from the aqueous phase with dichloromethane. The combined dichloromethane phases were dried with Na_2SO_4 and the solvent was then removed under reduced pressure producing the targeted complex **II-C1** with a 29% yield (25 mg).

^{1}H NMR (400 MHz, CD_3CN) δ = 9.04 (s, 2H, H*e*'), 9.02 (s, 2H, H*d*), 8.96 (dd, 2H, H*g*'), 8.66 (d, 2H, H*d*'), 8.58 (d, 2H, H*c*), 8.21 (d, 2H, H*e*), 8.14 (dd, 2H, H*f*'), 7.96 (td, 2H, H*c*'), 7.49 (dd, 2H, H*a*'), 7.23 (m, 4H, Ha/H*b*'), 7.13 (dd, 2H, H*b*), 7.06 (d, 2H, H*f*), 3.15 (s, 6H, H*g*), 1.32 (s, 18H, H*h*).

^{13}C NMR (101 MHz, CD_3CN) δ 164.0, 159.0, 157.0, 155.9, 153.3, 153.2, 152.7, 152.1, 150.0, 145.4, 145.1, 138.8, 129.8, 128.6, 125.5, 125.2, 123.9, 123.0, 122.8, 122.6, 120.7, 113.4, 40.4, 36.2, 30.4.

ESI-MS: calculated for $[M - 2PF_6]^{2+}$ 438.1602; found 438.1605; calculated for $[M - PF_6]^+$ 1021.2852; found 1021.2844.

Elemental analysis: calc. C: 51.74%, H: 4.43% and N: 9.46% for $C_{51}H_{50}N_8P_2F_{12}Ru \cdot H_2O$; found C: 51.76%, H: 4.31% and N: 9.51%.

II-C2 [Ru(Dtpy)(pz$_2$bpy)](PF$_6$)$_2$ was prepared following the procedure described for **II-C1** using 23 mg of **pz$_2$bpy**. Yield: 29% (25 mg)

^{1}H NMR (400 MHz, CD_3CN) δ = 9.77 (d, 2H, H*d*'), 9.23 (s, 2H, H*e*'), 9.03 (s, 2H, H*d*), 9.00 (m, 2H, H*g*'), 8.59 (d, 2H, H*c*), 8.39 (d, 2H, H*a*'), 8.23 (d, 2H, H*e*), 8.17 (d, 2H, H*f*'), 7.64 (dd, 2H, H*b*'), 7.14 (m, 2H, H*a*/H*b*), 7.06 (d, 2H, H*f*), 3.15 (s, 6H, H*g*), 1.32 (s, 18H, H*h*).

^{13}C NMR (101 MHz, CD_3CN) δ 164.7, 158.8, 155.9, 155.7, 154.5, 153.4, 152.1, 151.2, 149.2, 147.4, 145.8, 144.7, 130.2, 129.9, 125.3, 123.6, 123.3, 123.2, 122.8, 120.9, 113.3, 40.4, 36.3, 30.3.

ESI-MS: calculated for $[M - 2PF_6]^{2+}$ 439.1554; found 439.1521; calculated for $[M - PF_6]^+$ 1023.2756; found 1023.2654.

Elemental analysis: calc. C: 50.39%, H: 4.14% and N: 11.99% for $C_{49}H_{48}N_{10}P_2F_{12}Ru$; found C: 50.64%, H: 4.12% and N: 11.92%.

II-C3 [Ru(Dtpy)(bipytpy)](PF$_6$)$_2$ was prepared following the procedure described for **II-C1** using 40 mg of **bipytpy**. Yield: 39% (41 mg)

^{1}H NMR (400 MHz, CD3CN) δ = 9.20 (s, 2H, H*e*'), 9.05 (m, 2H, H*d*), 8.95 (t, 2H, H*d*'), 8.76 (d, 4H, H*i*'), 8.61 (m, 2H, H*c*), 8.23 (dd, 4H, H*e*/Hg'), 7.97 (d, 2H, H*f*'), 7.74 (dd, 4H, H*h*'), 7.60 (m, 2H, H*a*'), 7.53 (m, 2H, H*b*'), 7.31 (t, 2H, H*a*), 7.16 (dd, 2H, H*b*), 7.07 (d, 2H, H*f*), 3.15 (s, 6H, H*g*), 1.32 (s, 18H, H*h*).

^{13}C NMR (101 MHz, CD3CN) δ 164.1, 160.0, 159.1, 156.8, 156.0, 153.6, 153.3, 152.8, 151.8, 150.1, 147.9, 147.3, 143.7, 137.0, 133.7, 130.6, 129.9, 125.9, 125.4, 125.3, 123.9, 123.2, 123.0, 122.8, 122.5, 120.9, 113.4, 40.5, 36.3, 30.4.

ESI-MS: calculated for $[M - 2PF_6]^{2+}$ 554.6441; found 554.6391; calculated for $[M - PF_6]^+$ 1254.2530; found 1254.2395.

Elemental analysis: calc. C: 52.59%, H: 4.13% and N: 8.90% for $C_{62}H_{56}N_9P_2F_{12}BrRu \cdot H_2O$; found C: 52.39%, H: 4.13% and N: 8.90%.

II.5 Results and discussion

II.5.1 Synthesis

We synthetized **Dtpy** (4-(4,4"-di-*tert*-butyl-[2,2':6',2"-terpyridin]-4'-yl)-N,N-dimethylaniline) following our one pot procedure for terpyridines, starting with 4-*tert*-butyl-2-acetyl-pyridine instead of 2-acetyl-pyridine.[26-27] It was then used to prepare the ruthenium trichloride precursor **[Ru(Dtpy)Cl$_3$]** following a published procedure.[42] The standard procedure using aqueous ethanol instead of DCM/ethanol 95/5 only gives the homoleptic complex within an hour.

[Ru(Dtpy)Cl$_3$] was then used to prepare the complexes by combining it with the corresponding ligands (**pytpy**, **pz2bpy** and **bipytpy**, respectively) and three equivalents of $AgNO_3$ in ethylene glycol and heating the suspension for 16 h at 150 °C under inert atmosphere. The complex were isolated as PF_6^- salts, **II-C1 [Ru(Dtpy)(pytpy)](PF$_6$)$_2$**, **II-C2 [Ru(Dtpy)(pz$_2$bpy)](PF$_6$)$_2$** and **II-C3 [Ru(Dtpy)(bipytpy)](PF$_6$)$_2$** in modest yields after purification by column chromatography. The main side product is the homoleptic **[Ru(Dtpy)$_2$](PF$_6$)$_2$** complex. We tried to prepare the complexes by introducing first the acceptor ligand but obtained similar ligand scrambling during the second coordination step. The identity and purity of the complexes were confirmed by ^{1}H (Figure IX.1, Figure IX.2, Figure IX.3), ^{13}C NMR (Figure IX.4-IX.6), ESI-MS (Figure IX.7 to IX.10) and elemental analysis. For all complexes, the di-cationic ion shws the base peak in the ESI-MS analysis, In the NMR spectra, the symmetry of each terpyridine ligands is maintained, giving two series of resonances arising from each ligand. Attributions were made based on the correlation observed in COSY, HSQC and HMBC measurements.

II.5.2 Absorption and emission spectroscopies

The first insight into the electronic properties of our complexes was obtained by UV-visible absorption spectroscopy. Their absorption spectra are shown in Figure II.2 using their molar absorption coefficient as a function of wavelength. The values are tabulated in Table II.1, along with the value for **[Ru(toltpy)(bipytpy)](PF$_6$)$_2$** for comparison purpose. They possess the typical bis-terpyridine ruthenium absorption profile with a broad absorption around 500 nm

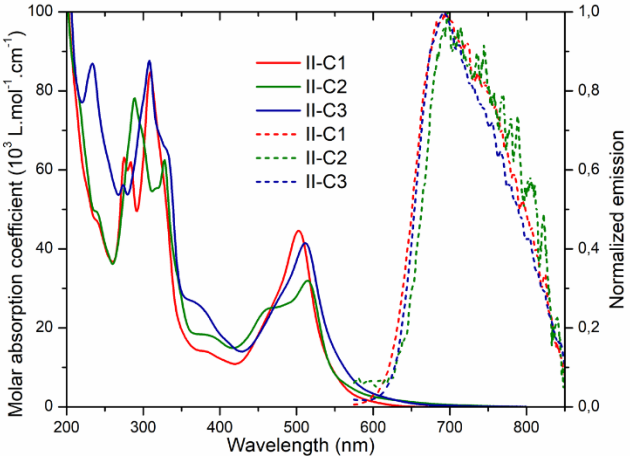

Figure II.2. Molecular absorption coefficients of complexes **II-C1**, **II-C2** and **II-C3** and their normalized luminescence spectra, measured in acetonitrile at room temperature.

corresponding to the ruthenium to terpyridine metal ligand charge transfer (MLCT) and several ligand centred (LC) transitions in the UV region. Compared to **[Ru(toltpy)(bipytpy)](PF$_6$)$_2$**, the MLCT band is slightly redshifted from 497 to 503, 515 and 512 nm for **II-C1**, **II-C2** and **II-C3**, respectively. Besides, **II-C1** and **II-C3** have higher molar absorption coefficient for this transition than **[Ru(toltpy)(bipytpy)](PF$_6$)$_2$**, with values of 45, 41 and 30 x 10^3 L mol^{-1} cm^{-1}, respectively. The lower coefficient of **II-C2** can be explained by the occurrence of a second MLCT transition at higher energy, decreasing the absorption coefficient of the lower energy transition. A similar observation was reported for other dipyrazinepyridyl Ru(II) complexes.[43]

In order to gain additional insight into the electronic properties of the complexes, we use DFT and TD/DFT calculation to obtain a theoretical model (Table IX.1, Table IX.2, Table IX.3, Table IX.4, Table IX.5). The calculated absorption transitions overlaid with the experimental absorption spectra are presented in Figure IX.17, Figure IX.18 and Figure IX.19. The contributions to the singlet-singlet transitions below 350 nm and the ten lowest singlet-triplet transitions are reported in Table IX.6, Table IX.7, Table IX.8. The lowest transition has the expected mixed MLCT and ligand to ligand charge transfer (LLCT) character, going from both DMAPh and Ru to the acceptor ligand transitions in all three complexes as presented *via* their natural transition orbitals in Figure II.3.

Table II.1. Absorption and luminescence properties of **II-C1**, **II-C2**, **II-C3** and **[Ru(toltpy)(bipytpy)]$^{2+}$** measured at room temperature in acetonitrile

Complex	λ_{abs} in nm (ε x10^3 L mol^{-1} cm^{-1})		λ_{em} in nm	Φ^a %	τ in ns (X^2)
	^{1}LC	^{1}MLCT			
II-C1	275 (63), 284 (62), 309 (85)	503 (45)	694	0.09	10.6 ± 0.4 (1.004)
II-C2	289 (78), 328 (62)	461 (25, sh), 515 (32)	697	0.02	16.5 ± 1,5 (1.061)
II-C3	234 (87), 274 (56), 308 (88), 332 (65, sh)	512 (41)	692	0.17	11.7 ± 0.3 (0.959)
[Ru(toltpy)(bipytpy)](PF$_6$)$_2$	234 (76), 301 (70), 331 (62)[b]	497 (30) [b]	658 [b]	0.07 ±0.03 [b]	3.8 ± 0.1 [b]

[a] Averaged from measurements against both $[Ru(bpy)_3]^{2+}$ and $[Ru(phtpy)_2]^{2+}$, with quantum yield of 9.40 and 0.004%, respectively. The error is 20%. [b] Ref 21

The TD/DFT model, however, attributes a low weight to this transition in the overall absorption spectra, the main contributing transitions having mixed ^{1}MLCT (Ru → Dtpy) and ^{1}MLCT (Ru → acceptor ligand) character.

Their luminescence properties were then examined in acetonitrile (with a concentration of about 5 µM). Their normalized luminescence spectra are shown in Figure II.2 while the emission maxima, quantum yields and lifetimes are reported in Table II.1. All three complexes emit around 695 nm and the emissions are redshifted by around 35 nm compared to those of **[Ru(toltpy)(bipytpy)](PF$_6$)$_2$**, most likely due to stronger donation from **Dtpy** than from **toltpy**. Stronger donation results in destabilization of the deactivating metal centred triplet state and disfavours its thermal population.[24] This was confirmed by their longer lifetime, between 10 and 16 ns against 3.8 ns for **[Ru(toltpy)(bipytpy)](PF$_6$)$_2$**. The quantum yields are all in the same order of magnitude, with similar quantum yield for **II-C1** and **[Ru(toltpy)(bipytpy)](PF$_6$)$_2$** (0.09 and 0.07%, respectively), the value for **II-C2** being lower (0.02%) and that of **II-C3** twice better (0.17%). This means that overall **II-C2** has both the longer lifetime and the lower quantum yield of the series.

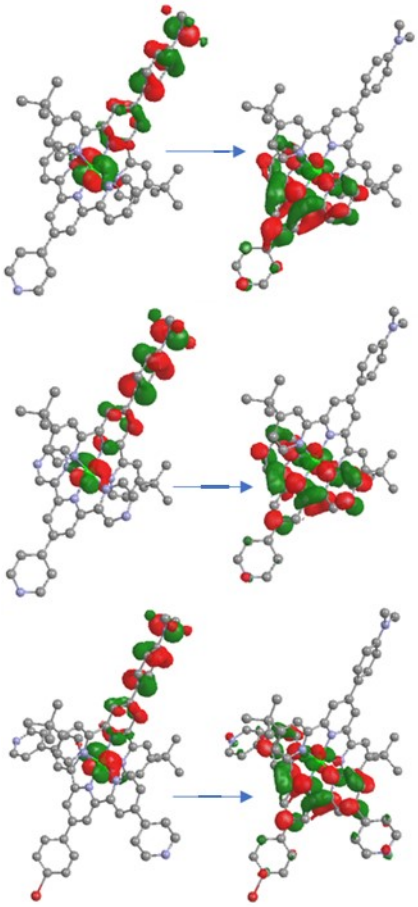

Figure II.3. Natural transition orbitals (hole→particle) for the $S_0 \rightarrow S_1$ transitions in different complexes (**II-C1**, **II-C2** and **II-C3**, top to bottom).

II.5.3 Electrochemical study

The three complexes were analysed by cyclic voltammetry in acetonitrile. The CVs at different scan rates are presented in Figure IX.11, Figure IX.12, Figure IX.13, as well as multiple cycles for each complex at 100 mV s^{-1} in Figure IX.14, Figure IX.15, Figure IX.16. The redox potentials are reported in Table II.2. Adsorption problems occurred during the measurements; so the working electrode was removed from the cell and rinsed between each scan.

In all three complexes, the first oxidation around 0.95 V *vs* SCE is related to the 4-(dimethylamino)phenyl (DMAPh) moiety.[44] Ru(II) to Ru(III) oxidation appears to be quasi reversible as it is affected by the electrochemically irreversible DMAPh oxidation. It takes place at 1.35 and 1.38 V *vs* SCE for **II-C1** and **II-C3** and even higher for **II-C2** with 1.58 V *vs* SCE which is in agreement with the expected reduced electron density at the metal centre in pyrazine-based complex. The electron poor character of this ligand is further confirmed by looking at the first reduction wave. **II-C2** is 200 mV easier to reduce than **II-C1**, itself slightly harder to reduce than **II-C3**, with a reduction potential of -0.89, -1.19 and-1.12 V *vs* SCE, respectively.

The values of **II-C1** and **II-C3**, are similar to that of **[Ru(toltpy)(bipytpy)](PF$_6$)$_2$**. Within the electrochemical window, **II-C1** presents one additional reduction at -1.54 V *vs* SCE. The attribution of the second reduction in heteroleptic bis-tridentate Ru complexes is complex. It is classically attributed to the ligand not reduced in the first wave due the increase repulsion caused to injected electron. For example, if we propose the attribution based on 1) the electron poor character of the ligand and 2) the fact that the electronic repulsion of the injected electron disfavour the subsequent reduction of the same ligand, then the second reduction is attributed to **tolyltpy** in **[Ru(toltpy)(bipytpy)](PF$_6$)$_2$**, around -1.45 V *vs* SCE.[21] The exact attribution of this second reduction is however uncertain and to gain additional insight we decided to get a model of the one electron reduced form of the complexes using DFT. The calculated frontier orbitals of these open shell configuration are presented in Table IX.12, Table IX.13, Table IX.14. For **II-C1**, the second reduction is predicted to take place on **Dtpy**, which agrees with the experimental reduction potential. For **II-C2** and **II-C3**, however, the situation is less decided with unoccupied energy levels located on each ligand very close in energy. However, looking at the less negative experimental potentials, these second reductions can be tentatively attributed to a second reduction of **pz$_2$bpy** in **II-C2**, and to a second of reduction of **bipytpy** in **II-C3**. These attributions are coherent with the more electron acceptor character of these ligand which are electron poor (**dpbp**) and possess extended delocalization (**bipytpy**).

Table II.2. Redox potentials at 100 mV/s for complexes **II-C1**, **II-C2** and **II-C3** (1 mM) measured in acetonitrile with 1 M TBAP

Complex	$E^{ox}_{Ru(II)}$	E^{ox}_{D}	$E^{Red}_{1/2}$		
II-C1	1.35[a]	0.95[b]	-1.19 (53)	-1.54 (64)	-
II-C2	1.58[a]	0.98[b]	-0.89 (59)	-1.32 (47)	-1.68 (69)
II-C3	1.38[a]	0.94[b]	-1.12 (58)	-1.44 (64)	-1.69 (133)
[Ru(toltpy)(bipytpy)](PF$_6$)$_2$	1.21 (85)[c]	-	-1.17 (75)[c]	-1.46 (71)[c]	-1.66 (86)[c]

[a] Quasi reversible, anodic value reported; [b] Irreversible, anodic value reported; [c] from Ref 21

Combining the cyclic voltammetry values and the emission data of the complexes, we then calculated the excited state redox potentials using the following equations:

$$E^*_{ox} = E_{ox} - E_{em} \quad \text{and} \quad E^*_{red} = E_{red} + E_{em}$$

where E_{em} (eV) ≈ 1240/λ_{onset}(nm) and λ_{onset} is obtained at the onset of the room-temperature emission (10% intensity). The excited state oxidation potentials are estimated to be −1.05, −0.98 and −1.03 V, while the excited state reduction potentials are estimated to be 0.81, 1.07 and 0.85 V *vs* SCE for **II-C1***, **II-C2*** and **II-C3***, respectively. These values are well consistent with the excited state potentials of **[Ru(toltpy)(bipytpy)](PF$_6$)$_2$** at −0.86 V and 0.90 V vs SCE, re-evaluated using the onset instead of the emission maximum. These values give us an indication of the hypothetical performances of the complexes in photocatalytic hydrogen evolution. Indeed, the study of **[Ru(toltpy)(bipytpy)](PF$_6$)$_2$** pointed out to a reductive quenching rate limited activity.[21] This reductive quenching efficiency would correlate with the excited state reduction potential as the driving force would depend on the difference between this potential and the oxidation potential of the sacrificial electron donor, typically triethanolamine whose oxidation potentials are estimated to be about 0.6 and 0.8 V *vs* SCE.[45] Based on this simple model (see Fig. IX-23), we would thus expect **II-C2** to be the most active PS as it has the stronger oxidative excited state, followed by **II-C3**, while **II-C1** would be the least efficient.

II.5.4 Photocatalysis

Light driven H_2 evolution experiments were conducted with the three complexes as photosensitizers (PSs) using the same conditions as in the study of **[Ru(toltpy)(bipytpy)](PF$_6$)$_2$**. The tests were conducted in DMF, using 1 M triethanolamine (TEOA) as a sacrificial electron

donor and 0.1 M tetrafluoroboric acid (HBF_4) as proton source. The complex $[Co(dmgH)_2(H_2O)_2](BF_4)_2$ ($dmgH_2$: dimethylglyoxime) was prepared *in situ* from $[Co(H_2O)_6](BF_4)_2$ and six equivalents of dimethylglyoxime, as reported in other studies with Ru and Re PSs.[46-47] The photosensitizers were at 0.1 mM and the cobalt complex used as catalyst at 1 mM. Both blue and green light LEDs were used as light source, centred at 445 and 525 nm, respectively. Their intensities were adjusted to get the same photon flux of approx. 0.3 µmol cm^{-2} s^{-1} by adjusting their output at 62 mW and 53 mW, respectively. The performances indicators, i.e. the turnover Frequencies (TOF), turnover number (TON), amount of H_2 and induction time are reported in Table II.3, along with the value for **[Ru(toltpy)(bipytpy)](PF$_6$)$_2$** under identical conditions.[21]

Table II.3. Photocatalytic H_2 evolution performances of the different PSs under different irradiation conditions in DMF with 1M TEOA and 0.1 M HBF_4. The PSs are at 0.1 mM and the catalyst is prepared *in situ* using 1 mM of $[Co(H_2O)_6](BF_4)_2$ and 6 mM of $dmgH_2$

PS	TOF_{max} ($mmol_{H2}$ /mol_{PS} /min)[a]	TON 24h[a]	n_{H2} 24h (µmol)[a]	Induction time (h)[a]
II-C1[b]	18	18	9	1.6
II-C2[b]	58	35	18	0.1
II-C3[b]	41	52	26	0.6
II-C1[c]	15	14	7	2.5
II-C2[c]	35	20	10	0.1
II-C3[c]	38	47	24	0.9
Ref. 21[b]	55	75	38	0.4

[a] Average of multiple runs. [b] under 450 nm 62 mW LED irradiation; [c] under 525 nm 53 mW LED irradiation

First, in the case of the blue light irradiated photosystems (Figure II.4 and Figure IX.21), we can observe the expected trend in activity by noting the TOFs at the peak of activity (TOF_{max}). **II-C2** is the most active, followed by **II-C3** and finally **II-C1** with TOFs of 58, 41 and 18 $mmol_{H2}$ mol_{PS}^{-1} min^{-1}, respectively. However, the activity of **II-C2** decreased over time while **II-C1** and **II-C3** showed a steady rate of activity over 48 h, as observed for **[Ru(toltpy)(bipytpy)](PF$_6$)$_2$**. Overall, all three PSs are less efficient than **[Ru(toltpy)(bipytpy)](PF$_6$)$_2$**, as hypothesized based on the excited state reduction potentials, except for **II-C2** whose instability under photocatalytic conditions makes it faster only at the beginning of the catalytic run.

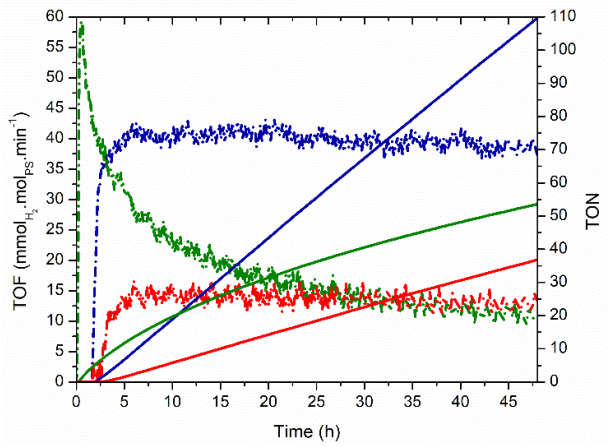

Figure II.4. Evolution of the photocatalytic H_2 production performances over time (TOF in dash, TON plain line) for complexes **II-C1** (red), **II-C2** (green) and **II-C3** (blue) under blue light (450 nm - 62 mW) irradiation in DMF with 1 M TEOA and 0.1 M HBF_4. The PSs are at 0.1 mM and the catalyst is prepared in-situ using 1 mM of $[Co(H_2O)_6](BF_4)_2$ and 6 mM of $dmgH_2$.

As observed for **[Ru(toltpy)(bipytpy)](PF$_6$)$_2$**, there is some induction after the LED is turned on.[21] Since no precautions were taken to prepare the cobalt complex *in situ*, partial oxidation by atmospheric O_2 of the easily oxidized $[Co(dmgH)_2(H_2O)_2](BF_4)_2$ complex could have occurred.[48] To explain this induction period, we first excluded the formation of colloidal active species by mercury poisoning in the initial study,[21] as did Alberto *et al.* in their study of a Re(I) PS in similar conditions.[46] Besides, the induction period correlates with the TOF_{max} of each PS: the lower the initial rate of activity, the longer the induction period. This is in agreement with the proposed mechanisms involving accumulation of the Co(I) species that will undergo oxidative addition of a proton to a Co(III) hydride species (Figure II.6).[6,21] The induction period is thus necessary to ensure reduction of all Co(III) species before further reduction of the catalyst from Co(II) to Co(I), the active state in this catalytic cycle.

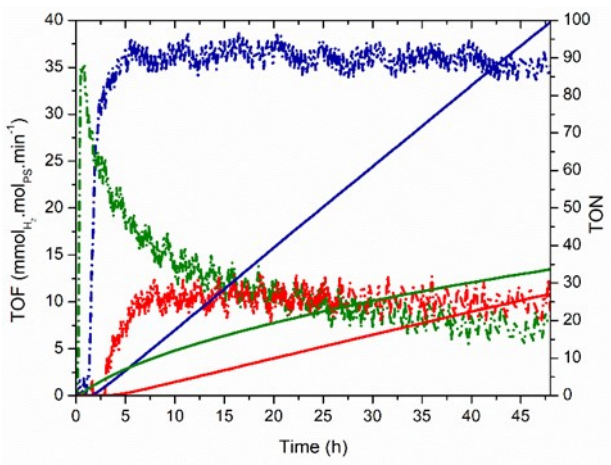

Figure II.5. Evolution of the photocatalytic H_2 production performances over time (TOF in dash, TON plain line) for complexes **II-C1** (red), **II-C2** (green) and **II-C3** (blue) under green light (525 nm - 53 mW) irradiation in DMF with 1 M TEOA and 0.1 M HBF_4. The PSs are at 0.1mM and the catalyst is prepared in-situ using 1 mM of $[Co(H_2O)_6](BF_4)_2$ and 6 mM of $dmgH_2$.

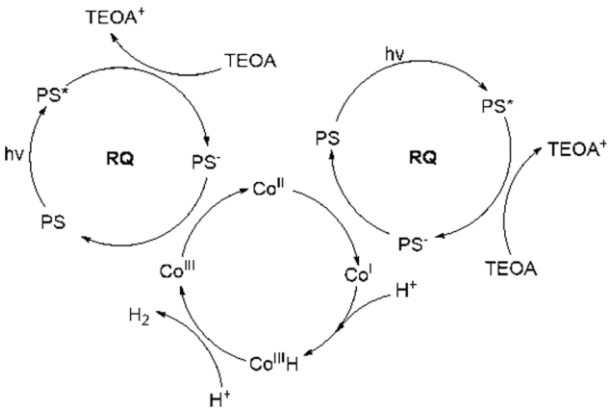

Figure II.6. Proposed mechanism for the photocatalytic production of H_2 with the reported photocatalytic system.

We then decided to study the activity of the three PSs under green light. Indeed, Ru bis-terpyridine complexes are ideal candidates for green light driven photoreaction with their strongly absorbing MLCT transitions usually located around 500 nm. All three complexes present similar activity under the irradiation of blue and green light (Figure II.5 and Figure IX.22), although with a slight decrease in TOF in all cases. Looking at the overlap between absorption and LED emission (Figure IX.20), a similar absorptivity at the LED maxima is observed, however, the lower energy part of the green LED has a lower overlap with the rapidly decreasing absorptivity than the homogeneous profile over then entire blue LED range. **II-C2** has the largest loss of activity (TOF_{max} going from 58 to 38 $mmol_{H2}$ mol_{PS}^{-1} min^{-1}), most likely due to his lower absorptivity under 500 nm compared to **II-C1** and **II-C3**. Overall, all three complexes exhibit similar activity under identical photon flux at two different wavelengths.

II.6 Conclusions

We prepared and characterized three new heteroleptic Ru(II) bis-terpyridine complexes with redshifted emission compared to **[Ru(toltpy)(bipytpy)](PF$_6$)$_2$**. These three complexes are capable of driving the photo-evolution of H_2 when combined with a cobaloxime catalyst under both blue and green light, in the presence of TEOA as an electron donor and HBF_4 as a proton source. By comparing their activities and photo-electrochemical properties, we were able to establish a trend between excited state reduction potentials and activity. Complex **II-C2**, equipped with a 2,6-di(pyrazin-2-yl)-4,4'-bipyridine appeared as a promising candidate but resulted in poor photostability when used in a photocatalytic system. **II-C1** and **II-C3**, however, exhibit photostability like **[Ru(toltpy)(bipytpy)](PF$_6$)$_2$** and maintained a stable rate of activity over 48 h, resulting in TON of 35 and 110 under blue irradiation and 25 and 100 under green light, respectively. However, while the complexes reported herein possess promising photostability compared to archetypical complexes such as **[Ru(bpy)$_3$](PF$_6$)$_2$**, the trade-off between activity and stability is the main topic our future work will focus on.

II.7 References

1. S. Ardo, D. F. Rivas, M. A. Modestino, V. S. Greiving, F. F. Abdi, E. Alarcon Llado, V. Artero, K. Ayers, C. Battaglia, J. P. Becker, D. Bederak, A. Berger, F. Buda, E. Chinello, B. Dam, V. Di Palma, T. Edvinsson, K. Fujii, H. Gardeniers, H. Geerlings, S. M. H. Hashemi, S. Haussener, F. Houle, J. Huskens, B. D. James, K. Konrad, A. Kudo, P. P. Kunturu, D. Lohse, B. Mei, E. L. Miller, G. F. Moore, J. Muller, K. L. Orchard, T. E. Rosser, F. H. Saadi, J. W. Schuttauf, B. Seger, S. W. Sheehan, W. A. Smith, J. Spurgeon, M. H. Tang, R. van de Krol, P. C. K. Vesborg and P. Westerik, *Energy Environ. Sci.*, 2018, **11**, 2768-2783.
2. *The Future of Hydrogen*, Report from the International Energy Agency, OECD/IEA, Paris, 2019.
3. M. Kirch, J.-M. Lehn and J.-P. Sauvage, *Helv. Chim. Acta*, 1979, **62**, 1345-1384.
4. S. Berardi, S. Drouet, L. Francas, C. Gimbert-Surinach, M. Guttentag, C. Richmond, T. Stoll and A. Llobet, *Chem. Soc. Rev.*, 2014, **43**, 7501-7519.
5. W. T. Eckenhoff, *Coord. Chem. Rev.*, 2018, **373**, 295-316.
6. N. Queyriaux, R. T. Jane, J. Massin, V. Artero and M. Chavarot-Kerlidou, *Coord. Chem. Rev.*, 2015, **304-305**, 3-19.
7. Y. J. Yuan, Z. T. Yu, D. Q. Chen and Z. G. Zou, *Chem. Soc. Rev.*, 2017, **46**, 603-631.
8. R. Gueret, L. Poulard, M. Oshinowo, J. Chauvin, M. Dahmane, G. Dupeyre, P. P. Laine, J. Fortage and M. N. Collomb, *ACS Catal.*, 2018, **8**, 3792-3802.
9. P. Lang, J. Habermehl, S. I. Troyanov, S. Rau and M. Schwalbe, *Chem. Eur. J.*, 2018, **24**, 3225-3233.
10. C. B. Larsen and O. S. Wenger, *Chem. Eur. J.*, 2018, **24**, 2039-2058.
11. G. Li, M. F. Mark, H. Lv, D. W. McCamant and R. Eisenberg, *J. Am. Chem. Soc.*, 2018, **140**, 2575-2586.
12. K. E. Dalle, J. Warnan, J. J. Leung, B. Reuillard, I. S. Karmel and E. Reisner, *Chem. Rev.*, 2019, **119**, 2752-2875.
13. B. M. Hockin, C. F. Li, N. Robertson and E. Zysman-Colman, *Catal. Sci. Technol.*, 2019, **9**, 889-915.
14. R. W. Hogue, O. Schott, G. S. Hanan and S. Brooker, *Chem. Eur. J.*, 2018, **24**, 9820-9832.

15. K. Yamamoto, A. Call and K. Sakai, *Chem. Eur. J.*, 2018, **24**, 16620-16629.

16. Y. V. Geletii, B. Botar, P. Kogerler, D. A. Hillesheim, D. G. Musaev and C. L. Hill, *Angew. Chem. Int. Ed.*, 2008, **47**, 3896-3899.

17. L. Sun, M. K. Raymond, A. Magnuson, D. LeGourriérec, M. Tamm, M. Abrahamsson, P. Huang Kenéz, J. Mårtensson, G. Stenhagen, L. Hammarström, S. Styring and B. Åkermark, *J. Inorg. Biochem.*, 2000, **78**, 15-22.

18. C. Lentz, O. Schott, T. Auvray, G. Hanan and B. Elias, *Inorg. Chem.*, 2017, **56**, 10875-10881.

19. M. Dave, A. Rajagopal, M. Damm-Ruttensperger, B. Schwarz, F. Nagele, L. Daccache, D. Fantauzzi, T. Jacob and C. Streb, *Sustainable Energy Fuels*, 2018, **2**, 1020-1026.

20. S. Saeedi, C. C. Xue, B. J. McCullough, S. E. Roe, B. J. Neyhouse and T. A. White, *ACS Appl. Energy Mater.*, 2019, **2**, 131-143.

21. M. Rupp, T. Auvray, E. Rousset, G. M. Mercier, V. Marvaud, D. G. Kurth and G. S. Hanan, *Inorg. Chem.*, 2019, **58**, 9127-9134.

22. J. P. Collin, S. Guillerez, J. P. Sauvage, F. Barigelletti, L. Flamigni, L. Decola and V. Balzani, *Coord. Chem. Rev.*, 1991, **111**, 291-296.

23. M. Maestri, N. Armaroli, V. Balzani, E. C. Constable and A. M. W. C. Thompson, *Inorg. Chem.*, 1995, **34**, 2759-2767.

24. A. K. Pal and G. S. Hanan, *Chem. Soc. Rev.*, 2014, **43**, 6184-6197.

25. K. L. Mulfort and D. M. Tiede, *J. Phys. Chem. B*, 2010, **114**, 14572-14581.

26. B. Laramee-Milette, T. Auvray, S. Nguyen, S. Tremblay, C. Lachance-Brais, M. Donguy, V. Taylor, D. Deschenes and G. S. Hanan, *Synthesis-Stuttgart*, 2015, **47**, 3849-3858.

27. J. H. Wang and G. S. Hanan, *Synlett*, 2005, **2005**, 1251-1254.

28. R. G. Miller and S. Brooker, *Inorg. Chem.*, 2015, **54**, 5398-5409.

29. J. N. Demas and G. A. Crosby, *J. Phys. Chem.*, 1971, **75**, 991-1024.

30. K. E. Spettel and N. H. Damrauer, *J. Phys. Chem. A*, 2014, **118**, 10649-10662.

31. N. G. Connelly and W. E. Geiger, *Chem. Rev.*, 1996, **96**, 877-910.

32. C. Adamo and V. Barone, *J. Chem. Phys.*, 1999, **110**, 6158-6170.

33. M. J. Frisch, G. W. Trucks, H. B. Schlegel, G. E. Scuseria, M. A. Robb, J. R. Cheeseman, G. Scalmani, V. Barone, G. A. Petersson, H. Nakatsuji, X. Li, M. Caricato, A. V. Marenich, J. Bloino, B. G. Janesko, R. Gomperts, B. Mennucci, H. P. Hratchian, J. V. Ortiz, A. F. Izmaylov,

J. L. Sonnenberg, Williams, F. Ding, F. Lipparini, F. Egidi, J. Goings, B. Peng, A. Petrone, T. Henderson, D. Ranasinghe, V. G. Zakrzewski, J. Gao, N. Rega, G. Zheng, W. Liang, M. Hada, M. Ehara, K. Toyota, R. Fukuda, J. Hasegawa, M. Ishida, T. Nakajima, Y. Honda, O. Kitao, H. Nakai, T. Vreven, K. Throssell, J. A. Montgomery Jr., J. E. Peralta, F. Ogliaro, M. J. Bearpark, J. J. Heyd, E. N. Brothers, K. N. Kudin, V. N. Staroverov, T. A. Keith, R. Kobayashi, J. Normand, K. Raghavachari, A. P. Rendell, J. C. Burant, S. S. Iyengar, J. Tomasi, M. Cossi, J. M. Millam, M. Klene, C. Adamo, R. Cammi, J. W. Ochterski, R. L. Martin, K. Morokuma, O. Farkas, J. B. Foresman and D. J. Fox, Gaussian 16 Rev. B.01, 2016, Wallingford, CT

34. T. H. Dunning and P. J. Hay, *Modern Theoretical Chemistry III ed.*, Plenum, New York, 1977.

35. P. J. Hay and W. R. Wadt, *J. Chem. Phys.*, 1985, **82**, 270-283.

36. P. J. Hay and W. R. Wadt, *J. Chem. Phys.*, 1985, **82**, 299-310.

37. W. R. Wadt and P. J. Hay, *J. Chem. Phys.*, 1985, **82**, 284-298.

38. M. Cossi, N. Rega, G. Scalmani and V. Barone, *J. Comput. Chem.*, 2003, **24**, 669-681.

39. N. M. O'Boyle, A. L. Tenderholt and K. M. Langner, *J. Comput. Chem.*, 2008, **29**, 839-845.

40. S. Leonid, *V 4.53*, 2005-2017, www.chemissian.com.

41. R. L. Martin, *J. Chem. Phys.*, 2003, **118**, 4775-4777.

42. B. Laramee-Milette, F. Nastasi, F. Puntoriero, S. Campagna and G. S. Hanan, *Chem. Eur. J.*, 2017, **23**, 16497-16504.

43. A. Stublla and P. G. Potvin, *Eur. J. Inorg. Chem.*, 2010, **2010**, 3040-3050.

44. P. Lainé, F. Bedioui, E. Amouyal, V. Albin and F. Berruyer-Penaud, *Chem. Eur. J.*, 2002, **8**, 3162-3176.

45. Y. Pellegrin and F. Odobel, *C. R. Chim.*, 2017, **20**, 283-295.

46. B. Probst, A. Rodenberg, M. Guttentag, P. Hamm and R. Alberto, *Inorg. Chem.*, 2010, **49**, 6453-6460.

47. E. Rousset, D. Chartrand, I. Ciofini, V. Marvaud and G. S. Hanan, *Chem. Commun.*, 2015, **51**, 9261-9264.

48. M. Razavet, V. Artero and M. Fontecave, *Inorg. Chem.*, 2005, **44**, 4786-4795.

Chapitre III. Electronic properties of rhenium(I) carbonyl complexes with hexahydro-pyrimidopyrimidine based ligands

III.1 Contexte et résumé

Des travaux précédents dans le groupe ont permis le développement de ligands polypyridines portant un groupement hexahydro-pyrimidopyrimidine (Hhpp), une guanidine bicyclique. Ces ligands sont apparus comme étant fortement donneurs et ont permis d'obtenir de prometteuses propriétés photophysiques pour les complexes de Ru(II), d'Ir(III) ou encore de Co(III) correspondants.

Dans cette étude, nous nous appuyons sur les résultats initiaux présentés par Dr. Amlan K. Pal dans une communication introduisant l'obtention de complexes de Re(I) dans lesquelles les ligands tridentés adoptent une coordination faciale, peu courante. En utilisant des ligands portant un ou deux groupements hpp, nous avons préparé quatre complexes dont deux nouvellement rapportés et approfondi l'étude de leurs propriétés électroniques et photophysiques par une combinaison de techniques de caractérisation : RMN, ESI-MS, analyse élémentaire, spectroscopies vibrationnelle, d'absorption et d'émission (y compris à basse température) et électrochimie ; un modèle théorique (DFT/TD-DFT) est également développé. La structure tridimensionnelle des deux nouveaux complexes est également obtenue par diffraction des rayons X sur monocristaux. Ces composés apparaissent non émissifs à température ambiante mais présentent une émission à 77 K correspondant à une transition de transfert de charge intra-ligand possédant également un faible caractère de transfert de charge métal-ligand. Les composés portant une pyrazine émettent 100 nm plus bas en énergie que leurs équivalents pyridines (580 vs 480 nm, respectivement).

Electronic properties of rhenium(I) carbonyl complexes with hexahydro-pyrimidopyrimidine based ligands

Thomas Auvray,[a] Amlan K. Pal,[a,b] and Garry S. Hanan*[a]

[a] Département de Chimie, Université de Montréal, Montréal, Canada, H3T-1J4

[b] Organic Semiconductor Centre, EaStCHEM School of Chemistry, University of St Andrews, St Andrews, Fife, U.K., KY16 9ST.

Full paper

Revised and resubmitted for publication in *New Journal of Chemistry*

Contributions :

Thomas Auvray : Conception du projet. Synthèse et caractérisation complète des ligands et complexes (RMN, ESI-MS, IR, AE). Collecte et affinement des données de diffraction sur monocristaux. Analyse des propriétés optiques et électroniques par électrochimie et spectroscopies, incluant luminescence à basse température. Calcul DFT / TD-DFT. Rédaction de l'article.

Amlan K. Pal. : Conception du projet, études préliminaires, révision de l'article.

Garry S. Hanan : Supervision, conception du projet, révision de l'article.

III.2 Abstract

We have recently been exploring the coordination chemistry of strongly donating neutral bicyclic guanidyl based ligands with various d^6 metals such as Ru(II), Ir(III) and Co(III) to modulate their electronic and photophysical properties compared to the structuraly related bipyridine and terpyridine complexes. Herein, we describe Re(I) tricarbonyl complexes based on bi- and tridentate ligands consisting of one or two hexahydro-pyrimidopyrimidine (hpp) units attached to a pyridine or a pyrazine ring. The complexes have been characterized by NMR, ESI-MS, vibrational and optical spectroscopies as well as electrochemistry. Their structures were determined via single-crystal X-ray crystallography and modeled using both DFT and TD-DFT methods. The complexes are non emissive at room temperature but display emission with mixed intra ligand (major) and metal-ligand (minor) charge transfer characters at 77 K, with maxima around 480 and 580 nm for the pyridine and pyrazine based compounds, respectively.

III.3 Introduction

The photophysical properties of coordination compounds based on d^6 metal, such as Ru(II), Ir(III) and Re(I), is a vibrant area of research, especially driven by the efforts to develop better dyes for light harvesting or emitting devices. Over the past few years, our group has been studying the impact of introducing a bicyclic guanidine fragment in ligands derived from 2,2'-bipyridine and 2,2';6',2''-terpyridine, ligands classically used with d^6 metal ions. We were interested in using the 1,3,4,6,7,8-hexahydro-2H-pyrimido[1,2-a]pyrimidine (Hhpp) moiety, which has already been used to coordinate various metal ions.[1-2] For example, a methylene bridged bis(hpp) ligand, studied by Coles *et al.,* was shown to be able to accommodate multiple coordination geometries.[3-4] To prepare the targeted ligands derived from 2,2'-bipyridine and 2,2';6',2''-terpyridine, cross-coupling between halo-N-heterocycles and the Hhpp precursor proved to be an efficient method.[5-6] The hpp-pyridyl derivatives obtained were successfully used to tune the absorption and emission properties of Ru(II)[7-10] and Ir(III)[11]

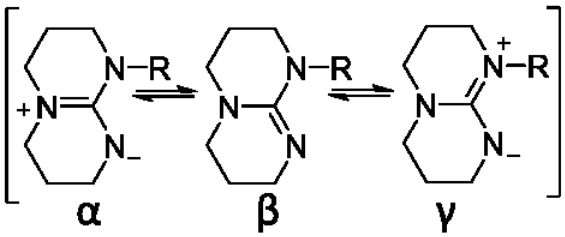

Figure III.1. Contributing resonance structures of the bicyclic hpp fragment.

photosensitizers. The partially saturated heterocycle of the Hhpp fragment, along with its resonance forms giving the coordinating nitrogen an amide character (R_2N^-), thus making these ligands strong σ and π donors (Figure III.1). This strong donation destabilizes the metal centred orbitals, leading to redshifted absorption and emission of the corresponding Ru(II) and Ir(III) complexes. The strong donating ability is accompanied by a larger bite angle due to the formation of a six-membered coordination ring *vs* five-membered in the cases of polypyridyl ligands. This difference proved to be highly beneficial in the case of bis-tridentate Ru(II) complexes where destabilization of the ligand field triplet state favours the radiative deactivation pathway. Indeed, this metal-centred triplet state (^{3}MC) is known to cause non-radiative deactivation after its thermal population.[8-9] Using this strategy, the lowest excited state of a Ru(II) complex was tuned to be lower than that of an Os(II) complex, leading to a rare example of Os(II) to Ru(II) energy transfer.[12] Furthermore, when used to chelate a Co(III) centre, hpp-based tridentate ligands led to the report of the first room temperature luminescent Co(III) complex with blue emission arising from a ligand-to-metal charge transfer excited state (LMCT) and making it a powerful oxidant used in photocatalytic trifluoromethylation.[13]

Amongst d^6 metal, the coordination chemistry of Re(I) carbonyl complexes has been the object of a tremendous amount of interest over the past decades.[14] This focus is related to the variety of fields in which these compounds can be applied. Indeed, they have been extensively used in photocatalysis,[15] especially as CO_2 reduction catalysts,[16-21] in organic light emitting diodes[22-23] and in chemical biology,[24-26] taking advantage mainly of their photophysical properties.[27-30] To fulfil the respective design criteria of these applications, numerous bi- and tridentate ligands have been developed, bidentate diimine ligands being used in the majority of the studies due to their attractive photophysical properties as evidenced by Wrighton *et al.* who identified the emissive excited state to be a metal-to-ligand charge transfer (MLCT).[27]

In order to expand the types of ligand used in the study of Re(I) coordination compounds,[31-38] we previously reported two cationic complexes based on 2,6-bis(3,4,7,8-tetrahydro-2H-pyrimido[1,2-a]pyrimidin-1(6H)-yl)pyridine (**III-L3**) and 2,6-bis(3,4,7,8-tetrahydro-2H-pyrimido [1,2-a]pyrimidin-1(6H)-yl)pyrazine (**III-L4**). In these complexes, the tridentate ligands adopt the less common facial configuration[39-41] due to the increased flexibility of the ligand.[42] The strong donation from the two hpp fragments causes a substantial decrease of the

Re(I) oxidation potential while the reduction potential depends on the nature of the unsaturated N-heterocycle, opening the possibility to tune oxidation and reduction of the complex separately. Motivated by these initial results, we report herein the complexes based on the mono-hpp ligand, namely 1-(pyridin-2-yl)-1,3,4,6,7,8-hexahydro-2H-pyrimido[1,2-a] pyrimidine (**III-L1**) and 1-(pyrazin-2-yl)-1,3,4,6,7,8-hexahydro-2H-pyrimido[1,2-a]pyrimidine (**III-L2**) in order to further study the impact of varied donation strength on the metal centred states and the related changes in electronic and photophysical properties of the Re(I) complexes.

III.3 Experimental section

III.3.1 Materials

$Re_2(CO)_{10}$ was obtained from Pressure Chemical and converted to $Re(CO)_5Br$ via titration with bromine.[43] Solvents were of ACS or spectroscopic grade (for absorption and emission measurements) and used as received, like other reagents, from commercial sources (Millipore Sigma or Fisher Scientific). Acetonitrile for electrochemistry was distilled from CaH_2 and stored under N_2.

III.3.2 Physical measurements

^1H and ^{13}C NMR spectra were acquired on a Bruker AV400 (400 MHz). Chemical shifts are reported in part per million (ppm) relative to the residual proton (7.26 ppm for $CDCl_3$, 2.50 ppm for DMSO-d^6) or carbon resonances (77.16 ppm for $CDCl_3$, 39.52 ppm for DMSO-d^6) of the solvent. All photophysical measurements were carried out in deaerated solutions (acetonitrile). Absorption spectra were measured on an Agilent Cary6000i UV-Vis-NIR spectrophotometer and luminescence spectra at room temperature and 77 K on a Perkin-Elmer LS55 fluorescence spectrometer. Infra-red vibration spectroscopy measurements were conducted on a Perkin-Elmer Spectrum2 in ATR mode. Electrochemical measurements involved a three-electrode set-up with a glassy carbon disk (d = 3 mm) working electrode, a platinum coil as counter electrode and a platinum wire as pseudo-reference. Measurements were made using a SP-50 BioLogic potentiostat interfaced to a computer equipped with the EC-lab software V11.21. The potentials were referenced internally using the ferrocenium/ferrocene couple in acetonitrile (0.40 V *vs.*

SCE).[44] The concentration of analyte was approximatively 1 mM while the supporting electrolyte (tetrabutylammonium hexafluorophosphate TBAP) was at 0.1 M.

III.3.3 Computational studies

The singlet ground state geometries of ligands and complexes were optimized by DFT method with the PBE0 hybrid functional[45] without symmetry constraints using Gaussian16 Rev. B01.[46] The lowest triplet excited state T_1 geometries were also optimized in the case of the complexes. All elements were assigned the LANL2DZ basis set.[47-49] Frequency calculations were performed to ensure that local minima had been reached. The absorption and emission properties were modelled by time dependent DFT (TD-DFT). All calculations were made for acetonitrile solution using a conductor-like polarizable continuum model (CPCM).[50] The results were visualized and tabulated using Gaussview6.0, GaussSum3.0[51] and Chemissian4.53.[52]

III.3.4 Crystallographic studies

Crystals suitable for X-ray diffraction analysis were obtained by slow evaporation of concentrated solution of each complex in acetone. The crystals were mounted on a glass fiber loop and datasets were collected with a Bruker Venture Metaljet diffractometer using Ga-Kα radiation (λ = 1.34139 Å) and equipped with a Photon 100 CMOS Detector, a Helios MX optics and a Kappa goniometer. The crystal-to-detector distance was 4.0 cm, and the data collection was carried out in 1024 x 1024 pixel mode. The temperature was set at 150 K using an Oxford Cryosystem liquid N_2 device. The cell parameters were determined from reflections taken from three sets of omega scans (104 frames, 1° per frame) using the APEX3 software package.[53] Data reduction was performed with SAINT, adsorption correction with SADABS. The structures were solved by intrinsic phasing via SHELXT[54] in OLEX2.[55] The non-H atoms were refined using weighted full-matrix least-squares on F^2. The H-atoms were included in calculated positions and treated as riding atoms (SHELXL) [56] Figures were prepared using OLEX2 or Mercury.[57] Additional refinement details are available in the corresponding section of Chapter X.

III.3.5 Synthesis

The two newly prepared neutral complexes **III-C1** and **III-C2** were obtained in excellent yield following literature procedures using ligands **III-L1** and **III-L2**, respectively (details in Chapter X).[58]

III-C1 *fac*-[Re(CO)$_3$(L$_1$)Br] beige powder, yield = 93% on a 0.5 mmol scale ; ^{1}H NMR (400 MHz, $CDCl_3$) δ 8.99 (dd, J = 2 Hz, 1H), 7.85 (m, 1H), 7.21 (d, J = 8 Hz, 1H), 7.15 (m, 1H), 3.97 (dt, J= 14, 4 Hz, 1H), 3.84 (m, 1H), 3.73 (m, 2H), 3.54 – 3.37 (m, 3H), 3.30 – 3.20 (m, 1H), 2.30 (m, 2H), 2.06 – 1.85 (m, 2H) ; ^{13}C NMR (101 MHz, DMSO-d^6) δ 198.17, 196.87, 192.64, 154.75, 153.29, 153.02, 141.15, 120.94, 115.56, 51.09, 48.20, 48.06, 46.30, 22.03, 21.68 ; ESI-MS (CH_3CN): $[M\text{-}Br]^+$ calc. for $C_{15}H_{16}N_4O_3Re$ 487.0780, found 487.0834 ; IR-ATR ν_{CO} (cm^{-1}) : 2009, 1860 ; Elemental analysis calc. (%) for $C_{15}H_{16}N_4O_3ReBr$, $(C_7H_8)_{0.1}$: C 32.76, H 2.94, N 9.73; found: C 32.45, H 2.95, N 9.76.

III-C2 *fac*-[Re(CO)$_3$(L$_2$)Br] yellow powder, yield = 94% on a 0.5 mmol scale ; ^{1}H NMR (400 MHz, $CDCl_3$) δ 8.89 (dd, J= 3, 1 Hz, 1H), 8.62 (d, J = 1 Hz, 1H), 8.38 (d, J= 3 Hz, 1H), 4.07 (dt, J= 14, 4 Hz, 1H), 3.84 (m, 2H), 3.71 (m, 1H), 3.49 (m, 3H), 3.30 (m, 1H), 2.37 (m, 2H), 1.95 (m, 2H) ; ^{13}C NMR (101 MHz, DMSO-d^6) δ 198.04, 196.10, 192.11, 152.83, 150.31, 145.41, 140.27, 139.11, 51.43, 48.32, 48.12, 46.12, 22.06, 21.68 ; ESI-MS (CH_3CN): $[M\text{-}Br]^+$ calc. for $C_{14}H_{15}N_5O_3Re$ 488.0732, found 488.0724. ; IR-ATR ν_{CO} (cm^{-1}) : 2006, 1868 ; Elemental analysis calc. (%) for $C_{14}H_{15}N_5O_3ReBr$: C 29.64, H 2.66, N 12.34; found: C 29.89, H 2.68, N 12.23.

III.4 Results and discussion

III.4.1 Synthesis and structural characterization

The hpp bearing ligands **III-L1-L4** were prepared following published procedures.[5] The hpp fragments are introduced either by Pd-catalyzed coupling between the suitable halide substituted N-heterocycle and 1,3,4,6,7,8-hexahydro-2H-pyrimido[1,2-a] pyrimidine (Hhpp) or by direct reaction with halogenated precursors. Their identities and purities were confirmed by ESI-MS and ^{1}H NMR. The expected number of resonances is observed in each case by ^{1}H NMR (see experimental section of Chapter X), the aromatic region showing only signals from the

N-heterocycles. The protons of each CH_2 groups are equivalent in NMR time scale, due to pseudorotation in the free ligands. By ESI-MS, they were all observed as mono-protonated species.

The complexes were then prepared following standard procedures for neutral diimine tricarbonyl rhenium(I) halide complex in excellent yield using the corresponding ligand (Figure III.2).[58] Under these conditions, when using **III-L3** and **III-L4**, the cationic complexes **III-C3** and **III-C4** are obtained after autoionization of the bromide ligand. Their ^{1}H NMR spectra matched the literature report (see experimental section of Chapter X).[42] Their identity was also confirmed by ESI-MS. For the new neutral complexes, **III-C1** and **III-C2**, their purity and identity were confirmed by ^{1}H, ^{13}C NMR, ESI-MS and elemental analysis. In the ^{1}H NMR spectra of the complexes (Fig. X.1, X.3), the methylene protons become inequivalent on the NMR time scale and their resonances are less resolved due to overlap and additional coupling. This is due to the different environment for the protons facing either bromide or carbonyl ligand. Looking at the ^{13}C NMR of **III-C1** and **III-C2** (Fig. X.2, X.4), three distinct resonances for the carbonyls are observed, at 198.2, 196.9, 192.6 and 198.0, 196.1 and 192.1 ppm, respectively. While all the complexes studied here have the CO ligands in a facial configuration, the facial coordination of **III-L3** and **III-L4** leads to one resonance for the three equivalent CO at 197.4 and 197.2 ppm, in **III-C3** and **III-C4**, respectively. No clear indication of increased electron richness of the complexes bearing an additional strongly donating hpp moieties can be observed from these values.

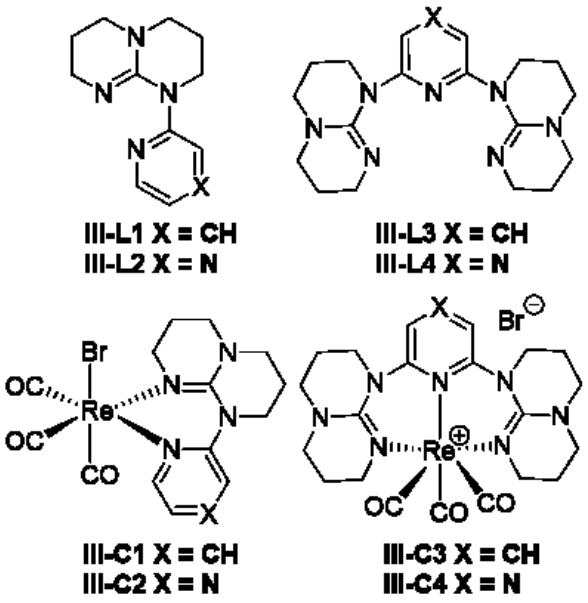

Figure III.2. Structures of the ligands **III-L1-L4** and complexes **III-C1-C4** studied.

A similar conclusion comes from the IR measurements conducted in the solid state. Both neutral and cationic complexes exhibit similar wavenumbers for the symmetric vibration mode, around 2009 cm^{-1} for **III-C1**/**C2** and 2004 cm^{-1} for **III-C3**/**C4**, implying that replacement of a π donating bromide by a stronger σ and π donating hpp fragment does not lead to a substantial

increase in backdonation from the rhenium centre to the carbonyls. Regarding the asymmetric modes, they appeared as one broad signal at 1860 and 1868 cm^{-1} for **III-C1** and **III-C2**, respectively, against two bands at 1895, 1867 cm^{-1} for **III-C3** and 1901, 1872 cm^{-1} for **III-C4**. The DFT models (PBE0/LANL2DZ, with acetonitrile continuum via CPCM) gave similar indications, the values being presented in Table X.5. A slight trend can however be seen in both experimental and theoretical values, with the vibrational frequencies of the complexes bearing the less electron donating pyrazine ring having slightly higher wavenumbers than those of pyridine analogues.

Further information was obtained by looking at the structural parameters from the crystal structures of the complexes. Single crystals suitable for diffraction analysis were obtained for both complexes [see corresponding section of Chapter X, Tables X.1 and X.2 for refinement details]. Both **III-C1** and **III-C2** crystallized in the $P2_1/n$ space group, but the cell content differed with two enantiomers present in the asymmetric unit of **III-C1** against one for **III-C2** (Fig. 1). The only observed intermolecular interactions are weak hydrogen bonds (Fig. X.7, X.8). The structures of **III-C3** and **III-C4** were obtained previously, both crystallizing in the P-1 space group.[42] This allowed us to compare the coordination environment of the rhenium centre with the different ligands (Table X.3). The bond length and angles were also compared to those in $[Re(CO)_3(bpy)Br]$, although the reported dataset is affected by positional disorder or the bromide,[59] and to $[Re(dqp)(CO)_3]^+$ (where dqp is 2,6-bis(8′-quinolinyl)pyridine).[39] In all cases, the rhenium is in a distorted octahedral coordination environment, the main distortion being caused by the restricted bite angle of the chelate ligand. The bpy ligand

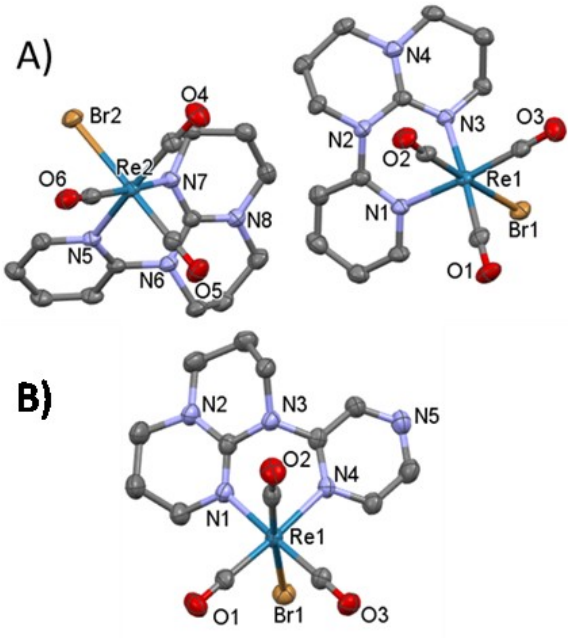

Figure III.3. Ellipsoid representation of the content of the asymmetric unit of (A) **III-C1** with two enantiomers and (B) **III-C2** with one of the enantiomer (50% probability, H atoms omitted for clarity).

has the smallest bite angle, around 75°, followed by **III-L1** (77°), **III-L3** and **III-L4** (78-79°), **III-L2** (80°) and finally dqp (82°). This range of bite angle is quite narrow considering that the bpy ligand forms a 5-membered coordination ring as oppose to the 6-membered ring formed by dqp and the hpp based ligands. The trend in bite angle follows the one observed in Ru(II) complexes,[9] although with smaller angles in all cases.

Carbonyl ligands are commonly used as probes for the electron donation of ligands. As seen in the vibrational and NMR spectroscopic data, there is no indication of increased backdonation in the presence of the hpp based ligands as no major differences in bond lengths are observed. The only bond showing significant variation is the Re-Br bond, with appears elongated in **III-C1** and **III-C2** compared to that in [$Re(CO)_3$(bpy)Br], with bond distances of 2.63(1), 2.65(1) and 2.58(1) Å, respectively. This elongation may reflect the increased donation to the metal by the hpp ligands, reducing the strength of the σ donation from the bromide. This would also make the bromide more prone to decoordination upon change in the electron density of the complex. The DFT optimized geometries agree with the crystallographic values (Table X.6).

The C-N bond lengths within the guanidine system were then analysed to estimate the weight of the resonance forms in Scheme 1. We thus looked at the values for our complexes and compared them to those in **III-L3** and the protonated form of **III-L1** as their structures have been previously reported (Fig. X.9 and Table X.4).[8,60] In the crystal structure of **III-L3**, the C=N double bonds appear localized, with a bond length around 1.27 Å in both hpp fragments, giving a large weight to the β form presented in Scheme 1. In the protonated form of **III-L1**, however, all three C-N bonds have bond lengths in the expected range for a guanidinium cation,[61] around 1.33 Å. The bond involving the nitrogen connected to the pyridine is, however, slightly longer, at 1.37 Å, which can be explained by the proximity of the electron withdrawing pyridine, disfavouring the γ form. In all four complexes, the bond pattern is similar with a double bond character to the three C-N bonds of the hpp moiety. The coordinated nitrogen has the shortest C-N bond, around 1.31 Å, followed by the one in the aliphatic backbone with C-N bond length around 1.34-1.35 Å, while the nitrogen attached to the N-heterocycle has, as expected, the longest C-N bond. This bond is elongated compared to that in the guanidinium salt (1.38-1.41 *vs.* 1.37 Å), since the N-heterocycle is now more electron withdrawing as it is donating part of its density to the rhenium centre. Finally, the angles between the plane of the pyridyl ring and

the planar {CN_3} core of the guanidyl moiety were compared (Table X.4) and showed torsion angles of 47 to 57° which suggest limited conjugation between guanidyl and N-heterocycle. In the case of the protonated ligand, the angle is reduced as the pyridine gets involved in stabilizing the proton. Complex **III-C2** stands out with the lowest torsion, possibly being affected by the H-bonding involving the pyrazine in its intermolecular arrangement (Fig. X.8).

III.4.2 Electrochemical properties

Based on the structural characterization, the nature of the N-heterocycle, along with the overall charge of the complex, should be the main factor differentiating complexes regarding their electronic and photophysical properties. Before analysing the complexes properties to test this hypothesis, we decided to characterize the ligands, as our previous study of **III-C3** and **III-C4** indicated important contribution of ligand centred energy levels on the electronic and photophysical properties of the complexes.[42] Electrochemical characterization of the ligands in acetonitrile, using cyclic voltammetry (Table 1), shows that the bis(hpp) ligands **III-L3** and **III-L4** are almost 300 mV easier to oxidize than the mono-hpp ones. Ligand **III-L2** appears harder to oxidize compared to **III-L1**, as would be expected for the more electron withdrawing pyrazine ring, although the potential of **III-L2** is approximative due to complication in the electrochemical measurement, i.e. adsorption on the electrode during the analysis. The difference in potentials reflects, however, the value predicted by the DFT calculations, indicating the oxidations are mainly centred on the hpp unit. In the case of the bis(hpp) ligand, two successive mono-electronic oxidations are observed, indicating there is some communication between the two hpp fragments via the N-heterocycle, in agreement with the calculated HOMOs. No clear reductions were observed for the ligands.

Cyclic voltammetry of the complexes (Fig. X.10, X.11) showed the expected effect of the nature of the N-heterocycle. Indeed, the pyridyl-based complexes present a reduction around -2 V *vs.* SCE while the pyrazine ones are anodically shifted by 500 mV due to the increased electron withdrawing nature of the N-heterocycle. The first oxidations match the ligand oxidations, indicating ligand centred processes. Surprisingly, the ligands appear easier to oxidize within the complexes, potentially due to the enhanced delocalization of the π bonding orbital in the hpp core after coordination as discussed in the crystallographic section.

The third oxidation, centred on the Re(I), are reversible in the case of the cationic complexes **III-C3** and **C4**. The attribution based on comparison with the ligands properties agrees with our DFT models (Tables X.17, X.18), with major hpp contributions to the HOMO and HOMO-1 while the HOMO-2 is centred on the {$Re(CO)_3$} core. In **III-C1** and **III-C2**, the situation is different (Tables X.15, X.16) with the HOMO being mainly hpp centred and the HOMO-1 corresponding to the antibonding π-donation interaction with the bromide. This oxidation is known to cause loss of the halide. Indeed, the third oxidation, appearing bielectronic, corresponds to the dimeric by-product formed after loss of the bromide as described by Bullock *et al.* for Re(I) tricarbonyl bipyridine halide complexes.[62] Compared to $[Re(bpy)(CO)_3(py)]^+$, the Re centre is easier to oxidize by around 300 mV in all our complexes, as expected due to the strong donation of the ligands. However, it is easier to oxidize the Re centre in $[Re(bpy)(CO)_3Br]$ than in **III-C1** and **III-C2**. The presence of a ligand centred oxidation taking place before oxidation of a Re centre may cause it to be anodically shifted.

Table III.1. Redox potentials of ligands and complexes in acetonitrile, 0.1 M $TBAPF_6$, measured against ferrocene as internal standard.

Compound	E_{ox} (V *vs* SCE)	E_{red} (V *vs* SCE)
III-L1	1.04[a]	-
III-L2	≈1.2[b]	-
III-L3[c]	0.77[a], 1.11(308)	-
III-L4[c]	0.77[a], 1.14(189)	-
III-C1	1.09[a], 1.42[a],1.94[d]	-2.05[e]
III-C2	1.11[a], 1.42[a], 1.96[d]	-1.52[e]
III-C3[c]	0.73[a], 1.08(80),1.43(100)	-1.99[e]
III-C4[c]	0.72[a], 1.09(82),1.43(80)	-1.49(73)
$[Re(bpy)(CO)_3Br]$[f]	1.36, 1.78	-
$[Re(bpy)(Py)(CO)_3]^+$[g]	1.74	-1.09, -1.39

[a] irreversible, anodic value reported; [b] adsorption at the electrode; [c] ref. 42; [d] two electron wave; [e] quasi-reversible; [f] ref. 63; [g] ref. 34

III.4.3 Photophysical properties

Based on the electrochemical data, we expected important contributions of the ligand centred transitions to the optical properties of our complexes. Thus, the absorption and emission spectra of the ligands were collected in dearated acetonitrile (Fig. 2). They only absorb in the UV region,

with the expected red-shifted absorption for the pyrazine-based species compared to the pyridine ones, with a shift of around 30 nm. Based on the TD-DFT models, the absorption bands below 280 nm are intra-ligand charge transfer (ILCT) with electron density transferred from the hpp to the heterocycle (Fig. X.12-15 and Tables X.11-14). The emissions are attributed to the expected ^{3}ILCT, as confirmed by the increased intensity after degassing the samples. The pyridine-based ligands have identical emission profiles, with a broad band centred at 351 nm, while the pyrazine ones have redshifted emission (with maxima at 391 and 398 nm, for **III-L2** and **III-L4**, respectively (Table 2). The emission spectra of **L4** had to be recorded at lower excitation wavelength as there is overlap between its absorption and emission profile. While we did not evaluate the respective quantum yields of the compounds, the solutions were of similar absorbances (around 0.05), where **III-L4** appears to have a weaker emission compared to the other ligands, and **III-L2** is the strongest emitter.

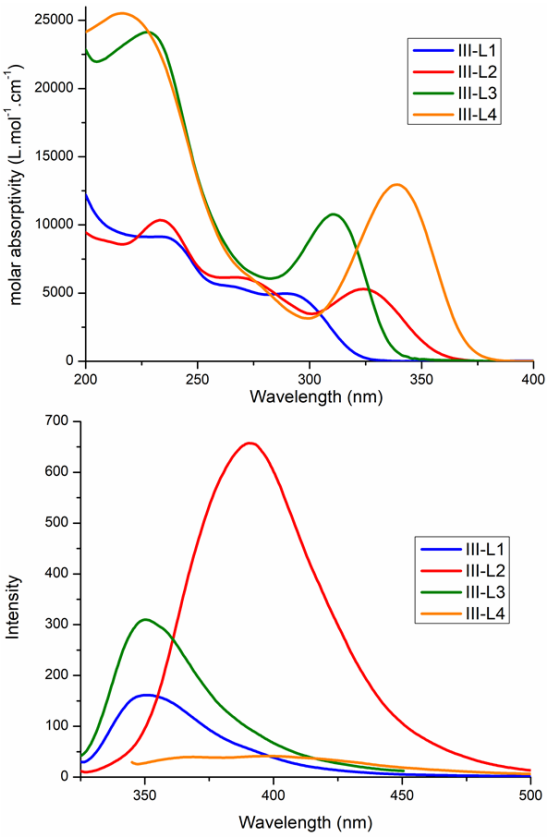

Figure III.4 Absorption (top) and emission (bottom) spectra of the ligands in deaerated acetonitrile at room temperature. (λexc = 310 nm for **III-L1 - III-L3**, 330 nm for **III-L4**)

The absorption and emission spectra of the complexes were then measured at room temperature in deaerated acetonitrile (Fig. 3, Table 2). There is an overall redshift of around 30 nm for the lowest energy absorption of all complexes compared to those of the ligands, as expected for Re(I) complexes. Complexation of the metal ion is expected to introduce additional metal-to-ligand charge-transfer (MLCT) character to the lower energy transitions. According to the TD-DFT calculations, there is indeed some MLCT contribution, but the transitions remain mostly ILCT in character (Fig. X.16-19 and Tables X.19-23).

In degassed acetonitrile at room temperature, no clear emission of **III-C1-C4** could be observed in the expected region for emission with MLCT or mixed ILCT/MLCT character as typically observed in Re(I) complexes.[14] Extremely weak or completely absent emission at room temperature is not unprecedented in Re(I) chemistry and examples involving various ligand structures have been reported.[63-66]

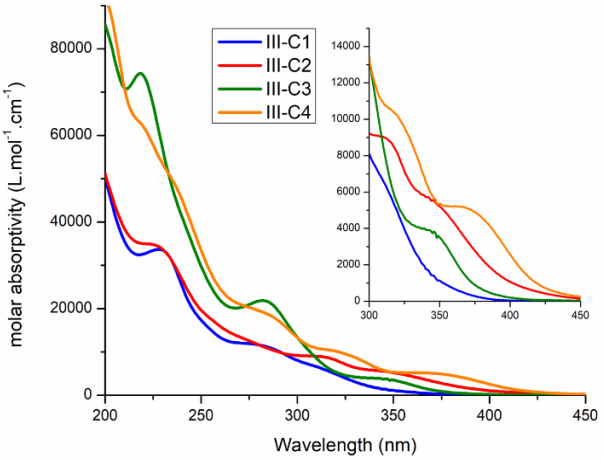

Figure III.5 Absorption profiles of the complexes in deaerated acetonitrile at room temperature

Table III.2 Photophysical data in degassed acetonitrile at room temperature unless stated otherwise.

Compound	λ_{abs} nm(ε x10^3 L mol^{-1} cm^{-1})	λ_{em} nm
III-L1	233 (9.2), 266 (5.6), 289 (5.0)	351
III-L2	234 (10), 265 (6.1), 324 (5.3)	391
III-L3	229 (24), 310 (11)	351
III-L4	218 (25), 339 (13)	398
III-C1[a]	228 (34), 280 (12), 311 (6.4, sh)	484
III-C2[a]	226 (35), 314 (9.0), 350 (5.2, sh)	586
III-C3[a]	218 (74), 282 (22), 349 (3.7)	488
III-C4[a]	220 (62), 284 (19), 324 (9.9), 370 (5.2)	572
[Re(bpy)(CO)$_3$Br][b]	370	575
[Re(bpy)(CO)$_3$(py)]$^{+}$[c]	366 (2.4)	558
Re(dqp)(CO)$_3$]$^{+}$[d]	340 (22)	606

[a] emission at 77 K in dearated acetonitrile; [b] ref. 19; [c] ref. 34; [d] ref. 39

Several quenching mechanisms are possible such as strong vibrational coupling, low lying ligand field state or even intramolecular electron transfer.[30] In order to get additional insight into the excited states, we measured the emission spectra at 77 K in deaerated acetonitrile (Fig. 4). The spectra are reminiscent of the ligand emission spectra, except for **III-C2** that presents a structured emission. This points to major ^{3}ILCT character of the emission in each case, as proposed in our TD-DFT models. The observed trend of emission energy maxima also follows

the one observed in the DFT models (Table X19) with **III-C1** and **III-C3** having similar emission energy and **III-C4** emitting at slightly higher energy than **III-C2**. This result is in good agreement with the trend observed in the lowest energy adsorption maxima of complexes **III-C1-C4**. By having a further look at the calculated triplet manifold of our complexes, we observed transition possibly responsible for the room temperature quenching. Indeed, aside from the mixed charge transfer MLCT/ILCT/LLCT (ligand to ligand charge transfer, from the CO or the bromide to the N^N ligand) transitions, there are some π→π* transitions involving the heterocycle as well as Re(I)→CO π* MLCT transitions located around the absorption maxima of the compounds, such as the $S_0 \rightarrow T_3$ transition in **III-C1** (Table S20). Intermolecular interactions should also be considered as we observed intermolecular H-bonding involving the pyrazine ring in **III-C2**. We have no definitive explanation for the lack of emission at room temperature, although several potentials causes have been identified.

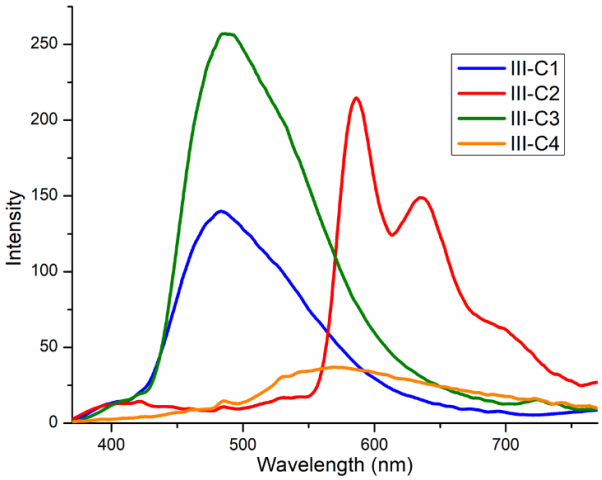

Figure III.6 Emission spectra at 77 K in deaerated acetonitrile of the hpp-based Re(I) complexes **III-C1-C4** (λexc = 330 nm).

III.5 Conclusions

Two new Re(I) carbonyl complexes based on the bicyclic guanidyl hpp moiety attached to a pyridyl or a pyrazine ring have been prepared through two simple steps with excellent yields. Their electrochemical and photophysical properties were compared to the previously reported complexes based on tridentate bis(hpp)-heterocycle ligands adopting a facial configuration in the Re(I) complexes. Structural investigation showed little evidence of the expected impact of having one or two hpp moieties, unlike the observed trend in Ru(II) complexes.[9] In all cases the electrochemical and photophysical properties appeared to be dictated by the ligands, the coordination leading to easier ligand-centred reduction due to decreased electron density after donation to the metal centre and redshifted emission due to additional minor MLCT character.

Based on the easy access to multiple derivatives for this class of ligands and the various handles available to further tune the complexes properties, such as exchanging the bromide for other axial ligands, we are currently exploring strategies to lower the MLCT energy in order to decrease the coupling between ILCT and MLCT states.

III.6 References

1. M. P. Coles, *Chem. Commun.*, 2009, 3659-3676.
2. J. F. Berry, F. Albert Cotton, P. Huang and C. A. Murillo, *Dalton Trans.*, 2003, 1218-1219.
3. S. H. Oakley, M. P. Coles and P. B. Hitchcock, *Inorg. Chem.*, 2004, **43**, 7564-7566.
4. M. P. Coles, M. S. Khalaf and P. B. Hitchcock, *Inorg. Chim. Acta*, 2014, **422**, 228-234.
5. A. K. Pal, P. K. Mandali, D. K. Chand and G. S. Hanan, *Synlett*, 2015, **26**, 1408-1412.
6. J. E. Allen, W. S. Kassel and N. A. Piro, *Polyhedron*, 2018, **155**, 77-84.
7. S. Nag, J. G. Ferreira, L. Chenneberg, P. D. Ducharme, G. S. Hanan, G. La Ganga, S. Serroni and S. Campagna, *Inorg. Chem.*, 2011, **50**, 7-9.
8. A. K. Pal, S. Serroni, N. Zaccheroni, S. Campagna and G. S. Hanan, *Chem. Sci.*, 2014, **5**, 4800-4811.
9. B. Laramee-Milette and G. S. Hanan, *Dalton Trans.*, 2016, **45**, 12507-12517.
10. A. K. Pal and V. N. K. B. Adusumalli, *New J. Chem.*, 2019, **43**, 14669-14673.
11. K. Hasan, A. K. Pal, T. Auvray, E. Zysman-Colman and G. S. Hanan, *Chem. Commun.*, 2015, **51**, 14060-14063.
12. B. Laramee-Milette and G. S. Hanan, *Chem. Commun.*, 2017, **53**, 10496-10499.
13. A. K. Pal, C. Li, G. S. Hanan and E. Zysman-Colman, *Angew. Chem. Int. Ed.*, 2018, **57**, 8027-8031.
14. R. A. Kirgan, B. P. Sullivan and D. P. Rillema, in *Photochemistry and Photophysics of Coordination Compounds II*, eds. V. Balzani and S. Campagna, Springer Berlin Heidelberg, Berlin, Heidelberg, 2007, pp. 45-100.
15. A. Zarkadoulas, E. Koutsouri, C. Kefalidi and C. A. Mitsopoulou, *Coord. Chem. Rev.*, 2015, **304**, 55-72.
16. J. Hawecker, J.-M. Lehn and R. Ziessel, *J. Chem. Soc., Chem. Commun.*, 1983, 536-538.
17. J. Hawecker, J.-M. Lehn and R. Ziessel, *J. Chem. Soc., Chem. Commun.*, 1984, 328-330.

18. B. P. Sullivan, C. M. Bolinger, D. Conrad, W. J. Vining and T. J. Meyer, *J. Chem. Soc., Chem. Commun.*, 1985, 1414-1416.

19. P. Kurz, B. Probst, B. Spingler and R. Alberto, *Eur. J. Inorg. Chem.*, 2006, **2006**, 2966-2974.

20. Y. Kuramochi, O. Ishitani and H. Ishida, *Coord. Chem. Rev.*, 2018, **373**, 333-356.

21. H. Takeda, K. Koike, H. Inoue and O. Ishitani, *J. Am. Chem. Soc.*, 2008, **130**, 2023-2031.

22. W. K. Chu, C. C. Ko, K. C. Chan, S. M. Yiu, F. L. Wong, C. S. Lee and V. A. L. Roy, *Chem. Mater.*, 2014, **26**, 2544-2550.

23. T. Klemens, A. Switlicka-Olszewska, B. Machura, M. Grucela, E. Schab-Balcerzak, K. Smolarek, S. Mackowski, A. Szlapa, S. Kula, S. Krompiec, P. Lodowski and A. Chrobok, *Dalton Trans.*, 2016, **45**, 1746-1762.

24. S. Hostachy, C. Policar and N. Delsuc, *Coord. Chem. Rev.*, 2017, **351**, 172-188.

25. L. C. Lee, K. K. Leung and K. K. Lo, *Dalton Trans.*, 2017, **46**, 16357-16380.

26. N. Manav, P. E. Kesavan, M. Ishida, S. Mori, Y. Yasutake, S. Fukatsu, H. Furuta and I. Gupta, *Dalton Trans.*, 2019, **48**, 2467-2478.

27. M. Wrighton and D. L. Morse, *J. Am. Chem. Soc.*, 1974, **96**, 998-1003.

28. J. C. Luong, L. Nadjo and M. S. Wrighton, *J. Am. Chem. Soc.*, 1978, **100**, 5790-5795.

29. J. V. Caspar and T. J. Meyer, *J. Phys. Chem.*, 1983, **87**, 952-957.

30. A. Vogler and H. Kunkely, *Coord. Chem. Rev.*, 2000, **200**, 991-1008.

31. C. B. Anderson, A. B. S. Elliott, C. J. McAdam, K. C. Gordon and J. D. Crowley, *Organometallics*, 2013, **32**, 788-797.

32. A. J. Huckaba, E. A. Sharpe and J. H. Delcamp, *Inorg. Chem.*, 2016, **55**, 682-690.

33. T. Mukuta, P. V. Simpson, J. G. Vaughan, B. W. Skelton, S. Stagni, M. Massi, K. Koike, O. Ishitani and K. Onda, *Inorg. Chem.*, 2017, **56**, 3404-3413.

34. L. Sacksteder, A. P. Zipp, E. A. Brown, J. Streich, J. N. Demas and B. A. Degraff, *Inorg. Chem.*, 1990, **29**, 4335-4340.

35. J. G. Vaughan, B. L. Reid, S. Ramchandani, P. J. Wright, S. Muzzioli, B. W. Skelton, P. Raiteri, D. H. Brown, S. Stagni and M. Massi, *Dalton Trans.*, 2013, **42**, 14100-14114.

36. V. W.-W. Yam, V. C.-Y. Lau and K.-K. Cheung, *Organometallics*, 1996, **15**, 1740-1744.

37. B. Laramee-Milette, N. Zaccheroni, F. Palomba and G. S. Hanan, *Chem. Eur. J.*, 2017, **23**, 6370-6379.

38. C. B. Larsen and O. S. Wenger, *Inorg. Chem.*, 2018, **57**, 2965-2968.

39. D. J. Losey, B. A. Frenzel, W. M. Smith, S. E. Hightower and C. G. Hamaker, *Inorg. Chem. Commun.*, 2013, **30**, 46-48.

40. P. A. Anderson, F. R. Keene, E. Horn and E. R. T. Tiekink, *Appl. Organomet. Chem.*, 1990, **4**, 523-533.

41. D. L. Reger, K. J. Brown and M. D. Smith, *J. Organomet. Chem.*, 2002, **658**, 50-61.

42. A. K. Pal and G. S. Hanan, *Dalton Trans.*, 2014, **43**, 11811-11814.

43. S. P. Schmidt, W. C. Trogler and F. Basolo, *Inorg. Synth.*, 1990, **28**, 160-165.

44. N. G. Connelly and W. E. Geiger, *Chem. Rev.*, 1996, **96**, 877-910.

45. C. Adamo and V. Barone, *J. Chem. Phys.*, 1999, **110**, 6158-6170.

46. M. J. Frisch, G. W. Trucks, H. B. Schlegel, G. E. Scuseria, M. A. Robb, J. R. Cheeseman, G. Scalmani, V. Barone, G. A. Petersson, H. Nakatsuji, X. Li, M. Caricato, A. V. Marenich, J. Bloino, B. G. Janesko, R. Gomperts, B. Mennucci, H. P. Hratchian, J. V. Ortiz, A. F. Izmaylov, J. L. Sonnenberg, Williams, F. Ding, F. Lipparini, F. Egidi, J. Goings, B. Peng, A. Petrone, T. Henderson, D. Ranasinghe, V. G. Zakrzewski, J. Gao, N. Rega, G. Zheng, W. Liang, M. Hada, M. Ehara, K. Toyota, R. Fukuda, J. Hasegawa, M. Ishida, T. Nakajima, Y. Honda, O. Kitao, H. Nakai, T. Vreven, K. Throssell, J. A. Montgomery Jr., J. E. Peralta, F. Ogliaro, M. J. Bearpark, J. J. Heyd, E. N. Brothers, K. N. Kudin, V. N. Staroverov, T. A. Keith, R. Kobayashi, J. Normand, K. Raghavachari, A. P. Rendell, J. C. Burant, S. S. Iyengar, J. Tomasi, M. Cossi, J. M. Millam, M. Klene, C. Adamo, R. Cammi, J. W. Ochterski, R. L. Martin, K. Morokuma, O. Farkas, J. B. Foresman and D. J. Fox, Gaussian 16 Rev. B.01, 2016, Wallingford, CT

47. T. H. Dunning and P. J. Hay, *Modern Theoretical Chemistry III ed.*, Plenum, New York, 1977.

48. P. J. Hay and W. R. Wadt, *J. Chem. Phys.*, 1985, **82**, 299-310.

49. W. R. Wadt and P. J. Hay, *J. Chem. Phys.*, 1985, **82**, 284-298.

50. M. Cossi, N. Rega, G. Scalmani and V. Barone, *J. Comput. Chem.*, 2003, **24**, 669-681.

51. N. M. O'Boyle, A. L. Tenderholt and K. M. Langner, *J. Comput. Chem.*, 2008, **29**, 839-845.

52. S. Leonid, *V 4.53*, 2005-2017, www.chemissian.com.

53. *APEX3, SAINT, SADABS*, 2016, **Bruker AXS Inc.**

54. G. M. Sheldrick, *Acta Crystallogr., Sect. A*, 2015, **71**, 3-8.

55. O. V. Dolomanov, L. J. Bourhis, R. J. Gildea, J. A. K. Howard and H. Puschmann, *J. Appl. Crystallogr.*, 2009, **42**, 339-341.

56. G. M. Sheldrick, *Acta Crystallogr., Sect, C*, 2015, **71**, 3-8.

57. C. F. Macrae, I. J. Bruno, J. A. Chisholm, P. R. Edgington, P. McCabe, E. Pidcock, L. Rodriguez-Monge, R. Taylor, J. van de Streek and P. A. Wood, *J. Appl. Crystallogr.*, 2008, **41**, 466-470.

58. A. Juris, S. Campagna, I. Bidd, J. M. Lehn and R. Ziessel, *Inorg. Chem.*, 1988, **27**, 4007-4011.

59. R. Kia and F. Safari, *Inorg. Chim. Acta*, 2016, **453**, 357-368.

60. R. J. Schwamm, R. Vianello, A. Marsavelski, M. A. Garcia, R. M. Claramunt, I. Alkorta, J. Saame, I. Leito, C. M. Fitchett, A. J. Edwards and M. P. Coles, *J. Org. Chem.*, 2016, **81**, 7612-7625.

61. F. H. Allen, O. Kennard, D. G. Watson, L. Brammer, A. G. Orpen and R. Taylor, *J. Chem. Soc. Perk. Trans. 2*, 1987, S1.

62. J. P. Bullock, E. Carter, R. Johnson, A. T. Kennedy, S. E. Key, B. J. Kraft, D. Saxon and P. Underwood, *Inorg. Chem.*, 2008, **47**, 7880-7887.

63. N. M. Shavaleev, A. Barbieri, Z. R. Bell, M. D. Ward and F. Barigelletti, *New J. Chem.*, 2004, **28**, 398-405.

64. L. Wei, J. W. Babich, W. Ouellette and J. Zubieta, *Inorg. Chem.*, 2006, **45**, 3057-3066.

65. N. Pizarro, M. Saldías, N. Guzmán, C. Sandoval-Altamirano, S. Kahlal, J.-Y. Saillard, J.-R. Hamon and A. Vega, *New J. Chem.*, 2019, **43**, 2449-2457.

66. J. G. Vaughan, B. L. Reid, P. J. Wright, S. Ramchandani, B. W. Skelton, P. Raiteri, S. Muzzioli, D. H. Brown, S. Stagni and M. Massi, *Inorg. Chem.*, 2014, **53**, 3629-3641.

Chapitre IV. In depth study of the electronic properties of NIR emissive κ^3N terpyridine rhenium(I) dicarbonyl complexes

IV.1 Contexte et résumé

L'étude des complexes de Re(I) équipés de ligands tridentés, dérivés de 2,2';6',2''-terpyridine, fait l'objet d'un nombre limité de travaux dans la littérature. Cela peut s'expliquer par la publication en 1988 par Lehn *et al.* d'une étude de divers complexes de Re(I) où ils indiquaient que le complexe (faussement) identifié comme étant [Re(tpy)$(CO)_2$Cl] n'était pas émissif à température ambiante. Les études subséquentes rétablirent l'identité de ce complexe comme étant [Re(tpy)$(CO)_3$Cl], dans lequel le ligand tpy agit comme un ligand bidenté, indiqué par la nomenclature κ^2N. Le caractère dynamique de cette coordination fut rigoureusement étudié en utilisant la spectroscopie RMN. En 1993, Orrell *et al.* ont préparé le complexe [Re(κ^3N-tpy)$(CO)_2$Cl] par thermolyse du complexe κ^2N. Le domaine fut alors dormant pendant presque 20 ans, jusqu'aux travaux d'Hightower *et al.* sur ces mêmes dérivés κ^3N. Il y avait alors un renouveau d'intérêt pour l'étude de composés portant des ligands substitués 4'-aryle-tpy, [Re(κ^2N-4'R-tpy)$(CO)_3$Cl], porté par la communauté des dispositifs électroluminescents. À cette période, le groupe Hanan étudiait les dérivés comportant une pyridine en position 4' de la tpy pour la préparation d'assemblages discrets, bénéficiant de l'organisation prévisible de la sphère de coordination du Re(I). Étudié dans le cadre de son assemblage en carré moléculaire, le composé [Re(4'(4-py)-κ^3N-tpy)$(CO)_2$L], absorbant une large gamme du spectre visible, présenta une émission dans le proche infra-rouge.

Dans cette étude systématique, nous avons établi une relation entre structures et propriétés en étudiant une série de composés [Re(κ^xN-R'-tpy)$(CO)_y$L] avec une combinaison de mesures expérimentales (spectroscopiques et électrochimiques) et modélisation par DFT/TD-DFT. Pour cela, nous avons fait varier 1) la coordination des ligands entre les modes κ^2N et κ^3N, 2) les substituants R sur les ligands et 3) la nature du ligand axial complétant la sphère de coordination (Br^-, py ou PPh_3). Chacune de ces variations permet de moduler, avec différentes amplitudes, les propriétés photophysiques des complexes et leur émission, notamment dans l'infra-rouge.

In depth study of the electronic properties of NIR emissive κ^3N terpyridine rhenium(I) dicarbonyl complexes

Thomas Auvray,[a] Amélie Dubreuil,[a] Benedetta Del Secco,[b] Nelsi Zaccheroni,[b*] and Garry S. Hanan[a,*]

Département de Chimie, Université de Montréal, Montréal, Canada, H3T-1J4

Dipartimento di Chimica 'G. Ciamician',Università degli Studi di Bologna, Via S.Giacomo 11, 40126, Bologna, Italy

Full paper

Manuscript in preparation

Contributions :

Thomas Auvray : Conception du projet. Synthèse et caractérisation complète des composés (RMN, ESI-MS, IR, EA). Analyse des propriétés optiques et électroniques. Calcul DFT / TD-DFT. Rédaction de l'article.

Amélie Dubreuil : Synthèse et caractérisation partielle de certains complexes.

Benedetta Del Secco : Mesure d'émission dans le proche infrarouge.

Nelsi Zaccheroni : Supervision (B.D.S.), révision de l'article

Garry S. Hanan : Supervision (T.A., A.D.), révision de l'article.

IV.2 Abstract

The structure-properties relationship in a series of carbonyl rhenium(I) complexes based on substituted terpyridine ligands of general formula $[Re(\kappa^{x}N\text{-}Rtpy)(CO)_{y}L]^{n+}$ is explored by both experimental and theoretical methods. In these compounds, the terpyridines can adopt both bidentate (κ^2N) and terdentate (κ^3N) coordination modes associated with three or two carbonyls, respectively. Conversion from the κ^2N to the κ^3N coordination mode leads to large change in the absorption spectra and oxidation potentials due to destabilization of the HOMO level. The κ^3N complexes absorption profiles cover the whole visible spectra with lower maxima around 700 nm, tailing till 800 nm, while no emission is observed with Br^- as axial ligand L. When the axial ligand is modified from the native halide to pyridine or triphenylphosphine, the lowest absorption band is blueshifted by 60 and 90 nm, respectively. These cationic complexes are near-infrared emitter with emission maxima between 840-950 nm for the pyridine compounds and 780-800 nm for the triphenylphosphine ones.

IV.3 Introduction

The chemistry of rhenium(I) complexes has sparked a tremendous amount of research efforts over the past decades. Their photophysical and electrochemical properties have been thoroughly studied[1-5] and applied in a multitude of the fields such as solar energy harvesting devices[6] and solar to chemical energy conversion,[7-11] light emitting devices[12-13] as well as photodynamic therapy and cellular imaging.[14-15] While the breadth of their application is large, most of the studies regarding these complexes are following the seminal work from J.M. Lehn *et al.*[10] and T.J. Meyer *et al.*[11] who showed in the 1980's that $[Re(CO)_3(bpy)X]$ complexes (where bpy is 2,2'-bipyridine and X an halide) are able to catalyze the selective reduction of carbon dioxide into carbon monoxide either photo or electrochemically. Their photophysical properties were also applied to photocatalytic hydrogen evolution, using the Re(I) complex as photosensitizer with cobalt catalyst.[9,16] Efforts focused on tuning the photophysical properties of the complexes lead to several structural variations, either by ligand design keeping the diimine core[17-20] or introduction of other ligands such as phosphine,[21-27] N-heterocyclic carbene,[28] alcyne[29-30] or more isocyanide.[31-32] These complexes were also used as building blocks in supramolecular assemblies[33-36] and extended periodic structures.[37-38]

We recently focused on tridentate ligand-based complexes as they offer a suitable geometry for predictable assembly depending on the facial or meridional arrangement of the ligands. Others

investigated related complexes at the same time, leading to the report of several complexes with tridentate N,N,N ligand in a meridional[39-42] or facial geometry[43-44] (Figure IV.1). Interestingly, the meridionally coordinated κ^3N terpyridine and N,N,N pincer based complexes[45] proved to have extended absorption in the visible compared to their κ^2N equivalent or the facial isomers which are usually exhibiting absorption limited to the high energy visible, with some exception involving excited state mixing with other absorbing units.[46] In a recent report, Dempsey *et al.* working with a Re bipyridine complex successfully pushed its absorption to the low energy visible region, matching the κ^3N terpyridine values, by modifying the nature of the ligands completing the coordination sphere.[47]

However, to our knowledge, our report of the κ^3N terpyridine based complex $[Re(CO)_2(py)(\kappa^3N\text{-}4pytpy)]^+$ and the corresponding metallasquare (with *py* standing for pyridine and *4pytpy* for 4'(4-pyridyl)-2,2':6',2''-terpyridine) is the only case where this type of complex was shown to possess a near-infrared emission band at room temperature, with an emission maximum around 940 nm.[36] The study of the κ^2N and κ^3N terpyridine complexes has been the object of successive corrections in the literature following technological improvements of the spectrophotometer. As an example, in their initial report, Lehn *et al.* observed only emission in cryogenic condition for the κ_2N complex, which are now found to be applicable in luminescent devices.[12,17] We thus decided to investigate the effect of varying substituent and ancillary ligand on the emission of κ_3N terpyridine rhenium complexes in order to gain a better understanding of the parameters influencing their electronic properties.

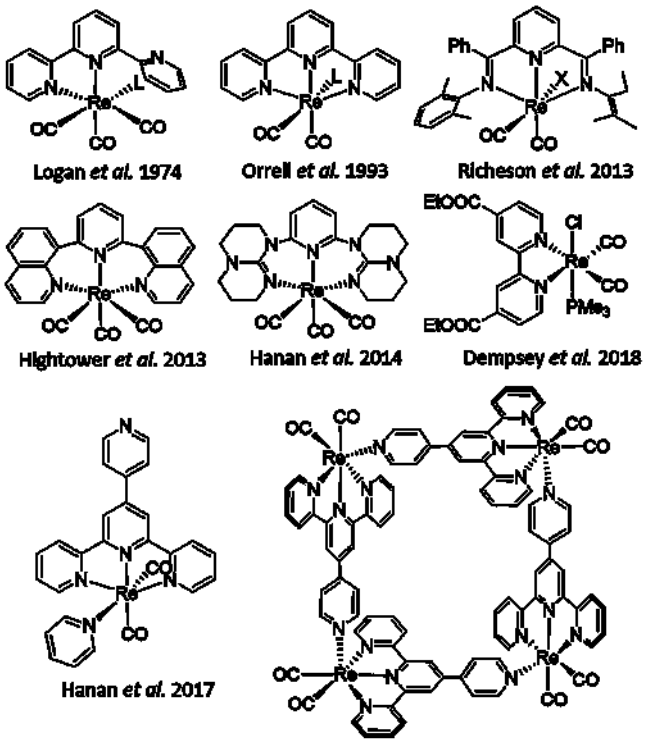

Figure IV.1. Selected rhenium complexes with either N,N,N coordination or related properties.

IV.4 Results and discussion

IV.4.1 Synthesis

We chose the terpyridine ligands presented in Figure IV.2A to study the effect of the substituent on the photophysical properties of the targeted complexes. All the ligands were prepared following literature procedures. The detailed synthesis for each compound can be found in the supplementary materials (Chapter XI).

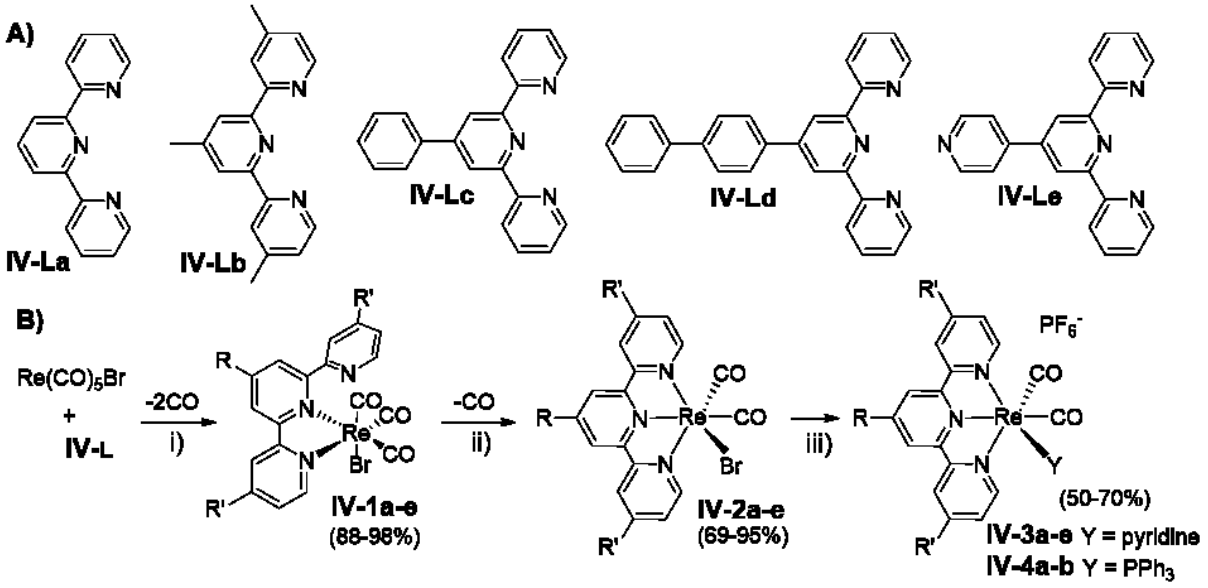

Figure IV.2. A) Selected substituted terpyridines. B) Synthethic pathways for the complexes. i) toluene, reflux, 4 h; ii) under N2, 270 °C, 6 h; iii) for **3a-e** : pyridine, AgOTf (1 eq.), reflux 5 h, $KPF_{6(aq)}$, for **4a-b** : THF, PPh_3, AgOTf (1 eq.), reflux 5 h, $KPF_{6(aq)}$

The κ^2N tpy coordinated complexes **IV-1a-e** were prepared following classical Re tricarbonyl diimine preparation procedures from $Re(CO)_5Br$ (Fig. IV.2B) in excellent yield (88-98%). The loss of a third CO is known to require harsher conditions such as UV irradiation,[48] oxido-decarbonylation[47,49] or pyrolysis.[39] The tricarbonyl complexes obtained were converted into the dicarbonyl κ^3N form **IV-2a-e** using the latter. The targeted quantity of the suitable complex **IV-1** was placed in an oven dried vial which was then sealed in a glovebox to maintain an inert atmosphere throughout the reaction. This vial was then placed in a sand bath heated to 270°C. The solids changed color as the reaction proceeded, from orange/yellow to dark brown/black. This procedure yielded the corresponding complexes **IV-2a-e** in good to excellent yield (69-

95%), but manipulation of these solids is made difficult by their tendency to stick to every surface used. Also, these solids are hygroscopic as shown by NMR and CHN analysis in which water was still observed even after careful drying. Finally, following the procedures reported by Hightower *et al*., we prepared complexes **IV-3a-e** and **IV-4a-b** by bromide abstraction with silver triflate, followed by replacement either by pyridine or triphenylphosphine. These cationic complexes were isolated in medium to good yield (50-70%) as their PF_6^- salts and purified on alumina to remove any unreacted materials or silver salt. The lower yield comes from losses in the precipitation step in water. The neutral complexes **IV-1a-e** and **IV-2a-e** have lower solubility in common solvents than the cationic complexes **IV-3a-e** and **IV-4a-b**.

IV.4.2 Structural characterization

To confirm the identity and purity of all the complexes, we used a combination of proton and carbon NMR spectroscopy, infrared (IR) spectroscopy, mass spectrometry (MS) and elemental analysis (CHN). All compounds were observed by MS as mono-cationic species presenting the typical pattern of rhenium compounds caused by its two natural isotopes ^{185}Re and ^{187}Re (with 37/63 % abundancy). The NMR spectra of complexes **IV-1a-e** are asymmetric (Fig. XI.1-5), as expected for the κ^2N coordination of the ligand which leads to no equivalent center except for the ortho and meta positions of the 4'aryl substituent in **IV-Lc-e**. In some cases, we observed splitting of signals that we ascribed to the fluxionality of such complexes. Indeed, the rhenium center can move between the two bidentate coordination sites *via* different mechanisms well documented by Orrell *et al.* and others via variable temperature NMR studies.[39,50-53] The facial geometry was confirmed by solid state IR spectroscopy where the characteristic bands for the CO vibrations were observed, the experimental and theoretical values obtained by DFT being listed in Table XI.1. No clear effect of the donor / acceptor substituent can be seen for these vibrations, with similar values for all compounds of the same family. The κ^3N coordinated complexes **IV-2a-e** obtained by pyrolysis present symmetrical NMR spectra typical for meridional terpyridine based complexes (Fig. XI.6-10). The *mer*-tpy*, cis*-CO conformation was confirmed by IR spectroscopy with the expected two bands for the CO vibrations. These bands are shifted to lower wavenumber compared to the κ^2N complexes **IV-1a-e**, from an average of 2020, 1910 and 1900 cm^{-1} to 1880 and 1800 cm^{-1} respectively. This shift is due to the back-donation from the d^6 metal center being now only shared between the two remaining carbonyl

ligands. This shift is also indicative of a somewhat more electron rich metal center, which would be easier to oxidize. The NMR spectra of **IV-3a-e** and **IV-4a-b** are like those of **IV-2a-e**, with additional peaks from the pyridine or phosphine ligand respectively. Replacing the bromide by a pyridine has moderate effect on the CO vibrations bands that are shifted to slightly higher wavenumbers ($\Delta\nu \approx 20$ cm^{-1}), a more significant shift being observed in the case of **IV-4a-b** with a triphenylphosphine ligand ($\Delta\nu \approx 40$ cm^{-1}). These variations were predicted by DFT calculations (*vide infra*) and indicate a trend in ease of oxidation, i.e. **IV-2a-e** should be easier to oxidize than **IV-3a-e**, followed by **IV-4a-b** and finally **IV-1a-e**. A similar trend was presented recently by Dempsey *et al.* on a series of Re-bipyridine compounds.[47]

IV.4.3 Computational studies

In parallel to the synthesis of the targeted compounds, we performed DFT calculations to model them using Gaussian16 rev. A03 and support our interpretation of the spectroscopic measurements. We used the hybrid PBE0 method with the LanL2DZ basis set for all atoms. All calculations were performed without symmetry constraints and the effect of the solvent (acetonitrile) was included via a conductor-like polarizable continuum (CPCM). Frequency calculations after optimization were performed to confirm that local minima had been reached and obtain theoretical vibrational values (see Table XI.1). The energy diagram presented in Fig. IV.4 allows for a simple observation of the trend predicted for the successive modifications leading to complexes **IV-1**, **IV-2**, **IV-3** or **IV-4**. The energy values for orbitals from LUMO+2 to HOMO-2 with their Mulliken population analysis are reported in Tables XI.2-18.

The conversion of **IV-1a-e** into **IV-2a-e**, i.e. from κ^2N to κ^3N coordination of the ligands, causes a significant increase in energy for the higher occupied levels, i.e. by almost 1eV. This change is expected as the replacement of a strongly π-accepting CO ligand by the weak π accepting pyridine of the terpyridine ligand should lead to destabilization of the metal centered π orbitals. In addition to the contribution from the bonding π-backdonation between rhenium and carbonyls

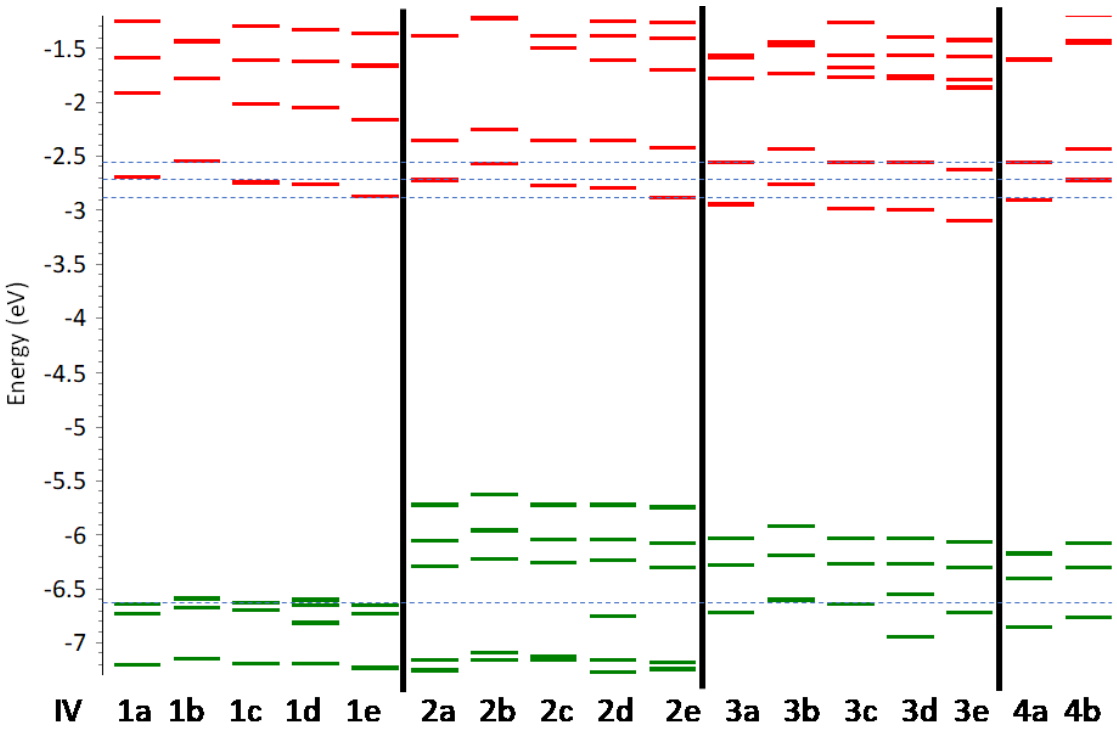

Figure IV.3 Partial energy diagram centered on frontier orbitals for all complexes modeled in an acetonitrile continuum by DFT (PBE0/LanL2DZ).

in **IV-1a-e**, the HOMO and HOMO-1 levels also have an antibonding π* character linked to the donation from the bromide (Figure IV.4). This antibonding interaction has a lower contribution in the κ^3N complexes **IV-2a-e**. This can be explained by the destabilization of the metal centered π orbital which reduces the mixing between the bonding π overlap corresponding to the retrodonation to the carbonyl and the antibonding π overlap associated with the donation from the bromide.

Considering the LUMO of **IV-1a-e** and **IV-2a-e**, almost no energy variation is observed, while the LUMO+1 are stabilized by 250 to 480 meV and the LUMO+2 destabilized to a lesser extent. These changes result from the increased conjugation of the terpyridine once in its meridional coordination mode. The LUMO of complexes **IV-1a-e** is delocalized over the coordinated bipyridine-like moiety and the increase in conjugation does not really affect its energy while the LUMO+1 and LUMO+2 involve individual pyridine rings and the extended conjugation modifies their relative energies. Going from the neutral **IV-2a-e** to the cationic complexes **IV-3a-e** and **IV-4a-b** leads to an overall stabilization by several hundred meV, , with a stronger

impact on the occupied levels from the σ-donating triphenylphosphine in **IV-4a-b** compared to the pyridine in **IV-3a-e**.

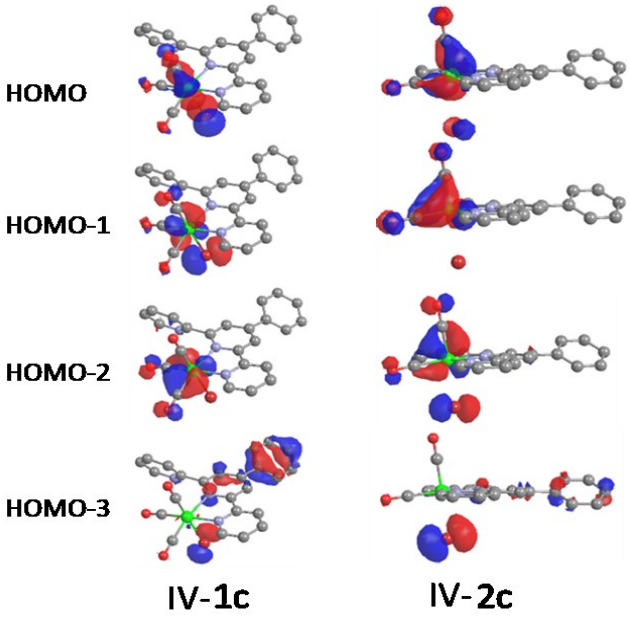

Figure IV.4. Selected molecular orbitals (isovalue 0.05 e/Å^3) for complexes **IV-1c** and **IV-2c** (top to bottom: HOMO to HOMO-3)

The different substituents introduced on the terpyridine ligand appear, however, to have a minor effect on the energy level as observed in Figure IV.3. The larger effect comes from trimethyl substituted ligand **IV-Lb**, a stronger donor, resulting in a general destabilization of all orbitals for the corresponding complexes. In the case of the phenyl (**IV-Lc**) or biphenyl (**IV-Ld**) substituent on the 4' position, they caused only a slight stabilization of the LUMO compared to the parent compound. Interestingly, however, **IV-Ld** based complexes exhibit significant contribution of the biphenyl in the HOMO-2 level of all complex and the HOMO in **IV-1d**. The 4-pyridyl in **IV-Le** leads to a lower LUMO in the related complexes, as expected from an electron accepting substituent. **IV-Lc**, **IV-Ld** and **IV-Le** exhibit contributions of the aromatic ring in the 4' position to the LUMO+2, reducing the impact of the κ^2N to κ^3N conversion on its energy compared to the LUMO+1 as mentioned above.

Furthermore, as we were expecting large differences in the photophysical properties between κ^2N and κ^3N complexes, based on previous reports,[36,44] we conducted time dependent DFT (TD-DFT) calculations to provide information regarding the positions and nature of the electronic transitions. The calculated transitions are represented in Figure XI.18-34 along with the experimental spectra (*vide infra*). The natural transition orbitals[54] for the lowest allowed singlet to singlet transition and the lowest forbidden singlet to triplet transition of each complexes are reported in Figure XI.60-76. In all cases, these transitions are mainly corresponding to the HOMO-LUMO transition and can be describe as a combination of a metal-to-ligand charge

transfer (MLCT, i.e. Re(d)→L(π*)) with various ligand-to-ligand charge transfer involving either the Br^- or the CO. In the triplet transitions of the κ^2N complexes **IV-1a-e**, especially in **IV-1c-d**, the model indicates contribution of a ligand centred transition (LC, i.e. π→π*). In these κ^2N compounds, there is also a non negligible contribution of the Br^-(n)→L(π*) LLCT transition, leading a complex mix of transitions, like other reports in the literature.[4] The contribution of the LLCT involving the bromide is reduced after conversion to the κ^3N coordination, following the change in orbital contributions discussed above. There is, however, an increased contribution from the density corresponding to the backdonation from the Re(I) to the carbonyls which is also transferred to the ligand. This transition is thus better described as a metal-ligand-to-ligand charge transfer (MLLCT, {Re(CO)}→L(π*)). Following the removal of the Br^- in **IV-3a-e** and **IV4-a-b**, the MLLCT becomes the only contributing transition, according to the theoretical model.

The TD-DFT predicted emission value gives unreasonable value for rhenium or iridium complexes and more precise values can be obtained by calculating the energy of the optimized geometry of the first triplet, as well as the energy of the singlet state in the same geometry, as described by Zysman-Colman *et al.,*[55] giving the values in Table IV.1.

Table IV.1. Calculated wavelengths for the $S_0 \rightarrow T_1$ transition corresponding to the expected emission wavelengths.

Compound	**IV-1a**	**IV-1b**	**IV-1c**	**IV-1d**	**IV-1e**	**IV-2a**	**IV-2b**	**IV-2c**	**IV-2d**
$\lambda_{TD\text{-}DFT}$ (nm)	444.0	434.0	457.6	479.2	460.6	691.1	663.8	696.4	698.0
$\lambda_{0.0}$ (nm)	476.5	466.0	493.7	502.0	510.1	808.0	778.8	819.5	822.7
λ_{ae} (nm)	580.8	553.3	615.6	617.9	649.2	959.1	931.7	972.1	976.0
Compound	**IV-2e**	**IV-3a**	**IV-3b**	**IV-3c**	**IV-3d**	**IV-3e**	**IV-4a**	**IV-4b**	
$\lambda_{TD\text{-}DFT}$ (nm)	722.6	670.2	639.3	671.4	672.6	693.9	610.1	582.4	
$\lambda_{0.0}$ (nm)	865.9	779.8	754.2	786.4	788.3	826.4	699.1	684.9	
λ_{ae} (nm)	1042.0	924.3	900.1	929.5	932.6	989.9	854.8	822.3	

$\lambda_{TD\text{-}DFT}$ = wavelength of $S_0 \rightarrow T_1$ transition obtained by TDDFT at the S_0 optimized geometry

$\lambda_{0,0} = 1240/[E(T_1) - E(S_0)]$ at their respective optimized geometries obtained by DFT

$\lambda_{AE} = 1240/[E(T_1) - E(S_0)]$ at the T_1 optimized geometry (adiabatic electronic emission) obtained by DFT

DFT/TD-DFT modelization allowed us to extract trends throughout the family of complexes reported herein. Based on these theoretical values, we expected the reduction potentials of the

complexes to show little to no variations while the oxidation potentials should better reflect the variation between the four series. The electrochemical characterisation would thus be an efficient method to verify this hypothesis. We thus acquired the experimental values using absorption spectroscopy and electrochemistry to confirm the predicted effect of the different structural change.

IV.4.4 UV-Vis absorption spectroscopy

The absorption spectrum of each complex was measured in acetonitrile. The spectra are presented in the SI (Figure XI.18-34) with the corresponding calculated transitions from time dependent DFT. The absorption maxima and molar absorption coefficient are reported in Table X.19, while selected values for the transitions discussed below are displayed in Table IV.2.

A large bathochromic shift between the κ^2N and κ^3N coordination modes can be observed in Fig. IV.5 presenting the spectra of the complexes based on **IV-Lb**. While the κ^2N compounds barely absorb in the visible with maxima around 360-390 nm with tailing into the visible region, all the κ^3N complexes absorption spectra cover the whole visible region with three large additional transitions between 400 nm and 700 nm. The replacement of the bromide by pyridine in **IV-3a-e** leads to a ≈40 nm blueshift, while the triphenylphosphine complexes **IV-4a-b** present an even stronger blueshift of ≈80 nm. The transitions in the visible correspond in all cases to Metal-Ligand-to-Ligand Charge Transfer (MLLCT), with the electron originating from an energy level involving the bonding π orbital of the retrodonation from the rhenium center to the carbonyls ligands and being promoted to terpyridine centered energy levels. As discussed earlier, the bonding π orbital is primarily affected by the change of coordination mode and its subsequent effect on the mixing between the different ligand-metal interaction, explaining the large shift in wavelength without major change in localization.

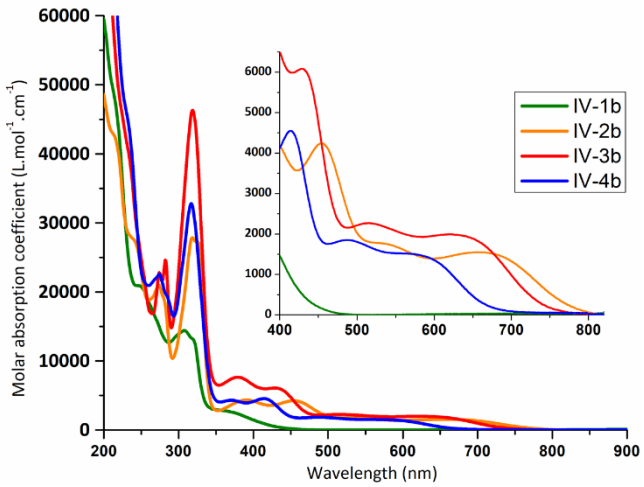

Figure IV.5. Absorption spectra for all complexes based on ligand **IV-Lb** (measured in acetonitrile)

Table IV.2 Absorption maxima and molar absorption coefficients of all complexes in acetonitrile

Complex	λ_{max} *nm* (ε x10^3 L mol^{-1} cm^{-1})			
IV-1a	367 (2.2)			
IV-2a	395 (3.3)	465 (3.3)	547 (1.2)	690 (1.1)
IV-3a	380 (6.0)	440 (4.8)	516 (1.7)	647 (1.5)
IV-4a	374 (3.2)	421 (3.8)	488 (1.4)	590 (1.1)
IV-1b	360 (2.8)			
IV-2b	390 (4.3)	454 (4.2)	534 (1.8, sh)	660 (1.6)
IV-3b	379 (7.7)	428 (6.1)	514 (2.2)	621 (2.0)
IV-4b	371 (4.3)	415 (4,5)	487 (1.8)	579 (1.5, sh)
IV-1c	386 (3.7)			
IV-2c	398 (4.6)	473 (6.0)	569 (1.3,sh)	700 (1.2)
IV-3c	382 (6.1)	448 (7.0)	529 (1.4, sh)	661 (1.2)
IV-1d	364 (12.6, sh)			
IV-2d	401 (5.8)	475 (8.8)	569 (1.4, sh)	705 (1.4)
IV-3d	386 (8.5, sh)	449 (10.0)	544 (1.4, sh)	661 (1.3)
IV-1e	388 (5.1)			
IV-2e	402 (2.8)	481 (3.5)	591 (0.7, sh)	721 (0.6)
IV-3e	385 (7.2)	454 (8.2)	539 (1.6, sh)	678 (1.4)
[Re(bpy)(CO)$_3$Br] [18]	370			
[Re(mer-NNN)(CO)$_2$Cl] [44]	367	485	≈ 620	≈ 720
[Re(fac-dqp)(CO)$_3$]Cl [42]	340			

The various substituents allow for subtle tuning of the absorption maxima, the more electron rich ligand **IV-Lb** leading to higher wavelengths in all cases for example. The aromatic substituents on the 4' position for **IV-Lc**, **IV-Ld** and **IV-Le** cause a slight redshift compare to **IV-La**, the 4-pyridyl in **IV-Le** having a stronger effect, in agreement with its higher electron withdrawing properties.

IV.4.5 Electrochemistry

Based on the IR spectroscopy results and the theoretical model, we were expecting the oxidation potentials to be significantly modified by the various structural modification while the reduction potentials should remain almost unchanged for complexes bearing the same ligands. We thus investigated these changes by cyclic voltammetry for all complexes in N,N-dimethylformamide,

using a three electrodes set-up, tetrabutylammonium hexafluorophosphate (TABPE, 0.1 M) as electrolyte and ferrocene as internal reference (0.45 V *vs.* SCE). We had to used DMF due to the limited solubility of the neutral complexes **IV-1a-e** and **IV-2a-e**. The values are reported in Table 3, along with literature values, while the cyclic voltammograms are shown in Figure XI.35-51. Several of the redox events observed are irreversible or quasi reversible in nature, as commonly observed in Re(I) carbonyl complexes.[56] This is commonly attributed to the loss of ligand after injection or removal of an electron. Indeed, a redox process can be observed in all the cyclic voltammograms for **IV-1a-e** and **IV-2a-e** at 0.76 V *vs.* SCE and is attributed to the released Br^- ligand, as evidenced by Bullock *et al.,* as it matches the reported redox potential of Br_2/Br^- in acetonitrile.[56-57] The values for chloride and triflate equivalent complexes reported by Amoroso *et al.* and Hightower *et al.*,[41,58] show unchanged reduction potentials in the different coordination environment while the oxidation potential follow the trend predicted by IR measurements and DFT models.

Looking at the oxidation potentials of our complexes, we observed the expected trend with the κ^3N bromide complexes (**IV-2a-e**) being easier to oxidize than the κ^3N pyridine cationic species (**IV-3a-e**), followed by the κ^3N triphenylphosphine forms (**IV-4a-b**) and finally the κ^2N complexes (**IV-1a-e**) are the most difficult to oxidize. The oxidation potential are reduced by 800 mV going from **IV-1a-e** to **IV-2a-e**, matching the shift observed in our DFT model.

The irreversibility of the oxidation from Re(I) to Re(II) in **IV-1a-e** makes for a difficult analysis of the variation between the different ligands. However, conversion from κ^2N to κ^3N coordination makes the oxidation processes reversible, revealing that complexes based on the more electron donating 4,4',4''-trimethyl-2,2';6',2''-terpyridine ligand **IV-Lb** are easier to oxidize by around 100 mV. The reduction potentials on the other hand are not affected by the changes in coordination mode. They are however related to the nature of the terpyridine substituents, the complexes based on ligand **IV-Le** with a 4-pyridyl substituent being the easier to reduce, while the more electron rich ligand **IV-Lb** makes the corresponding complexes harder to reduce.

Table IV.3 Redox potentials of the different Re(I) complexes (V *vs.* SCE)

	IV-1a [a]	**IV-1b** [a]	**IV-1c** [a]	**IV-1d** [a]	**IV-1e** [a]	[Re(κ^{2}N-tpy)(CO)$_3$Cl][b]
E_{ox} (ΔE, mV)	1.31 (irr)	1.42 (irr)	1.23 (irr)	1.19 (irr)	1.45 (irr)	1.19
E_{red} (ΔE, mV)	-1.30 (77)	-1.40 (155)	-1.25 (63) -1.74 (irr)	-1.25 (60) -1.70 (irr)	-0.99 (79) -1.16 (irr) -1.33 (irr)	-1.34
	IV-2a [a]	**IV-2b** [a]	**IV-2c** [a]	**IV-2d** [a]	**IV-2e** [a]	[Re(κ^{3}N-tpy)(CO)$_3$Cl][c]
E_{ox} (ΔE, mV)	0.55 (52)	0.45[d]	0.55 (63)	0.50 (76) 1.26 (irr)	0.56 (48)	0.48 (65) 1.22 (irr)
E_{red} (ΔE, mV)	-1.31 (qr)	-1.42 (qr)	-1.27 (qr)	-1.26 (irr)	-0.89 (95)[d] -1.23 (irr)	-1.17 (irr) -1.34 (irr)
	IV-3a [a]	**IV-3b** [a]	**IV-3c** [a]	**IV-3d** [a]	**IV-3e** [a]	[Re(κ^{3}N-tpy)(CO)$_2$(py)](OTf)[c]
E_{ox} (ΔE, mV)	0.82 (91)	0.77 (144)	0.82 (63)	0.81 (69)	0.83 (77)	0.86 (irr) 1.35 (irr)
E_{red} (ΔE, mV)	-1.14 (qr) -1.38 (irr)	-1.25 (qr)	-1.11 (qr) -1.35 (irr)	-1.11 (qr) -1.29 (irr)	-0.96 (qr) -1.27 (qr)	-1.21 (irr)
	IV-4a [a]	**IV-4b** [a]				[Re(κ^{3}N-tpy)(CO)$_2$(PPh$_3$)](OTf)[c]
E_{ox} (ΔE, mV)	0.95 (89)	0.80 (qr) 1.21 (irr)				0.94 (irr) 1.31 (irr)
E_{red} (ΔE, mV)	-1.11 (80)	-1.38 (qr) -1.68 (irr)				-1.19 (irr)

irr. Irreversible, qr. quasi reversible, [a] measured in DMF/TBAP 0.1 M, [b] ref. 58, measured in MeCN/TBAP, initially reported *vs.* Fc^+/Fc, [c] ref. 41, measured in MeCN/TBAP, [d] affected by the addition of ferrocene

IV.4.6 Luminescence spectroscopy

The emission spectra of the complexes were acquired in acetonitrile (concentration of 20 to 50 μM) and are reported in Table IV.4. The κ^2N complexes **IV-1a-e** are emitting around 650 nm (Figure XI.52). The emission wavelengths vary with the substituent of the terpyridine from 625 nm for the electron rich ligand **IV-Lb** to 682 nm for the electron poor ligand **IV-Le**. The emission maxima and quantum yields are similar to those reported for related chloro complexes, though the quantum yield of our bromo derivatives are lower, in agreement with the energy gap law.[2,19] Conversion to the neutral κ^3N complexes **IV-2a-e** resulted in a massive redshift of the lower absorption maxima. These complexes appear, however, to be non emissive at room temperature, despite the emission predicted by TD-DFT below 900 nm. Exchanging the bromide ligand for pyridine or triphenylphosphine caused a blueshift of the lowest absorption maxima and the TD-DFT predicted emission value follows the same trend. These complexes are indeed emissive in the NIR region, with maxima between 780 and 950 nm (Figure XI53-59).

When looking at the emission maxima of complexes **IV-3a-e**, the same substituent effect is observed, with complex **IV-3b** emitting at 840 nm with **IV-3e** emits at 950 nm, as previously reported by some of us.[36] The triphenylphosphine complexes **IV-4a-b** emit at higher wavelength (800 and 782 nm, respectively), in agreement with the stronger blueshift observed in absorption compared to the pyridine complexes **IV-3a-b**. These complexes are amongst the most NIR emissive Re(I) complexes.[59]

Surprisingly, the quantum yield of the cationic complexes **IV-3a-e** and **IV-4a-b** are higher than those of the neutral κ^2N complexes **IV-1a-e**, despite emission maxima redshifted by at least 220 nm (see Table IV-4). This is contradicting the energy gap law since lower emission energy should be associated with a lower quantum yield. This contradiction can be explained by the change in the nature of the emissive state, as discussed in the theoretical section. Indeed, while the κ^2N-tpy halide complexes have a complex mix of MLCT, LLCT and LC contributions in their lowest transition, in the κ^3N complexes, the lowest transition are purely metal-ligand-to-ligand (MLLCT) in nature, the density being transfer from the $\{Re(CO)_2\}$ fragment to the terpyridine ligand π^* orbital.

Table IV.4 Emission data for different Re(I) complexes in deaerated acetonitrile at RT.

	IV-1a	**IV-1b**	**IV-1c**	**IV-1d**	**IV-1e**	**IV-2a**	**IV-2b**	**IV-2c**	**IV-2d**	**IV-2e**
λ_{em} *nm*	640	625	659	527 653	682	N.D.	N.D.	N.D.	N.D.	N.D.
Φ %	0.03	0.05	0.06	0.10	0.02	-	-	-	-	-
	IV-3a	**IV-3b**	**IV-3c**	**IV-3d**	**IV-3e**	**IV-4a**	**IV-4b**			
λ_{em} *nm*	870	840	876	865	950	800	782			
Φ %	0.13	0.18	0.13	0.11	0.02	0.71	0.40			
	[Re(bpy)(CO)$_3$Br][a]			[Re(bpy)(CO)$_3$Br][b]			[Re(κ^3N-pydiimine)(CO)$_2$X][c]			
λ_{em} *nm*	575			606			N.D.			

N.D. not detected; [a] determined relative to [Re(bpy)(CO)$_3$Cl] with Φ = 0.5 %[2]; b determined relative to IR125 with Φ = 23 %[60]; [c] ref. 18; [d] ref. 44, [e] ref. 42

IV.5 Conclusion

By varying the coordination modes of terpyridines ligands, their substituent and the nature of the axial ligands L of Re(I) carbonyl complexes of general formula [Re(κ^xN-Rtpy)(CO)$_y$L]$^{n+}$, we were able to tune with varying amplitude the electronic and photophysical properties of these complexes. Conversion from κ^2N to κ^3N coordination mode of the terpyridines ligands has a major impact on the HOMO levels of these complexes which are destabilized by almost 800 meV, a shift observed in the electrochemical analysis, while the LUMO levels remain unchanged. The HOMO destabilization also leads to a large redshift of the absorption maxima by 300 nm, making the κ^3N bromo complexes **IV-2a-e** panchromatic while the κ^2N bromo complexes **IV-1a-e** were barely absorbing in the visible region. Replacing the bromide ligand by a pyridine (**IV-3a-e**) or a triphenylphosphine ligand (**IV-4a-b**) allows to lessen the HOMO destabilization and is accompanied by blueshifted absorption maxima. These complexes show NIR emission between 780 and 950 nm depending of the ligand used, with unusually high quantum yield between 0.02 and 0.7 % for this class of complexes, attributed to a change in the nature of the excited state. We have thus demonstrated the possibility to finely tune the properties of these complexes via simple structural variations, opening a path to the design of application specific complexes such as biological probes, a context where NIR emission properties are desirable.[61]

IV.6 References

1. M. Wrighton and D. L. Morse, *J. Am. Chem. Soc.*, 1974, **96**, 998-1003.
2. J. V. Caspar and T. J. Meyer, *J. Phys. Chem.*, 1983, **87**, 952-957.
3. A. B. P. Lever, *Inorg. Chem.*, 1991, **30**, 1980-1985.
4. A. Vogler and H. Kunkely, *Coord. Chem. Rev.*, 2000, **200**, 991-1008.
5. R. A. Kirgan, B. P. Sullivan and D. P. Rillema, in *Photochemistry and Photophysics of Coordination Compounds II*, eds. V. Balzani and S. Campagna, Springer Berlin Heidelberg, Berlin, Heidelberg, 2007, pp. 45-100.
6. L. Veronese, E. Quartapelle Procopio, T. Moehl, M. Panigati, K. Nonomura and A. Hagfeldt, *Phys. Chem. Chem. Phys.*, 2019, **21**, 7534-7543.
7. Y. Kuramochi, O. Ishitani and H. Ishida, *Coord. Chem. Rev.*, 2018, **373**, 333-356.
8. G. Calzaferri, K. Hädener and J. Li, *J. Photochem. Photobiol., A*, 1992, **64**, 259-262.
9. B. Probst, C. Kolano, P. Hamm and R. Alberto, *Inorg. Chem.*, 2009, **48**, 1836-1843.
10. J. Hawecker, J.-M. Lehn and R. Ziessel, *J. Chem. Soc., Chem. Commun.*, 1983, 536-538.
11. B. P. Sullivan, C. M. Bolinger, D. Conrad, W. J. Vining and T. J. Meyer, *J. Chem. Soc., Chem. Commun.*, 1985, 1414-1416.
12. T. Klemens, A. Switlicka-Olszewska, B. Machura, M. Grucela, E. Schab-Balcerzak, K. Smolarek, S. Mackowski, A. Szlapa, S. Kula, S. Krompiec, P. Lodowski and A. Chrobok, *Dalton Trans.*, 2016, **45**, 1746-1762.
13. D. Wang, Q. L. Xu, S. Zhang, H. Y. Li, C. C. Wang, T. Y. Li, Y. M. Jing, W. Huang, Y. X. Zheng and G. Accorsi, *Dalton Trans.*, 2013, **42**, 2716-2723.
14. S. Hostachy, C. Policar and N. Delsuc, *Coord. Chem. Rev.*, 2017, **351**, 172-188.
15. F. X. Wang, J. H. Liang, H. Zhang, Z. H. Wang, Q. Wan, C. P. Tan, L. N. Ji and Z. W. Mao, *ACS Appl. Mater. Interfaces*, 2019, **11**, 13123-13133.
16. A. Fihri, V. Artero, A. Pereira and M. Fontecave, *Dalton Trans.*, 2008, 5567-5569.
17. A. Juris, S. Campagna, I. Bidd, J. M. Lehn and R. Ziessel, *Inorg. Chem.*, 1988, **27**, 4007-4011.
18. P. Kurz, B. Probst, B. Spingler and R. Alberto, *Eur. J. Inorg. Chem.*, 2006, **2006**, 2966-2974.

19. T. Klemens, A. Switlicka-Olszewska, B. Machura, M. Grucela, H. Janeczek, E. Schab-Balcerzak, A. Szlapa, S. Kula, S. Krompiec, K. Smolarek, D. Kowalska, S. Mackowski, K. Erfurt and P. Lodowski, *RSC Adv.*, 2016, **6**, 56335-56352.

20. T. Klemens, A. Switlicka, A. Szlapa-Kula, S. Krompiec, P. Lodowski, A. Chrobok, M. Godlewska, S. Kotowicz, M. Siwy, K. Bednarczyk, M. Libera, S. Mackowski, T. Pedzinski, E. Schab-Balcerzak and B. Machura, *Appl. Organomet. Chem.*, 2018, **32**, e4611.

21. J. Rohacova, A. Sekine, T. Kawano, S. Tamari and O. Ishitani, *Inorg. Chem.*, 2015, **54**, 8769-8777.

22. A. Kamecka, K. Prachnio and A. Kapturkiewicz, *J. Lumin.*, 2018, **203**, 409-419.

23. A. Loibl, M. Weber, M. Lutz and C. Müller, *Eur. J. Inorg. Chem.*, 2019, **2019**, 1575-1585.

24. M. R. Crawley, K. J. Kadassery, A. N. Oldacre, A. E. Friedman, D. C. Lacy and T. R. Cook, *Organometallics*, 2019, **38**, 1664-1676.

25. C. C. Addison, R. Davis and N. Logan, *J. Chem. Soc., Dalton Trans.*, 1974, 2070-2071.

26. H. Tsubaki, A. Sekine, Y. Ohashi, K. Koike, H. Takeda and O. Ishitani, *J. Am. Chem. Soc.*, 2005, **127**, 15544-15555.

27. T. Morimoto, C. Nishiura, M. Tanaka, J. Rohacova, Y. Nakagawa, Y. Funada, K. Koike, Y. Yamamoto, S. Shishido, T. Kojima, T. Saeki, T. Ozeki and O. Ishitani, *J. Am. Chem. Soc.*, 2013, **135**, 13266-13269.

28. T. Mukuta, P. V. Simpson, J. G. Vaughan, B. W. Skelton, S. Stagni, M. Massi, K. Koike, O. Ishitani and K. Onda, *Inorg. Chem.*, 2017, **56**, 3404-3413.

29. V. W.-W. Yam, V. C.-Y. Lau and K.-K. Cheung, *Organometallics*, 1996, **15**, 1740-1744.

30. W. K. Chung, M. Ng, N. Y. Zhu, S. K. L. Siu and V. W. W. Yam, *J. Organomet. Chem.*, 2017, **847**, 278-288.

31. C. B. Larsen and O. S. Wenger, *Inorg. Chem.*, 2018, **57**, 2965-2968.

32. C. C. Ko, L. T. Lo, C. O. Ng and S. M. Yiu, *Chem. Eur. J.*, 2010, **16**, 13773-13782.

33. P. H. Dinolfo, M. E. Williams, C. L. Stern and J. T. Hupp, *J. Am. Chem. Soc.*, 2004, **126**, 12989-13001.

34. B. Laramee-Milette, C. Lachance-Brais and G. S. Hanan, *Dalton Trans.*, 2015, **44**, 41-45.

35. J. Rohacova and O. Ishitani, *Chem. Sci.*, 2016, **7**, 6728-6739.

36. B. Laramee-Milette, N. Zaccheroni, F. Palomba and G. S. Hanan, *Chem. Eur. J.*, 2017, **23**, 6370-6379.

37. C. Wang, Z. Xie, K. E. deKrafft and W. Lin, *J. Am. Chem. Soc.*, 2011, **133**, 13445-13454.

38. D. A. Popov, J. M. Luna, N. M. Orchanian, R. Haiges, C. A. Downes and S. C. Marinescu, *Dalton Trans.*, 2018, **47**, 17450-17460.

39. E. W. Abel, V. S. Dimitrov, N. J. Long, K. G. Orrell, A. G. Osborne, H. M. Pain, V. Šik, M. B. Hursthouse and M. A. Mazid, *J. Chem. Soc., Dalton Trans.*, 1993, 597-603.

40. D. R. Black and S. E. Hightower, *Inorg. Chem. Commun.*, 2012, **24**, 16-19.

41. B. A. Frenzel, J. E. Schumaker, D. R. Black and S. E. Hightower, *Dalton Trans.*, 2013, **42**, 12440-12451.

42. T. Jurca, W. C. Chen, S. Michel, I. Korobkov, T. G. Ong and D. S. Richeson, *Chem. Eur. J.*, 2013, **19**, 4278-4286.

43. A. K. Pal and G. S. Hanan, *Dalton Trans.*, 2014, **43**, 11811-11814.

44. D. J. Losey, B. A. Frenzel, W. M. Smith, S. E. Hightower and C. G. Hamaker, *Inorg. Chem. Commun.*, 2013, **30**, 46-48.

45. P. Bulsink, A. Al-Ghamdi, P. Joshi, I. Korobkov, T. Woo and D. Richeson, *Dalton Trans.*, 2016, **45**, 8885-8896.

46. P. H. Lee, C. C. Ko, N. Zhu and V. W. Yam, *J. Am. Chem. Soc.*, 2007, **129**, 6058-6059.

47. D. A. Kurtz, K. R. Brereton, K. P. Ruoff, H. M. Tang, G. A. N. Felton, A. J. M. Miller and J. L. Dempsey, *Inorg. Chem.*, 2018, **57**, 5389-5399.

48. K. Koike, J. Tanabe, S. Toyama, H. Tsubaki, K. Sakamoto, J. R. Westwell, F. P. Johnson, H. Hori, H. Saitoh and O. Ishitani, *Inorg. Chem.*, 2000, **39**, 2777-2783.

49. D. A. Kurtz, B. Dhakal, E. S. Donovan, G. S. Nichol and G. A. N. Felton, *Inorg. Chem. Commun.*, 2015, **59**, 80-83.

50. E. W. Abel, N. J. Long, K. G. Orrell, A. G. Osborne, H. M. Pain and V. Šik, *J. Chem. Soc., Chem. Commun.*, 1992, 303-304.

51. A. Gelling, D. R. Noble, K. G. Orrell, A. G. Osborne and V. Šik, *J. Chem. Soc., Dalton Trans.*, 1996, 3065-3070.

52. A. Freyer, C. DiMeglio and A. Freyer, *J. Chem. Educ.*, 2006, **83**, 788.

53. A. Gelling, K. G. Orrell, A. G. Osborne and V. Sik, *J. Chem. Soc., Dalton Trans.*, 1998, 937-945.

54. R. L. Martin, *J. Chem. Phys.*, 2003, **118**, 4775-4777.

55. S. Ladouceur, K. N. Swanick, S. Gallagher-Duval, Z. F. Ding and E. Zysman-Colman, *Eur. J. Inorg. Chem.*, 2013, **2013**, 5329-5343.

56. J. P. Bullock, E. Carter, R. Johnson, A. T. Kennedy, S. E. Key, B. J. Kraft, D. Saxon and P. Underwood, *Inorg. Chem.*, 2008, **47**, 7880-7887.

57. G. D. Allen, M. C. Buzzeo, C. Villagran, C. Hardacre and R. G. Compton, *J. Electroanal. Chem.*, 2005, **575**, 311-320.

58. A. J. Amoroso, A. Banu, M. P. Coogan, P. G. Edwards, G. Hossain and K. M. Malik, *Dalton Trans.*, 2010, **39**, 6993-7003.

59. H. Xiang, J. Cheng, X. Ma, X. Zhou and J. J. Chruma, *Chem. Soc. Rev.*, 2013, **42**, 6128-6185.

60. C. Wurth, M. Grabolle, J. Pauli, M. Spieles and U. Resch-Genger, *Nat. Protoc.*, 2013, **8**, 1535-1550.

61. L. C. Lee, K. K. Leung and K. K. Lo, *Dalton Trans.*, 2017, **46**, 16357-16380.

Chapitre V. De la chimie des polyoxométallates

Afin d'introduire les chapitres suivants, il nous parut nécessaire d'introduire plus en détails la famille des polyoxométallates (POMs), mentionnée dans l'introduction. Ces clusters sont constitués principalement de ligands oxo O^{2-} et de métaux du début de la série des métaux de transitions, tels que le vanadium, le molybdène et le tungstène, tous dans leur état d'oxydation le plus élevé, i.e. V^{V}, Mo^{VI} et W^{VI} ayant tous une configuration électronique d^0. Bien qu'apparentés aux oxides, ces composés se distinguent par leurs structures définies et leur bonne solubilité permettant des études en solution. Une différence est faite entre isopolyanions et hétéropolyanions, de formule générale respective $[M_mO_y]^{p-}$ et $[X_xM_mO_y]^{q-}$, où X est un hétéroatome tel que le bore, le phosphore ou l'arsenic.[1] Le premier POM fut préparé en 1826 par Berzelius qui observa la formation d'un précipité lors de la combinaison de molybdate d'ammonium et d'acide phosphorique.[2] Il fallut attendre plus d'un siècle pour que la structure de ce composé soit déterminée. Cette structure porte depuis le nom du chimiste qui l'a résolue à partir de diagramme de diffraction sur poudre : J.F. Keggin (Figure V.1).[3] S'en suivirent dans les années 40 de nombreuses avancées dans la compréhension des mécanismes de formation, accélérée par l'utilisation de nouvelles techniques de caractérisations, notamment à l'initiative de P. Souchay, fondateur de ' l'école française des POMs'.[2]

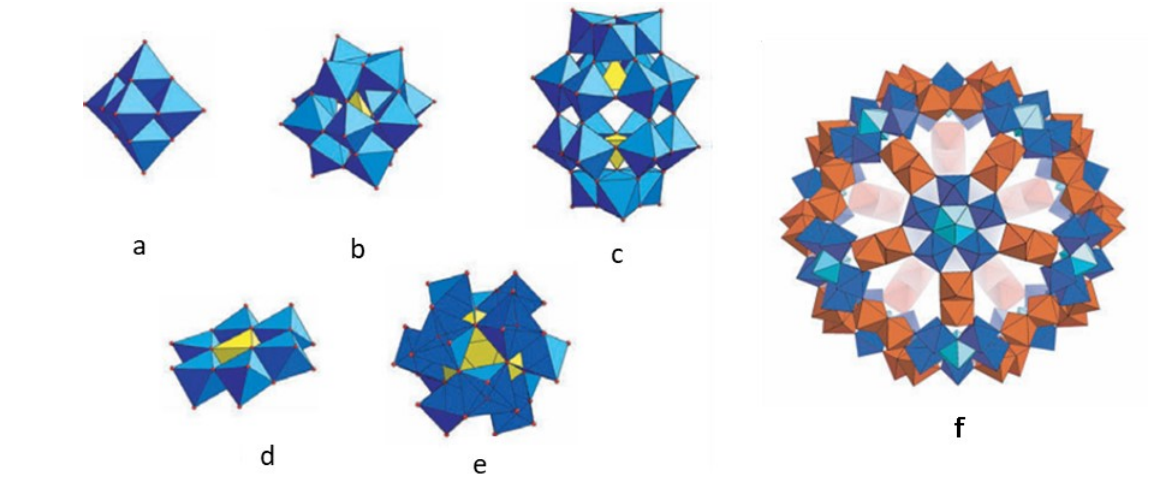

Figure V.1. Structures tridimensionnelles de POMs choisis de type a) Lindqvist, b) Keggin, c) Dawson, d) Anderson, e) Dexter-Silverton et f) Keplerate (Adapté de P. Gouzerh and M. Che, *L'actualité chimique*, 2006, **298**, 9-22, Copyright 2006 Société Chimique de France)

Depuis, de nombreuses autres structures ont été rapportées, comprenant les fullerènes inorganiques, encore appelés keplerates (Figure V.1f). On trouve ainsi des POMs constitués de six à plusieurs centaines d'atomes métalliques. Ceux-ci sont classiquement représentés à l'aide de polyèdres de coordination, comme sur la figure V.1, le métal se trouvant au centre du polyèdre défini par les ligands oxo agissant comme ligand pontant entre un à quatre centres. Dans la majorité des cas, le métal est dans un environnement octaédrique, parfois déformé du fait du caractère double d'une des liaisons métal oxo (M=O).

Ces composés sont aujourd'hui appliqués dans une multitude de champ d'études, allant de la catalyse,[4] aux matériaux magnétiques,[5] en passant par la biologie[6] et diverses applications photo(électro)chimiques.[7-8] Pour l'application qui nous intéresse plus immédiatement ici, la photocatalyse, ces composés occupent une place particulière, faisant le lien entre molécule et matériaux. Ils disposent de propriétés électroniques uniques et sont capables d'accepter un grand nombre d'électrons – des exemples dans la littérature impliquent le stockage réversible de 18[9] ou même 24[10] électrons sur un unique cluster – ce qui en fait des candidats idéals pour s'attaquer au défi que représente les réactions multi-électroniques d'intérêt pour la photosynthèse artificielle.[11]

Au moment où Lehn et Grätzel étudiaient les systèmes présentés dans l'introduction, Savinov (1981) puis Papaconstantinou (1985) démontraient que les hétéropolyoxotungstates $[XW_{12}O_{40}]^{q-}$ peuvent photocatalyser l'oxydation d'alcool couplée à la production de dihydrogène sous irradiation UV.[12] Cette transformation implique la réduction du POM *via* réaction entre sa forme excitée et un alcool (piégeage réductif), suivi de la régénération du POM oxydé via évolution de dihydrogène, la réduction des protons étant thermodynamiquement favorisée dans le cas des polyoxotungstates. Peu de temps après, l'inclusion d'atome de titane dans un POM à structure de Keggin, $[PTi_2W_{10}O_{40}]^{7-}$, permit à Yamase *et al.* de réaliser la réduction de CO_2 en CH_4 sous lumière UV en solution aqueuse, la réaction étant couplée à l'oxydation du méthanol en formaldehyde.[13] Les limites de ce système se trouvent dans les hautes énergies requises pour exciter les transferts de charge ligand à métal (LMCT, $O(\pi) \rightarrow M(d)$). Cette situation rappelle les conclusions des travaux avec le dioxyde de titane, illustrant les similarités entre POMs et oxides métalliques. Cependant, à l'image du domaine de la photosynthèse artificielle en général, peu d'avancées furent rapportés au cours des décennies

suivantes. Les connaissances fondamentales des propriétés photophysiques et des transferts d'électron impliquant les POMs continuèrent cependant de progresser.[14-15]

En 2008, les groupes de M. Bonchio et C. Hill publièrent simultanément un composé de type 'sandwich' dans lequel deux POMs vacants servent de ligands pour un coeur polymétalliques composé de quatre atomes de ruthénium pontés par différents ligands oxygénés, $\{Ru_4(\mu\text{-}O)_4(\mu\text{-}OH)_2(H_2O)_4\}^{6+}$.[16-17] Ce composé est un catalyseur efficace pour l'oxydation de l'eau et donna un nouveau souffle au développement de cette réaction.[18] Poursuivant avec cette famille de composés robustes, Hill *et al.* publièrent d'autres composés 'sandwich' contenant des cœurs tetramétalliques pour l'oxydation de l'eau (cobalt)[19] ou la réduction des protons (manganèse, nickel ou cuivre).[20]

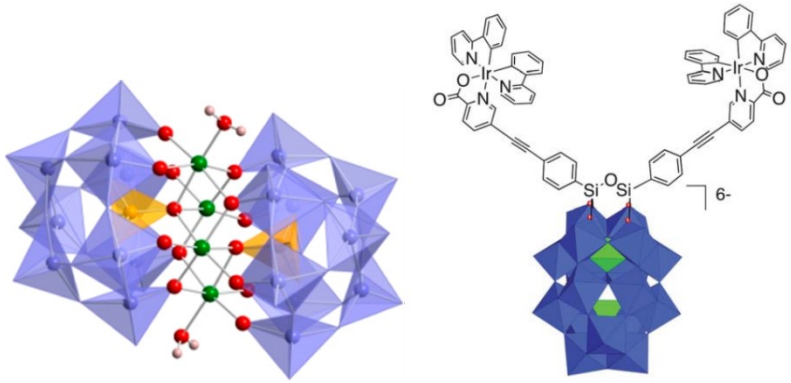

Figure V.2 Exemples choisis de composés comportant une unité POM utilisés pour la photoréduction des protons. (Gauche, catalyseur POM-Ni4-POM Adapté, avec permission, de C. L. Hill, *J. Am. Chem. Soc.*, 2014, **136**, 14015-14018. Copyright 2014 American Chemical Society) (Droite, dyade Ir_2-POM, adapté, avec permission, de A. Proust, *Energy Environ. Sci.*, 2013, **6**, 1504-1508, Copyright 2013 Royal Chemical Society).

Explorant les possibilités offertes par la fonctionnalisation covalente de POMs,[21] Proust *et al.* reportèrent la dyade présentée dans la Figure V.2.[22] Dans ce système, les complexes d'iridium servent de photosensibilisateurs et transfèrent les électrons vers le POM servant à la fois de réservoir à électrons et de catalyseur. Les deux systèmes présentés dans la Figure V.2 sont particulièrement intéressants en raison de la stabilité sur plusieurs jours des systèmes photocatalytiques correspondants.

Ainsi, les POMs constituent des modèles attractifs pour les oxydes métalliques omniprésents dans la littérature et combinent robustesse et propriétés rédox ajustables, tout en tolérant des modifications structurales permettant leur fonctionnalisation dans le cadre d'assemblage covalents. Ces caractéristiques peuvent expliquer pourquoi, au cours de la dernière décennie, le nombre de publications liées à l'utilisation de polyoxométallates pour des applications en photosynthèse artificielle a augmenté au rythme effréné récemment mis en évidence.[23]

Références

1. M. T. Pope, *Heteropoly and Isopoly Oxometalates*, Springer-Verlag Berlin Heidelberg GmbH, 1983.
2. P. Gouzerh and M. Che, *L'actualité chimique*, 2006, **298**, 9-22.
3. J. F. Keggin, *Nature*, 1933, **131**, 908-909.
4. I. V. Kozhevnikov, *Chem. Rev.*, 1998, **98**, 171-198.
5. J. J. Baldoví, S. Cardona-Serra, A. Gaita-Ariño and E. Coronado, in *Polyoxometalate Chemistry*, 2017, pp. 213-249.
6. A. Bijelic, M. Aureliano and A. Rompel, *Angew. Chem. Int. Ed.*, 2019, **58**, 2980-2999.
7. J. J. Walsh, A. M. Bond, R. J. Forster and T. E. Keyes, *Coord. Chem. Rev.*, 2016, **306**, 217-234.
8. L. Chen, W. L. Chen, X. L. Wang, Y. G. Li, Z. M. Su and E. B. Wang, *Chem. Soc. Rev.*, 2019, **48**, 260-284.
9. J. J. Chen, M. D. Symes and L. Cronin, *Nat. Chem.*, 2018, **10**, 1042-1047.
10. H. Wang, S. Hamanaka, Y. Nishimoto, S. Irle, T. Yokoyama, H. Yoshikawa and K. Awaga, *J. Am. Chem. Soc.*, 2012, **134**, 4918-4924.
11. S. M. Lauinger, Q. Yin, Y. V. Geletii and C. L. Hill, in *Polyoxometalate Chemistry*, 2017, pp. 117-154.
12. A. Ioannidis and E. Papaconstantinou, *Inorg. Chem.*, 1985, **24**, 439-441.
13. T. Yamase and M. Sugeta, *Inorg. Chim. Acta*, 1990, **172**, 131-134.
14. T. Yamase, *Catalysis Surveys from Asia*, 2003, **7**, 203-217.
15. I. A. Weinstock, *Chem. Rev.*, 1998, **98**, 113-170.
16. A. Sartorel, M. Carraro, G. Scorrano, R. De Zorzi, S. Geremia, N. D. McDaniel, S. Bernhard and M. Bonchio, *J. Am. Chem. Soc.*, 2008, **130**, 5006-5007.

17. Y. V. Geletii, B. Botar, P. Kogerler, D. A. Hillesheim, D. G. Musaev and C. L. Hill, *Angew. Chem. Int. Ed.*, 2008, **47**, 3896-3899.

18. H. Lv, Y. V. Geletii, C. Zhao, J. W. Vickers, G. Zhu, Z. Luo, J. Song, T. Lian, D. G. Musaev and C. L. Hill, *Chem. Soc. Rev.*, 2012, **41**, 7572-7589.

19. Q. Yin, J. M. Tan, C. Besson, Y. V. Geletii, D. G. Musaev, A. E. Kuznetsov, Z. Luo, K. I. Hardcastle and C. L. Hill, *Science*, 2010, **328**, 342-345.

20. H. Lv, W. Guo, K. Wu, Z. Chen, J. Bacsa, D. G. Musaev, Y. V. Geletii, S. M. Lauinger, T. Lian and C. L. Hill, *J. Am. Chem. Soc.*, 2014, **136**, 14015-14018.

21. A. Proust, B. Matt, R. Villanneau, G. Guillemot, P. Gouzerh and G. Izzet, *Chem. Soc. Rev.*, 2012, **41**, 7605-7622.

22. B. Matt, J. Fize, J. Moussa, H. Amouri, A. Pereira, V. Artero, G. Izzet and A. Proust, *Energy Environ. Sci.*, 2013, **6**, 1504-1508.

23. C. Bozal-Ginesta and J. R. Durrant, *Faraday Discuss.*, 2019, **215**, 439-451.

Chapitre VI. Covalent hybrids based on Re(I) tricarbonyl complexes and polypyridine-functionalized polyoxometalate: synthesis, characterization and electronic properties

VI.1 Contexte et résumé

Comme démontré dans le chapitre précédent, les POMs possèdent de multiples propriétés les rendant attractifs pour le développement de systèmes photocatalytiques robustes et efficaces. Dans la continuité des travaux de thèse de Marie-Pierre Santoni, nous avons exploré les propriétés d'hybrides covalents combinant les propriétés de complexes de Re(I) carbonyle diimine et d'un polyoxométallate (ici un polyoxovanadotungstate de type Dawson). La structure tridimensionnelle d'une de ces espèces hybrides organique-inorganique est résolue par diffraction des rayons-X sur monocristal. Ce type de structure est peu abondant dans les bases de données cristallographiques comparativement à leurs équivalents basés sur des interactions électrostatiques. Dans l'esprit de la chimie supramoléculaire, telle que définie par J.M. Lehn, nous nous attendions à ce que les propriétés de ces dyades covalentes surpassent la somme des propriétés de leur unités constituantes.

Dans les faits, à l'état fondamental, aucune preuve de communication ou synergie entre le complexe et le cluster n'est observée. Cependant, lors de l'étude des propriétés photophysiques, seul le complexe de Re(I) isolé est émissif. En combinant mesures électrochimiques, études de désactivation de l'état excité et modèle théorique, nous démontrons la présence d'un transfert d'électron photoinduit intramoléculaire surpassant le piégeage oxydatif observé dans le système bimoléculaire en termes d'efficacité.

Covalent hybrids based on Re(I) tricarbonyl complexes and polypyridine-functionalized polyoxometalate: synthesis, characterization and electronic properties

Thomas Auvray,[a] Marie-Pierre Santoni,[b*] Bernold Hasenknopf,[c*] Garry S. Hanan[a*]

a. Département de Chimie, Université de Montréal, Montréal, Canada, H3T-1J4

b. Université Paris Diderot, Sorbonne Paris Cité, ITODYS, UMR CNRS 7086, 15 rue J.-A. de Baïf, 75013 Paris, France

c. Sorbonne Universités, UPMC Univ. Paris 6, Institut Parisien de Chimie Moléculaire, CNRS UMR 8232, 4 Place Jussieu, 75005 Paris, France

Full paper

Published online on 07 July 2017

Reproduced with permission of The Royal Society of Chemistry from *Dalton Trans.*, **2017**, 46, 10029–10036

Contributions :

Thomas Auvray : Conception du projet. Synthèse et caractérisation complète des ligands, hybrides et complexes. Analyse structurelle par diffraction des rayons X, analyse des propriétés optiques et électroniques. Calcul théorique. Rédaction de l'article.

Marie-Pierre Santoni : Conception du projet, études préliminaires, révision de l'article.

Bernold Hasenknopf : Conception du projet, révision de l'article.

Garry S. Hanan : Supervision, conception du projet, révision de l'article.

VI.2 Abstract

A series of $[Re(CO)_3Br(N^N)]$ (N^N = substituted 2,2'-bipyridine ligand) complexes based on polypyridine functionalized Dawson polyoxometalate (**VI-1-3**) has been synthesized. The new hybrids (**VI-4-6**) were characterized by various analytical techniques, including absorption, vibrational and luminescence spectroscopies as well as electrochemistry. Both units, the polyoxometalate and the transition metal complex, retain their intrinsic properties. Their combination in the newly prepared hybrids results in improved photosensitization in the high-energy visible region. However, a complete quenching of the emission for the $[Re(CO)_3Br(N^N)]$ complexes is observed due to formation of a charge separated state, $Re(II) - POM^-$, as shown by quenching experiments as well as theoretical modelling via DFT.

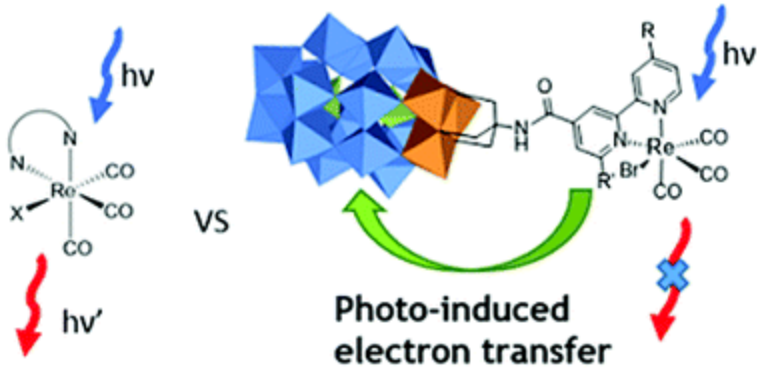

VI.3 Introduction

Polyoxometalates (POMs) are a class of anionic oxo-clusters of early-transition metals (mainly V(V), Mo(VI) and W(VI)) that exhibit a remarkable variety of structures and potential applications.[1-3] They have been used in catalysis, magnetism, material science and even medicine.[4-7] One of the most active areas of POM research focuses on their covalent functionalization to combine their unique properties with the properties of the grafted organic or organometallic components and develop new synergistic functionality in the hybrids.[8-12] This interest also arises from the analogy between POMs and metal oxide surfaces: POMs are considered as soluble analogues of metal oxides and, consequently, potential models for understanding elementary steps of heterogenous processes.[13-14] Among the covalent functionalization strategies, substitution of oxo ligand by poly-alcohol (triol and diol-amide,

Figure VI.1b, VI.1c and VI.1e) is one of the most extensively used.[15-17] It has been applied to various POM structures (Lindqvist, Anderson and Dawson)[18-20] and the grafting reaction has been extensively studied.[21-23] While the use of diol-amide has been shown to induce electronic communication between the sub-unit of the prepared hybrids,[17,24] the use of triol such as tris-(hydroxymethyl) aminomethane (TRIS) has proven to be a viable route for the grafting of various moieties with limited electronic communication between the constitutive units,[25] in a true supramolecular approach.[26] We and others have used TRIS functionalized POMs to prepare polymeric[27-29] and discrete coordination species by introducing polypyridine ligands via an amide[30] or an imine[31] group. Many studies on covalently functionalized POMS aimed to combine them with known chromophores.[32] Both organics and organometallic dyes were explored, such as benzospiropyran[33], porphyrins,[25,28,34-35] and Ru(II), [20,36] Ir(III)[37-40] and Re(I)[41] polypyridines complexes (Fig. VI.1). Other examples are focused towards catalysis.[42]

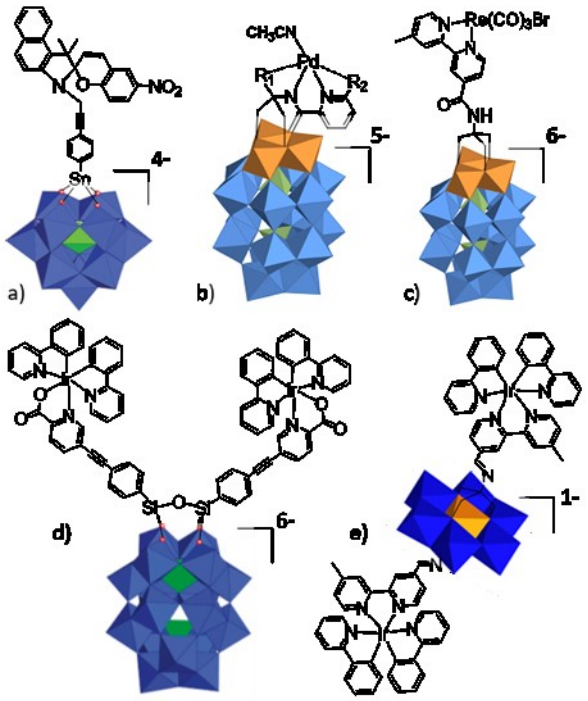

Figure VI.1. 1 Selected examples for different modes of grafting used to prepare covalently modified POMs (**a** Parrot *et al.*[33], **b** Riflade *et al.*[42], **c** Santoni *et al.*[41], **d** Matt *et al.*[39] and **e** Streb *et al.*[40]).

Re(I) carbonyl diimine complexes have been the object of numerous studies in the past decades since the pioneering studies by Wrighton *et al.* of their photophysical properties.[43] Nowadays, these complexes are mostly being studied for their selective CO_2 to CO photocatalytic reduction abilities shown for the first time by Lehn *et al.*[44-45] They have also found application in other catalytic systems,[46] electroluminescent devices[47] and for biomedical purposes[48]. However, a few systems combining POM and Re(I) chromophore had been reported, based on non-covalent electrostatic interactions, such as counter-cation recognition via a crown-ether modified ligand,[49] or hydrogen bonding via a pendant amine on the Re complex.[50] We noted that there are several reports of Re carbonyl compounds based on POMs, in which the fac-$\{Re(CO)_3\}$ coordination sphere is completed by oxo or alkoxo ligands from the POM skeleton.[51-56] While those compounds exhibit interesting structural and electronic properties due that unique coordination environment, they don't present metal-to-ligand charge-transfer (MLCT) bands as observed in the Re tricarbonyl diimine complexes such as *fac*-$[Re(CO)_3Br(bpy)]$ (where bpy is 2,2'-bipyridine).

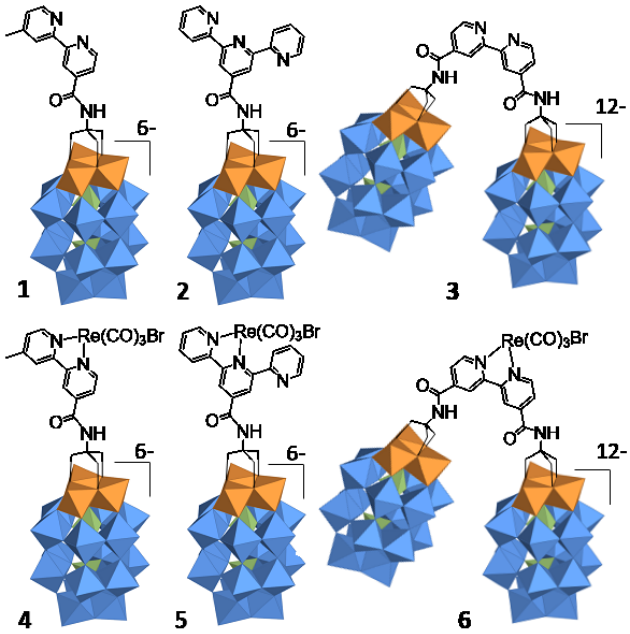

Figure VI.2 Structure of the discussed functionalized POMs (**VI-1-3**) and their Re complexes (**VI-4-6**) (Orange octahedron: $\{VO_6\}$, Blue octahedron: $\{WO_6\}$, Green tetrahedron: $\{PO_4\}$).

Herein, we extend the family of hybrids combining Re(I) carbonyl complexes and polypyridine-functionalized POMs, by complexation of the $\{Re(CO)_3Br\}$ moiety onto the available

coordination site of covalently modified POMs. The bipyridine-functionalized Dawson (**VI-1**), terpyridine-substituted (**VI-2**) and bridging-bipyridine-substituted (**VI-3**) act as ligand for Re(I) thus affording hybrids **VI-4-6**.

VI.3 Results and discussion

VI.3.1. Synthesis and characterization of triol-functionalized polypyridine

To prepare the targeted hybrids, the triol moiety was introduced via trans-esterification on the ethyl-carboxylate functionalized polypyridine ligands with TRIS, followed by an intramolecular rearrangement.[57] The three ligands thus obtained had been previously reported either by us (**VI-L1**, **VI-L2**)[20,41] or by Cronin *et al.* (**VI-L3**)[58]. The detailed synthetic pathways are described in the Supporting Information (Chap. 12). The identity of the compounds was confirmed by ESI-MS, ^{1}H and ^{31}P NMR spectra. The presence of amide groups was confirmed by singlets at 7.65, 7.81 and 7.69 ppm for **VI-L1**, **VI-L2** and **VI-L3**, respectively. The amide also appears on the IR spectra through its characteristic C=O stretching vibration at 1644, 1658 and 1645 cm^{-1} (Fig. XII.2).

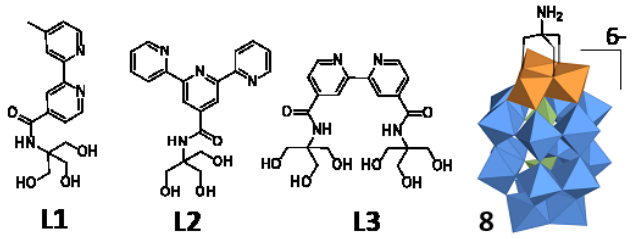

Figure VI.3. Structure of the polypyridine triol-functionalized ligands **VI-L1-L3** and the reference TRIS-capped POM **VI-8** (Orange octahedron: {VO_6}, Blue octahedron: {WO_6}, Green tetrahedron: {PO_4}).

VI.3.2. Synthesis and characterization of polypyridine-POM hybrids

Following published procedures,[19-20] the triol functionalized ligands were grafted on the tri-substituted Dawson type POM $[P_2V_3W_{15}O_{62}]^{9-}$ **VI-7**, affording compounds **VI-1-3** (Fig. VI.2) with high yield by combining the ligands and starting POM in stoichiometric amounts and heating them in the dark for several days at 80 °C in *N,N*-dimethylacetamide (DMAc). The

starting POM **VI-7** was obtained by condensation of sodium metavanadate with the tri-vacant Dawson phosphotungstate $[P_2W_{15}O_{56}]^{12-}$ whose reproducible preparation has been extensively studied by Finke *et al.*.[59-60] The TRIS-capped POM **VI-8**, previously reported by Cronin *et al.*[61], was prepared in a similar way, as a reference. In all cases, the grafting takes place on the $\{V_3\}$ cap (Fig. **VI-**2, **VI-**3), due to the higher basicity of the oxo ligands linked to V^V centers instead of W^{VI} center,[62] maintaining the C_3v geometry of the cluster as shown by the crystallographic structure (*vide infra*). The reaction requires several days to ensure that the three alkoxide groups have replaced bridging μ^2-oxo ligands.[21] The identity of the three hybrids was confirmed by ESI-MS (see Fig. XII.6-XII.8, XII.12) and their purity by ^1H and ^{31}P NMR, as well as elemental analysis. When comparing their IR spectra with that of the starting POM **VI-7**, two features allow to confirm the grafting of the organic unit : (i) the enlarged splitting between the M-O-M vibrations between 700 and 800 cm^{-1} [15](Fig. XII.3), (ii) the additional vibration bands corresponding to the amide C=O, C-O stretching and the aromatic C=C stretching and bending modes (albeit with weak intensities when compared to the tetrabutylammonium (TBA) C-N stretching bands at 1482 cm^{-1}) (Fig. XII.3).

When compared with the starting compound **VI-7**, all the functionalized species exhibit a shift of both phosphate signals in their ^{31}P NMR spectra. This is mainly due to the decreased negative charge of the cluster after replacing the three oxo ligands by three alkoxo ligands. However, from one hybrid to another, there is almost no difference in the ^{31}P NMR spectra, indicating that there is almost no communication between the constitutive units, as expected for triol functionalized POM hybrids.

VI.3.3. Complexation of {Re(CO)$_3$Br} on functionalized POMs

Compounds **VI-4**, **VI-5,** and **VI-6** were obtained by combining one equivalent of $Re(CO)_5Br$ with the corresponding functionalized POM in DMAc and heating the mixture overnight at 80°C in the dark. The complexation process was monitored by ^1H and ^{31}P NMR in CD_3CN as shown in Fig. VI.4. Upon complexation on **VI-1** and **VI-3**, the proton peaks of the bipyridine ligand are deshielded, as expected for this type of complex. In the case of compound **VI-5**, the ^1H NMR spectrum becomes more complex when compared to hybrid **VI-2** as the coordination on the terpyridine ligand only involves two of the pyridyls, thus making the external pyridyls

inequivalent. This κ^2N coordination is expected as the formation of κ^3N terpyridine complexes typically requires high temperatures.[63-64] The coordination geometry is confirmed by the presence of three distinct vibration bands arising from the carbonyl ligands as shown on the IR spectra of Fig XII.4. We also studied a known Re complex as a reference: we chose [Re(dmb)(CO)$_3$Br] (dmb = 4,4'-dimethyl-2,2'-bipyridine), referred as **VI-9** hereafter. The values are tabulated in Table VI.1 and show that the carbonyl bands of **VI-4-6** appear at higher frequency than in **VI-9**. These shifts in wavenumber are in agreement with the stronger π-accepting character arising from the introduction of weakly electron-withdrawing amide group. The molecular formulas were confirmed by ESI-MS (Fig. XII.9-XII.11) and their purity checked by ^{1}H and ^{31}P NMR and EA.

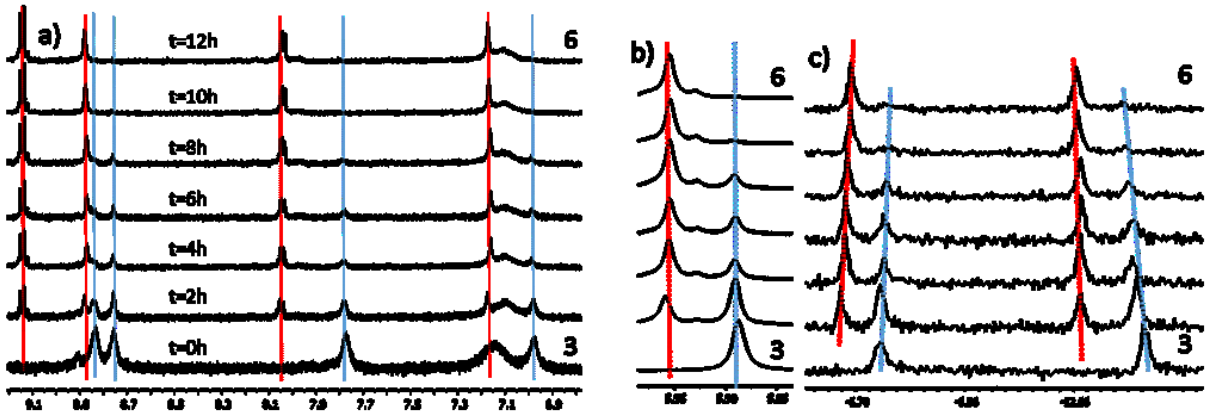

Figure VI.4. Follow-up of the complexation reaction using hybrid **VI-3** in CD_3CN at 80 °C. Spectra acquired every 2 h. a) Aromatic region of the ^{1}H NMR, b) Methylene proton of the triol moiety and c) ^{31}P NMR

Table VI.1. CO stretching modes of compounds **VI4 - VI6** as well as the reference **VI9**

Compound	Wavenumber (σ / cm^{-1})
VI-4	2019, 1916, 1891
VI-5	2020, 1916, 1894
VI-6	2023, 1925, 1899
VI-9	2012, 1882, 1865

VI.3.4. Crystallographic study

We obtained crystals suitable for X-ray analysis by slow diffusion of di-isopropyl ether into an acetonitrile solution of **VI-1**. It crystallizes in the orthorhombic space group $P2_12_12_1$ (complete details on the dataset and refinement are in the SI). The structure, presented in Fig. VI.5, confirms the expected grafting of the triol moiety by replacement of the three bridging μ^2-oxo ligands of the $\{V_3\}$ cap by the μ^2-alkoxo groups. The non-crystallographic C_3v symmetry of the cluster is also unaffected, confirming the IR and NMR results.

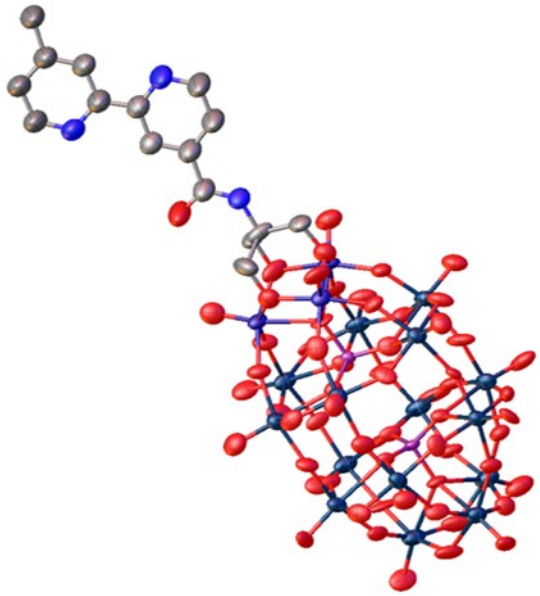

Figure VI.5. X-ray structure of compound **VI-1** (Ellipsoids are at 50% probability. Hydrogens and counter cations are omitted for clarity).

VI.3.5. UV-visible absorption and luminescence properties

The absorption spectra of the different compounds were collected: in both CH_3CN (Fig. VI.6) and DMF (Fig. XII.5b,c) for compounds **VI-1 − VI-9** and only in DMF for the ligands (Fig. XII.5a), due to their insolubility in CH_3CN. Absorption maxima and molar absorption coefficient in CH_3CN are reported in Table VI.2. The absorption spectra of the ligands are dominated by $\pi \rightarrow \pi^*$ transitions in the UV part of the spectra. Noteworthy, **VI-L3** absorbs at lower energy than the other ligands as expected from its stronger π-accepting character due to the presence of two amide groups. The native POM **VI-7** exhibits intense absorption in the UV

region, which is attributed to the multiple ligand-to-metal charge transfer ($O \rightarrow W^{VI}$ and $O \rightarrow V^{V}$ LMCTs), tailing into the high-energy part of the visible region (inset Fig. VI.5). Hybrid **VI-8** exhibits similar absorption properties, as the TRIS fragment brings no additional transitions. The absorption spectra of the functionalized POMs **VI-1** − **VI-3** thus correspond to the combination of the LMCT transitions observed in **VI-7** with the ligand centered (LC) transitions of the ligand, indicating minimal electronic communication between the two parts of the hybrid. Upon coordination of the $\{Re(CO)_3Br\}$ fragment, the LC transitions are slightly red-shifted while an additional transition emerges in the visible part of the spectra, corresponding to the Re(d)→π* metal-to-ligand charge transfer (MLCT). This additional transition leads to an increase of the molar absorption coefficient in the high energy visible region (*i.e* in the case of ε_{450}, its value is almost twice as high in **VI-6** as compared to **VI-3**), as observed when comparing the insets of Fig. VI.6.

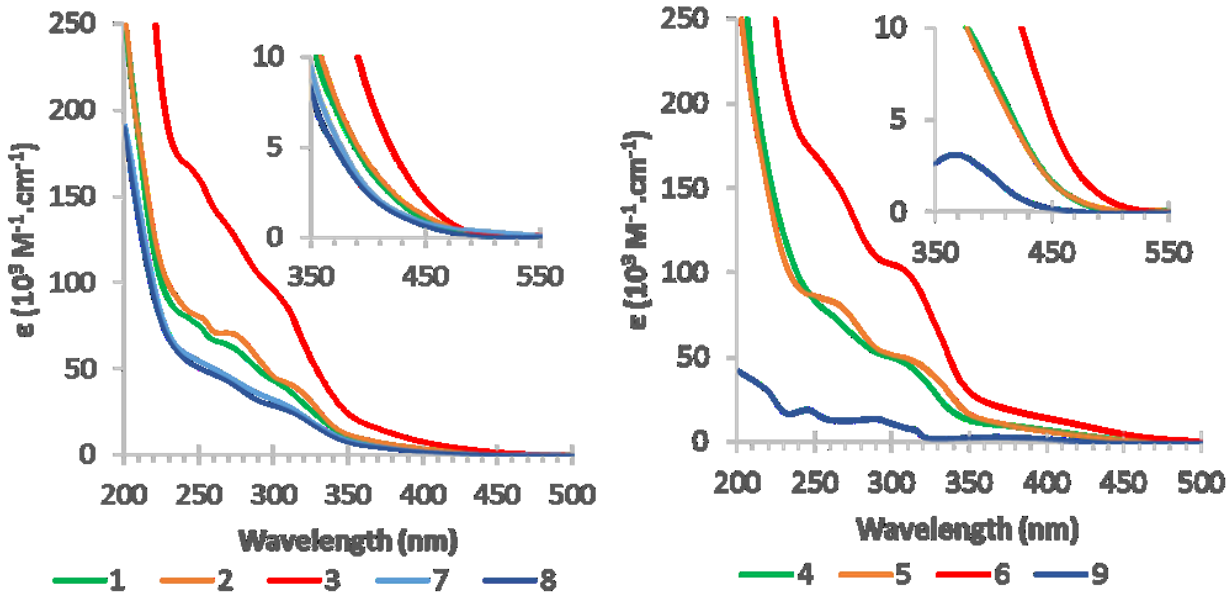

Figure VI.6. Absorption spectra at 298 K in CH_3CN of compounds **VI-1** − **VI-9**.

Re(I) bipyridine complexes are known to be emissive, displaying intense luminescence when excited in their ^{1}MLCT band. The reference compound **VI-9**, for example, emits with a maximum at 584 nm,[65] while a complex based on a bis-amide bipyridine as in **VI-6** has been reported to emit around 650nm.[66] However, in the case of our covalently modified POM based

Re complexes, no luminescence could be detected upon excitation of the ^{1}MLCT transition (see Fig. XII.27). The causes of this complete luminescence quenching will be discussed below.

Table VI.2. Absorption data for compounds **VI-1**−**VI-9**. All measurements were done in CH_3CN at RT

Compounds	Absorption (λ/nm) (ε/10^3 M^{-1} cm^{-1})
VI-1	308 (sh, 38.6), 269 (63.7), 251 (74.1), 241 (80.2)
VI-2	314 (40.1), 272 (71.1), 253 (sh, 79.4)
VI-3	307 (sh, 87.7), 269 (sh, 132.1), 247 (sh, 142,9)
VI-4	375 (sh, 8.2), 304 (49.2), 260 (sh, 73.9)
VI-5	381 (sh, 8.1), 313 (46.8), 264 (80.4)
VI-6	381 (sh, 17.1), 305 (102.1), 263 (sh, 151.3)
VI-7	309 (sh, 28.9), 258 (sh, 51.1)
VI-8	315 (sh, 29.2), 270 (sh, 49.5)
VI-9	372 (2.8), 314 (sh, 7.1), 290 (13.7), 218 (sh, 30.2)

VI.3.6. Electrochemical studies

To confirm that the electronic communication between the complex and the cluster is negligible, the electrochemical properties of the different compounds were investigated using both cyclic voltammetry (CV) and square-wave (SW) measurements. The results are gathered in Table VI.3 while the cyclic voltammograms can be found in Fig XII.14-XII.25. Regarding redox properties for the ligands, they all exhibit several reductions and one oxidation. **VI-L1** is harder to reduce than **VI-L3**, itself harder to reduce than **VI-L2**, in agreement with the increasing electron-accepting character correlated to the additional amide group in the case of **VI-L3** and the extended conjugation in the case of **VI-L2**.

The oxidation process, also observed in **VI-8**, is attributed to the triol moiety, as it was not observed in the model with a *tert*-butyl amide we reported elsewhere.[20] The oxidation of compound **VI-8** is harder than in the ligand due the electron withdrawing nature of the POM, thus confirming the existence of some communication, albeit with a limited spatial range as discussed by some of us on a similar system.[28]

In the case of the POM based species, increasingly problematic adsorption phenomena on the glassy carbon electrode were observed upon reduction. Using CH_3CN instead of DMF reduced the impact of the adsorption, however, the redox processes remained ill-defined in some cases

and the values in Table VI.3 are thus extracted from the SW measurements. In addition, ferrocene could not be used as an internal reference as it partially overlapped with the first reduction process and appeared to react with the reduced species produced. To increase the reference potential, we chose a derivative of ferrocene, namely acetyl-ferrocene (AcFc).[67]

Table VI.3. Redox potentials of ligands **VI-L1-L3**, hybrids **VI-1-3** and **VI-8**, POM **VI-7** and Re complexes **VI-4-6** and **VI-9**

Compound	Reductions (V vs SCE)	Oxidations (V vs SCE)
VI-L1[a]	-1.78 (irr), -2.15 (qr,170), -2.46 (irr)	1.05 (irr)
VI-L2[a]	-1.62 (qr, 280), -2.07 (qr, 200), -2.59 (irr)	0.92 (irr)
VI-L3[a]	-1.72 (irr), -1.98 (qr, 80), -2.36 (irr)	0.88 (irr)
VI-1[b]	0.25, -0.06, -0.75, -1.09, -1.51, -1.94, -2.23	-
VI-2[b]	0.25, 0.01, -0.14, -0.78, -1.09, -1.50, -1.84, -2.23	-
VI-3[b]	0.30, -0.51, -1.03, -1.28, -1.59, -1.77, -1.94	-
VI-4[b]	0.38, -0.60, -1.08, -1.17, -1.56, -1.90, -2.24	0.88 (irr), 1.42 (irr), 1.88(irr)
VI-5[b]	0.35, -0.61, -1.03, -1.13, -1.53, -1.80, -2.26	0.88 (irr), 1.33 (irr), 2.08(irr)
VI-6[b]	0.36, -0.48, -0.97, -1.40, -2.32	0.90 (irr), 1.45(irr)
VI-7[b]	0.37, 0.09, -0.81, -1.17, -1.45, -1.95, -2.24	-
VI-8[b]	0.17, -0.04, -1.03, -1.48, -1.57, -1.95, -2.20	1.51 (irr)
VI-9[c]	-1.41 (qr, 94), -1.80 (irr), -2.18 (irr), -2.50 (qr, 140)	0.86 (irr), 1.36(irr), 1.88 (irr)

All redox potentials were measured (V vs. SCE) at RT in degassed solutions with 1 mM of analyte and 0.1 M $TBAPF_6$ as supporting Electrolyte. [a] in DMF with Fc as internal reference (0.45V vs SCE), [b] in CH_3CN with AcFc as internal reference (0.71 V vs SCE), reduction potentials are extracted from SW experiments due to increased problems of adsorption of multi-charged species; [c] in CH_3CN with Fc as internal reference (0.40V vs SCE)

The tri-vanadium substituted Dawson polyoxotungstate is a class I POM per Pope's classification.[68] According to previous electrochemical investigation,[15,28,62] the first three reduction processes take place on the three V^V centers. These reductions were described as two (mono and bi-electronic) or three separated waves. When compared to the starting POM **VI-7**, the functionalized POMs **VI-1**, **VI-2**, **VI-3** and **VI-8** are reduced at lower potential. This shift of the first reduction shows that there is some electronic communication between the organic part and the POM. Indeed, one would expect the presence of an electron donating group such as the amine in **VI-8** would make the reduction of the spatially close V^V center harder. Besides, the reduction is harder in the case of **VI-8** than for **VI-1-3**, in agreement with the reduced electron donating properties of the amine group once it is included in the amide function. However, the first V^V reduction is similar in the POM based Re complexes **VI-4-6** and the native

POM **VI-7**. This can be explained by the further diminished electronic density on the amide function after coordination, as the {$Re(CO)_3Br$} moiety is an electron withdrawing group, due to the back-electron transfer towards the carbonyls. Less attention has been given in the literature to the following reduction that are expected to take place on the W^{VI} centers. In their initial report, Pope *et al.* studied **VI-7** in water and reported two polyelectronic reduction at -0.70 V and -0.84 V (*vs* Ag/AgCl), with 2 and 4 electrons involved, respectively.[62] In our hands, **VI-7** gave a first W centered reduction at -0.81 V (*vs* SCE in CH_3CN), with four additional reductions at lower potentials. Similar reductions are observed in our functionalized POMs and their equivalent Re complexes. Due to the adsorption problem encountered, we chose not to extend the discussion on these processes any further. Besides, we were unable to distinguish between ligand and POM based reductions as the ligand-based redox processes, monoelectronic, are hidden by the polyelectronic reductions on the cluster. To assign the oxidation potential observed for the Re complexes **VI-4− VI-6**, we referred to the study by Bullock *et al.* on the multiple oxidation processes of **VI-9** in CH_3CN.[69] This work proved that a disproportionation reaction via a bromide-bridged intermediate dimer takes place after the oxidation to form the Re^{II} species around 1.3 V. This disproportionation leads to the formation of an acetonitrile adduct, where the solvent is replacing the bromide anion. This acetonitrile complex is reversibly oxidized at higher potential (i.e. around 1.8 V). Noteworthy, this adduct was not observed for compound **VI-6**. This is not surprising as the size of the compound should disfavour the dimerization step. The presence of free bromide is confirmed by the oxidation peak of the Br_2/Br^- couple around 0.88 V. When compared to reference **VI-9**, our POM based Re complexes **VI-4-6** are slightly harder to oxidize, as expected due to the electron withdrawing nature of the ligand used.

VI.3.7. Investigation of the luminescence quenching

Based on the reduction potentials described above, we propose that the absence of luminescence in compound **VI-4**, **VI-5** and **VI-6** can be caused by intramolecular electron transfer, leading to a transient charge-separated excited state, relaxing to the ground state via back electron transfer. Indeed, using the Rehm-Weller equation, the excited state oxidation potential $E^*_{(ReII/Re^*I)}$ of the different compounds is estimated to be around 1.3 – (1240/650) = -0.6 V, thus lower in potential than the three vanadium centered reductions previously described. To confirm this hypothesis,

we decided to investigate the bimolecular luminescence quenching of **VI-9** by **VI-7** in solution, since the native POM **VI-7** exhibits similar redox properties with the hybrid rhenium complexes **VI-4-6**. Due to the overlapping absorption spectra leading to a strong inner-filter effect, we followed the quenching by measuring the lifetime variation of **VI-9** (τ_0 = 73 ns). A diffusion limited quenching was observed with k_q = 5.9 x 10^9 $mol^{-1}.L.s^{-1}$. (Fig. XII.26) This result confirms the possibility of quenching by electron transfer which would be much more efficient and possibly faster in the prepared hybrids as the covalent link between Re complex and the functionalized POM favours the intramolecular electron transfer process, overcoming the diffusion rate limitation. Theoretical calculations were also performed to model the electronic properties of **VI-4** and obtain more insight into the different accessible excited states upon excitation of the Re(d)→π* ^{1}MLCT bands. Complex **VI-9** was also investigated to verify the model validity and complete details on the computational data can be found in the Chap. XII.

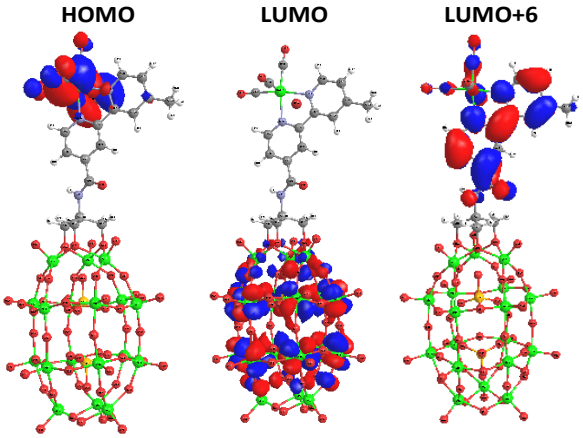

Figure VI.7. Selected Molecular Orbitals for **VI-4** (Isovalue 0.03 e A-3).

The LUMOs are centered on the POM except LUMO+6 which is ligand centered, as shown in part in Fig. VI.7 and more extensively in Table XII.3, which displays the electronic contribution of the different units of **VI-4** in the orbitals from LUMO+6 to HOMO-4. On the other hand, HOMO to HOMO-2 are centered on the {$Re(CO)_3Br$} moiety, while HOMO-3 and HOMO-4 have mixed contributions located around the triol-amide fragment, illustrating the limited range of electron delocalization as expected for a triol modified POM.[28] Analysis of the TD-DFT results, presented in part in Table VI.4 (see Table XII.4 for complete data), confirm the attribution of the UV-vis transition proposed above and show the existence of several optically dark states surrounding the MLCTs and LMCTs transitions. The presence of these dark states,

corresponding to effective charge separated states (CSS) (i.e. charge transfer from the {Re(CO)$_3$Br} moiety to the POM), is expected to facilitate electron transfer from the π* orbital of the bipyridine ligand to the vacant d orbitals on the POM after population of the $^{1/3}$MLCT levels. Noteworthy, the lowest CSSs appear to have mixed singlet and triplet nature, probably due to the strong spin-orbit coupling expected for third-row transition metal like Re and W. Similar results were obtained from the theoretical study conducted by Proust *et al.* on an Ir-POM hybrid.[39] Based on these results, we propose the schematic energy diagram on Fig. 6.8 to explain the luminescence quenching by intramolecular charge transfer.

Table VI.4. First predicted singlet and triplet transitions with their respective wavelength, main contribution, oscillator strength and attribution for **VI-4.**

S_0 to	λ(nm)	Contribution	Osc. Strength	Attribution
S_1/T_1	523	H→L	0	Re→POM CSS
S_2/T_2	511	H-1→L	0	Re→POM CSS
S_3/T_3	472	H→L+1	0	Re→POM CSS
S_4/T_4	471	H→L+2	0	Re→POM CSS
T_5	465	H→L+6	0	Re(d)→π* MLCT
S_5/T_6	463	H-1→L+1	0	Re→POM CSS
S_6/T_7	462	H-1→L+2	0	Re→POM CSS
T_{10}	453	H-1→L+6	0	Re(d)→π* MLCT
S_7	447	H-3→L	0	O→V^V(d) LMCT
S_8	446	H→L+6	0.004	Re(d)→π* MLCT
S_9	436	H-3→L+1	0.011	O→V^V(d) LMCT
S_{10}	423	H-1→L+6	0.091	Re(d)→π* MLCT

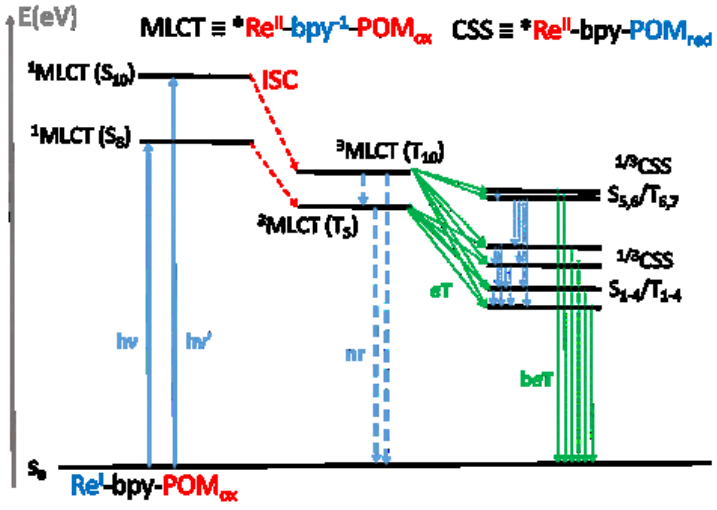

Figure VI.8. Energy diagram showing the pathway for luminescence quenching via intramolecular electron transfer. (nr : non-radiative, eT : electron transfer, beT : back electron transfer, ISC : intersystem crossing).

VI.4. Conclusion

Herein, we have reported the synthesis and characterization of three new hybrid Re(I) carbonyl complexes based on polypyridine functionalized polyoxometalate. These covalent hybrids exhibit enhanced photosensitization in the visible, up to 500 nm, while maintaining the properties of each of their constitutive units. In all cases, the well documented emission arising from the ^{3}MLCT state of Re diimine complexes is quantitatively quenched. We proposed that an intramolecular electron transfer from the excited Re center to the POM is responsible for this quenching. We are currently investigating the possibility of using the theorized charge-separated state in photocatalytic reactions such as light-driven hydrogen production.

VI.5. References

1. M. T. Pope, *Heteropoly and Isopoly Oxometalates*, Springer-Verlag Berlin Heidelberg GmbH, 1983.
2. M. T. Pope and A. Muller, *Angew. Chem. Int. Ed.*, 1991, **30**, 34-48.
3. P. Gouzerh and M. Che, *L'actualité chimique*, 2006, **298**, 9-22.
4. M. T. Pope and A. Muller, eds., *Topics in molecular organization and engineering*, Polyoxometalates : from platonic solids to anti-retroviral activity, Springer, 1994.
5. L. Cronin and A. Muller, eds., *Chem. Soc. Rev.*, Polyoxometalate cluster science (theme collection), 2012.
6. R. v. Eldik and L. Cronin, eds., *Advances in Inorganic Chemistry*, Polyoxometalate Chemistry, Elsevier, 2017.
7. C. L. Hill, ed., *Chem. Rev.*, Special Issue on polyoxometalates chemistry, 1998.
8. A. Dolbecq, E. Dumas, C. R. Mayer and P. Mialane, *Chem. Rev.*, 2010, **110**, 6009-6048.
9. A. Proust, B. Matt, R. Villanneau, G. Guillemot, P. Gouzerh and G. Izzet, *Chem. Soc. Rev.*, 2012, **41**, 7605-7622.
10. M. P. Santoni, G. S. Hanan and B. Hasenknopf, *Coord. Chem. Rev.*, 2014, **281**, 64-85.
11. A. Blazevic and A. Rompel, *Coord. Chem. Rev.*, 2016, **307**, 42-64.
12. G. Izzet, F. Volatron and A. Proust, *Chem. Rec.*, 2017, **17**, 250-266.
13. C. Streb, *Dalton Trans.*, 2012, **41**, 1651-1659.

14. S. Piccinin, A. Sartorel, G. Aquilanti, A. Goldoni, M. Bonchio and S. Fabris, *Proc. Natl. Acad. Sci. U.S.A.*, 2013, **110**, 4917-4922.

15. Y. Hou and C. L. Hill, *J. Am. Chem. Soc.*, 1993, **115**, 11823-11830.

16. B. Hasenknopf, R. Delmont, P. Herson and P. Gouzerh, *Eur. J. Inorg. Chem.*, 2002, **2002**, 1081-1087.

17. J. Li, I. Huth, L. M. Chamoreau, B. Hasenknopf, E. Lacote, S. Thorimbert and M. Malacria, *Angew. Chem. Int. Ed.*, 2009, **48**, 2035-2038.

18. A. Müller, J. Meyer, H. Bögge, A. Stammler and A. Botar, *Z. Anorg. Allg. Chem.*, 1995, **621**, 1818-1831.

19. P. R. Marcoux, B. Hasenknopf, J. Vaissermann and P. Gouzerh, *Eur. J. Inorg. Chem.*, 2003, **2003**, 2406-2412.

20. M. P. Santoni, A. K. Pal, G. S. Hanan, A. Proust and B. Hasenknopf, *Inorg. Chem.*, 2011, **50**, 6737-6745.

21. H. Zeng, G. R. Newkome and C. L. Hill, *Angew. Chem. Int. Ed.*, 2000, **39**, 1771-1774.

22. E. F. Wilson, H. N. Miras, M. H. Rosnes and L. Cronin, *Angew. Chem. Int. Ed.*, 2011, **50**, 3720-3724.

23. P. Wu, P. Yin, J. Zhang, J. Hao, Z. Xiao and Y. Wei, *Chem. Eur. J.*, 2011, **17**, 12002-12005.

24. D. Lachkar, D. Vilona, E. Dumont, M. Lelli and E. Lacote, *Angew. Chem. Int. Ed.*, 2016, **55**, 5961-5965.

25. C. Allain, D. Schaming, N. Karakostas, M. Erard, J. P. Gisselbrecht, S. Sorgues, I. Lampre, L. Ruhlmann and B. Hasenknopf, *Dalton Trans.*, 2013, **42**, 2745-2754.

26. J. M. Lehn, *Supramolecular Chemistry, Concepts and Perspectives*, VCH Verlagsgesellschaft mbH, 1995.

27. S. Favette, B. Hasenknopf, J. Vaissermann, P. Gouzerh and C. Roux, *Chem. Commun.*, 2003, 2664-2665.

28. I. Azcarate, I. Ahmed, R. Farha, M. Goldmann, X. Wang, H. Xu, B. Hasenknopf, E. Lacote and L. Ruhlmann, *Dalton Trans.*, 2013, **42**, 12688-12698.

29. A. Abhervé, M. Palacios-Corella, J. M. Clemente-Juan, R. Marx, P. Neugebauer, J. van Slageren, M. Clemente-León and E. Coronado, *J. Mater. Chem. C.*, 2015, **3**, 7936-7945.

30. M. P. Santoni, A. K. Pal, G. S. Hanan, M. C. Tang, K. Venne, A. Furtos, P. Menard-Tremblay, C. Malveau and B. Hasenknopf, *Chem. Commun.*, 2012, **48**, 200-202.

31. C. Allain, S. Favette, L. M. Chamoreau, J. Vaissermann, L. Ruhlmann and B. Hasenknopf, *Eur. J. Inorg. Chem.*, 2008, **2008**, 3433-3441.

32. J. J. Walsh, A. M. Bond, R. J. Forster and T. E. Keyes, *Coord. Chem. Rev.*, 2016, **306**, 217-234.

33. A. Parrot, A. Bernard, A. Jacquart, S. A. Serapian, C. Bo, E. Derat, O. Oms, A. Dolbecq, A. Proust, R. Metivier, P. Mialane and G. Izzet, *Angew. Chem. Int. Ed.*, 2017, **56**, 4872-4876.

34. A. Harriman, K. J. Elliott, M. A. H. Alamiry, L. Le Pleux, M. Severac, Y. Pellegrin, E. Blart, C. Fosse, C. Cannizzo, C. R. Mayer and F. Odobel, *J. Phys. Chem. C*, 2009, **113**, 5834-5842.

35. Z. H. Huo, D. J. Zang, S. Yang, R. Farha, M. Goldmann, B. Hasenknopf, H. L. Xu and L. Ruhlmann, *Electrochim. Acta*, 2015, **179**, 326-335.

36. B. Matt, C. Coudret, C. Viala, D. Jouvenot, F. Loiseau, G. Izzet and A. Proust, *Inorg. Chem.*, 2011, **50**, 7761-7768.

37. B. Matt, J. Moussa, L. M. Chamoreau, C. Afonso, A. Proust, H. Amouri and G. Izzet, *Organometallics*, 2012, **31**, 35-38.

38. B. Matt, J. Fize, J. Moussa, H. Amouri, A. Pereira, V. Artero, G. Izzet and A. Proust, *Energy Environ. Sci.*, 2013, **6**, 1504-1508.

39. B. Matt, X. Xiang, A. L. Kaledin, N. N. Han, J. Moussa, H. Amouri, S. Alves, C. L. Hill, T. Q. Lian, D. G. Musaev, G. Izzet and A. Proust, *Chem. Sci.*, 2013, **4**, 1737-1745.

40. S. Schonweiz, S. A. Rommel, J. Kubel, M. Micheel, B. Dietzek, S. Rau and C. Streb, *Chem. Eur. J.*, 2016, **22**, 12002-12005.

41. M. P. Santoni, A. K. Pal, G. S. Hanan, M. C. Tang, A. Furtos and B. Hasenknopf, *Dalton Trans.*, 2014, **43**, 6990-6993.

42. B. Riflade, J. Oble, L. Chenneberg, E. Derat, B. Hasenknopf, E. Lacote and S. Thorimbert, *Tetrahedron*, 2013, **69**, 5772-5779.

43. M. Wrighton and D. L. Morse, *J. Am. Chem. Soc.*, 1974, **96**, 998-1003.

44. J. Hawecker, J.-M. Lehn and R. Ziessel, *J. Chem. Soc., Chem. Commun.*, 1983, 536-538.

45. Y. Yamazaki, H. Takeda and O. Ishitani, *J. Photochem. Photobiol., C*, 2015, **25**, 106-137.

46. A. Zarkadoulas, E. Koutsouri, C. Kefalidi and C. A. Mitsopoulou, *Coord. Chem. Rev.*, 2015, **304**, 55-72.

47. T. Klemens, A. Switlicka-Olszewska, B. Machura, M. Grucela, H. Janeczek, E. Schab-Balcerzak, A. Szlapa, S. Kula, S. Krompiec, K. Smolarek, D. Kowalska, S. Mackowski, K. Erfurt and P. Lodowski, *RSC Adv.*, 2016, **6**, 56335-56352.

48. R. Alberto, R. Schibli, R. Waibel, U. Abram and A. P. Schubiger, *Coord. Chem. Rev.*, 1999, **190-192**, 901-919.

49. J. Ettedgui, Y. Diskin-Posner, L. Weiner and R. Neumann, *J. Am. Chem. Soc.*, 2011, **133**, 188-190.

50. E. Haviv, L. J. Shimon and R. Neumann, *Chem. Eur. J.*, 2017, **23**, 92-95.

51. R. Villanneau, R. Delmont, A. Proust and P. Gouzerh, *Chemistry-a European Journal*, 2000, **6**, 1184-1192.

52. R. Villanneau, A. Proust, F. Robert and P. Gouzerh, *Chem. Eur. J.*, 2003, **9**, 1982-1990.

53. C. Zhao, W. Rodriguez-Cordoba, A. L. Kaledin, Y. Yang, Y. V. Geletii, T. Lian, D. G. Musaev and C. L. Hill, *Inorg. Chem.*, 2013, **52**, 13490-13495.

54. C. Zhao, E. N. Glass, J. M. Sumliner, J. Bacsa, D. T. Kim, W. Guo and C. L. Hill, *Dalton Trans.*, 2014, **43**, 4040-4047.

55. J. G. Jia, Y. H. Zhang, P. P. Zhang, P. T. Ma, D. D. Zhang, J. P. Wang and J. Y. Niu, *RSC Adv.*, 2016, **6**, 108335-108342.

56. J. Li, J. Guo, J. Jia, P. Ma, D. Zhang, J. Wang and J. Niu, *Dalton Trans.*, 2016, **45**, 6726-6731.

57. G. R. Newkome, G. R. Baker, S. Arai, M. J. Saunders, P. S. Russo, K. J. Theriot, C. N. Moorefield, L. E. Rogers and J. E. Miller, *J. Am. Chem. Soc.*, 1990, **112**, 8458-8465.

58. C. P. Pradeep, F. Y. Li, C. Lydon, H. N. Miras, D. L. Long, L. Xu and L. Cronin, *Chem. Eur. J.*, 2011, **17**, 7472-7479.

59. R. G. Finke, B. Rapko, R. J. Saxton and P. J. Domaille, *J. Am. Chem. Soc.*, 1986, **108**, 2947-2960.

60. W. W. Laxson, S. Ozkar and R. G. Finke, *Inorg. Chem.*, 2014, **53**, 2666-2676.

61. C. P. Pradeep, D. L. Long, G. N. Newton, Y. F. Song and L. Cronin, *Angew. Chem. Int. Ed.*, 2008, **47**, 4388-4391.

62. S. P. Harmalker, M. A. Leparulo and M. T. Pope, *J. Am. Chem. Soc.*, 1983, **105**, 4286-4292.

63. E. W. Abel, V. S. Dimitrov, N. J. Long, K. G. Orrell, A. G. Osborne, H. M. Pain, V. Šik, M. B. Hursthouse and M. A. Mazid, *J. Chem. Soc., Dalton Trans.*, 1993, 597-603.

64. B. Laramee-Milette, N. Zaccheroni, F. Palomba and G. S. Hanan, *Chem. Eur. J.*, 2017, **23**, 6370-6379.

65. C. Bruckmeier, M. W. Lehenmeier, R. Reithmeier, B. Rieger, J. Herranz and C. Kavakli, *Dalton Trans.*, 2012, **41**, 5026-5037.

66. C. Liu, K. D. Dubois, M. E. Louis, A. S. Vorushilov and G. Li, *ACS Catal.*, 2013, **3**, 655-662.

67. J. R. Aranzaes, M. C. Daniel and D. Astruc, *Can. J. Chem.*, 2006, **84**, 288-299.

68. M. T. Pope, *Inorg. Chem.*, 1972, **11**, 1973-1974.

69. J. P. Bullock, E. Carter, R. Johnson, A. T. Kennedy, S. E. Key, B. J. Kraft, D. Saxon and P. Underwood, *Inorg. Chem.*, 2008, **47**, 7880-7887.

Chapitre VII. Tuning the electron transfer kinetics in covalent dyads based on polyoxometalate and rhenium photosensitizer

VII.1 Contexte et résumé

Nous avons étendu la famille de dyades décrites au chapitre précédent par l'intégration d'espaceurs phényles entre POM et complexes, faisant l'hypothèse que cela permettrait de moduler le transfert électronique, en accord avec la théorie de Marcus. Nous avons également vérifié s'il était possible de piéger l'état de séparation de charge créé par le transfert d'électron intramoléculaire photoinduit mis en évidence dans l'étude précédente. Nous supposions qu'en réduisant le centre métallique, il serait possible de bloquer le transfert d'électron en retour. Ce piégeage réductif permettrait alors l'accumulation de charge sur le cluster, potentiellement utilisable pour conduire la réaction de réduction de protons pour former du dihydrogène.

Expérimentalement, notre hypothèse est confirmée par la restauration partielle de l'émission dans le cadre des dyades avec espaceurs. Des mesures d'absorption transitoires ont permis d'obtenir des informations relatives aux constantes de vitesse de séparation et de recombinaison de charge. En présence de triéthanolamine, une transition additionnelle est observée dans le spectre UV-visible de la dyade placée sous irradiation lumineuse ($\lambda = 410$ nm). Cette transition d'intervalence indique que le cluster est réduit, l'électron étant présent pour une durée au moins égale à l'échelle de temps caractéristique des mesures d'absorption (de l'ordre de la seconde). En nous appuyant sur ces résultats, les dyades furent testées pour la production photocatalysée de dihydrogène. Contrairement aux études similaires dans la littérature, le système bimoléculaire performe bien mieux que nos dyades, quasiment inactives. Nous avons donc décidé d'ajouter un co-catalyseur à base de platine afin d'accélérer la réoxydation du cluster. Dans ce système, le POM joue alors le rôle de médiateur d'électrons et conduit à une amélioration de la stabilité dans le cas des dyades et du système bimoléculaire, dans une moindre mesure.

Tuning the electron transfer kinetics in covalent dyads based on polyoxometalate and rhenium photosensitizer

Thomas Auvray,[a] Georges Turner,[a] Mirco Natali,[b]* Garry S. Hanan[a]*

a. Département de Chimie, Université de Montréal, Montréal, Canada, H3T-1J4

b. Dipartimento di Scienze Chimiche e Farmaceutiche, Università degli Studi di Ferrara, Via L. Borsari, 46, 44121 Ferrara

Full paper

Manuscript in preparation

Contributions :

Thomas Auvray : Conception du projet. Synthèse et caractérisation complète des ligands, hybrides et complexes. Analyse des propriétés optiques et électroniques. Mesures photocatalytiques. Rédaction de l'article.

Georges Turner : Synthèse et caractérisation partielle de ligands et POMs.

Mirco Natali : Absorption transitoire (picosecondes), spectro-électrochimie, révision de l'article.

Garry S. Hanan : Supervision, révision de l'article.

VII.2 Abstract

As a model for heterogenization on metal oxides, functionalized polyoxometalates (POMs) in which a catalyst is covalently attached have attracted attention in the past decade. Covalent dyads combining Ir(III) photosensitizers (PSs) and POMs have been shown to outperformed the corresponding bimolecular system in photocatalytic hydrogen evolution both in term of activity and stability. In this study, we applied our previously reported Re(I) complexes based on polypyridyl functionalized Dawson polyoxovanadotungstates for photocatalytic hydrogen evolution. The dyads themselves showed poor activity and are less efficient than the bimolecular systems, unlike similar systems reported in the literature. However, addition of a platinum co-catalyst to favour re-oxidation of the reduced POMs allows for significant enhancement of the activity which is sustained for a longer period for the dyads than the dissociated system. In addition, the electron transfer dynamic within the dyads was investigated using two new dyads with phenyl spacers between PS and POM units. Transient absorption measurements showed fast charge separation and recombination within the dyads, with the expected increase in electron transfer rates induced by the phenyl spacers unit, proving the versatility of our grafting design.

VII.3 Introduction

As an answer to the need of replacing fossil fuels by cleaner, renewable energy sources as soon as possible to address the current global climate crisis, the field of artificial photosynthesis has developed over the past decades.[1-3] Inspired by the finely tuned photosynthetic process found in Nature, catalysts and photosensitizers were developed to create photocatalytic systems capable of converting water (H_2O) or carbon dioxide (CO_2) into oxygen (O_2) and potential energy sources, called solar fuels, such as hydrogen (H_2), methanol (CH_3OH) or methane (CH_4), using (sun)light as energy input.[4-5] Transition-metal coordination compounds are of particular interest to address the challenge of driving these multielectron redox processes from 2 electron reactions such as H_2 evolution up to 8 electron reductions of CO_2 to CH_4, and their large tunability through variation of the ligands in the coordination sphere offers a vast scope of optimization path for both activity and selectivity, crucial in the case of CO_2 reduction.[6-7] The structurally well-defined catalytic sites also allow for mechanistic studies as each metal centre is an active

site, unlike in materials such as metal oxides where defect and surface elements act differently from the bulk. Building on these advantages, stepwise increase of the intrinsic activity of the catalyst and optimization of the energy collection of the photosensitizer have been reported, which combined led to increased activity of the photocatalytic systems. However, doubt have started to emerge regarding their integration in actual commercial devices as the long-term stability of these systems is problematic.[3] There is indeed a need for improvement in that aspect and a proposed solution is the heterogenization of the molecular species, combining their tunability with the manufacturability of materials. This approach comes with additional challenges due to the change in the nature of the electron transfer, now occurring at the material-molecule interface.[8]

Polyoxometalates (POMs), oxo-cluster of early transition metals,[9] have been compared to metal oxide due to the similarity in their electronic properties.[10-11] They have also been used as catalyst for water oxidation and more recently hydrogen evolution.[12] Over the past decades, there has been tremendous research efforts to functionalise these clusters,[13-14] especially focused on improving the light harvesting properties of the resulting organic-inorganic hybrids.[15-16] Covalently functionalized POMs can be seen as model platforms for heterogenization of molecular species on metal oxide. Successful demonstration of that possibility related to the field of artificial photosynthesis was reported by Proust *et coll.* using a silanol derived vacant polyoxotungstate decorated with iridium photosensitizers in a photocatalytic system for H_2 production stable for at least a weak.[17] In addition, their dyad outperformed the corresponding bimolecular system. Since, Streb *et coll.* reported a conceptually similar system using a different grafting approach, i.e. alkoxide replacement of the native oxo ligand, and their Ir-POM covalent system showed better activity than the previous system, while again outperforming the bimolecular system.[18] The grafting approach in their study[19-20] is similar to the one we used in our report of a covalently modified polyoxovanadotungstate applied as ligands for rhenium carbonyl complexes.[21-22] Initial photophysical study indicated the presence of an efficient photoinduced electron transfer within the Re-POM dyads quenching the Re(I) complex emission.[22] Based on this observation and the proofs of concept in the literature, we decided to investigate the potential of our dyads for photocatalytic H_2 evolution. We were also interested to gain additional insight regarding the intramolecular photoinduced electron transfer and thus

prepared dyads containing phenyl spacers between the two redox centres, in order to tune the transfer and possibly observe an impact of these modifications on the photocatalytic activity.

VII.4 Experimental section

VII.4.1 Materials

$Re_2(CO)_{10}$ was obtained from Pressure Chemical and converted to $Re(CO)_5Br$ via titration with bromine.[23] Solvents were of ACS or spectroscopic grade (for absorption and emission measurements) and used as received, like other reagents, from commercial sources (Millipore Sigma or Fisher Scientific). Acetonitrile for electrochemistry was distilled from CaH_2 and stored under N_2.

VII.4.2 Physical measurements

^1H and ^{13}C NMR spectra were acquired on a Bruker AV400 (400MHz). Chemical shifts are reported in part per million (ppm) relative to the residual proton (7.26 ppm for $CDCl_3$, 2.50 ppm for DMSO-d^6, 1.94 ppm for CD_3CN) or carbon resonances (77.16 ppm for $CDCl_3$, 39.52 ppm for DMSO-d^6) of the solvent. All photophysical measurements were carried out in deaerated solutions (acetonitrile). ESI-MS measurements were made on a Bruker Daltonics MicrOTOF II. Absorption spectra were measured on an Agilent Cary6000i UV-Vis-NIR spectrophotometer and luminescence spectra at room temperature and 77 K on a Perkin-Elmer LS55 fluorescence spectrometer. Infra-red vibration spectroscopy measurements were conducted on a Perkin-Elmer Spectrum2 in ATR mode. Electrochemical measurements involved a three-electrode set-up with a glassy carbon disk (d = 3 mm) working electrode, a platinum coil as counter electrode and a platinum wire as pseudo-reference. Measurements were made using a SP-50 BioLogic potentiostat interfaced to a computer equipped with the EC-lab software V11.21. The potentials were referenced internally using the ferrocenium/ferrocene (0.40 V *vs.* SCE)[24] or the acetylferrocenium/acetylferrocene couple (0.71 V *vs.* SCE).[25] The concentration of analyte was approximatively 1 mM while the supporting electrolyte (tetrabutylammonium hexafluorophosphate TBAP) was at 0.1 M.

VII.4.3 Synthesis of the ligands

Ligands **VII-L1-3** were prepared following our previous report.[22] The acid and ethyl ester precursors for **VII-L4-7** were prepared following literature procedures.[26-28]

VII-L4 4-([2,2':6',2"-terpyridin]-4'-yl)-N-(1,3-dihydroxy-2-(hydroxymethyl) propan-2-yl) benzamide

The ethyl ester precursor (1 eq.) was dissolved in dry DMSO, then K_2CO_3 (1 eq.) and TRIS (tris(hydroxymethyl)aminomethane, 1 eq.) were added and the suspension was stirred under N_2. It turned progressively to a limpid yellow solution. After two days, the desired compound was obtained by pouring the mixture in excess water to give a white suspension. The product was then extracted with $CHCl_3$, the organic phase dried with Na_2SO_4 and the solvent removed under reduced pressure. The white residue was recrystallized in MeOH/Et_2O at -20 °C overnight. Yield: 370 mg (81% on a 1 mmol scale).

^{1}H NMR (DMSO-d^6, 400 MHz) : δ 8.79 (d, 2H), 8.76 (s, 2H), 8.69 (d, 2H), 8.06 (td, 2H), 8.03 (s, 4H), 7.55 (ddd, 2H), 7.45 (br, 1H, NH), 4.80 (t, 3H), 3.74 (d, 6H) ; ^{13}C NMR (DMSO-d^6, 100 MHz, 298 K) : δ 166.7, 155.8, 154.9, 149.4, 148.7, 139.9, 137.6, 136.0, 128.4, 126.8, 124.7, 121.0, 118.1, 62.8 and 60.3 ; ESI-MS (MeOH, positive mode) Calc. $[M+Na]^+$ 479.1690, Found 476.1630.

VII-L5 4'-([2,2':6',2"-terpyridin]-4'-yl)-N-(1,3-dihydroxy-2-(hydroxymethyl) propan-2-yl)-[1,1'-biphenyl]-4-carboxamide

Prepared using the same protocol than **VII-L4**, starting from the appropriate ethyl ester. Yield: 170 mg (71% on a 0.45 mmol scale)

^{1}H NMR (DMSO-d^6, 400 MHz) : δ 8.78 (br, 4H), 8.71 (d, 2H), 8.07 (m, 4H), 7.96 (m, 4H), 7.89 (d, 2H), 7.55 (m, 2H), 7.40 (br, 1H, NH), 4.81 (br, 3H), 3.73 (br, 6H). ^{13}C NMR (DMSO-d^6, 100 MHz, 298 K) : δ 166.9, 155.8, 154.9, 149.4, 148.8, 141.6, 140.1, 137.5, 136.9, 134.3, 128.3, 127.8, 127.6, 126.3, 124.6, 120.9, 117.8, 62.9 and 60.4. ; ESI-MS (MeOH, positive mode) Calc. $[M+Na]^+$ 555.2003, Found 555.1967.

VII-L6 N-(tert-butyl)-4'-methyl-[2,2'-bipyridine]-4-carboxamide

4'-methyl-[2,2'-bipyridine]-4-carboxylic acid (130 mg, 0.6 mmol) was refluxed in $SOCl_2$ (10 mL) for 3 h. The unreacted $SOCl_2$ was then distilled out under reduced pressure and the oily product cooled to RT. It was then dissolved in DCM (10 mL) and *tert*-butylamine (5 eq.) diluted

in DCM (10 mL) was added dropwise. The suspension was then left to stir overnight under nitrogen at RT. The next day, aqueous Na_2CO_3 (20 mL, 1 M) was added and the phases separated. The organic phase was washed with water (20mL) then brine (20mL) and finally dried on Na_2SO_4. The solvent was removed under reduced pressure, affording the desired product as an off-white waxy solid. Yield: 120 mg (74%).

^{1}H NMR ($CDCl_3$, 400 MHz) δ = 8.78 (dd, 1H), 8.55 (d, 1H), 8.52 (s, 1H), 8.27 (m, 1H), 7.74 (dd, 1H), 7.18 (dd, 1H), 6.19 (br. s, 1H, NH), 2.46 (s, 3H), 1.50 (s, 9H) ; ^{13}C NMR (101 MHz, $CDCl_3$) δ 165.33, 155.57, 150.48, 149.32, 144.46, 125.60, 122.64, 122.17, 117.48, 52.60, 29.17, 21.63.

VII-L7 4-([2,2':6',2"-terpyridin]-4'-yl)-N-(tert-butyl)benzamide

Prepared similarly to **VII-L6** starting from 4-([2,2':6',2"-terpyridin]-4'-yl)benzoic acid. Yield: 205 mg (73% on a 0.5 mmol scale).

^{1}H NMR ($CDCl_3$, 400 MHz) δ = 8.75 (m, 4H), 8.68 (dt, 2H), 7.95 (m, 2H), 7.88 (m, 4H), 7.37 (ddd, 2H), 6.01 (br. s, 1H, NH), 1.52 (s, 9H) ; ^{13}C NMR (101 MHz, $CDCl_3$) δ 166.52, 156.30, 156.27, 149.41, 149.34, 141.35, 137.07, 136.41, 127.62, 127.53, 124.10, 121.57, 119.04, 51.95, 29.08.

VII.4.4 Synthesis of the polypyridyl functionalized POM

The functionalized POMs **VII-D1-3** were prepared following our previous report using the polyoxovanadotungstate **VII-P1**.[22] The POM itself was prepared following the detailed procedures from Finke *et al*. as its TBA salt.[29]

VII-D4 $(C_{16}H_{36}N)_5H[P_2V_3W_{15}O_{63}C_{26}H_{21}N_4]$

This compound was prepared following the protocol previously reported. A 1:1 stoichiometric mixture of **VII-P1** and **VII-L4** was dissolved in DMAc (3 mL for 520 mg / 0.1 mmol of **VII-P1**) under N_2 and heated in the dark for 14 days at 80 °C. Once the solution had returned to room temperature, it was added dropwise to excess Et_2O yielding a greenish solid which was re-dissolved in a minimum of MeCN and re-precipitated twice in Et_2O to obtain a yellow powder that was dried at 50 °C. Yield : 98 mg (88% on a 20 µmol scale).

^{1}H NMR (CD_3CN, 400 MHz) : δ 8.78 (s,2H), 8.76 (d, 2H), 8.72 (d, 2H), 8.03-7.95 (m, 6H), 7.46 (dd, 2H), 6.72 (s, 1H, NH), 5.87 (s, 6H) in addition to the TBA resonances ; ^{31}P NMR (162 MHz, CD_3CN) δ -6.72 (s), -12.82 (s) ; ESI-MS (MeCN, negative mode) Calc. for $[M\text{-}4TBA]^{5-}$

922.6398, Found 922.6204 and Calc. for $[M-2TBA]^{3-}$ 1669.2560, Found 1699.2341 ; Elemental analysis calc. (%) for $C_{106}H_{202}N_9O_{63}P_2V_3W_{15}$: C 22.78, H 3.62, N 2.26; found: C 22.48, H 3.66, N 2.28.

VII-D5 $(C_{16}H_{36}N)_5H[P_2V_3W_{15}O_{63}C_{32}H_{25}N_4]$

Prepared as **VII-D4** using **VII-L5**. Yield : 99 mg (87% on a 20 µmol scale))

^{1}H NMR (CD_3CN, 400 MHz) : δ 8.82 (d, 2H), 8.76 (d, 2H), 8.73 (d, 2H), 8.02 (m, 4H), 7.93 (m, 4H), 7.83 (d, 2H), 7.47 (m, 2H), 6.67 (s, 1H, NH), 5.86 (s, 6H) in addition to the TBA resonances ; ^{31}P NMR (162 MHz, CD_3CN) δ -6.71, -12.80 ; ESI-MS (MeCN, negative mode) Calc. for $[M-4TBA]^{5-}$ 937.8461, Found 937.8259 and Calc. for $[M-2TBA]^{3-}$ 1724.5998, Found 1724.5482 ; Elemental analysis calc. (%) for $C_{112}H_{1206}N_9O_{63}P_2V_3W_{15}$: C 23.77, H 3.67, N 2.23; found: C 23.39, H 3.72, N 2.19.

VII.4.5 Synthesis of the Re(I) complexes

VII-C1 $[Re(CO)_3Br($**VII-L6**$)]$

An equimolar mix of $Re(CO)_5Br$ (45 mg, 0.11 mmol) and **VII-L6** (30 mg, 0.11mmol) wasrefluxed in cyclohexane (20 mL) for 3 h. The desired complex precipitated out progressively during this time. The suspension was cooled to RT, then filtered and the yellow solid washed with diethyl ether. Yield: 60 mg (87%)

^{1}H NMR (400 MHz, $CDCl_3$) δ = 9.05 (d, 1H), 8.83 (d, 1H), 8.50 (d, 1H), 8.28 (s, 1H), 7.82 (dd, 1H), 7.27 (m, 1H), 6.45 (s, 1H), 2.44 (s, 3H), 1.55 (s, 9H) ; ^{13}C NMR (101 MHz, $CDCl_3$) δ 196.80, 194.05, 188.73, 162.03, 156.95, 154.94, 153.80, 152.84, 152.19, 145.32, 128.77, 125.27, 124.81, 120.81, 53.58, 29.13, 21.92 ; IR (ATR, cm-1) : 2022 (vs), 1926 (s), 1890 (vs) ; ESI-MS (MeCN, negative mode), Calc for $[M-H]^-$ 618.0021, Found 618.0006 ; Elemental analysis calc. (%) for $C_{19}H_{19}N_3O_4ReBr$: C 36.84, H 3.09, N 6.52; found: C 37.00, H 2.97, N 6.52.

VII-C2 $[Re(CO)_3Br($**VII-L7**$)]$

Prepared as **VII-C1** using **VII-L7**. Yield: 105 mg (92% on a 0.15 mmol scale)

^{1}H NMR (400 MHz, $CDCl_3$) δ = 9.13 (d, 1H), 8.86 (d, 1H), 8.40 (m, 2H), 8.09 (t, 1H), 7.94 (m, 3H), 7.91 (d, 2H), 7.82 (d, 2H), 7.53 (m, 2H), 6.02 (br. s, 1H, NH), 1.53 (s, 9H) ; ^{13}C NMR (101 MHz, $CDCl_3$) δ 197.18, 193.63, 190.01, 166.12, 163.10, 158.18, 157.82, 157.10, 153.51, 150.61, 150.12, 139.08, 138.38, 138.12, 137.51, 128.39, 128.00, 127.05, 125.78, 125.55,

125.44, 124.57, 120.60, 52.46, 29.26 ; IR (ATR, cm-1) : 2024 (vs), 1907 (vs, br) ; ESI-MS (MeCN, negative mode), Calc for $[M+Br]^-$ 838.9694, Found 838.9676 ; Elemental analysis calc. (%) for $C_{29}H_{24}N_4O_4ReBr,H_2O$: C 44.85, H 3.37, N 7.21; found: C 44.90, H 3.02, N 7.11.

VII-D9 $(C_{16}H_{36}N)_5H[P_2V_3W_{15}O_{66}C_{29}H_{21}N_4ReBr]$

The complexation procedure previously reported was used. **VII-D4** was combined to 1 eq. of $Re(CO)_5Br$ in DMAc (3 mL for 520 mg / 0.1 mmol of functionalized POM) under N_2 and heated in the dark overnight at 80 °C. Once the solution had returned to room temperature, it was added dropwise to excess Et_2O yielding a yellow solid which was washed with cold DCM before being re-dissolved in a minimum of MeCN and re-precipitated twice in Et_2O to obtain a yellow-orange powder that was dried at 50 °C. Yield : 50 mg (94 % on a 10 µmol scale)

^1H NMR (CD_3CN, 400 MHz, 298 K) : δ 9.08 (m,2H), 8.81 (m, 2H), 8.55 (m, 1H), 8.39 (m, 2H), 8.05 (m, 4H), 7.87 (m, 1H), 7.65 (m, 1H), 7.59 (m, 1H), 6.69 (br. s, 1H, NH), 5.85 (m, 6H), in addition to the TBA resonances. ^{31}P NMR (162 MHz, CD_3CN) δ -6.75 (s), -12.69 (s). IR (ATR, cm^{-1}) : 2019 (m), 1914 (m), 1891 (m) ; ESI-MS (MeCN, negative mode) Calc. for $[M-4TBA]^{5-}$ 992.6111, Found 992.6150 and Calc. for $[M-2TBA]^{3-}$ 1816.2087, Found 1816.2128 ; Elemental analysis calc. (%) for $C_{109}H_{202}N_9O_{66}P_2V_3W_{15}ReBr$: C 22.06, H 3.43, N 2.12; found: C 21.95, H 3.42, N 2.17.

VII-D10 $(C_{16}H_{36}N)_5H[P_2V_3W_{15}O_{66}C_{35}H_{25}N_4ReBr]$

Prepared as **VII-D9** using **VII-D5**. 91 mg (85% on a 10 µmol scale).

^1H NMR (CD_3CN, 400 MHz, 298 K) : δ 9.08 (t, 1H), 8.80 (m, 2H), 8.74 (d, 1H), 8.28 (m, 1H), 8.13 (m, 3H), 8.00 (t, 1H), 7.96 (m, 4H), 7.88 (d, 2H), 7.82 (m, 2H), 7.65 (m, 1H), 7.58 (m, 1H), 6.69 (br. s, 1H, NH), 5.87 (br. s, 6H) in addition to the TBA resonances ; ^{31}P NMR (162 MHz, CD_3CN) δ -6.72, -12.76 ; IR (ATR, cm^{-1}) : 2018 (m), 1914 (m), 1886 (m); ESI-MS (MeCN, negative mode) Calc. for $[M-4TBA]^{5-}$ 1007.8174, Found 1007.7842 and Calc. for $[M-2TBA]^{3-}$ 1841.5525, Found 1841.5847 ; Elemental analysis calc. (%) for $C_{115}H_{1206}N_9O_{66}P_2V_3W_{15}ReBr$: C 22.98, H 3.46, N 2.10; found: C 22.27, H 3.58, N 2.12.

VII.5 Results and discussion

VII.5.1 Synthesis and structural characterization

The synthetic pathways for the dyads **VII-D6-10** (Figure VII-1) combining Re(I) carbonyl complexes and polypyridyls functionalized POMs are described in the experimental section and schematized in Figures XIII-1 XIII-2. We used the optimized procedures reported previously to obtain the triol equipped ligands **VII-L1-5** and the polypyridyl functionalized POMs **VII-D1-5**.[22] The newly reported functionalized POMs **VII-D4-5** were then prepared *via* the same procedures from the suitable triol equipped terpyridine ligands **VII-L4-5.** These ligands were obtained with higher yield than the ones previously reported due to the lower solubility in water brought by the phenyl spacers and were characterized by ^{1}H, ^{13}C NMR and ESI-MS. The polypyridyl functionalized POMs **VII-D1-5** were characterized by ^{1}H, ^{13}C NMR ESI-MS and EA.

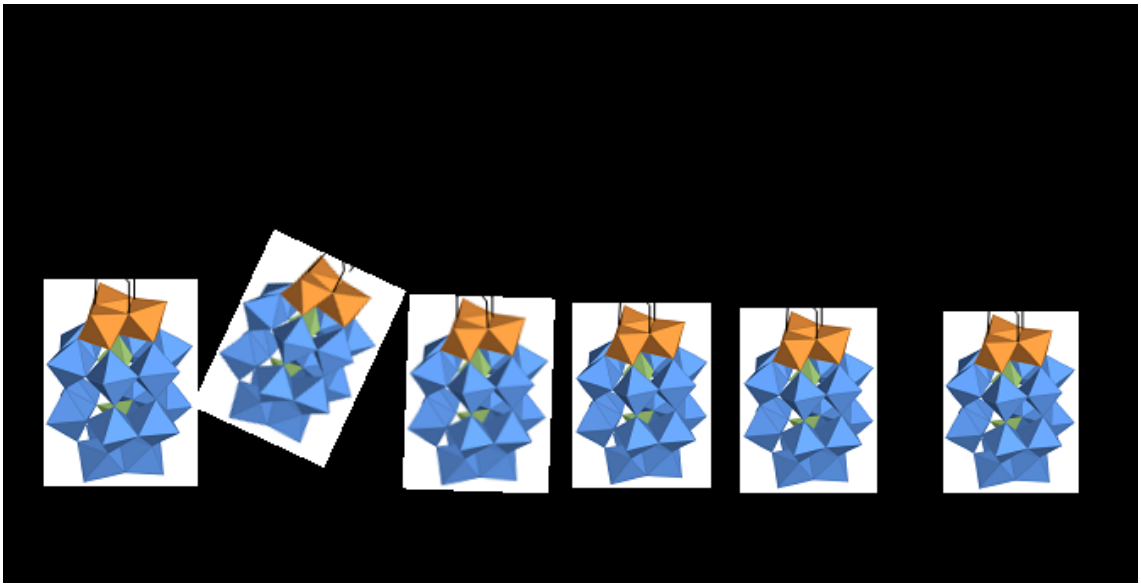

Figure VII.1. Structures of the Re(I) polypyridyl dyads in this study.

They were then used in the complexation reaction allowing integration of the $\{Re(CO)_3Br\}$ moiety as previously reported, affording **VII-D9-10** in good to excellent yield.[22] Their ^{1}H NMR spectra are poorly resolved in the aromatic region, an observation attributed to the fluxionality associated with the bidentate coordination of the 2,2'-6',2''-terpyridine ligands, indicating that the complexation took place. This dynamic phenomenon has been widely studied previously

and we believe the rigid link connecting the complex to the cluster hindered some of the movement.[30-33] The monophenyl spaced species **VII-D9** is more severely affected than the other terpyridine derivatives, tentatively because free rotation the phenyl spacer is affected by both the grafting and the dynamic coordination sites exchange. The success of the complexation reaction can also be observed by IR spectroscopy with the three characteristic CO bands (one symmetric, two antisymmetric vibrations modes) of the facial conformation of the three carbonyls (Figure XIII-13).

For comparison purpose, we prepared two model Re(I) complexes **VII-C1** and **VII-C2** (Figure VII.2) based on *tert*-butyl amide polypyridyl ligands. The identity and purity of these complexes were confirmed by ^{1}H and ^{13}C NMR, ESI-MS, IR spectroscopy as well as EA. The resolved aromatic resonances in the NMR spectra of **VII-C2** confirms that the grafting slows down the site exchange of the Re(I) center in the dyads compared to the complex itself. Theses model complexes exhibit the same three vibrations patterns in their IR spectra, confirming the facial geometry of the carbonyls.

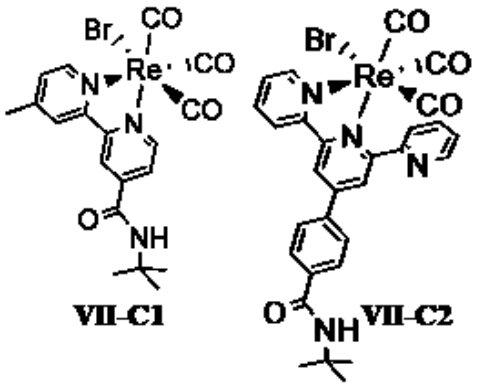

Figure VII.2. Model Re(I) complexes.

VII.5.2 Electronic and photophysical properties

Having prepared the targeted dyads, the next step was to evaluate their electronic and photophysical properties compared to the other in the series, confirming that no unexpected modifications was introduced alongside the spacers. As shown in the previous study, in the ground state, the dyads behave as the sum of their sub-units.[22] The two references complexes were also characterized to provide better comparison values.

Electrochemical measurements were first conducted, in acetonitrile with TBAP (0.1 M) as electrolyte. As in our previous study, poor resolution of the redox processes was observed in cyclic voltammetry as the compounds tend to adsorb at the glassy carbon electrode. The vanadium centred reduction and the irreversible rhenium oxidation could not be clearly observed, even using square wave analysis. The extended phenyl spacer might worsen the adsorption problem, and, in these measurements, the acetylferrocene reference was also

affected. Re(I) carbonyl complexes also have usually poorly resolved cyclic voltammogram due to the irreversibility of all the process, commonly attributed to the loss of the halide ligand.[34]

Table VII.1 Redox potentials of the Re-POMs dyads and model Re(I) complexes in acetonitrile with TBAP 0.1M.

	VII-D6	**VII-D7**	**VII-D8**	**VII-D9**	**VII-D10**	**VII-C1**	**VII-C2**
E_{red}[a] V *vs.* SCE	0.38 -0.60 -1.08 -1.17 -1.56 -1.90 -2.24	0.36 -0.48 -0.97 -1.40 -2.32	0.35 -0.61 -1.03 -1.13 -1.53 -1.80 -2.26	-1.07 -1.37 -1.81 -2.18	-0.48 -1.05 -1.16 -1.54 -2.02 -2.22	-1.26 (qr)	-1.35 (qr)
E_{ox} V *vs.* SCE	0.88 (irr) 1.42 (irr) 1.88 (irr)	0.90 (irr) 1.45 (irr)	0.88 (irr) 1.33 (irr) 2.08 (irr)	1,5 (w, irr)	n.d.	1.39 (irr) 1.95 (irr)	1,18 (irr) 1.93 (irr)

qr quasi reversible; irr irreversible; w weak; [a] from square wave measurement

The overall values obtained for the new extended dyads **VII-D9** and **VII-D10** are in agreement with the previous report, confirming the lack of communication in the ground state.[22] A similar conclusion can be drawn from the absorption spectra of the compounds in acetonitrile, the values being reported in Table VII.2.

Table VII.2. Absorption and emission data for the Re-POM dyads and model complexes in deaerated acetonitrile at room temperature.

Compounds	**Absorption (λ/nm) (ε x 10^3 L mol^{-1} cm^{-1})**	**Emission (λ nm)**
VII-D6	375 (sh, 8.2), 304 (49.2), 260 (sh, 73.9)	N.D.
VII-D7	381 (sh, 17.1), 305 (102.1), 263 (sh, 151.3)	N.D.
VII-D8	381 (sh, 8.1), 313 (46.8), 264 (80.4)	N.D.
VII-D9	377 (sh, 17.1) 300 (103), 265 (125)	660
VII-D10	368 (sh, 29.9), 321 (77), 269 (99)	610
VII-C1	384 (3.4), 297 (13.9), 248 (20.4), 218 (sh, 33.9)	660
VII-C2	385 (4.4), 301 (29.2), 268 (28.9)	665

In the emission spectra of the extended dyads, however, we observed a residual emission at 660 and 610 nm, for **VII-D9** and **VII-D10**, respectively. Due to the weakness of the signal we could not quantify with a reasonable error the quantum yield of the emission of these Re(I) complexes. These weak emissions are however in agreement with the value reported for related complexes. Indeed, a Re(I) complex bearing a 4'(4-py)-tpy ligand in a bidentate coordination mode as the compound analysed here is reported to have a quantum yield of 7.2×10^{-5} in degassed acetonitrile.[35] In the case of **VII-C2** and **VII-D9**, both having the phenyl fragment in the 4' position of the terpyridine, they have similar emission maxima, around 660 nm. The presence of emission for the dyad with phenyl spacers indicates that our design strategy allowed to tune the electron transfer rate. In order to confirm this, transient absorption measurements were conducted.

VII.5.3 Photoinduced electron transfer dynamics and charge accumulation

Based on the proposed photophysical diagram established in our previous study and readapted in Figure VII.4, we expected the spectroscopic signature of the reduced POMs to be the main feature observed during the ultrafast spectroscopic measurements, due to the broadness of the intervalence charge transfer.[36] Besides, the reduced forms of **VII.P1** have been studied spectroscopically by Pope *et al.*, indicating that the transitions have low molar absorption coefficient between 500 and 1000 L mol^{-1} cm^{-1}.[37] Based on these data, the spectral evolution following irradiation at 400nm were recorded. The results are summarized in Table VII.3 while the spectral evolution and fitting curve are presented in Figures XIII-22-27.

The kinetic fit gave three components to the temporal evolution, the first τ_1 being attributed to molecular and/or solvent relaxation within the ^{3}MLCT state populated after excitation at 400nm, followed by the charge separation τ_{CS} via intramolecular electron transfer, creating the charge separated state, and finally τ_{CR} for the recombination regenerating the ground state configuration. The first information is the absence of difference (within the experimental error) in the case of **VII-D6** and **VII-D7** having one and two POM units, respectively. This is coherent as the compounds have similar electrochemical properties, although the presence of two POM units could have favoured enhanced charge separation.

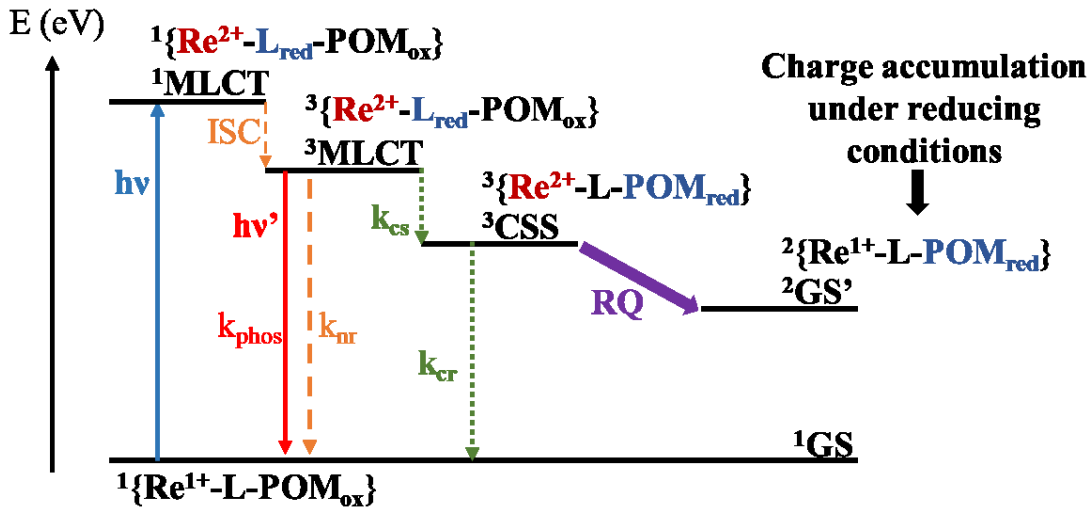

Figure VII.3. Energy diagram of the different states accessed after excitation of the ^{1}MLCT in the Re-POMs dyad with the hypothetical reductive quenching (RG) in the preence of a sacrificial electron donor. (ISC: intersystem crossing, nr: non radiative, phos: phosphorescence, cs : charge separation, cr: charge recombination, CSS: charge separated state)

Secondly, there is a net difference between the bipyridine and terpyridine based dyads **VII-D6** and **VII-D8**. This could be attributed to the different photophysical properties between bipyridine and terpyridine based Re(I) complexes, as observed in the photophysical studies. Finally, as observed in emission spectra and predicted by Marcus' theory, there is an increase in the constant rate for charge separation and recombination with increasing linker length, thus validating the hypothesis behind our synthetic efforts for **VII-D8-D10**. Interestingly, the charge recombination is slowed down to a lesser extent than the charge separation (Figure VII.3). This could suggest an additional path for recombination, i.e. a hole mediated recombination process, based on the superexchange theory.[38] There is indeed some, albeit minor, contribution from the phenyl and biphenyl bridges in the LUMO of structurally related Re(I) complexes, and more importantly, the biphenyl had an important contribution in the HOMO of the corresponding complex.[39]

Table VII.3 Time components extracted from the fitting of the spectral evolution following 400 nm excitation of the different dyads in degassed acetonitrile.

	τ_1 (ps)	τ_{CS} (ps)	τ_{CR} (ps)
VII-D6	0.7	6.7	88
VII-D7	0.2	8.0	90
VII-D8	1.0	12	241
VII-D9	1.9	29	254
VII-D10	5.5	71	514

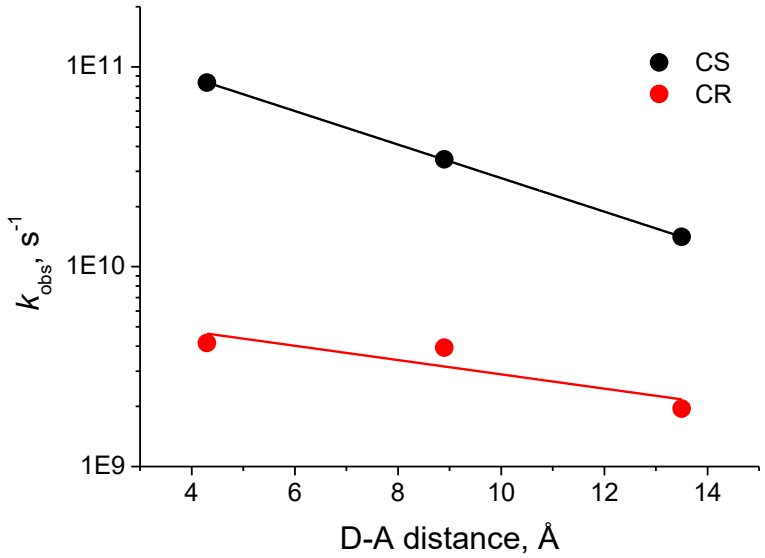

Figure VII.4. Variation of the charge separation and charge recombination rates with the approximated distance between Re and POM.

Based on the experimental values discussed above and the theoretical model built in the previous study (Figure VII.3),[22] introduction of a sacrificial electron donor[40] within the system should allow for charge accumulation by regenerating the oxidised Re centre after excitation and electron transfer. We thus conducted irradiation experiment using **VII-D6** in DMF with triethanolamine as a sacrificial electron donor. The change in absorption during irradiation were

followed by UV-vis spectroscopy. The spectral evolution is presented in Figure XIII-28. While the expect growth of the intervalence charge transfer band was observed, we will refrain to discuss it further as it would need to be reacquired. The measurement will be conducted in sealable cuvette and with extended spectral window, as the intervalence band of the mono electron reduced species has a maxima at 1150 nm (8700 cm^{-1}) disappearing with further reduction, which could allow us to determine the number of electrons injected.[37]

VII.5.4 Photocatalytic hydrogen evolution

Having shown that we could accumulate electrons on the POM unit under irradiation, we then decided to test if these electrons could be recruited to achieve a photocatalytic reaction. Izzet *et al.* as well as Streb *et al.* have shown that their dyads combining Ir(III) PS and POM were capable to photocatalyse hydrogen evolution, outperforming the equivalent bimolecular photocatalytic system.[17-18] The Re(I) dyad **VII-D6** was thus tested under standard photocatalytic conditions (concentration of 0.1 mM in DMF with TEOA 1 M as sacrificial electron donor and HBF_4 0.1 M as proton source)[41] under blue light irradiation (410 nm, 50 mW). The equivalent bimolecular system combining **VII-C1** and **VII-P1** was analysed in parallel for comparison. The dyad appeared to be almost inactive while the bimolecular system proved to be somewhat active for at least 24h, with a fast decay of the activity within 5 hours (Fig. VII-5). These results are in stark contrast compared to what was observed in the structurally related systems.[17-18] The very weak activity is tentatively explained by slow intrinsic catalytic activity from the POM itself. Besides competition with other intramolecular electron transfer process could reduce the overall charge transfer efficiency. To test this, we used the dyad with the lowest charge recombination rate **VII-D10**. No significant difference in activity was observed. In addition, in the case of the related model complex **VII-C2**, we observed lower activity than with the bipyridine based complex **VII-C1**, as expected due to its inferior photophysical characteristics.[42]

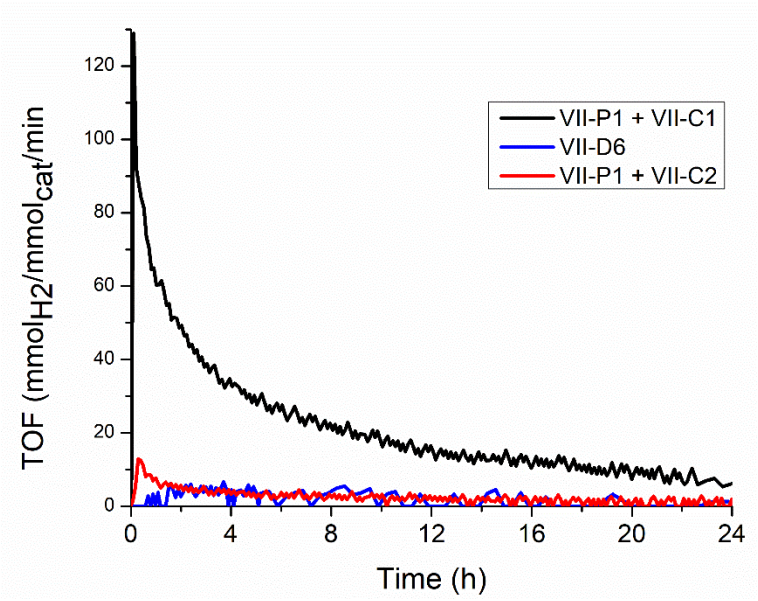

Figure VII.5. Photocatalytic hydrogen evolution rate of the dyad **VII-D6** and the two bimolecular systems based on VII-P1 and either VII-C1 or VII-C2 (irradiation at 410 nm (50 mW) with 0.1mM **VII-P1/VII-C1/VII-C2/VII-D6** in DMF, TEOA 1M, HBF_4 0.1M)

To solve this situation, we used a commonly used solution in photocatalytic experiments with POMs. We introduced colloidal platinum as catalyst to assist the POM reoxidation by proton reduction.[43-44] Indeed, platinum has been showed to efficiently produced hydrogen in the presence of reduced POMs as electron sources.[45]

The photocatalytic system can now be described as containing a photosensitizer (**VII-C1** or **VII-C2**), an electron shuttle (**VII-P1**) and a hydrogen evolution catalyst (Pt coll.). The dyads in this approach would thus conceptually be related to different systems in the literature using extended aromatic ligands[46] or tethered methylviologen as electron accepting sites.[47] In order to observed if **VII-P1**, the POM used in this study, itself is an efficient electron mediator, we thus studied the multicomponent catalytic system, comparing the activity of the Re(I) complexes with platinum in the absence or presence of the redox mediator. The colloidal platinum was obtained in situ by reduction of the precursor salt K_2PtCl_4.[48]

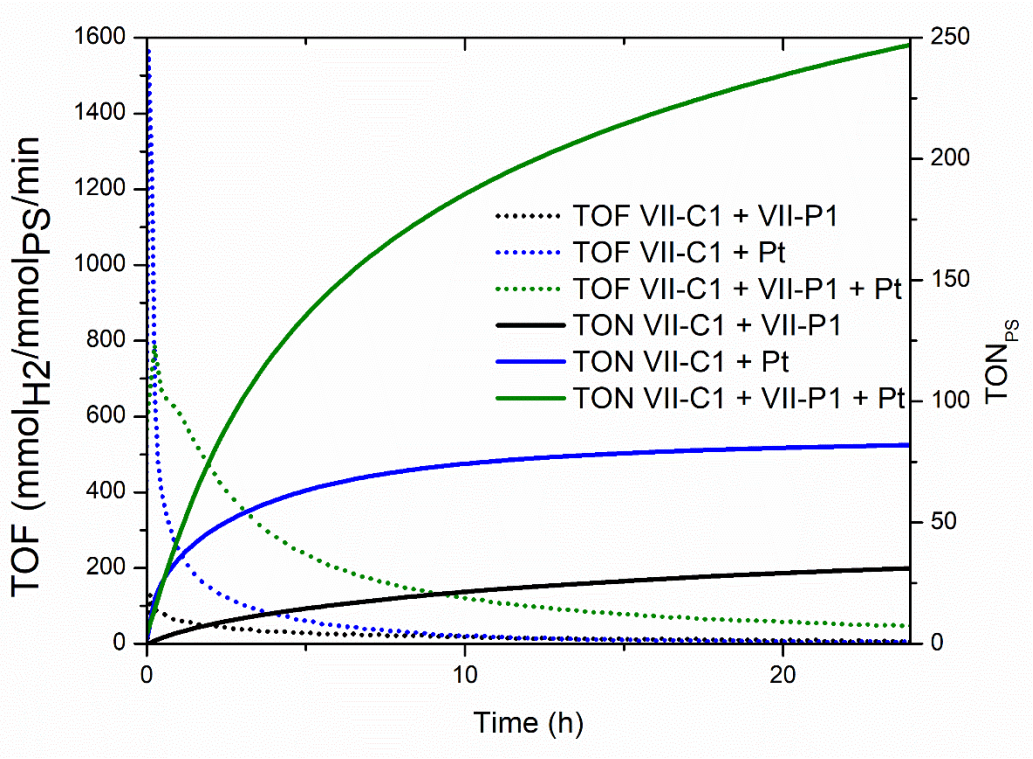

Figure VII.6. Photocatalytic hydrogen evolution activity of dissociated systems based on **VII-C1** and different catalyst (irradiation at 410 nm (50 mW) with 0.1mM **VII-P1**/**VII-C1**, 0.05mM K_2PtCl_4 in DMF, TEOA 1M, HBF_4 0.1M)

As expected, complex **VII-C1** combined with colloidal Pt is a more efficient photocatalytic system than when **VII-C1** is combined with the POM **VII-P1** (Figure VII.6, blue and black curve. respectibely). However, both systems are almost inactive after 10h, while when both **VII-P1** and colloidal Pt are combined with **VII-C1** (Figure VII.6, green curve), the activity is maintained for a longer period of time. This increased stability, at the cost of a decrease in initial rate (the TOFmax is roughly halved), allows for a TON after 24 h three times higher for this multicomponent system than with Pt alone. A similar effect is observed when we used **VII-C2** instead of **VII-C1** (Figure XIII-29), though the system is overall less efficient, as expected from the initial catalytic test.

These experiments based on dissociated systems showed that the POM **VII-P1** can act as an efficient redox mediator. We thus examined the activity of our dyads in the presence of Pt as catalyst in order to see if it keeps this potential within the covalent hybrids. We first ran control

experiments with **VII-P1** alone or in the presence of platinum, as well as an experiment with platinum alone. As expected, no activity was observed in these conditions. In the case of dyad **VII-D7** bearing two POM units, the catalytic solution became cloudy after irradiation and no activity was observed, even in the presence of Pt. This is most likely due to aggregation of the compound as the related Zn complex was shown to form globular structure by Cronin *et al.*[49]

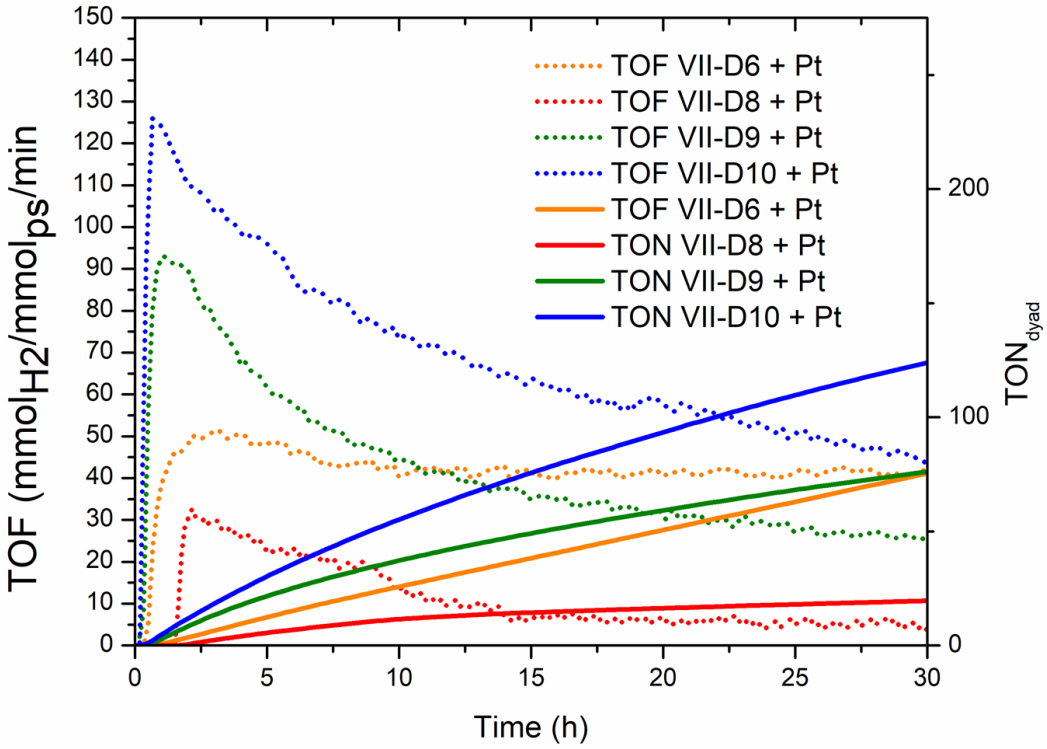

Figure VII.7. Photocatalytic hydrogen evolution activity of dyads **VII-D6**, **VII-D8**, **VII-D9** and **VII-D10** with Pt as catalyst (irradiation at 410 nm (50 mW) with 0.1 mM **VII-D**, 0.05 mM K_2PtCl_4 in DMF, TEOA 1 M, HBF_4 0.1 M)

In the case of the dyads **VII-D6**, **VII-D8**, **VII-D9** and **VII-D10**, the addition of colloidal platinum leads to reasonable activity. Two trends appear in these experiments (Figure VII.7). First, **VII-D6** appears more stable than **VII-D8**, **VII-D9** and **VII-D10**, with an almost constant rate of activity compared to the steadily decaying activity of the two other dyads. The second trend concerns the TOFmax of each dyad, which appear to follow the trend in recombination time. Dyad **VII-D10**, with a recombination time of 510 ps is the most active with a TOFmax of approx. 130 $mmol_{H2}/mmol_{dyad}$/min, followed by dyad **VII-D9** (254/ 90) and finally **VII-D6** (88 / 45). VII-D8 does not follow that trend as it has a lower TOFmax around 30

$mmol_{H2}/mmol_{dyad}/min$ while having a recombination time of 241 ps. This could be explained by its poor photophysical properties, with complete quenching of the luminescence

However, in long term experiment, the superior stability of dyad **VII-D6** allows it to match the TON of the more active dyads as their activity decreases. On the long term, **VII-D6** shows activity even after five days (Figure XIII.30). These systems are overall less efficient than the dissociated systems based on **VII-P1**, **VII-C1** and Pt colloids with rate of activity lower by an order of magnitude. The increased stability of the dyad **VII-D6** allows it, however, to reach similar turn-over number after 5 days (250 mol_{H2}/mol_{dyad}).

VII.6 Conclusion

The insertion of phenyl spacers proved to be a successful approach to tune the electron transfer kinetic within the Re(I)-POM dyads reported in this study. Indeed, partial emission was restored as the electron transfer kinetic was decreased, as confirmed by ultrafast spectroscopy measurements. The possibility of trapping the charge separate states using a sacrificial electron donor was confirmed. Furthermore, the stored electron could be used in photocatalytic hydrogen evolution, though a catalyst – colloidal platinum - had to be introduced to increase the rate of activity. This addition revealed the possibility of enhancing the stability of the photocatalytic system based solely on a Re(I) photosensitizer and colloidal platinum by introducing the POM as a redox mediator, allowing for a threefold increase in TurnOver Number. The dyad based on the bipyridine modified polyoxovanadotungstate, **VII-D6**, is stable for at least five days under photocatalytic conditions, reaching a TON of 270 after 120 hours. These results confirm the benefit of covalent attachment of the photosensitizer on the POM to enhance its photostability, although at the cost of decreased activity compared to the multi components systems.

VII.7 References

1. S. Berardi, S. Drouet, L. Francas, C. Gimbert-Surinach, M. Guttentag, C. Richmond, T. Stoll and A. Llobet, *Chem. Soc. Rev.*, 2014, **43**, 7501-7519.
2. C. Bozal-Ginesta and J. R. Durrant, *Faraday Discuss.*, 2019, **215**, 439-451.
3. B. Zhang and L. Sun, *Chem. Soc. Rev.*, 2019, **48**, 2216-2264.

4. K. E. Dalle, J. Warnan, J. J. Leung, B. Reuillard, I. S. Karmel and E. Reisner, *Chem. Rev.*, 2019, **119**, 2752-2875.

5. Y. H. Luo, L. Z. Dong, J. Liu, S. L. Li and Y. Q. Lan, *Coord. Chem. Rev.*, 2019, **390**, 86-126.

6. N. Elgrishi, M. B. Chambers, X. Wang and M. Fontecave, *Chem. Soc. Rev.*, 2017, **46**, 761-796.

7. J. W. Wang, D. C. Zhong and T. B. Lu, *Coord. Chem. Rev.*, 2018, **377**, 225-236.

8. E. S. Andreiadis, M. Chavarot-Kerlidou, M. Fontecave and V. Artero, *Photochem. Photobiol.*, 2011, **87**, 946-964.

9. M. T. Pope, *Heteropoly and Isopoly Oxometalates*, Springer-Verlag Berlin Heidelberg GmbH, 1983.

10. B. E. Petel, W. W. Brennessel and E. M. Matson, *J. Am. Chem. Soc.*, 2018, **140**, 8424-8428.

11. T. Zhang, A. Sole-Daura, S. Hostachy, S. Blanchard, C. Paris, Y. Li, J. J. Carbo, J. M. Poblet, A. Proust and G. Guillemot, *J. Am. Chem. Soc.*, 2018, **140**, 14903-14914.

12. S. M. Lauinger, Q. Yin, Y. V. Geletii and C. L. Hill, in *Polyoxometalate Chemistry*, 2017, pp. 117-154.

13. A. Proust, B. Matt, R. Villanneau, G. Guillemot, P. Gouzerh and G. Izzet, *Chem. Soc. Rev.*, 2012, **41**, 7605-7622.

14. M. P. Santoni, G. S. Hanan and B. Hasenknopf, *Coord. Chem. Rev.*, 2014, **281**, 64-85.

15. J. J. Walsh, A. M. Bond, R. J. Forster and T. E. Keyes, *Coord. Chem. Rev.*, 2016, **306**, 217-234.

16. J. M. Cameron, D. J. Wales and G. N. Newton, *Dalton Trans.*, 2018, **47**, 5120-5136.

17. B. Matt, J. Fize, J. Moussa, H. Amouri, A. Pereira, V. Artero, G. Izzet and A. Proust, *Energy Environ. Sci.*, 2013, **6**, 1504-1508.

18. S. Schonweiz, M. Heiland, M. Anjass, T. Jacob, S. Rau and C. Streb, *Chem. Eur. J.*, 2017, **23**, 15370-15376.

19. Y. Hou and C. L. Hill, *J. Am. Chem. Soc.*, 1993, **115**, 11823-11830.

20. P. R. Marcoux, B. Hasenknopf, J. Vaissermann and P. Gouzerh, *Eur. J. Inorg. Chem.*, 2003, **2003**, 2406-2412.

21. M. P. Santoni, A. K. Pal, G. S. Hanan, M. C. Tang, A. Furtos and B. Hasenknopf, *Dalton Trans.*, 2014, **43**, 6990-6993.

22. T. Auvray, M. P. Santoni, B. Hasenknopf and G. S. Hanan, *Dalton Trans.*, 2017, **46**, 10029-10036.

23. S. P. Schmidt, W. C. Trogler and F. Basolo, *Inorg. Synth.*, 1990, **28**, 160-165.

24. N. G. Connelly and W. E. Geiger, *Chem. Rev.*, 1996, **96**, 877-910.

25. J. R. Aranzaes, M. C. Daniel and D. Astruc, *Can. J. Chem.*, 2006, **84**, 288-299.

26. Z. Popovic, M. Busby, S. Huber, G. Calzaferri and L. De Cola, *Angew. Chem. Int. Ed.*, 2007, **46**, 8898-8902.

27. D. M. Ryan, M. K. Coggins, J. J. Concepcion, D. L. Ashford, Z. Fang, L. Alibabaei, D. Ma, T. J. Meyer and M. L. Waters, *Inorg. Chem.*, 2014, **53**, 8120-8128.

28. A. Stublla and P. G. Potvin, *Eur. J. Inorg. Chem.*, 2010, **2010**, 3040-3050.

29. W. W. Laxson, S. Ozkar and R. G. Finke, *Inorg. Chem.*, 2014, **53**, 2666-2676.

30. P. A. Anderson, F. R. Keene, E. Horn and E. R. T. Tiekink, *Appl. Organomet. Chem.*, 1990, **4**, 523-533.

31. E. W. Abel, N. J. Long, K. G. Orrell, A. G. Osborne, H. M. Pain and V. Šik, *J. Chem. Soc., Chem. Commun.*, 1992, 303-304.

32. E. W. Abel, V. S. Dimitrov, N. J. Long, K. G. Orrell, A. G. Osborne, H. M. Pain, V. Šik, M. B. Hursthouse and M. A. Mazid, *J. Chem. Soc., Dalton Trans.*, 1993, 597-603.

33. A. Freyer, C. DiMeglio and A. Freyer, *J. Chem. Educ.*, 2006, **83**, 788.

34. J. P. Bullock, E. Carter, R. Johnson, A. T. Kennedy, S. E. Key, B. J. Kraft, D. Saxon and P. Underwood, *Inorg. Chem.*, 2008, **47**, 7880-7887.

35. B. Laramee-Milette, C. Lachance-Brais and G. S. Hanan, *Dalton Trans.*, 2015, **44**, 41-45.

36. M. T. Pope, *Inorg. Chem.*, 1972, **11**, 1973-1974.

37. S. P. Harmalker, M. A. Leparulo and M. T. Pope, *J. Am. Chem. Soc.*, 1983, **105**, 4286-4292.

38. M. Natali, S. Campagna and F. Scandola, *Chem. Soc. Rev.*, 2014, **43**, 4005-4018.

39. T. Klemens, A. Switlicka-Olszewska, B. Machura, M. Grucela, H. Janeczek, E. Schab-Balcerzak, A. Szlapa, S. Kula, S. Krompiec, K. Smolarek, D. Kowalska, S. Mackowski, K. Erfurt and P. Lodowski, *RSC Adv.*, 2016, **6**, 56335-56352.

40. Y. Pellegrin and F. Odobel, *C. R. Chim.*, 2017, **20**, 283-295.

41. B. Probst, A. Rodenberg, M. Guttentag, P. Hamm and R. Alberto, *Inorg. Chem.*, 2010, **49**, 6453-6460.

42. T. Klemens, A. Switlicka-Olszewska, B. Machura, M. Grucela, E. Schab-Balcerzak, K. Smolarek, S. Mackowski, A. Szlapa, S. Kula, S. Krompiec, P. Lodowski and A. Chrobok, *Dalton Trans.*, 2016, **45**, 1746-1762.

43. E. Papaconstantinou, *Chem. Soc. Rev.*, 1989, **18**.

44. A. Ioannidis and E. Papaconstantinou, *Inorg. Chem.*, 1985, **24**, 439-441.

45. B. Rausch, M. D. Symes, G. Chisholm and L. Cronin, *Science*, 2014, **345**, 1326-1330.

46. J. F. Lefebvre, J. Schindler, P. Traber, Y. Zhang, S. Kupfer, S. Grafe, I. Baussanne, M. Demeunynck, J. M. Mouesca, S. Gambarelli, V. Artero, B. Dietzek and M. Chavarot-Kerlidou, *Chem. Sci.*, 2018, **9**, 4152-4159.

47. K. Yamamoto, A. Call and K. Sakai, *Chem. Eur. J.*, 2018, **24**, 16620-16629.

48. B. F. DiSalle and S. Bernhard, *J. Am. Chem. Soc.*, 2011, **133**, 11819-11821.

49. P. Yin, T. Li, R. S. Forgan, C. Lydon, X. Zuo, Z. N. Zheng, B. Lee, D. Long, L. Cronin and T. Liu, *J. Am. Chem. Soc.*, 2013, **135**, 13425-13432.

Chapitre VIII. Conclusions et perspectives

Les différentes études présentées dans cette thèse illustrent les approches de design moléculaire accessibles pour atteindre certains des objectifs identifiés dans la littérature et favoriser l'implantation de technologies transposant la photosynthèse artificielle du laboratoire à l'application.[1]

Les premiers chapitres démontrent la valeur du design de ligands pour l'étude des complexes de coordination. L'importance de cette approche se reflète dans le travail quotidien d'un chimiste de coordination, la synthèse des ligands occupant généralement près de deux tiers du temps de travail de synthèse au laboratoire.

Dans le chapitre II, nous avons démontré que des modifications simples sur la structure de ligands de type 2,2' :6',2''-terpyridines impactent fortement les propriétés photophysiques des complexes de Ru(II) correspondants. Malgré leurs modestes performances, ces photosensibilisateurs (PSs), longtemps négligés car possédant des propriétés photophysiques initialement peu engageantes (courts temps de vie et faibles rendements quantiques) comparées à celles de complexes dérivés de la 2,2-bipyridine, conduisent à une meilleure photostabilité du système photocatalytique. Il s'agit maintenant d'améliorer les propriétés intrinsèques de ces complexes tout en conservant leur photostabilité. Les multiples stratégies explorées pour améliorer ces composés doivent vraisemblablement être réexplorées, de nombreux complexes déjà rapportés mais simplement jamais considérés constituant éventuellement un bassin de PSs viables.[2]

Les chapitres III et IV contribuent à l'avancement des connaissances fondamentales associées à la chimie de coordination du Re(I). Alors que les complexes pyridyl-guanidine du chapitre III voient leur propriétés photophysiques dépendre fortement de celles des ligands utilisés, la transition entre la coordination de deux ou trois des pyridines de ligands terpyridines, i.e. κ^2N à κ^3N, permet de découpler les transferts de charge métal-ligand (MLCT) des transitions intraligand (LC) et des transferts de charge ligand-ligand (ILCT). Ces changements tirent leur origine de la combinaison des différentes interactions orbitalaires, impliquant les carbonyls,

ligands fortement σ donneurs et π accepteurs, le ligand polydenté (le plus souvent faible σ donneur et faible π accepteur) et le ligand axial dont la nature varie plus largement.

Les tests initiaux indiquent que les complexes pyridyl-guanidine ne sont pas actifs lorsqu'utilisés comme catalyseurs pour la réduction du CO_2. Cette observation n'est pas si surprenante compte tenu de la main-mise des ligands sur les propriétés de ces complexes. À l'opposé, les faibles variations des potentiels de réduction entre composés κ^2N et κ^3N sont prometteuses pour une possible application pour la réduction du CO_2 ; la validation de cette hypothèse sera la priorité des travaux subséquents.

Les chapitres VI et VII introduisent une classe de composés prometteurs. Les hybrides Re-POMs possèdent d'intéressantes propriétés photophysiques, i.e. un efficace transfert d'électron du photosensibilisateur vers un réservoir d'électrons. Bien que les performances des dyades par elles-mêmes soient faibles, vraisemblablement parce que le POM choisi pour ces études - choix dirigé par la stratégie de greffage choisie – n'est pas un catalyseur efficace pour la réduction des protons et requiert l'assistance d'un catalyseur, ici le platine. Cependant, en présence de platine, une amélioration significative de la stabilité des systèmes photocatalytiques, basés sur dyade covalente ou système bimoléculaire, est observée. Pour la suite de cette étude, l'extension à d'autres PSs afin de valider l'impact de la stratégie de greffage sur la photostabilité sous conditions catalytiques est envisagée. Des travaux initiaux sur un dérive basé sur un PS d'Ir(III) semblent prometteurs, ce chromophore possédant de meilleures propriétés photophysiques intrinsèques. Ces études de préparation d'espèces hybrides organique-inorganique constituent une transition intéressante entre le développement d'espèces moléculaires et leur intégration par hétérogénéisation via la fonctionnalisation de surfaces de semi-conducteurs.[3-4]

Ce dernier point nous amène aux perspectives s'ouvrant après cette thèse. Au vue de la vitalité du domaine de la photosynthèse artificielle, comme discuté dans l'introduction, il n'est pas surprenant de voir que de multiples tendances aient émergés.

Le principal changement est une prise de conscience de la nécessité de considérer l'impact des composantes des systèmes photocatalytiques développés. La majorité des composés développés comme photosensibilisateurs ou catalyseurs sont basés sur des métaux au coût modéré à élevé. En effet, le ruthénium, l'iridium ou le platine sont peu abondants et l'augmentation exponentielle de la demande dans divers domaines technologiques ne peut qu'empirer la situation. Le cas du rhénium est ici ambigu. Celui-ci est certes peu abondant, mais il n'existe pas autant d'applications compétitives que dans le cas des autres métaux. En réponse à ces considérations, le développement de systèmes basés uniquement sur la première rangée des éléments de transitions est en pleine effervescence.[5-6] Cette substitution des métaux de deuxième et troisième rangées semble plus facilement prendre place dans le cas catalyseurs que des photosensibilisateurs. En effet, l'utilisation de métaux de première rangée modifie fortement la nature des états excités de plus basse énergie, ceux-ci étant souvent liés au champ de ligand et donc non-radiatif. Plusieurs exemples ont été reportés, et plus important encore, une connaissance des paramètres permettant de relever le défi des métaux de première rangée se développe.[7] Les composés de cuivre Cu(I) sont activement explorés et proposent un défi de synthèse car ils nécessitent la présence d'un encombrement stérique contrôlé pour s'ajuster à la déformation de Jahn-Teller observée dans les états excités.[8] Une autre approche, centrée sur les transferts de charge de ligand à métal, a déjà été introduite durant cette thèse lorsque l'on a discuté des composés de cobalt Co(III) pyridyl-guanidine rapportés par le groupe Hanan. Celle-ci est également applicable aux composés de fer, métal le plus abondant.[7,9]

Les deux autres tendances s'attachent à améliorer l'efficacité des systèmes catalytiques en couplant réactions d'oxydation et de réduction. Ce couplage permet d'éliminer le recours aux donneurs et accepteurs sacrificiels, intrinsèquement problématique pour une intégration économiquement viable.

Une première voie pour améliorer les perspectives économiques des dispositifs de photosynthèse artificielle est de coupler les réactions usuelles avec des réactions 'photorédox' organiques développées ces dernières années, ou la valorisation de la biomasse.[10-12] Ces approches sont cependant énergeantes et apportent de nombreux défis, notamment la séparation des produits désirés.

D’un point de vue ingénierie, lorsque l’on parle de dispositifs de photosynthèse artificielle, il est difficile d’imaginer l’utilisation de solutions contenant PS, catalyseurs, produits et autres additifs. Aussi, les efforts vers l’hétérogénéisation des systèmes moléculaires deviennent inévitables. Cette approche n’élimine pas pour autant la nécessité de développer de nouvelles espèces actives en solution, mais impose de considérer également l’activité une fois ancrées sur une surface.[13] De multiples approches d’hétérogénéisation existent, visant principalement à la préparation de photoélectrodes.[14-15] L’intégration des espèces moléculaires actives au sein de polymères de coordination, ou Metal Organic Framework (MOF), est un domaine extrêmement actif.[16-17]

Pour conclure cette thèse, nous souhaitons introduire le récent travail de T.J. Meyer *et al.*. Ce système hétérogène, obtenu par greffage sur une nanoparticule d’oxyde conducteur, est inspiré du photosystème II, un système hétérogène en lui-même du fait de son encapsulation dans la bicouche lipidique de la membrane cellulaire. Il s’agit de l’illustration élégante d’une vaste part des connaissances développées dans le domaine de la photosynthèse artificielle, combinées dans un système hétérogène.[18]

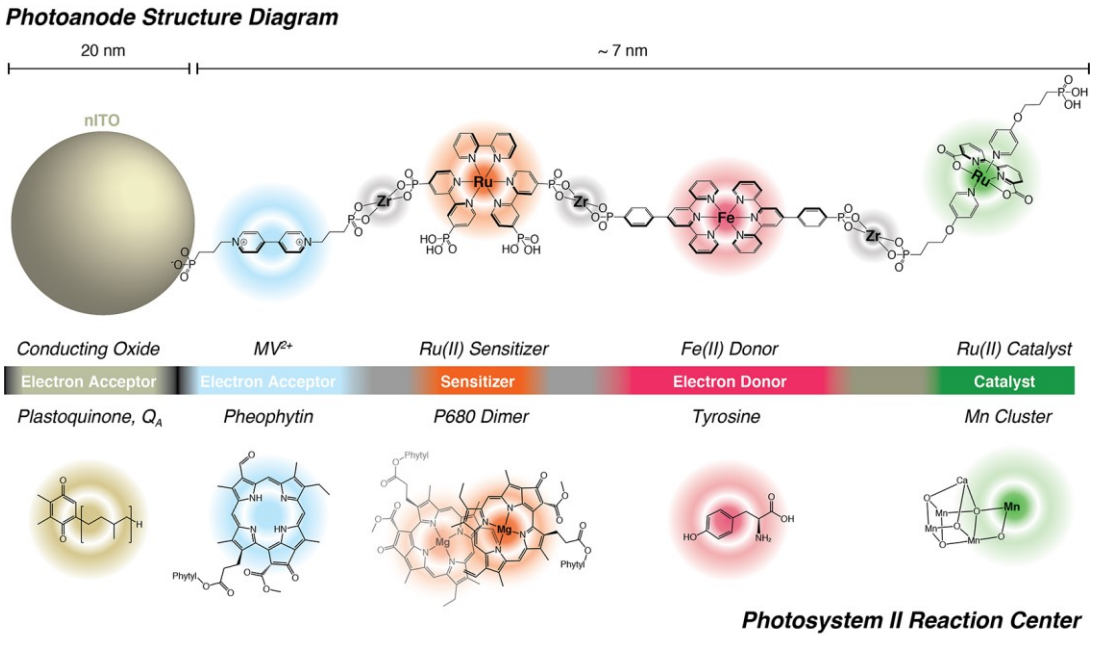

Figure VIII.1 Assemblage supramoléculaire pour l’oxydation de l’eau photocatalysée. (Reproduit, avec permission, de T. J. Meyer et al., *J. Am. Chem. Soc.*, 2019, **141**, 7926-7933., Copyright 2019 American Chemical Society)

Références

1. B. Zhang and L. Sun, *Chem. Soc. Rev.*, 2019, **48**, 2216-2264.
2. A. K. Pal and G. S. Hanan, *Chem. Soc. Rev.*, 2014, **43**, 6184-6197.
3. S. M. Lauinger, Q. Yin, Y. V. Geletii and C. L. Hill, in *Polyoxometalate Chemistry*, 2017, pp. 117-154.
4. J. M. Cameron, D. J. Wales and G. N. Newton, *Dalton Trans.*, 2018, **47**, 5120-5136.
5. K. E. Dalle, J. Warnan, J. J. Leung, B. Reuillard, I. S. Karmel and E. Reisner, *Chem. Rev.*, 2019, **119**, 2752-2875.
6. B. M. Hockin, C. F. Li, N. Robertson and E. Zysman-Colman, *Catal. Sci. Technol.*, 2019, **9**, 889-915.
7. O. S. Wenger, *Chem. Eur. J.*, 2019, **25**, 6043-6052.
8. Y. Zhang, M. Schulz, M. Wachtler, M. Karnahl and B. Dietzek, *Coord. Chem. Rev.*, 2018, **356**, 127-146.
9. A. K. Pal, C. Li, G. S. Hanan and E. Zysman-Colman, *Angew. Chem. Int. Ed.*, 2018, **57**, 8027-8031.
10. M. H. Shaw, J. Twilton and D. W. MacMillan, *J. Org. Chem.*, 2016, **81**, 6898-6926.
11. L. M. Reid, T. F. Li, Y. Cao and C. P. Berlinguette, *Sustainable Energy Fuels*, 2018, **2**, 1905-1927.
12. M. F. Kuehnel and E. Reisner, *Angew. Chem. Int. Ed.*, 2018, **57**, 3290-3296.
13. X. Liu, S. Inagaki and J. Gong, *Angew. Chem. Int. Ed.*, 2016, **55**, 14924-14950.
14. Z. Yu, F. Li and L. C. Sun, *Energy Environ. Sci.*, 2015, **8**, 760-775.
15. K. Morita, K. Sakai and H. Ozawa, *ACS Appl. Energy Mater.*, 2019, **2**, 987-992.
16. A. Dhakshinamoorthy, Z. Li and H. Garcia, *Chem. Soc. Rev.*, 2018, **47**, 8134-8172.
17. M. B. Majewski, A. W. Peters, M. R. Wasielewski, J. T. Hupp and O. K. Farha, *Acs Energy Letters*, 2018, **3**, 598-611.
18. D. Wang, R. N. Sampaio, L. Troian-Gautier, S. L. Marquard, B. H. Farnum, B. D. Sherman, M. V. Sheridan, C. J. Dares, G. J. Meyer and T. J. Meyer, *J. Am. Chem. Soc.*, 2019, **141**, 7926-7933.

Chapitre IX. Matériels supplémentaires au chapitre II

IX.1 Synthesis

In a 250 mL round-bottomed flask, 4-*tert*-butylpyridine (5 g), $AgNO_3$ (0.5 g) and pyruvic acid (9 g) were combined, followed by dichloromethane (50 mL) and water (10 mL). This mixture is cooled to 0 °C using an ice-water bath. Separately, $(NH_4)_2S_2O_8$ (12.5 g) was dissolved in water (40 mL) and concentrated H_2SO_4 (3 mL). This aqueous solution is then added dropwise over a period of about 15 minutes in the cooled round-bottomed flask, under stirring. Once the addition is complete, the biphasic mixture is slowly warmed-up to room temperature then refluxed for 4 hours. Once cooled down, the reaction mixture is poured onto ice (100 mL). Carefully, NaOH (10 M) is added until the pH is basic (9-10). The mixture is then filtered to remove the grey Ag_2O that formed upon addition of base. The two phases are then separated. The aqueous phase is washed with dichloromethane (50 mL). The two dichloromethane fractions are then combined and dried on Na_2SO_4. The Na_2SO_4 is washed with diethyl ether (50 mL) and the filtrate is added to the dichloromethane solution. The solvents are then removed under reduced pressure, until only about 20-30 mL of solution is left. It is then diluted with diethyl ether (75 mL), and this organic phase is washed three times with an aqueous citric acid solution (0.75M, 25 mL) [to remove the remaining 4-*tert*-butylpyridine which can be recycled using the workup described below]. The organic phase is then washed three times with hydrochloric acid (1 M, 25 mL). [The organic phase only contains the bis-acetyl by-product at this point.] The acidic aqueous phase is poured onto ice (50 ml) and neutralize with caution with NaOH (10 M) till pH 9-10. It is then extracted twice with diethyl ether (50 ml). The ether solution is filtered over a 1 cm bed of silica gel, the silica being washed with diethyl ether (30 mL). The diethyl ether is then removed under reduced pressure without heat, affording 2-acetyl-4-*tert*-butylpyridine as a light orange oil whose ^{1}H NMR spectra matched the literature. The yield varies between 25-30 % of 2-acetyl-4-*tert*-butylpyridine.
The reaction and purification can be followed by TLC on SiO_2 with 7/3 Hexane/Diethyl ether.

1) G. Hanan, B. Laramée-Milette, T. Auvray, S. Nguyen, S. Tremblay, C. Lachance-Brais, M. Donguy, V. Taylor and D. Deschênes, *Synthesis*, 2015, **47**, 3849-3858.

IX.2 ^{1}H NMR spectra

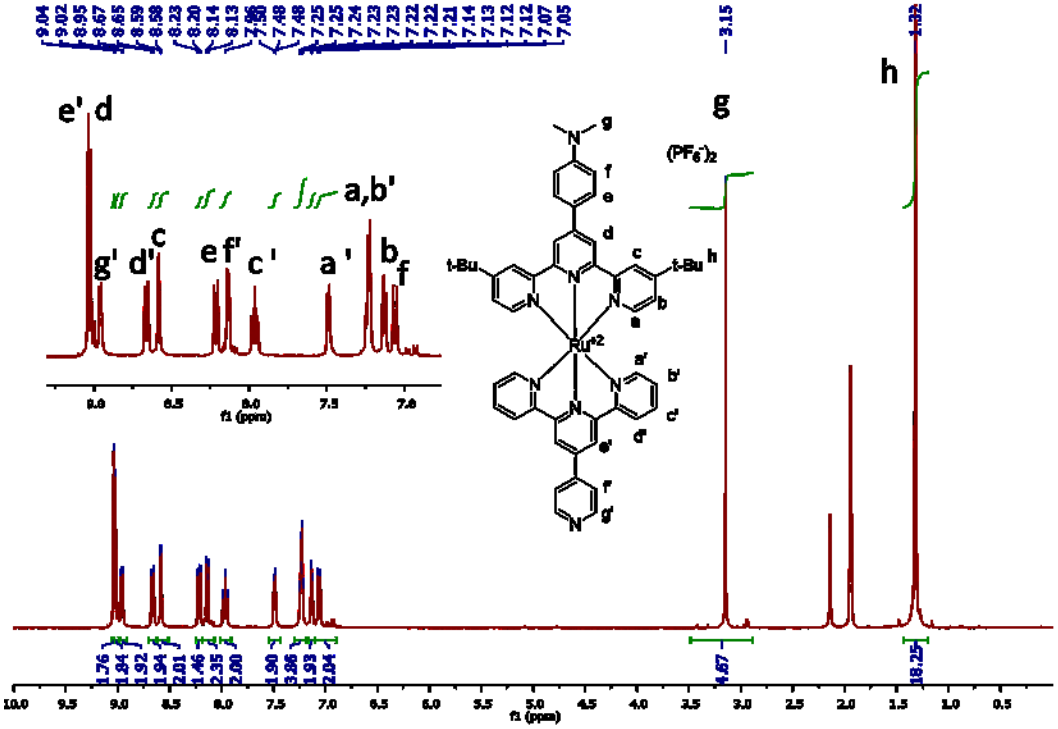

Figure IX.1. ^{1}H NMR spectra of complex **II-C1** in CD_3CN

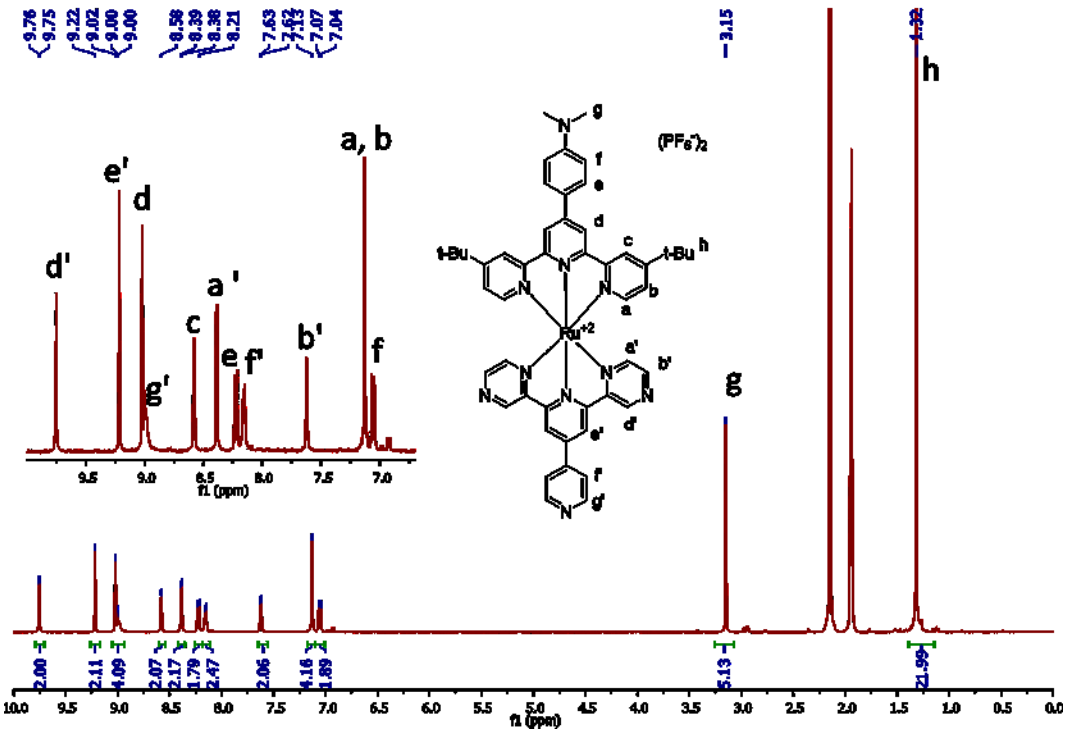

Figure IX.2. ^{1}H NMR spectra of complex **II-C2** in CD_3CN

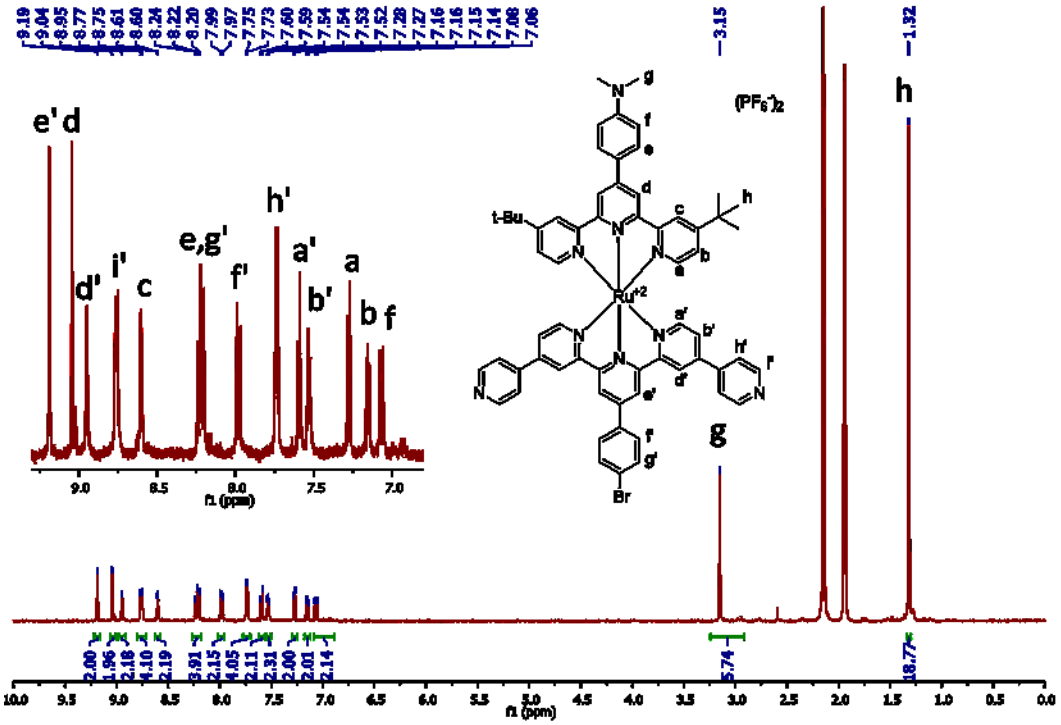

Figure IX.3. ^{1}H NMR spectra of complex **II-C3** in CD_3CN

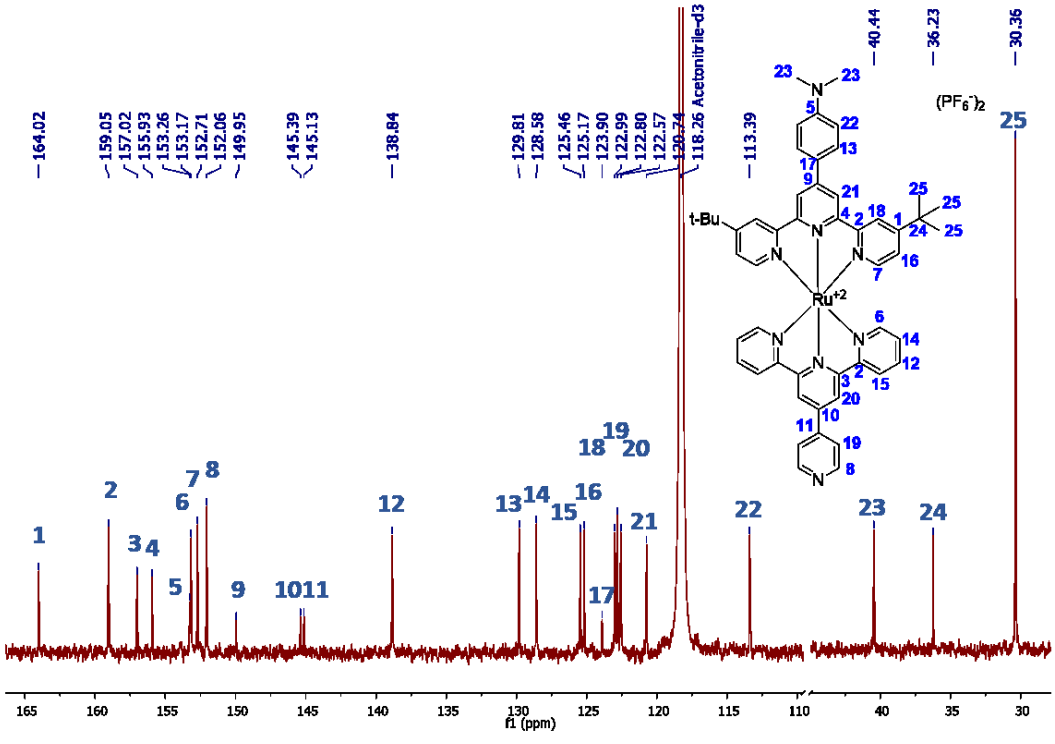

Figure IX.4. ^{13}C NMR spectra of complex **II-C1** in CD_3CN

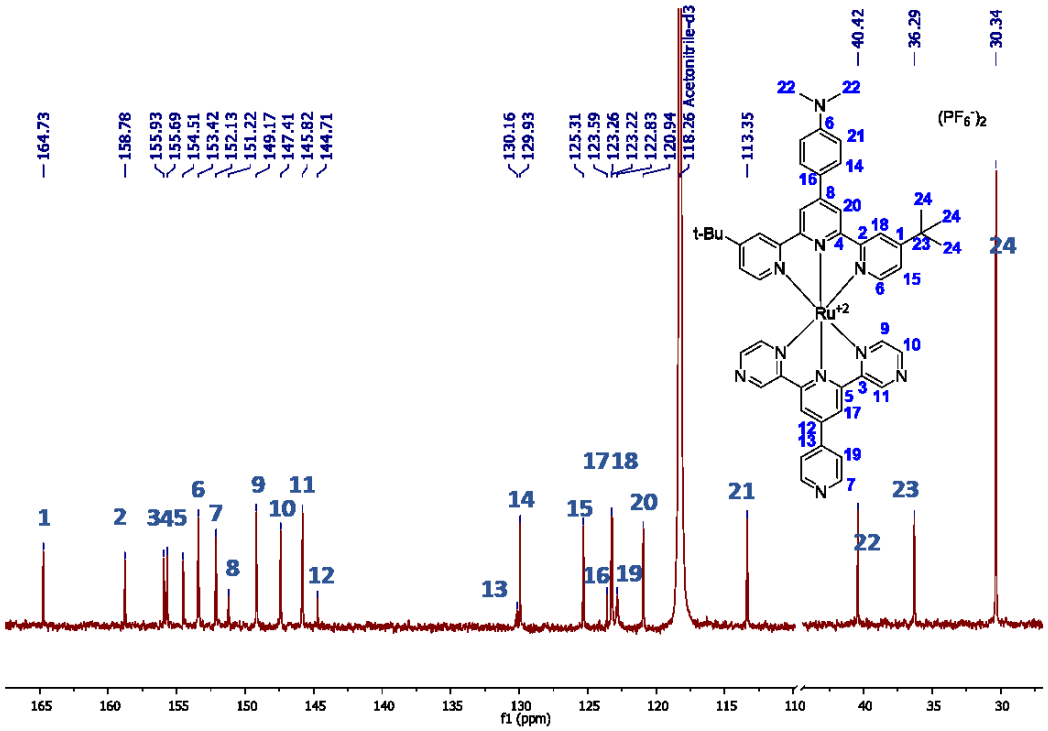

Figure IX.5. ^{13}C NMR spectra of complex **II-C2** in CD_3CN

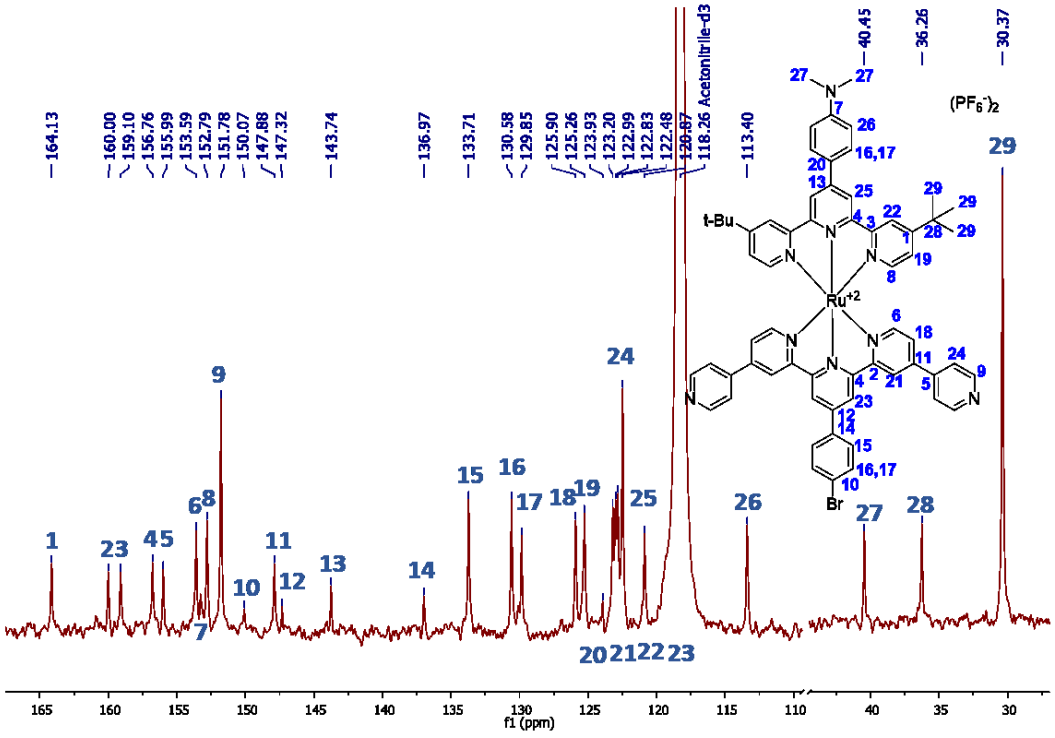

Figure IX.6. ^{13}C NMR spectra of complex **II-C3** in CD_3CN

IX.3 ESI-MS (MeCN)

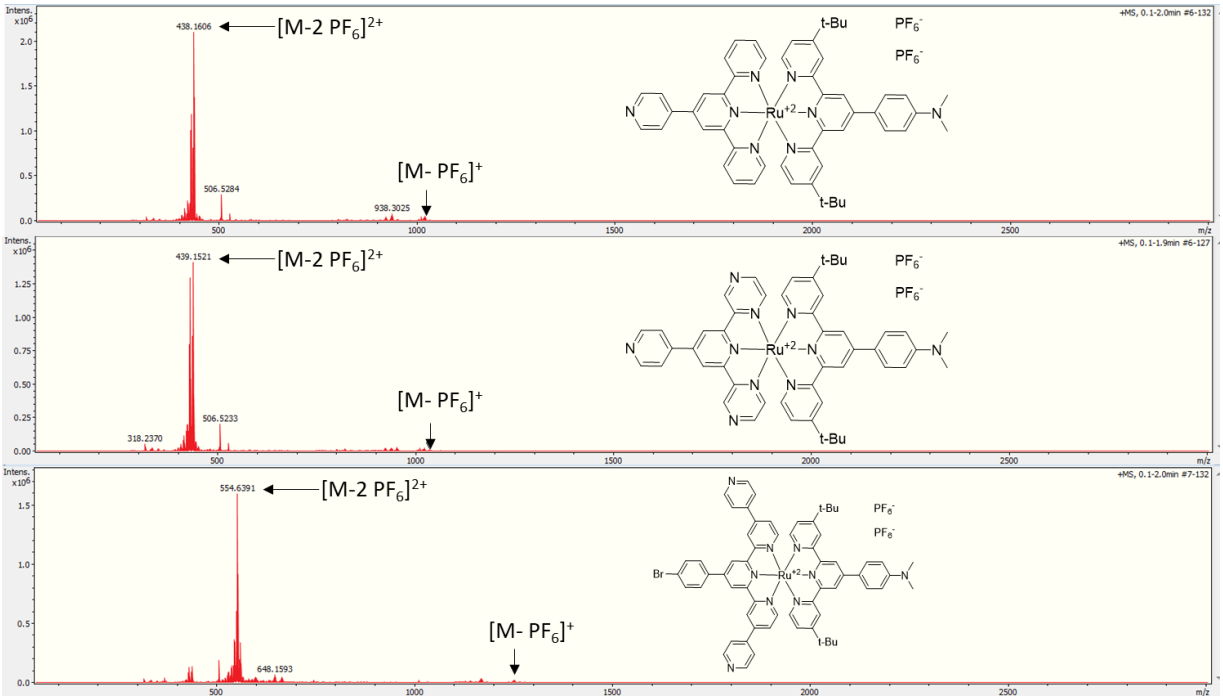

Figure IX.7. Complete chromatograms obtained by ESI-MS (CH_3CN, positive mode) for complexes **II-C1-C3**.

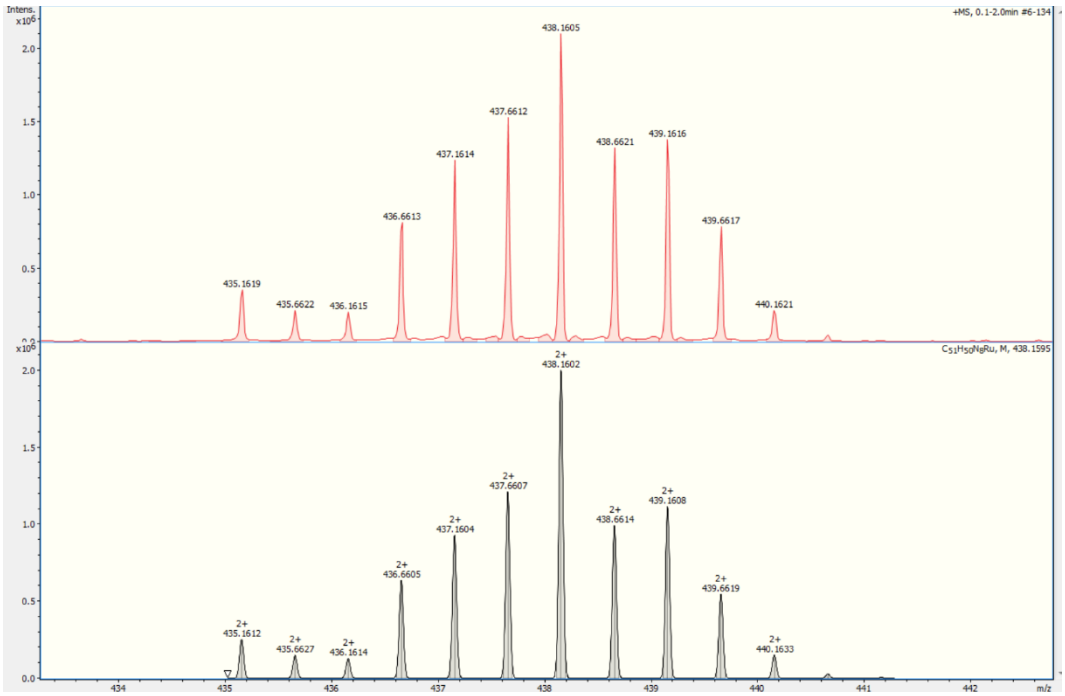

Figure IX.8. Experimental (top) and calculated (bottom) isotopic pattern for complex **II-C1**$^{2+}$

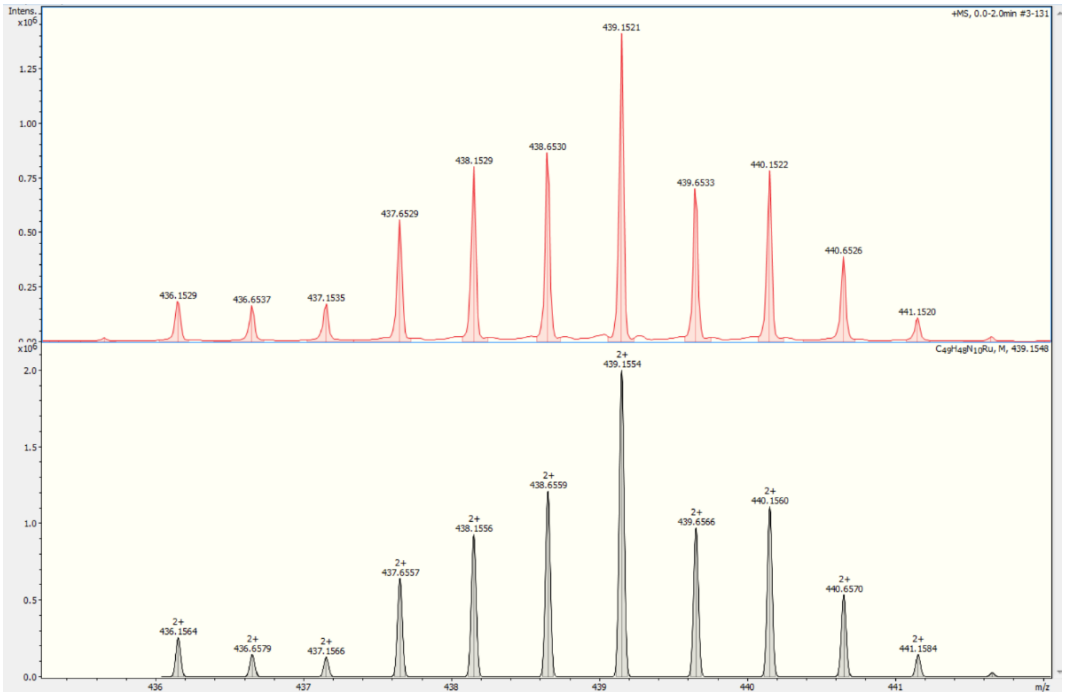

Figure IX.9. Experimental (top) and calculated (bottom) isotopic pattern for complex **II-C2**$^{2+}$

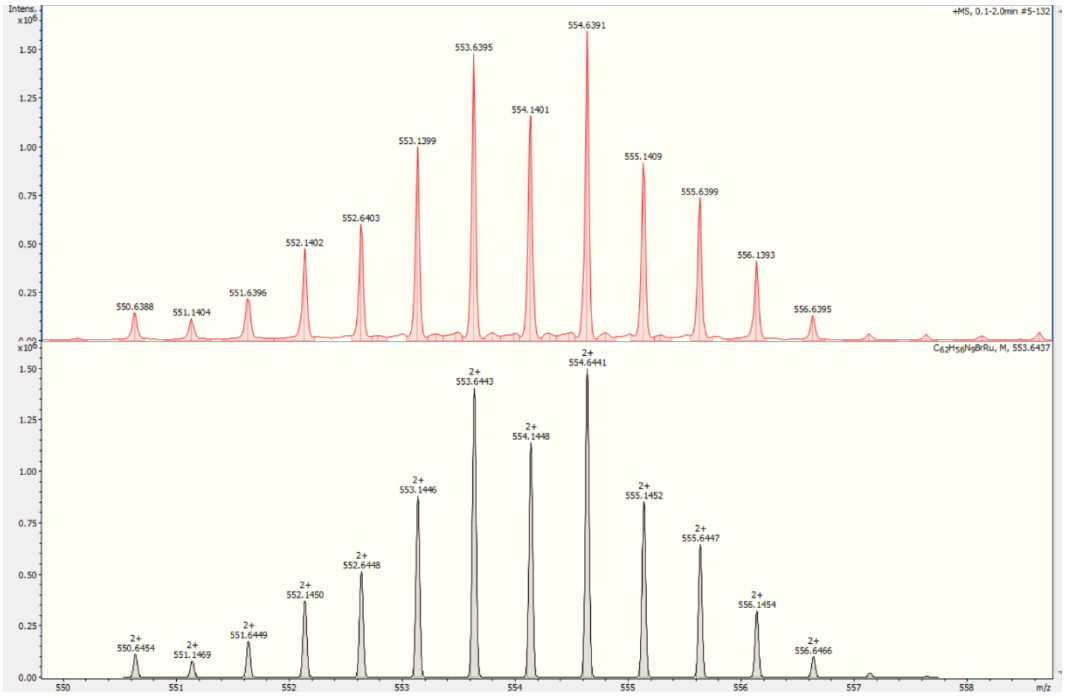

Figure IX.10. Experimental (top) and calculated (bottom) isotopic pattern for complex **II-C3**$^{2+}$

IX.4 Electrochemical studies

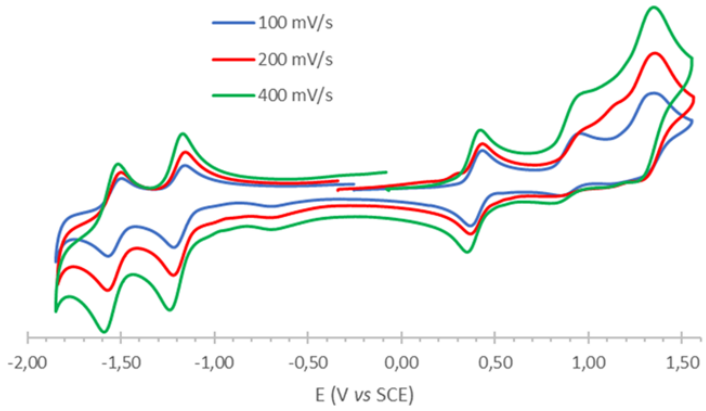

Figure IX.11. Cyclic voltammograms for **II-C1** in MeCN/TBAP with ferrocene, measured at various scan rates.

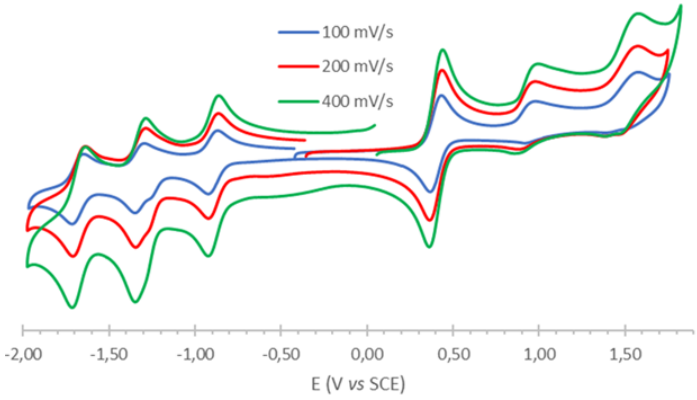

Figure IX.12. Cyclic voltammograms for **II-C2** in MeCN/TBAP with ferrocene, measured at various scan rates.

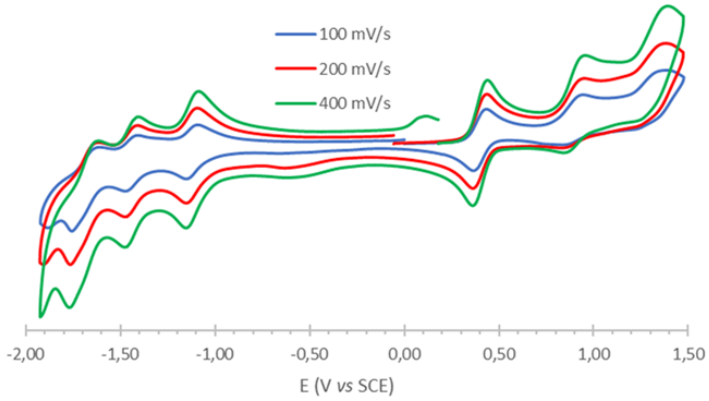

Figure IX.13. Cyclic voltammograms for **II-C3** in MeCN/TBAP with ferrocene, measured at various scan rates.

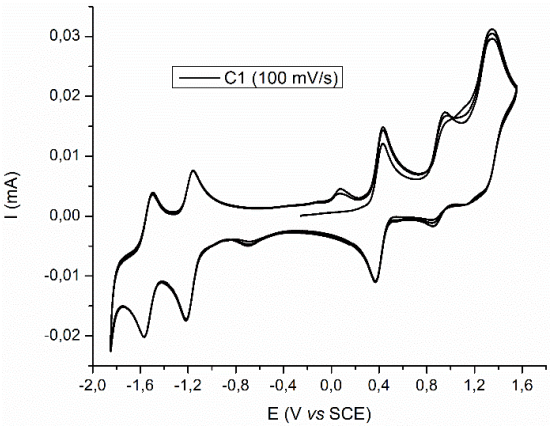

Figure IX.14. Cyclic voltammograms for **II-C1** in MeCN/TBAP at 100mV/s with ferrocene as internal standard.

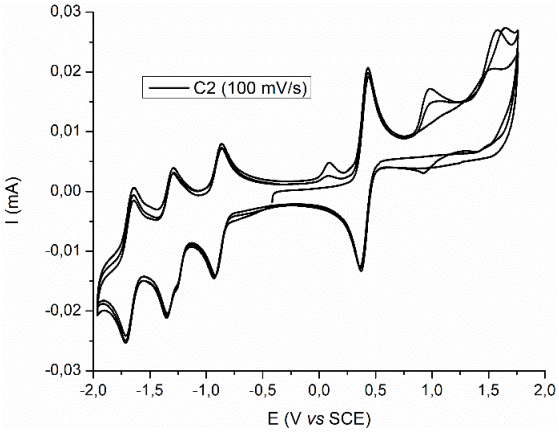

Figure IX.15. Cyclic voltammograms for **II-C2** in MeCN/TBAP at 100mV/s with ferrocene as internal standard.

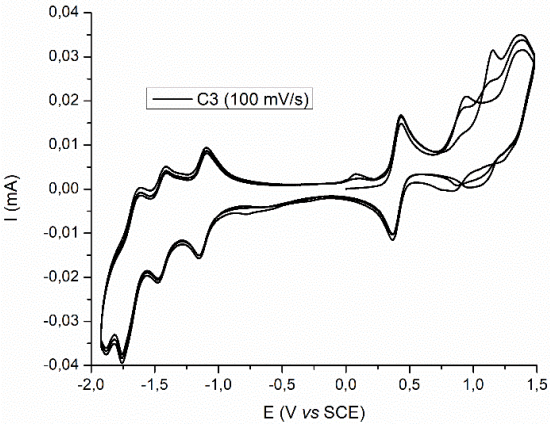

Figure IX.16. Cyclic voltammograms for **II-C3** in MeCN/TBAP at 100mV/s with ferrocene as internal standard.

IX.5 Theoretical studies

Table IX.1. Kohn-Sham representation of the first three unoccupied orbitals of **II-C1**$^{2+}$, **II-C2**$^{2+}$ and **II-C3**$^{2+}$.

Complex	LUMO	LUMO+1	LUMO+2
II-C1	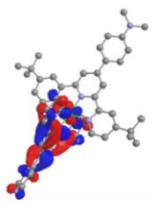	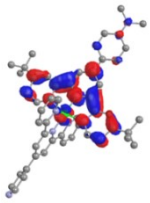	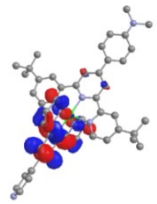
II-C2	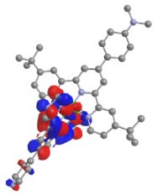	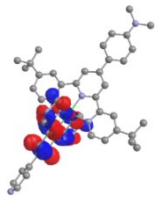	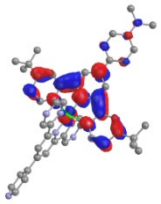
II-C3	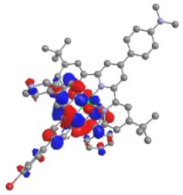	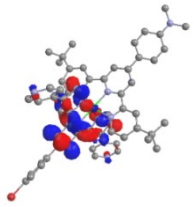	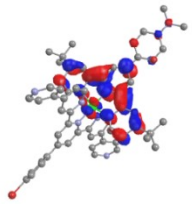

Table IX.2. Kohn-Sham representation of the first three occupied orbitals of **II-C1**$^{2+}$, **II-C2**$^{2+}$ and **II-C3**$^{2+}$.

Complex	HOMO	HOMO-1	HOMO-2
II-C1	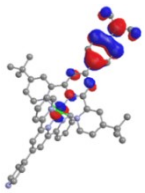	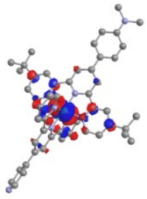	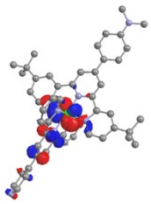
II-C2	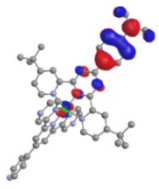	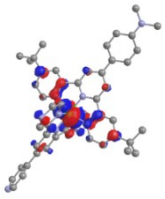	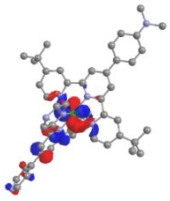
II-C3	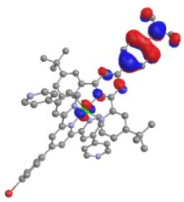	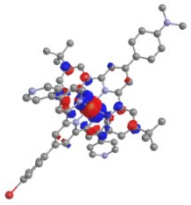	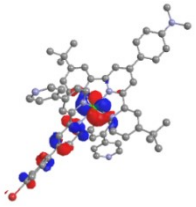

Table IX.3. Contributions of each unit to selected frontiers orbitals of **II-C1**$^{2+}$

MO	eV	DMAPh	tbu_2tpy	Ru	4-py	tpy
L+2	-2.6	0	9	1	0	90
L+1	-2.61	7	85	7	0	1
LUMO	-2.84	0	2	9	11	79
HOMO	-5.69	82	9	8	0	1
H-1	-6.39	0	18	67	0	15
H-2	-6.51	0	9	67	4	20

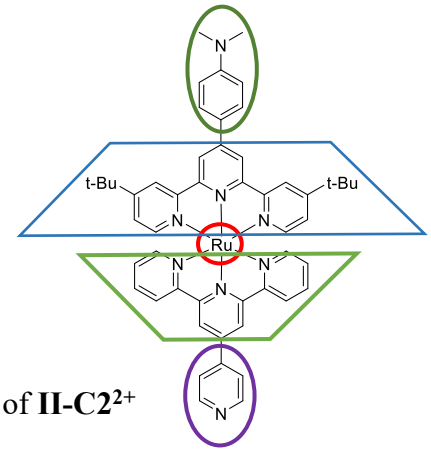

Table IX.4. Contributions of each unit to selected frontiers orbitals of **II-C2**$^{2+}$

MO	eV	DMAPh	tbu_2tpy	Ru	4-py	pzpypz
L+2	-2.73	7	86	6	0	1
L+1	-2.95	0	2	3	0	95
LUMO	-3.26	0	2	9	4	85
HOMO	-5.75	85	9	5	0	1
H-1	-6.75	0	21	64	0	15
H-2	-6.79	0	9	65	4	22

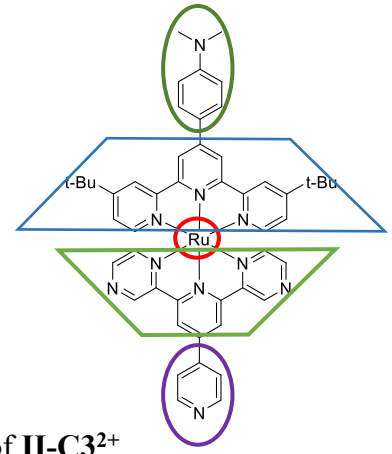

Table IX.5. Contributions of each unit to selected frontiers orbitals of **II-C3**$^{2+}$

MO	eV	DMAP	tbu_2tpy	Ru	4'(4BrPh)	tpy	4 and 4'' py
L+2	-2.62	7	85	6	0	1	0
L+1	-2.7	0	5	2	0	85	8
LUMO	-2.95	0	1	8	4	76	11
HOMO	-5.7	82	9	8	0	1	0
H-1	-6.39	0	17	65	0	15	3
H-2	-6.48	0	8	63	9	19	1

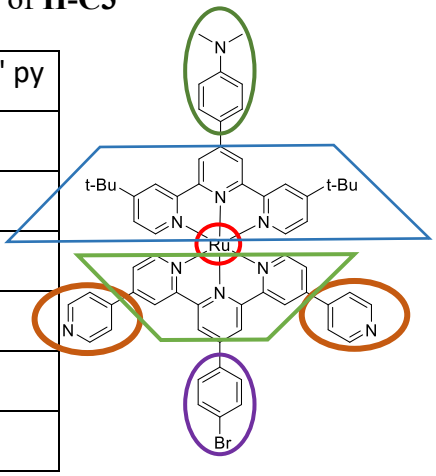

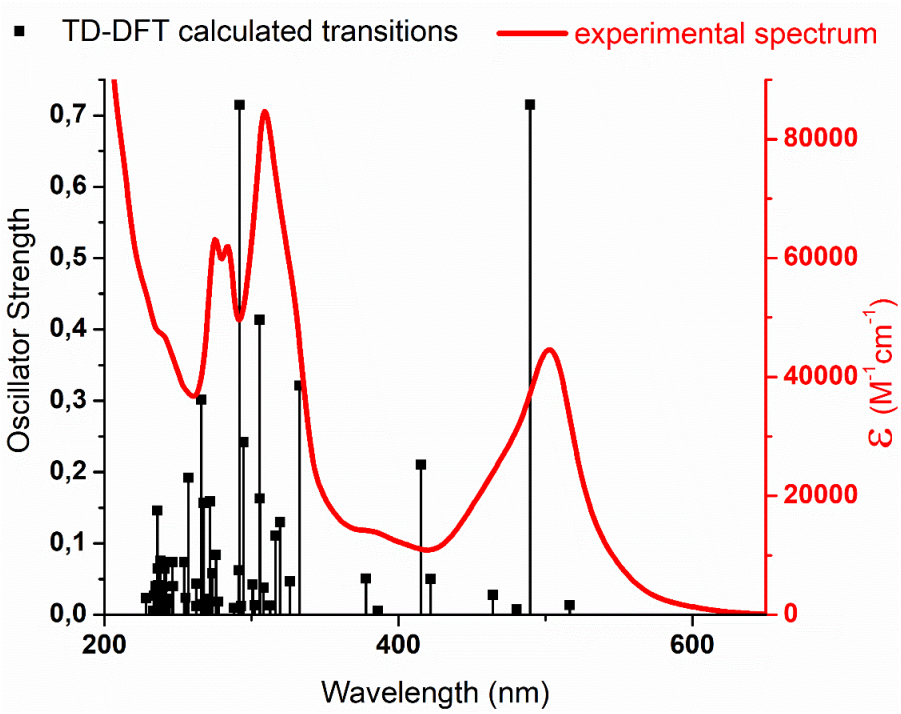

Figure IX.17. Overlap of the experimental absorption spectra and calculated transitions for **II-C1**$^{2+}$

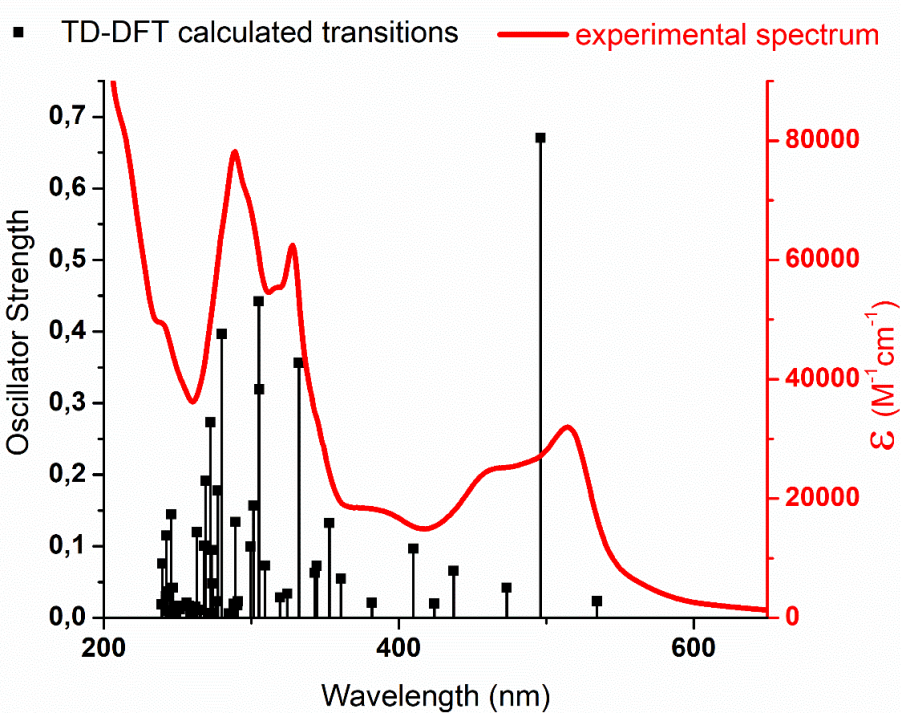

Figure IX.18. Overlap of the experimental absorption spectra and calculated transitions for **II-C2**$^{2+}$

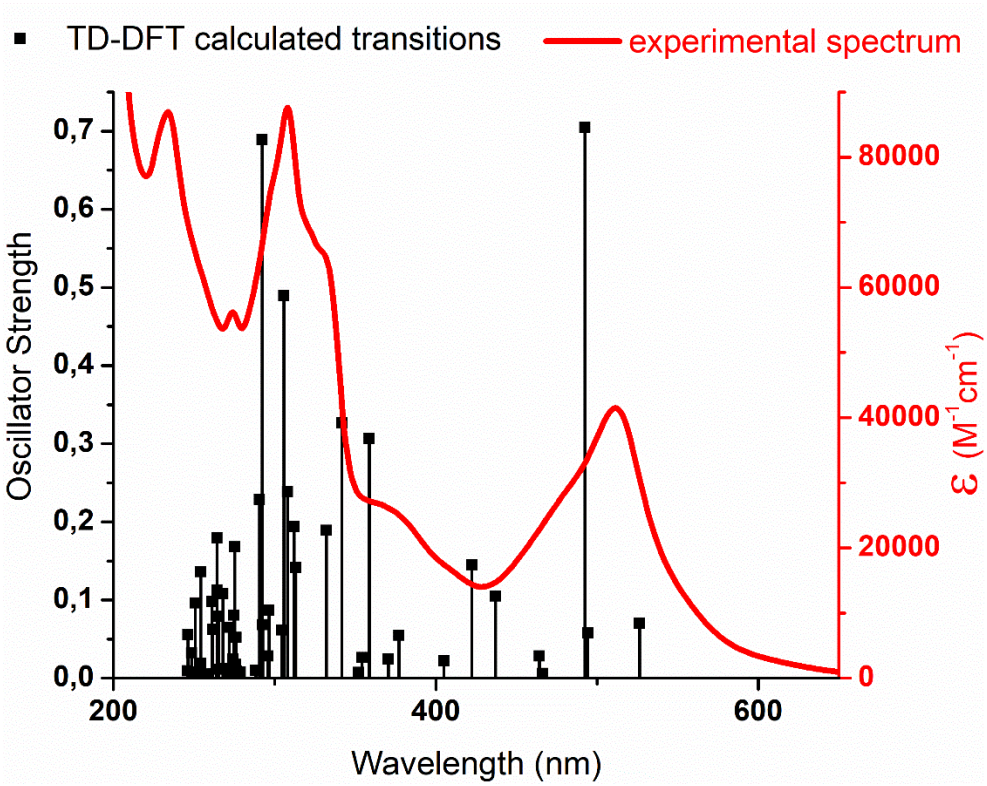

Figure IX.19. Overlap of the experimental absorption spectra and calculated transitions for **II-C3**$^{2+}$

Table IX.6. Calculated transitions and contributions of each unit for **II-C1^{2+}**.

$S_0 \rightarrow S_x$	λ (nm)	Osc. Strength	Major contribs	DMAP	tbu2tpy	Ru	4-py	tpy
1	551.60	0.0	H-3->LUMO (25%), HOMO->LUMO (73%)	64-->0 (-64)	11-->2 (-9)	22-->9 (-13)	0-->11 (11)	3-->78 (75)
2	516.58	0.0135	H-1->LUMO (97%)	0-->0 (0)	18-->2 (-16)	67-->9 (-58)	0-->11 (11)	15-->78 (63)
3	489.53	0.7149	H-2->LUMO (10%), HOMO->L+1 (84%)	69-->6 (-63)	9-->77 (68)	17-->7 (-10)	0-->1 (1)	3-->9 (6)
4	480.32	0.0071	HOMO->L+2 (69%), HOMO->L+3 (22%)	76-->0 (-76)	10-->28 (18)	13-->1 (-12)	0-->0 (0)	2-->70 (68)
5	468.48	0.0013	H-1->L+1 (35%), HOMO->L+3 (50%)	48-->3 (-45)	13-->80 (67)	33-->4 (-29)	0-->0 (0)	7-->14 (7)
6	464.22	0.0279	H-1->L+1 (61%), HOMO->L+2 (12%), HOMO->L+3 (22%)	29-->4 (-25)	15-->75 (60)	46-->5 (-41)	0-->0 (0)	10-->16 (6)
7	450.10	0.0044	H-2->LUMO (51%), H-1->L+2 (32%)	5-->1 (-4)	13-->17 (4)	64-->5 (-59)	2-->6 (4)	17-->71 (54)
8	449.36	0.0	H-2->L+1 (90%)	4-->6 (2)	9-->78 (69)	64-->7 (-57)	3-->1 (-2)	19-->8 (-11)
9	433.28	0.0	H-3->LUMO (68%), HOMO->LUMO (23%)	28-->1 (-27)	15-->8 (-7)	49-->9 (-40)	0-->10 (10)	7-->73 (66)
10	421.89	0.0499	H-2->L+2 (92%)	0-->0 (0)	9-->13 (4)	66-->1 (-65)	4-->1 (-3)	21-->85 (64)
11	415.30	0.21	H-2->LUMO (14%), H-1->L+2 (60%), H-1->L+3 (24%)	1-->0 (-1)	16-->28 (12)	66-->2 (-64)	1-->2 (1)	16-->67 (51)
12	404.20	0.0009	H-3->L+1 (51%), H-1->L+3 (29%)	14-->4 (-10)	16-->78 (62)	59-->5 (-54)	0-->1 (1)	10-->12 (2)
13	396.17	0.0004	H-2->L+3 (92%)	0-->1 (1)	9-->84 (75)	67-->3 (-64)	4-->0 (-4)	20-->13 (-7)
14	386.11	0.0051	H-3->L+2 (86%), HOMO->L+2 (11%)	22-->0 (-22)	16-->10 (-6)	55-->1 (-54)	0-->0 (0)	7-->89 (82)
15	377.95	0.0508	H-3->L+3 (91%)	17-->1 (-16)	17-->88 (71)	58-->3 (-55)	0-->0 (0)	7-->8 (1)
16	363.50	0.0013	H-3->L+1 (37%), H-2->LUMO (10%), H-1->L+3 (36%)	6-->3 (-3)	17-->72 (55)	63-->5 (-58)	1-->2 (1)	13-->18 (5)
17	358.07	0.0	HOMO->L+4 (87%)	76-->0 (-76)	10-->0 (-10)	13-->0 (-13)	0-->32 (32)	2-->67 (65)
$S_0 \rightarrow T_x$								
1	630.55	0.0	H-2->LUMO (57%), HOMO->L+1 (28%)	26-->3 (-23)	10-->34 (24)	46-->7 (-39)	4-->7 (3)	14-->48 (34)
2	616.53	0.0	H-2->LUMO (36%), HOMO->L+1 (45%)	42-->5 (-37)	11-->52 (41)	34-->7 (-27)	2-->4 (2)	10-->32 (22)
3	572.41	0.0	H-3->LUMO (34%), HOMO->LUMO (64%)	57-->0 (-57)	12-->2 (-10)	27-->9 (-18)	0-->11 (11)	3-->78 (75)
4	568.81	0.0	H-1->LUMO (94%)	0-->0 (0)	18-->2 (-16)	65-->8 (-57)	0-->11 (11)	16-->78 (62)
5	517.38	0.0	H-1->L+1 (43%), HOMO->L+3 (43%)	42-->4 (-38)	15-->82 (67)	36-->4 (-32)	0-->0 (0)	8-->10 (2)
6	508.09	0.0	H-1->L+1 (49%), HOMO->L+2 (13%), HOMO->L+3 (32%)	38-->4 (-34)	15-->76 (61)	38-->4 (-34)	0-->0 (0)	8-->16 (8)
7	494.89	0.0	H-1->L+2 (48%), H-1->L+3 (24%)	2-->0 (-2)	18-->32 (14)	54-->2 (-52)	5-->2 (-3)	21-->64 (43)
8	476.22	0.0	H-3->L+2 (12%), HOMO->L+2 (66%), HOMO->L+3 (15%)	69-->0 (-69)	11-->25 (14)	18-->1 (-17)	0-->0 (0)	2-->73 (71)
9	471.515	0.0	H-4->L+3 (11%), H-3->L+1 (15%), H-1->L+2 (13%), H-1->L+3 (35%)	17-->3 (-14)	28-->74 (46)	44-->3 (-41)	1-->0 (-1)	11-->19 (8)
10	465.13	0.0	H-2->L+1 (95%)	2-->7 (5)	9-->83 (74)	66-->7 (-59)	4-->0 (-4)	20-->4 (-16)

Table IX.7. Calculated transitions and contributions of each unit for **II-C2**$^{2+}$.

$S_0 \rightarrow S_x$	λ(nm)	Osc. Strength	Major contribs	DMAP	tbu2tpy	Ru	4-py	pzpypz
1	635.36	0.0	H-3->LUMO (16%), HOMO->LUMO (83%)	73-->0 (-73)	11-->2 (-9)	15-->9 (-6)	0-->4 (4)	2-->84 (82)
2	534.44	0.0235	H-1->LUMO (97%)	0-->0 (0)	21-->2 (-19)	64-->9 (-55)	0-->4 (4)	15-->84 (69)
3	529.96	0.0001	HOMO->L+1 (92%)	79-->0 (-79)	10-->2 (-8)	10-->3 (-7)	0-->0 (0)	1-->95 (94)
4	496.14	0.6709	H-2->LUMO (26%), HOMO->L+2 (69%)	60-->5 (-55)	9-->63 (54)	23-->6 (-17)	1-->1 (0)	7-->24 (17)
5	484.37	0.0	H-3->LUMO (81%), HOMO->LUMO (16%)	23-->0 (-23)	17-->2 (-15)	53-->9 (-44)	0-->4 (4)	8-->84 (76)
6	473.31	0.0034	HOMO->L+3 (97%)	83-->1 (-82)	10-->95 (85)	7-->2 (-5)	0-->0 (0)	1-->2 (1)
7	473.22	0.0419	H-2->LUMO (48%), H-1->L+1 (22%), HOMO->L+2 (25%)	21-->2 (-19)	12-->25 (13)	50-->7 (-43)	2-->2 (0)	14-->65 (51)
8	437.24	0.0656	H-2->L+1 (94%)	0-->0 (0)	9-->3 (-6)	64-->3 (-61)	4-->1 (-3)	22-->93 (71)
9	424.04	0.0198	H-1->L+2 (86%)	4-->6 (2)	20-->76 (56)	62-->5 (-57)	0-->0 (0)	14-->13 (-1)
10	417.41	0.0	H-2->L+2 (97%)	0-->7 (7)	9-->85 (76)	65-->6 (-59)	5-->0 (-5)	21-->2 (-19)
11	413.93	0.0018	H-3->L+1 (62%), H-1->L+2 (12%), HOMO->L+5 (12%)	23-->1 (-22)	16-->15 (-1)	52-->4 (-48)	0-->0 (0)	9-->81 (72)
12	410.94	0.0004	HOMO->L+4 (93%)	81-->0 (-81)	10-->0 (-10)	8-->0 (-8)	0-->18 (18)	1-->81 (80)
13	409.85	0.0968	H-2->LUMO (15%), H-1->L+1 (69%)	4-->1 (-3)	18-->13 (-5)	62-->4 (-58)	1-->1 (0)	15-->81 (66)
14	398.74	0.0001	H-3->L+1 (16%), HOMO->L+5 (80%)	71-->0 (-71)	11-->4 (-7)	16-->2 (-14)	0-->0 (0)	2-->93 (91)
15	381.70	0.0206	H-3->L+2 (58%), H-1->L+3 (36%)	7-->5 (-2)	19-->88 (69)	62-->4 (-58)	0-->0 (0)	11-->4 (-7)
16	371.33	0.0004	H-2->L+3 (95%)	0-->1 (1)	9-->93 (84)	65-->3 (-62)	5-->0 (-5)	22-->4 (-18)
17	360.73	0.0548	H-3->L+3 (92%)	13-->1 (-12)	18-->93 (75)	60-->2 (-58)	0-->0 (0)	9-->4 (-5)
18	352.87	0.1326	H-3->L+2 (20%), H-2->L+4 (17%), H-1->L+3 (46%), H-1->L+5 (11%)	3-->2 (-1)	19-->65 (46)	63-->3 (-60)	1-->3 (2)	15-->27 (12)
$S_0 \rightarrow T_x$								
1	665.94	0.0	H-2->LUMO (93%)	1-->0 (-1)	9-->3 (-6)	62-->9 (-53)	5-->5 (0)	23-->83 (60)
2	657.22	0.0	H-3->LUMO (25%), HOMO->LUMO (74%)	65-->0 (-65)	11-->2 (-9)	20-->9 (-11)	0-->4 (4)	3-->84 (81)
3	614.85	0.0	HOMO->L+2 (80%)	76-->8 (-68)	11-->85 (74)	11-->5 (-6)	0-->0 (0)	2-->2 (0)
4	604.86	0.0	H-1->LUMO (94%)	0-->0 (0)	21-->2 (-19)	62-->9 (-53)	0-->5 (5)	16-->84 (68)
5	537.01	0.0	HOMO->L+1 (86%)	77-->0 (-77)	10-->5 (-5)	11-->3 (-8)	0-->0 (0)	2-->91 (89)
6	518.61	0.0	H-1->L+1 (69%)	1-->0 (-1)	19-->7 (-12)	52-->3 (-49)	3-->2 (-1)	25-->88 (63)
7	511.59	0.0	HOMO->L+3 (88%)	79-->1 (-78)	10-->92 (82)	9-->2 (-7)	0-->0 (0)	2-->5 (3)
8	499.78	0.0	H-3->LUMO (71%), HOMO->LUMO (26%)	30-->0 (-30)	16-->2 (-14)	47-->9 (-38)	0-->4 (4)	8-->84 (76)
9	475.07	0.0	H-2->L+1 (92%)	0-->0 (0)	9-->5 (-4)	63-->3 (-60)	5-->0 (-5)	23-->92 (69)
10	465.79	0.0	H-1->L+2 (87%)	3-->7 (4)	25-->86 (61)	57-->5 (-52)	0-->0 (0)	14-->2 (-12)

Table IX.8. Calculated transitions and contributions of each unit for **II-C3**$^{2+}$.

$S_0 \rightarrow S_x$	λ (nm)	Osc. Strength	Major contributions	DMAP	tpyd	Ru	4'(4BrPh)	tpy	4 and 4'' py
1	569.73	0.0	H-3->LUMO (21%), HOMO->LUMO (77%)	67-->0 (-67)	11-->2 (-9)	20-->8 (-12)	0-->4 (4)	2-->75 (73)	0-->11 (11)
2	526.49	0.0703	H-1->LUMO (96%)	0-->0 (0)	17-->2 (-15)	65-->8 (-57)	0-->4 (4)	15-->75 (60)	3-->11 (8)
3	494.26	0.058	H-3->L+1 (10%), HOMO->L+1 (82%)	73-->0 (-73)	10-->10 (0)	14-->2 (-12)	0-->0 (0)	2-->79 (77)	0-->7 (7)
4	492.51	0.7051	H-2->LUMO (17%), HOMO->L+2 (72%)	64-->5 (-59)	9-->66 (57)	21-->6 (-15)	2-->1 (-1)	5-->19 (14)	0-->2 (2)
5	471.84	0.0039	HOMO->L+3 (91%)	76-->1 (-75)	10-->91 (81)	12-->3 (-9)	0-->0 (0)	2-->5 (3)	0-->1 (1)
6	466.04	0.0059	H-2->LUMO (48%), H-1->L+1 (32%), HOMO->L+2 (12%)	10-->1 (-9)	12-->18 (6)	56-->5 (-51)	5-->2 (-3)	15-->65 (50)	1-->8 (7)
7	464.27	0.0285	H-1->L+2 (94%)	3-->7 (4)	17-->83 (66)	63-->6 (-57)	0-->0 (0)	14-->3 (-11)	3-->0 (-3)
8	453.44	0.0001	H-3->LUMO (26%), H-2->L+2 (60%), HOMO->LUMO (11%)	12-->4 (-8)	11-->53 (42)	56-->7 (-49)	7-->2 (-5)	14-->30 (16)	0-->4 (4)
9	444.07	0.0001	H-3->LUMO (49%), H-2->L+2 (36%), HOMO->LUMO (12%)	17-->3 (-14)	13-->32 (19)	55-->7 (-48)	4-->3 (-1)	11-->48 (37)	0-->7 (7)
10	436.95	0.105	H-2->L+1 (93%)	0-->0 (0)	8-->7 (-1)	62-->2 (-60)	9-->1 (-8)	19-->82 (63)	1-->8 (7)
11	422.21	0.1452	H-2->LUMO (17%), H-1->L+1 (60%), H-1->L+3 (15%)	3-->0 (-3)	15-->21 (6)	62-->3 (-59)	2-->1 (-1)	15-->66 (51)	2-->7 (5)
12	404.91	0.0223	H-3->L+2 (44%), H-1->L+3 (44%)	12-->4 (-8)	17-->85 (68)	59-->5 (-54)	0-->0 (0)	11-->5 (-6)	1-->1 (0)
13	399.05	0.0	HOMO->L+5 (86%)	74-->0 (-74)	10-->4 (-6)	14-->1 (-13)	0-->0 (0)	2-->65 (63)	0-->30 (30)
14	398.00	0.0013	H-2->L+3 (93%)	0-->1 (1)	8-->89 (81)	62-->3 (-59)	10-->0 (-10)	19-->6 (-13)	1-->1 (0)
15	397.64	0.0	HOMO->L+4 (91%)	77-->0 (-77)	10-->1 (-9)	12-->1 (-11)	0-->11 (11)	1-->62 (61)	0-->25 (25)
16	396.44	0.0008	H-3->L+1 (80%), HOMO->L+1 (10%)	25-->0 (-25)	16-->6 (-10)	52-->2 (-50)	0-->0 (0)	7-->82 (75)	0-->9 (9)
17	377.07	0.0548	H-3->L+3 (92%)	16-->1 (-15)	17-->91 (74)	59-->3 (-56)	0-->0 (0)	7-->5 (-2)	0-->1 (1)
18	370.54	0.0242	H-3->L+2 (35%), H-1->L+3 (25%), H-1->L+5 (26%)	5-->3 (-2)	17-->57 (40)	63-->4 (-59)	1-->1 (0)	13-->25 (12)	2-->10 (8)
19	358.61	0.3067	H-1->L+4 (91%)	0-->0 (0)	17-->1 (-16)	64-->1 (-63)	0-->11 (11)	16-->62 (46)	3-->25 (22)
20	354.08	0.0262	H-2->L+4 (52%), H-1->L+5 (39%)	0-->0 (0)	12-->5 (-7)	63-->1 (-62)	5-->6 (1)	18-->61 (43)	2-->26 (24)
21	351.93	0.0072	H-2->L+5 (93%)	0-->0 (0)	8-->3 (-5)	62-->1 (-61)	9-->1 (-8)	19-->64 (45)	1-->31 (30)
$S_0 \rightarrow T_x$									
1	632.70	0.0	H-2->LUMO (66%), HOMO->L+2 (18%)	16-->2 (-14)	9-->22 (13)	50-->7 (-43)	8-->4 (-4)	16-->56 (40)	1-->9 (8)
2	617.24	0.0	H-3->L+2 (11%), H-2->LUMO (21%), HOMO->L+2 (56%)	53-->6 (-47)	11-->63 (52)	26-->6 (-20)	2-->2 (0)	7-->20 (13)	1-->3 (2)
3	589.98	0.0	H-1->LUMO (87%)	4-->0 (-4)	17-->2 (-15)	60-->7 (-53)	0-->4 (4)	15-->75 (60)	4-->12 (8)
4	588.89	0.0	H-3->LUMO (28%), HOMO->LUMO (64%)	57-->0 (-57)	12-->2 (-10)	27-->8 (-19)	0-->4 (4)	4-->75 (71)	0-->11 (11)
5	520.75	0.0	H-1->L+1 (64%), H-1->L+3 (11%)	1-->0 (-1)	16-->16 (0)	53-->2 (-51)	1-->1 (0)	21-->71 (50)	8-->10 (2)
6	516.56	0.0	H-1->L+2 (29%), HOMO->L+3 (57%)	54-->3 (-51)	13-->84 (71)	27-->4 (-23)	0-->0 (0)	6-->8 (2)	1-->1 (0)
7	509.09	0.0	H-1->L+2 (52%), HOMO->L+1 (26%), HOMO->L+3 (13%)	34-->4 (-30)	15-->62 (47)	40-->4 (-36)	0-->0 (0)	9-->27 (18)	2-->3 (1)
8	493.84	0.0	H-3->L+1 (11%), H-1->L+2 (11%), HOMO->L+1 (52%), HOMO->L+3 (21%)	62-->1 (-61)	12-->36 (24)	22-->3 (-19)	0-->0 (0)	4-->55 (51)	0-->5 (5)
9	470.99	0.0	H-5->L+3 (12%), H-3->L+2 (13%), H-1->L+3 (43%)	17-->3 (-14)	29-->83 (54)	42-->4 (-38)	0-->0 (0)	10-->9 (-1)	2-->1 (-1)
10	468.15	0.0	H-2->L+1 (81%)	1-->1 (0)	8-->16 (8)	61-->3 (-58)	9-->0 (-9)	20-->73 (53)	1-->7 (6)

Table IX.9. Atomic coordinates of **II-C1**$^{2+}$ after optimization

Center Number	Atomic number	Coordinates (Angstroms)			Center Number	Atomic number	Coordinates (Angstroms)		
		X	Y	Z			X	Y	Z
1	6	3.934175	0.000089	0.000057	56	7	-1.237261	0.008663	2.039348
2	7	1.143358	0.000023	0.000216	57	6	-2.066182	0.020984	4.712428
3	6	3.200113	-1.211804	0.004842	58	6	0.327652	0.014761	3.041171
4	6	3.200015	1.211923	0.004874	59	6	-2.581745	0.008613	2.349418
5	6	1.805961	1.188470	0.000176	60	6	-3.011533	0.014451	3.680530
6	6	1.806058	-1.188462	0.000137	61	6	0.702850	0.021189	4.386793
7	1	3.722064	-2.159821	0.037364	62	1	0.715067	0.014361	2.749363
8	1	3.721899	2.159981	0.037260	63	1	-4.069689	0.013812	3.912344
9	6	0.895459	2.348799	0.006929	64	1	0.061228	0.025995	5.154839
10	6	0.956081	4.390234	0.018781	65	1	-2.387815	0.025726	5.747681
11	7	0.445061	2.038622	0.008008	66	6	-7.086148	0.000042	0.000702
12	6	1.329723	3.678182	0.011113	67	7	-9.922954	0.000150	0.001075
13	6	0.410622	4.740138	0.017622	68	6	-7.818490	0.648932	1.014196
14	6	-1.342002	3.052836	0.013638	69	6	-7.818708	0.649071	-1.012599
15	1	2.392717	3.880184	0.009058	70	6	-9.217719	0.624130	0.972451
16	1	-2.388725	2.775241	0.014012	71	6	-9.217510	0.623883	0.974416
17	1	-1.731173	5.148055	0.023389	72	1	-7.322115	-1.189970	1.812516
18	6	0.895646	-2.348861	0.006467	73	1	-7.322503	1.190073	-1.811050
19	6	0.955745	-4.390432	0.017908	74	1	-9.797516	1.123923	-1.741854
20	6	1.330009	-3.678213	0.010376	75	1	-9.797143	-1.123632	1.743972
21	7	0.444895	-2.038782	0.007618	76	7	9.657062	0.000325	0.000708
22	6	-1.341764	-3.053061	0.013047	77	6	10.392322	-1.147654	0.526745
23	6	0.410984	-4.740236	0.016668	78	1	10.155438	-2.068434	0.023252
24	1	2.393019	-3.880136	0.008249	79	1	11.463534	0.964974	0.430051
25	1	-2.388505	-2.775535	0.013502	80	1	10.172906	-1.317225	-1.589727
26	1	-1.730782	-5.148311	0.022362	81	6	10.392078	1.148471	0.528127
27	6	5.404792	0.000151	0.000223	82	1	10.172099	1.318394	1.590931
28	6	8.280993	0.000266	0.000540	83	1	10.155518	2.069087	0.022298
29	6	6.145440	1.092583	0.507902	84	1	11.463336	0.965710	0.432094
30	6	6.145640	-1.092217	0.507309	85	6	0.835589	-6.209636	0.022052
31	6	7.537274	-1.100217	0.515655	86	6	0.835122	6.209566	0.023336
32	6	7.537073	1.100700	0.516539	87	6	0.265932	6.891137	-1.291218
33	1	5.630869	1.947376	0.938278	88	1	0.827999	6.841010	-1.326876
34	1	5.631228	-1.947044	0.937806	89	1	0.661112	6.422060	-2.200107
35	1	8.050181	-1.958523	0.933651	90	6	2.364537	6.375134	0.021290
36	1	8.049822	1.959068	0.934604	91	1	2.822521	5.934294	0.872624
37	44	0.849396	0.000096	0.000114	92	1	2.610374	7.442815	0.025643
38	7	-1.237808	0.008881	-2.039471	93	1	2.825770	5.926282	0.909529
39	6	-2.067392	0.021225	-4.712338	94	1	0.553734	7.948984	-1.298087
40	6	-2.582368	0.008811	-2.349203	95	6	0.261253	6.902576	1.236203
41	6	0.328445	0.015019	-3.041515	96	1	0.653270	6.441916	2.150748
42	6	0.703978	0.021458	-4.387044	97	1	0.832788	6.852516	1.268413
43	6	-3.012489	0.014660	-3.680208	98	1	0.548805	7.960514	1.234441
44	1	0.714342	0.014645	-2.749951	99	6	0.266487	-6.891519	1.289806
45	1	0.059908	0.026293	-5.155280	100	1	0.661671	-6.422616	2.198783
46	1	-4.070703	0.014006	-3.911758	101	1	0.554354	-7.949350	1.296434
47	1	-2.389282	0.025972	-5.747512	102	1	0.827446	-6.841466	1.325514
48	7	-2.830762	0.000108	0.000138	103	6	0.261729	-6.902418	-1.237617
49	6	-5.604615	0.000014	0.000507	104	1	0.832317	-6.852439	-1.269776
50	6	-3.490482	0.001357	1.191545	105	1	0.549365	-7.960333	-1.236094
51	6	-3.490802	0.001525	-1.191093	106	1	0.653676	-6.441528	-2.152076
52	6	-4.886968	0.001920	-1.213396	107	6	2.365015	-6.375096	0.019920
53	6	-4.886644	0.001846	1.214218	108	1	2.826246	-5.926405	0.908242
54	1	-5.416357	0.026783	-2.158086	109	1	2.822938	-5.934027	0.873912
55	1	-5.415782	0.026750	2.159047	110	1	2.610929	-7.442760	0.024030

Table IX.10. Atomic coordinates of **II-C2**$^{2+}$ after optimization.

Center Number	Atomic number	Coordinates (Angstroms)			Center Number	Atomic number	Coordinates (Angstroms)		
		X	Y	Z			X	Y	Z
1	6	3.937218	0.000006	0.000015	55	7	-1.234519	0.007055	2.027363
2	7	1.147051	0.000005	0.000103	56	7	-2.093625	0.015939	4.698760
3	6	3.202251	-1.212005	0.004609	57	6	0.344937	0.012170	3.045456
4	6	3.202241	1.212012	0.004521	58	6	-2.579578	0.006560	2.337355
5	6	1.808835	1.188035	0.000453	59	6	-2.979315	0.010585	3.680975
6	6	1.808845	-1.188039	0.000277	60	6	0.780484	0.016851	4.375136
7	1	3.723199	-2.160344	0.037060	61	1	0.707093	0.012340	2.795181
8	1	3.723178	2.160356	0.037016	62	1	-4.028602	0.009328	3.950360
9	6	0.898927	2.349276	0.005577	63	1	0.064885	0.021126	5.188236
10	6	0.951668	4.391814	0.015412	64	6	-7.089534	0.000013	0.000313
11	7	0.441511	2.041189	0.006533	65	7	-9.924603	0.000021	0.000475
12	6	1.333872	3.677716	0.008900	66	6	-7.820884	0.653100	1.010886
13	6	0.415069	4.740408	0.014370	67	6	-7.820764	0.653130	-1.011596
14	6	-1.338704	3.054879	0.011156	68	6	-9.219829	0.628081	0.971497
15	1	2.396829	3.879295	0.006924	69	6	-9.219944	0.628042	0.970627
16	1	-2.385726	2.778959	0.011429	70	1	-7.324903	-1.197640	1.807054
17	1	-1.726375	5.149845	0.019223	71	1	-7.324688	1.197668	-1.807706
18	6	0.898945	-2.349287	0.005798	72	1	-9.799629	1.130929	-1.738791
19	6	0.951639	-4.391834	0.015782	73	1	-9.799834	-1.130887	1.737855
20	6	1.333897	-3.677724	0.009228	74	7	9.657609	0.000052	0.000344
21	7	0.441496	-2.041207	0.006713	75	6	10.393246	-1.157434	0.506891
22	6	-1.338683	-3.054901	0.011407	76	1	10.152018	-2.068712	0.056596
23	6	0.415100	-4.740421	0.014781	77	1	11.464268	0.975197	0.407987
24	1	2.396855	-3.879296	0.007288	78	1	10.178115	-1.342874	-1.568012
25	1	-2.385706	-2.778986	0.011632	79	6	10.393310	1.157485	0.506229
26	1	-1.726341	-5.149869	0.019649	80	1	10.178321	1.342825	1.567398
27	6	5.406411	0.000012	0.000057	81	1	10.152008	2.068817	0.057139
28	6	8.282456	0.000037	0.000235	82	1	11.464319	0.975263	0.407157
29	6	6.147489	1.099986	0.491776	83	6	0.840924	-6.209114	0.019567
30	6	6.147448	-1.099954	0.491974	84	6	0.840883	6.209105	0.019034
31	6	7.538497	-1.108003	0.500612	85	6	0.271431	6.891589	-1.286418
32	6	7.538540	1.108059	0.500243	86	1	0.822541	6.842825	-1.321612
33	1	5.633849	1.960984	0.910479	87	1	0.665823	6.422936	-2.195814
34	1	5.633770	-1.960962	0.910608	88	6	2.370389	6.373361	0.017280
35	1	8.051349	-1.971898	0.906838	89	1	2.828414	5.931817	0.876245
36	1	8.051424	1.971961	0.906412	90	1	2.616733	7.440858	0.020836
37	44	0.851075	0.000011	0.000053	91	1	2.831166	5.925244	0.906108
38	7	-1.234271	0.007081	-2.027299	92	1	0.560405	7.949042	-1.292386
39	7	-2.093076	0.015963	-4.698797	93	6	0.267476	6.901011	1.241435
40	6	-2.579297	0.006576	-2.337446	94	1	0.659184	6.439284	2.155520
41	6	0.344576	0.012207	-3.045294	95	1	0.826590	6.852311	1.273692
42	6	0.779972	0.016887	-4.375023	96	1	0.556252	7.958536	1.240329
43	6	-2.978880	0.010602	-3.681112	97	6	0.271546	-6.891484	1.287045
44	1	0.707427	0.012389	-2.794907	98	1	0.665965	-6.422728	2.196376
45	1	0.064279	0.021169	-5.188040	99	1	0.560550	-7.948928	1.293107
46	1	-4.028136	0.009340	-3.950615	100	1	0.822427	-6.842750	1.322285
47	7	-2.832960	0.000009	0.000060	101	6	0.267451	-6.901141	-1.240807
48	6	-5.608161	0.000008	0.000227	102	1	0.826615	-6.852425	-1.273019
49	6	-3.494747	0.000562	1.190259	103	1	0.556211	-7.958670	-1.239607
50	6	-3.494603	0.000570	-1.190460	104	1	0.659125	-6.439512	-2.154957
51	6	-4.890518	0.001538	-1.214381	105	6	2.370430	-6.373360	0.017746
52	6	-4.890664	0.001548	1.214013	106	1	2.831259	-5.925059	0.906454
53	1	-5.420059	0.026102	-2.159132	107	1	2.828396	-5.931995	0.875898
54	1	-5.420316	0.026122	2.158701	108	1	2.616782	-7.440855	0.021500

Table IX.11. Atomic coordinates of **II-C3^{2+}** after optimization.

Center Number	Atomic number	Coordinates (Angstroms)			Center Number	Atomic number	Coordinates (Angstroms)		
		X	Y	Z			X	Y	Z
1	6	-5.061183	0.000331	0.022569	66	6	6.681791	-1.015713	0.696659
2	7	-2.270583	0.001359	0.007409	67	6	8.081518	-1.022328	0.709268
3	6	-4.320438	0.012562	-1.230392	68	6	8.089453	1.016606	0.628873
4	6	-4.333653	0.014097	1.193242	69	1	6.171279	1.793362	-1.177081
5	6	-2.939537	0.019065	1.177314	70	1	6.156908	-1.796464	1.238411
6	6	-2.926597	0.016505	-1.199359	71	1	8.615460	-1.805250	1.236481
7	1	-4.837204	0.005407	-2.181619	72	1	8.629637	1.798885	-1.150655
8	1	-4.860616	0.004361	2.138837	73	7	-10.783768	0.003814	0.054976
9	6	-2.035339	0.030477	2.342671	74	6	-11.512010	0.550795	-1.198321
10	6	0.195192	0.051902	4.394432	75	1	-11.271981	0.014460	-2.126315
11	7	0.693042	0.024387	2.040293	76	1	-12.584352	0.454271	-1.022355
12	6	-2.477043	0.048098	3.669438	77	1	-11.288961	-1.615655	-1.350296
13	6	-1.563859	0.059195	4.736511	78	6	-11.525825	0.541991	1.080016
14	6	0.198237	0.035167	3.059323	79	1	-11.305679	1.607036	1.234886
15	1	-3.541156	0.053773	3.865427	80	1	-11.296061	0.005621	2.010597
16	1	1.246445	0.030326	2.787430	81	1	-12.595945	0.444433	0.891541
17	1	0.575629	0.059606	5.156564	82	6	-1.929174	0.072923	-6.214972
18	6	-2.009868	0.027495	-2.354874	83	6	-1.996683	0.078405	6.203382
19	6	0.147533	0.048971	-4.386535	84	6	-1.434610	-1.179755	6.908505
20	6	-2.437097	0.043882	-3.686388	85	1	0.340540	-1.219095	6.864731
21	7	0.670982	0.022241	-2.037951	86	1	-1.829829	-2.095098	6.452198
22	6	0.231369	0.033160	-3.047230	87	6	-3.526992	0.087129	6.360203
23	6	-1.512380	0.054932	-4.743467	88	1	-3.980064	0.974826	5.902038
24	1	-3.498980	0.048521	-3.894038	89	1	-3.778827	0.101100	7.426397
25	1	1.276612	0.029187	-2.764117	90	1	-3.988117	0.807227	5.923578
26	1	0.631480	0.056903	-5.140278	91	1	-1.727997	-1.168624	7.964779
27	6	-6.531676	0.000733	0.030758	92	6	-1.423433	1.347531	6.879200
28	6	-9.407797	0.002878	0.047115	93	1	-1.809901	2.255506	6.401185
29	6	-7.278957	0.522558	1.049759	94	1	0.329013	1.375869	6.835660
30	6	-7.265879	0.525209	-1.119650	95	1	-1.717653	1.363892	7.935165
31	6	-8.657398	0.534946	-1.135461	96	6	-1.357128	1.184336	-6.913647
32	6	-8.670588	0.530214	1.049717	97	1	-1.755660	2.100314	-6.461513
33	1	-6.769672	0.966043	1.900996	98	1	-1.638973	1.173917	-7.973065
34	1	-6.746282	0.968007	-1.964993	99	1	0.263527	1.221739	-6.857946
35	1	-9.165052	0.966121	-1.990365	100	6	-1.350889	-1.342998	-6.884717
36	1	-9.188592	0.960579	1.898793	101	1	0.257073	-1.373479	-6.828961
37	44	0.277826	0.000895	0.003325	102	1	-1.633366	-1.358534	-7.943898
38	7	0.110783	-2.034203	0.027448	103	1	-1.744407	-2.250337	-6.411265
39	6	0.952330	-4.727487	0.052008	104	6	-3.457688	0.078769	-6.388514
40	6	1.454246	-2.347327	0.030881	105	1	-3.921912	0.816210	-5.956473
41	6	0.791138	-3.042694	0.039987	106	1	-3.917388	0.965854	-5.935815
42	6	0.413183	-4.383674	0.052923	107	1	-3.697861	0.091750	-7.457404
43	6	1.884444	-3.674811	0.042726	108	6	8.772024	0.003317	0.043581
44	1	-1.836040	-2.759793	0.033030	109	35	10.723055	0.004608	0.053188
45	1	-1.186022	-5.143176	0.040709	110	6	1.396647	6.141971	0.060811
46	1	2.946098	-3.888912	0.066254	111	7	2.234484	8.850819	0.096384
47	7	1.705491	0.000207	0.011588	112	6	2.597276	6.528369	0.688192
48	6	4.483766	0.000823	0.022331	113	6	0.627893	7.153749	0.546837
49	6	2.366644	1.190118	0.001157	114	6	1.080258	8.477794	0.506221
50	6	2.365644	-1.190212	0.027305	115	6	2.971623	7.877239	0.682171
51	6	3.761344	-1.213229	0.029897	116	1	3.227137	5.807510	-1.198085
52	6	3.762350	1.212103	0.007501	117	1	0.296259	6.925567	1.066276
53	1	4.289848	-2.158503	0.013850	118	1	0.503940	9.269312	0.974430
54	1	4.291422	2.157017	0.026202	119	1	3.890233	8.193949	-1.165612
55	7	0.112418	2.035683	0.015729	120	6	1.391914	-6.141432	0.059660
56	6	0.956059	4.728403	0.042278	121	7	2.228114	-8.850848	0.073894
57	6	0.788708	3.044911	0.024931	122	6	0.625168	-7.140469	0.690450
58	6	1.456110	2.347831	0.016892	123	6	2.589661	-6.540757	0.565097
59	6	1.887319	3.674975	0.030199	124	6	2.963292	-7.889491	0.534136
60	6	0.409729	4.385593	0.037318	125	6	1.076691	-8.465335	0.674010
61	1	-1.833818	2.762718	0.029088	126	1	0.296630	-6.901443	1.209226
62	1	2.949168	3.888445	0.010493	127	1	3.217539	-5.830280	-1.091781
63	1	-1.182053	5.145167	0.065997	128	1	3.879620	-8.216270	-1.015200
64	6	5.964468	0.001522	0.029571	129	1	0.502009	-9.247136	1.160221
65	6	6.689665	1.011816	0.630246					

Table IX.12. Contributions of each unit to selected frontiers orbitals of **II-C1**$^{+}$

MO	eV	DMAPh	tbu$_2$tpy	Ru	4-py	tpy
α L+2	-2.05	0	13	4	1	82
α L+1	-2.24	1	84	1	0	14
α LUMO	-2.33	6	83	9	0	2
α SOMO	-3.61	0	1	8	15	76
α H-1	-5,50	65	11	22	0	3
α H-2	-6.51	0	16	67	0	17
β L+2	-2.01	0	2	8	17	73
β L+1	-2.22	1	93	1	0	5
β LUMO	-2.32	6	82	10	0	2
β HOMO	-5.48	62	11	25	0	3
β H-1	-5.69	0	7	62	6	25
β H-2	-5.81	0	16	67	0	17

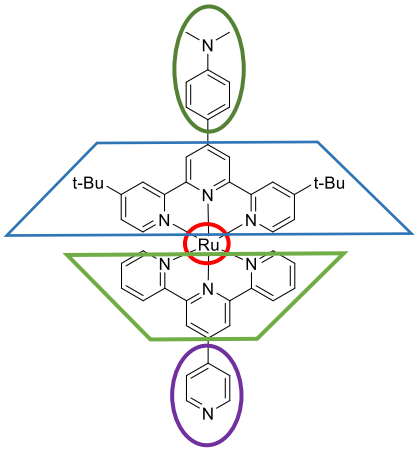

Table IX.13. Contributions of each unit to selected frontiers orbitals of **II-C2**$^{+}$

MO	eV	DMAPh	tbu$_2$tpy	Ru	4-py	pzpypz
α L+2	-2.26	1	91	4	0	5
α L+1	-2.42	6	84	8	0	1
α LUMO	-2.60	0	7	4	0	88
α SOMO	-3.96	0	2	8	4	85
α H-1	-5.58	75	9	14	0	2
α H-2	-6.11	0	16	64	0	20
β L+2	-2.32	0	69	0	0	31
β L+1	-2.38	0	2	9	9	80
β LUMO	-2.42	6	84	8	0	2
β HOMO	-5.57	73	10	16	0	2
β H-1	-6.01	0	7	65	4	24
β H-2	-6.11	0	16	65	0	19

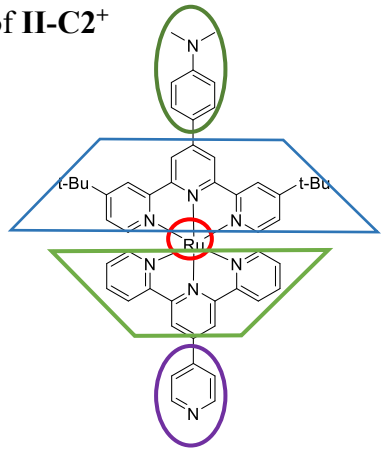

Table IX.14. Contributions of each unit to selected frontiers orbitals of **II-C3**$^{+}$

MO	eV	DMAPh	tbu$_2$tpy	Ru	4'(4BrPh)	tpy	4 and 4'' py
α L+2	-2.21	1	89	4	0	5	2
α L+1	-2.35	6	83	9	0	2	0
α LUMO	-2.47	0	9	3	0	69	18
α SOMO	-3.65	0	1	7	4	78	10
α H-1	-5.52	68	10	19	0	2	0
α H-2	-5.86	0	15	65	0	18	3
β L+2	-2.05	0	9	5	1	70	14
β L+1	-2.24	1	83	2	0	11	3
β LUMO	-2.35	4	55	8	1	24	8
β HOMO	-5.51	66	10	21	0	3	0
β H-1	-5.82	0	14	63	1	19	3
β H-2	-6.16	29	17	48	0	6	0

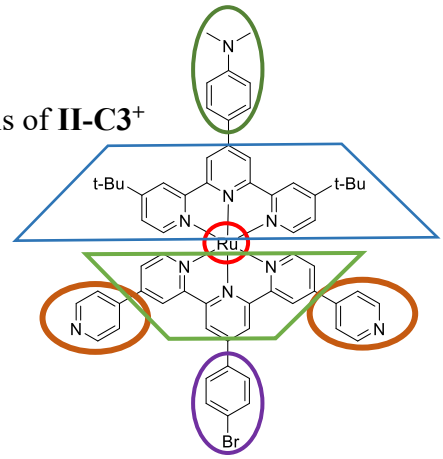

Table IX.15. Atomic coordinates of **II-C1**$^{+}$ after optimization.

Center Number	Atomic number	Coordinates (Angstroms)			Center Number	Atomic number	Coordinates (Angstroms)		
		X	Y	Z			X	Y	Z
1	6	3.940614	0.000035	0.000066	56	7	-1.240576	0.013654	2.037235
2	7	1.149055	0.000010	0.000364	57	6	-2.064210	0.032410	4.719138
3	6	3.208431	-1.212196	0.009224	58	6	0.328806	0.021896	3.044193
4	6	3.208393	1.212241	0.009494	59	6	-2.595240	0.014185	2.349447
5	6	1.813166	1.190623	0.004628	60	6	-3.009268	0.023385	3.695447
6	6	1.813206	-1.190623	0.004066	61	6	0.692730	0.031533	4.387791
7	1	3.732910	-2.159288	0.044745	62	1	0.713192	0.020712	2.746248
8	1	3.732849	2.159351	0.044861	63	1	-4.067479	0.023405	3.930834
9	6	0.900151	2.348890	0.015115	64	1	0.074259	0.038053	5.153331
10	6	0.957500	4.387315	0.033324	65	1	-2.381050	0.039931	5.756541
11	7	0.441369	2.035888	0.014252	66	6	-7.092033	0.000010	0.000775
12	6	1.331047	3.681076	0.024696	67	7	-9.967600	0.000011	0.001248
13	6	0.409590	4.740127	0.034731	68	6	-7.852202	0.294641	1.164511
14	6	-1.340414	3.049019	0.022859	69	6	-7.852590	0.294652	-1.162717
15	1	2.393866	3.885492	0.024251	70	6	-9.247326	0.282087	-1.116505
16	1	-2.384593	2.760262	0.021300	71	6	-9.246961	0.282068	1.118752
17	1	-1.733252	5.144859	0.040214	72	1	-7.373084	0.554223	2.101755
18	6	0.900224	-2.348916	0.014498	73	1	-7.373762	0.554211	-2.100115
19	6	0.957372	-4.387393	0.032585	74	1	-9.822251	0.512799	-2.009106
20	6	1.331157	-3.681091	0.024034	75	1	-9.821581	0.512788	2.011549
21	7	0.441305	-2.035951	0.013634	76	7	9.669127	0.000237	0.000402
22	6	-1.340322	-3.049107	0.022157	77	6	10.403179	-1.135224	0.553380
23	6	0.409728	-4.740168	0.034029	78	1	10.168960	-2.068439	0.023007
24	1	2.393982	-3.885476	0.023580	79	1	11.474762	0.953997	0.456449
25	1	-2.384508	-2.760377	0.020568	80	1	10.180804	-1.282915	-1.619233
26	1	-1.733104	-5.144958	0.039415	81	6	10.403001	1.135402	0.555025
27	6	5.414147	0.000064	0.000095	82	1	10.180921	1.282123	1.621086
28	6	8.291076	0.000150	0.000361	83	1	10.168313	2.068980	0.025526
29	6	6.154567	1.080211	0.531552	84	1	11.474609	0.954622	0.457540
30	6	6.154729	-1.080067	0.531168	85	6	0.830204	-6.211470	0.046293
31	6	7.547577	-1.088377	0.538895	86	6	0.830027	6.211440	0.047025
32	6	7.547413	1.088589	0.539567	87	6	0.258800	6.887250	-1.316889
33	1	5.638566	1.925146	0.979777	88	1	0.835018	6.833121	-1.351789
34	1	5.638859	-1.925059	0.979436	89	1	0.654712	6.415289	-2.224078
35	1	8.060367	-1.938104	0.974556	90	6	2.359052	6.381480	0.047151
36	1	8.060073	1.938276	0.975460	91	1	2.818806	5.944943	0.848001
37	44	0.831603	0.000037	0.000257	92	1	2.602558	7.449824	0.056300
38	7	-1.241238	0.013722	-2.037599	93	1	2.820376	5.929332	0.933711
39	6	-2.065691	0.032465	-4.719261	94	1	0.543162	7.946164	-1.328785
40	6	-2.596015	0.014228	-2.349406	95	6	0.256415	6.909474	1.209649
41	6	0.329777	0.021981	-3.044839	96	1	0.650949	6.453841	2.125737
42	6	0.694106	0.031613	-4.388327	97	1	0.837438	6.855541	1.243653
43	6	-3.010442	0.023423	-3.695288	98	1	0.540360	7.968551	1.203234
44	1	0.712308	0.020812	-2.747194	99	6	0.258951	-6.887336	1.316116
45	1	0.072660	0.038148	-5.154091	100	1	0.654820	-6.415393	2.223333
46	1	-4.068725	0.023427	-3.930361	101	1	0.543342	-7.946243	1.327987
47	1	-2.382854	0.039983	-5.756566	102	1	0.834869	-6.833240	1.350983
48	7	-2.823841	0.000049	0.000061	103	6	0.256650	-6.909480	-1.210422
49	6	-5.627988	0.000013	0.000525	104	1	0.837202	-6.855568	-1.244458
50	6	-3.498986	0.002886	1.203993	105	1	0.540619	-7.968550	-1.204030
51	6	-3.499394	0.002925	-1.203683	106	1	0.651204	-6.453808	-2.126482
52	6	-4.887384	0.000269	-1.220478	107	6	2.359233	-6.381472	0.046468
53	6	-4.886966	0.000289	1.221268	108	1	2.820514	-5.929322	0.933049
54	1	-5.406344	0.021256	-2.171570	109	1	2.819008	-5.944913	0.848663
55	1	-5.405601	0.021322	2.172534	110	1	2.602765	-7.449810	0.055610

Table IX.16. Atomic coordinates of **II-C2**$^{+}$ after optimization.

Center Number	Atomic number	Coordinates (Angstroms)			Center Number	Atomic number	Coordinates (Angstroms)		
		X	Y	Z			X	Y	Z
1	6	3.937951	0.000003	0.000025	55	7	-1.227109	0.008062	2.018109
2	7	1.148354	0.000008	0.000060	56	7	-2.103519	0.019701	4.709496
3	6	3.205370	-1.212309	0.005598	57	6	0.343359	0.012615	3.055128
4	6	3.205366	1.212301	0.005594	58	6	-2.589128	0.008569	2.336056
5	6	1.810519	1.189883	0.000719	59	6	-2.977639	0.014174	3.690461
6	6	1.810524	-1.189897	0.000636	60	6	0.772736	0.018619	4.375513
7	1	3.729250	-2.159597	0.038376	61	1	0.710418	0.011509	2.806707
8	1	3.729246	2.159590	0.038330	62	1	-4.030149	0.014165	3.954067
9	6	0.898279	2.349894	0.007843	63	1	0.058723	0.022622	5.190236
10	6	0.955545	4.391629	0.020154	64	6	-7.089485	0.000015	0.000197
11	7	0.443105	2.040570	0.008166	65	7	-9.940974	0.000033	0.000306
12	6	1.331690	3.680562	0.013227	66	6	-7.832414	0.551616	1.067628
13	6	0.411745	4.741524	0.020140	67	6	-7.832489	0.551655	-1.067177
14	6	-1.340795	3.053839	0.013876	68	6	-9.230198	0.529052	-1.026082
15	1	2.394670	3.883438	0.011907	69	6	-9.230126	0.528995	1.026639
16	1	-2.385887	2.768978	0.013409	70	1	-7.341250	-1.019490	1.913864
17	1	-1.730093	5.150233	0.024854	71	1	-7.341384	1.019522	-1.913452
18	6	0.898288	-2.349911	0.007716	72	1	-9.808136	0.955556	-1.840352
19	6	0.955530	-4.391653	0.019909	73	1	-9.808007	0.955492	1.840954
20	6	1.331703	-3.680579	0.013030	74	7	9.664273	0.000011	0.000235
21	7	0.443097	-2.040591	0.008051	75	6	10.398703	-1.137744	0.548961
22	6	-1.340784	-3.053863	0.013702	76	1	10.164250	-2.068619	0.014802
23	6	0.411762	-4.741543	0.019884	77	1	11.470171	0.955995	0.452309
24	1	2.394684	-3.883451	0.011706	78	1	10.176575	-1.289361	-1.614226
25	1	-2.385876	-2.769005	0.013254	79	6	10.398655	1.137888	0.549241
26	1	-1.730076	-5.150259	0.024557	80	1	10.176398	1.289744	1.614443
27	6	5.410463	0.000002	0.000079	81	1	10.164288	2.068652	0.014846
28	6	8.286949	0.000009	0.000179	82	1	11.470132	0.956088	0.452784
29	6	6.150909	1.082972	0.526431	83	6	0.835352	-6.211726	0.027271
30	6	6.150952	-1.082961	0.526226	84	6	0.835331	6.211708	0.027617
31	6	7.543352	-1.091111	0.534378	85	6	0.265561	6.892161	-1.295732
32	6	7.543307	1.091132	0.534674	86	1	0.828346	6.840792	-1.330992
33	1	5.635421	1.930049	0.971020	87	1	0.660673	6.422235	-2.204273
34	1	5.635501	-1.930040	0.970854	88	6	2.364663	6.378572	0.026612
35	1	8.056137	-1.942545	0.966561	89	1	2.823323	5.938575	0.867389
36	1	8.056060	1.942575	0.966876	90	1	2.610010	7.446456	0.032217
37	44	0.836245	0.000011	0.000038	91	1	2.825561	5.928718	0.914538
38	7	-1.227268	0.008081	-2.018157	92	1	0.552401	7.950366	-1.304093
39	7	-2.103861	0.019710	-4.709480	93	6	0.262260	6.906371	1.231249
40	6	-2.589306	0.008581	-2.336008	94	1	0.655234	6.446903	2.146041
41	6	0.343588	0.012635	-3.055234	95	1	0.831716	6.855112	1.264395
42	6	0.773058	0.018634	-4.375591	96	1	0.548807	7.964687	1.228301
43	6	-2.977913	0.014182	-3.690384	97	6	0.265732	-6.892223	1.295430
44	1	0.710205	0.011535	-2.806881	98	1	0.660926	-6.422305	2.203941
45	1	0.059102	0.022637	-5.190364	99	1	0.552604	-7.950419	1.303739
46	1	-4.030441	0.014168	-3.953918	100	1	0.828173	-6.840888	1.330808
47	7	-2.830763	0.000010	0.000032	101	6	0.262137	-6.906350	-1.231551
48	6	-5.612581	0.000006	0.000140	102	1	0.831841	-6.855062	-1.264582
49	6	-3.496282	0.000343	1.203848	103	1	0.548659	-7.964672	-1.228654
50	6	-3.496377	0.000352	-1.203730	104	1	0.655027	-6.446872	-2.146374
51	6	-4.890659	0.001749	-1.219329	105	6	2.364684	-6.378585	0.026084
52	6	-4.890565	0.001742	1.219551	106	1	2.825695	-5.928623	0.913897
53	1	-5.421092	0.022582	-2.164434	107	1	2.823228	-5.938693	0.868027
54	1	-5.420928	0.022597	2.164696	108	1	2.610035	-7.446468	0.031780

Table IX.17. Atomic coordinates of **II-C3**$^{+}$ after optimization.

Center Number	Atomic number	Coordinates (Angstroms)			Center Number	Atomic number	Coordinates (Angstroms)		
		X	Y	Z			X	Y	Z
1	6	-5.064006	0.009230	0.019465	66	6	6.696134	-1.056806	0.604942
2	7	-2.272725	0.014324	0.010255	67	6	8.095861	-1.069423	0.599177
3	6	-4.335511	0.018746	-1.194669	68	6	8.094980	1.026923	0.643186
4	6	-4.327561	0.037443	1.228840	69	1	6.175104	1.831074	-1.137022
5	6	-2.932571	0.044040	1.202315	70	1	6.177332	-1.859094	1.120445
6	6	-2.940334	0.021053	-1.177300	71	1	8.632648	-1.877043	1.085304
7	1	-4.862609	0.014991	-2.140853	72	1	8.630715	1.831888	-1.134855
8	1	-4.848497	0.028776	2.178412	73	7	-10.791856	0.002983	0.040099
9	6	-2.016608	0.066885	2.358130	74	6	-11.529316	0.581548	-1.077700
10	6	0.154561	0.102972	4.391869	75	1	-11.297140	0.077154	-2.025654
11	7	0.676239	0.055599	2.042302	76	1	-12.600350	0.478842	0.896517
12	6	-2.444525	0.098260	3.690747	77	1	-11.307922	-1.651199	-1.196543
13	6	-1.520611	0.117456	4.747643	78	6	-11.522400	0.585671	1.163385
14	6	0.225044	0.072931	3.052891	79	1	-11.302716	1.655850	1.280645
15	1	-3.506791	0.108045	3.897574	80	1	-11.281950	0.081798	2.109553
16	1	1.268961	0.062064	2.763672	81	1	-12.594499	0.480378	0.990170
17	1	0.623114	0.115115	5.147309	82	6	-1.977609	0.163846	-6.199874
18	6	-2.031829	0.050526	-2.338827	83	6	-1.937708	0.152500	6.219455
19	6	0.182782	0.109930	-4.383825	84	6	-1.371896	-1.099260	6.932580
20	6	-2.468278	0.089321	-3.668494	85	1	0.278462	-1.142150	6.876719
21	7	0.689423	0.041351	-2.031509	86	1	-1.774329	-2.018250	6.489925
22	6	0.205382	0.071333	-3.047525	87	6	-3.466299	0.166468	6.392669
23	6	-1.551115	0.120181	-4.730975	88	1	-3.921961	1.050242	5.929448
24	1	-3.531880	0.096548	-3.868509	89	1	-3.707273	0.192070	7.461299
25	1	1.251115	0.064193	-2.764805	90	1	-3.933785	0.731099	5.969553
26	1	0.590096	0.132627	-5.143928	91	1	-1.653389	-1.076762	7.992074
27	6	-6.537236	0.007674	0.024547	92	6	-1.355348	1.426836	6.877146
28	6	-9.414031	0.004562	0.035047	93	1	-1.745020	2.330706	6.393774
29	6	-7.274475	0.567433	1.092611	94	1	0.261378	1.452517	6.820943
30	6	-7.281012	0.553613	-1.038165	95	1	-1.637851	1.455043	7.936226
31	6	-8.673735	0.563287	-1.041157	96	6	-1.411398	1.080777	-6.925093
32	6	-8.667162	0.574103	1.105794	97	1	-1.807624	2.004349	-6.486368
33	1	-6.756164	1.039120	1.923198	98	1	-1.699403	1.052088	-7.982689
34	1	-6.767829	-1.024194	-1.872547	99	1	0.317484	1.119776	-6.876102
35	1	-9.189046	-1.022748	-1.876684	100	6	-1.404401	-1.444920	-6.852474
36	1	-9.177356	1.032423	1.945086	101	1	0.310178	-1.474261	-6.803661
37	44	0.292294	0.012926	0.003854	102	1	-1.694292	-1.479539	-7.909361
38	7	0.090223	-2.015218	0.048044	103	1	-1.794013	-2.343923	-6.360072
39	6	0.945449	-4.730932	0.093914	104	6	-3.507305	0.173008	-6.363408
40	6	1.455989	-2.337182	0.055720	105	1	-3.968656	0.729296	-5.943641
41	6	0.807927	-3.039095	0.063377	106	1	-3.963449	-1.051759	-5.891198
42	6	0.441043	-4.373433	0.082753	107	1	-3.755098	0.205099	-7.430305
43	6	1.868985	-3.679704	0.081200	108	6	8.783733	0.023603	0.026889
44	1	-1.854140	-2.754252	0.065700	109	35	10.738312	0.029412	0.037967
45	1	-1.219534	-5.126247	0.117588	110	6	1.414378	6.151651	0.133106
46	1	2.932727	-3.890188	0.063970	111	7	2.255907	8.868723	0.194598
47	7	1.702937	0.008740	0.000317	112	6	0.613501	7.159870	0.710086
48	6	4.487099	0.009503	0.002384	113	6	2.650846	6.554326	0.414989
49	6	2.375695	1.200159	0.028735	114	6	3.025117	7.901138	0.362031
50	6	2.358624	-1.204151	0.030763	115	6	1.067131	8.483334	0.719088
51	6	3.759464	-1.216637	0.028739	116	1	0.340683	6.927057	-1.169661
52	6	3.766112	1.218253	0.030892	117	1	3.310794	5.843964	0.900887
53	1	4.286990	-2.163958	0.024600	118	1	3.971630	8.223800	0.784586
54	1	4.299720	2.161304	0.025292	119	1	0.462407	9.266713	-1.165428
55	7	0.119151	2.039787	0.044000	120	6	1.377233	-6.138787	0.105628
56	6	0.973954	4.741479	0.102845	121	7	2.201666	-8.874289	0.120306
57	6	0.778571	3.060710	0.073822	122	6	2.660111	-6.529988	0.556538
58	6	1.471465	2.353677	0.047271	123	6	0.523843	-7.178545	0.331904
59	6	1.898383	3.686129	0.074526	124	6	0.969503	-8.503702	0.308230
60	6	0.400787	4.395937	0.105062	125	6	3.022436	-7.879290	0.544212
61	1	-1.824773	2.779712	0.065408	126	1	3.369422	-5.803638	0.937905
62	1	2.962174	3.892592	0.098321	127	1	0.470162	-6.968680	0.710619
63	1	-1.173439	5.155939	0.105524	128	1	0.319782	-9.304495	0.648924
64	6	5.965978	0.014788	0.009315	129	1	4.004485	-8.184670	0.893008
65	6	6.694930	1.023900	0.630339					

IX.6 Photocatalytic studies

Hydrogen evolution was monitored using a Perkin Elmer Clarus-480 gas chromatograph (GC) with a thermal conductivity detector, argon as carrier and eluent gas, a 7 ft. HayeSep N 60/80 pre-column, a 9 ft. molecular sieve 13 x 45/60 column and a 2 ml injection loop. Three distinct solutions for the sacrificial electron donor and proton source, the photosensitizer and the catalyst were prepared and mixed together to obtain 5 ml of solutions in standard 20 ml headspace vials. Using DMF as a solvent, the resulting molar concentration of photocatalytic medium are: 1 M for triethanolamine (TEOA), 0.1 M for HBF4, 0.56 M for water (*pH*apparent= 8.9). The concentration of active species were: 0.1 mM for the photosensitizer, 1 mM of cobalt pre-catalyst $[Co(H_2O)_6](BF_4)_2$ and 6 mM of dimethylglyoxime.

The vials were placed on top of a LED in an aluminum cast connected to a thermostatic bath set at 20 °C. They were sealed with a rubber septum pierced with two stainless steel tubes. The first tube carried an argon flow pre-bubbled in DMF. The flow was set between at 5 ml/min (adjusted with calibrated mass flow MCseries from Alicat) and referenced with a digital flowmeter (Perkin Elmer FlowMark). The second tube led the flow to the GC sample loop through a 2 ml overflow protection vial, then through an 8-port stream select valve (VICCI) and finally to GC sample loop. A microprocessor (Arduino Uno) coupled with a custom PC interface allowed for timed injections. For calibration testing, stock cylinders of known concentration of H_2 in argon replaced the argon flow (inserted at the pre-bubbler, to keep the same vapor matrix). The measured results, independent of flow rate (under same pressure) can be easily converted into a rate of hydrogen production following equation 1. The errors associated to the *TON* (TurnOver Number) and *TOF* (TurnOver Frequency) were estimated to be within 10 %. They are calculated using the equations below.

(Eq. 1) H_2 rate (µL/min) = [H_2 standard] (ppm) × Ar flow rate (mL/min)

(Eq. 2) H_2 rate (nmol/min) = H_2 rate (µL/min) / 24.45 × 1000

(Eq. 3) $TOF\ (mmol_{H2}.mol_{PS}.min^{-1}) = H_2$ rate (nmol/min) / n_{PS} (mol) / 10^6

The amount of hydrogen produced between two injections is calculated using the average rate over that period of time [t_i ; t_j], multiplied by the time between two injections (tj-ti).

(Eq. 4) $n_{H2\ total}$ (nmol) = $\sum_{t0}^{tf} n_{H2}[ti\ ;tj] = \sum_{t0}^{tf}($ (H_2 rate (ti) + H_2 rate (tj)) /2) × (tj-ti))

(Eq. 5) For a chosen length of experiment (t_f) $TON(t_f) = n_{H2(tf)} / n_{PS}$

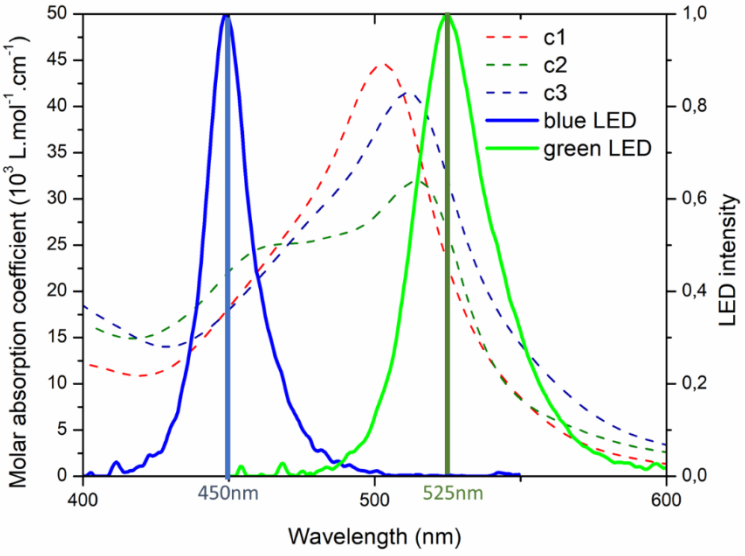

Figure IX.20. Overlap of the emission spectra of the LEDs used for photocatalytic experiments with the absorption spectra of the photosensitizers in this study.

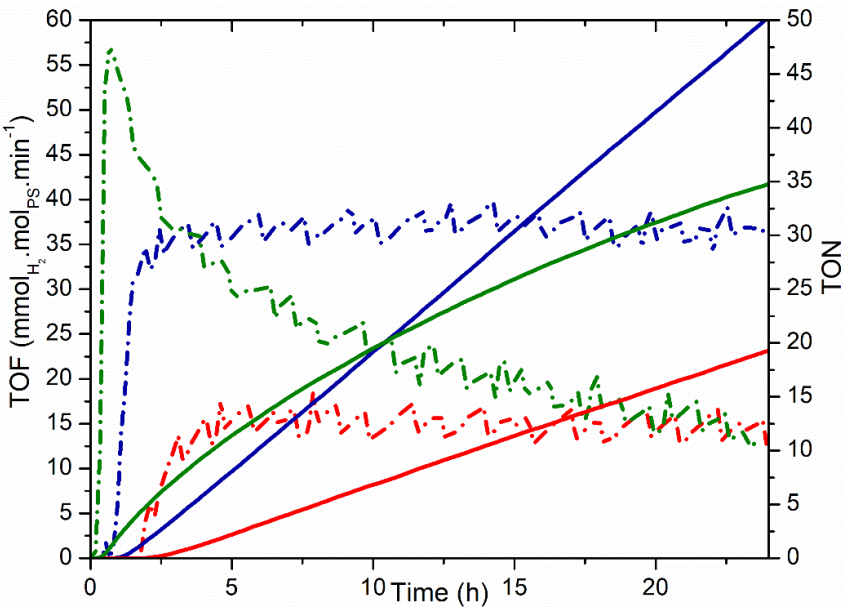

Figure IX.21. Photocatalytic hydrogen evolution performances obtained using fresh stock solutions of **II-C1**, **II-C2** or **II-C3** in DMF with 1M TEOA and 0.1M HBF4 under 450 nm irradiation (62 mW) with 1mM $[Co(H_2O)_6](BF_4)_2$ and 6mM $dmgH_2$ as precursors for the catalyst.

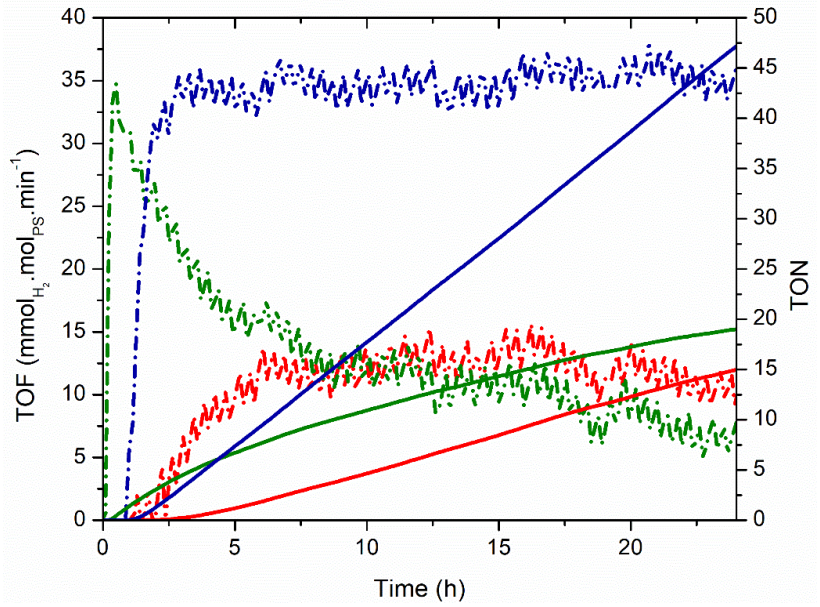

Figure IX.22. Photocatalytic hydrogen evolution performances obtained using fresh stock solutions of **II-C1**, **II-C2** or **II-C3** in DMF with 1M TEOA and 0.1M HBF4 under 525 nm irradiation (53mW) with 1mM $[Co(H_2O)_6](BF_4)_2$ and 6mM $dmgH_2$ as precursors for the catalyst.

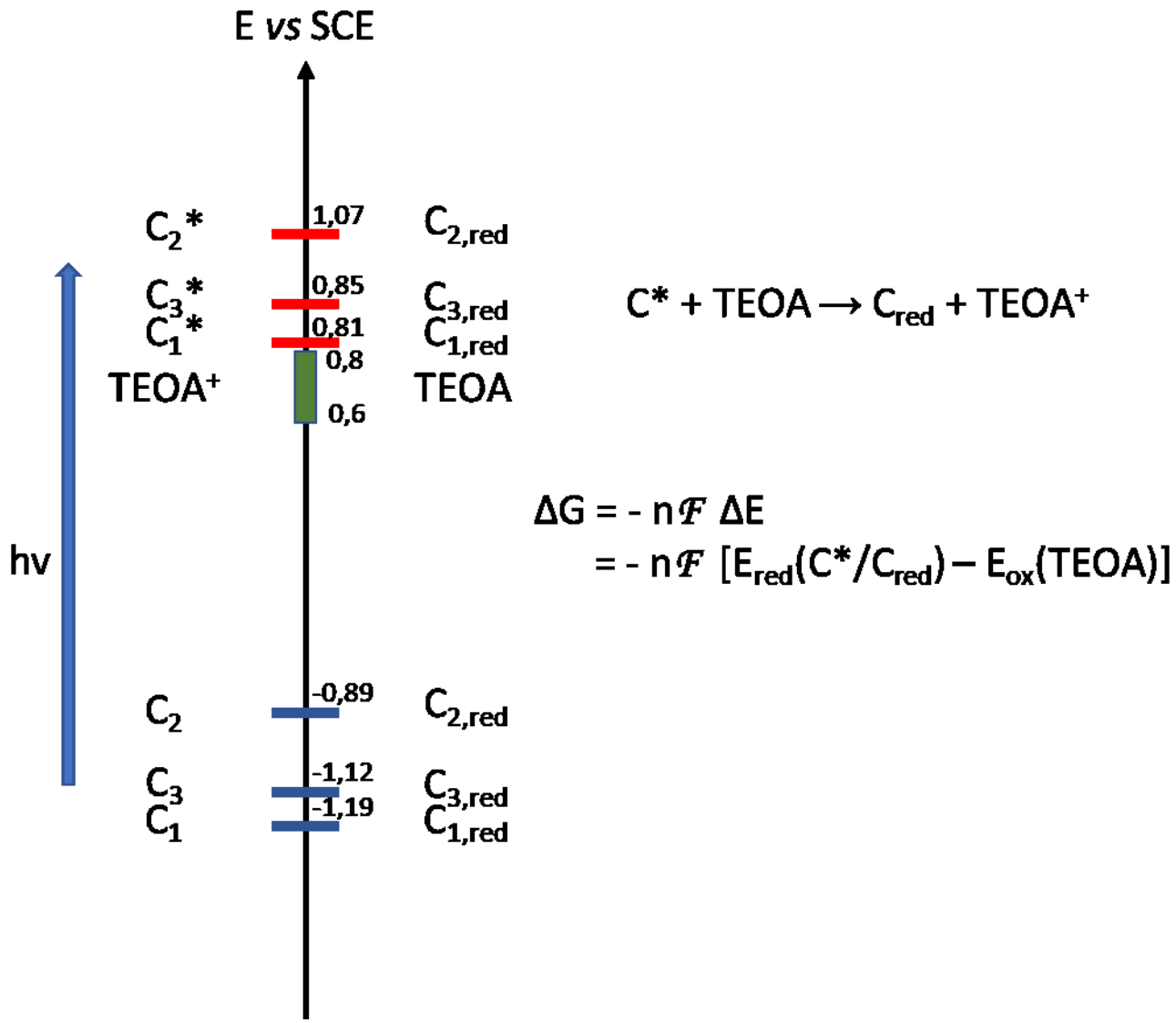

Figure IX.23. Scale of redox potentials highlighting the variation in driving force based on the relative position of the excited state reduction potential of the different PS (determined using the emission onset) compared to the oxidation range of triethanolamine.

Chapitre X. Matériels supplémentaires au chapitre III

X.1 Experimental details

Ligands **III-L1** to **III-L4** as well as complexes **III-C3** and **III-C4** were prepared following our previous report.[1] Complexes **III-C1** and **III-C2** were prepared similarly to **III-C3** and **III-C4**.[2]

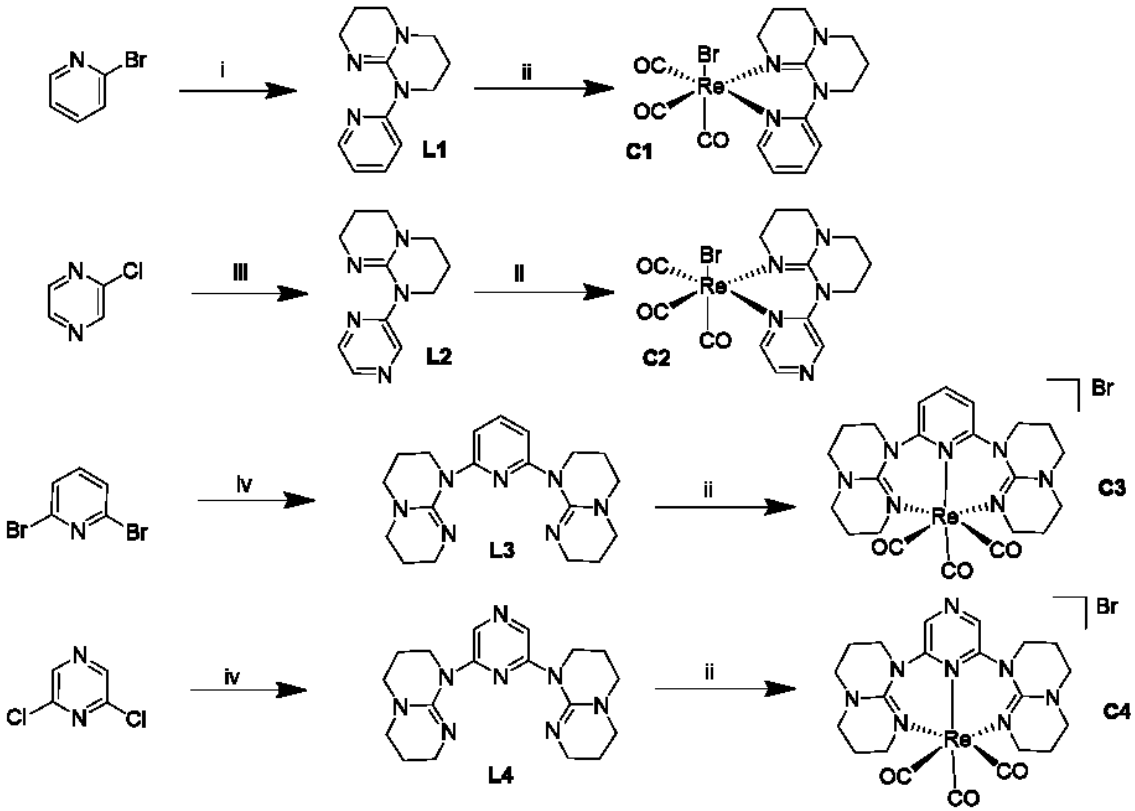

Scheme X.1. Synthetic pathways for complexes III-C1 to III-C4 (i Hhpp 1.1 eq, KOtBu 1.4 eq, $Pd(OAc)_2$ 1 mol%, BINAP 1.5 mol% in toluene, 90°C under N_2 ; ii $Re(CO)_5Br$ 1 eq in toluene, reflux ; iii Hhpp 2.1 eq, 95°C ; iv Hhpp 2.15 eq, KOtBu 2.8 eq, $Pd(OAc)_2$ 2 mol%, BINAP 3 mol% in toluene, 90°C under N_2)

III-L1 ^{1}H NMR (400 MHz, $CDCl_3$) δ 8.24 (ddd, J= 5, 2, 1 Hz, 1H), 7.67 (dt, J= 9, 1 Hz, 1H), 7.47 (ddd, J= 9, 7, 1 Hz, 1H), 6.77 (ddd, J = 7, 5, 1 Hz, 1H), 3.89 (t, J= 6 Hz, 2H), 3.42 (t, J= 6 Hz, 2H), 3.24 (t, J= 6 Hz, 2H), 3.19 (t, J= 6 Hz, 2H), 2.03 (quint, J= 6 Hz, 2H), 1.89 (quint, J= 6 Hz, 2H). ESI-MS (MeOH): $[M+H]^+$ calc. for $C_{12}H_{16}N_4$ 217.1448, found 217.1459.

III-L2 ^{1}H NMR (400 MHz, $CDCl_3$) δ 9.08 (d, J = 2 Hz, 1H), 8.12 (dd, J= 3, 2 Hz, 1H), 7.95 (d, J = 3 Hz, 1H), 3.84 (t, J= 6 Hz, 2H), 3.43 (t, J= 6 Hz, 2H), 3.26 (t, J= 6 Hz, 2H), 3.22 (t, J= 6 Hz, 2H), 2.06 (quint, J= 6 Hz, 2H), 1.91 (quint, J= 6 Hz, 2H). ESI-MS (MeOH): $[M+H]^+$ calc. for $C_{11}H_{15}N_5$ 218.1400, found 218.1370.

III-L3 ^{1}H NMR (400 MHz, $CDCl_3$) δ 7.34 (t, J = 8 Hz, 1H), 7.12 (d, J = 8 Hz, 2H), 3.84 (t, J= 6 Hz, 4H), 3.41 (t, J= 6 Hz, 4H), 3.21 (t, J= 6 Hz, 4H), 3.14 (t, J= 6 Hz, 4H), 1.96 (quint, J= 6 Hz, 4H), 1.86 (quint, J= 6 Hz, 4H). ESI-MS (MeOH): $[M+H]^+$ calc. for $C_{19}H_{27}N_7$ 354.2401, found 354.2419.

III-L4 ^{1}H NMR (400 MHz, $CDCl_3$) δ 8.46 (s, 2H), 3.79 (t, J= 6 Hz, 4H), 3.40 (t, J= 6 Hz, 4H), 3.22 (t, J= 6 Hz, 4H), 3.16 (t, J= 6 Hz, 4H), 1.97 (quint, J= 6 Hz, 4H), 1.88 (quint, J= 6 Hz, 4H). ESI-MS (MeOH): $[M+H]^+$ calc. for $C_{18}H_{26}N_8$ 355.2353, found 355.2324.

General procedures for the complexes: $Re(CO)_5Br$ and the suitable ligand were combined in equimolar ratio in toluene. The solution was refluxed for 5h during which a small amount of precipitate formed. After being left to cool back to RT, the suspension was concentrated *in vacuo* and additional precipitation was induced by addition of diethyl ether. The solid was filtered and air-dried.

III-C1 beige solid, Yield = 93% on a 0.5 mmol scale.
^{1}H NMR (400 MHz, $CDCl_3$) δ 8.99 (dd, J = 2 Hz, 1H), 7.85 (m, 1H), 7.21 (d, J = 8 Hz, 1H), 7.15 (m, 1H), 3.97 (dt, J= 14, 4 Hz, 1H), 3.84 (m, 1H), 3.73 (m, 2H), 3.54 – 3.37 (m, 3H), 3.30 – 3.20 (m, 1H), 2.30 (m, 2H), 2.06 – 1.85 (m, 2H).
^{13}C NMR (101 MHz, DMSO) δ 198.17, 196.87, 192.64, 154.75, 153.29, 153.02, 141.15, 120.94, 115.56, 51.09, 48.20, 48.06, 46.30, 22.03, 21.68.
ESI-MS (CH_3CN): $[M-Br]^+$ calc. for $C_{15}H_{16}N_4O_3Re$ 487.0780, found 487.0834.
IR-ATR ν_{CO} (cm^{-1}) : 2009, 1860 (br).
Elemental analysis calc. (%) for $C_{15}H_{16}N_4O_3ReBr$, $(C_7H_8)_{0.1}$: C 32.76, H 2.94, N 9.73; found: C 32.45, H 2.95, N 9.76. The presence of residual toluene was confirmed separately in the NMR spectra of the sample sent to EA.

III-C2 yellow solid, Yield = 94% on a 0.5 mmol scale.
^{1}H NMR (400 MHz, $CDCl_3$) δ 8.89 (dd, J= 3, 1 Hz, 1H), 8.62 (d, J = 1 Hz, 1H), 8.38 (d, J= 3 Hz, 1H), 4.07 (dt, J= 14, 4 Hz, 1H), 3.84 (m, 2H), 3.71 (m, 1H), 3.49 (m, 3H), 3.30 (m, 1H), 2.37 (m, 2H), 1.95 (m, 2H).
^{13}C NMR (101 MHz, DMSO) δ 198.04, 196.10, 192.11, 152.83, 150.31, 145.41, 140.27, 139.11, 51.43, 48.32, 48.12, 46.12, 22.06, 21.68.
ESI-MS (CH_3CN): $[M-Br]^+$ calc. for $C_{14}H_{15}N_5O_3Re$ 488.0732, found 488.0724.

IR-ATR ν_{CO} (cm^{-1}) : 2006, 1868 (br).
Elemental analysis calc. (%) for $C_{14}H_{15}N_5O_3ReBr$: C 29.64, H 2.66, N 12.34; found: C 29.89, H 2.68, N 12.23.

III-C3 off-white solid, Yield = 79% on a 0.25 mmol scale.
^1H NMR (400 MHz, $CDCl_3$) δ 8.13 (t, J = 8 Hz, 1H), 7.35 (d, J = 8 Hz, 2H), 4.11 (dt, J= 14, 4 Hz, 2H), 3.75 – 3.59 (m, 6H), 3.54 (m, 2H), 3.45 (dd, J = 8, 5 Hz, 4H), 3.36(m, 2H), 2.50 (m, 2H), 2.32 (m, 2H), 2.04 (m, 4H).
ESI-MS (CH_3CN): $[M-Br]^+$ calc. for $C_{22}H_{27}N_7O_3Re$ 624.1726, found 624.1656. ; IR-ATR ν_{CO} (cm^{-1}) : 2004, 1895, 1867.

III-C4 pale olive-green solid, Yield 72% on a 0.25 mmol scale.
^1H NMR (400 MHz, $CDCl_3$) δ 8.42 (s, 2H), 4.15 (dt, J= 14, 4 Hz, 2H), 3.76 (m, 6H), 3.55 (m, 4H), 3.36 (m, 4H), 2.52 (m, 2H), 2.32 (m, 2H), 2.05 (m, 4H).
ESI-MS (CH_3CN): $[M-Br]^+$ calc. for $C_{21}H_{26}N_8O_3Re$ 624.1680, found 624.1662.
IR-ATR ν_{CO} (cm^{-1}) : 2005, 1901, 1872.

1. A. K. Pal, P. K. Mandali, D. K. Chand and G. S. Hanan, *Synlett*, 2015, **26**, 1408-1412.
2. A. K. Pal and G. S. Hanan, *Dalton Trans.*, 2014, **43**, 11811-11814.

X.2 NMR spectra

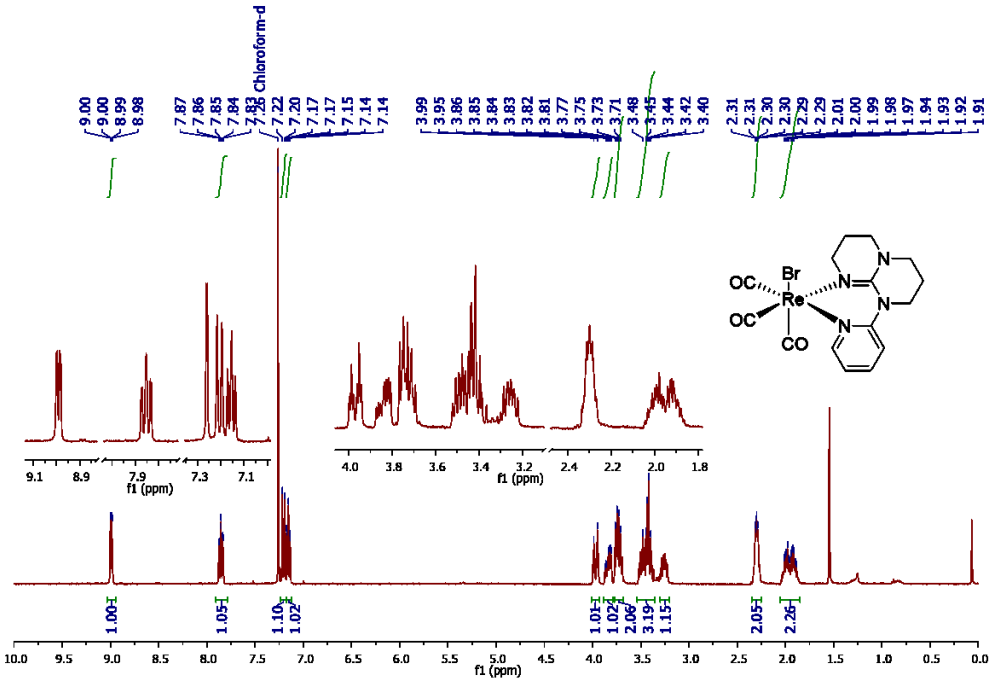

Figure X.1. ^{1}H NMR spectra for **III-C1** in $CDCl_3$

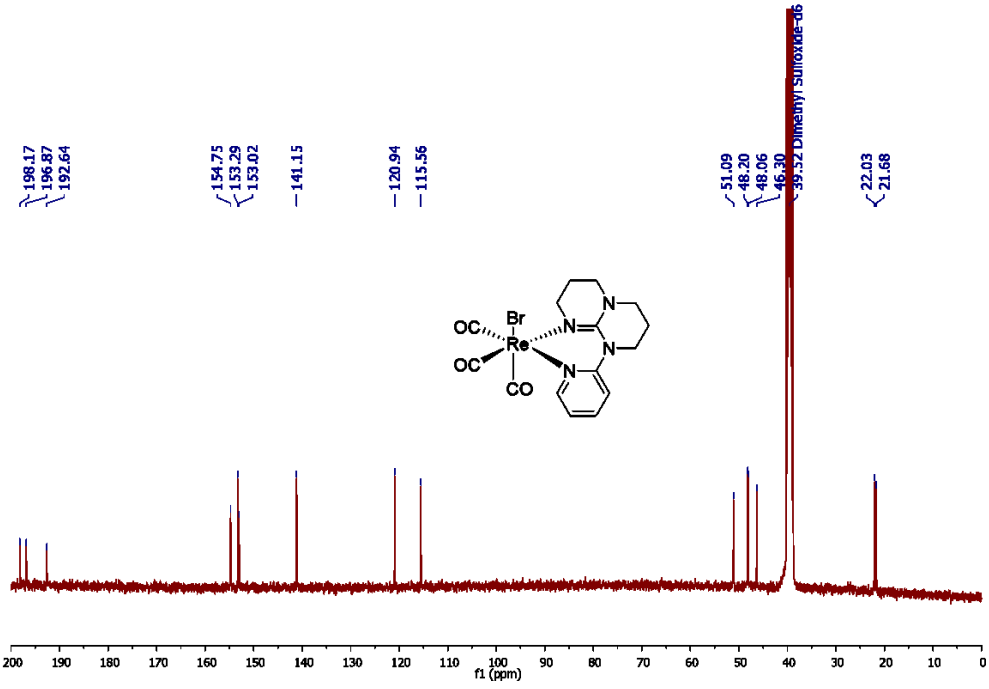

Figure X.2. ^{13}C NMR spectra for **III-C1** in DMSO-d^{6}

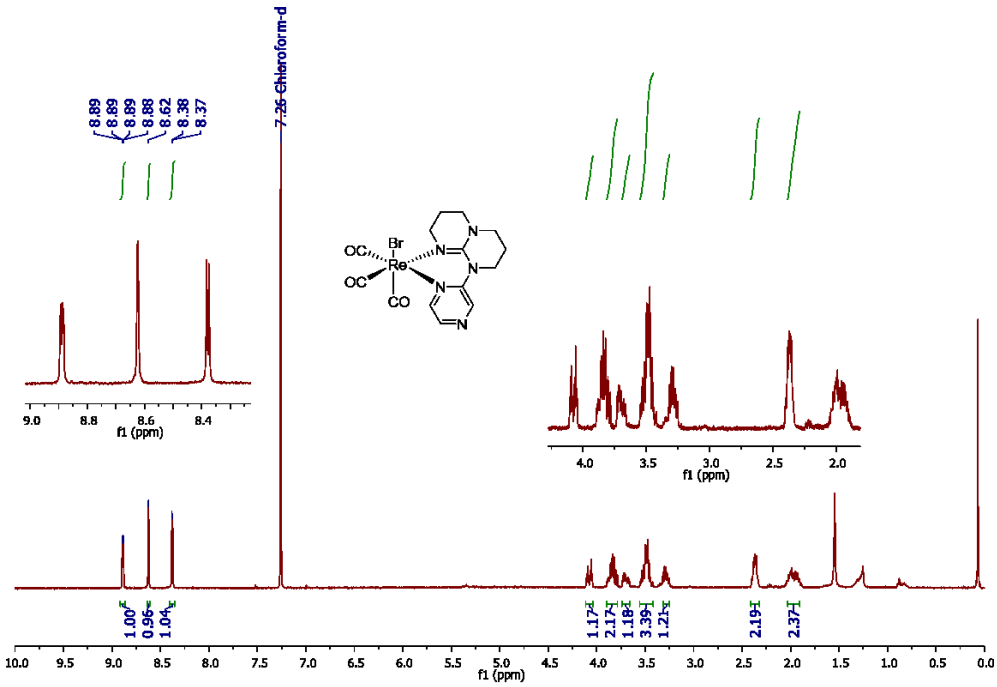

Figure X.3. ^{1}H NMR spectra for **III-C2** in $CDCl_3$

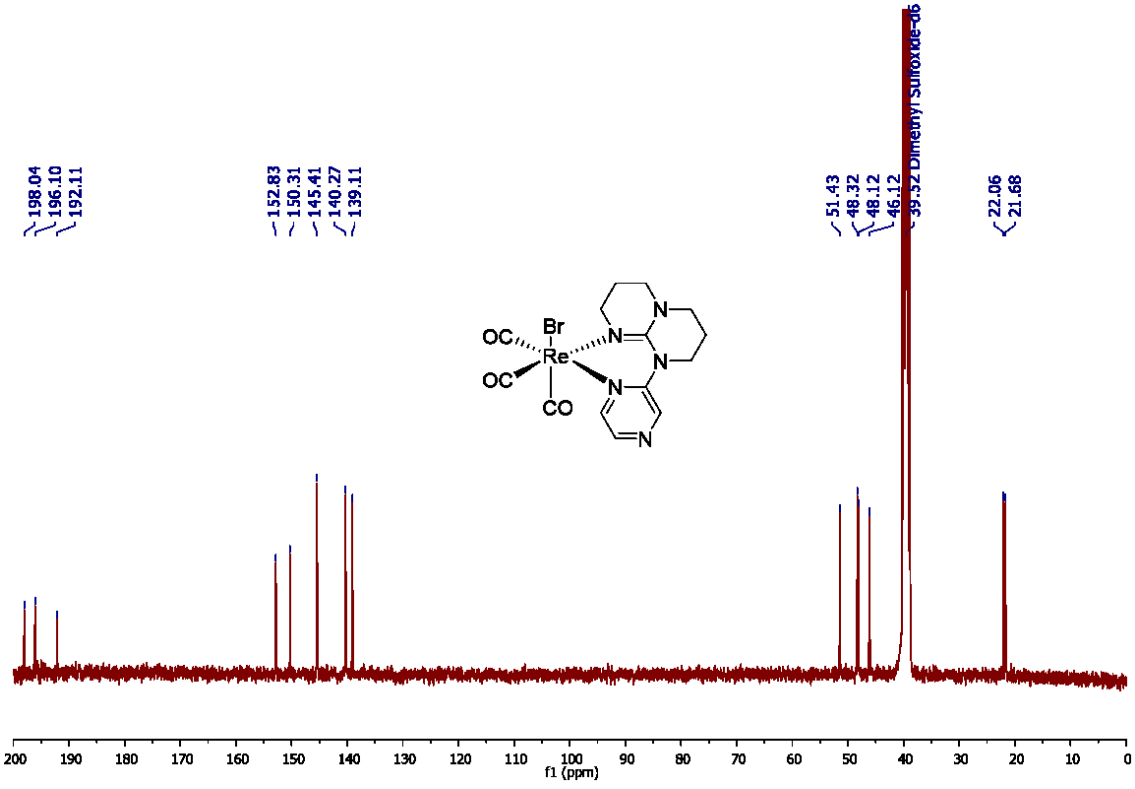

Figure X.4.^{13}C NMR spectra for **III-C2** in DMSO-d^{6}

X.3 Crystallographic study

Table X.1. Refinement parameters for the structure of complex **III-C1**

Identification code	**III-C1** (CCDC 1877927)
Empirical formula	$C_{15}H_{16}BrN_4O_3Re$
Formula weight	566.43
Temperature/K	150
Crystal system	monoclinic
Space group	$P2_1/n$
a/Å	17.754(2)
b/Å	11.744(1)
c/Å	17.956(2)
α/°	90
β/°	115.446(4)
γ/°	90
Volume/Å^3	3380.6(7)
Z/Z'	8/2
ρ_{calc}g/cm^3	2.226
μ/mm^{-1}	11.112
F(000)	2144.0
Crystal size/mm^3	0.14 × 0.07 × 0.04
Radiation	GaKα (λ = 1.34139)
2Θ range for data collection/°	5.094 to 121.668
Index ranges	$-22 \leq h \leq 23$, $-15 \leq k \leq 15$, $-23 \leq l \leq 21$
Reflections collected	46928
Independent reflections	7785 [R_{int} = 0.0545, R_{sigma} = 0.0303]
Data/restraints/parameters	7785/0/434
Goodness-of-fit on F^2	1.073
Final R indexes [I>=2σ (I)]	R_1 = 0.0355, wR_2 = 0.0993
Final R indexes [all data]	R_1 = 0.0359, wR_2 = 0.1000
Largest diff. peak/hole / e Å^{-3}	1.96/-1.42

Table X.2. Refinement parameters for the structure of complex **III-C2**

Identification code	**III-C2** (CCDC 1877926)
Empirical formula	$C_{14}H_{15}BrN_5O_3Re$
Formula weight	567.42
Temperature/K	150
Crystal system	monoclinic
Space group	$P2_1/n$
a/Å	13.6283(8)
b/Å	9.2290(5)
c/Å	13.8140(8)
α/°	90
β/°	107.120(2)
γ/°	90
Volume/Å^3	1660.5(2)
Z/Z'	4/1
ρ_{calc}g/cm^3	2.270
μ/mm^{-1}	11.325
F(000)	1072.0
Crystal size/mm^3	0.14 × 0.1 × 0.03
Radiation	GaKα (λ = 1.34139)
2Θ range for data collection/°	6.968 to 121.346
Index ranges	$-17 \leq h \leq 17$, $-11 \leq k \leq 11$, $-17 \leq l \leq 17$
Reflections collected	41041
Independent reflections	3802 [R_{int} = 0.0534, R_{sigma} = 0.0218]
Data/restraints/parameters	3802/0/218
Goodness-of-fit on F^2	1.272
Final R indexes [I>=2σ (I)]	R_1 = 0.0297, wR_2 = 0.0817
Final R indexes [all data]	R_1 = 0.0298, wR_2 = 0.0817
Largest diff. peak/hole / e Å^{-3}	1.42/-1.19

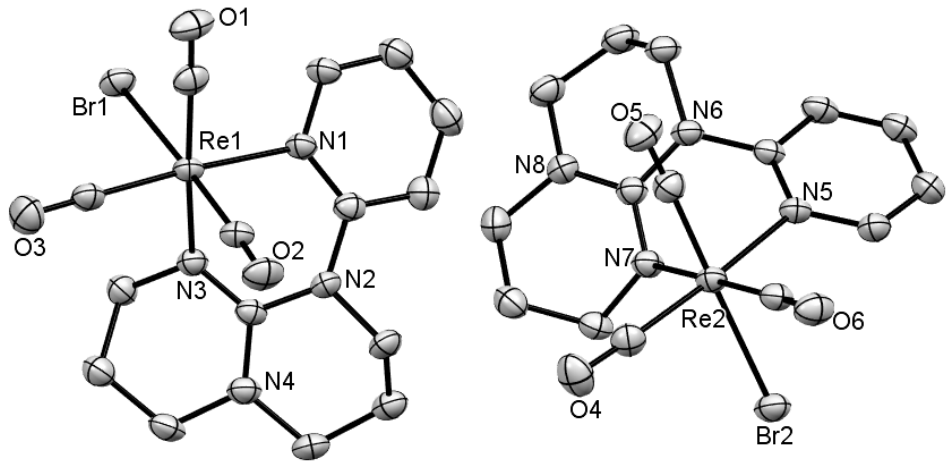

Figure X.5. Figure S5. ORTEP projection of the two inequivalent complexes in the asymmetric unit of **III-C1** (ellipsoid at 50% probability, H atoms omitted for clarity).

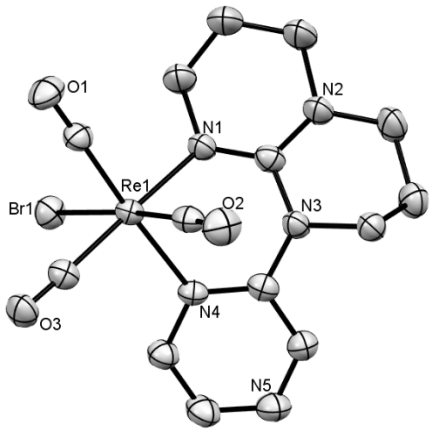

Figure X.6. ORTEP projection of complex in the asymmetric unit of **III-C2** (ellipsoid at 50% probability, H atoms omitted for clarity).

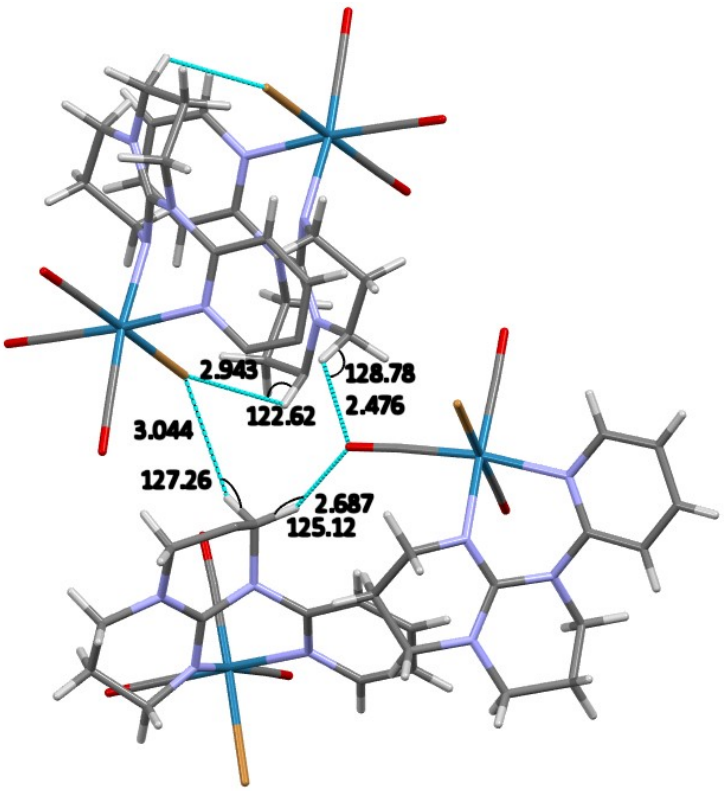

Figure X.7. Hydrogen bonds pattern in the crystal packing of **III-C1**

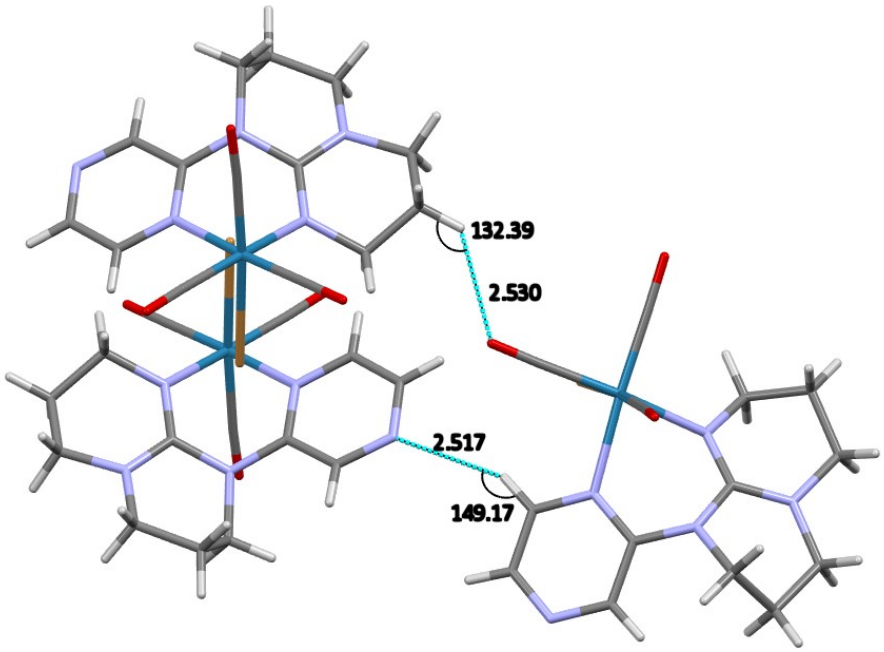

Figure X.8. Hydrogen bonds pattern in the crystal packing of **III-C2**

Table X.3. Selected bond lengths and angles from the crystal structures of complexes **III-C1**, **III-C2**, **III-C3**, **III-C4**, [Re(bpy)(CO)$_3$Br] and [Re(dqp)(CO)$_3$]$^+$.

Complex	**III-C1**‡	**III-C2**	**III-C3**$^+$	**III-C4**$^+$	**[Re(bpy)(CO)$_3$Br]**	**[Re(dqp)(CO)$_3$]$^+$**
CCDC	1877927	1877926	975057	922649	1476781	90586
Re-N_{het}	2.195(4) 2.197(4)	2.182(2)	2.174(3)	2.163(4)	2.160(10) 2.170(10)	2.164(7) 2.220(5) 2.210(6)
Re-N_{hpp}	2.174(3) 2.179(3)	2.152(4)	2.199(3) 2.183(4)	2.195(3) 2.194(4)	-	-
Re-CO	1.920(3) 1.914(3) 1.904(4) 1.910(4) 1.919(3) 1.923(3)	1.911(4) 1.916(5) 1.922(5)	1.922(4) 1.902(6) 1.933(5)	1.934(5) 1.931(6) 1.899(6)	1.920(10) 1.910(10) 2.060(10)*	1.930(7) 1.920(10) 1.917(7)
Re-Br	2.629(1) 2.628(1)	2.647(2)	-	-	2.576(2)*	-
C=O	1.144(5) 1.137(4) 1.159(6) 1.149(6) 1.128(4) 1.146(4)	1.157(5) 1.123(7) 1.145(6)	1.153(6) 1.171(7) 1.144(5)	1.141(8) 1.135(7) 1.184(8)	1.160(20) 1.150(20) 1.130(20)*	1.164(9) 1.148(9) 1.160(10)
OC-Re-CO	90.4(2) 88.6(2) 88.3(2) 88.8(2) 89.9(2) 89.0(2)	86.4(2) 89.3(2) 90.1(2)	88.1(2) 89.5(2) 89.2(2)	88.6(2) 89.6(2) 87.9(2)	90.1(6) 90.7(6) 86.1(5)*	87.8(3) 86.5(3) 88.1(3)
N_{het}-Re-N_{het}	-	-	-	-	74.7(4)	80.7(2) 82.5(2) 92.1(2)
N_{het}-Re-N_{hpp}	77.1(1) 77.3(1)	79.6(1)	78.1(1) 78.8(1)	77.9(1) 78.6(1)	-	-
N_{hpp}-Re-N_{hpp}	-	-	88.4(1)	89.1(1)	-	-

N_{het} = N in pyridine or pyrazine

‡ Values for both inequivalent complexes present in the unit cell

*Affected by positional disorder of the bromide. The Re-Br value is for the main occupied site.

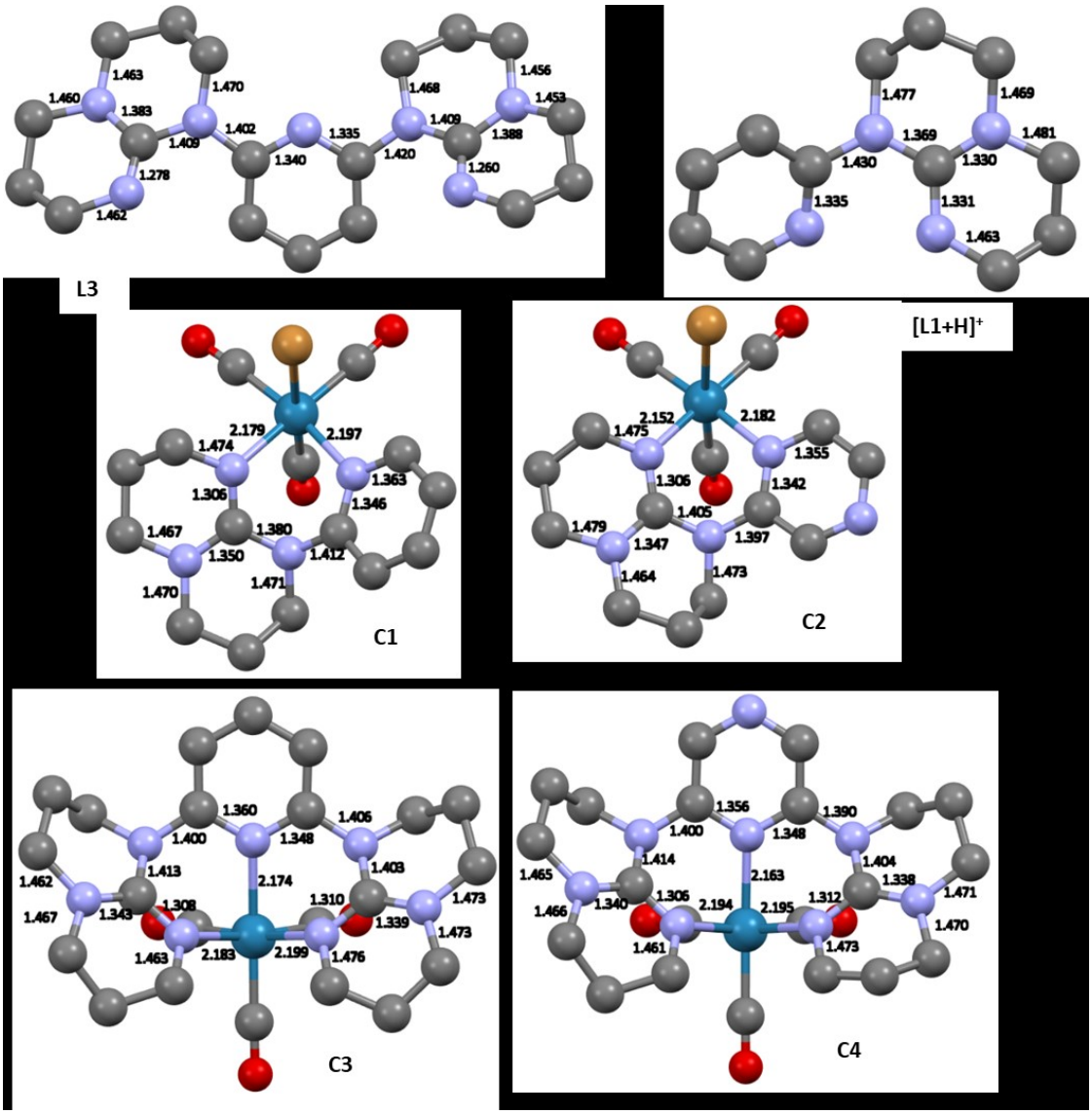

Figure X.9. Analysis of the bond lengths within the hpp-N-heterocycle of **III-L3** (CCDC 988217), protonated **III-L1** (CCDC 1457787), **III-C1**, **III-C2**, **III-C3** and **III-C4** (H atomes and anions omitted for clarity).

Table X.4. Torsion angle between the hpp moiety and the N-heterocycle **[III-L1+H]$^+$**, **III-C1**, **III-C2**, **III-C3** and **III-C4**.

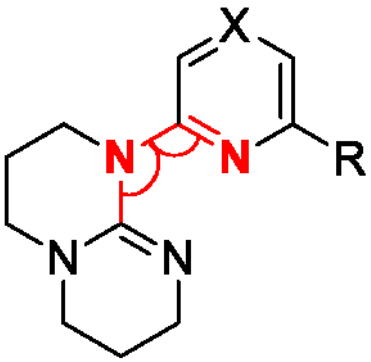

Complex	III-C1	III-C2	III-C3	III-C4	III-L3	[III-L1+H]$^+$
Torsion angles	52.8(5) -57.3(5)	-47.3(6)	52.8(5) -53.0(5)	-53.0(6) 52.5(6)	-20.4(3) -176.4(2)	-42.6(2)

X.4 Electrochemical study

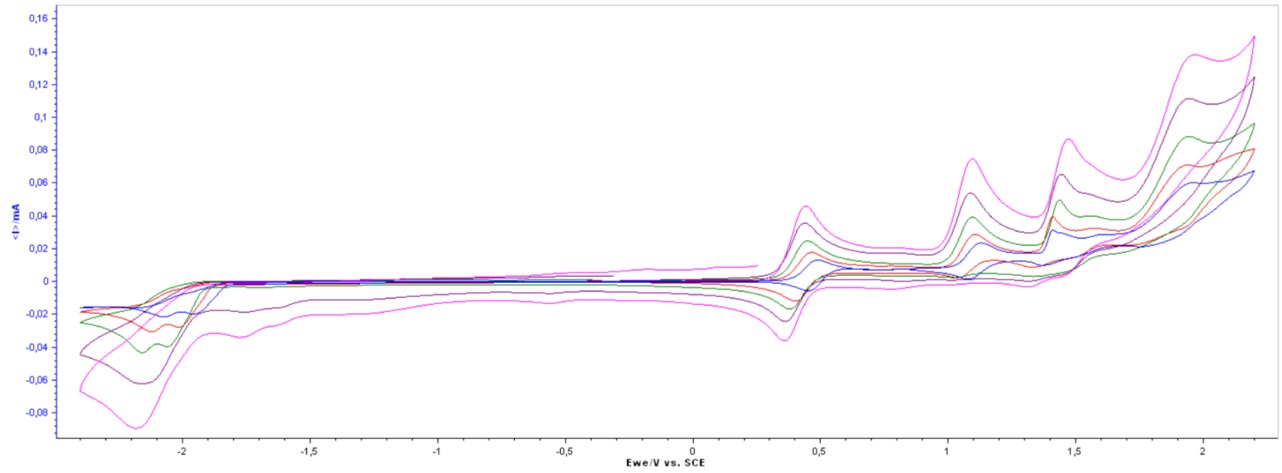

Figure X.10. Cyclic voltammograms of complex **III-C1** (1mM) in acetonitrile with 0.1M $TBAPF_6$ and ferrocene as internal standard at various scan speed (25, 50, 100, 200 and 400 mV/s – only the first cycle out of three are shown).

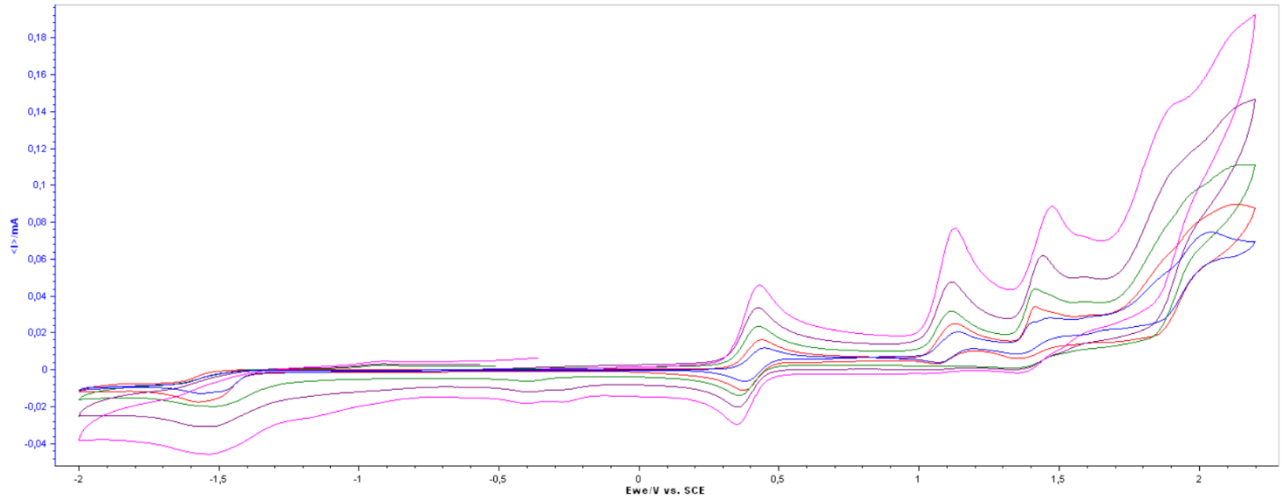

Figure X.11. Cyclic voltammograms of complex **III-C2** (1mM) in acetonitrile with 0.1M $TBAPF_6$ and ferrocene as internal standard at various scan speed (25, 50, 100, 200 and 400 mV/s – only the first cycles out of three are shown).

X.5 Theoretical study

Table X.5. Calculated CO vibrations wavenumbers (cm-1) for the acetonitrile solvated complexes **III-C1** to **III-C4**

Vibration mode	**III-C1**	**III-C2**	**III-C3**	**III-C4**
C=O elongation symmetrical	1995	1998	1993	1996
C=O elongation asymmetrical	1856	1864	1845	1854
C=O elongation asymmetrical	1840	1846	1845	1851

Table X.6. Comparison between chosen experimental and calculated structural parameters for **III-C1**, **III-C2**, **III-C3** and **III-C4**.

Exp.	Re-CO	Re-N_{het}	Re-N_{hpp}	Re-Br	N_{het}-Re-N_{hpp}	OC-Re-CO
III-C1	1.920(3) 1.913(4) 1.904(4) 1.910(4) 1.919(3) 1.923(3)	2.195(4) 2.197(4)	2.174(3) 2.179(3)	2.629(1) 2.628(1)	77.1(1) 77.3(1)	90.4(2) 88.6(2) 88.3(2) 88.8(2) 89.9(2) 89.0(2)
III-C2	1.911(4) 1.916(5) 1.922(5)	2.182(2)	2.152(4)	2.647(2)	79.6(1)	86.4(2) 89.3(2) 90.1(2)
III-C3	1.902(6) 1.922(4) 1.933(5)	2.174(3)	2.183(4) 2.199(3)	-	78.8(1) 78.1(1)	88.1(2) 89.2(2) 89.5(2)
III-C4	1.899(6) 1.931(6) 1.934(5)	2.163(4)	2.194(4) 2.195(3)	-	78.6(1) 77.9(1)	87.9(2) 89.6(2) 88.6(3)
Calc.	Re-CO	Re-N_{het}	Re-N_{hpp}	Re-Br	N_{het}-Re-N_{hpp}	OC-Re-CO
III-C1	1.905 1.881 1.911	2.176	2.131	2.735	81.25	91.19 91.61 88.64
III-C2	1.912 1.883 1.907	2.168	2.133	2.726	81.31	91.28 91.52 88.56
III-C3	1.910 1.910 1.905	2.151	2.163 2.163	-	80.44 80.44	88.88 89.42 88.89
III-C4	1.911 1.907 1.911	2.143	2.164 2.164	-	80.19 80.19	88.74 89.55 88.74

Table X.7. Calculated frontiers orbitals with contribution of each unit of **III-L1**.

Orbitals	Energy (eV)	py	hpp
L+2	1.4	16	84
L+1	-0.32	82	18
LUMO	-0.61	97	3
HOMO	-5.77	16	84
H-1	-6.31	29	71
H-2	-6.79	3	97

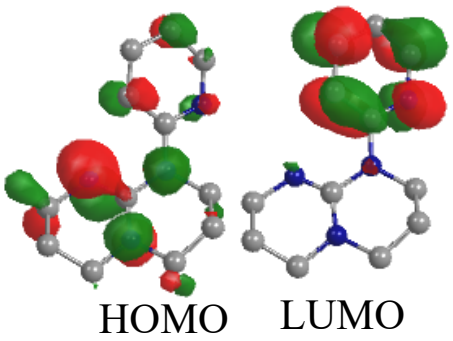

Table X.8. Calculated frontiers orbitals with contribution of each unit of **III-L2**.

Orbitals	Energy (eV)	pz	hpp
L+2	1.19	16	84
L+1	-0.63	84	16
LUMO	-1.28	97	3
HOMO	-5.94	10	90
H-1	-6.49	34	66
H-2	-7.0	5	95

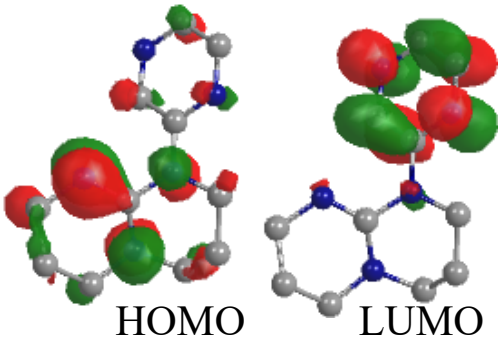

Table X.9. Calculated frontiers orbitals with contribution of each unit of **III-L3**.

Orbitals	Energy (eV)	py	hpp
L+2	1.24	9	91
L+1	-0.18	72	28
LUMO	-0.34	89	11
HOMO	-5.45	34	66
H-1	-5.84	2	98
H-2	-6.12	15	85

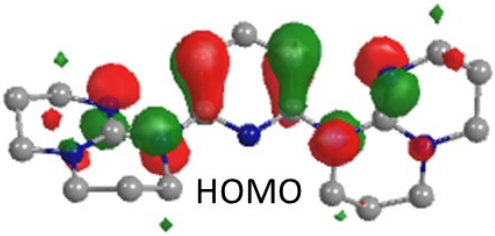

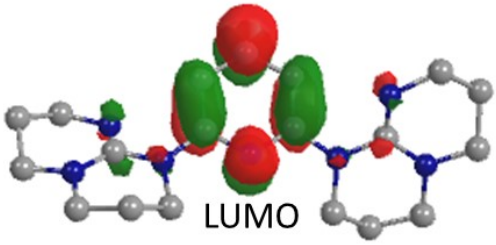

Table X.10. Calculated frontiers orbitals with contribution of each unit of **III-L4**.

Orbitals	Energy (eV)	pz	hpp
L+2	1.09	8	92
L+1	-0.42	73	27
LUMO	-0.96	91	9
HOMO	-5.64	30	70
H-1	-5.93	2	98
H-2	-6.23	19	81

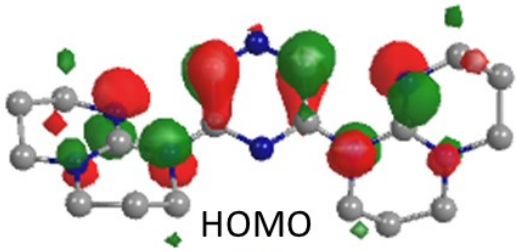

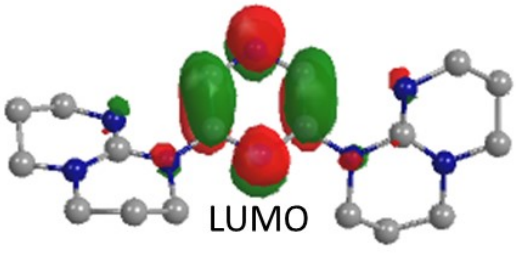

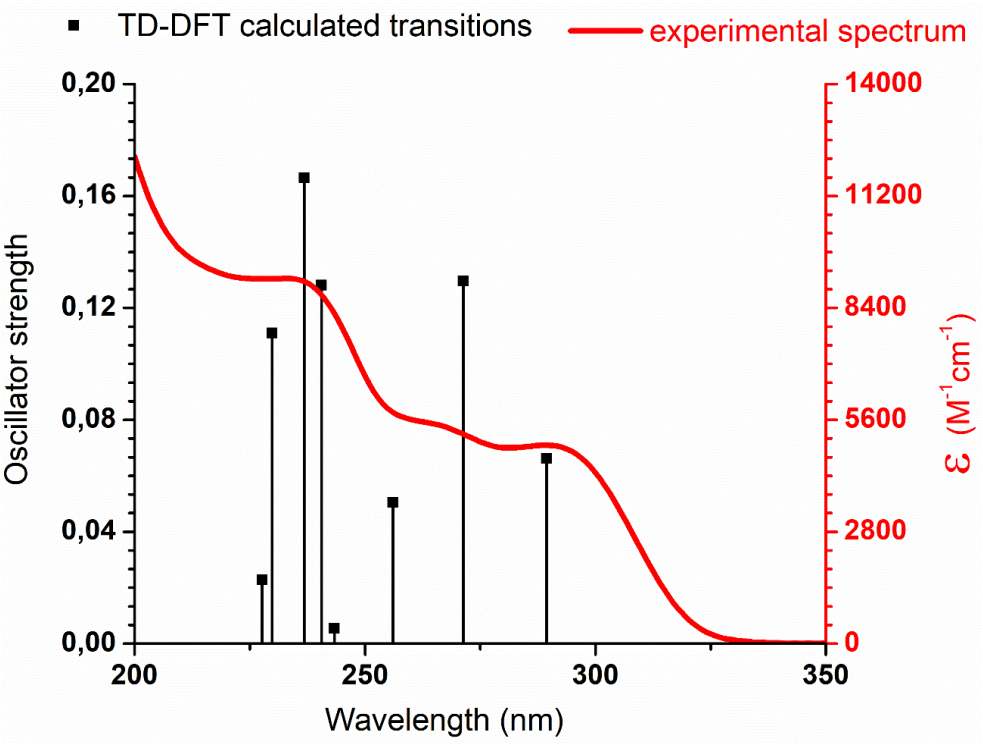

Figure X.12. Experimental absorption spectrum and theoretical transition for **III-L1**.

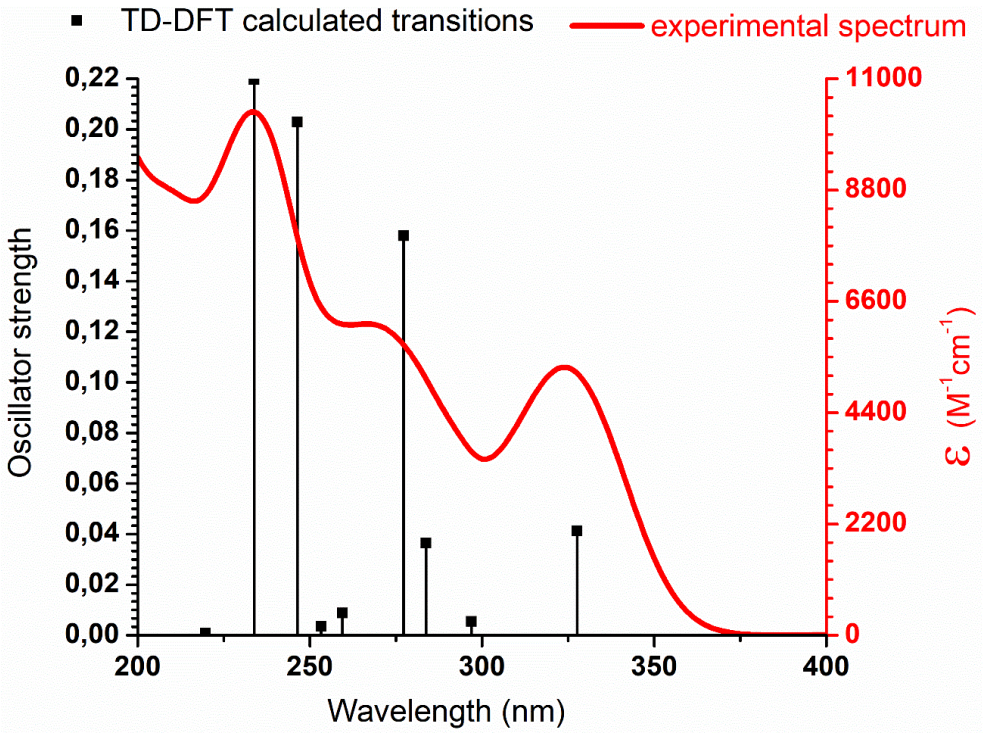

Figure X.13. Experimental absorption spectrum and theoretical transition for **III-L2**.

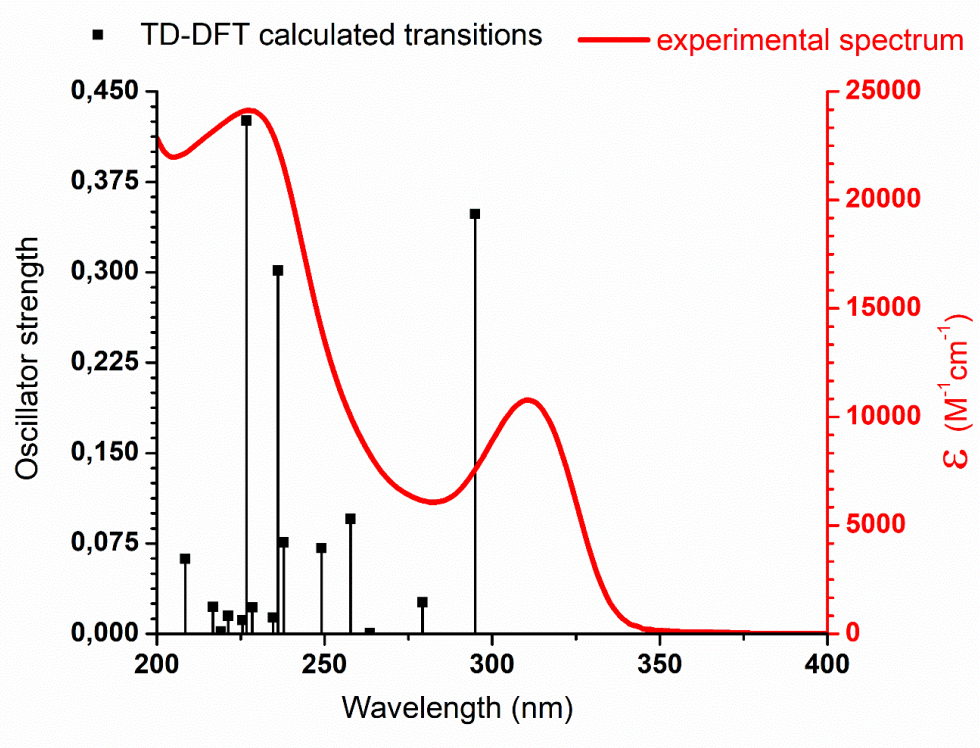

Figure X.14. Experimental absorption spectrum and theoretical transition for **III-L3**.

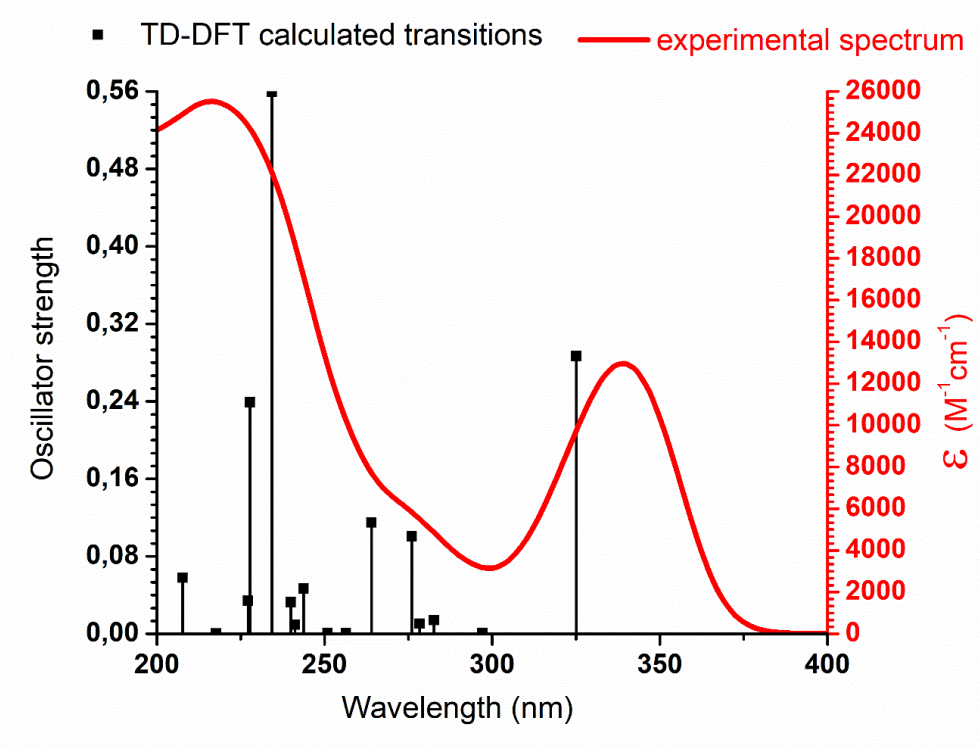

Figure X.15. Experimental absorption spectrum and theoretical transition for **III-L4**.

Table X.11. Calculated singlet-singlet transitions below 200nm and ten lowest singlet-triplet transitions of **III-L1** in acetonitrile.

Transition	λ(nm)	Osc. Strength	Major contribs	py %	Hpp %
1	289.40	0.0662	HOMO->LUMO (94%)	17-->96 (79)	83-->4 (-79)
2	271.28	0.1296	HOMO->L+1 (94%)	16-->82 (66)	84-->18 (-66)
3	256.01	0.0505	H-1->LUMO (93%)	30-->96 (66)	70-->4 (-66)
4	243.35	0.0054	H-3->LUMO (98%)	94-->97 (3)	6-->3 (-3)
5	240.58	0.1282	H-2->LUMO (34%), H-2->L+1 (16%), H-1->L+1 (47%)	16-->86 (70)	84-->14 (-70)
6	236.79	0.1665	H-2->LUMO (31%), H-2->L+1 (16%), H-1->L+1 (47%)	18-->85 (67)	82-->15 (-67)
7	229.83	0.1111	H-2->LUMO (31%), H-2->L+1 (58%)	7-->85 (78)	93-->15 (-78)
8	227.66	0.0229	H-3->L+1 (94%)	92-->82 (-10)	8-->18 (10)

Transition	λ(nm)	Osc. Strength	Major contribs	py %	Hpp %
1	367.66	0.0	H-4->LUMO (10%), H-1->L+1 (20%), HOMO->L+1 (57%)	30-->81 (51)	70-->19 (-51)
2	343.44	0.0	H-1->LUMO (24%), HOMO->LUMO (64%)	23-->94 (71)	77-->6 (-71)
3	315.85	0.0	H-1->LUMO (12%), H-1->L+1 (30%), HOMO->L+1 (15%), HOMO->L+2 (28%)	27-->64 (37)	73-->36 (-37)
4	284.67	0.0	H-3->LUMO (96%)	95-->95 (0)	5-->5 (0)
5	267.56	0.0	H-1->LUMO (56%), HOMO->LUMO (33%)	27-->96 (69)	73-->4 (-69)
6	265.83	0.0	H-5->LUMO (13%), H-4->LUMO (43%), H-2->LUMO (18%), H-1->L+1 (13%)	52-->90 (38)	48-->10 (-38)
7	254.83	0.0	H-2->L+1 (68%), H-2->L+2 (17%)	8-->72 (64)	92-->28 (-64)
8	235.85	0.0	H-2->LUMO (35%), H-1->L+1 (10%), HOMO->L+2 (32%)	18-->66 (48)	82-->34 (-48)
9	233.69	0.0	H-3->L+1 (94%)	93-->81 (-12)	7-->19 (12)
10	232.45	0.0	H-2->LUMO (40%), H-1->L+1 (14%), HOMO->L+2 (23%)	19-->73 (54)	81-->27 (-54)

Table X.12. Calculated parameters for the singlet-singlet transitions below 200nm and the ten lowest singlet-triplet transitions of **III-L2** in acetonitrile.

Transition	λ(nm)	Osc. Strength	Major contribs	pz %	Hpp %
1	327.59	0.0414	HOMO->LUMO (92%)	15-->97 (82)	85-->3 (-82)
2	296.90	0.0055	H-3->LUMO (85%)	84-->97 (13)	16-->3 (-13)
3	283.74	0.0365	H-1->LUMO (64%), HOMO->L+1 (27%)	31-->93 (62)	69-->7 (-62)
4	277.13	0.1579	H-1->LUMO (27%), HOMO->L+1 (62%)	20-->88 (68)	80-->12 (-68)
5	259.45	0.0088	H-2->LUMO (89%)	10-->95 (85)	90-->5 (-85)
6	253.28	0.0035	H-3->L+1 (78%)	80-->84 (4)	20-->16 (-4)
7	246.36	0.2028	H-3->L+1 (12%), H-1->L+1 (75%)	39-->82 (43)	61-->18 (-43)
8	233.78	0.2196	H-2->L+1 (83%), H-1->L+1 (10%)	8-->82 (74)	92-->18 (-74)
9	219.63	0.0008	H-5->LUMO (73%), H-4->LUMO (25%)	81-->96 (15)	19-->4 (-15)
Transition	λ(nm)	Osc. Strength	Major contribs	pz %	Hpp %
1	399.69	0.0	H-3->LUMO (10%), H-1->LUMO (36%), HOMO->LUMO (48%)	28-->96 (68)	72-->4 (-68)
2	371.56	0.0	H-1->L+1 (32%), HOMO->L+1 (44%)	27-->82 (55)	73-->18 (-55)
3	364.53	0.0	H-3->LUMO (83%)	84-->96 (12)	16-->4 (-12)
4	330.31	0.0	H-1->LUMO (11%), H-1->L+1 (28%), HOMO->L+1 (17%), HOMO->L+2 (27%)	23-->67 (44)	77-->33 (-44)
5	305.03	0.0	H-1->LUMO (35%), HOMO->LUMO (44%)	22-->92 (70)	78-->8 (-70)
6	270.41	0.0	H-5->LUMO (11%), H-2->LUMO (64%)	20-->92 (72)	80-->8 (-72)
7	266.41	0.0	H-5->LUMO (55%), H-4->LUMO (27%)	74-->93 (19)	26-->7 (-19)
8	263.48	0.0	H-3->L+1 (86%)	85-->82 (-3)	15-->18 (3)
9	253.72	0.0	H-2->L+1 (54%), H-2->L+2 (10%)	16-->75 (59)	84-->25 (-59)
10	249.45	0.0	H-7->LUMO (14%), H-2->LUMO (20%), H-2->L+1 (14%)	35-->88 (53)	65-->12 (-53)

Table X.13. Calculated parameters for the singlet-singlet transitions below 200nm and the ten lowest singlet-triplet transitions of **III-L3** in acetonitrile.

Transition	λ(nm)	Osc. Strength	Major contribs	py %	Hpp %
1	294.84	0.3483	HOMO->LUMO (95%)	35-->89 (54)	65-->11 (-54)
2	279.12	0.0262	HOMO->L+1 (97%)	34-->71 (37)	66-->29 (-37)
3	263.52	0.0006	H-1->LUMO (99%)	3-->89 (86)	97-->11 (-86)
4	257.74	0.0955	H-1->L+1 (92%)	3-->71 (68)	97-->29 (-68)
5	249.05	0.0712	H-2->LUMO (95%)	16-->88 (72)	84-->12 (-72)
6	237.81	0.0761	H-3->LUMO (23%), H-2->L+1 (71%)	15-->75 (60)	85-->25 (-60)
7	236.03	0.3014	H-4->LUMO (27%), H-3->L+1 (63%)	10-->74 (64)	90-->26 (-64)
8	234.61	0.0136	H-5->LUMO (11%), H-4->L+1 (16%), H-3->LUMO (45%), H-2->L+1 (24%)	11-->80 (69)	89-->20 (-69)
9	228.47	0.0222	H-6->LUMO (98%)	90-->89 (-1)	10-->11 (1)
10	226.66	0.4258	H-5->L+1 (34%), H-4->LUMO (27%), H-3->L+1 (22%)	9-->69 (60)	91-->31 (-60)
11	225.55	0.0115	H-5->LUMO (20%), H-4->L+1 (41%), H-3->LUMO (30%)	7-->78 (71)	93-->22 (-71)
12	221.28	0.015	H-5->L+1 (29%), H-4->LUMO (44%), HOMO->L+2 (13%)	9-->70 (61)	91-->30 (-61)
13	219.03	0.0021	H-6->L+1 (79%), H-5->LUMO (13%)	74-->73 (-1)	26-->27 (1)
14	216.67	0.0224	H-6->L+1 (19%), H-5->LUMO (54%), H-4->L+1 (24%)	21-->80 (59)	79-->20 (-59)
15	208.45	0.0624	H-5->L+1 (25%), HOMO->L+2 (70%)	26-->27 (1)	74-->73 (-1)
Transition	λ(nm)	Osc. Strength	Major contribs	py %	Hpp %
1	389.08	0.0	HOMO->L+1 (77%)	34-->70 (36)	66-->30 (-36)
2	357.17	0.0	HOMO->LUMO (86%)	31-->86 (55)	69-->14 (-55)
3	318.77	0.0	H-2->LUMO (14%), H-1->L+1 (44%), H-1->L+3 (10%), HOMO->L+2 (18%)	12-->52 (40)	88-->48 (-40)
4	315.18	0.0	H-2->L+1 (35%), H-1->LUMO (20%), H-1->L+2 (22%), HOMO->L+3 (12%)	14-->53 (39)	86-->47 (-39)
5	282.86	0.0	H-7->LUMO (11%), H-3->LUMO (39%), H-1->LUMO (29%), HOMO->L+1 (10%)	20-->86 (66)	80-->14 (-66)
6	261.24	0.0	H-6->LUMO (96%)	90-->88 (-2)	10-->12 (2)
7	258.65	0.0	H-3->LUMO (22%), H-2->L+1 (11%), H-1->LUMO (35%)	15-->78 (63)	85-->22 (-63)
8	257.22	0.0	H-3->L+1 (33%), H-2->LUMO (35%), H-1->L+1 (12%)	13-->77 (64)	87-->23 (-64)
9	252.42	0.0	H-5->L+1 (16%), H-4->LUMO (11%), H-3->L+1 (19%), H-2->LUMO (28%)	11-->71 (60)	89-->29 (-60)
10	247.78	0.0	H-5->LUMO (13%), H-4->L+1 (45%)	12-->64 (52)	88-->36 (-52)

Table X.14. Calculated parameters for the singlet-singlet transitions below 200nm and the ten lowest singlet-triplet transitions of **III-L4** in acetonitrile.

Transition	λ(nm)	Osc. Strength	Major contribs	pz %	Hpp %
1	325.04	0.2867	HOMO->LUMO (96%)	30-->91 (61)	70-->9 (-61)
2	297.09	0.0011	H-1->LUMO (98%)	3-->91 (88)	97-->9 (-88)
3	282.65	0.0142	HOMO->L+1 (94%)	30-->73 (43)	70-->27 (-43)
4	278.35	0.0105	H-6->LUMO (45%), H-2->LUMO (51%)	54-->91 (37)	46-->9 (-37)
5	275.98	0.1005	H-6->LUMO (51%), H-2->LUMO (45%)	57-->90 (33)	43-->10 (-33)
6	263.99	0.115	H-1->L+1 (92%)	3-->73 (70)	97-->27 (-70)
7	256.36	0.0008	H-3->LUMO (91%)	9-->90 (81)	91-->10 (-81)
8	250.89	0.0011	H-4->LUMO (88%)	3-->88 (85)	97-->12 (-85)
9	243.68	0.0468	H-6->L+1 (28%), H-5->LUMO (12%), H-2->L+1 (57%)	39-->74 (35)	61-->26 (-35)
10	241.13	0.0094	H-6->L+1 (48%), H-5->LUMO (34%)	51-->78 (27)	49-->22 (-27)
11	239.86	0.0329	H-6->L+1 (19%), H-5->LUMO (37%), H-2->L+1 (36%)	29-->80 (51)	71-->20 (-51)
12	234.27	0.5599	H-3->L+1 (86%)	9-->72 (63)	91-->28 (-63)
13	227.70	0.2392	H-5->L+1 (76%), HOMO->L+2 (13%)	11-->62 (51)	89-->38 (-51)
14	227.18	0.0342	H-5->LUMO (10%), H-4->L+1 (79%)	5-->71 (66)	95-->29 (-66)
15	217.61	0.0003	H-7->LUMO (95%)	86-->90 (4)	14-->10 (-4)
16	207.59	0.0579	H-5->L+1 (16%), HOMO->L+2 (77%)	26-->20 (-6)	74-->80 (6)
Transition	λ(nm)	Osc. Strength	Major contribs	pz %	Hpp %
1	415.37	0.0	H-2->LUMO (13%), HOMO->LUMO (83%)	28-->90 (62)	72-->10 (-62)
2	395.13	0.0	HOMO->L+1 (70%)	26-->72 (46)	74-->28 (-46)
3	337.52	0.0	H-6->LUMO (93%)	92-->89 (-3)	8-->11 (3)
4	329.75	0.0	H-2->LUMO (18%), H-1->L+1 (45%), H-1->L+3 (10%), HOMO->L+2 (17%)	12-->55 (43)	88-->45 (-43)
5	327.33	0.0	H-2->L+1 (26%), H-1->LUMO (48%), H-1->L+2 (13%)	10-->68 (58)	90-->32 (-58)
6	307.60	0.0	H-5->LUMO (12%), H-3->LUMO (25%), H-1->LUMO (18%), HOMO->L+1 (15%)	13-->75 (62)	87-->25 (-62)
7	283.54	0.0	H-2->LUMO (62%), H-1->L+1 (16%), HOMO->LUMO (15%)	19-->86 (67)	81-->14 (-67)
8	277.51	0.0	H-3->LUMO (46%), H-2->L+1 (14%), H-1->LUMO (26%)	9-->82 (73)	91-->18 (-73)
9	262.23	0.0	H-4->LUMO (47%), H-3->L+1 (32%)	6-->73 (67)	94-->27 (-67)
10	258.31	0.0	H-5->LUMO (51%), H-4->L+1 (25%)	7-->76 (69)	93-->24 (-69)

Table X.15. Selected molecular orbitals with energies and Mulliken contributions for **III-C1** (isovalue 0.006 $e/Å^3$)

Orbital	Energy and contributions	Orbital	Energy and contributions
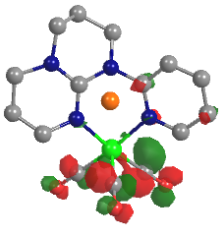 LUMO+3	-0.769 eV Re: 15% CO: 67% Br: 2% Py: 14% hpp: 2%	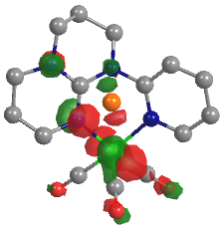 HOMO	-6.075 eV Re: 30% CO: 18% Br: 11% Py: 2% hpp: 39%
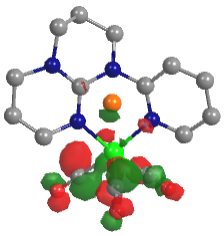 LUMO+2	-0.981 eV Re: 22% CO: 66% Br: 5% Py: 3% hpp: 5%	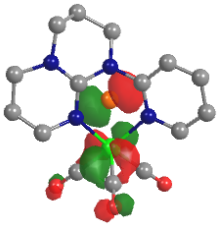 HOMO-1	-6.504 eV Re: 37% CO: 18% Br: 40% Py: 2% hpp: 3%
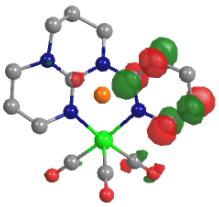 LUMO+1	-1.101 eV Re: 3% CO: 12% Br: 0% Py: 78% hpp: 7%	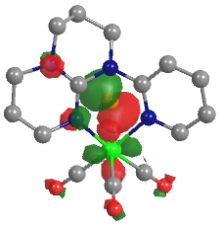 HOMO-2	-6.726 eV Re: 24% CO: 11% Br: 44% Py: 1% hpp: 20%
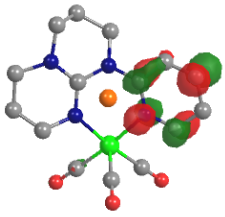 LUMO	-1.704 eV Re: 3% CO: 7% Br: 1% Py: 86% hpp: 4%	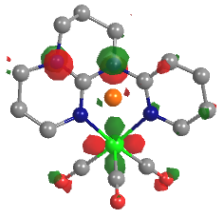 HOMO-3	-7.016 eV Re: 23% CO: 11% Br: 7% Py: 15% hpp: 44%

Table X.16. Selected molecular orbitals with energies and Mulliken contributions for **III-C2** (isovalue 0.006 *e*/Å^3)

Orbital	Energy and contributions	Orbital	Energy and contributions
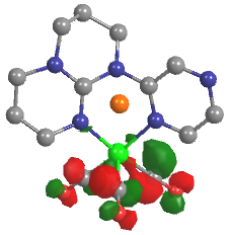 LUMO+3	-0.873 eV Re: 18% CO: 74% Br: 2% Pz: 5% hpp: 1%	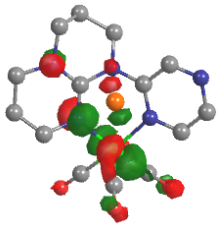 HOMO	-6.178 eV Re: 31% CO: 18% Br: 11% Pz: 1% hpp: 39%
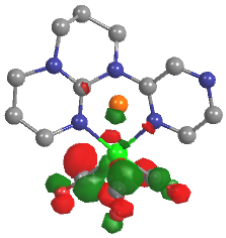 LUMO+2	-1.069 eV Re: 22% CO: 66% Br: 5% Pz: 1% hpp: 5%	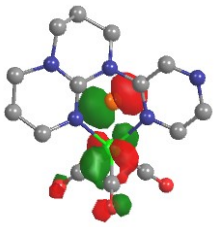 HOMO-1	-6.591 eV Re: 36% CO: 17% Br: 43% Pz: 2% hpp: 3%
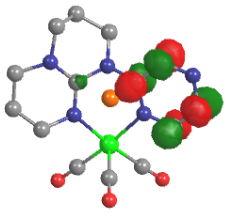 LUMO+1	-1.435 eV Re: 1% CO: 5% Br: 0% Pz: 86% hpp: 7%	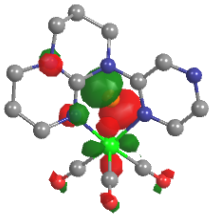 HOMO-2	-6.798 eV Re: 23% CO: 10% Br: 45% Pz: 0% hpp: 21%
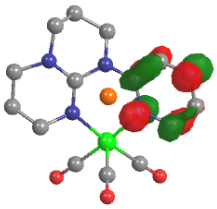 LUMO	-2.391eV Re: 1% CO: 4% Br: 1% Pz: 90% hpp: 4%	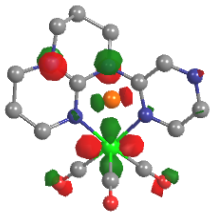 HOMO-3	-7.134 eV Re: 29% CO: 14% Br: 10% Pz: 11% hpp: 36%

Table X.17. Selected molecular orbitals with energies and Mulliken contributions for **III-C3** (isovalue 0.006 *e*/Å^3)

Orbital	Energy and contributions	Orbital	Energy and contributions
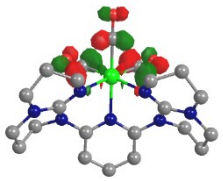 LUMO+3	-0.826 eV Re: 19% CO: 69% Py: 6% hpp: 6%	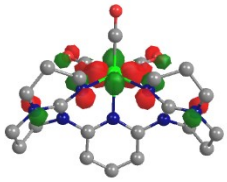 HOMO	-6.185 eV Re: 34% CO: 19% Py: 0% hpp: 46%
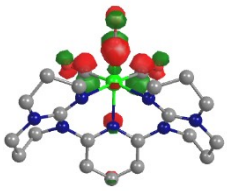 LUMO+2	-0.878 eV Re: 20% CO: 67% Py: 11% hpp: 3%	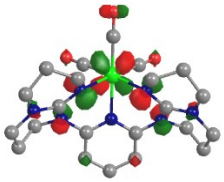 HOMO-1	-6.415 eV Re: 24% CO: 12% Py: 11% hpp: 53%
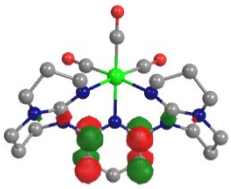 LUMO+1	-1.079 eV Re: 1% CO: 5% Py: 75% hpp: 18%	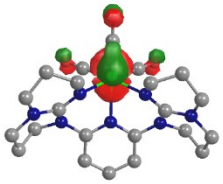 HOMO-2	-6.865 eV Re: 60% CO: 29% Py: 5% hpp: 5%
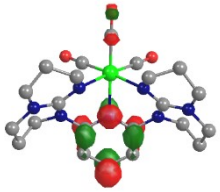 LUMO	-1.794eV Re: 5% CO: 10% Py: 77% hpp: 8%	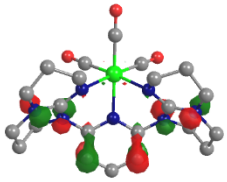 HOMO-3	-7.103 eV Re: 6% CO: 3% Py: 34% hpp: 57%

Table X.18. Selected molecular orbitals with energies and Mulliken contributions for **III-C4** (isovalue 0.006 $e/Å^3$)

Orbital	Energy and contributions	Orbital	Energy and contributions
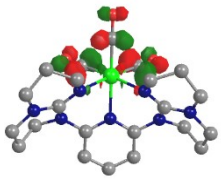 LUMO+3	-0.920 eV Re: 20% CO: 71% Pz: 2% hpp: 8%	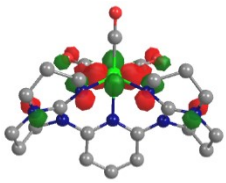 HOMO	-6.273 eV Re: 34% CO: 19% Pz: 0% hpp: 47%
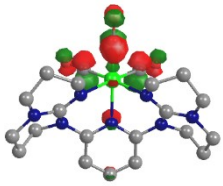 LUMO+2	-1.012 eV Re: 23% CO: 71% Pz: 5% hpp: 2%	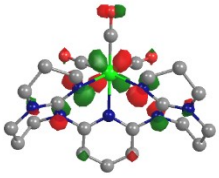 HOMO-1	-6.573 eV Re: 27% CO: 13% Pz: 7% hpp: 53%
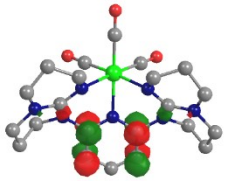 LUMO+1	-1.401 eV Re: 0% CO: 2% Pz: 81% hpp: 16%	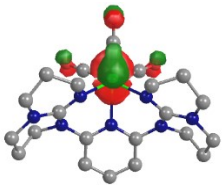 HOMO-2	-6.987 eV Re: 61% CO: 29% Pz: 4% hpp: 6%
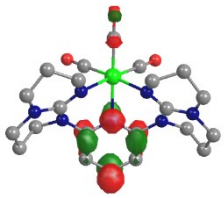 LUMO	-2.435eV Re: 3% CO: 5% Pz: 84% hpp: 8%	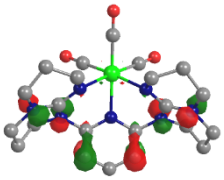 HOMO-3	-7.303 eV Re: 2% CO: 1% Pz: 33% hpp: 64%

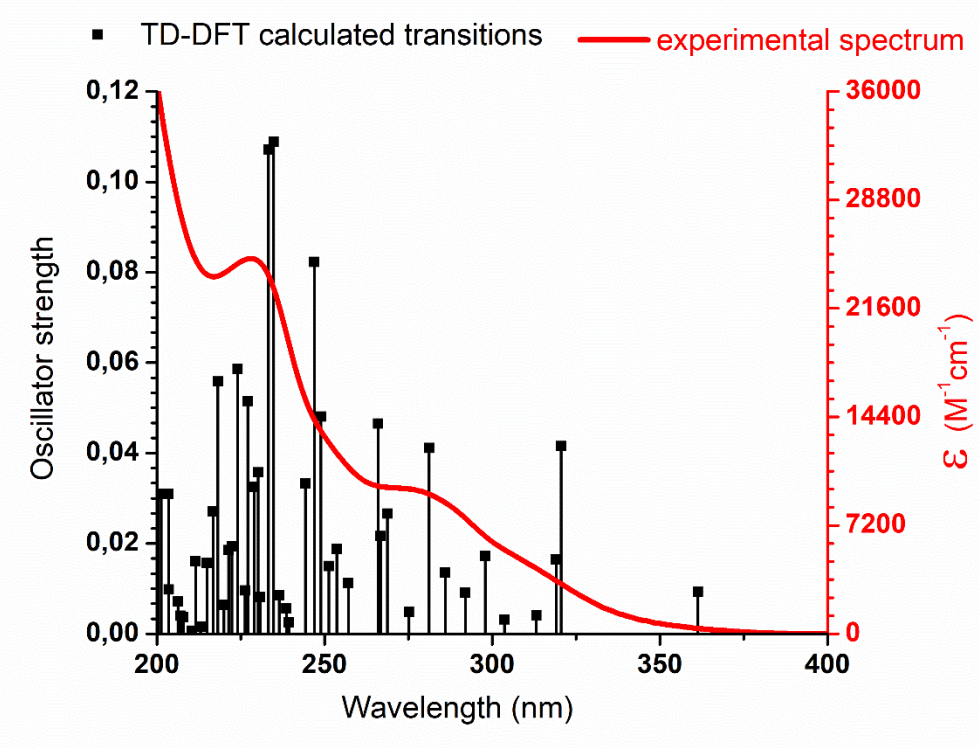

Figure X.16. Experimental absorption spectrum and theoretical transition for **III-C1**

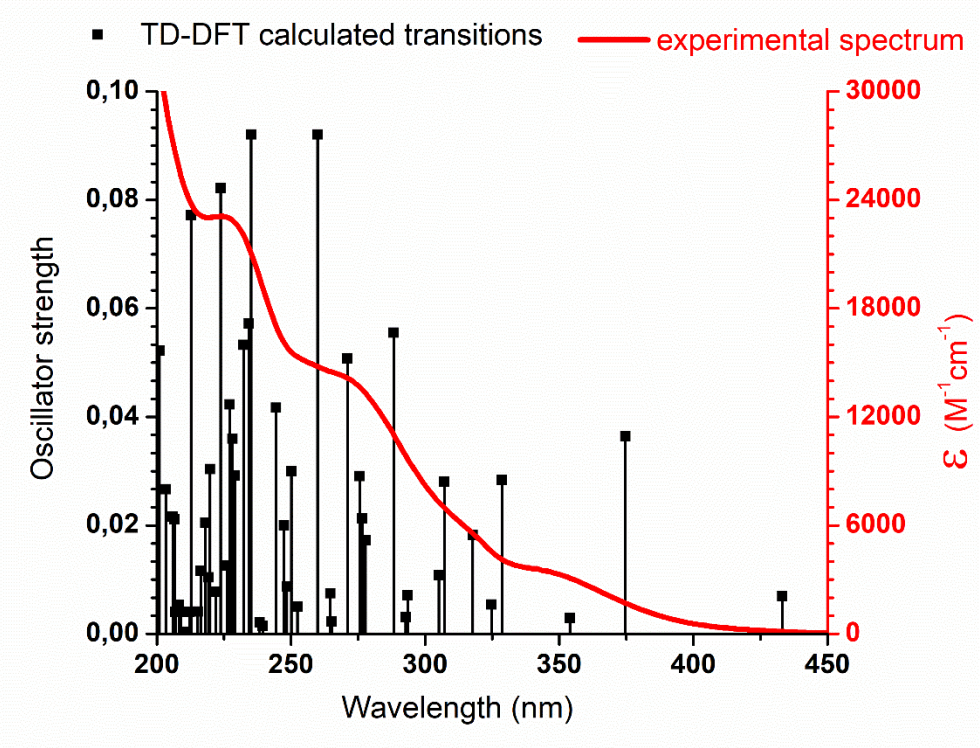

Figure X.17. Experimental absorption spectrum and theoretical transition for **III-C2**

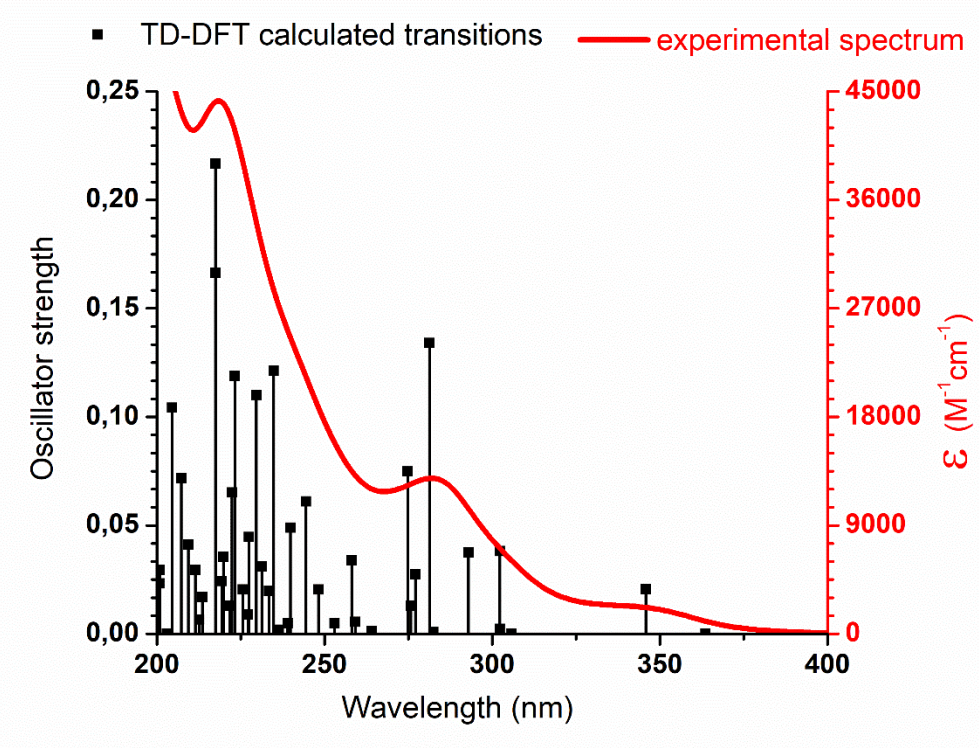

Figure X.18. Experimental absorption spectrum and theoretical transition for **III-C3**

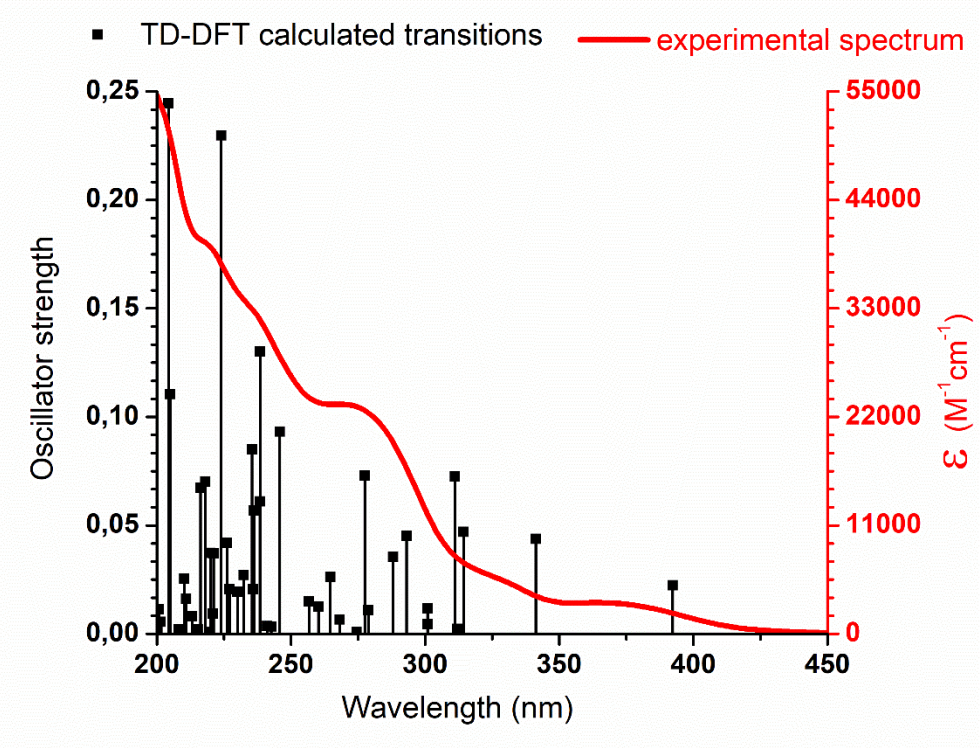

Figure X.19. Experimental absorption spectrum and theoretical transition for **III-C4**

Table X.19. Theoretical emission value for complexes **III-C1** to **III-C4**

Complex	$\lambda_{td\text{-}dft}$ (nm)	$\lambda_{0,0}$ (nm)	λ_{ae} (nm)
III-C1	387	436	537
III-C2	460	541	699
III-C3	381	422	503
III-C4	441	523	680

λ_{TDDFT} = wavelength of S0→T_1 transition obtained by TDDFT at the S_0 optimized geometry.

$\lambda_{0,0}$ = 1240/[E(T_1) – E(S_0)] at their respective optimized geometries.

λ_{ae} = 1240/[E(T_1) – E(S_0)] at the T_1 optimized geometry (adiabatic electronic emission).

Table X.20. Calculated parameters for the first ten singlet-singlet and singlet-triplet transitions of **III-C1** in acetonitrile

Transition	λ(nm)	Oscillator strength	Major contribution(s)	Re %	Br %	py %	CO %	hpp %
$S_0 \rightarrow S_1$	361	0.0093	HOMO->LUMO (97%)	30-->3 (-27)	11-->1 (-10)	2-->84 (82)	18-->8 (-10)	39-->4 (-35)
$S_0 \rightarrow S_2$	321	0.0415	H-1->LUMO (82%)	36-->5 (-31)	37-->1 (-36)	2-->73 (71)	17-->16 (-1)	7-->4 (-3)
$S_0 \rightarrow S_3$	319	0.0165	H-1->LUMO (10%), HOMO->L+2 (63%)	30-->17 (-13)	16-->3 (-13)	2-->21 (19)	17-->54 (37)	34-->5 (-29)
$S_0 \rightarrow S_4$	313	0.0041	HOMO->L+1 (43%), HOMO->L+2 (18%), HOMO->L+3 (24%)	31-->11 (-20)	14-->2 (-12)	2-->41 (39)	18-->41 (23)	36-->5 (-31)
$S_0 \rightarrow S_5$	304	0.0032	H-2->LUMO (82%)	25-->5 (-20)	41-->1 (-40)	2-->76 (74)	11-->13 (2)	21-->4 (-17)
$S_0 \rightarrow S_6$	298	0.0172	H-1->L+2 (14%), HOMO->L+1 (43%), HOMO->L+3 (35%)	31-->10 (-21)	17-->1 (-16)	2-->42 (40)	17-->41 (24)	33-->5 (-28)
$S_0 \rightarrow S_7$	292	0.0091	H-2->L+2 (14%), H-1->L+2 (43%), HOMO->L+3 (15%)	32-->19 (-13)	33-->4 (-29)	3-->15 (12)	15-->59 (44)	17-->4 (-13)
$S_0 \rightarrow S_8$	286	0.0135	H-3->LUMO (33%), H-1->L+1 (32%), H-1->L+3 (23%)	31-->6 (-25)	29-->1 (-28)	7-->62 (55)	15-->26 (11)	18-->5 (-13)
$S_0 \rightarrow S_9$	281	0.0411	H-3->LUMO (55%), H-1->L+1 (19%), H-1->L+3 (16%)	28-->5 (-23)	21-->1 (-20)	10-->69 (59)	13-->20 (7)	28-->4 (-24)
$S_0 \rightarrow S_{10}$	275	0.0049	H-4->LUMO (14%), H-3->L+2 (10%), H-2->L+2 (30%), H-1->L+3 (14%)	28-->15 (-13)	34-->3 (-31)	6-->25 (19)	13-->52 (39)	19-->4 (-15)
$S_0 \rightarrow T_1$	387	0.0	HOMO->LUMO (72%)	29-->4 (-25)	13-->1 (-12)	5-->78 (73)	17-->12 (-5)	37-->5 (-32)
$S_0 \rightarrow T_2$	360	0.0	H-3->L+1 (10%), H-1->LUMO (26%)	25-->6 (-19)	21-->1 (-20)	16-->69 (53)	13-->19 (6)	26-->5 (-21)
$S_0 \rightarrow T_3$	356	0.0	HOMO->L+2 (72%)	30-->19 (-11)	14-->4 (-10)	3-->17 (14)	17-->55 (38)	37-->6 (-31)
$S_0 \rightarrow T_4$	338	0.0	H-3->LUMO (12%), HOMO->L+1 (20%), HOMO->L+3 (37%)	28-->9 (-19)	14-->1 (-13)	7-->48 (41)	15-->37 (22)	36-->4 (-32)
$S_0 \rightarrow T_5$	332	0.0	H-1->LUMO (26%), H-1->L+2 (29%)	31-->11 (-20)	32-->2 (-30)	8-->43 (35)	15-->39 (24)	14-->5 (-9)
$S_0 \rightarrow T_6$	323	0.0	H-1->L+2 (50%)	34-->17 (-17)	35-->3 (-32)	4-->19 (15)	16-->56 (40)	11-->5 (-6)
$S_0 \rightarrow T_7$	322	0.0	H-4->LUMO (19%), H-3->LUMO (26%), H-2->LUMO (16%)	24-->6 (-18)	19-->1 (-18)	12-->68 (56)	12-->20 (8)	33-->5 (-28)
$S_0 \rightarrow T_8$	317	0.0	H-3->LUMO (11%), H-2->LUMO (14%), HOMO->L+1 (25%)	28-->8 (-20)	21-->1 (-20)	5-->58 (53)	15-->27 (12)	32-->6 (-26)
$S_0 \rightarrow T_9$	310	0.0	H-3->LUMO (10%), H-2->LUMO (19%), HOMO->L+1 (17%), HOMO->L+3 (10%)	27-->8 (-19)	24-->1 (-23)	5-->54 (49)	14-->29 (15)	30-->8 (-22)
$S_0 \rightarrow T_{10}$	303	0.0	H-3->L+2 (10%), H-2->LUMO (14%), H-2->L+2 (23%)	26-->13 (-13)	31-->2 (-29)	6-->32 (26)	12-->46 (34)	25-->7 (-18)

Table X.21. Calculated parameters for the first ten singlet-singlet and singlet-triplet transitions of **III-C2** in acetonitrile

Transition	λ(nm)	Oscillator strength	Major contribution(s)	Re %	Br %	pz %	CO %	hpp %
$S_0 \rightarrow S_1$	433	0.007	HOMO->LUMO (99%)	31-->1 (-30)	11-->1 (-10)	1-->90 (89)	18-->4 (-14)	39-->4 (-35)
$S_0 \rightarrow S_2$	375	0.0364	H-1->LUMO (98%)	36-->2 (-34)	43-->1 (-42)	2-->89 (87)	17-->4 (-13)	3-->4 (1)
$S_0 \rightarrow S_3$	354	0.0029	H-2->LUMO (95%)	23-->2 (-21)	44-->1 (-43)	1-->89 (88)	10-->4 (-6)	21-->4 (-17)
$S_0 \rightarrow S_4$	329	0.0284	H-3->LUMO (81%)	27-->2 (-25)	11-->1 (-10)	17-->89 (72)	13-->4 (-9)	33-->4 (-29)
$S_0 \rightarrow S_5$	325	0.0054	HOMO->L+1 (83%)	31-->4 (-27)	12-->0 (-12)	2-->76 (74)	18-->13 (-5)	38-->7 (-31)
$S_0 \rightarrow S_6$	318	0.0182	HOMO->L+2 (79%)	30-->20 (-10)	13-->4 (-9)	3-->10 (7)	17-->61 (44)	38-->5 (-33)
$S_0 \rightarrow S_7$	307	0.028	H-8->LUMO (10%), H-4->LUMO (50%), HOMO->L+3 (20%)	20-->6 (-14)	15-->1 (-14)	22-->66 (44)	10-->23 (13)	32-->4 (-28)
$S_0 \rightarrow S_8$	305	0.0108	H-4->LUMO (19%), H-1->L+2 (13%), HOMO->L+3 (44%)	27-->14 (-13)	17-->2 (-15)	9-->30 (21)	15-->50 (35)	31-->3 (-28)
$S_0 \rightarrow S_9$	293	0.0071	H-1->L+1 (57%), H-1->L+2 (21%)	34-->9 (-25)	40-->2 (-38)	4-->54 (50)	16-->29 (13)	7-->6 (-1)
$S_0 \rightarrow S_{10}$	293	0.0031	H-2->L+2 (13%), H-1->L+1 (21%), H-1->L+2 (29%)	31-->15 (-16)	37-->3 (-34)	6-->32 (26)	15-->46 (31)	11-->5 (-6)
$S_0 \rightarrow T_1$	460	0.0	HOMO->LUMO (84%)	30-->2 (-28)	12-->1 (-11)	4-->89 (85)	17-->5 (-12)	37-->4 (-33)
$S_0 \rightarrow T_2$	401	0.0	H-1->LUMO (71%)	31-->2 (-29)	34-->1 (-33)	8-->88 (80)	15-->5 (-10)	12-->4 (-8)
$S_0 \rightarrow T_3$	394	0.0	H-8->LUMO (17%), H-4->LUMO (29%), H-3->LUMO (22%)	19-->2 (-17)	15-->1 (-14)	29-->88 (59)	9-->5 (-4)	29-->4 (-25)
$S_0 \rightarrow T_4$	363	0.0	H-2->LUMO (50%), HOMO->L+2 (21%)	26-->7 (-19)	30-->2 (-28)	4-->64 (60)	13-->21 (8)	28-->5 (-23)
$S_0 \rightarrow T_5$	355	0.0	H-8->LUMO (15%), H-4->L+1 (14%), H-2->LUMO (15%), HOMO->L+1 (10%)	19-->2 (-17)	19-->1 (-18)	25-->85 (60)	9-->7 (-2)	28-->6 (-22)
$S_0 \rightarrow T_6$	353	0.0	H-2->LUMO (23%), HOMO->L+2 (56%)	27-->15 (-12)	20-->3 (-17)	6-->34 (28)	15-->43 (28)	32-->5 (-27)
$S_0 \rightarrow T_7$	352	0.0	H-8->LUMO (41%), H-3->LUMO (14%)	15-->2 (-13)	12-->1 (-11)	45-->85 (40)	7-->7 (0)	20-->5 (-15)
$S_0 \rightarrow T_8$	341	0.0	HOMO->L+1 (28%), HOMO->L+3 (43%)	29-->11 (-18)	15-->2 (-13)	4-->37 (33)	16-->45 (29)	36-->5 (-31)
$S_0 \rightarrow T_9$	327	0.0	H-4->LUMO (13%), H-3->LUMO (17%), HOMO->L+1 (18%), HOMO->L+3 (28%)	28-->10 (-18)	13-->1 (-12)	7-->49 (42)	15-->34 (19)	37-->6 (-31)
$S_0 \rightarrow T_{10}$	323	0.0	H-1->L+2 (81%)	35-->21 (-14)	42-->4 (-38)	2-->4 (2)	16-->65 (49)	5-->5 (0)

Table X.22. Calculated parameters for the first ten singlet-singlet and singlet-triplet transitions of **III-C3**$^{+}$ in acetonitrile

Transition	λ(nm)	Oscillator strength	Major contribution(s)	Re %	py %	CO %	hpp %
$S_0 \rightarrow S_1$	364	0.0001	HOMO->LUMO (95%)	34-->6 (-28)	0-->75 (75)	19-->12 (-7)	46-->8 (-38)
$S_0 \rightarrow S_2$	346	0.0206	H-1->LUMO (95%)	24-->6 (-18)	11-->75 (64)	12-->11 (-1)	53-->8 (-45)
$S_0 \rightarrow S_3$	306	0.0	HOMO->L+2 (86%)	35-->19 (-16)	1-->17 (16)	19-->61 (42)	45-->4 (-41)
$S_0 \rightarrow S_4$	302	0.0023	H-1->L+2 (20%), HOMO->L+1 (25%), HOMO->L+3 (33%)	30-->12 (-18)	6-->36 (30)	16-->43 (27)	48-->9 (-39)
$S_0 \rightarrow S_5$	302	0.0381	H-2->LUMO (82%)	55-->7 (-48)	6-->66 (60)	27-->19 (-8)	13-->8 (-5)
$S_0 \rightarrow S_6$	293	0.0375	H-1->L+2 (10%), HOMO->L+1 (69%)	31-->5 (-26)	4-->61 (57)	17-->19 (2)	48-->15 (-33)
$S_0 \rightarrow S_7$	282	0.0008	H-1->L+1 (37%), H-1->L+3 (43%)	29-->11 (-18)	10-->36 (26)	14-->41 (27)	47-->11 (-36)
$S_0 \rightarrow S_8$	281	0.134	H-3->LUMO (71%), HOMO->L+3 (15%)	14-->8 (-6)	26-->61 (35)	7-->23 (16)	53-->8 (-45)
$S_0 \rightarrow S_9$	277	0.0274	H-2->L+3 (37%), H-1->L+2 (26%), HOMO->L+3 (14%)	43-->16 (-27)	7-->16 (9)	21-->61 (40)	29-->7 (-22)
$S_0 \rightarrow S_{10}$	276	0.0129	H-2->L+3 (46%), H-1->L+2 (17%), HOMO->L+3 (16%)	45-->16 (-29)	6-->13 (7)	23-->65 (42)	26-->7 (-19)
$S_0 \rightarrow T_1$	381	0.0	HOMO->LUMO (66%)	33-->6 (-27)	5-->70 (65)	18-->14 (-4)	45-->10 (-35)
$S_0 \rightarrow T_2$	378	0.0	H-3->LUMO (10%), H-1->LUMO (81%)	22-->6 (-16)	13-->73 (60)	11-->12 (1)	53-->9 (-44)
$S_0 \rightarrow T_3$	368	0.0	H-3->L+1 (21%), H-2->LUMO (22%), H-1->L+1 (15%), HOMO->LUMO (20%)	28-->5 (-23)	15-->69 (54)	15-->13 (-2)	42-->13 (-29)
$S_0 \rightarrow T_4$	344	0.0	H-3->LUMO (13%), HOMO->L+1 (13%), HOMO->L+3 (59%)	29-->14 (-15)	6-->25 (19)	16-->50 (34)	49-->10 (-39)
$S_0 \rightarrow T_5$	336	0.0	H-2->LUMO (38%), H-2->L+2 (27%), H-1->L+1 (12%)	46-->10 (-36)	9-->51 (42)	23-->30 (7)	22-->9 (-13)
$S_0 \rightarrow T_6$	330	0.0	HOMO->L+2 (59%), HOMO->L+4 (13%)	33-->18 (-15)	3-->15 (12)	18-->51 (33)	46-->16 (-30)
$S_0 \rightarrow T_7$	327	0.0	H-4->LUMO (10%), H-3->LUMO (34%), H-1->L+2 (28%), HOMO->L+3 (11%)	22-->12 (-10)	16-->44 (28)	11-->38 (27)	51-->6 (-45)
$S_0 \rightarrow T_8$	320	0.0	HOMO->L+1 (28%), HOMO->L+3 (13%), HOMO->L+6 (11%)	29-->10 (-19)	6-->34 (28)	16-->32 (16)	49-->24 (-25)
$S_0 \rightarrow T_9$	315	0.0	H-1->L+1 (18%), H-1->L+3 (43%)	27-->13 (-14)	9-->26 (17)	13-->46 (33)	50-->14 (-36)
$S_0 \rightarrow T_{10}$	299	0.0	H-2->L+2 (16%), H-1->L+3 (19%), HOMO->L+2 (17%), HOMO->L+4 (13%)	35-->16 (-19)	7-->17 (10)	18-->48 (30)	41-->18 (-23)

Table X.23. Calculated parameters for the first ten singlet-singlet and singlet-triplet transitions of **III-C4**$^+$ in acetonitrile

Transition	λ (nm)	Oscillator strength	Major contribution(s)	Re %	pz%	CO %	hpp %
$S_0 \rightarrow S_1$	428	0.0001	HOMO->LUMO (99%)	34-->3 (-31)	0-->84 (84)	19-->5 (-14)	47-->8 (-39)
$S_0 \rightarrow S_2$	392	0.0224	H-1->LUMO (98%)	27-->3 (-24)	7-->83 (76)	13-->5 (-8)	53-->8 (-45)
$S_0 \rightarrow S_3$	341	0.0438	H-2->LUMO (97%)	60-->3 (-57)	4-->83 (79)	29-->6 (-23)	7-->8 (1)
$S_0 \rightarrow S_4$	314	0.047	H-4->LUMO (14%), H-3->LUMO (51%), HOMO->L+1 (20%)	18-->5 (-13)	18-->73 (55)	9-->13 (4)	55-->10 (-45)
$S_0 \rightarrow S_5$	312	0.0023	HOMO->L+2 (92%)	33-->22 (-11)	1-->6 (5)	18-->70 (52)	47-->2 (-45)
$S_0 \rightarrow S_6$	311	0.0726	H-3->LUMO (23%), HOMO->L+1 (75%)	27-->1 (-26)	8-->81 (73)	15-->3 (-12)	51-->15 (-36)
$S_0 \rightarrow S_7$	301	0.0044	H-7->LUMO (11%), H-6->LUMO (24%), H-5->LUMO (62%)	15-->3 (-12)	26-->82 (56)	7-->6 (-1)	52-->8 (-44)
$S_0 \rightarrow S_8$	301	0.0117	H-4->LUMO (45%), H-3->LUMO (22%), H-1->L+2 (14%), HOMO->L+3 (10%)	28-->8 (-20)	11-->61 (50)	13-->23 (10)	48-->7 (-41)
$S_0 \rightarrow S_9$	293	0.0451	H-4->LUMO (38%), H-1->L+2 (20%), HOMO->L+3 (36%)	35-->14 (-21)	4-->34 (30)	17-->46 (29)	45-->7 (-38)
$S_0 \rightarrow S_{10}$	288	0.0354	H-1->L+1 (94%)	27-->1 (-26)	7-->78 (71)	13-->5 (-8)	52-->16 (-36)
$S_0 \rightarrow T_1$	441	0.0	HOMO->LUMO (93%)	34-->3 (-31)	1-->82 (81)	19-->6 (-13)	46-->9 (-37)
$S_0 \rightarrow T_2$	439	0.0	H-3->LUMO (20%), H-1->LUMO (75%)	21-->3 (-18)	13-->83 (70)	10-->6 (-4)	55-->8 (-47)
$S_0 \rightarrow T_3$	400	0.0	H-3->L+1 (13%), H-2->LUMO (51%)	37-->3 (-34)	14-->81 (67)	18-->6 (-12)	31-->10 (-21)
$S_0 \rightarrow T_4$	368	0.0	H-7->LUMO (19%), H-6->LUMO (33%), H-5->LUMO (26%)	16-->4 (-12)	30-->80 (50)	7-->7 (0)	47-->9 (-38)
$S_0 \rightarrow T_5$	366	0.0	H-3->LUMO (56%), H-1->LUMO (15%)	14-->5 (-9)	21-->72 (51)	7-->13 (6)	58-->10 (-48)
$S_0 \rightarrow T_6$	352	0.0	H-3->L+1 (24%), H-2->LUMO (32%), H-1->L+1 (24%)	34-->4 (-30)	13-->73 (60)	16-->11 (-5)	37-->12 (-25)
$S_0 \rightarrow T_7$	341	0.0	HOMO->L+1 (18%), HOMO->L+3 (57%)	32-->13 (-19)	3-->28 (25)	17-->47 (30)	47-->12 (-35)
$S_0 \rightarrow T_8$	335	0.0	HOMO->L+2 (74%)	33-->21 (-12)	3-->8 (5)	18-->61 (43)	46-->9 (-37)
$S_0 \rightarrow T_9$	330	0.0	H-4->LUMO (12%), H-1->L+2 (11%), HOMO->L+1 (28%), HOMO->L+3 (23%)	32-->10 (-22)	4-->37 (33)	17-->37 (20)	47-->16 (-31)
$S_0 \rightarrow T_{10}$	320	0.0	H-1->L+1 (15%), H-1->L+3 (27%), HOMO->L+4 (18%)	29-->12 (-17)	9-->25 (16)	14-->39 (25)	48-->24 (-24)

Table X.24. Optimized geometry of **III-L1** in acetonitrile.

Center number	Atomic number	Coordinates (angstroms)			Center number	Atomic number	Coordinates (angstroms)		
		X	Y	Z			X	Y	Z
1	1	2.182753	0.369888	1.584898	17	1	-1.364422	-4.314957	3.899093
2	6	1.162255	0.172196	1.899321	18	1	-1.989347	-3.926434	6.870312
3	7	-1.452013	0.369452	2.712084	19	1	-2.702001	-1.911987	5.263548
4	6	0.929619	0.643990	3.005366	20	1	-2.934342	-4.352445	4.722295
5	6	0.078205	0.727407	1.190634	21	1	0.914945	-5.130171	6.144577
6	6	-1.207406	0.418599	1.638332	22	1	-2.569489	-2.154821	3.520959
7	6	0.409330	0.903600	3.394923	23	6	0.645863	-3.426961	7.478254
8	1	1.745739	-1.069468	3.570648	24	1	0.667284	-4.506539	7.662648
9	1	0.226885	1.367414	0.328422	25	1	0.136379	-2.956581	8.334477
10	1	-2.084486	0.813013	1.132703	26	6	2.062992	-2.875822	7.337282
11	7	0.745090	-1.771617	4.447500	27	1	2.597005	-3.444654	6.565958
12	7	0.115852	-3.199678	6.241369	28	1	2.608894	-2.991484	8.279990
13	6	-1.950018	-3.872400	4.713064	29	6	1.976503	-1.399185	6.938263
14	6	-1.266643	-4.094826	6.055303	30	1	2.963861	-1.026659	6.638023
15	6	-2.091417	-2.373827	4.474541	31	1	1.672463	0.798988	7.809523
16	6	0.112549	-2.017833	5.547357	32	7	1.035954	-1.141650	5.838391

Table X.25. Optimized geometry of **III-L2** in acetonitrile.

Center number	Atomic number	Coordinates (angstroms)			Center number	Atomic number	Coordinates (angstroms)		
		X	Y	Z			X	Y	Z
1	7	0.320572	1.299503	2.883815	17	1	-2.292286	-2.379284	6.513654
2	7	-1.117475	-1.007844	2.212594	18	1	-2.566009	-2.429580	3.696950
3	6	0.269202	0.254906	3.721200	19	1	-2.950673	-4.320093	5.024251
4	6	0.336743	1.206092	1.693980	20	1	-1.824345	-3.918780	7.254184
5	6	-1.054346	0.054774	1.374573	21	1	-1.381442	-3.533911	3.010414
6	6	0.456667	0.930054	3.393949	22	6	0.619056	-3.232411	7.564314
7	1	0.804208	0.333295	4.656197	23	1	0.272577	-4.193498	7.961413
8	1	0.285966	2.055529	1.023779	24	1	0.503254	-2.485455	8.362533
9	1	-1.590535	0.031783	0.435643	25	6	2.086147	-3.328499	7.139935
10	7	0.601341	-2.008117	4.261154	26	1	2.233088	-4.223224	6.522325
11	7	0.226981	-2.872153	6.416849	27	1	2.719892	-3.423921	8.027909
12	6	-1.915217	-3.968699	5.079580	28	6	2.463787	-2.082749	6.328905
13	6	-1.640444	-3.257713	6.403231	29	1	3.484542	-2.171978	5.942525
14	6	-1.658548	-2.997191	3.924689	30	1	2.449763	-1.197270	6.983761
15	6	0.320940	-2.247843	5.317505	31	7	1.563824	-1.869878	5.182095
16	1	-1.260654	-4.844896	5.011958					

Table X.26. Optimized geometry of **III-L3** in acetonitrile.

Center number	Atomic number	Coordinates (angstroms)			Center number	Atomic number	Coordinates (angstroms)		
		X	Y	Z			X	Y	Z
1	7	0.000015	0.202663	0.000112	28	1	-5.278574	-1.020037	2.506320
2	6	-1.216792	-1.874357	0.084425	29	7	-3.709738	0.988635	1.110842
3	6	1.216863	-1.874299	0.084137	30	7	2.320653	0.340869	0.234177
4	6	1.174581	0.465008	0.078873	31	7	4.678832	0.585915	0.408115
5	6	-1.174582	0.465071	0.079117	32	6	3.189536	1.921243	1.873430
6	1	-2.161496	-2.394674	0.135572	33	6	4.585340	1.759584	1.287367
7	1	2.161593	-2.394570	0.135254	34	6	2.164020	1.706659	0.766624
8	7	-2.320676	0.340775	0.234404	35	6	3.606476	0.062448	0.195428
9	7	-4.678888	0.585983	0.407834	36	1	3.016257	1.192931	2.674018
10	6	-3.189834	1.921073	-1.873591	37	1	4.852200	2.662803	0.714420
11	6	-4.585513	1.759571	-1.287194	38	1	2.297554	2.450262	0.032491
12	6	-2.164080	1.706509	0.767002	39	1	3.088034	2.924940	2.299995
13	6	-3.606436	0.062505	0.195419	40	1	5.330775	1.651992	2.085247
14	1	-3.016784	1.192692	-2.674161	41	1	1.142788	1.801775	1.133100
15	1	-4.852165	2.662862	0.714262	42	7	3.709901	0.988514	-1.110881
16	1	-2.297371	2.450195	0.032076	43	6	5.034576	-1.467541	-1.530423
17	1	-3.088350	2.924734	-2.300247	44	1	4.969948	-2.550204	-1.697359
18	1	-5.331140	1.651988	-2.084898	45	1	5.278969	-1.019782	-2.506098
19	1	-1.142931	1.801531	-1.133738	46	6	6.026019	0.315192	0.113903
20	6	-6.025977	0.315248	0.114424	47	1	6.744601	0.555179	0.677346
21	1	-6.744708	0.555378	0.676647	48	1	6.246491	0.973584	0.969600
22	1	-6.246243	0.973537	0.970253	49	6	6.148859	-1.149339	0.528261
23	6	-6.148806	-1.149330	0.528624	50	1	6.051097	-1.785547	0.360247
24	1	-6.051222	-1.785440	0.359973	51	1	7.133653	-1.336440	0.970333
25	1	-7.133532	-1.336432	0.970847	52	6	0.000055	-2.560680	0.000151
26	6	-5.034353	-1.467689	1.530553	53	1	0.000077	-3.647154	0.000167
27	1	-4.969727	-2.550373	1.697353					

Table X.27. Optimized geometry of **III-L4** in acetonitrile.

Center number	Atomic number	Coordinates (angstroms)			Center number	Atomic number	Coordinates (angstroms)		
		X	Y	Z			X	Y	Z
1	7	0.000102	-2.495942	0.000910	27	6	-5.002148	-1.571594	1.472733
2	7	0.000039	0.269363	0.000492	28	1	-4.907404	-2.656543	1.604334
3	6	-1.165624	-1.820920	0.055908	29	1	-5.265420	-1.162752	2.460164
4	6	1.165464	-1.821034	0.057532	30	7	-3.688642	-1.041770	1.079439
5	6	1.171333	0.404864	0.060465	31	7	2.326213	0.372459	0.201874
6	6	-1.171373	0.404759	0.059284	32	7	4.689433	0.562405	0.385740
7	1	-2.083328	-2.387679	0.073664	33	6	3.224172	1.990838	1.786209
8	1	2.083123	-2.387867	0.075535	34	6	4.619589	1.771563	1.218296
9	7	-2.326109	0.372741	0.200842	35	6	2.199299	1.762123	0.681963
10	7	-4.689207	0.562621	0.386472	36	6	3.608125	0.080251	0.201107
11	6	-3.222986	1.991126	-1.785816	37	1	3.026873	1.298936	2.612947
12	6	-4.618794	1.771846	-1.218881	38	1	4.914342	2.643984	0.612791
13	6	-2.198928	1.762432	0.680805	39	1	2.356167	2.468240	0.145671
14	6	-3.608308	0.079998	0.201187	40	1	3.145314	3.012317	2.172906
15	1	-3.025077	1.299211	-2.612398	41	1	5.355451	1.675396	2.026109
16	1	-4.913911	2.644236	0.613502	42	1	1.179195	1.896771	1.039056
17	1	-2.356497	2.468477	0.146751	43	7	3.687809	-1.041954	-1.079500
18	1	-3.143855	3.012601	-2.172470	44	6	5.001055	-1.571679	-1.473833
19	1	-5.354124	1.675764	-2.027183	45	1	4.906254	-2.656617	-1.605461
20	1	-1.178565	1.897150	-1.037111	46	1	5.263574	-1.162726	-2.461418
21	6	-6.034159	0.230324	0.106716	47	6	6.034046	0.230138	0.108380
22	1	-6.749239	0.473487	0.686561	48	1	6.749663	0.473178	0.684455
23	1	-6.286332	0.852480	0.980206	49	1	6.285665	0.852399	0.981953
24	6	-6.115122	-1.250838	0.469955	50	6	6.114761	-1.250981	0.471847
25	1	-5.989577	-1.853198	0.438328	51	1	5.989927	-1.853452	0.436459
26	1	-7.098063	-1.482029	0.894553	52	1	7.097392	-1.482087	0.897213

Table X.28. Optimized geometry of **III-C1** in acetonitrile.

Center number	Atomic number	Coordinates (angstroms)			Center number	Atomic number	Coordinates (angstroms)		
		X	Y	Z			X	Y	Z
1	1	1.006230	0.305137	0.755467	21	1	0.951008	-4.172121	7.213259
2	6	0.266989	0.240921	1.542079	22	1	-2.470162	-3.240020	3.325740
3	6	-1.520860	0.001481	3.594845	23	6	1.272824	-4.559970	6.126636
4	7	0.227700	0.939481	2.232606	24	1	0.758367	-5.510013	6.316471
5	6	0.577665	1.307954	1.808951	25	1	1.663629	-4.195811	7.084441
6	6	-1.491618	1.184165	2.867910	26	6	2.407096	-4.749723	5.122341
7	6	0.658690	-1.066944	3.258038	27	1	2.118590	-5.458583	4.338091
8	1	0.509324	2.210678	1.214747	28	1	3.284688	-5.154922	5.635046
9	1	-2.149443	2.003659	3.135745	29	6	2.721117	-3.396952	4.482070
10	1	-2.182725	0.095078	4.445183	30	1	3.003798	-2.669984	5.257602
11	7	0.738103	-2.259761	4.006801	31	1	3.552680	-3.473024	3.782370
12	7	0.281807	-3.578758	5.638037	32	7	1.531011	-2.905631	3.749824
13	6	-2.106176	-3.841541	5.391155	33	75	1.636577	-2.495949	1.660875
14	6	0.989917	-3.481170	6.369013	34	6	1.540627	-2.123653	0.211343
15	6	-2.104447	-2.806482	4.263582	35	8	1.458838	-1.901739	-1.376128
16	6	0.398485	-2.940370	4.441632	36	6	2.782526	-3.965583	1.263869
17	1	-1.925450	-4.849894	5.003651	37	8	3.479608	-4.894571	1.016933
18	1	-1.127204	-2.467196	6.764837	38	6	3.113273	-1.349391	1.867150
19	1	-2.760112	-1.980821	4.542628	39	8	4.054830	0.626060	1.977428
20	1	-3.084124	-3.839959	5.881521	40	35	0.504889	-4.156419	1.292596

Table X.29. Optimized geometry of **III-C2** in acetonitrile.

Center number	Atomic number	Coordinates (angstroms)			Center number	Atomic number	Coordinates (angstroms)		
		X	Y	Z			X	Y	Z
1	1	1.014751	0.376495	0.814242	21	1	-2.441914	-3.304675	3.332236
2	6	0.275547	0.256696	1.592736	22	6	1.278157	-4.550956	6.146821
3	6	-1.519731	0.017055	3.570709	23	1	0.757649	-5.488094	6.378091
4	7	0.252879	0.941014	2.250653	24	1	1.689073	-4.157201	7.084188
5	6	0.609598	1.278687	1.903190	25	6	2.390677	-4.785481	5.128668
6	7	-1.512427	1.144736	2.908503	26	1	2.075638	-5.507715	4.367256
7	6	0.648847	-1.094763	3.256912	27	1	3.269433	-5.194357	5.636123
8	1	0.591230	2.216010	1.362359	28	6	2.722079	-3.455428	4.451349
9	1	-2.211137	0.098581	4.399104	29	1	3.035770	-2.716360	5.202821
10	7	0.733888	-2.276574	4.001040	30	1	3.538214	-3.567580	3.738719
11	7	0.287861	-3.579251	5.638952	31	7	1.530168	-2.950277	3.728731
12	6	-2.107635	-3.817601	5.429093	32	75	1.651264	-2.485545	1.650551
13	6	0.974252	-3.442837	6.381190	33	6	1.573940	-2.058360	0.211417
14	6	-2.100377	-2.829458	4.258611	34	8	1.504017	-1.802583	-1.369108
15	6	0.406630	-2.964763	4.432358	35	6	2.781730	-3.958636	1.216405
16	1	-1.951261	-4.843473	5.079505	36	8	3.466580	-4.888444	0.945980
17	1	-1.092048	-2.416000	6.748682	37	6	3.141221	-1.360581	1.898185
18	1	-2.769801	-2.000416	4.489761	38	8	4.088923	0.651565	2.033851
19	1	-3.078825	-3.778011	5.930791	39	35	0.509243	-4.095956	1.237493
20	1	0.934309	-4.109444	7.244544					

Table X.30. Optimized geometry of **III-C3**$^{+}$ in acetonitrile.

Center number	Atomic number	Coordinates (angstroms)			Center number	Atomic number	Coordinates (angstroms)		
		X	Y	Z			X	Y	Z
1	1	0.000494	5.194659	0.066828	31	1	5.330486	2.834646	0.561097
2	6	0.000384	4.112638	0.005101	32	1	4.817390	1.221658	-2.636006
3	7	0.000104	1.342956	0.221918	33	1	3.420830	2.778626	1.112262
4	6	-1.208476	3.416112	0.011560	34	7	1.533091	0.782467	0.724034
5	6	1.207800	3.416346	0.011297	35	6	4.063282	-1.296772	-2.031473
6	6	1.180599	2.016299	0.092408	36	1	4.031828	-1.146620	-3.118500
7	6	-1.180980	2.016113	0.092636	37	1	5.100693	-1.523688	-1.759122
8	1	-2.141344	3.952584	0.084016	38	7	-1.532699	0.782306	0.724456
9	1	2.140554	3.952975	0.084520	39	6	-4.062536	-1.296926	-2.032439
10	7	-2.374652	1.274654	0.074836	40	1	-4.031352	-1.146116	-3.119380
11	7	-3.690093	0.027092	-1.375180	41	1	-5.099778	-1.524529	-1.760017
12	6	-4.397448	2.317098	0.800930	42	6	-1.694369	-1.919540	-1.656543
13	6	-4.710718	1.029436	-1.560793	43	1	-1.010385	-2.711042	-1.355455
14	6	-3.640518	1.929062	0.465740	44	1	-1.420540	-1.611661	-2.675367
15	6	-2.509924	0.112379	0.708307	45	6	-3.133318	-2.429049	-1.622285
16	1	-3.788723	2.995014	-1.408171	46	1	-3.371273	-2.778988	0.611154
17	1	-5.661177	0.613297	-1.203906	47	1	-3.260525	-3.271994	-2.307962
18	1	-4.222117	1.213512	1.057589	48	6	1.695472	-1.920392	-1.655189
19	1	-5.330879	2.833913	0.560778	49	1	1.421494	-1.613547	-2.674279
20	1	-4.818577	1.220910	-2.635460	50	1	1.011957	-2.712056	-1.353421
21	1	-3.421322	2.777929	1.112712	51	6	3.134697	-2.429085	-1.620472
22	7	2.374392	1.275154	0.074413	52	1	3.262371	-3.272506	-2.305475
23	6	4.397058	2.317843	0.801282	53	1	3.372825	-2.778095	0.609060
24	7	3.690317	0.026770	-1.374837	54	75	0.000050	0.728625	0.801378
25	6	4.710333	1.030204	-1.561252	55	6	1.343536	0.521683	2.142820
26	6	2.509984	0.112558	0.708187	56	8	2.153406	0.395250	3.004580
27	6	3.640170	1.929745	0.465364	57	6	0.000167	-2.602485	1.143170
28	1	3.788320	2.995794	-1.408467	58	8	0.000327	-3.772479	1.361952
29	1	5.661208	0.614495	-1.204989	59	6	-1.343743	0.521750	2.142765
30	1	4.221850	1.214328	1.057303	60	8	-2.153507	0.395324	3.004634

Table X.31. Optimized geometry of **III-C4**$^{+}$ in acetonitrile.

Center number	Atomic number	Coordinates (angstroms)			Center number	Atomic number	Coordinates (angstroms)		
		X	Y	Z			X	Y	Z
1	7	4.096537	0.081228	0.000000	31	1	1.270931	-2.651330	4.785957
2	7	1.324170	0.247991	0.000000	32	1	2.802835	1.116543	3.414209
3	6	3.412557	0.074706	-1.155910	33	7	0.771186	0.724246	1.536986
4	6	3.412557	0.074706	1.155910	34	6	-1.255494	-2.056512	4.060456
5	6	2.004114	0.125946	1.175407	35	1	-1.094277	-3.141476	4.021065
6	6	2.004114	0.125946	-1.175407	36	1	-1.477262	-1.792130	5.100861
7	1	3.993070	0.002988	-2.064720	37	7	0.771186	0.724246	-1.536986
8	1	3.993070	0.002988	2.064720	38	6	-1.255494	-2.056512	-4.060456
9	7	1.289825	0.083198	-2.372306	39	1	-1.094277	-3.141476	-4.021065
10	7	0.006604	-1.385608	-3.683169	40	1	-1.477262	-1.792130	-5.100861
11	6	2.356622	0.809040	-4.373382	41	6	-1.898553	-1.669405	-1.699403
12	6	1.074720	-1.576467	-4.691691	42	1	-2.697344	-1.371586	-1.022434
13	6	1.958093	0.464838	-3.635771	43	1	-1.580553	-2.682266	-1.415990
14	6	0.128394	0.708397	-2.508958	44	6	-2.397808	-1.650327	-3.142107
15	1	3.031540	-1.406759	-3.751954	45	1	-2.756455	0.644765	-3.389996
16	1	0.666217	-1.230736	-5.649321	46	1	-3.232764	-2.345462	-3.269766
17	1	1.246303	1.049690	-4.228400	47	6	-1.898553	-1.669405	1.699403
18	1	2.881477	0.576358	-5.303987	48	1	-1.580553	-2.682266	1.415990
19	1	1.270931	-2.651330	-4.785957	49	1	-2.697344	-1.371586	1.022434
20	1	2.802835	1.116543	-3.414209	50	6	-2.397808	-1.650327	3.142107
21	7	1.289825	0.083198	2.372306	51	1	-3.232764	-2.345462	3.269766
22	6	2.356622	0.809040	4.373382	52	1	-2.756455	0.644765	3.389996
23	7	0.006604	-1.385608	3.683169	53	75	0.746969	0.799540	0.000000
24	6	1.074720	-1.576467	4.691691	54	6	0.560301	2.143105	1.345743
25	6	0.128394	0.708397	2.508958	55	8	0.444609	3.004375	2.156307
26	6	1.958093	0.464838	3.635771	56	6	-2.626318	1.120363	0.000000
27	1	3.031540	-1.406759	3.751954	57	8	-3.797446	1.324614	0.000000
28	1	0.666217	-1.230736	5.649321	58	6	0.560301	2.143105	-1.345743
29	1	1.246303	1.049690	4.228400	59	8	0.444609	3.004375	-2.156307
30	1	2.881477	0.576358	5.303987					

Chapitre XI. Matériels supplémentaires au chapitre IV

XI.1 Experimental section

XI.1.1 Physical measurements

^{1}H and ^{13}C NMR spectra were acquired on a Bruker AV400 (400MHz). Chemical shifts are reported in part per million (ppm) relative to the residual proton (1.94 ppm for CD_3CN, 2.05 ppm for acetone-d^6, 2.50 ppm for DMSO-d^6) or carbon resonances (39.52 ppm for DMSO-d^6) of the solvent. ESI-MS measurements were made on a Bruker Daltonics MicroTOF II. All photophysical measurements were carried out in deaerated solutions (acetonitrile). Absorption spectra were measured on an Agilent Cary6000i UV-Vis-NIR spectrophotometer and luminescence spectra at room temperature on a Perkin-Elmer LS55 fluorescence spectrometer. Infra-red vibration spectroscopy measurements were conducted on a Perkin-Elmer Spectrum2 in ATR mode. Electrochemical measurements involved a three-electrode set-up with a glassy carbon disk (d=3mm) working electrode, a platinum coil as counter electrode and a platinum wire as pseudo-reference. Measurements were made using a SP-50 BioLogic potentiostat interfaced to a computer equipped with the EC-lab software V11.21. The potentials were referenced internally using the ferrocenium/ferrocene couple in DMF (0.45 V *vs.* ECS).[1] The concentration of analyte was approximatively 1 mM while the supporting electrolyte (tetrabutylammonium hexafluorophosphate TBAP) was at 0.1 M.

XI.1.2 Computational studies

The singlet ground state geometries of the complexes were optimized by DFT method with the PBE0 hybrid functional[2] without symmetry constraints using Gaussian16 Rev. A03.[3] The lowest triplet excited state T_1 geometries were also optimized in the case of the complexes. All elements were assigned the LANL2DZ basis set.[4-6] Frequency calculations were performed to ensure that local minima had been reached and get a model of the IR spectra. The absorption and emission properties were modelled by time dependent DFT (TD-DFT). All calculations were made for acetonitrile solution using a

conductor-like polarizable continuum model (CPCM).[7] The results were visualized and tabulated using Gaussview6.0, GaussSum3.0[8] and Chemissian4.53[9].

XI.1.3 Materials

$Re_2(CO)_{10}$ was obtained from Pressure Chemical and converted to $Re(CO)_5Br$ via titration with bromine.[10] Solvents were of ACS or spectroscopic grade (for absorption and emission measurements) and used as received, like other reagents, from commercial sources (Millipore Sigma or Fisher Scientific). Acetonitrile for electrochemistry was distilled from CaH_2 and stored under N_2. Compounds **IV-1a**, **IV-1e**, **IV-2a**, **IV-2e**, **IV-3a**, **IV-3e** and **IV-4a** were prepared as previously reported and their spectra matched the literature.[11-13] Their purity was only verified by ^{1}H NMR.

XI.1.4 Synthetic procedures

All the complexes appeared to be hygroscopic and were thus stored in a desiccator with freshly activated $CaSO_4$ (Drierite) and covered with aluminium foil.

Complexes **IV-1a-e** were prepared via the typical Re diimine complex synthesis. $Re(CO)_5Br$ and the desired ligand were combined in a 1:1.05 molar ratio in toluene and refluxed for 4h (Typical scale: 0.5mmol in 75mL). The desired neutral complex, [$Re(CO)_3Br(\kappa^2$N-tpy)], which precipitated during the reaction, was filtered, washed with cold toluene then diethyl ether and finally air dried. Further drying at 100°C for one night was conducted before storage in a desiccator.

IV-1a *fac*-[$Re(CO)_3Br(\kappa^2$N-*La*)] Y=94% (550 mg, 1 mmol scale) yellow solid. ^{1}H NMR (400 MHz, CD_3CN) δ 9.08 (d, J = 6 Hz, 1H), 8.78 (d, J = 5 Hz, 1H), 8.50 (t, J = 8 Hz, 2H) 8.28 (t, J = 8 Hz, 1H), 8.21 (td, J = 8, 2 Hz, 1H), 7.97 (td, J = 8, 2 Hz, 1H), 7.78 (t, J = 7 Hz, 2H), 7.63 (ddd, J = 8, 6, 2 Hz, 1H), 7.55 (ddd, J = 8, 5, 2 Hz, 1H) ; ESI-MS (MeCN): Calculated 504.0352 for $[M-Br]^+$, Observed 504.0342

IV-1b *fac*-[$Re(CO)_3Br(\kappa^2$N-*Lb*)] Y=88% (275 mg) yellow solid.; ^{1}H NMR (400 MHz, CD_3CN) δ 8.89 (d, J = 6 Hz, 1H), 8.60 (d, J = 5 Hz, 1H), 8.35(d, J = 6 Hz, 2H), 7.62 (s, 2H), 7.45 (d, J = 5 Hz, 1H), 7.37 (d, J = 6 Hz, 1H), 2.60 (s, 3H), 2.58 (s, 3H), 2.44 (s, 3H) ; ^{13}C NMR (101 MHz,

DMSO-d^6) δ 197.5; 194.0, 190.6, 160.7, 157.8, 156.1 156.0, 152.3, 152.1, 151.9, 149.0, 147.6, 128.2, 128.0, 125.8, 125.42, 125.38, 124.2, 20.9, 20.7, 20.5 ; ESI-MS (MeCN): Calculated 546.0822 for $[M\text{-}Br]^+$, Observed 546.0869 ; Elemental analysis for $C_{21}H_{17}BrN_3O_3Re,H_2O$ Calculated: C(%) 39.20, N(%) 6.53, H(%) 2.98, Found: C(%) 39.40, N(%) 6.41, H(%) 2.57.

IV-1c *fac*-[Re(CO)$_3$Br(κ^2N-*Lc*)] Y=91% (301 mg) yellow solid. ^{1}H NMR (400 MHz, CD_3CN) δ = 9.10 (d, J = 6 Hz, 1H), 8.81 (d, J = 5 Hz, 1H), 8.75 (d, J = 2 Hz, 1H), 8.68 (d, J = 8 Hz, 1H), 8.24 (t, J = 8 Hz, 1H), 8.05 (d, J = 2 Hz, 1H), 8.03 – 7.98 (m, 3H), 7.85 (d, J = 8 Hz, 1H), 7.68 – 7.54 (m, 5H).; ^{13}C NMR (101 MHz, DMSO-d^6) δ 197.5, 194.0, 190.4, 161,6, 157.9, 157.3, 156.4, 152.8, 150.6, 149.2, 139.9, 137.0, 134.7, 131.0, 129.4, 127.9, 127.5, 125.5, 125.1, 125.0, 124.4, 120.7; ESI-MS (MeCN): Calculated 580.0672 for $[M\text{ -}Br]^+$, Observed 580.0754; Elemental analysis for $C_{24}H_{15}BrN_3O_3Re,H_2O$, Calculated: C(%) 42.55, N(%) 6.20, H(%) 2.53, Found: C(%) 42.71, N(%) 6.00, H(%) 2.17.

IV-1d *fac*-[Re(CO)$_3$Br(κ^2N-*Ld*)] Y=92% (339 mg) orange-red solid. ^{1}H NMR (400 MHz, CD_3CN) δ = 9.10 (d, J = 6 Hz, 1H), 8.81 (d, J = 5 Hz, 1H), 8.79 (s, 1H), 8.71 (d, J = 8 Hz, 1H), 8.24 (t, J = 8 Hz, 1H), 8.11 (s, 1H), 8.09 (s, 2H), 8.00 (t, J = 8 Hz, 1H), 7.89 (d, J = 8 Hz, 2H), 7.85 (d, J = 8 Hz, 1H), 7.76 (d, J = 7 Hz, 2H), 7.65 (t, J = 7 Hz, 1H), 7.58 (dd, J = 8, 5 Hz, 1H), 7.52 (t, J = 8 Hz, 2H), 7.44 (t, J = 7 Hz, 1H)$^{\cdot}$; ^{13}C NMR (101 MHz, DMSO-d^6) δ 197.5, 194.0, 190.4, 161,6, 158.0, 157.3, 156.4, 152.8, 150.0, 149.2, 142.5, 139.9, 138.9, 137.0, 133.6, 129.1, 128.5, 128.2, 127.5, 12.9, 125.5, 125.1, 125.0, 124.2, 120.4 ; ESI-MS (MeCN): Calculated 656.0985 for $[M\text{ -}Br]^+$, Observed 656.0888 ; Elemental analysis for $C_{30}H_{19}BrN_3O_3Re,H_2O$ Calculated: C(%) 47.81, N(%) 5.58, H(%) 2.81, Found: C(%) 48.09, N(%) 5.42, H(%) 2.60.

IV-1e *fac*-[Re(CO)$_3$Br(κ^2N-*Le*)] Y=95% (313 mg) yellow-orange solid. ^{1}H NMR (400 MHz, CD_3CN) δ = 9.11 (d, J = 5 Hz, 1H), 8.99 (d, J = 7 Hz, 1H), 8.80 (m, 3H), 8.67 (dd, J = 11, 9 Hz, 1H), 8.25 (m, 1H), 8.10 (m, 1H), 7.99 (d, J = 7 Hz, 2H), 7.91 (dd, J = 5, 2 Hz, 1H), 7.85 (m, 1H), 7.66 (m, 1H), 7.58 (m, 1H).; ESI-MS (MeCN): Calculated 581.0624 for $[M\text{ -}Br]^+$, Observed 581.0675

Complexes **IV-2a-e** were prepared as in our previous report, starting from the corresponding κ^2N-terpyridine complexes. The suitable κ^2N-terpyridine complex (100 mg) was ground into a

fine powder then placed in a 20mL Biotage® microwave vial, sealed in a nitrogen purged glovebox with a PTFE-silicon septum. The vial was then heated in a sand bath at 270 °C for 6 h. Once back to RT, the vial was opened, and the black brown solid was dispersed in 10mL of diethyl ether, filtered, washed with dichloromethane (2*10 mL) and finally air dried. Further drying at 100°C overnight was conducted before storage in a desiccator.

IV-2a [Re(CO)$_2$Br(κ^3N-*La*)] Y=90% (129 mg, starting with 150 mg) dark brown solid.; ^{1}H NMR (400 MHz, DMSO-d^6) δ = 8.89 (dd, J = 6, 1 Hz, 2H), 8.61 (d, J = 8 Hz, 2H), 8.56 (d, J = 8 Hz, 2H), 8.22 (t, J = 8 Hz, 1H), 8.03 (td, J = 8, 1 Hz, 2H), 7.51 – 7.43 (ddd, J = 8, 6, 1 Hz, 2H) ; ESI-MS (MeCN): Calculated 476.0409 for [M -Br]$^+$, Observed 476.0355

IV-2b *mer,cis*[Re(CO)$_2$Br(κ^3N-*Lb*)] Y=74% (72 mg) dark brown solid; ^{1}H NMR (400 MHz, Acetone-d^6) δ = 8.79 (d, J = 6 Hz, 2H), 8.32 (s, 2H), 8.27 (d, J = 1 Hz, 2H), 7.27 (dd, J = 6, 1 Hz, 2H), 2.72 (s, 3H), 2.58 (s, 6H) ; ^{13}C NMR (101 MHz, DMSO-d^6) δ 182.4, 156.4, 156.0, 155.7, 151.2, 149.2, 128.6, 125.0, 122.6, 21.4, 20.5 ; ESI-MS (MeCN): Calculated 518.0879 for [M -Br]$^+$,Observed 518.0859 ; Elemental analysis for $C_{20}H_{17}BrN_3O_2Re$, Calculated: C(%) 40.21, N(%) 7.03, H(%) 2.87, Found: C(%) 39.92, N(%) 6.78, H(%) 2.79.

IV-2c *mer,cis*[Re(CO)$_2$Br(κ^3N-*Lc*)] Y=73% (69 mg) dark brown solid; ^{1}H NMR (400 MHz, Acetone-d^6) δ = 9.03 (d, J = 5 Hz, 2H), 8.79 (s, 2H), 8.67 (d, J = 8 Hz, 2H), 8.12 (d, J = 7 Hz, 2H), 8.02 (t, J = 8 Hz, 2H), 7.65 (t, J = 7 Hz, 2H), 7.60 (d, J = 7 Hz, 1H), 7.48 (t, J 7 Hz, 2H) ; ^{13}C NMR (101 MHz, DMSO-d^6) δ 181.1, 156.9, 156.7, 156.6, 150.7, 137.5, 135.9, 130.6, 129.2, 128.3, 128.0, 124.8, 119.5; ESI-MS (MeCN): Calculated 552.0722 for [M -Br]$^+$, Observed 552.0734 ; Elemental analysis for $C_{23}H_{15}BrN_3O_2Re$,0.5 H_2O , Calculated: C(%) 43.13, N(%) 6.56, H(%) 2.52, Found: C(%) 43.08, N(%) 6.41, H(%) 2.28.

IV-2d *mer,cis*[Re(CO)$_2$Br(κ^3N-*Ld*)] Y=79% (76 mg) dark brown solid ; ^{1}H NMR (400 MHz, Acetone-d^6) δ = 9.04 (d, J = 6 Hz, 2H), 8.86 (s, 2H), 8.69 (d, J = 8 Hz, 2H), 8.25 (d, J = 9 Hz, 2H), 8.03 (t, J = 8 Hz, 2H), 7.95 (d, J = 8 Hz, 2H), 7.80 (d, J = 7 Hz, 2H), 7.60 – 7.40 (m, 5H) ; ^{13}C NMR (101 MHz, DMSO-d^6) δ 181.1, 156.9, 156.8, 156.7, 150.0, 142.2, 139.0, 137.5, 134.7, 129.1, 128.6, 128.3, 128.2, 127.3, 126.9, 124.8, 119.2; ESI-MS (MeCN): Calculated 628.1036

for [M -Br]$^+$,Observed 628.1021 ; Elemental analysis for $C_{29}H_{19}BrN_3O_2Re$,0.5 H_2O , Calculated: C(%) 48.61, N(%) 5.86, H(%) 2.81, Found: C(%) 48.48, N(%) 5.72, H(%) 2.52.

IV-2e *mer,cis*[Re(CO)$_2$Br(κ^3N-*Le*)] Y=90% (86 mg) dark brown solid ; ^{1}H NMR (400 MHz, DMSO-d^6) δ = 9.03 (s, 2H), 8.92 (d, J = 5 Hz, 2H), 8.89 (d, J = 6 Hz, 2H), 8.81 (d, J = 8 Hz, 2H), 8.21 (d, J = 6 Hz, 2H), 8.10 (t, J = 8 Hz, 2H), 7.52 (ddd, J = 8, 6, 1 Hz, 2H) ; ESI-MS (MeCN): Calculated 533.0675 for [M -Br]$^+$,Observed 533.0736

Complexes **IV-3a-e** were prepared following published procedures for **IV-3a** and **IV-3e**. The suitable precursor complex **IV-2** (50 mg) was dissolved in pyridine (10 mL) under N_2. To this solution, protected from light with aluminum foil, was added 1.25 eq. of silver triflate. The mixture was refluxed for 5 h, still under N_2, turning dark green. Once cooled to RT, it was filtered through Celite and precipitated by addition of an aqueous solution of KPF_6, then filtered and washed with water. The greyish green precipitate was purified on Al_2O_3 (DCM/acetone 2/8). The green fraction was collected, its volume reduced before being poured in Et_2O to precipitate the final compound. The solid was dried in air and then in a 100°C oven overnight before storage in a desiccator.

IV-3a *mer,cis*[Re(CO)$_2$(py)(κ^3N-*La*)](PF$_6$) Y=70 % (44mg) ^{1}H NMR (400 MHz, Acetone-d^6) δ = 9.14 (ddd, J = 6, 1, 1 Hz, 2H), 8.67 (d, J = 8 Hz, 2H), 8.60 (ddd, J = 8, 1, 1 Hz, 2H), 8.38 (t, J = 8 Hz, 1H), 8.28 (dd, J = 7, 2 Hz, 2H), 8.18 (td, J = 8, 2 Hz, 2H), 7.91 (tt, J = 8, 2 Hz, 1H), 7.68 (ddd, J = 8, 6, 1 Hz, 2H), 7.36 (ddd, J = 8, 5, 1 Hz, 2H). ; ESI-MS (MeCN): Calculated 555.0826 for [M -PF$_6$]$^+$, Observed 555.0796

IV-3b *mer,cis*[Re(CO)$_2$(py)(κ^3N-*Lb*)](PF$_6$) Y=71% (53 mg, starting with 60 mg of **VI-2b**) ^{1}H NMR (400 MHz, Acetone-d^6) δ = 8.93 (d, J = 6 Hz, 2H), 8.54 (s, 2H), 8.45 (d, J = 1 Hz, 2H), 8.24 (dd, J = 7, 1 Hz, 2H), 7.90 (tt, J = 8, 2 Hz, 2H), 7.49 (dd, J = 6, 1 Hz, 2H), 7.35 (ddd, J = 8, 6, 1 Hz, 2H), 2.76 (s, 3H), 2.62 (s, 6H) ; ^{13}C NMR (101 MHz, DMSO-d^6) δ 212.69, 187.76, 156.09, 156.07, 155.80, 152.93, 150.89, 149.97, 139.25, 130.06, 126.57, 126.01, 123.96, 21.62, 20.65 ; ESI-MS (MeCN): Calculated 597.1295 for [M -PF$_6$]$^+$,Observed 597.1353 ; Elemental analysis for $C_{25}H_{22}N_4O_2RePF_6$, Calculated: C(%) 40.49, N(%) 7.55, H(%) 2.99, Found: C(%) 40.63, N(%) 7.45, H(%) 2.84.

IV-3c *mer,cis*[Re(CO)$_2$(py)(κ^3N-*Lc*)](PF$_6$) Y=60% (37 mg) ^{1}H NMR (400 MHz, Acetone-d^6) δ = 9.16 (dd, J = 6, 1 Hz, 2H), 8.99 (s, 2H), 8.84 (d, J = 8 Hz, 2H), 8.33 (dd, J = 6, 2 Hz, 2H), 8.21 (td, J = 8, 2 Hz, 2H), 8.13 (dd, J = 8, 2 Hz, 2H), 7.92 (tt, J = 8, 2 Hz, 1H), 7.72 – 7.61 (m, 5H), 7.37 (ddd, J = 8, 6, 1 Hz, 2H) ; ^{13}C NMR (101 MHz, DMSO-d^6) δ 212.90, 186.75, 156.80, 156.76, 156.71, 151.67, 150.10, 139.38, 138.90, 135.33, 131.00, 129.79, 129.25, 128.06, 126.66, 125.71, 120.79 ; ESI-MS (MeCN): Calculated 631.1139 for [M -PF$_6$]$^+$, Observed 631.1070 ; Elemental analysis for $C_{28}H_{20}N_4O_2Re\ PF_6$,0.5$H_2O$, Calculated: C(%) 42.86, N(%) 7.14, H(%) 2.70, Found: C(%) 42.91, N(%) 6.99, H(%) 2.70.

IV-3d *mer,cis*[Re(CO)$_2$(py)(κ^3N-*Ld*)](PF$_6$) Y=59% (36 mg) ^{1}H NMR (400 MHz, Acetone-d^6) δ = 9.17 (dd, J = 6, 1 Hz, 2H), 9.07 (s, 1H), 8.87 (d, J = 8 Hz, 2H), 8.34 (dd, J = 7, 2 Hz, 2H), 8.27 (d, J = 9 Hz, 2H), 8.22 (td, J = 8, 2 Hz, 2H), 7.97 (d, J = 9 Hz, 2H), 7.92 (tt, J = 8, 2 Hz, 1H), 7.79 (d, J = 7 Hz, 2H), 7.70 (ddd, J = 8, 6, 1 Hz, 2H), 7.54 (t, J = 8 Hz, 2H), 7.45 (tt, J = 7, 2 Hz, 1H), 7.38 (ddd, J = 8, 5, 1 Hz, 2H) ; ^{13}C NMR (101 MHz, DMSO-d^6) δ 212.94, 186.82, 156.83, 156.75, 151.06, 150.11, 142.54, 139.39, 138.90, 138.80, 134.14, 129.79, 129.10, 128.68, 128.30, 127.64, 127.32, 126.93, 126.67, 125.73, 120.49 ; ESI-MS (MeCN): Calculated 707.1458 for [M -PF$_6$]$^+$, Observed 707.1436 ; Elemental analysis for $C_{34}H_{24}N_4O_2RePF_6$,H_2O , Calculated: C(%) 46.95, N(%) 6.44, H(%) 3.01, Found: C(%) 47.02, N(%) 6.21, H(%) 3.01.

IV-3e *mer,cis*[Re(CO)$_2$(py)(κ^3N-*Le*)](PF$_6$) Y=50% (30 mg) ^{1}H NMR (400 MHz, Acetone-d^6) δ = 9.18 (dd, J = 6, 1 Hz, 2H), 9.10 (s, 2H), 8.90 – 8.81 (m, 4H), 8.32 (dd, J = 7, 2 Hz, 2H), 8.23 (td, J = 8, 2 Hz, 2H), 8.09 (dd, J = 5, 2, 2H), 7.92 (tt, J = 8, 2 Hz, 1H), 7.72 (ddd, J = 8, 6, 1 Hz, 2H), 7.40 – 7.32 (m, 2H) ; ESI-MS (MeCN): Calculated 632.1097 for [M -PF$_6$]$^+$, Observed 632.1074.

Complexes **IV-4a** and **IV-4b** were prepared according to literature. The suitable complex **IV-2** (50 mg) were dissolved in THF (50 mL) under N_2. To this solution, protected from light with aluminum foil, was added 1.25 eq. of silver triflate and 10 eq. of triphenylphosphine. The mixture was refluxed for 5 h, still under N_2, turning dark green. The same work-up as for complexes **3** was used to obtain **4** as a green solid.

IV-4a *mer,cis*[Re(CO)$_2$(PPh$_3$)(κ^3N-*La*)](PF$_6$) Y=50% (42 mg) ^{1}H NMR (400 MHz, Acetone-d^6) δ = 9.22 (d, J = 6 Hz, 2H), 8.35 (d, J = 8 Hz, 2H), 8.29 (d, J = 8 Hz, 2H), 8.17 (t, J = 8 Hz, 2H), 7.96 (t, J = 8 Hz, 2H), 7.53 – 7.45 (m, 4H), 7.40 (td, J = 7, 1 Hz, 3H), 7.29 (td, J = 8, 2 Hz, 6H), 7.17 – 7.06 (m, 6H) ; ^{31}P NMR (162 MHz, Acetone-d^6) δ 14.91 ; ESI-MS (MeCN): Calculated 738.1322 for [M -PF$_6$]$^+$, Observed 738.1291

IV-4b *mer,cis*[Re(CO)$_2$(PPh$_3$)(κ^3N-*Lb*)](PF$_6$) Y=66% (61 mg, starting with 60 mg of **VI-2b**) ^{1}H NMR (400 MHz, Acetone-d^6) δ = 8.99 (d, J = 6 Hz, 2H), 8.19 (s, 2H), 8.15 (m, 2H), 7.40 (m, 3H), 7.30 (m, 6H), 7.14 (m, 6H), 2.72 (s, 3H), 2.53 (s, 6H) ; ^{31}P NMR (162 MHz, Acetone-d^6) δ 14.33 ; ^{13}C NMR (101 MHz, DMSO-d^6) δ 157.05, 155.42, 154.25, 151.54, 149.91, 132.45, 132.35, 130.30, 128.91, 128.82, 125.14, 123.56, 21.19, 20.33 ; ESI-MS (MeCN): Calculated 780.1784 for [M -PF$_6$]$^+$,Observed 780.1742 ; Elemental analysis for $C_{38}H_{32}N_4O_2ReP_2F_6$, Calculated: C(%) 49.35, N(%) 4.54, H(%) 3.49, Found: C(%) 49.26, N(%) 4.44, H(%) 3.48.

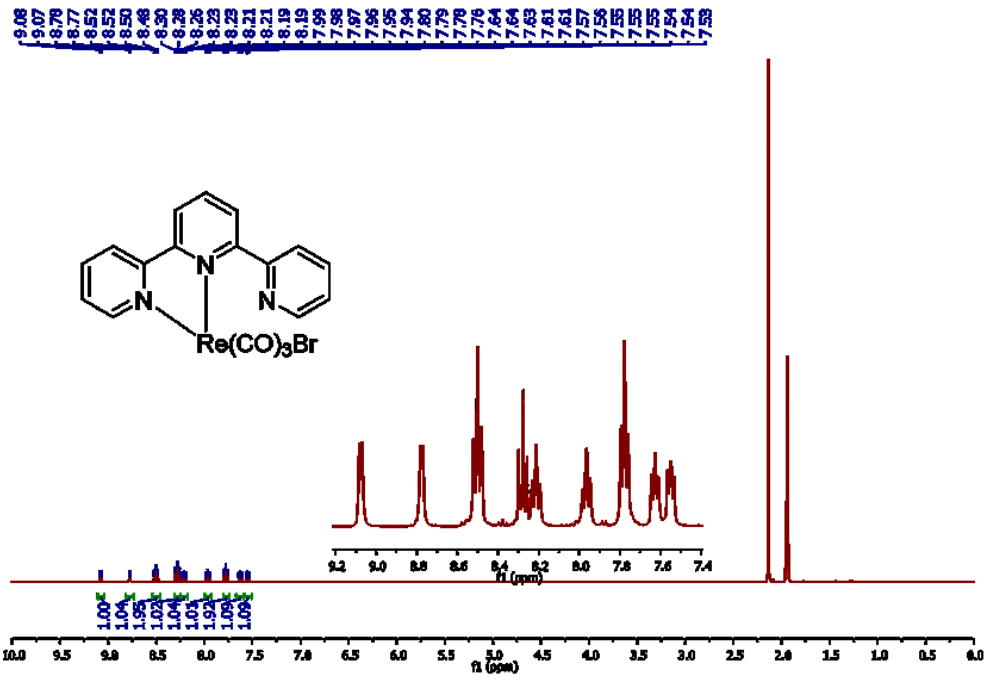

Figure XI.1. ^{1}H NMR spectra for complex **IV-1a** in CD_3CN

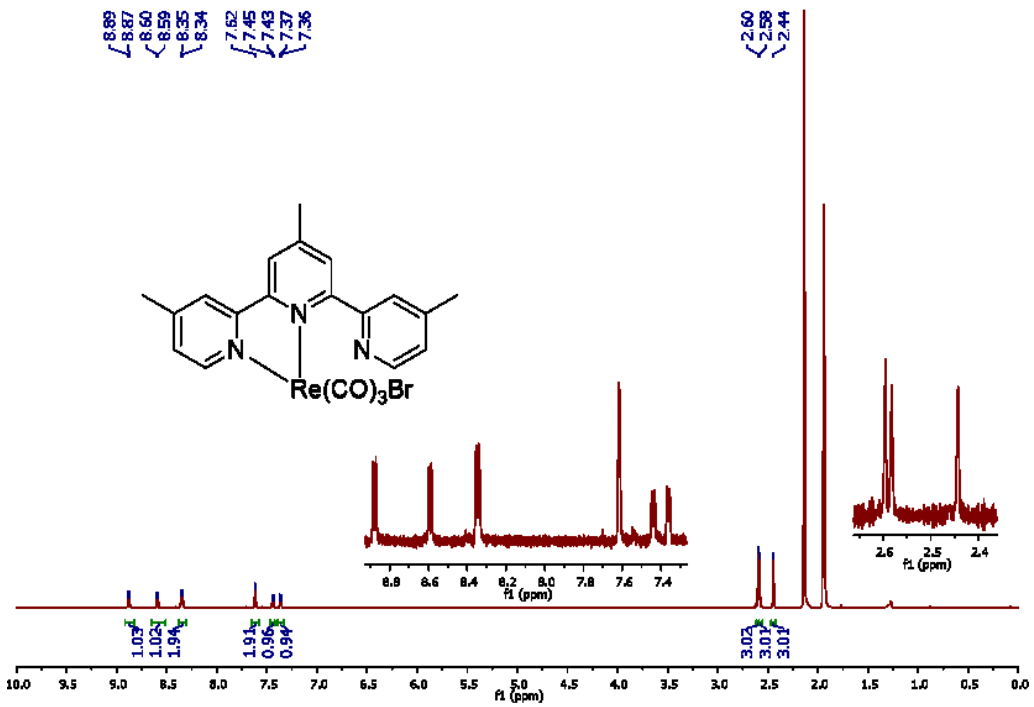

Figure XI.2. ^{1}H NMR spectra for complex **IV-1b** in CD_3CN

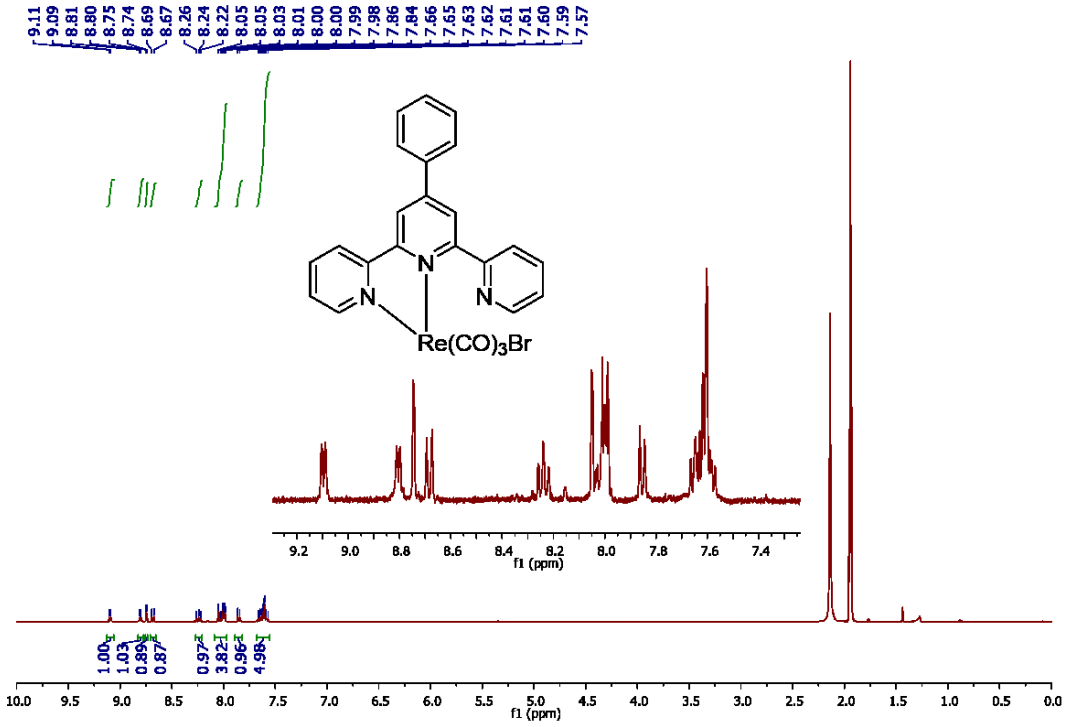

Figure XI.3. ^{1}H NMR spectra for complex **IV-1c** in CD_3CN

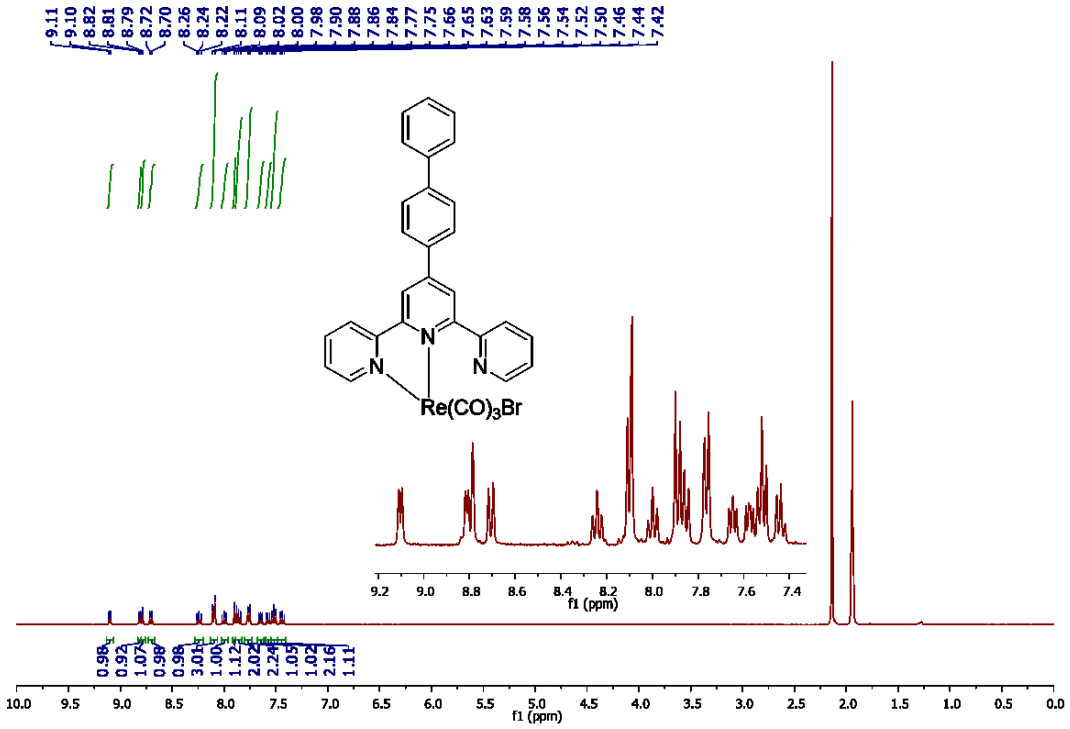

Figure XI.4. ^{1}H NMR spectra for complex **IV-1d** in CD_3CN

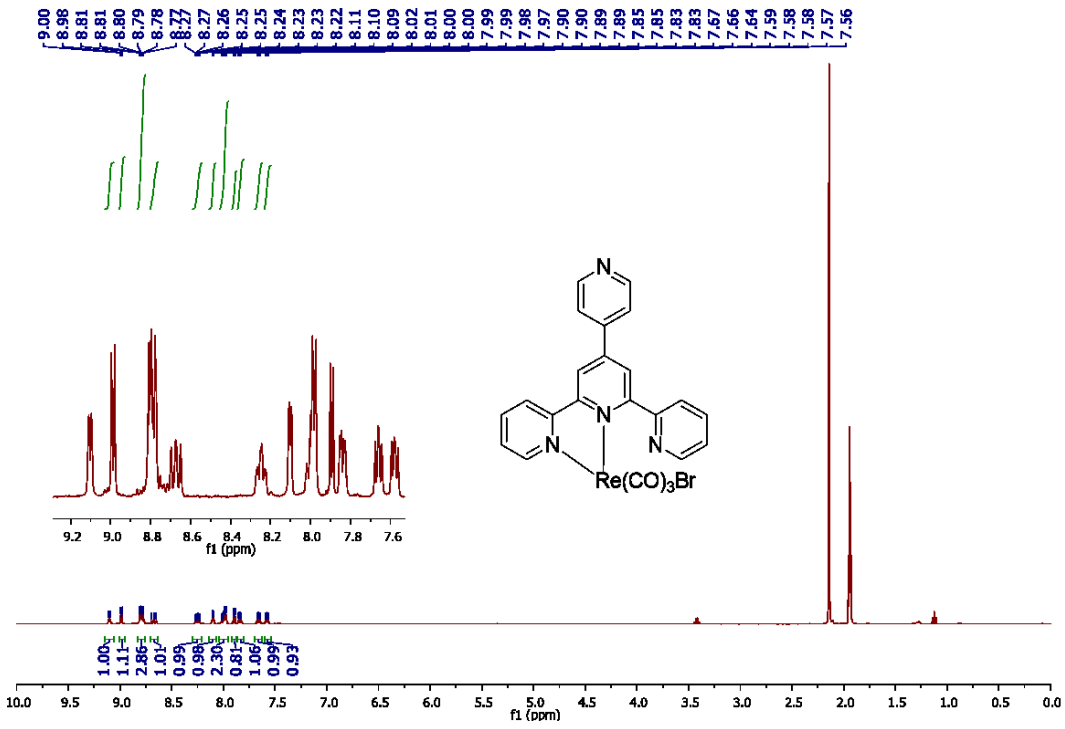

Figure XI.5. ^{1}H NMR spectra for complex **IV-1e** in CD_3CN

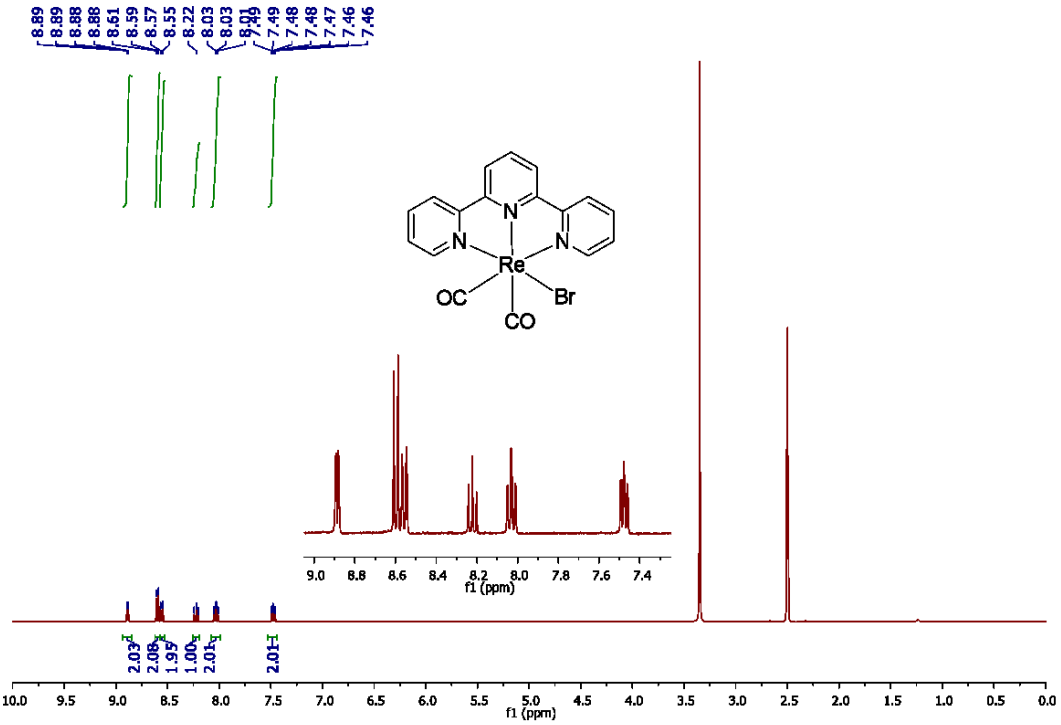

Figure XI.6. ^{1}H NMR spectra for complex **IV-2a** in (DMSO-d^{6})

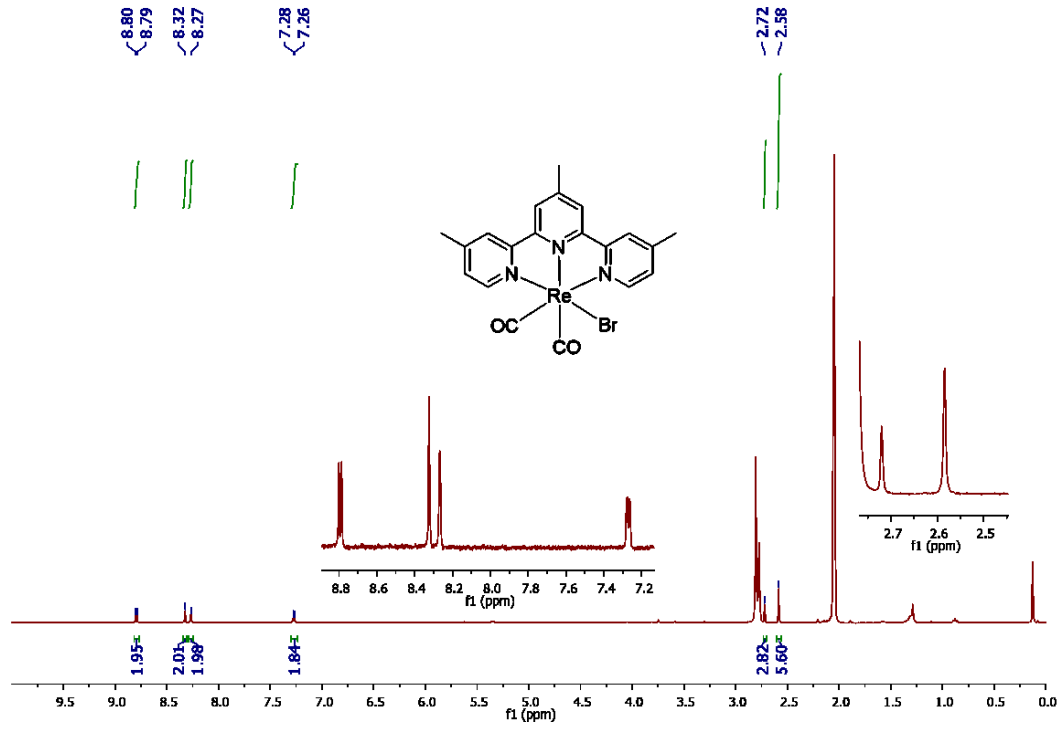

Figure XI.7. ^{1}H NMR spectra for complex **IV-2b** in (acetone-d^{6})

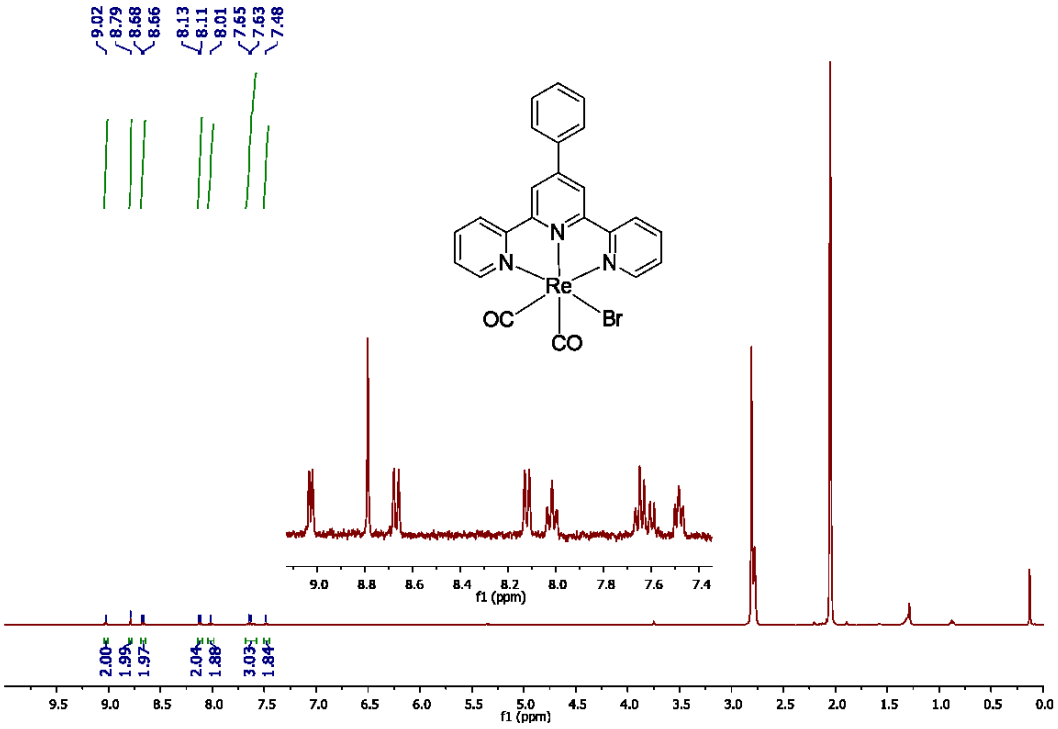

Figure XI.8.[1]H NMR spectra for complex **IV-2c** in (acetone-d[6])

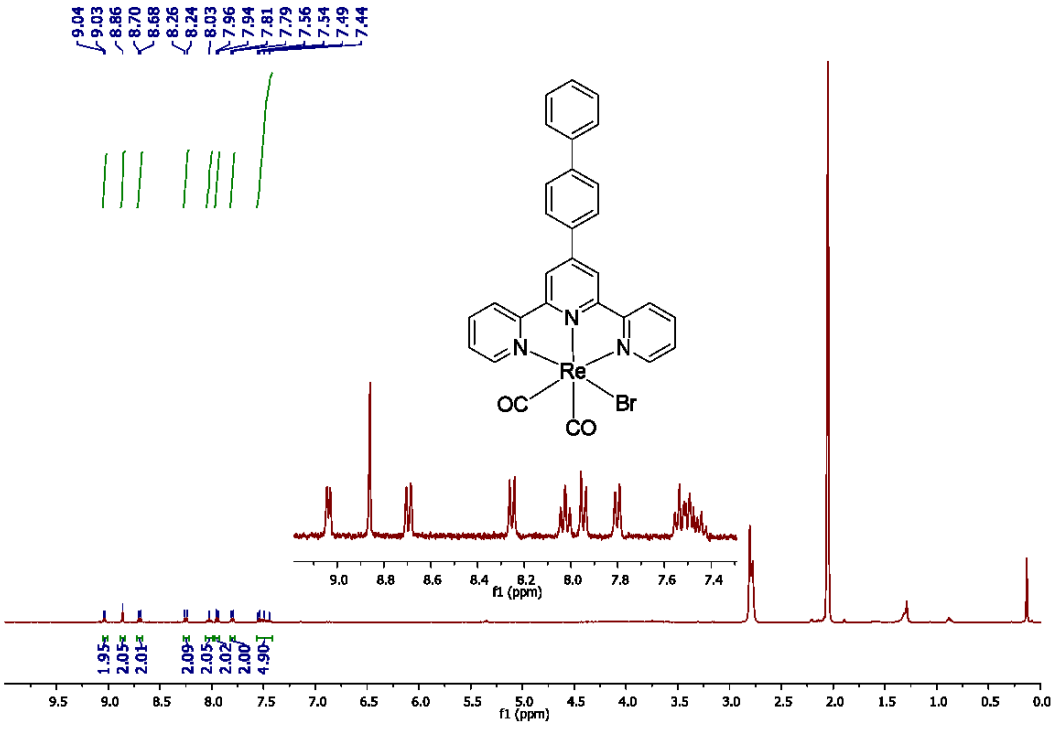

Figure XI.9. [1]H NMR spectra for complex **IV-2d** in (acetone-d[6])

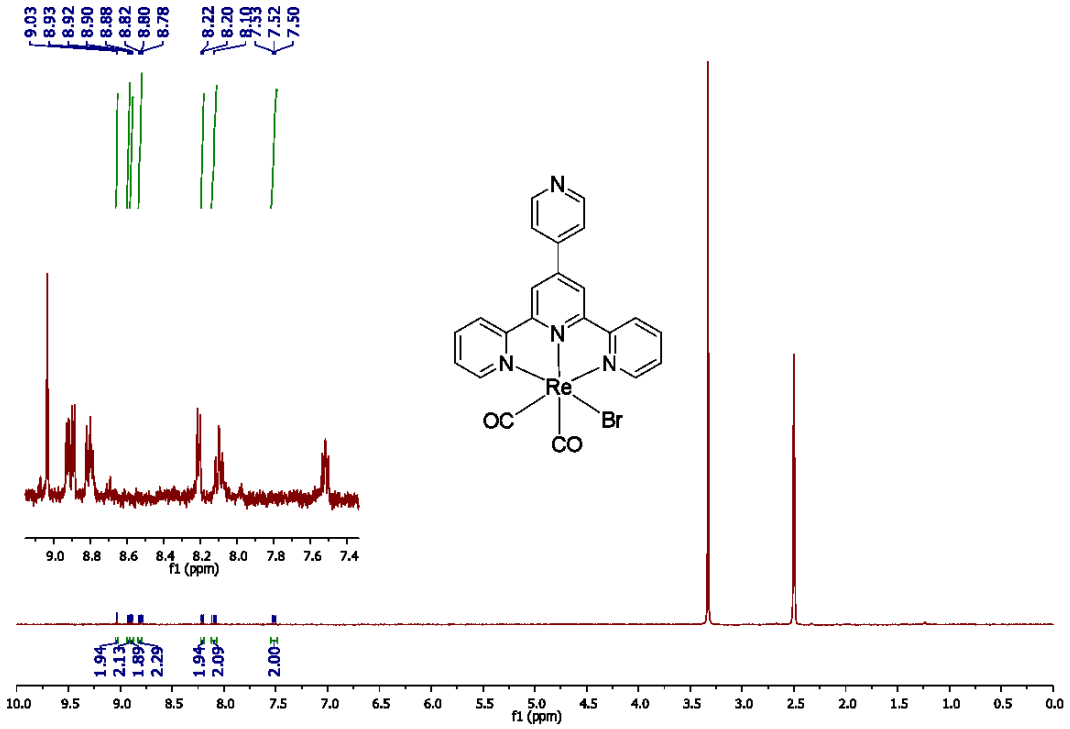

Figure XI.10. ^{1}H NMR spectra for complex **IV-2e** in (acetone-d^{6})

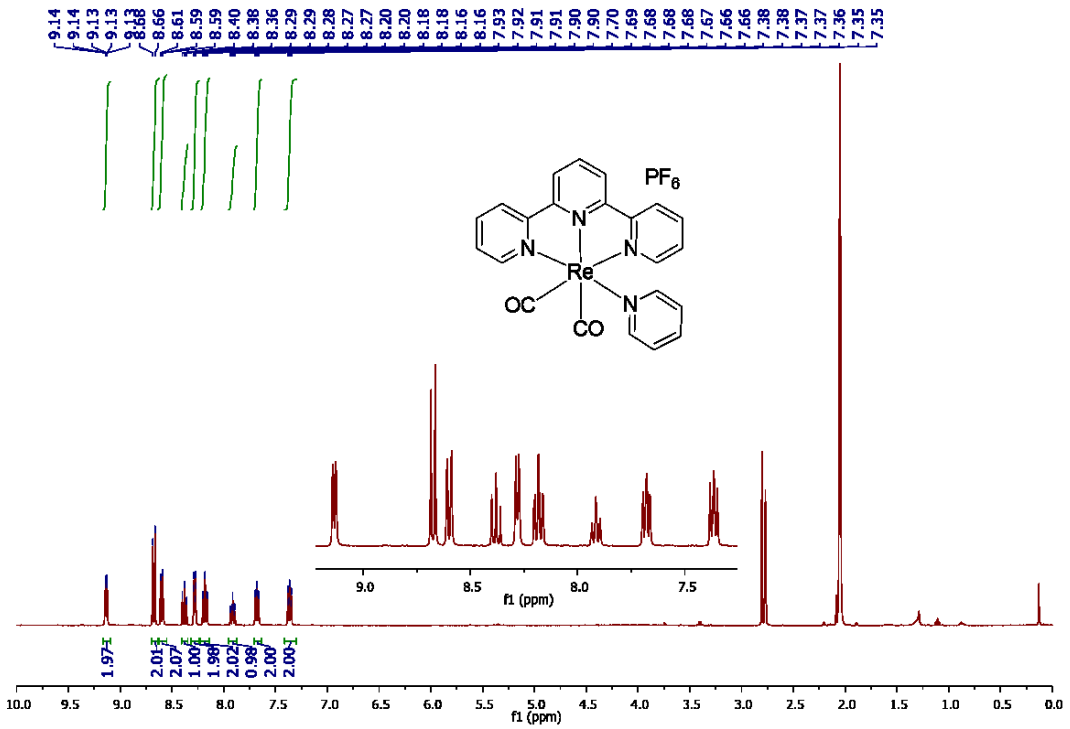

Figure XI.11. ^{1}H NMR spectra for complex **IV-3a** in (acetone-d^{6})

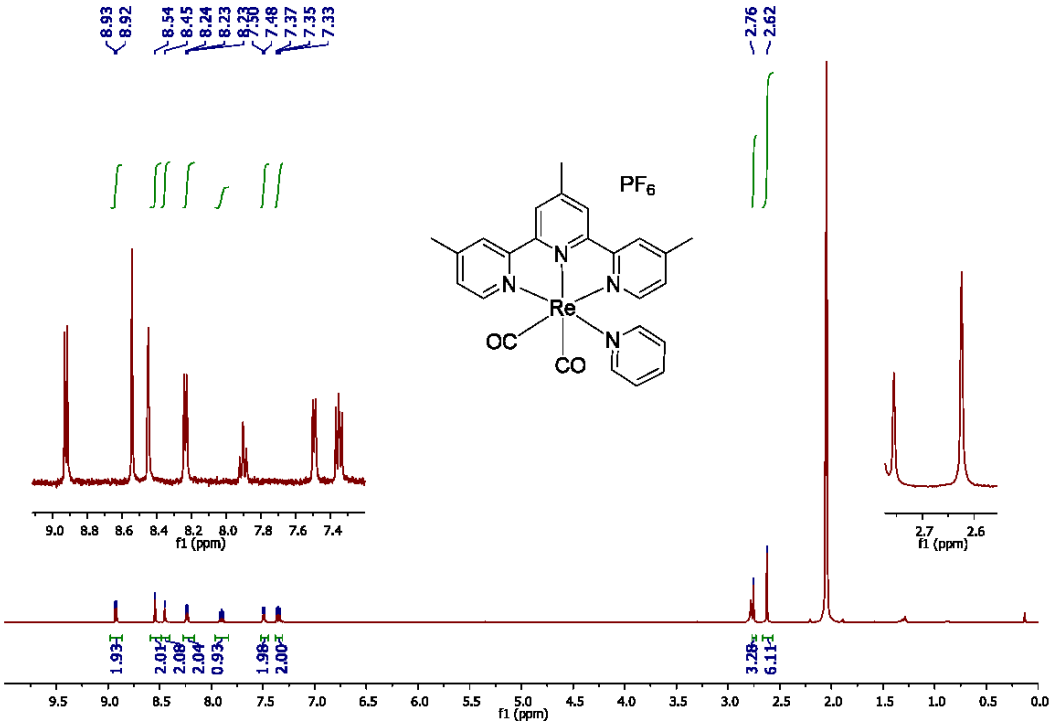

Figure XI.12. ^{1}H NMR spectra for complex **IV-3b** in (acetone-d^{6})

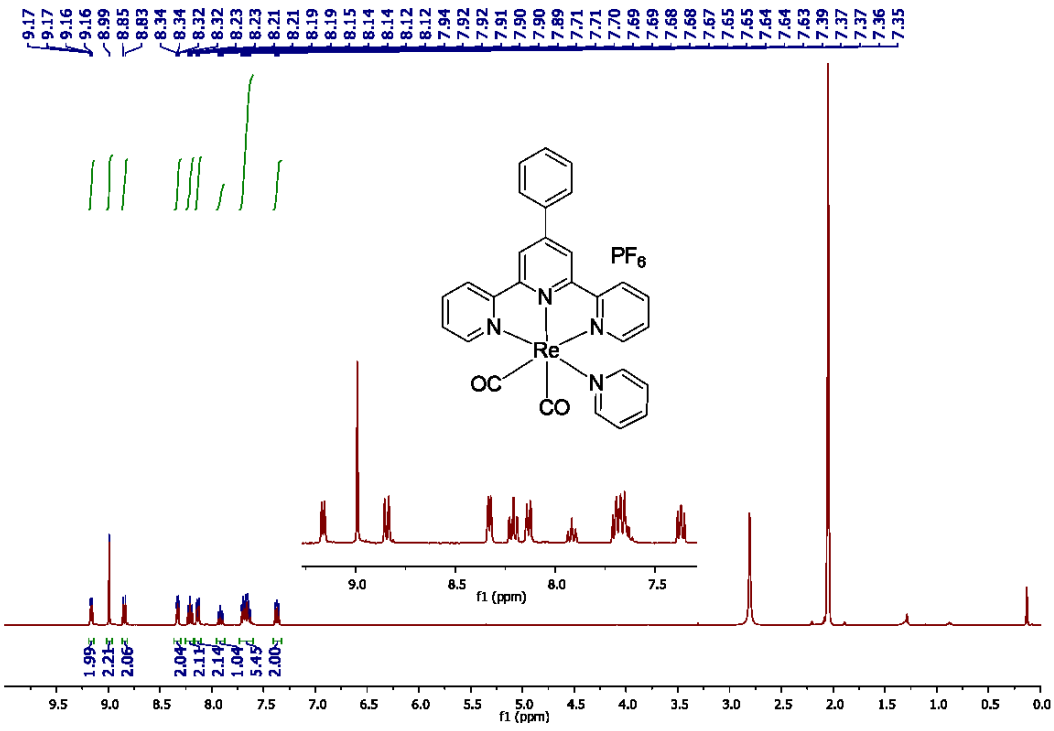

Figure XI.13. ^{1}H NMR spectra for complex **IV-3c** in (acetone-d^{6})

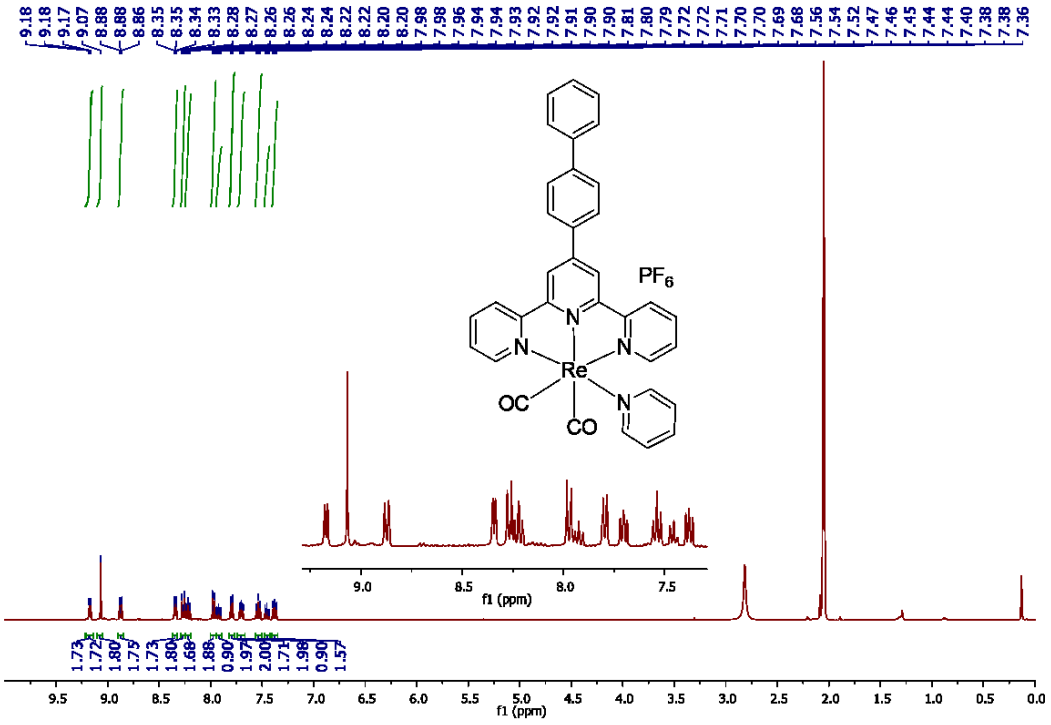

Figure XI.14. ^{1}H NMR spectra for complex **IV-3d** in (acetone-d^{6})

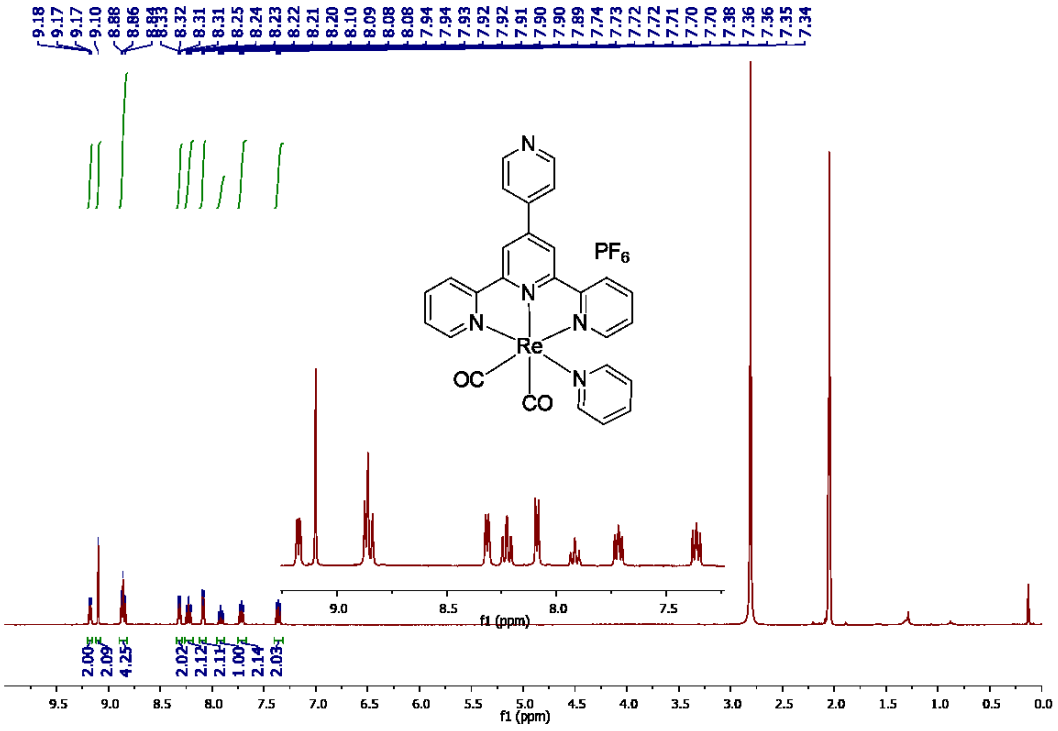

Figure XI.15. ^{1}H NMR spectra for complex **IV-3e** in (acetone-d^{6})

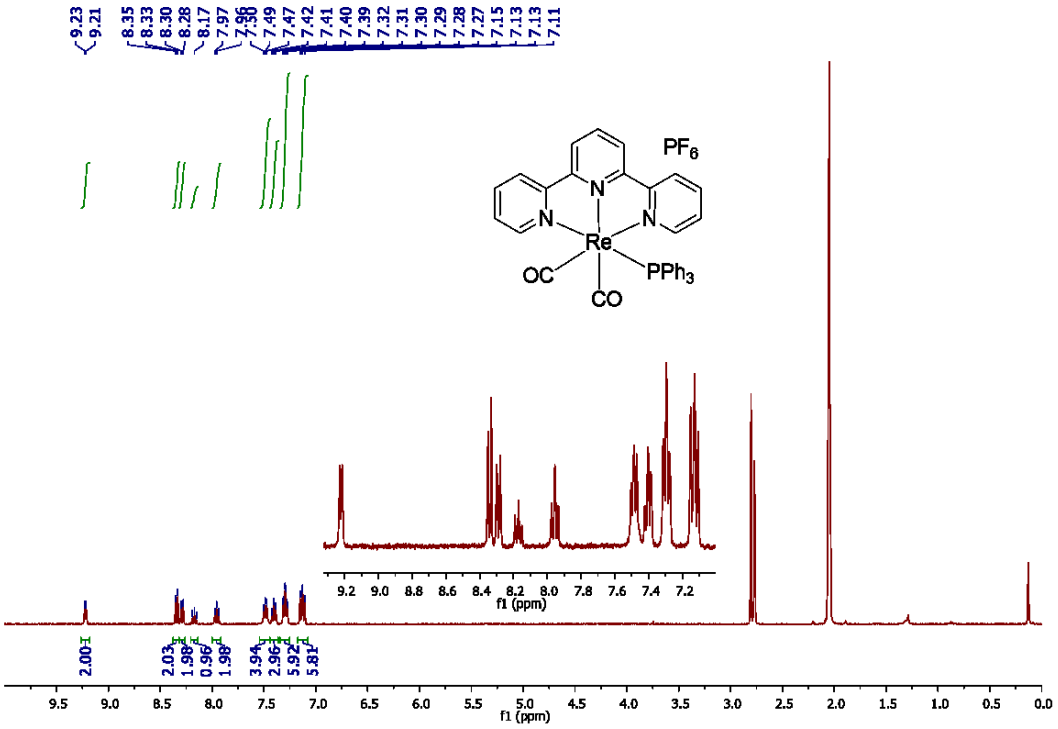

Figure XI.16. ^{1}H NMR spectra for complex **IV-4a** in (acetone-d^{6})

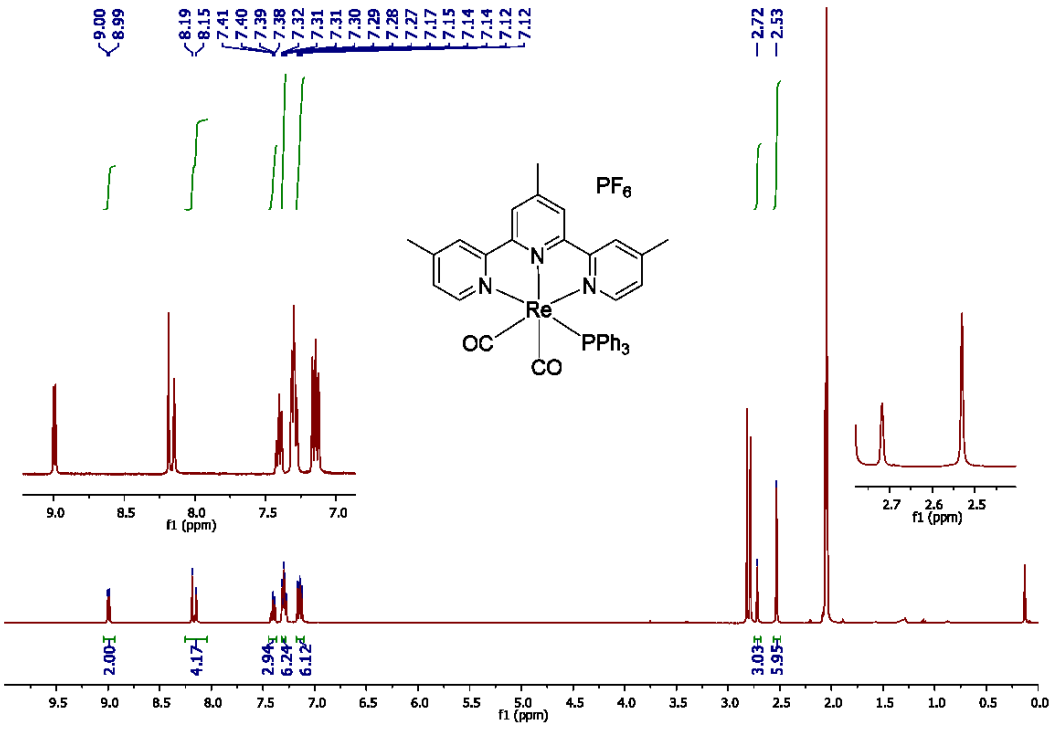

Figure XI.17. ^{1}H NMR spectra for complex **IV-4b** in (acetone-d^{6})

XI.2 Theoretical study and correlation with spectroscopic and electrochemical data

The theoretical absorption spectra were obtained by TD-DFT. We calculated the first 100 singlet-singlet transitions and the first 10 forbidden singlet-triplet transitions for all complexes. The geometries of the lower triplet state were optimized for all compounds and use to obtain a more precise value for the expected emission wavelength, involving single point calculation of the energy of the singlet state forced into the triplet geometry. These data are available in the corresponding section of the SI.

Table XI.1. Experimental and theoretical wavenumbers for the carbonyl IR active vibration modes

Compounds	**IV-1a**	**IV-1b**	**IV-1c**	**IV-1d**	**IV-1e**
ν(CO) exp. cm^{-1}	2021, 1913, 1891	2017, 1910, 1881	2013, 1908, 1875	2013, 1905, 1880	2019, 1925, 1880
ν(CO) calc. cm^{-1}	2003, 1881, 1859	2001, 1878, 1854	2003, 1881, 1858	2003, 1881, 1858	2003, 1883, 1860
Compounds	**IV-2a**	**IV-2b**	**IV-2c**	**IV-2d**	**IV-2e**
ν(CO) exp. cm^{-1}	1878, 1796	1880, 1793	1882, 1797	1884, 1801	1884, 1801
ν(CO) calc. cm^{-1}	1872, 1788	1867, 1780	1871, 1788	1871, 1788	1872, 1791
Compounds	**IV-3a**	**IV-3b**	**IV-3c**	**IV-3d**	**IV-3e**
ν(CO) exp. cm^{-1}	1905, 1819	1912, 1837	1897, 1813	1904, 1832	1912, 1859
ν(CO) calc. cm^{-1}	1887, 1805	1881, 1797	1885, 1804	1885, 1804	1887, 1809
Compounds	**IV-4a**	**IV-4b**			
ν(CO) exp. cm^{-1}	1929, 1862	1928, 1859			
ν(CO) calc. cm^{-1}	1895, 1811	1890, 1802			

XI.2.1 Orbitals data

Table XI.2. Selected molecular orbitals with relative Mulliken contributions of each fragments and energies for complex **IV-1a** (isovalue 0.05 e/Å^3)

Orbital	Energy and contributions	Orbital	Energy and contributions
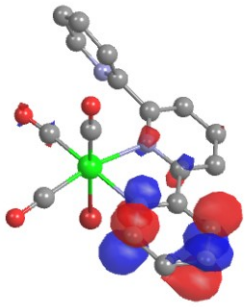 LUMO+2	-1.593 eV Re: 1% Br: 1% CO: 4% ''bpy'': 93% ''py'': 1%	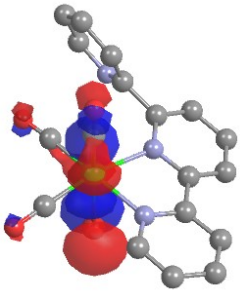 HOMO	-6.646 eV Re: 39% Br: 40% CO: 18% ''bpy'': 2% ''py'': 1%
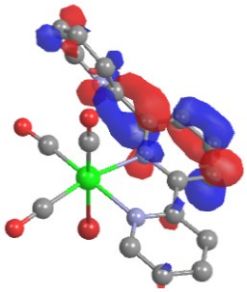 LUMO+1	-1.912 eV Re: 0% Br: 0% CO: 1% ''bpy'': 71% ''py'': 27%	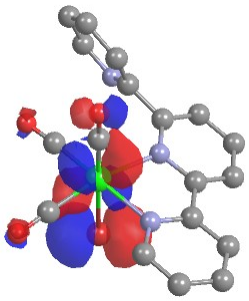 HOMO-1	-6.736 eV Re: 35% Br: 46% CO: 15% ''bpy'': 4% ''py'': 0%
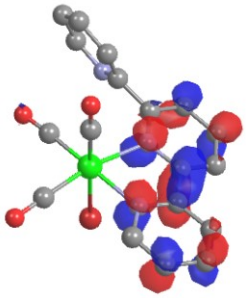 LUMO	-2.694 eV Re: 2% Br: 2% CO: 4% ''bpy'': 89% ''py'': 2%	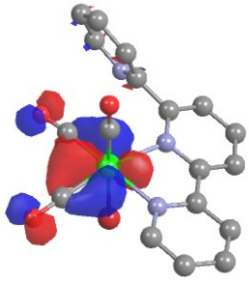 HOMO-2	-7.217 eV Re: 61% Br: 2% CO: 26% ''bpy'': 2% ''py'': 8%

Table XI.3. Selected molecular orbitals with relative Mulliken contributions of each fragments and energies for complex **IV-1b** (isovalue 0.05 e/Å^3)

Orbital	Energy and contributions	Orbital	Energy and contributions
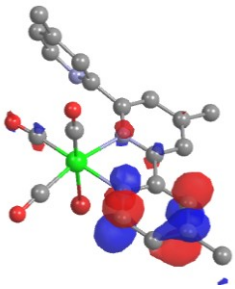 LUMO+2	-1.437 eV Re: 2% Br: 1% CO: 6% ''bpy'': 89% ''py'': 2%	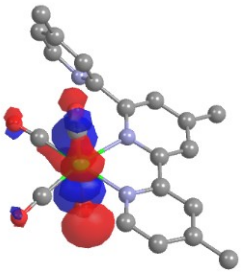 HOMO	-6.599 eV Re: 40% Br: 38% CO: 18% ''bpy'': 3% ''py'': 1%
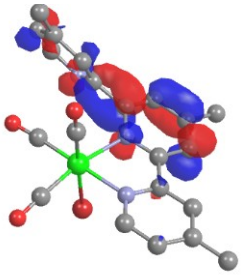 LUMO+1	-1.785 eV Re: 0% Br: 0% CO: 2% ''bpy'': 71% ''py'': 27%	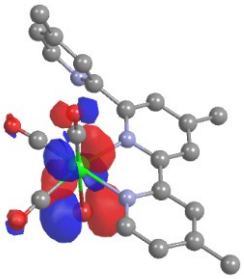 HOMO-1	-6.683 eV Re: 36% Br: 43% CO: 16% ''bpy'': 5% ''py'': 0%
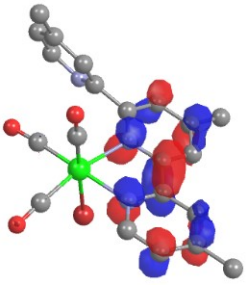 LUMO	-2.543 eV Re: 2% Br: 2% CO: 5% ''bpy'': 89% ''py'': 2%	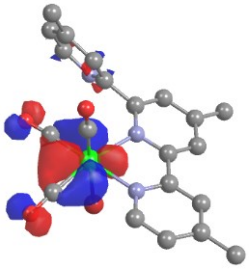 HOMO-2	-7.158 eV Re: 60% Br: 3% CO: 26% ''bpy'': 2% ''py'': 10%

Table XI.4. Selected molecular orbitals with relative Mulliken contributions of each fragments and energies for complex **IV-1c** (isovalue 0.05 e/Å^3)

Orbital	Energy and contributions	Orbital	Energy and contributions
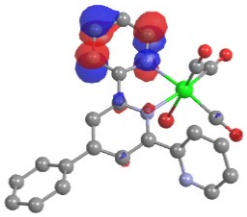 LUMO+2	-1.618 eV Re: 2% Br: 1% CO: 4% ''bpy'': 90% ''py'': 1% Ph: 2%	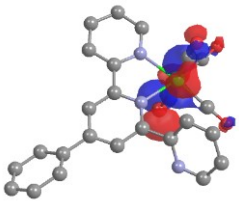 HOMO	-6.636 eV Re: 39% Br: 39% CO: 18% ''bpy'': 2% ''py'': 1% Ph: 1%
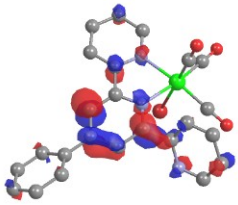 LUMO+1	-2.016 eV Re: 0% Br: 0% CO: 1% ''bpy'': 72% ''py'': 17% Ph: 9%	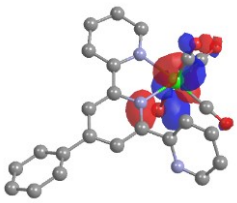 HOMO-1	-6.709 eV Re: 35% Br: 42% CO: 16% ''bpy'': 5% ''py'': 0% Ph: 2%
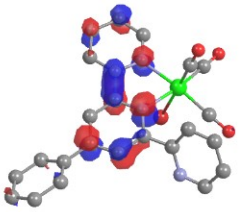 LUMO	-2.746 eV Re: 2% Br: 2% CO: 4% ''bpy'': 82% ''py'': 3% Ph: 7%	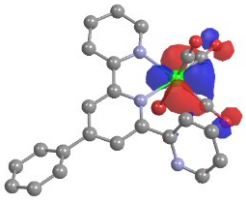 HOMO-2	-7.207 eV Re: 59% Br: 3% CO: 25% ''bpy'': 3% ''py'': 9% Ph: 2%

Table XI.5. Selected molecular orbitals with relative Mulliken contributions of each fragments and energies for complex **IV-1d** (isovalue 0.05 e/Å^3)

Orbital	Energy and contributions	Orbital	Energy and contributions
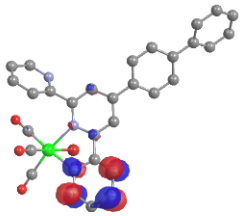 LUMO+2	-1.630 eV Re: 2% Br: 1% CO: 5% ''bpy'': 85% ''py'': 2% Ph_2: 5%	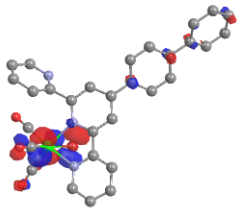 HOMO	-6.611 eV Re: 29% Br: 25% CO: 14% ''bpy'': 5% ''py'': 1% Ph_2: 26%
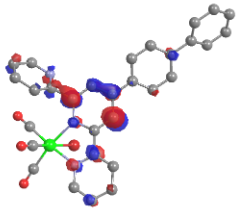 LUMO+1	-2.052 eV Re: 0% Br: 0% CO: 1% ''bpy'': 70% ''py'': 13% Ph_2: 15%	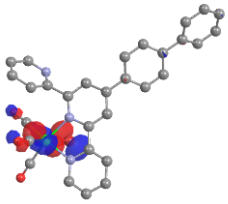 HOMO-1	-6.661 eV Re: 32% Br: 33% CO: 14% ''bpy'': 5% ''py'': 1% Ph_2: 16%
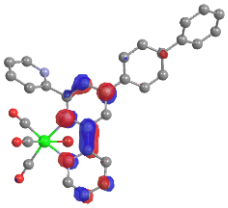 LUMO	-2.763 eV Re: 2% Br: 2% CO: 4% ''bpy'': 80% ''py'': 3% Ph_2: 10%	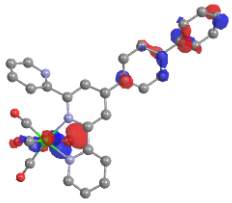 HOMO-2	-6.823 eV Re: 12% Br: 29% CO: 5% ''bpy'': 5% ''py'': 1% Ph_2: 48%

Table XI.6. Selected molecular orbitals with relative Mulliken contributions of each fragments and energies for complex **IV-1e** (isovalue 0.05 e/Å^3)

Orbital	Energy and contributions	Orbital	Energy and contributions
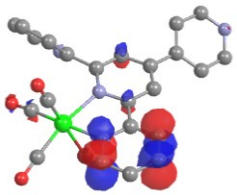 LUMO+2	-1.669 eV Re: 2% Br: 1% CO: 5% ''bpy'': 84% ''py'': 3% Py: 4%	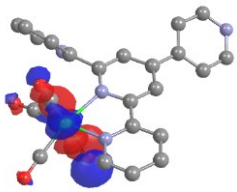 HOMO	-6.660 eV Re: 39% Br: 40% CO: 18% ''bpy'': 2% ''py'': 1% Py: 0%
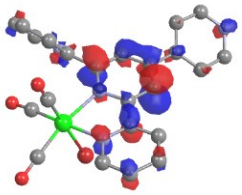 LUMO+1	-2.167 eV Re: 0% Br: 0% CO: 1% ''bpy'': 73% ''py'': 11% Py: 14%	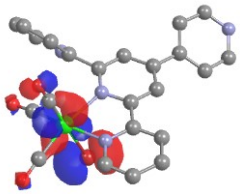 HOMO-1	-6.746 eV Re: 35% Br: 45% CO: 15% ''bpy'': 4% ''py'': 0% Py: 1%
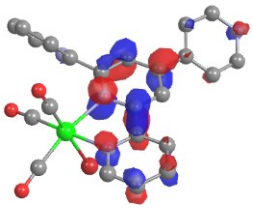 LUMO	-2.877 eV Re: 2% Br: 2% CO: 4% ''bpy'': 78% ''py'': 3% Py: 12%	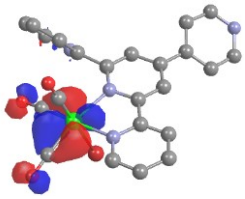 HOMO-2	-7.238 eV Re: 61% Br: 2% CO: 26% ''bpy'': 2% ''py'': 8% Py: 0%

Table XI.7. Selected molecular orbitals with relative Mulliken contributions of each fragments and energies for complex **IV-2a** (isovalue 0.05 e/Å^3)

Orbital	Energy and contributions	Orbital	Energy and contributions
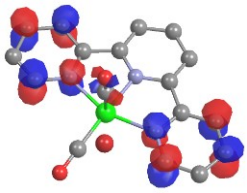 LUMO+2	-1.390 eV Re: 2% Br: 0% CO: 5% tpy: 93%	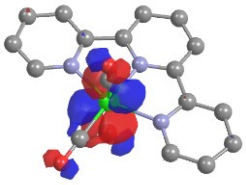 HOMO	-5.733 eV Re: 58% Br: 10% CO: 17% tpy: 15%
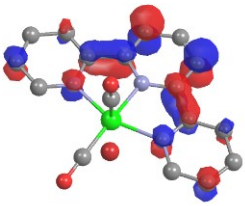 LUMO+1	-2.354 eV Re: 2% Br: 0% CO: 2% tpy: 96%	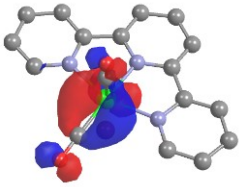 HOMO-1	-6.059 eV Re: 66% Br: 0% CO: 27% tpy: 7%
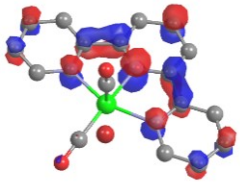 LUMO	-2.725 eV Re: 3% Br: 3% CO: 5% tpy: 90%	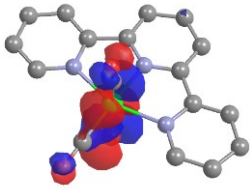 HOMO-2	-6.306 eV Re: 45% Br: 26% CO: 21% tpy: 8%

Table XI.8. Selected molecular orbitals with relative Mulliken contributions of each fragments and energies for complex **IV-2b** (isovalue 0.05 e/Å^3)

Orbital	Energy and contributions	Orbital	Energy and contributions
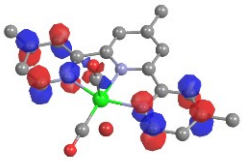 LUMO+2	-1.229 eV Re: 1% Br: 0% CO: 6% tpy: 93%	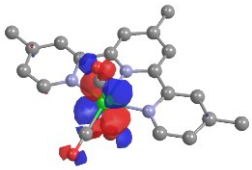 HOMO	-5.637 eV Re: 59% Br: 9% CO: 18% tpy: 15%
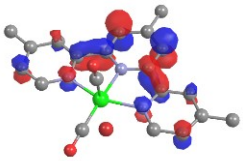 LUMO+1	-2.261 eV Re: 2% Br: 0% CO: 1% tpy: 97%	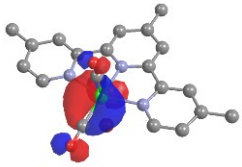 HOMO-1	-5.969 eV Re: 65% Br: 0% CO: 27% tpy: 8%
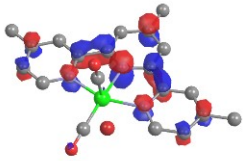 LUMO	-2.567 eV Re: 3% Br: 3% CO: 4% tpy: 90%	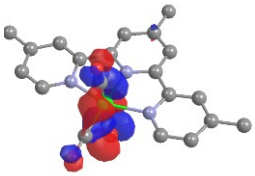 HOMO-2	-6.225 eV Re: 45% Br: 22% CO: 22% tpy: 8%

Table XI.9. Selected molecular orbitals with relative Mulliken contributions of each fragments and energies for complex **IV-2c** (isovalue 0.05 e/Å^3)

Orbital	Energy and contributions	Orbital	Energy and contributions
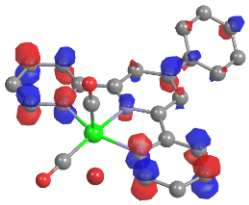 LUMO+2	-1.499 eV Re: 0% Br: 0% CO: 0% tpy: 85% ph: 15%	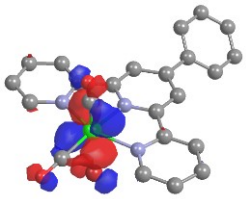 HOMO	-5.729 eV Re: 59% Br: 10% CO: 17% tpy: 14% ph: 0%
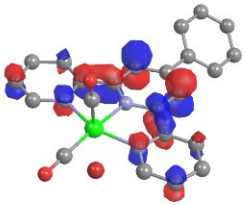 LUMO+1	-2.359 eV Re: 2% Br: 0% CO: 1% tpy: 96% ph: 1%	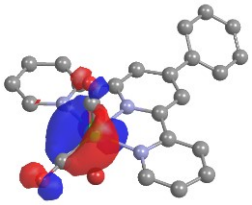 HOMO-1	-6.052 eV Re: 65% Br: 0% CO: 27% tpy: 8% ph: 0%
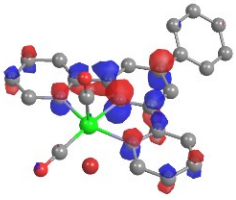 LUMO	-2.774 eV Re: 3% Br: 3% CO: 5% tpy: 84% ph: 6%	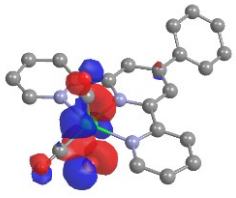 HOMO-2	-6.266 eV Re: 44% Br: 23% CO: 21% tpy: 8% ph: 3%

Table XI.10. Selected molecular orbitals with relative Mulliken contributions of each fragments and energies for complex **IV-2d** (isovalue 0.05 e/Å^3)

Orbital	Energy and contributions	Orbital	Energy and contributions
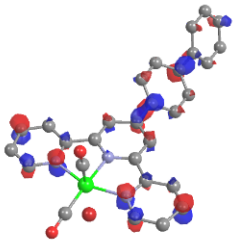 LUMO+2	-1.614 eV Re: 0% Br: 0% CO: 0% tpy: 60% ph2: 39%	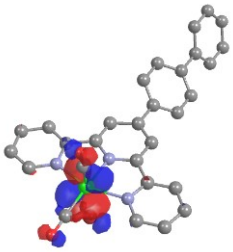 HOMO	-5.729 eV Re: 59% Br: 10% CO: 17% tpy: 14% ph2: 0%
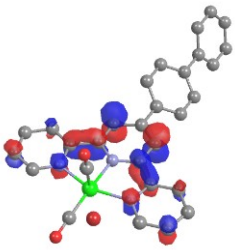 LUMO+1	-2.359 eV Re: 2% Br: 0% CO: 2% tpy: 96% ph2: 0%	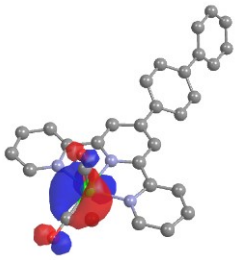 HOMO-1	-6.051 eV Re: 65% Br: 0% CO: 27% tpy: 8% ph2: 0%
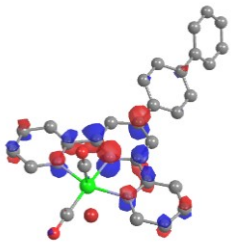 LUMO	-2.790 eV Re: 3% Br: 3% CO: 4% tpy: 82% ph2: 8%	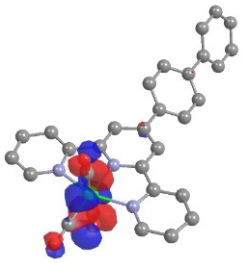 HOMO-2	-6.241 eV Re: 42% Br: 20% CO: 20% tpy: 8% ph2: 10%

Table XI.11. Selected molecular orbitals with relative Mulliken contributions of each fragments and energies for complex **IV-2e** (isovalue 0.05 e/Å^3)

Orbital	Energy and contributions	Orbital	Energy and contributions
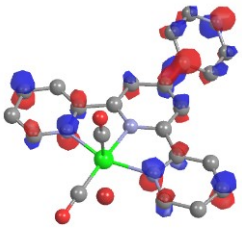 LUMO+2	-1.703 eV Re: 0% Br: 0% CO: 0% tpy: 63% py: 37%	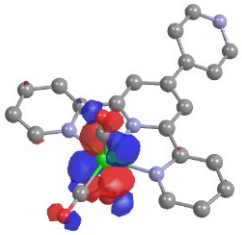 HOMO	-5.758 eV Re: 58% Br: 10% CO: 17% tpy: 14% py: 0%
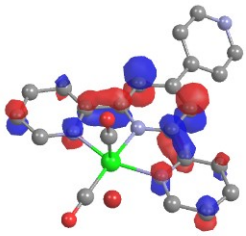 LUMO+1	-2.425 eV Re: 2% Br: 0% CO: 2% tpy: 96% py: 0%	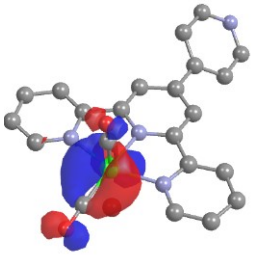 HOMO-1	-6.085 eV Re: 65% Br: 0% CO: 27% tpy: 8% py: 0%
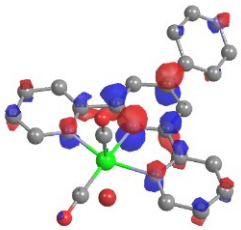 LUMO	-2.891 eV Re: 3% Br: 3% CO: 5% tpy: 80% py: 10%	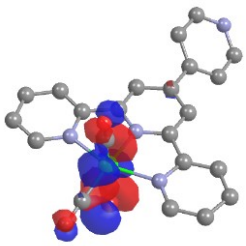 HOMO-2	-6.317 eV Re: 44% Br: 25% CO: 21% tpy: 8% py: 1%

Table XI.12. Selected molecular orbitals with relative Mulliken contributions of each fragments and energies for complex **IV-3a** (isovalue 0.05 e/Å^3)

Orbital	Energy and contributions	Orbital	Energy and contributions
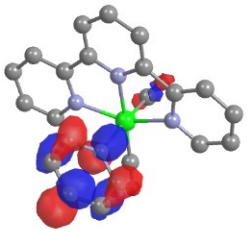 LUMO+2	-1.778 eV Re: 2% CO: 6% tpy: 4% py: 88%	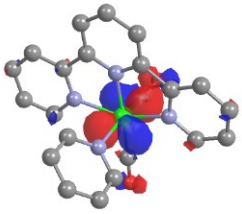 HOMO	-6.044 eV Re: 64% CO: 17% tpy: 17% py: 2%
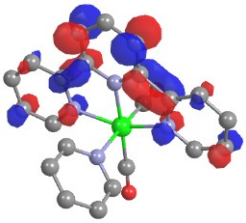 LUMO+1	-2.558 eV Re: 2% CO: 1% tpy: 96% py: 1%	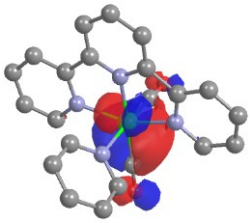 HOMO-1	-6.294 eV Re: 66% CO: 26% tpy: 8% py: 0%
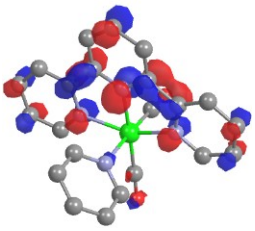 LUMO	-2.949 eV Re: 3% CO: 5% tpy: 91% py: 1%	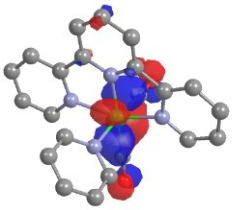 HOMO-2	-6.726 eV Re: 58% CO: 27% tpy: 12% py: 3%

Table XI.13. Selected molecular orbitals with relative Mulliken contributions of each fragments and energies for complex **IV-3b** (isovalue 0.05 e/Å^3)

Orbital	Energy and contributions	Orbital	Energy and contributions
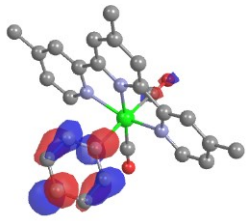 LUMO+2	-1.741 eV Re: 2% CO: 5% tpy: 3% py: 90%	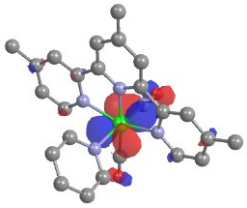 HOMO	-5.929 eV Re: 63% CO: 17% tpy: 18% py: 2%
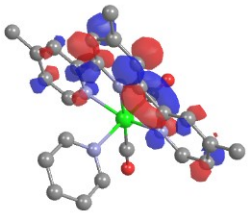 LUMO+1	-2.440 eV Re: 1% CO: 1% tpy: 97% py: 1%	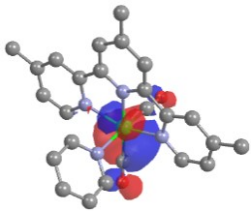 HOMO-1	-6.194 eV Re: 66% CO: 27% tpy: 8% py: 0%
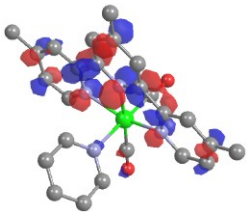 LUMO	-2.762 eV Re: 3% CO: 5% tpy: 92% py: 1%	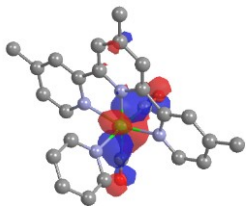 HOMO-2	-6.613 eV Re: 57% CO: 27% tpy: 13% py: 3%

Table XI.14. Selected molecular orbitals with relative Mulliken contributions of each fragments and energies for complex **IV-3c** (isovalue 0.05 e/Å^3)

Orbital	Energy and contributions	Orbital	Energy and contributions
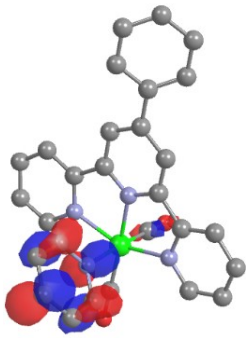 LUMO+2	-1.741 eV Re: 2% CO: 5% tpy: 5% ph: 0% py: 87%	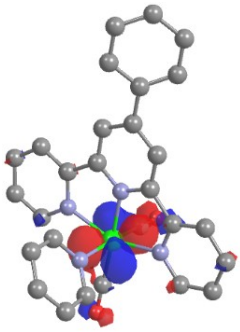 HOMO	-6.038 eV Re: 64% CO: 17% tpy: 17% ph: 0% py: 2%
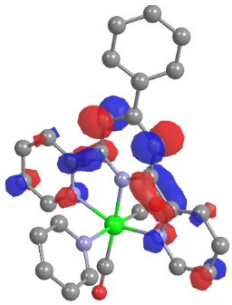 LUMO+1	-2.558 eV Re: 2% CO: 1% tpy: 96% ph: 0% py: 1%	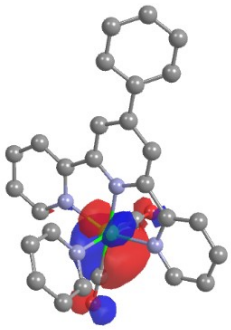 HOMO-1	-6.281 eV Re: 66% CO: 26% tpy: 8% ph: % py: 0%
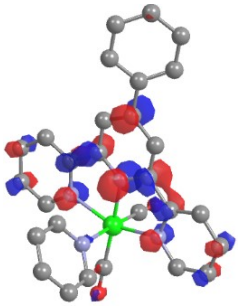 LUMO	-2.986 eV Re: 3% CO: 5% tpy: 86% ph: 6% py: 1%	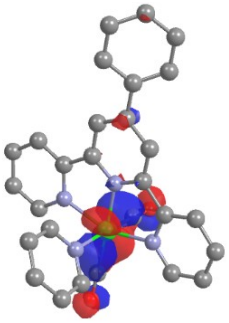 HOMO-2	-6.644 eV Re: 53% CO: 25% tpy: 12% ph: 7% py: 3%

Table XI.15. Selected molecular orbitals with relative Mulliken contributions of each fragments and energies for complex **IV-3d** (isovalue 0.05 e/Å^3)

Orbital	Energy and contributions	Orbital	Energy and contributions
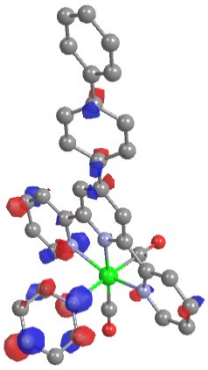 LUMO+2	-1.764 eV Re: 1% CO: 3% tpy: 38% ph2: 20% py: 38%	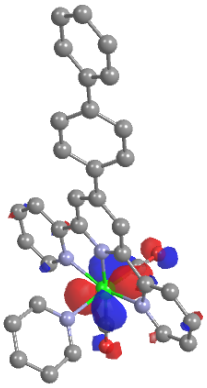 HOMO	-6.036 eV Re: 64% CO: 17% tpy: 17% ph2: 0% py: 2%
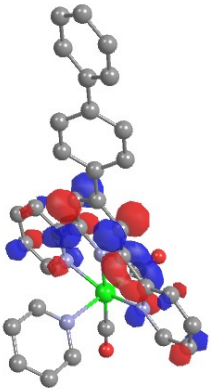 LUMO+1	-2.555 eV Re: 2% CO: 1% tpy: 96% ph2: 0% py: 1%	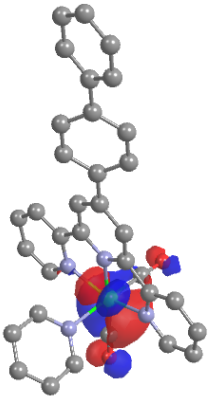 HOMO-1	-6.279 eV Re: 66% CO: 26% tpy: 8% ph2: 0% py: 0%
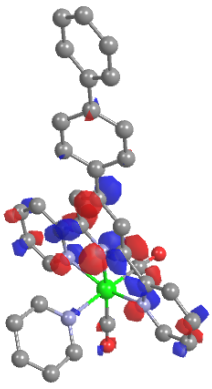 LUMO	-2.999 eV Re: 3% CO: 5% tpy: 84% ph2: 8% py: 1%	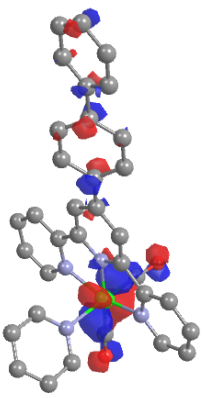 HOMO-2	-6.560 eV Re: 37% CO: 18% tpy: 11% ph2: 32% py: 2%

Table XI.16. Selected molecular orbitals with relative Mulliken contributions of each fragments and energies for complex **IV-3e** (isovalue 0.05 e/Å^3)

Orbital	Energy and contributions	Orbital	Energy and contributions
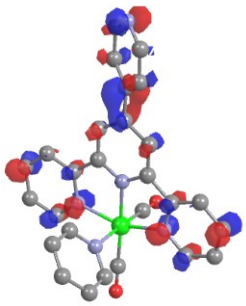 LUMO+2	-1.863 eV Re: 0% CO: 0% tpy: 66% 4py: 31% py: 2%	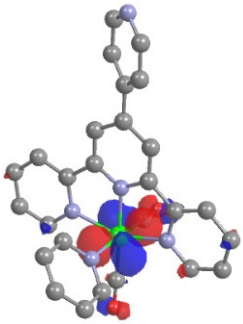 HOMO	-6.071 eV Re: 64% CO: 17% tpy: 17% 4py: 0% py: 2%
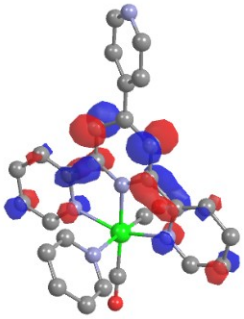 LUMO+1	-2.628 eV Re: 2% CO: 1% tpy: 96% 4py: 0% py: 1%	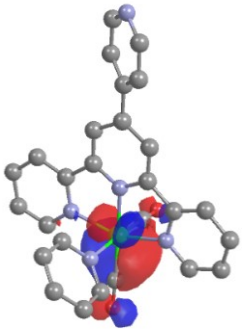 HOMO-1	-6.315 eV Re: 66% CO: 26% tpy: 8% 4py: 0% py: 0%
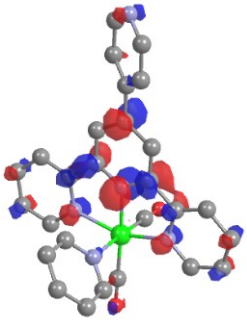 LUMO	-3.101 eV Re: 3% CO: 5% tpy: 82% 4py: 9% py: 1%	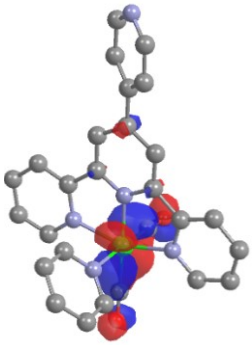 HOMO-2	-6.726 eV Re: 57% CO: 26% tpy: 12% 4py: 3% py: 3%

Table XI.17. Selected molecular orbitals with relative Mulliken contributions of each fragments and energies for complex **IV-4a** (isovalue 0.05 e/Å^3)

Orbital	Energy and contributions	Orbital	Energy and contributions
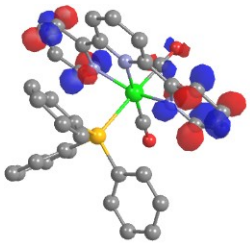 LUMO+2	-1.778 eV Re: 2% CO: 7% tpy: 86% PPh3: 4%	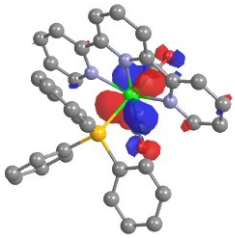 HOMO	-6.186 eV Re: 64% CO: 17% tpy: 17% PPh3: 2%
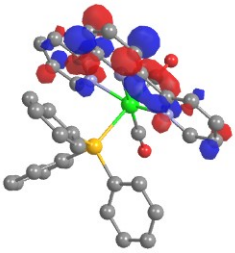 LUMO+1	-2.553 eV Re: 2% CO: 1% tpy: 96% PPh3: 1%	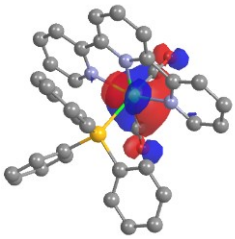 HOMO-1	-6.403 eV Re: 65% CO: 25% tpy: 10% PPh3: 0%
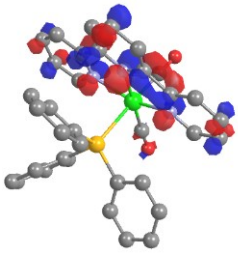 LUMO	-2.907 eV Re: 2% CO: 5% tpy: 90% PPh3: 3%	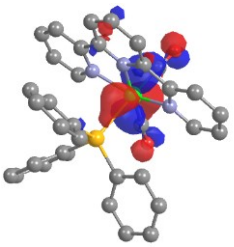 HOMO-2	-6.863 eV Re: 53% CO: 24% tpy: 15% PPh3: 8%

Table XI.18. Selected molecular orbitals with relative Mulliken contributions of each fragments and energies for complex **IV-4b** (isovalue 0.05 e/Å^3)

Orbital	Energy and contributions	Orbital	Energy and contributions
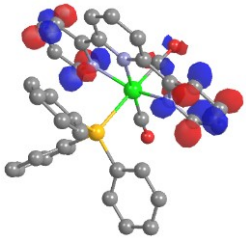 LUMO+2	-1.444 eV Re: 2% CO: 6% tpy: 83% PPh3: 10%	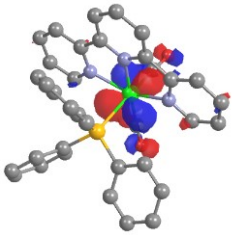 HOMO	-6.092 eV Re: 63% CO: 16% tpy: 18% PPh3: 2%
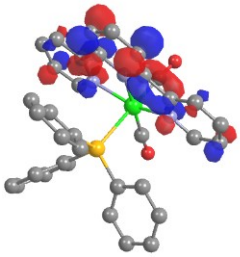 LUMO+1	-2.435 eV Re: 1% CO: 1% tpy: 97% PPh3: 1%	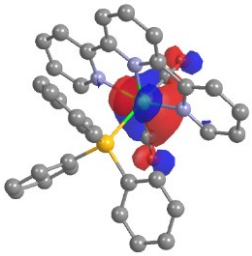 HOMO-1	-6.318 eV Re: 65% CO: 26% tpy: 9% PPh3: 0%
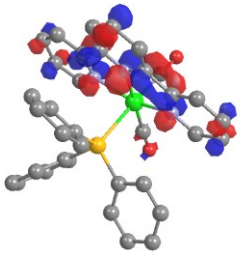 LUMO	-2.723 eV Re: 2% CO: 4% tpy: 91% PPh3: 2%	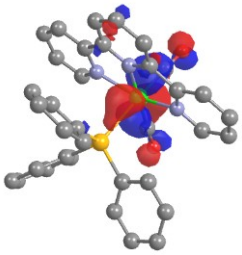 HOMO-2	-6.777 eV Re: 57% CO: 25% tpy: 16% PPh3: 6%

XI.2.2 Absorption spectra (experimental and theoretical)

Table XI.19. Complete list of absorption maxima and molar absorption coefficient for all complexes measured in acetonitrile

Complex	λ_{max} *nm* (ε $10^3 M^{-1}.cm^{-1}$)
IV-1a	367 (2.2), 322 (11.1, sh), 310 (12.6), 247 (17.0), 210 (31.1, sh)
IV-1b	360 (2.8), 319 (13.2, sh), 308 (14.5), 248 (20.9)
IV-1c	386 (3.7), 328 (12.8, sh), 266 (25.5), 218 (32.8, sh)
IV-1d	364 (12.6, sh), 320 (33.3), 276 (28.3), 248 (28.0)
IV-1e	388 (5.1), 322 (14.6), 265 (28.7), 251 (29.9)
IV-2a	690 (1.1), 547 (1.2), 446 (3.3), 395 (3.3), 330 (21.0, sh), 323 (22.0), 278 (16.5), 241 (20.2, sh) 229 (22.9, sh)
IV-2b	660 (1.6), 534 (1.8, sh), 454 (4.2, sh), 390 (4.3, sh), 326 (27.2, sh), 318 (27.8, sh), 241 (27.4), 214 (42.7, sh)
IV-2c	700 (1.2), 473 (6.0), 398 (4.6), 334 (22.5, sh), 323 (24.8), 286 (41.4), 239 (23.8, sh)
IV-2d	705 (1.4), 475 (8.8), 401 (5.8), 328 (46.6), 287 (37.6), 234 (32.4)
IV-2e	721 (0.6), 481 (3.5), 402 (2.8), 328 (13.5), 283 (23.9), 227 (24.6, sh)
IV-3a	647 (1.5), 516 (1.7), 440 (4.8), 380 (6.0), 322 (37.3), 281 (22.7), 274 (19.6, sh), 227 (29.5, sh)
IV-3b	621 (2.0), 514 (2.2), 428 (6.1), 379 (7.7), 318 (46.4), 283 (24.7), 274 (22.8), 234 (40.0, sh)
IV-3c	661 (1.2), 448 (7.0), 382 (6.1), 323 (31,8), 285 (38.4), 240 (21.9)
IV-3d	661 (1.3), 449 (10.0), 325 (46.4), 285 (43.2), 235 (30.7)
IV-3e	678 (1.4), 454 (8.2), 385 (7.2), 326 (33.8), 284 (44.5), 277 (38.0, sh), 263 (28.9), 242 (29.0)
IV-4a	590 (1.1), 488 (1.4), 421 (3.8), 374 (3.2), 320 (27.7), 273 (21.0)
IV-4b	579 (1.5, sh), 487 (1.8), 415 (4,5), 371 (4.3), 317 (32.8), 286 (19.1, sh), 274 (22.7)

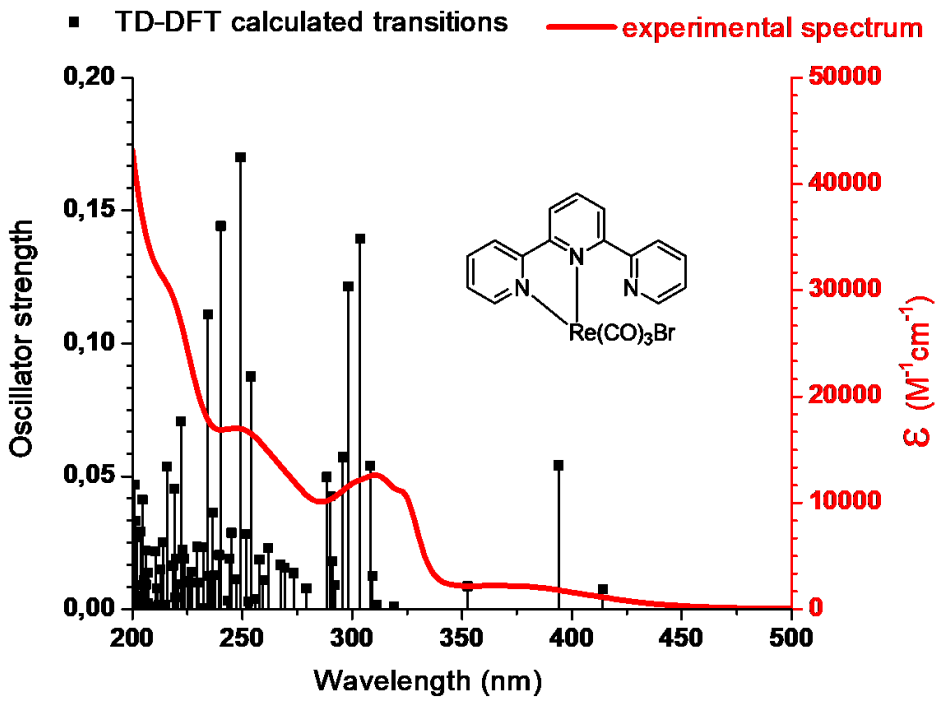

Figure XI.18. Theoretical and experimental absorption spectra for complex **IV-1a**

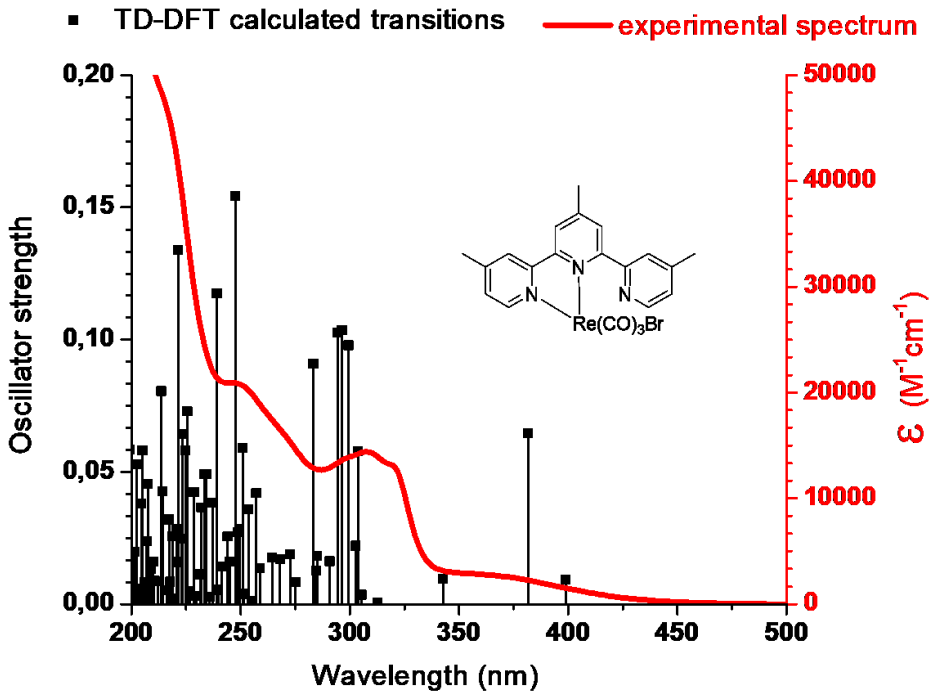

Figure XI.19. Theoretical and experimental absorption spectra for complex **IV-1b**

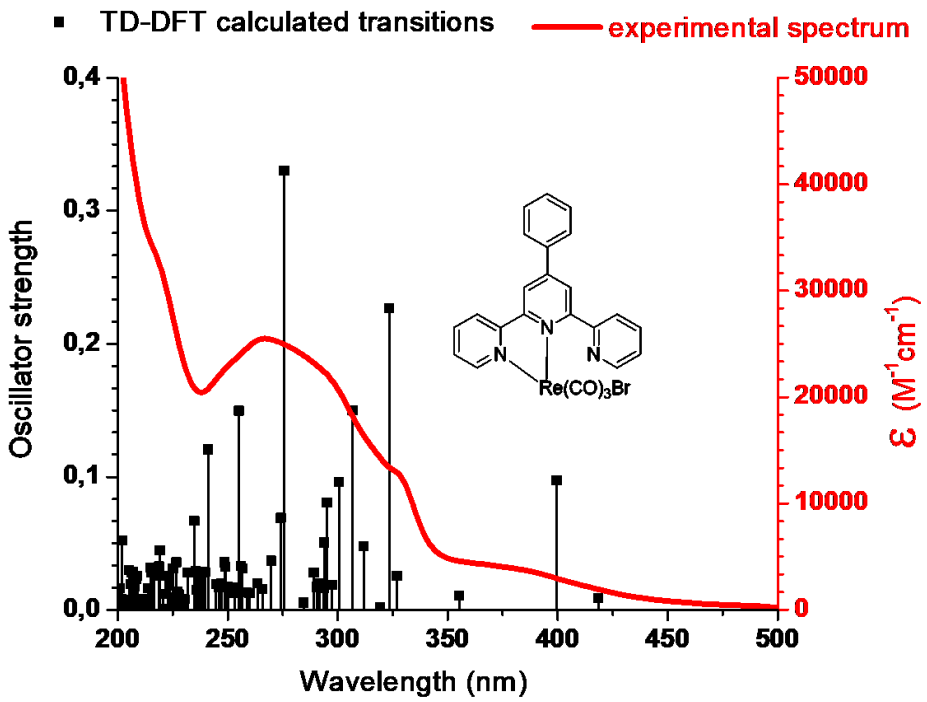

Figure XI.20. Theoretical and experimental absorption spectra for complex **IV-1c**

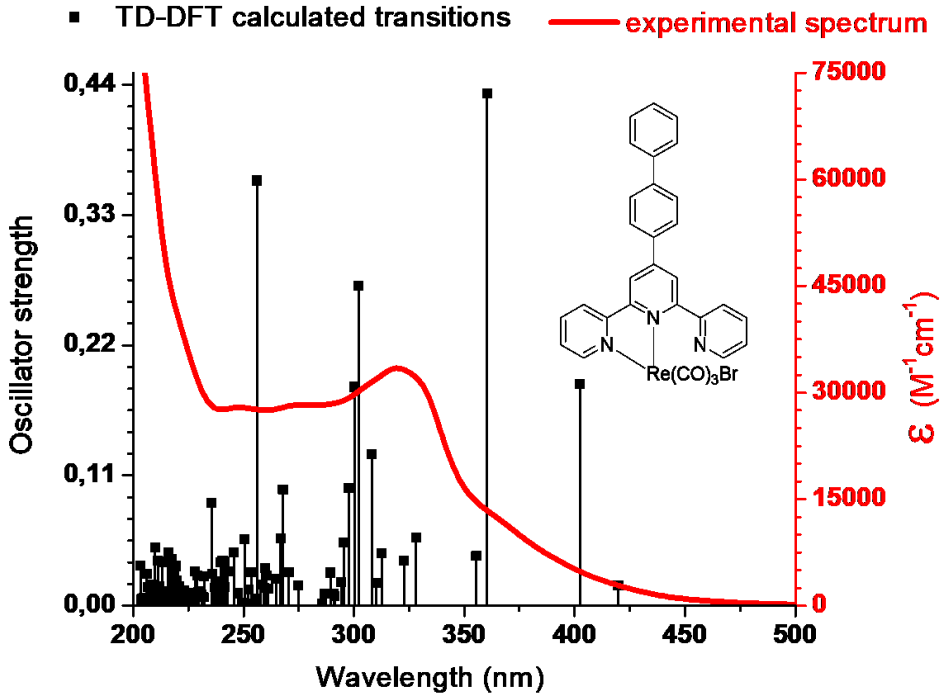

Figure XI.21. Theoretical and experimental absorption spectra for complex **IV-1d**

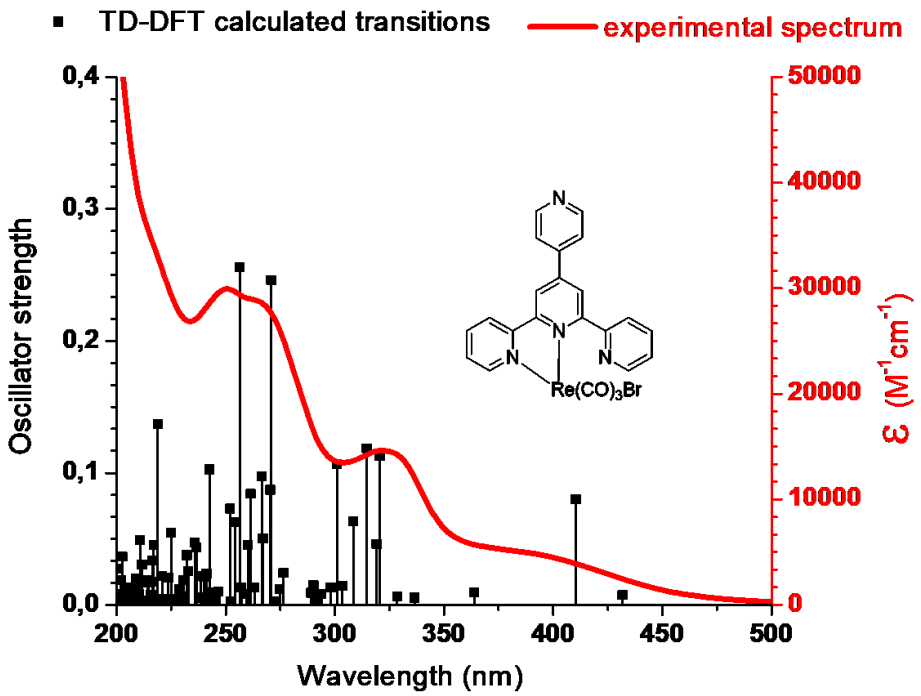

Figure XI.22. Theoretical and experimental absorption spectra for complex **IV-1e**

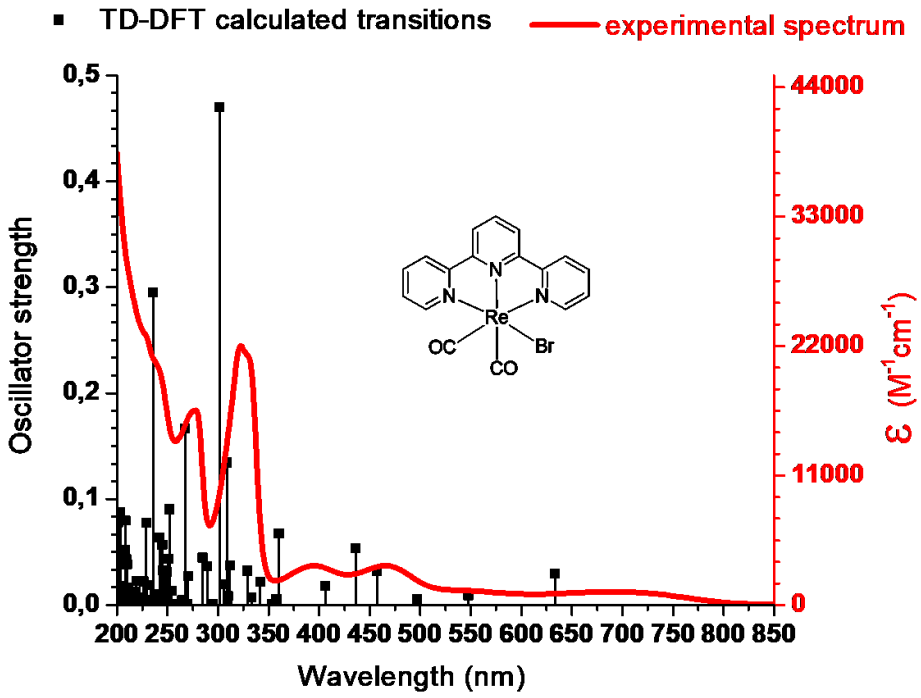

Figure XI.23. Theoretical and experimental absorption spectra for complex **IV-2a**

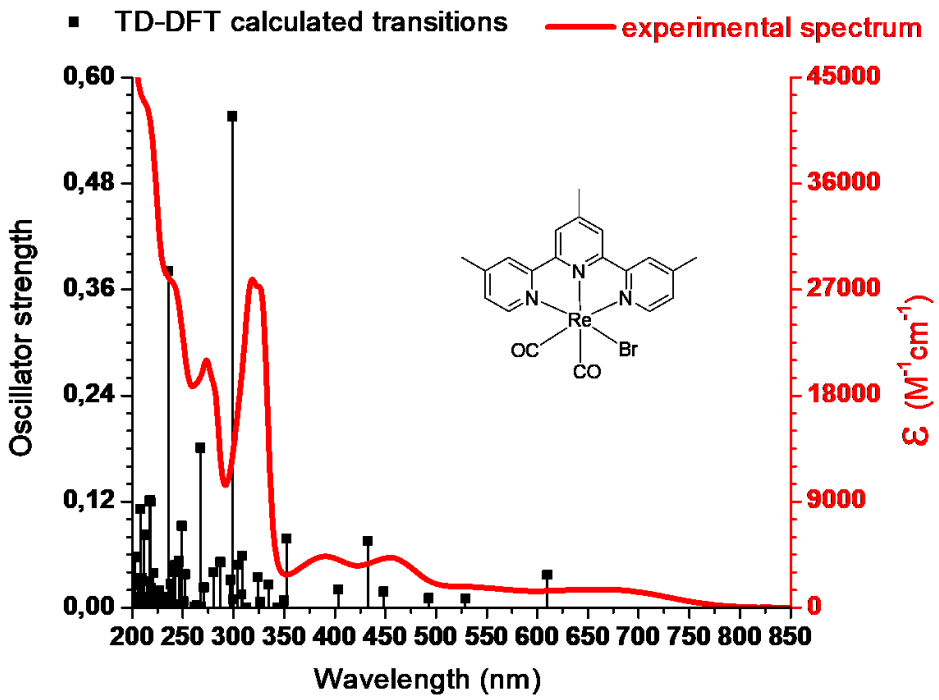

Figure XI.24. Theoretical and experimental absorption spectra for complex **IV-2b**

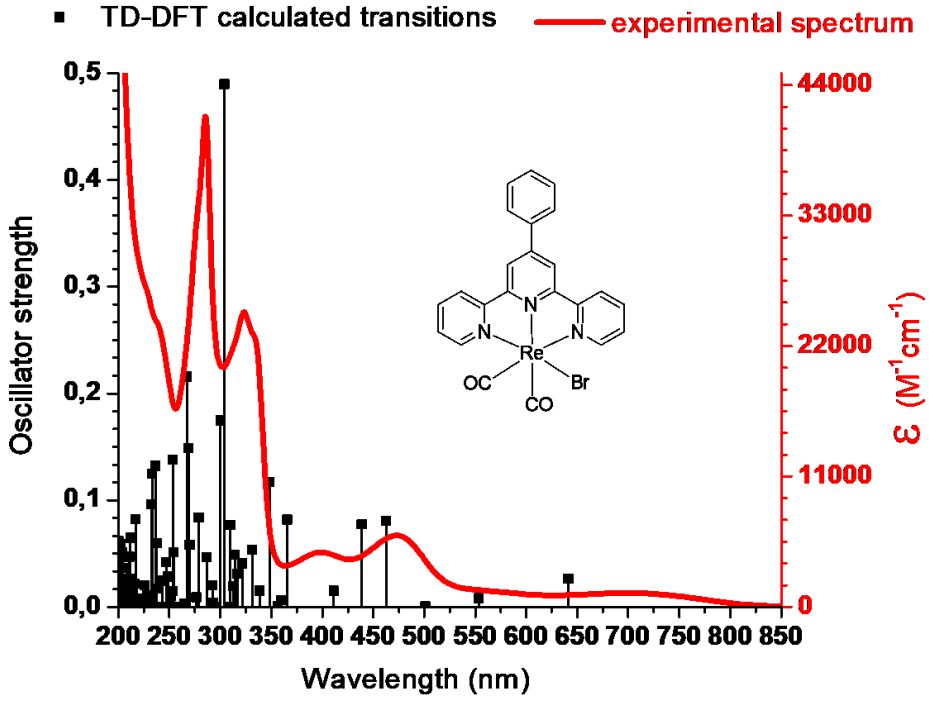

Figure XI.25. Theoretical and experimental absorption spectra for complex **IV-2c**

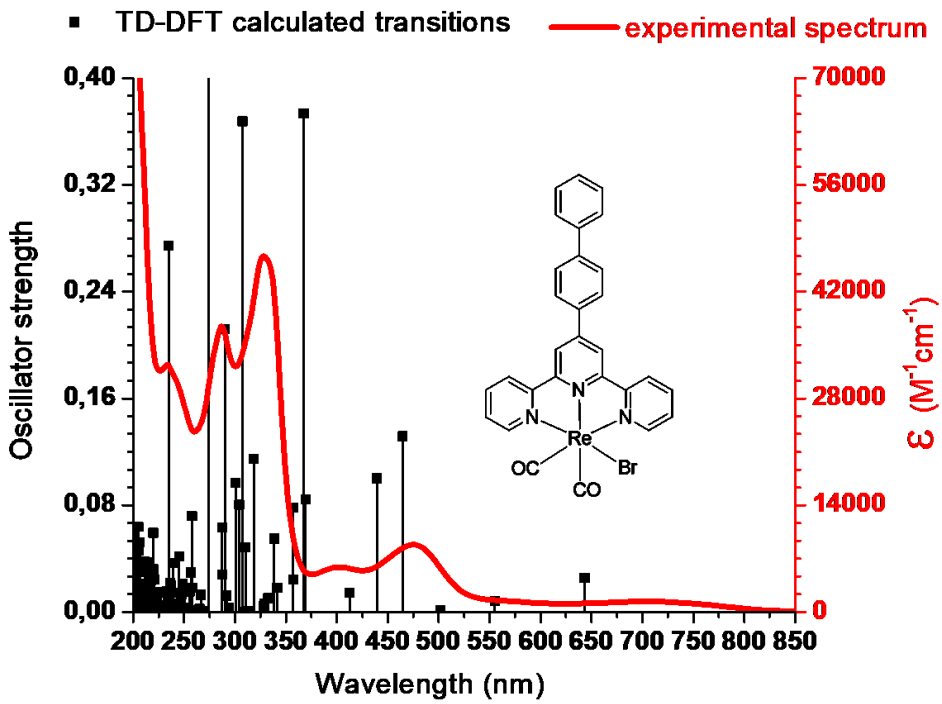

Figure XI.26. Theoretical and experimental absorption spectra for complex **IV-2d**

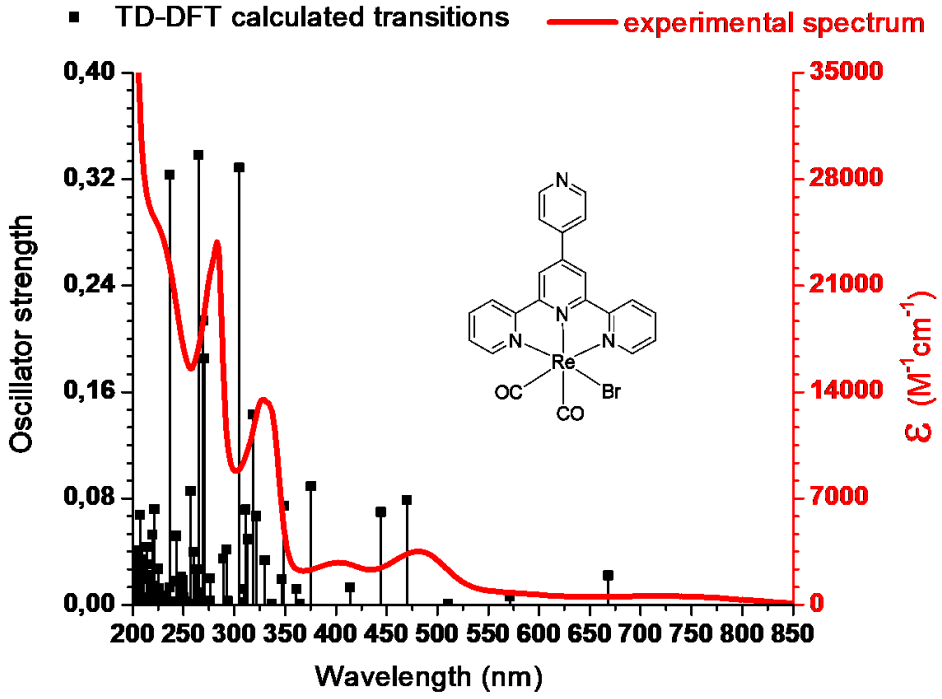

Figure XI.27. Theoretical and experimental absorption spectra for complex **IV-2e**

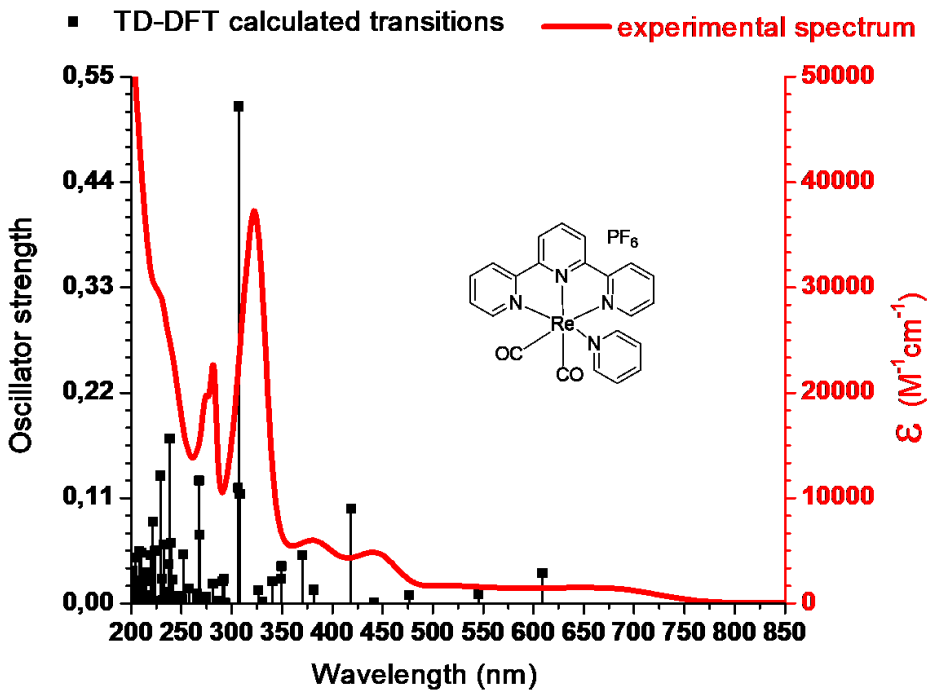

Figure XI.28. Theoretical and experimental absorption spectra for complex **IV-3a**

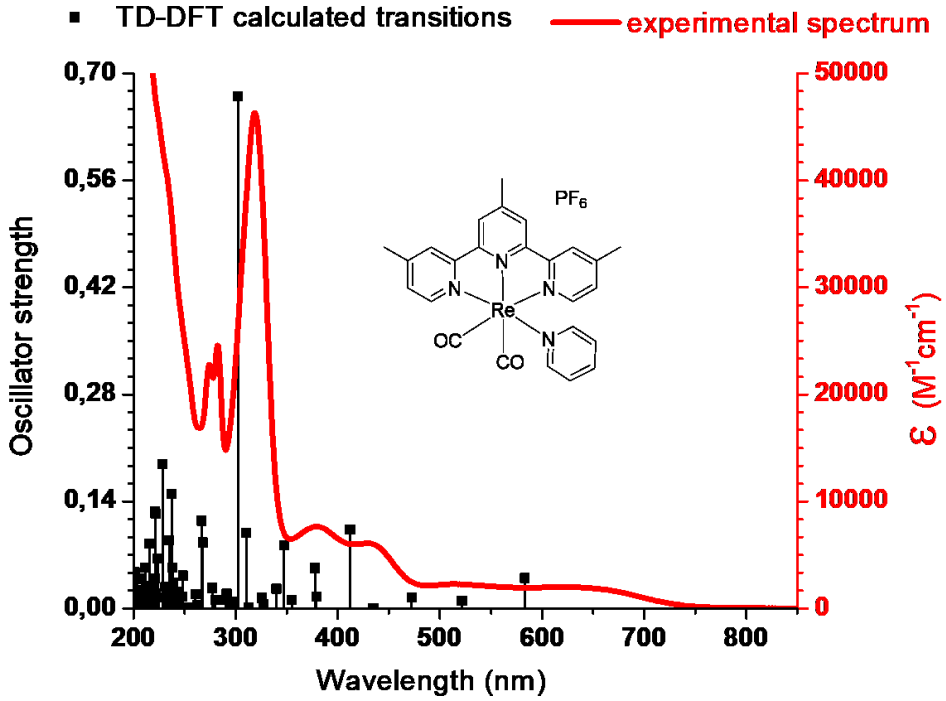

Figure XI.29. Theoretical and experimental absorption spectra for complex **IV-3b**

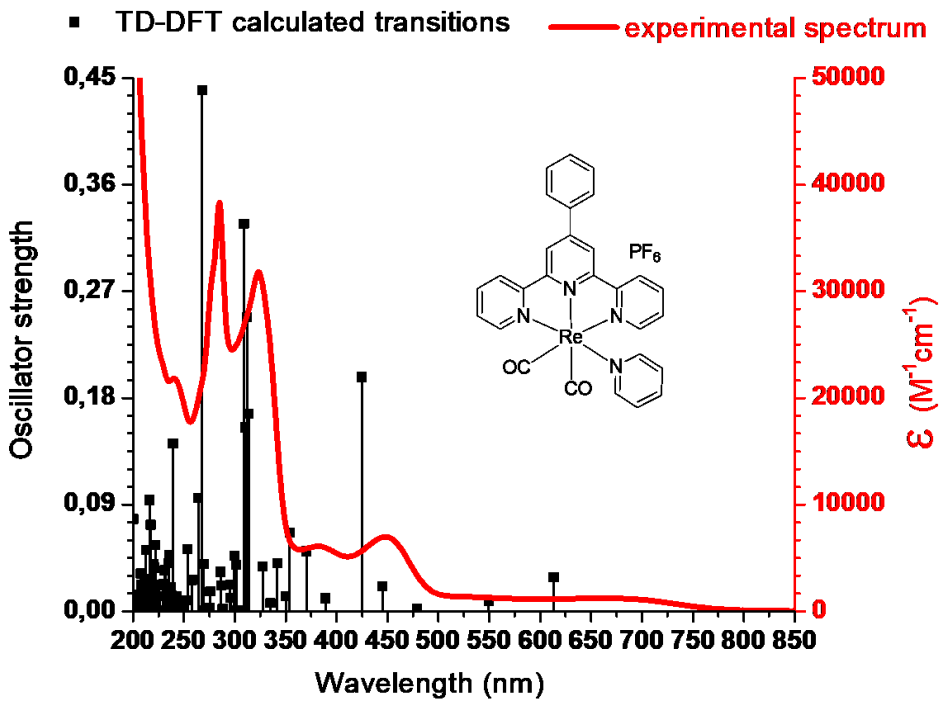

Figure XI.30. Theoretical and experimental absorption spectra for complex **IV-3c**

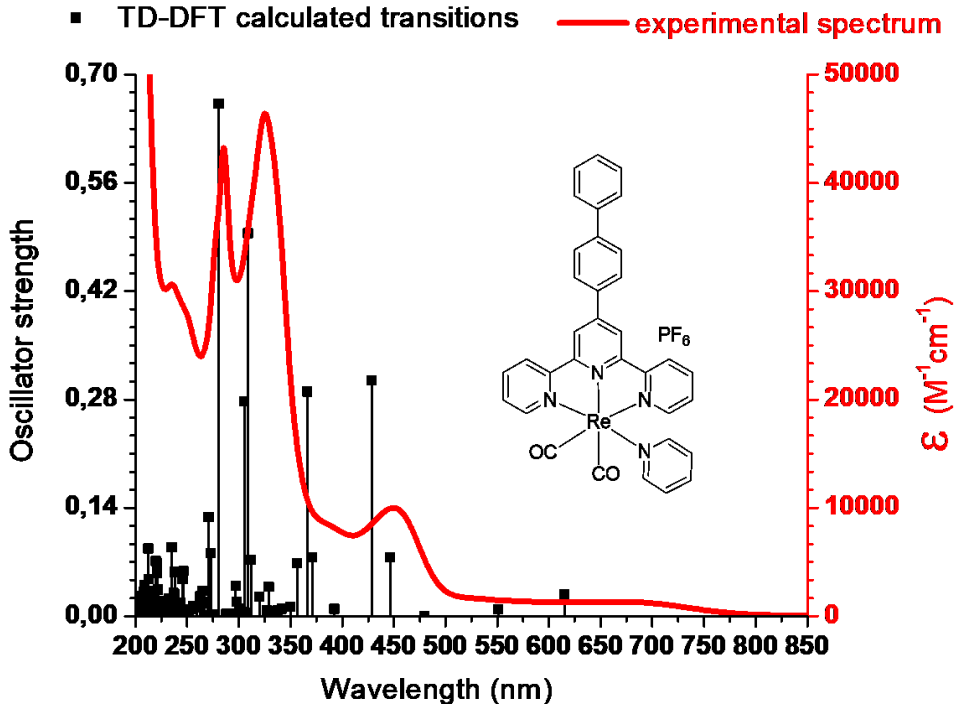

Figure XI.31. Theoretical and experimental absorption spectra for complex **IV-3d**

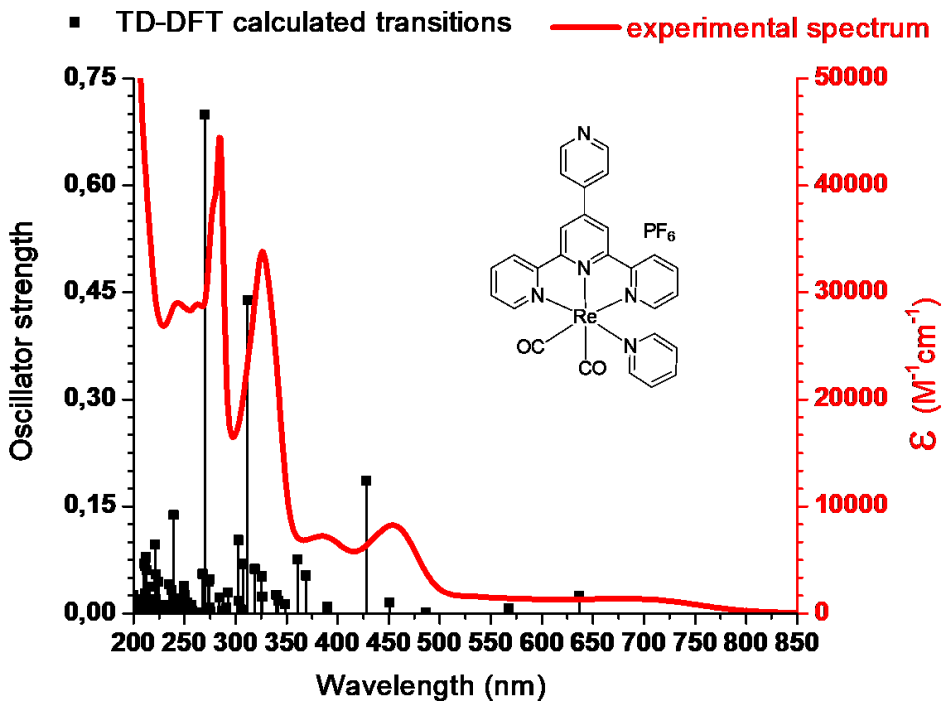

Figure XI.32. Theoretical and experimental absorption spectra for complex **IV-3e**

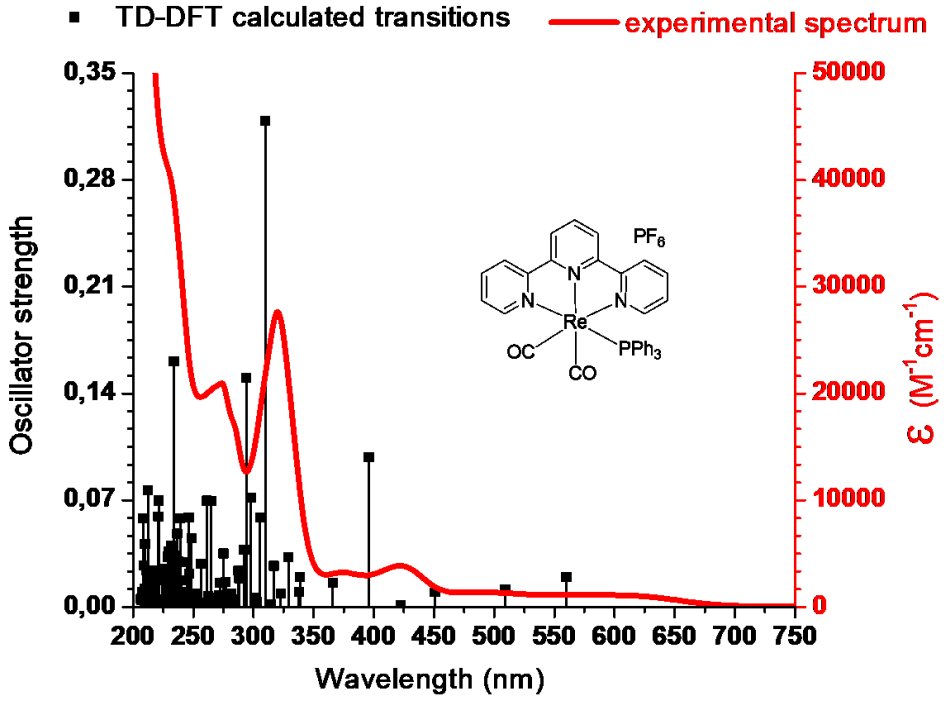

Figure XI.33. Theoretical and experimental absorption spectra for complex **IV-4a**

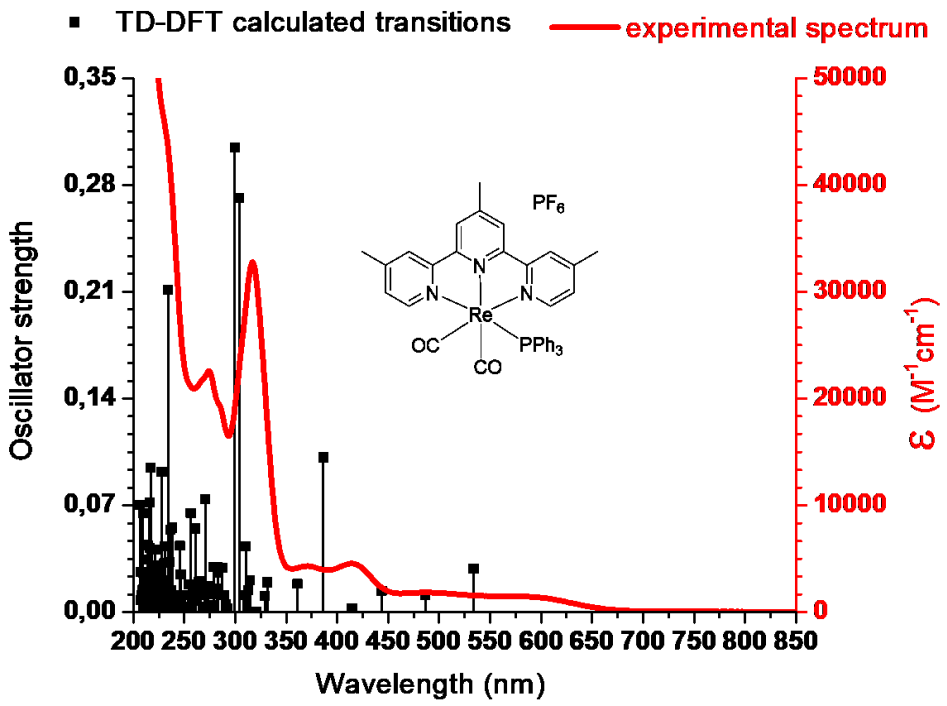

Figure XI.34. Theoretical and experimental absorption spectra for complex **IV-4b**

XI.2.3 Cyclic voltammetry

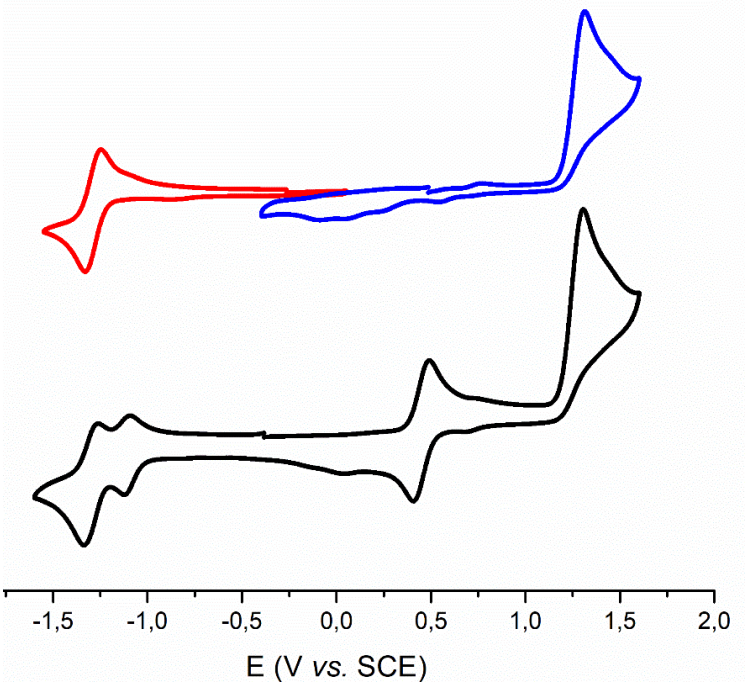

Figure XI.35. Cyclic voltammograms of **IV-1a** at 200 mV/s in DMF/DMAP 0.1 M (red and blue : without ferrocene, black : full range with ferrocene)

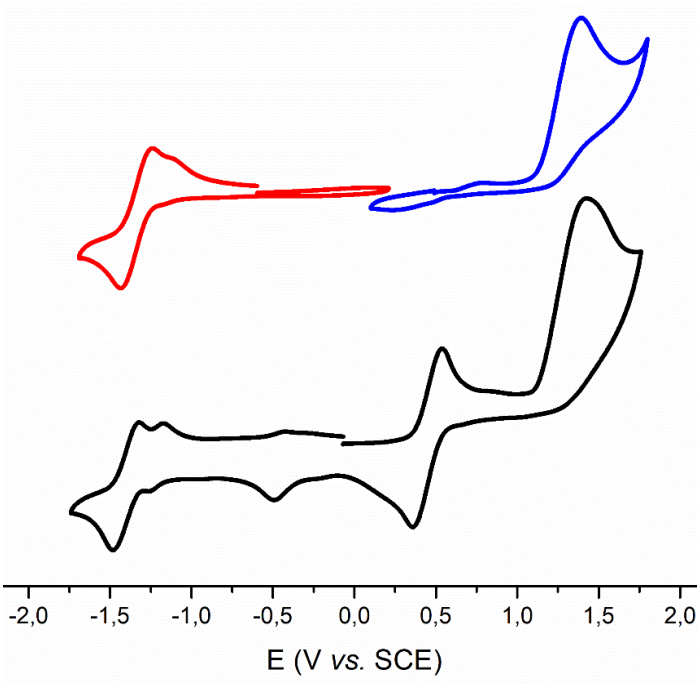

Figure XI.36. Cyclic voltammograms of **IV-1b** at 200 mV/s in DMF/DMAP 0.1 M (red and blue : without ferrocene, black : full range with ferrocene)

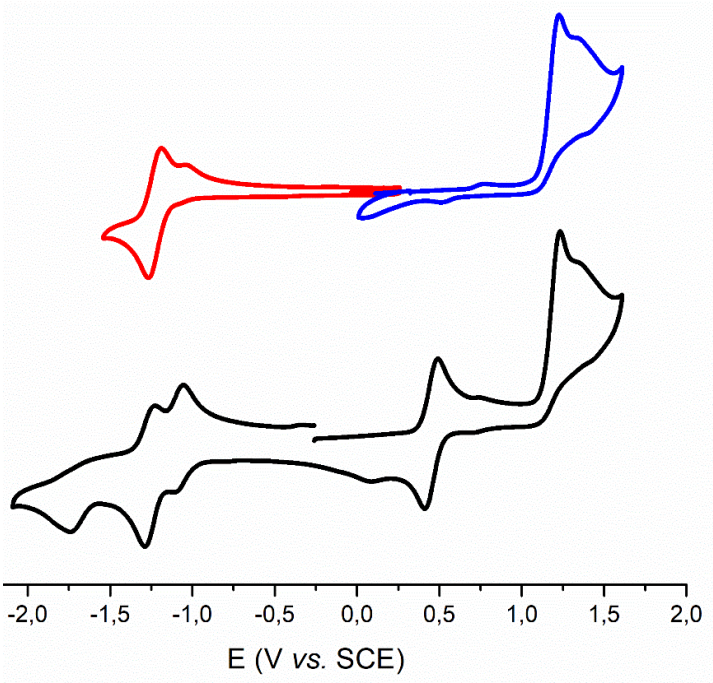

Figure XI.37. Cyclic voltammograms of **IV-1c** at 200 mV/s in DMF/DMAP 0.1 M (red and blue : without ferrocene, black : full range with ferrocene)

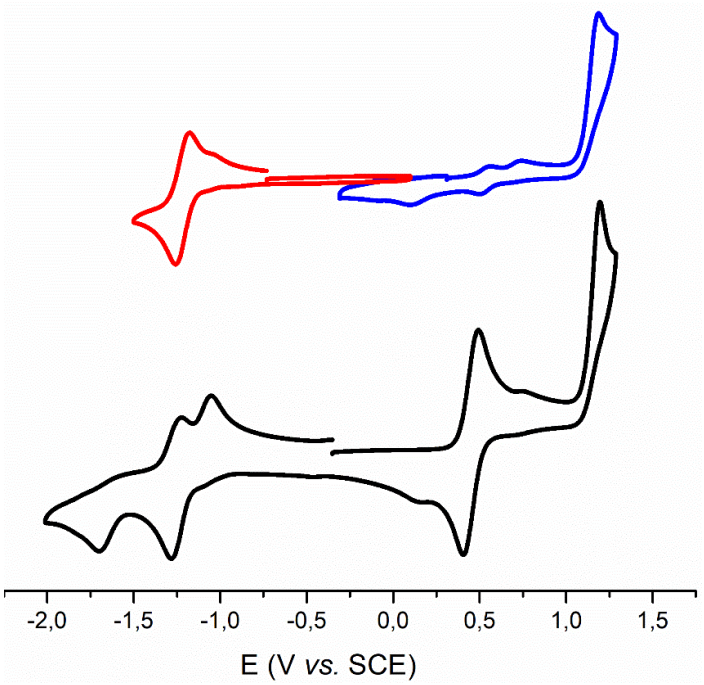

Figure XI.38. Cyclic voltammograms of **IV-1d** at 200 mV/s in DMF/DMAP 0.1 M (red and blue : without ferrocene, black : full range with ferrocene)

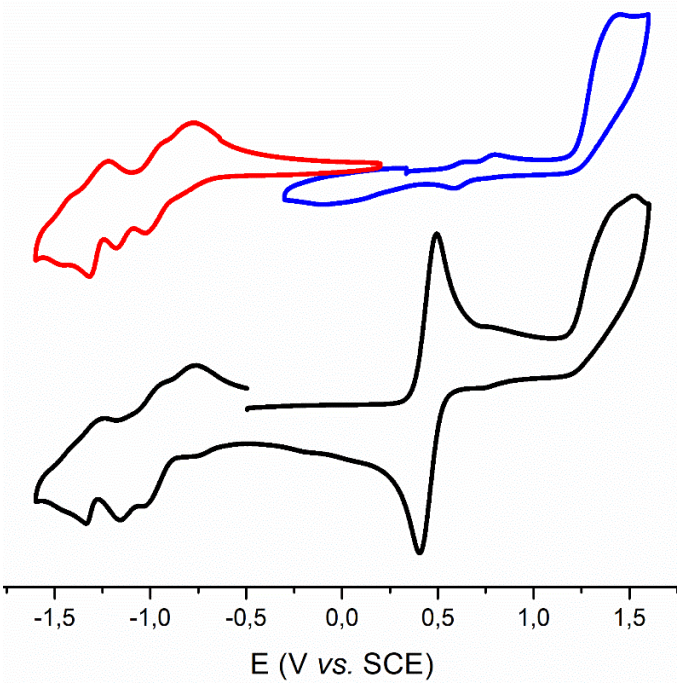

Figure XI.39. Cyclic voltammograms of **IV-1e** at 200 mV/s in DMF/DMAP 0.1 M (red and blue : without ferrocene, black : full range with ferrocene)

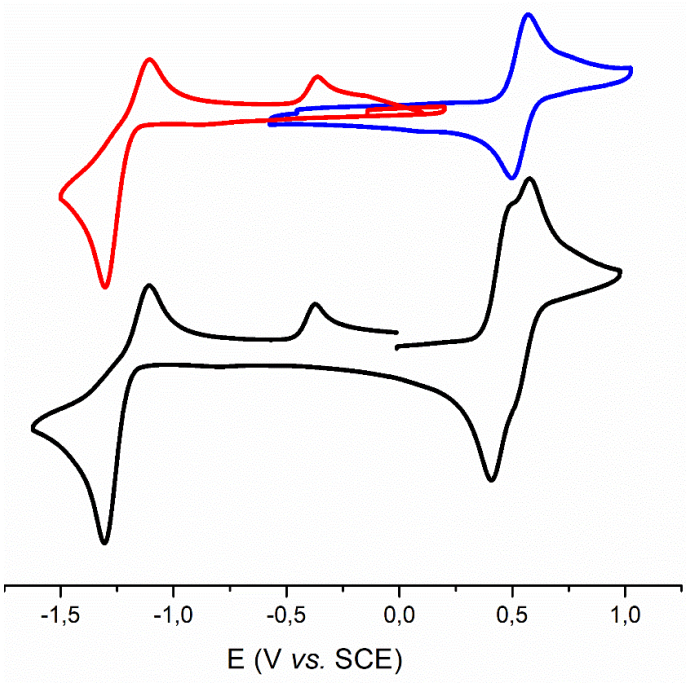

Figure XI.40. Cyclic voltammograms of **IV-2a** at 200 mV/s in DMF/DMAP 0.1 M (red and blue : without ferrocene, black : full range with ferrocene)

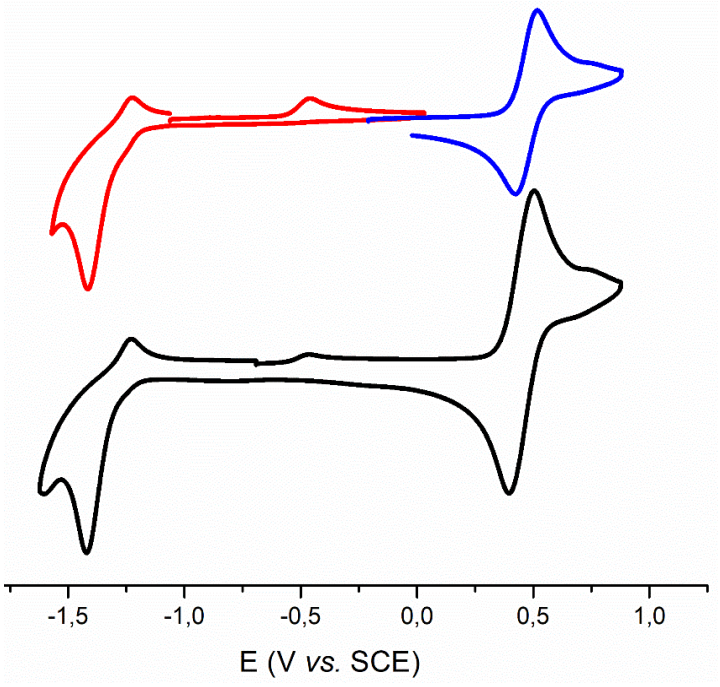

Figure XI.41. Cyclic voltammograms of **IV-2b** at 200 mV/s in DMF/DMAP 0.1 M (red and blue : without ferrocene, black : full range with ferrocene)

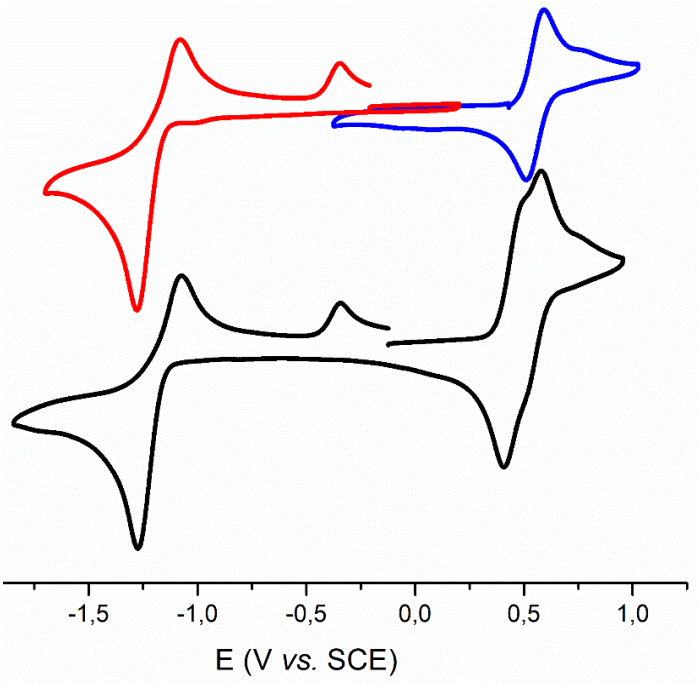

Figure XI.42. Cyclic voltammograms of **IV-2c** at 200 mV/s in DMF/DMAP 0.1 M (red and blue : without ferrocene, black : full range with ferrocene)

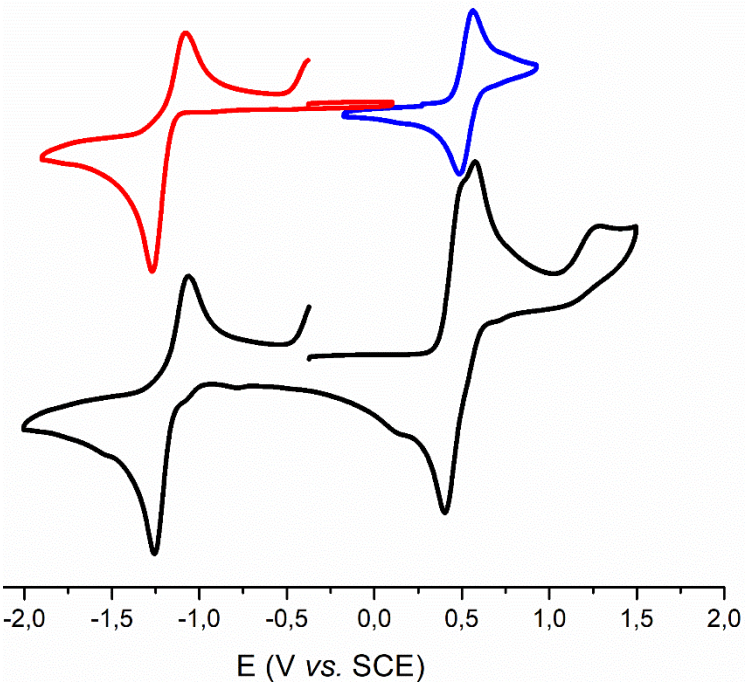

Figure XI.43. Cyclic voltammograms of **IV-2d** at 200 mV/s in DMF/DMAP 0.1 M (red, and blue : without ferrocene, black : full range with ferrocene)

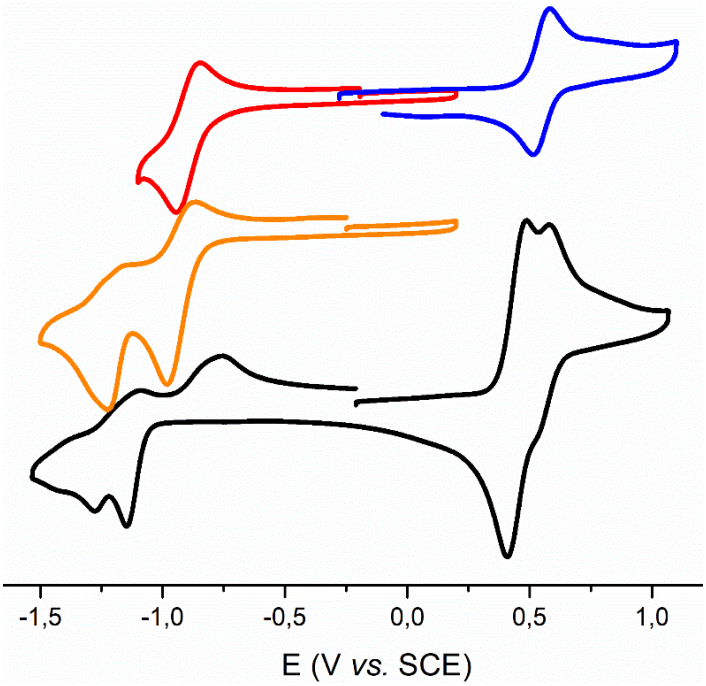

Figure XI.44. Cyclic voltammograms of **IV-2e** at 200 mV/s in DMF/DMAP 0.1 M (red, orange and blue : without ferrocene, black : full range with ferrocene)

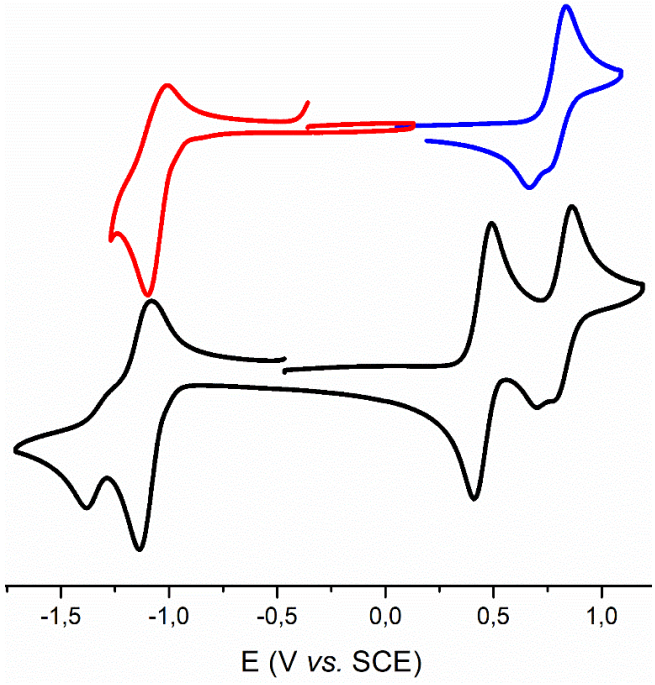

Figure XI.45. Cyclic voltammograms of **IV-3a** at 200 mV/s in DMF/DMAP 0.1 M (red and blue : without ferrocene, black : full range with ferrocene)

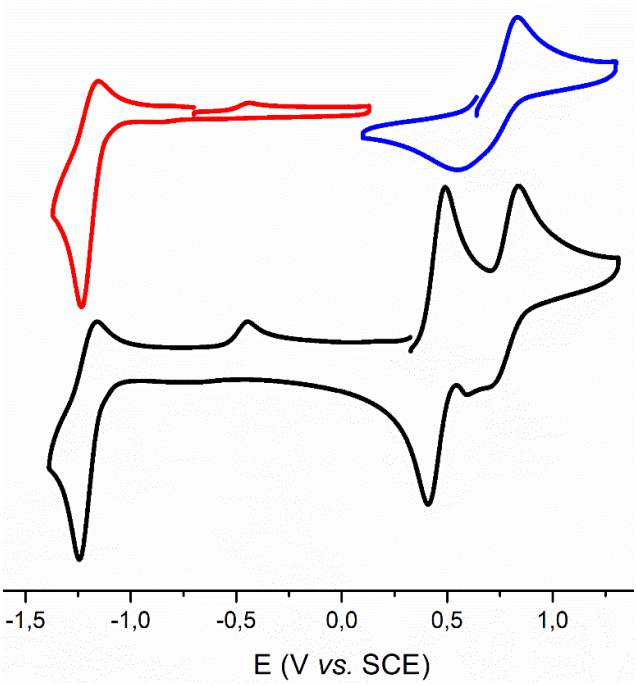

Figure XI.46. Cyclic voltammograms of **IV-3b** at 200 mV/s in DMF/DMAP 0.1 M (red and blue : without ferrocene, black : full range with ferrocene)

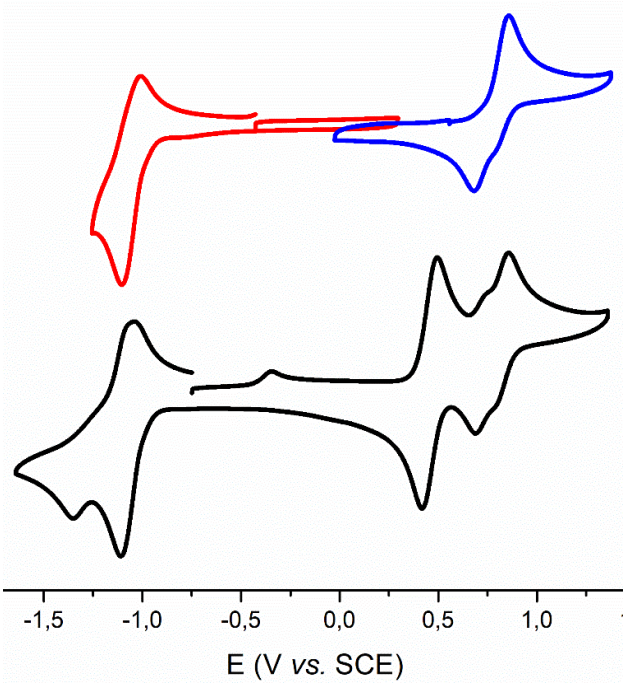

Figure XI.47. Cyclic voltammograms of **IV-3c** at 200 mV/s in DMF/DMAP 0.1 M (red and blue : without ferrocene, black : full range with ferrocene)

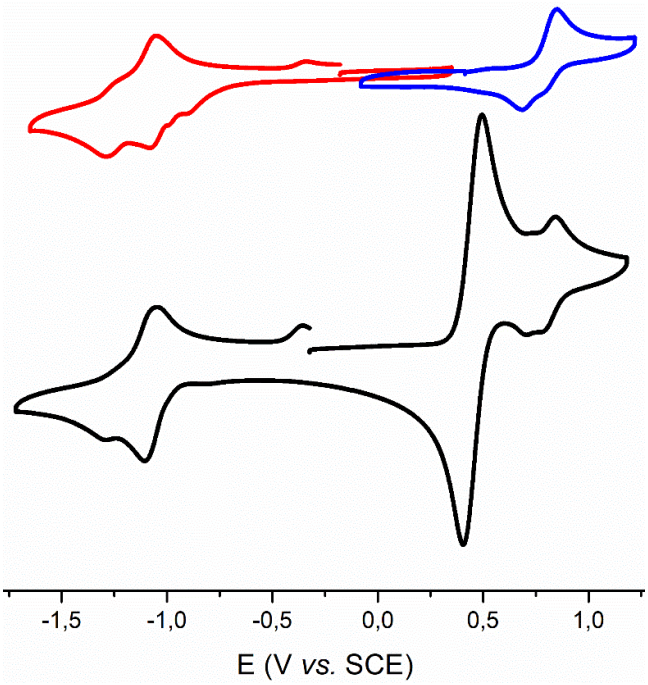

Figure XI.48. Cyclic voltammograms of **IV-3d** at 200 mV/s in DMF/DMAP 0.1 M (red and blue : without ferrocene, black : full range with ferrocene)

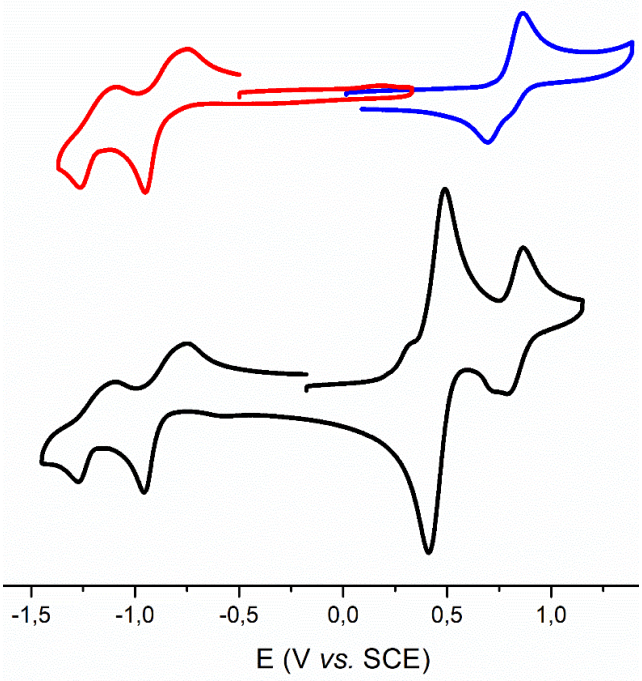

Figure XI.49. Cyclic voltammograms of **IV-3e** at 200 mV/s in DMF/DMAP 0.1 M (red and blue : without ferrocene, black : full range with ferrocene)

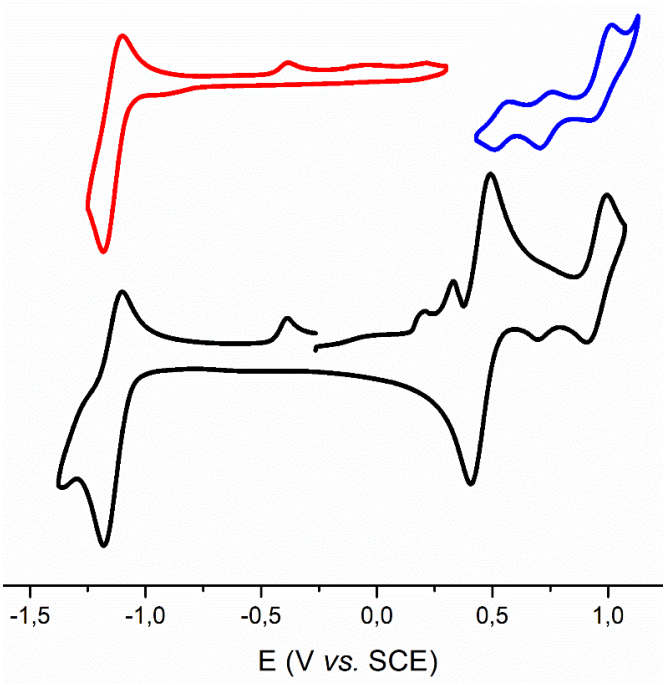

Figure XI.50. Cyclic voltammograms of **IV-4a** at 200 mV/s in DMF/DMAP 0.1 M (red and blue : without ferrocene, black : full range with ferrocene)

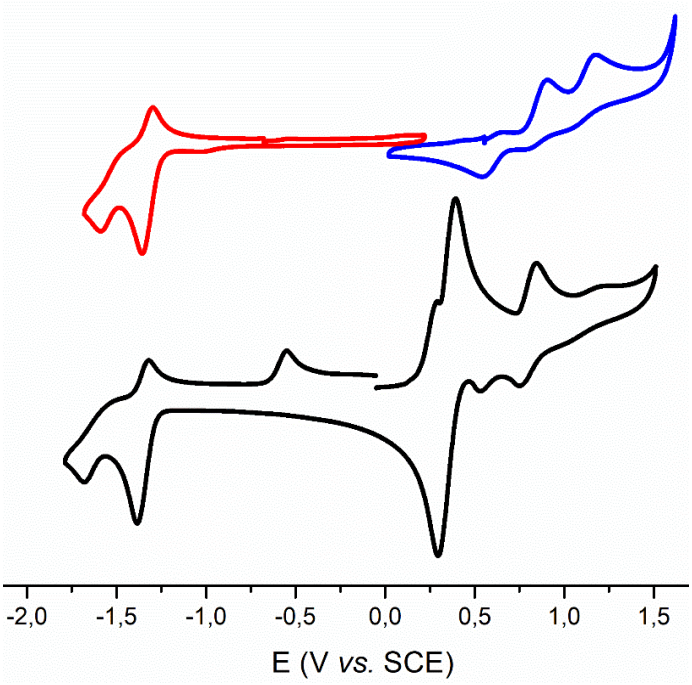

Figure XI.51. Cyclic voltammograms of **IV-4b** at 200 mV/s in DMF/DMAP 0.1 M (red and blue : without ferrocene, black : full range with ferrocene)

XI.2.4 Emission spectra

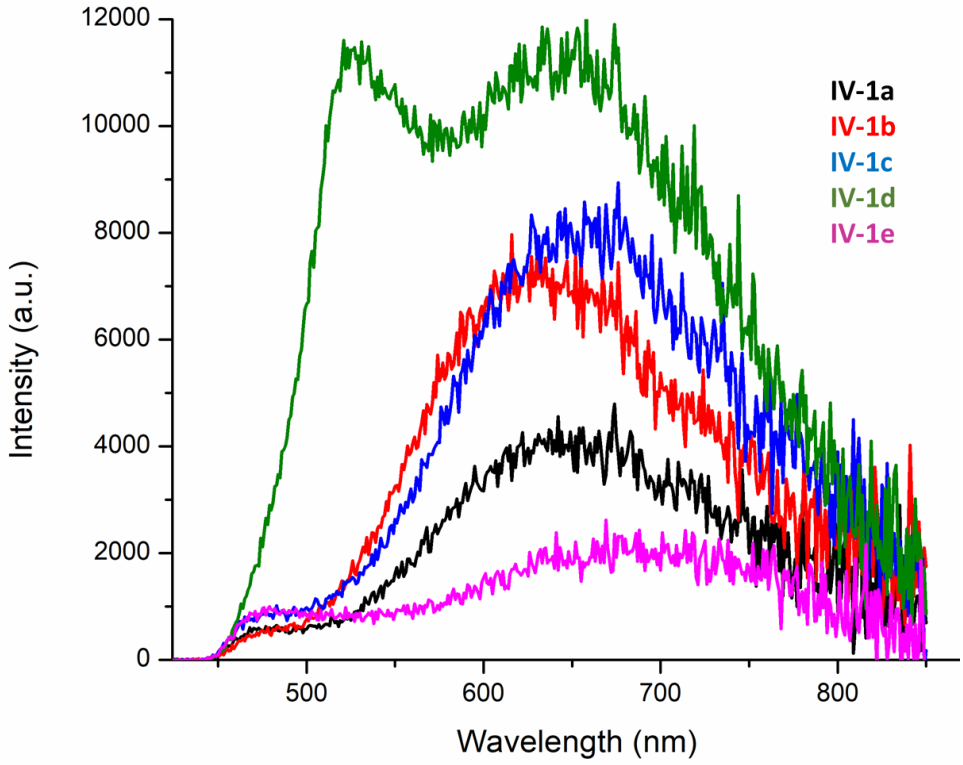

Figure XI.52. Emission spectra of the κ^2N complexes **IV-1a-e** in deaerated acetonitrile

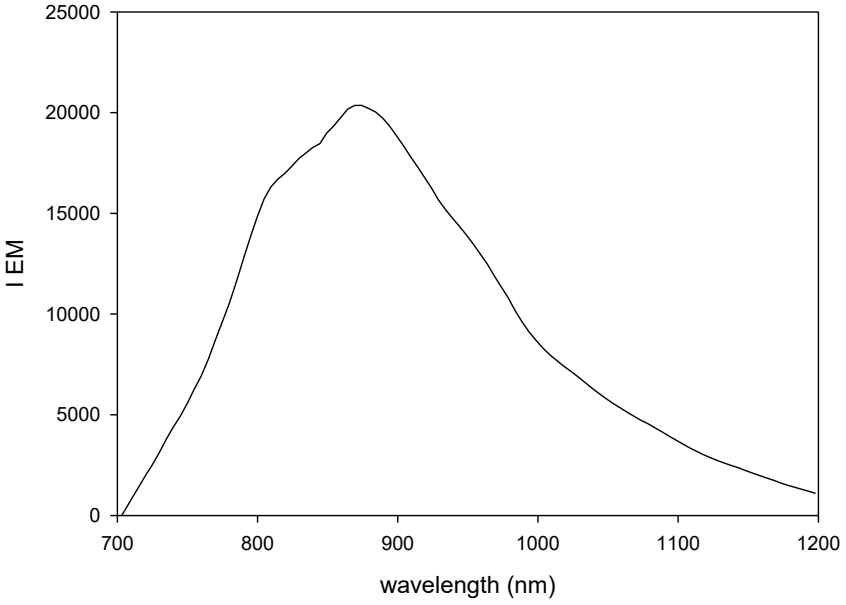

Figure XI.53. Emission spectra of **IV-3a** in deaerated acetonitrile (50 μM) with excitation at 440 nm.

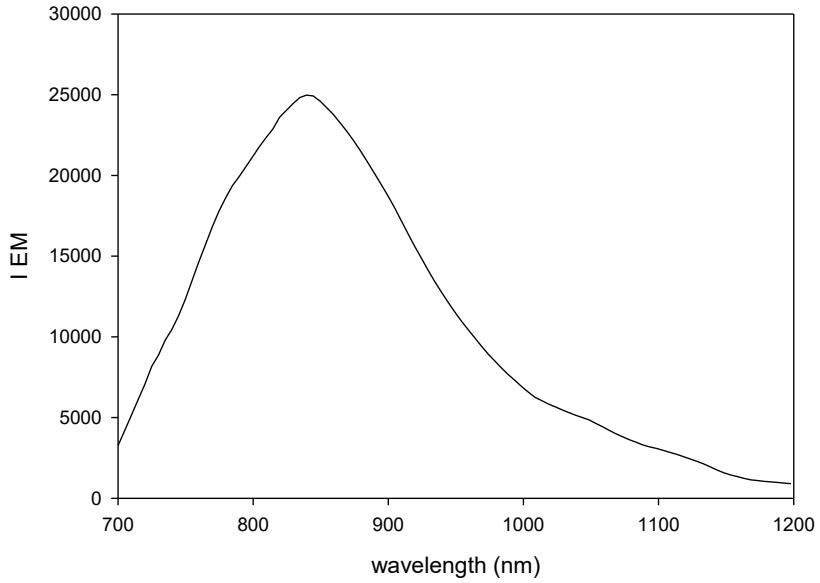

Figure XI.54. Emission spectra of **IV-3b** in deaerated acetonitrile (50 μM) with excitation at 440 nm.

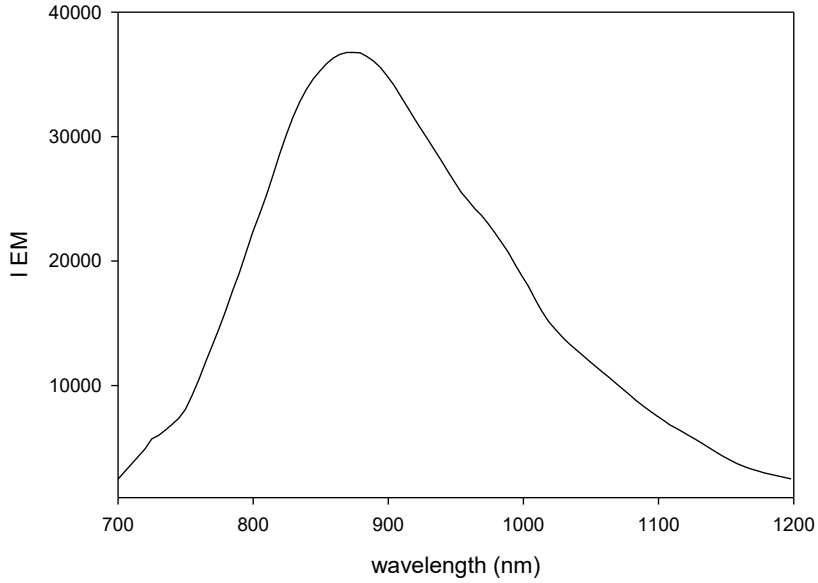

Figure XI.55. Emission spectra of **IV-3c** in deaerated acetonitrile (50 μM) with excitation at 440 nm.

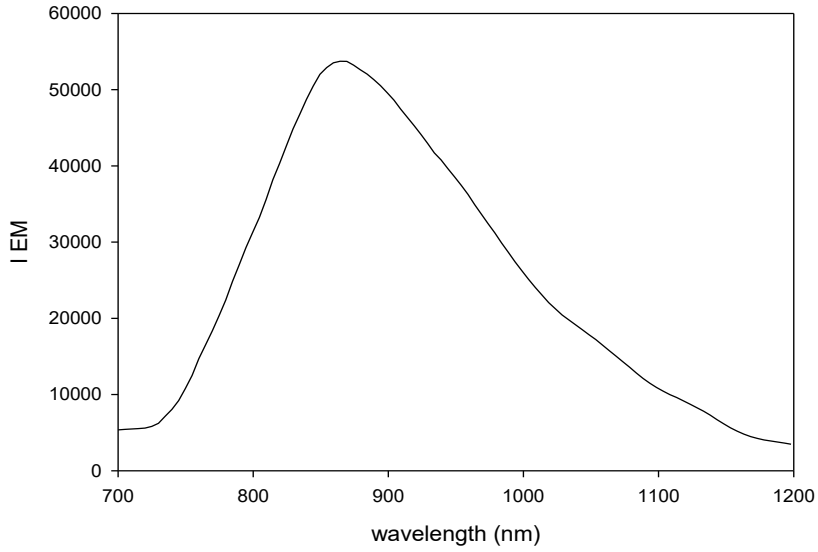

Figure XI.56. Emission spectra of **IV-3d** in deaerated acetonitrile (50 μM) with excitation at 440 nm.

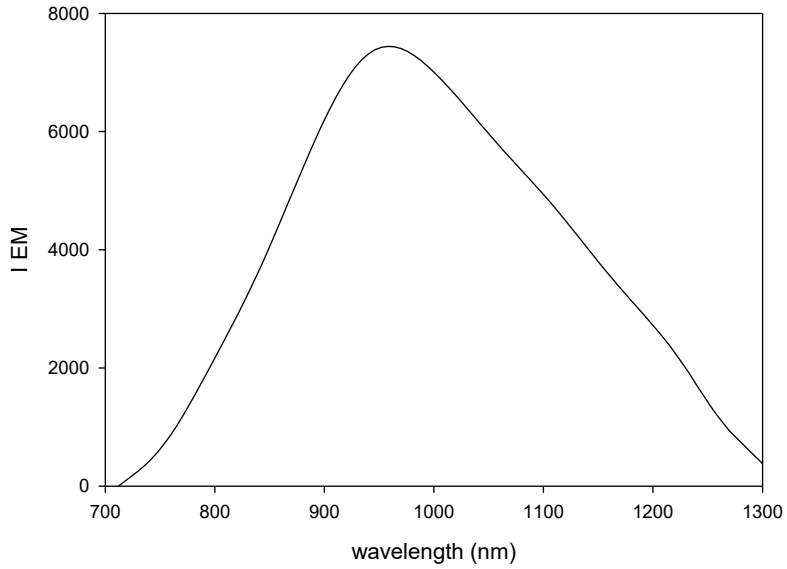

Figure XI.57. Emission spectra of **IV-3e** in deaerated acetonitrile (50 μM) with excitation at 440 nm.

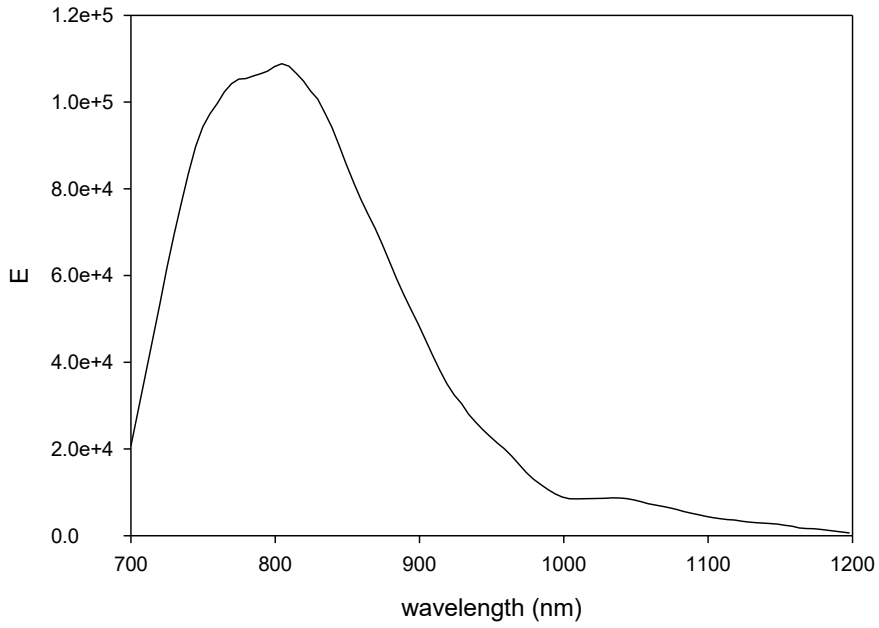

Figure XI.58. Emission spectra of **IV-4a** in deaerated acetonitrile (50 μM) with excitation at 440 nm.

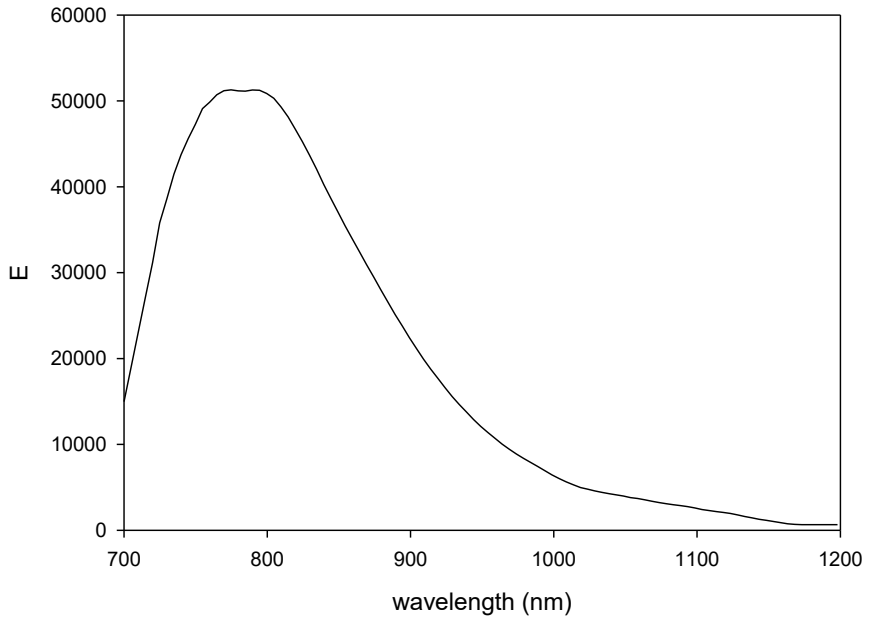

Figure XI.59. Emission spectra of **IV-4b** in deaerated acetonitrile (50 µM) with excitation at 440 nm.

XI.2.5 Natural transition orbitals

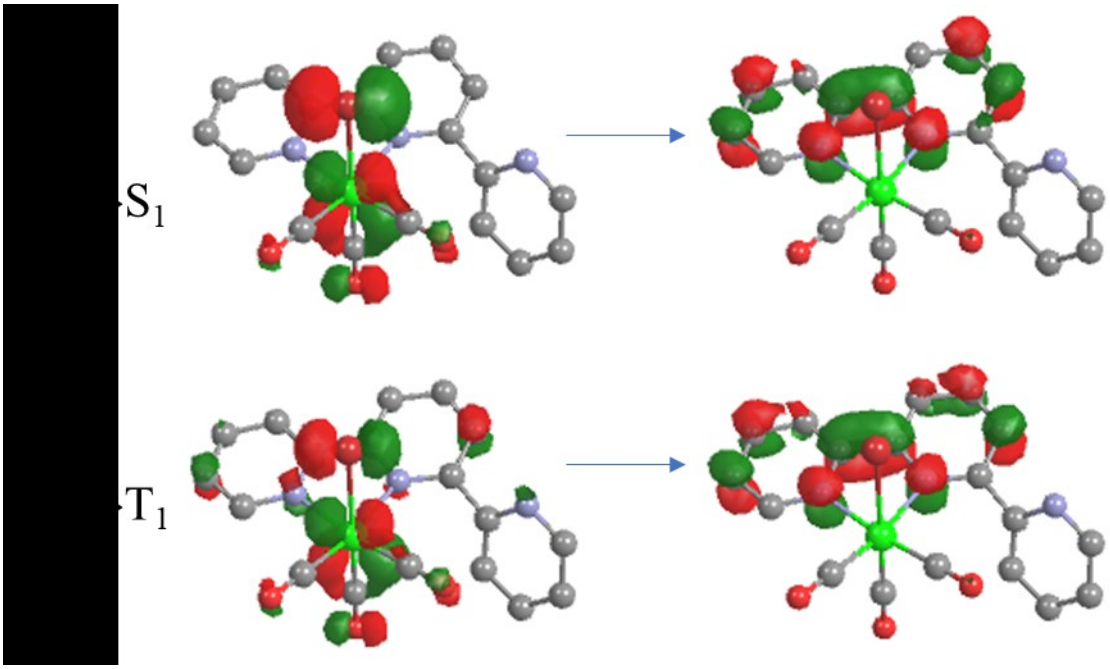

Figure XI.60. Natural transition orbitals for **IV-1a** lowest energy transitions.

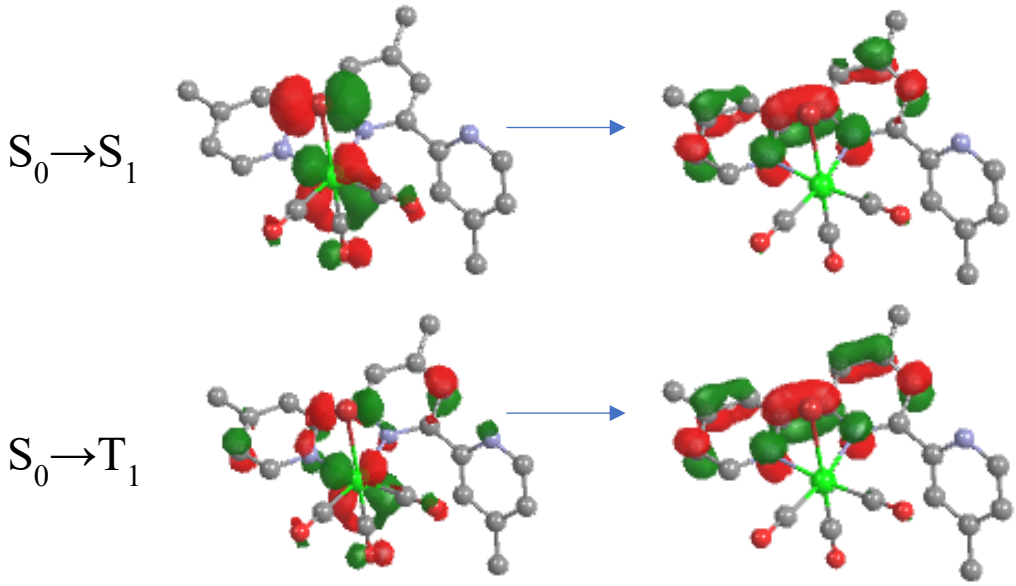

Figure XI.61. Natural transition orbitals for **IV-1b** lowest energy transitions.

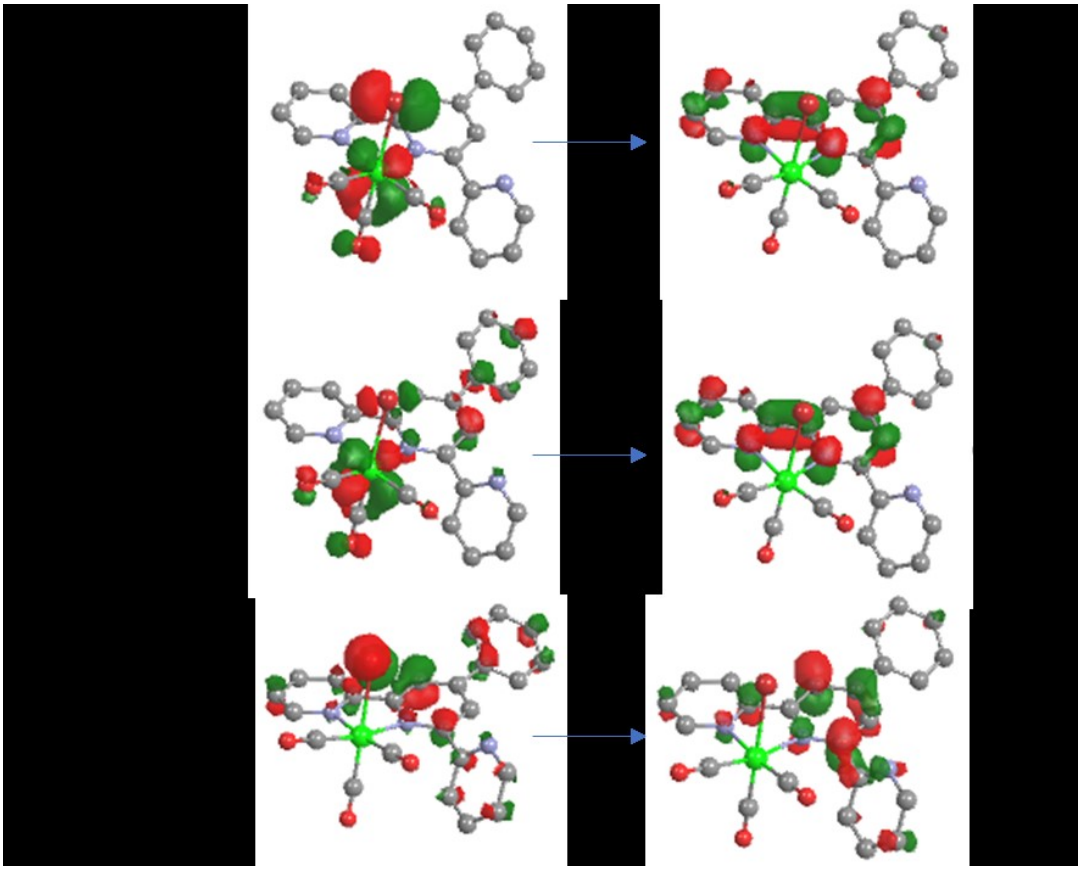

Figure XI.62. Natural transition orbitals for **IV-1c** lowest energy transitions.

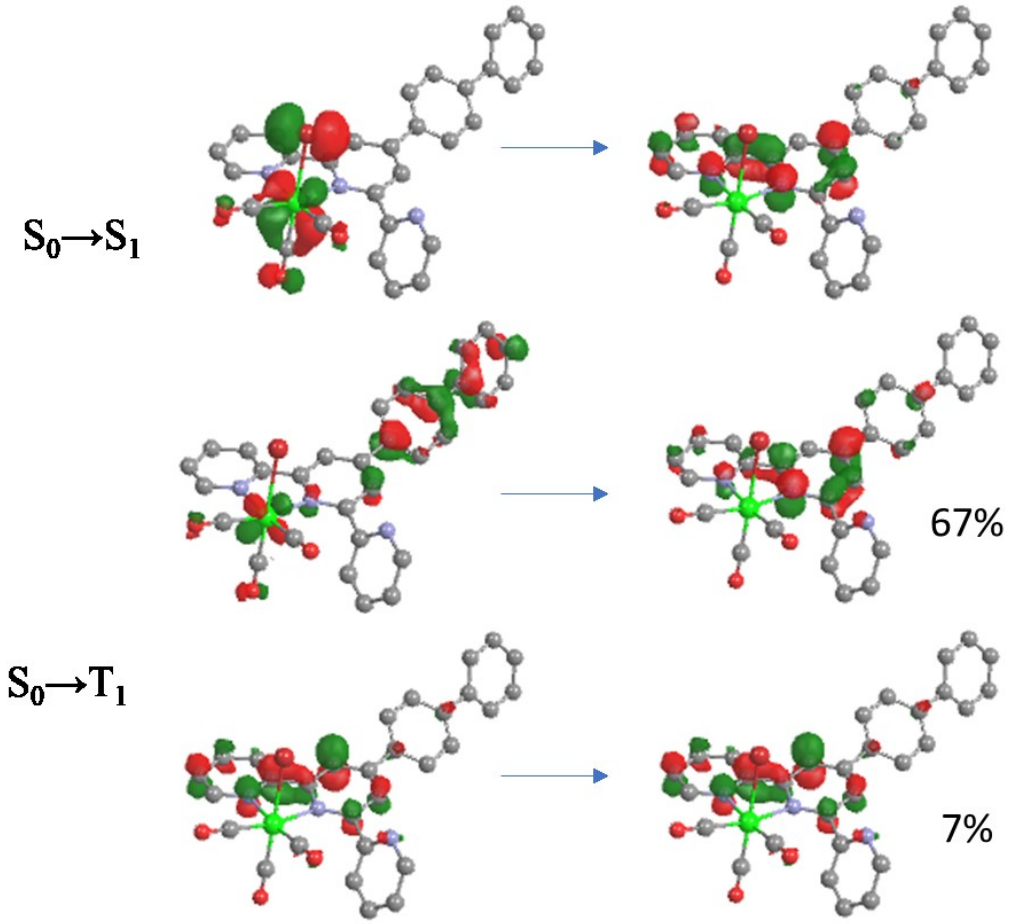

Figure XI.63. Natural transition orbitals for **IV-1d** lowest energy transitions.

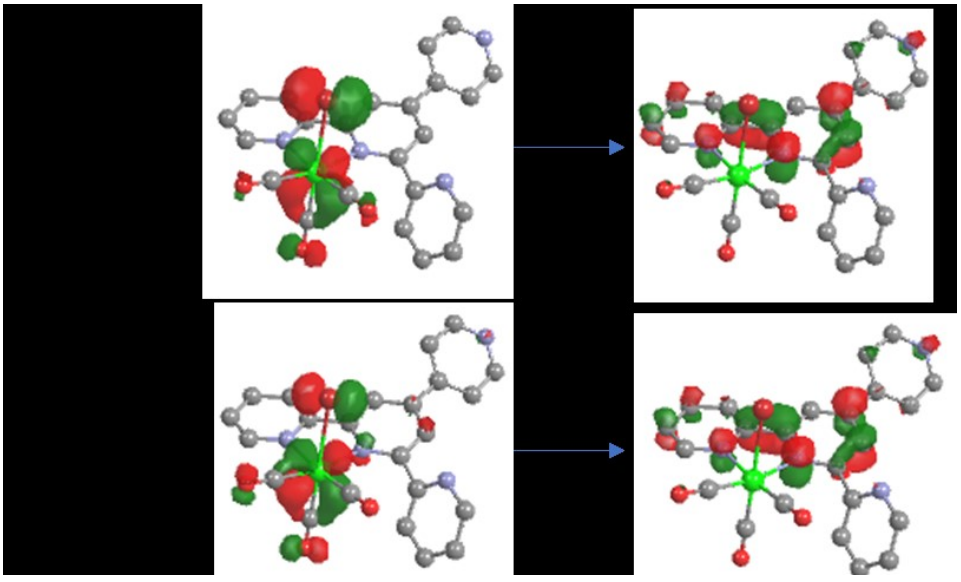

Figure XI.64. Natural transition orbitals for **IV-1e** lowest energy transitions.

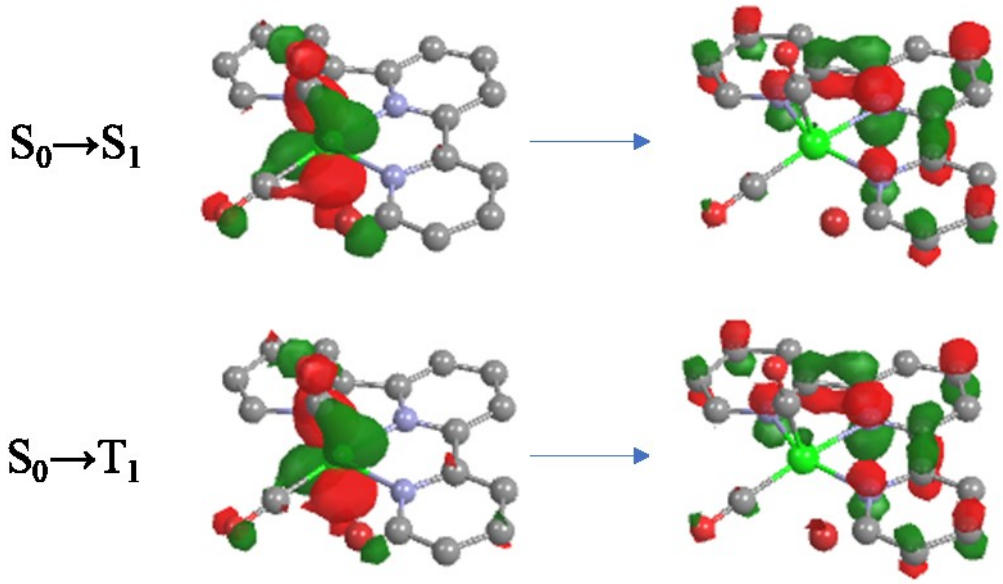

Figure XI.65. Natural transition orbitals for **IV-2a** lowest energy transitions.

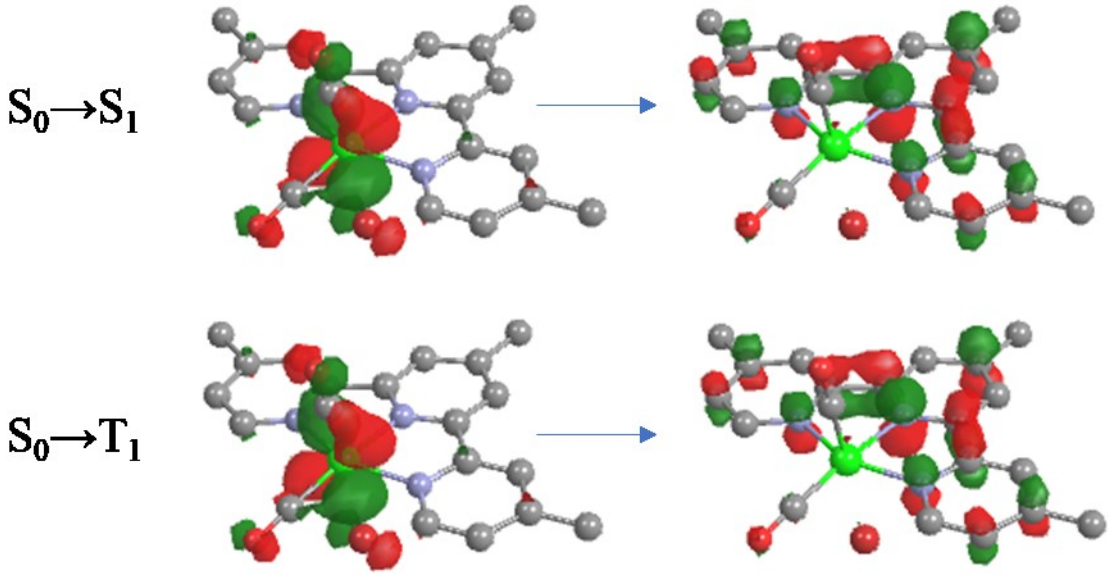

Figure XI.66. Natural transition orbitals for **IV-2b** lowest energy transitions.

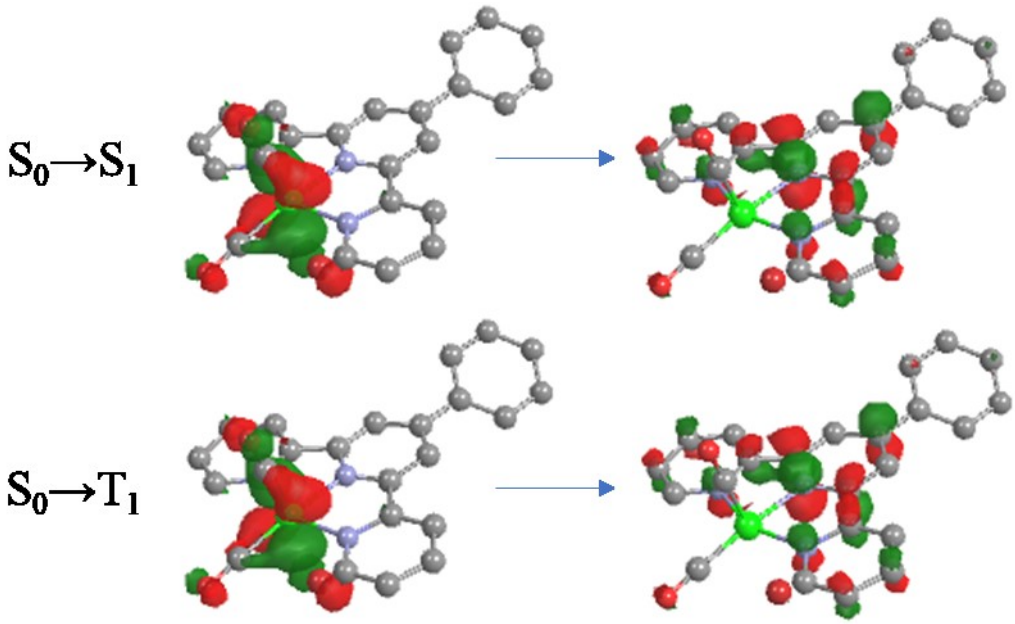

Figure XI.67. Natural transition orbitals for **IV-2c** lowest energy transitions.

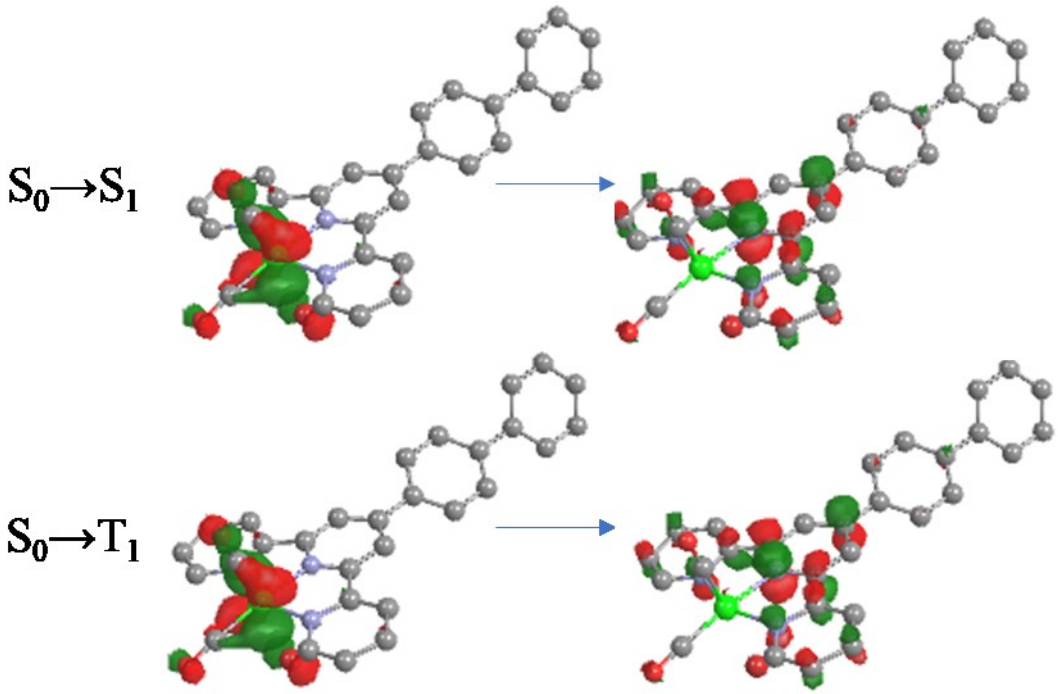

Figure XI.68. Natural transition orbitals for **IV-2d** lowest energy transitions.

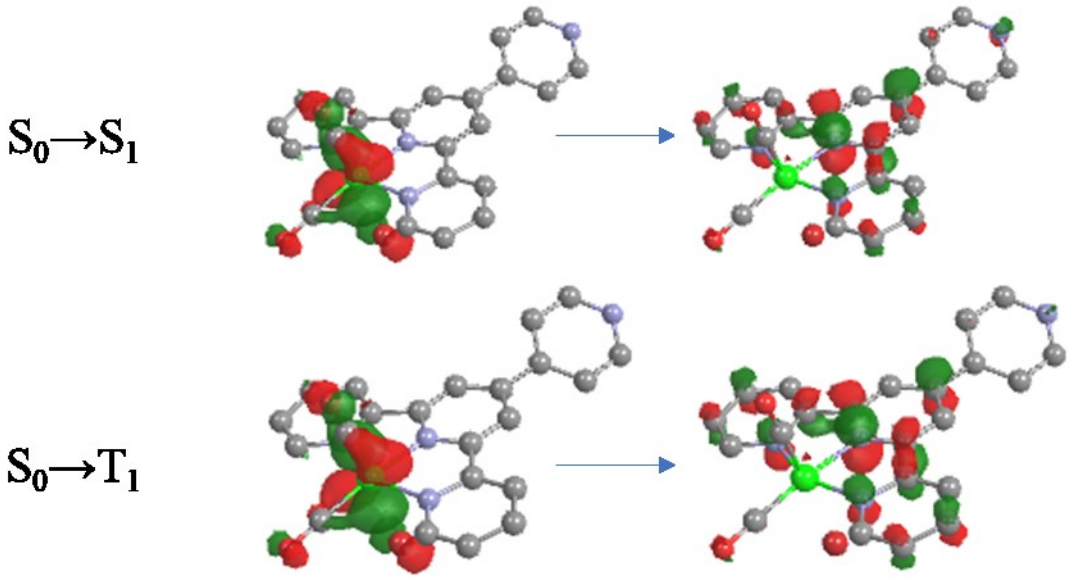

Figure XI.69. Natural transition orbitals for **IV-2e** lowest energy transitions.

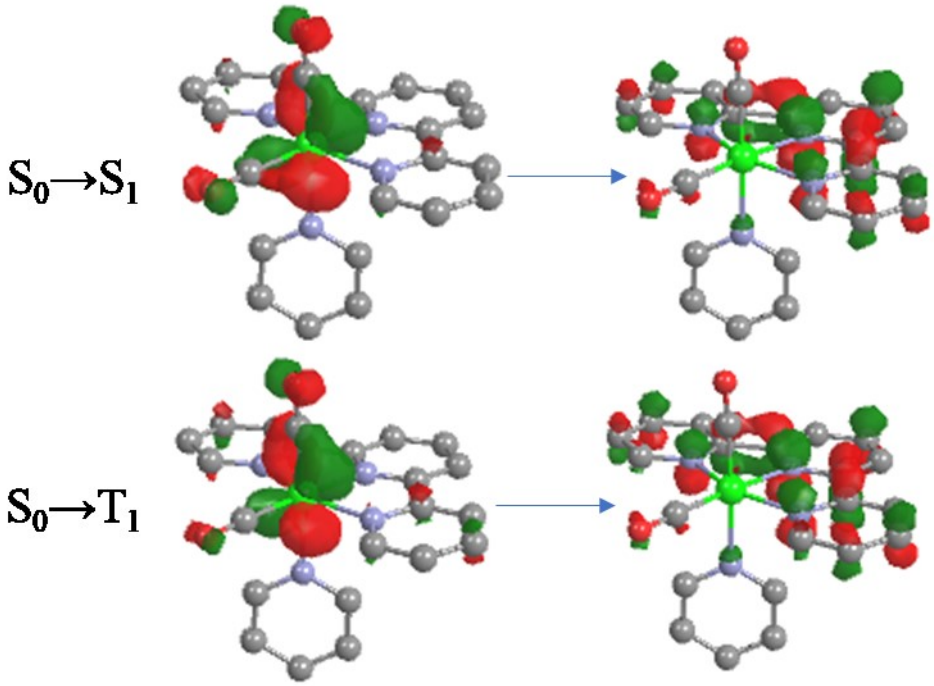

Figure XI.70. Natural transition orbitals for **IV-3a** lowest energy transitions.

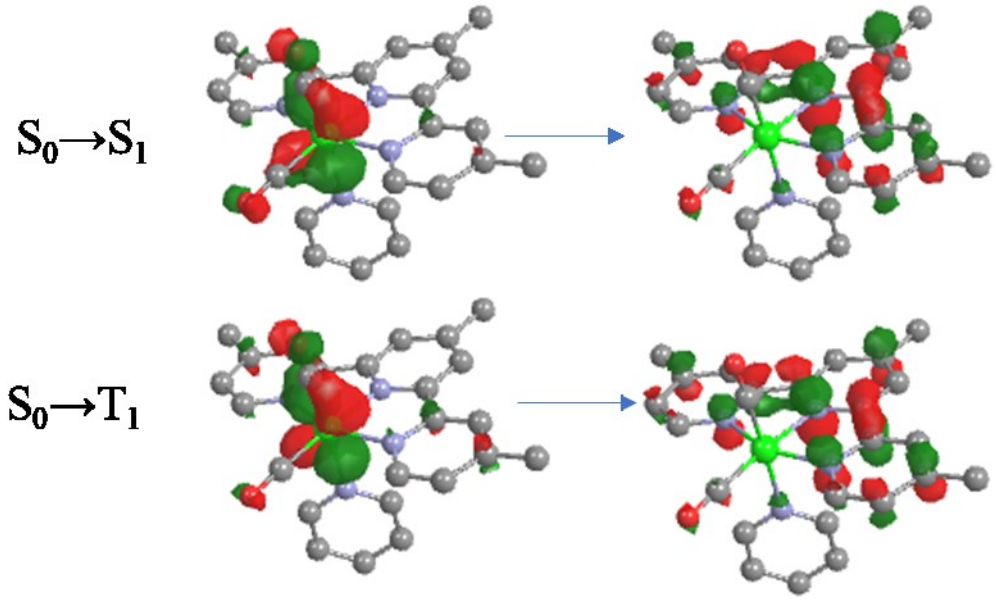

Figure XI.71. Natural transition orbitals for **IV-3b** lowest energy transitions.

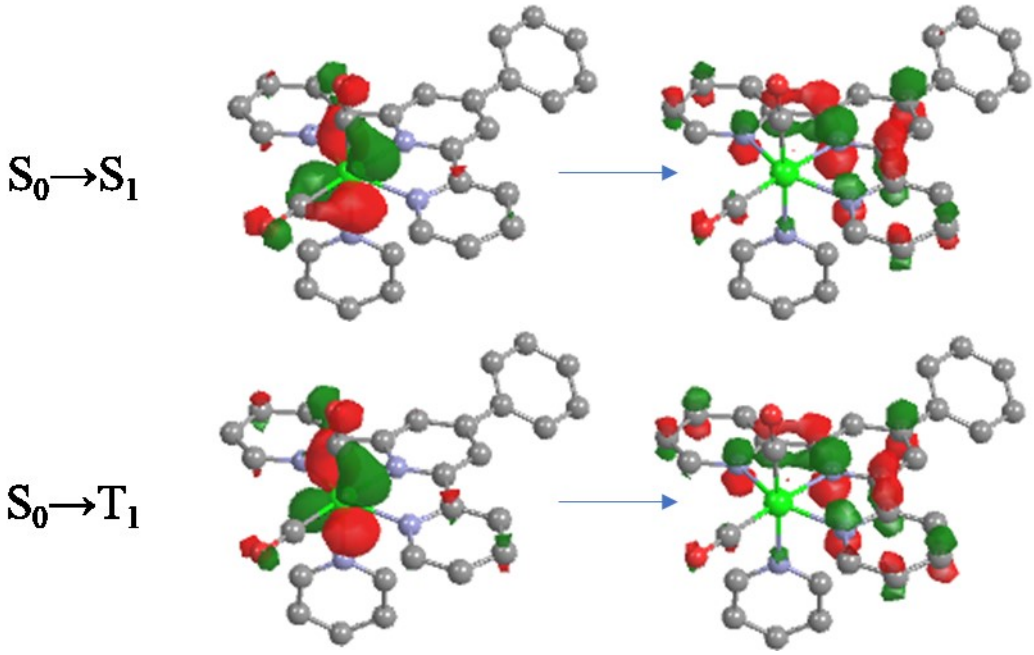

Figure XI.72. Natural transition orbitals for **IV-3c** lowest energy transitions.

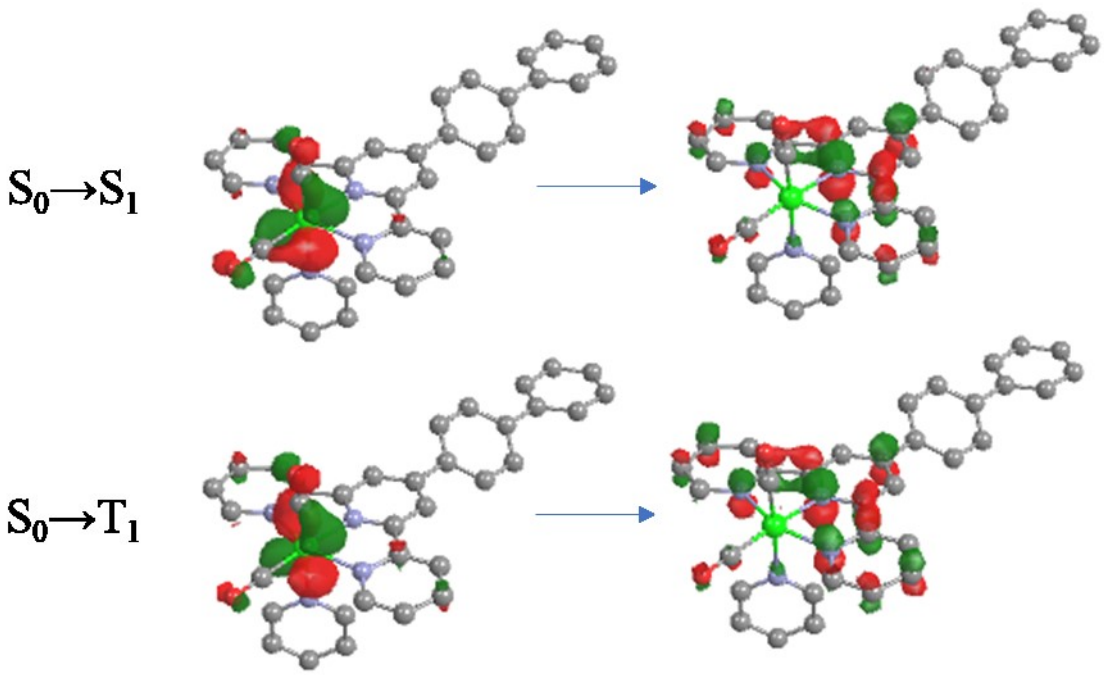

Figure XI.73. Natural transition orbitals for **IV-3d** lowest energy transitions.

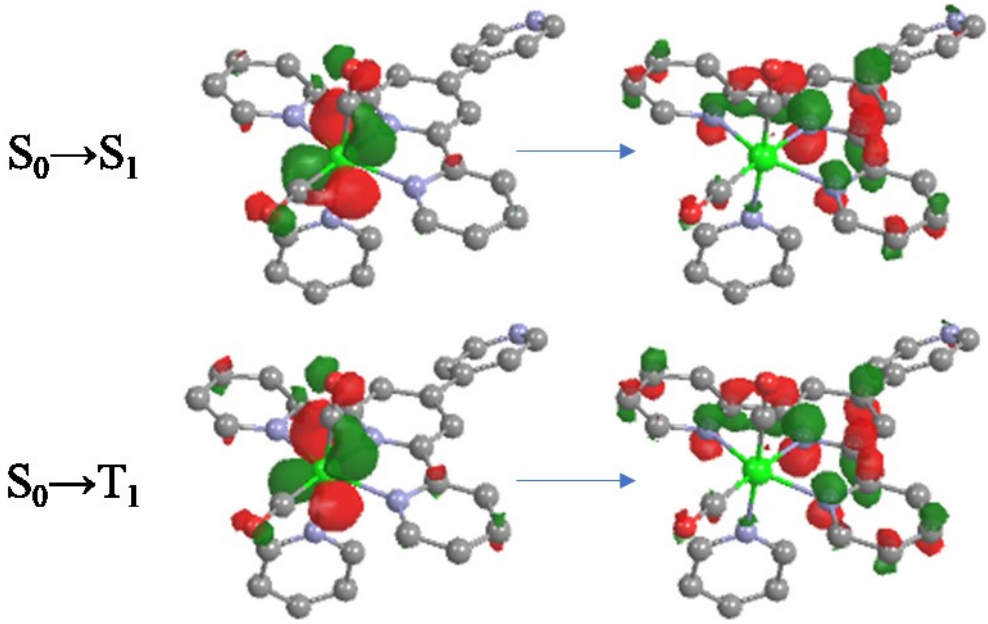

Figure XI.74. Natural transition orbitals for **IV-3e** lowest energy transitions.

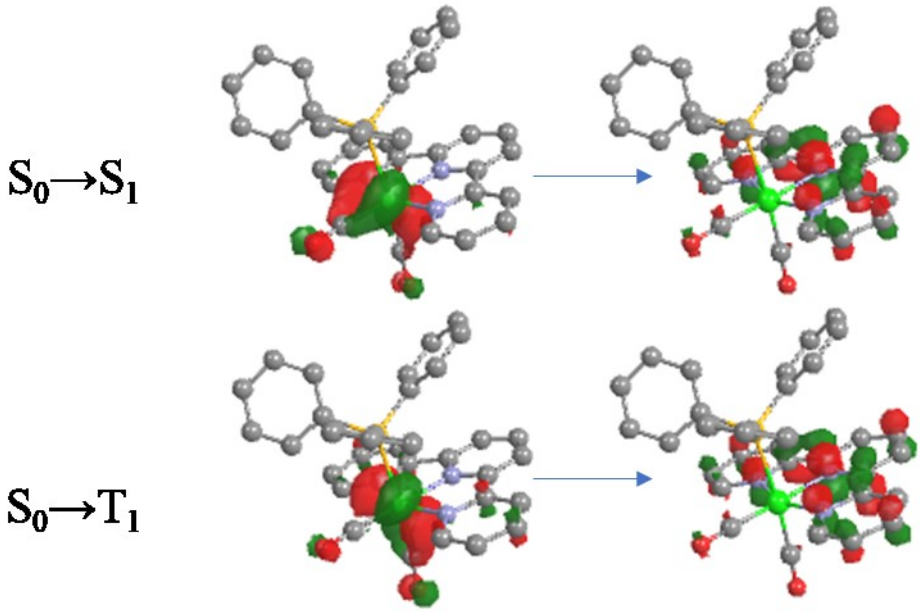

Figure XI.75. Natural transition orbitals for **IV-4a** lowest energy transitions.

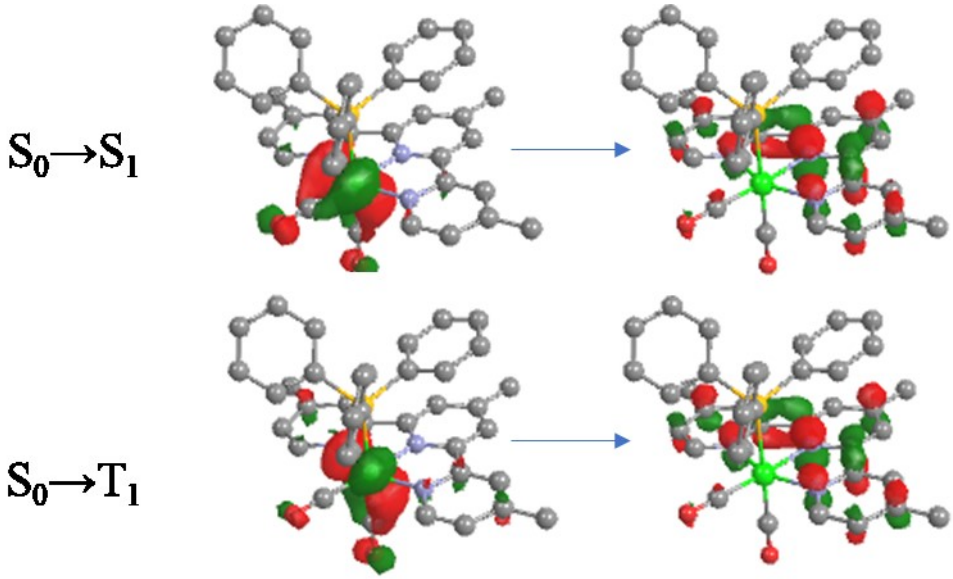

Figure XI.76. Natural transition orbitals for **IV-4b** lowest energy transitions.

XI.2.6 Optimized geometries

Table XI.20. Coordinates of the optimized geometry of **IV-1a**.

Center number	Atomic number	Coordinates (Å)			Center number	Atomic number	Coordinates (Å)		
		X	Y	Z			X	Y	Z
1	6	1.307778	0.225098	1.406016	20	6	0.237491	-4.820687	4.944150
2	7	0.233659	0.208298	4.003140	21	6	-1.061250	-2.625325	4.365493
3	6	1.117206	0.974312	2.093462	22	7	1.282710	-3.155260	4.066124
4	6	0.904927	1.416231	2.013471	23	6	1.037133	-4.396038	4.540432
5	6	0.376727	1.384140	3.308306	24	6	-1.305977	-3.918823	4.845543
6	6	0.549729	0.961570	3.376916	25	1	-1.869027	-1.912341	4.252483
7	1	1.380870	-1.926919	1.651920	26	1	1.888288	-5.067772	4.589190
8	1	1.021369	2.355284	1.489691	27	1	-2.310014	-4.215097	5.130271
9	6	0.060921	2.603459	4.004197	28	1	0.383650	-5.829928	5.312348
10	6	0.994915	4.774010	5.449568	29	75	0.113337	0.493781	6.148960
11	7	0.419255	2.439807	5.310958	30	35	2.507838	1.155211	6.151049
12	6	0.152093	3.857329	3.383747	31	6	0.360494	-1.240959	6.812556
13	6	0.619025	4.954946	4.111542	32	8	0.681497	-2.280686	7.278015
14	6	0.881105	3.504127	6.013902	33	6	0.245086	1.053249	7.962965
15	1	0.125681	3.982472	2.345691	34	8	0.312796	1.422686	9.087496
16	1	0.694012	5.929042	3.641700	35	6	-1.951012	0.068866	6.119429
17	1	-1.160931	3.326322	7.043192	36	8	-3.111130	0.195212	6.119677
18	1	-1.369113	5.594557	6.049290	37	1	1.743307	0.233016	0.413492
19	6	0.250016	-2.278404	3.998412					

Table XI.21. Coordinates of the optimized geometry of **IV-1b**.

Center number	Atomic number	Coordinates (Å)			Center number	Atomic number	Coordinates (Å)		
		X	Y	Z			X	Y	Z
1	6	1.159452	0.193887	1.187805	24	1	-1.684733	-2.060751	4.281487
2	7	0.347322	0.070927	3.903286	25	1	2.075411	-5.209793	4.122596
3	6	1.041443	-1.025810	1.868209	26	1	0.095553	-5.995464	5.058250
4	6	0.797966	1.349357	1.896535	27	75	0.229614	0.279950	6.081330
5	6	0.405099	1.268257	3.234025	28	35	2.832728	0.979985	5.826293
6	6	0.612236	-1.068263	3.200959	29	6	0.785520	-1.470340	6.629884
7	1	1.262419	-1.962852	1.370895	30	8	1.160032	-2.522886	7.021862
8	1	0.844862	2.310746	1.401007	31	6	0.288626	0.780479	7.915717
9	6	0.024474	2.458347	4.012337	32	8	0.338614	1.114544	9.052838
10	6	0.777311	4.563529	5.607147	33	6	-1.594387	0.169885	6.236954
11	7	0.185433	2.244490	5.343014	34	8	-2.744988	0.451471	6.355219
12	6	0.155225	3.726741	3.447014	35	6	0.728534	6.187262	3.657812
13	6	0.556050	4.813447	4.239145	36	1	0.162969	6.795959	3.856171
14	6	0.584335	3.284113	6.118249	37	1	-1.581167	6.704321	4.108644
15	1	0.003632	3.878428	2.386678	38	1	0.872433	6.152255	2.574609
16	1	0.751191	3.076014	7.166434	39	6	1.650016	0.263872	0.229182
17	1	-1.099616	5.356373	6.272690	40	1	2.740378	0.390034	0.243246
18	6	0.390552	-2.411004	3.800548	41	1	1.214830	1.113661	0.763046
19	6	0.005236	-4.972327	4.710411	42	1	1.418817	0.653060	0.778368
20	6	0.871210	-2.777719	4.292462	43	6	-2.415722	-4.500655	5.330666
21	7	1.430461	-3.279161	3.727768	44	1	-2.572676	-5.579009	5.234167
22	6	1.228164	-4.534023	4.186056	45	1	-3.240623	-3.981154	4.833248
23	6	-1.084142	-4.084413	4.767811	46	1	-2.469899	-4.253052	6.398896

Table XI.22. Coordinates of the optimized geometry of **IV-1c**.

Center number	Atomic number	Coordinates (Å)			Center number	Atomic number	Coordinates (Å)		
		X	Y	Z			X	Y	Z
1	6	0.139164	0.054416	1.100135	25	1	-2.107817	-1.920860	4.847599
2	7	0.150905	0.144669	3.924972	26	1	1.547383	-5.142644	4.178923
3	6	0.132165	-1.110860	1.883156	27	1	-2.295708	-4.184878	5.899149
4	6	0.064845	1.267379	1.780441	28	1	0.418670	-5.833654	5.565326
5	6	0.199913	1.289458	3.168279	29	6	0.330826	0.009207	0.365474
6	6	0.043755	-1.046875	3.269485	30	6	0.701419	0.076826	-3.165027
7	1	0.268559	-2.088551	1.438142	31	6	0.940761	1.086112	-1.043481
8	1	0.119357	2.192158	1.222192	32	6	0.089984	-1.111660	-1.112153
9	6	0.414460	2.541304	3.911584	33	6	0.091449	-1.152888	-2.500022
10	6	0.877484	4.775922	5.482467	34	6	1.126661	1.042153	-2.430726
11	7	0.374692	2.430351	5.271387	35	1	1.299048	1.948590	0.488881
12	6	0.682431	3.772773	3.297509	36	1	0.584973	-1.942525	0.618182
13	6	0.912266	4.902445	4.087141	37	1	0.247203	-2.018296	-3.061256
14	6	0.606466	3.525836	6.037104	38	1	1.607223	1.874350	-2.935780
15	1	0.724033	3.856776	2.219671	39	1	0.843749	0.109955	-4.240900
16	1	-1.120688	5.859525	3.622566	40	75	0.150823	0.509694	6.059961
17	1	0.572424	3.389050	7.109274	41	35	2.662740	1.123588	5.266154
18	1	-1.056332	5.622819	6.133419	42	6	0.782459	-1.210712	6.619982
19	6	0.161475	-2.339171	3.995696	43	8	1.215331	-2.241841	7.007660
20	6	0.376599	-4.839799	5.134065	44	6	0.565869	1.134456	7.809388
21	6	-1.310256	-2.646751	4.744132	45	8	0.836820	1.544425	8.888415
22	7	0.835627	-3.234971	3.788682	46	6	-1.616600	0.120112	6.591014
23	6	0.727005	-4.455009	4.358348	47	8	-2.727000	0.120918	6.944223
24	6	-1.416822	-3.919019	5.321349					

Table XI.23. Coordinates of the optimized geometry of **IV-1d**.

Center number	Atomic number	Coordinates (Å)			Center number	Atomic number	Coordinates (Å)		
		X	Y	Z			X	Y	Z
1	6	2.006258	0.050785	0.340086	30	6	6.323610	0.076242	0.044509
2	7	0.833034	0.126267	0.442304	31	6	4.139979	-1.141052	0.241199
3	6	1.290477	1.254419	0.232690	32	6	4.266388	1.112927	0.626261
4	6	1.246053	-1.111032	0.562731	33	6	5.659015	1.069905	0.531157
5	6	0.146391	-1.051862	0.604582	34	6	5.532483	-1.179995	0.340043
6	6	0.105513	1.273439	0.316654	35	1	3.568348	-2.005907	0.564849
7	1	1.796759	2.198514	0.075088	36	1	3.796441	2.008864	1.020469
8	1	1.745221	-2.059988	0.704797	37	1	6.232158	1.944860	0.822432
9	6	0.971357	-2.248486	0.835029	38	1	6.007755	-2.085470	0.704794
10	6	-2.692469	-4.367247	1.308653	39	75	-2.960836	0.142935	0.015004
11	7	-2.317218	-2.068887	0.695735	40	35	-2.041364	0.939962	-2.401162
12	6	0.446454	-3.492976	1.210378	41	6	-3.382705	1.564346	0.746286
13	6	-1.311739	-4.564545	1.446105	42	8	-3.684540	2.585981	-1.262161
14	6	-3.156878	-3.107562	0.932799	43	6	-4.711228	0.700160	0.484078
15	1	0.619964	-3.630625	1.329321	44	8	-5.791117	-1.069806	0.805085
16	1	0.916404	-5.531089	1.737235	45	6	-3.584684	0.374076	1.718164
17	1	-4.215009	-2.916861	0.817039	46	8	-3.997840	0.694469	2.787015
18	1	-3.400272	-5.167140	1.487822	47	6	7.803234	0.119152	0.059957
19	6	0.763867	2.606945	0.314371	48	6	10.628710	0.200572	0.259780
20	6	-1.767685	5.173708	0.316338	49	6	8.435742	0.862506	-1.079951
21	6	-1.561471	3.022123	1.394078	50	6	8.614447	0.582673	0.857811
22	7	0.446296	3.429382	0.716361	51	6	10.011790	0.542614	0.759725
23	6	0.950681	4.682531	0.712760	52	6	9.832975	0.902938	-1.179428
24	6	-2.069890	4.327826	1.392465	53	1	7.836607	-1.391799	-1.815460
25	1	-1.754815	2.351400	2.222607	54	1	8.155737	1.142758	1.667695
26	1	0.683403	5.309418	-1.557540	55	1	10.617118	1.083536	1.481249
27	1	-2.683256	4.676199	2.216734	56	1	10.298842	-1.474481	-1.976869
28	1	-2.142561	6.190217	0.275376	57	1	11.711506	0.231698	0.336446
29	6	3.479098	0.007280	0.242821					

Table XI.24. Coordinates of the optimized geometry of **IV-1e**.

Center number	Atomic number	Coordinates (Å)			Center number	Atomic number	Coordinates (Å)		
		X	Y	Z			X	Y	Z
1	6	0.199819	0.063083	1.116315	24	6	-1.384795	-3.933731	5.300513
2	7	0.137559	0.144688	3.927536	25	1	-2.087263	-1.940447	4.823146
3	6	0.191614	-1.105443	1.890359	26	1	1.603926	-5.129250	4.192061
4	6	0.025675	1.273974	1.788479	27	1	-2.268747	-4.208797	5.866066
5	6	0.186102	1.291581	3.174561	28	1	0.373484	-5.840212	5.552242
6	6	0.008173	-1.045508	3.274554	29	6	0.416305	0.021294	0.347294
7	1	0.344522	-2.080007	1.443649	30	6	1.053004	1.081155	-1.021649
8	1	0.076316	2.198578	1.229472	31	6	0.004187	-1.080675	-1.116650
9	6	0.425196	2.539186	3.916678	32	6	0.221624	-1.077635	-2.498142
10	6	0.937615	4.764523	5.483889	33	6	1.240186	0.997794	-2.406486
11	7	0.406993	2.424850	5.276621	34	1	1.424603	1.949403	0.488297
12	6	0.695318	3.768841	3.300381	35	1	0.520779	-1.920826	0.665658
13	6	0.950095	4.894272	4.088627	36	1	0.100914	-1.914638	-3.109006
14	6	0.663016	3.515921	6.040596	37	1	1.734641	1.801226	-2.942934
15	1	0.719817	3.855388	2.222201	38	75	0.126556	0.508228	6.068728
16	1	-1.160448	5.850257	3.622765	39	35	2.641743	1.147925	5.311814
17	1	0.645663	3.377314	7.112910	40	6	0.768004	-1.207298	6.634114
18	1	-1.136232	5.607930	6.133617	41	8	1.205753	-2.234841	7.025189
19	6	0.126009	-2.339964	3.996069	42	6	0.510460	1.133495	7.825136
20	6	0.334351	-4.844875	5.124200	43	8	0.761949	1.543896	8.908334
21	6	-1.281881	-2.658795	4.728316	44	6	-1.644441	0.099789	6.574708
22	7	0.880960	-3.226655	3.798259	45	8	-2.756749	0.152994	6.912445
23	6	0.775768	-4.448962	4.363246	46	7	0.834631	0.060013	-3.148569

Table XI.25. Coordinates of the optimized geometry of **IV-2a**.

Center number	Atomic number	Coordinates (Å)			Center number	Atomic number	Coordinates (Å)		
		X	Y	Z			X	Y	Z
1	6	0.071313	0.219079	0.959170	19	6	0.033448	-2.099406	3.984647
2	7	0.002763	0.251015	3.704797	20	6	0.076135	-4.143585	5.850320
3	6	0.051590	0.990598	1.668113	21	6	0.040429	-3.428472	3.549208
4	6	0.079339	1.444633	1.640536	22	7	0.043884	-1.787475	5.329404
5	6	0.047660	1.433855	3.040825	23	6	0.068680	-2.800626	6.232490
6	6	0.020527	0.947398	3.067791	24	6	0.060829	-4.466750	4.486749
7	1	0.067854	-1.933457	1.136233	25	1	0.030156	-3.652656	2.489626
8	1	0.116942	2.374593	1.087449	26	1	0.081667	-2.510327	7.274059
9	6	0.087061	2.605734	3.931366	27	1	0.065807	-5.500471	4.160424
10	6	0.176791	4.690129	5.750287	28	1	0.094686	-4.912792	6.613124
11	7	0.090734	2.324175	5.282843	29	75	0.009386	0.274340	5.776837
12	6	0.124208	3.924096	3.465947	30	35	2.726108	0.240110	5.487701
13	6	0.168500	4.982601	4.379744	31	6	0.253171	0.292735	7.646547
14	6	0.138840	3.356686	6.162764	32	8	0.436789	0.304103	8.835204
15	1	0.118772	4.124407	2.401558	33	6	-1.834474	0.298243	6.032342
16	1	0.196943	6.008287	4.030098	34	8	-3.022415	0.313947	6.223777
17	1	0.145478	3.089825	7.210643	35	1	0.093780	0.206550	0.124615
18	1	0.213059	5.475788	6.495483					

Table XI.26. Coordinates of the optimized geometry of **IV-2b**.

Center number	Atomic number	Coordinates (Å)			Center number	Atomic number	Coordinates (Å)		
		X	Y	Z			X	Y	Z
1	6	0.026659	0.131324	1.001953	23	6	0.229539	-4.485267	4.640004
2	7	0.023820	0.230089	3.773952	24	1	0.270356	-3.681035	2.639962
3	6	0.098887	-1.051225	1.763683	25	1	0.005803	-2.469214	7.390244
4	6	0.077856	1.362826	1.677491	26	1	0.164278	-4.868373	6.777289
5	6	0.082333	1.388310	3.075733	27	75	0.051665	0.298493	5.844589
6	6	0.090902	0.977835	3.160215	28	35	2.757841	0.087089	5.472816
7	1	0.151568	-2.009141	1.259926	29	6	0.353947	0.342747	7.703890
8	1	0.162462	2.280042	1.106783	30	8	0.574912	0.368824	8.887350
9	6	0.221580	2.577863	3.934960	31	6	-1.775443	0.443257	6.152485
10	6	0.491158	4.695391	5.681608	32	8	-2.955517	0.537701	6.377839
11	7	0.248544	2.326805	5.290665	33	6	0.597579	6.377927	3.782759
12	6	0.324282	3.878763	3.434942	34	1	1.651665	6.683901	3.780746
13	6	0.463061	4.974644	4.302244	35	1	0.055002	7.088327	4.414500
14	6	0.385366	3.381655	6.133971	36	1	0.224301	6.465594	2.758709
15	1	0.295305	4.045072	2.364106	37	6	0.067821	0.080713	0.499947
16	1	0.405437	3.147720	7.189694	38	1	0.351577	0.855071	0.880453
17	1	0.594455	5.494822	6.407277	39	1	0.481257	0.916163	0.943694
18	6	0.121712	-2.111010	4.102373	40	1	-1.105258	0.144069	0.852822
19	6	0.153957	-4.115933	5.996211	41	6	0.303278	-5.926470	4.222080
20	6	0.211935	-3.445170	3.696439	42	1	0.695063	-6.381883	4.247251
21	7	0.051475	-1.771013	5.436975	43	1	0.690652	-6.031327	3.204904
22	6	0.065171	-2.772037	6.353685	44	1	0.940133	-6.503765	4.899797

Table XI.27. Coordinates of the optimized geometry of **IV-2c**.

Center number	Atomic number	Coordinates (Å)			Center number	Atomic number	Coordinates (Å)		
		X	Y	Z			X	Y	Z
1	6	0.070968	0.080361	0.963500	24	6	0.001376	-4.499837	4.643581
2	7	0.050881	0.193401	3.738019	25	1	0.097822	-3.742531	2.627167
3	6	0.075772	-1.101506	1.734957	26	1	0.140372	-2.466737	7.371693
4	6	0.027715	1.320213	1.635861	27	1	0.014195	-5.542219	4.346457
5	6	0.008903	1.351133	3.032107	28	1	0.110422	-4.886681	6.779047
6	6	0.062180	-1.018925	3.129018	29	6	0.096307	0.019306	0.516279
7	1	0.059269	-2.066894	1.244956	30	6	0.147816	0.098875	-3.339788
8	1	0.026042	2.243190	1.069844	31	6	0.564962	0.996990	-1.289442
9	6	0.068858	2.550720	3.883782	32	6	0.783526	-1.018766	-1.180499
10	6	0.234251	4.687451	5.636240	33	6	0.810652	-1.076012	-2.579689
11	7	0.115606	2.309424	5.242481	34	6	0.541016	0.937156	-2.688517
12	6	0.100629	3.854568	3.378846	35	1	1.124952	1.790591	0.803274
13	6	0.182711	4.939241	4.258620	36	1	-1.323524	-1.768425	0.609270
14	6	0.200687	3.367178	6.089089	37	1	-1.352767	-1.875885	-3.074692
15	1	0.061979	4.024495	2.309866	38	1	1.063795	1.691941	-3.267924
16	1	0.206954	5.953814	3.877642	39	1	0.167690	0.144225	-4.424432
17	1	0.240716	3.131176	7.143598	40	75	0.035948	0.275838	5.802771
18	1	0.300893	5.494381	6.356173	41	35	2.742017	0.206932	5.418076
19	6	0.024967	-2.147143	4.075696	42	6	0.349340	0.345703	7.661348
20	6	0.069848	-4.139016	5.995956	43	8	0.577173	0.389772	8.841689
21	6	0.045548	-3.487943	3.678602	44	6	-1.796531	0.323312	6.126525
22	7	0.037494	-1.798128	5.410101	45	8	-2.976224	0.354882	6.362483
23	6	0.087012	-2.785945	6.339908					

Table XI.28. Coordinates of the optimized geometry of **IV-2d**.

Center number	Atomic number	Coordinates (Å)			Center number	Atomic number	Coordinates (Å)		
		X	Y	Z			X	Y	Z
1	6	1.951241	0.003689	0.164391	29	6	3.429835	0.000260	0.119371
2	7	0.824488	0.014253	0.275656	30	6	6.282230	0.002537	0.033418
3	6	1.229492	1.215927	0.110114	31	6	4.137875	-1.066227	0.472709
4	6	1.225955	-1.204365	0.248391	32	6	4.174434	1.065156	0.667915
5	6	0.169449	-1.173767	0.293795	33	6	5.570698	1.061891	0.626956
6	6	0.165611	1.195184	0.164216	34	6	5.534054	-1.065701	0.515827
7	1	1.756532	2.154756	0.004267	35	1	3.601110	-1.895511	0.923960
8	1	1.751449	-2.149758	0.294878	36	1	3.666857	1.895448	1.150139
9	6	-1.072853	-2.336361	0.348371	37	1	6.109958	1.905403	1.047210
10	6	-2.918580	-4.398305	0.429345	38	1	6.045252	-1.910221	0.967972
11	7	-2.421069	-2.038367	0.343706	39	75	-2.892323	0.018475	0.288477
12	6	0.624717	-3.660370	0.396089	40	35	-2.637805	0.137275	-2.430197
13	6	-1.551722	-4.707302	0.438635	41	6	-4.765480	0.008502	0.067667
14	6	-3.314016	-3.060241	0.379718	42	8	-5.956567	0.000481	0.100550
15	1	0.436855	-3.875212	0.400012	43	6	-3.127590	0.126840	2.131837
16	1	-1.214804	-5.736923	0.476834	44	8	-3.306512	0.197415	3.319833
17	1	-4.358491	-2.780537	0.368579	45	6	7.765633	0.003560	0.011965
18	1	-3.673736	-5.174687	0.458417	46	6	10.598213	0.005395	0.099230
19	6	-1.065544	2.358683	0.079196	47	6	8.456619	0.605015	-1.086105
20	6	-2.904306	4.421459	0.089201	48	6	8.522139	0.597101	1.017555
21	6	0.612953	3.677790	0.025966	49	6	9.922894	0.596433	0.975049
22	7	-2.414708	2.066289	0.104538	50	6	9.857317	0.606232	-1.129930
23	6	-3.304264	3.088059	0.017764	51	1	7.900234	-1.052673	-1.904701
24	6	-1.536465	4.725266	0.110764	52	1	8.017856	1.045733	1.868749
25	1	0.449373	3.888237	0.041906	53	1	10.485470	1.057369	1.781700
26	1	-4.349740	2.812465	0.036655	54	1	10.368540	-1.067778	-1.969728
27	1	-1.196136	5.751220	0.192525	55	1	11.683657	0.006062	0.132644
28	1	-3.656828	5.198191	0.154508					

Table XI.29. Coordinates of the optimized geometry of **IV-2e**.

Center number	Atomic number	Coordinates (Å)			Center number	Atomic number	Coordinates (Å)		
		X	Y	Z			X	Y	Z
1	6	0.073492	0.082087	0.970749	23	6	0.118107	-2.784600	6.339748
2	7	0.045789	0.194156	3.738013	24	6	0.037583	-4.499102	4.643414
3	6	0.072283	-1.101456	1.735818	25	1	0.072344	-3.742840	2.627383
4	6	0.032106	1.322890	1.637077	26	1	0.172890	-2.465335	7.371414
5	6	0.011977	1.353562	3.033919	27	1	0.027580	-5.541539	4.346377
6	6	0.051861	-1.019153	3.130363	28	1	0.155843	-4.885171	6.778372
7	1	0.056886	-2.065924	1.243895	29	6	0.103477	0.020914	0.509570
8	1	0.032621	2.245165	1.069839	30	6	0.559335	0.982668	-1.296632
9	6	0.061051	2.552718	3.885496	31	6	0.797379	-1.002878	-1.183563
10	6	0.217349	4.688710	5.638613	32	6	0.801670	-1.022590	-2.583303
11	7	0.113042	2.310334	5.243774	33	6	0.503821	0.883749	-2.691894
12	6	0.082799	3.856887	3.380983	34	1	1.133612	1.784288	0.845125
13	6	0.160351	4.941342	4.261398	35	1	-1.349749	-1.762590	0.641211
14	6	0.193574	3.367972	6.090871	36	1	-1.336357	-1.800100	-3.119465
15	1	0.039739	4.027768	2.312321	37	1	1.013879	1.611999	-3.314280
16	1	0.176867	5.956329	3.881219	38	75	0.047612	0.276329	5.801625
17	1	0.237982	3.131721	7.145121	39	35	2.750162	0.223099	5.410185
18	1	0.280713	5.495552	6.358923	40	6	0.366327	0.347497	7.659996
19	6	0.005074	-2.146891	4.076165	41	8	0.597402	0.392615	8.839041
20	6	0.108116	-4.137726	5.995492	42	6	-1.785105	0.312941	6.131672
21	6	0.018595	-3.487575	3.678578	43	8	-2.963605	0.337524	6.371385
22	7	0.059526	-1.797124	5.410213	44	7	0.164013	0.099233	-3.341644

Table XI.30. Coordinates of the optimized geometry of **IV-3a**.

Center number	Atomic number	Coordinates (Å)			Center number	Atomic number	Coordinates (Å)		
		X	Y	Z			X	Y	Z
1	6	0.030697	0.301535	0.961187	24	6	0.145060	-4.432597	4.422429
2	7	0.051714	0.297927	3.706575	25	1	0.181502	-3.588241	2.438808
3	6	0.083061	0.916382	1.654190	26	1	0.030019	-2.525056	7.238896
4	6	0.000573	1.518680	1.656762	27	1	0.168825	-5.460485	4.079313
5	6	0.018667	1.490432	3.056664	28	1	0.082199	-4.913711	6.540037
6	6	0.092905	0.891994	3.054398	29	75	0.050438	0.291592	5.781840
7	1	0.114129	-1.850740	1.108497	30	6	0.171649	0.305534	7.667214
8	1	0.029226	2.454894	1.114059	31	8	0.257466	0.322891	8.865620
9	6	0.029850	2.652729	3.963348	32	6	-1.825334	0.317458	5.963013
10	6	0.110179	4.711568	5.812572	33	8	-3.013204	0.328404	6.108079
11	7	0.104861	2.351032	5.311101	34	1	0.018647	0.302027	0.122720
12	6	0.019467	3.976964	3.520059	35	7	2.258377	0.207824	5.653907
13	6	0.017421	5.022667	4.450055	36	6	5.064434	0.036737	5.556478
14	6	0.152890	3.371717	6.204840	37	6	2.980951	1.015510	4.834072
15	1	0.083874	4.194124	2.461067	38	6	2.933788	0.688888	6.424064
16	1	0.022165	6.053314	4.116804	39	6	4.323852	0.800650	6.402827
17	1	0.218708	3.091040	7.246947	40	6	4.374090	0.959642	4.759769
18	1	0.147956	5.487204	6.567909	41	1	2.435312	1.726395	4.229546
19	6	0.123099	-2.057598	3.955832	42	1	2.338370	-1.321139	7.069168
20	6	0.098729	-4.132597	5.789631	43	1	4.808751	-1.530851	7.039771
21	6	0.154123	-3.378980	3.501011	44	1	4.898358	1.629676	4.088827
22	7	0.091474	-1.767175	5.306098	45	1	6.146408	0.028202	5.519621
23	6	0.074604	-2.795652	6.192487					

Table XI.31. Coordinates of the optimized geometry of **IV-3b**.

Center number	Atomic number	Coordinates (Å)			Center number	Atomic number	Coordinates (Å)		
		X	Y	Z			X	Y	Z
1	6	0.194597	3.934055	0.397778	28	6	0.054533	-2.673811	0.873540
2	7	0.088713	1.220662	0.163504	29	8	0.086487	-3.865205	-1.037417
3	6	1.044027	3.276839	0.249452	30	6	0.110974	0.597188	-2.469083
4	6	-1.376942	3.182661	0.264231	31	8	0.170613	0.493540	-3.661571
5	6	-1.299749	1.813476	0.013003	32	7	0.174945	-1.131729	1.582287
6	6	1.074235	1.909223	0.032750	33	6	0.473084	-1.605695	4.339252
7	1	1.962485	3.842270	0.354185	34	6	0.632769	0.521864	2.488947
8	1	-2.337043	3.670057	0.383190	35	6	1.135029	-1.976357	2.049227
9	6	-2.430426	0.875054	0.149030	36	6	1.310831	-2.236246	3.408333
10	6	-4.419817	-1.022566	0.373236	37	6	0.514928	0.733221	3.864190
11	7	-2.077051	0.444023	0.367623	38	1	-1.394326	0.143309	2.106891
12	6	-3.767217	1.261719	0.054369	39	1	1.765901	-2.451094	1.309497
13	6	-4.801464	0.315143	0.171137	40	1	2.089990	-2.920353	3.722962
14	6	-3.070044	-1.362980	0.465017	41	1	-1.188381	0.220839	4.540961
15	1	-4.014028	2.304000	0.113689	42	1	0.586994	-1.789473	5.402051
16	1	-2.759819	-2.386407	0.626016	43	6	6.086286	1.273448	0.308436
17	1	-5.165261	-1.805065	0.461173	44	1	6.193321	2.202813	0.878350
18	6	2.275399	1.076281	0.236388	45	1	6.815012	0.550623	0.683792
19	6	4.414887	0.600619	0.714295	46	1	6.342390	1.502710	0.733439
20	6	3.575664	1.575761	0.164428	47	6	0.240046	5.403657	0.708853
21	7	2.032717	0.251075	0.533822	48	1	-1.256050	5.799625	0.638767
22	6	3.097605	-1.057270	0.769857	49	1	0.400800	5.969471	0.024159
23	6	4.684494	0.741911	0.399720	50	1	0.127763	5.591620	1.724988
24	1	3.737566	2.621280	0.072596	51	6	-6.244087	0.726310	0.099097
25	1	2.873083	-2.086028	-1.018679	52	1	-6.892873	0.125531	0.121193
26	1	5.220707	-1.297142	0.916762	53	1	-6.566412	1.152146	-1.057984
27	75	0.006645	0.806862	0.602162	54	1	-6.401828	1.493451	0.665589

Table XI.32. Coordinates of the optimized geometry of **IV-3c**.

Center number	Atomic number	Coordinates (Å)			Center number	Atomic number	Coordinates (Å)		
		X	Y	Z			X	Y	Z
1	6	3.258249	0.057966	0.100586	29	75	-1.567937	0.071094	0.541809
2	7	0.492893	0.017584	0.340161	30	6	-3.455164	0.137847	0.604875
3	6	2.502906	-1.249925	0.142888	31	8	-4.655507	0.188248	0.637312
4	6	2.572724	1.173810	0.170768	32	6	-1.565732	0.133160	-2.425448
5	6	1.181364	1.186386	0.282810	33	8	-1.595361	0.168238	-3.621448
6	6	1.113620	-1.186766	0.266234	34	7	-1.660898	0.055577	1.665916
7	1	3.000658	-2.207536	0.057647	35	6	-1.843445	0.279928	4.464066
8	1	3.126925	2.103598	0.154908	36	6	0.883170	0.703636	2.481359
9	6	0.312762	2.376915	0.336958	37	6	-2.528732	0.930599	2.244504
10	6	-1.475849	4.489245	0.396520	38	6	-2.647045	-1.067630	3.627430
11	7	-1.044040	2.114769	0.399936	39	6	0.946832	0.620385	3.873704
12	6	0.796186	3.687781	0.316302	40	1	0.200093	1.397349	2.011706
13	6	0.102455	4.760501	0.349546	41	1	-3.138275	-1.523879	1.575902
14	6	-1.908487	3.161491	0.418794	42	1	-3.357040	-1.778652	4.032819
15	1	1.862243	3.873847	0.273031	43	1	0.303233	1.252271	4.474130
16	1	0.262308	5.781075	0.335856	44	1	-1.914707	0.365499	5.542869
17	1	-2.959735	2.911946	0.460154	45	6	4.733309	0.098833	0.019683
18	1	-2.209047	5.286529	0.417088	46	6	7.548775	0.176206	0.246880
19	6	0.184389	-2.329199	0.341403	47	6	5.427188	0.916921	0.711045
20	6	-1.693321	-4.352306	0.568588	48	6	5.472467	-1.153936	0.556135
21	6	0.599505	-3.662912	0.293184	49	6	6.868029	-1.190713	0.445435
22	7	-1.149370	-2.001201	0.491554	50	6	6.822289	0.877024	0.825611
23	6	-2.057197	-3.004536	0.605427	51	1	4.880595	1.725529	1.187563
24	6	0.344184	-4.690544	0.405042	52	1	4.965852	-1.933233	-1.118078
25	1	1.648885	-3.901991	0.173255	53	1	7.422449	-2.003841	0.903653
26	1	-3.087956	-2.704371	0.738120	54	1	7.339647	1.660908	1.370044
27	1	0.031446	-5.727744	0.369078	55	1	8.630587	0.205900	0.333969
28	1	-2.459381	-5.112019	0.666266					

Table XI.33. Coordinates of the optimized geometry of **IV-3d**.

Center number	Atomic number	Coordinates (Å)			Center number	Atomic number	Coordinates (Å)		
		X	Y	Z			X	Y	Z
1	6	2.031956	0.010401	0.225395	34	7	-2.821762	0.087923	1.701922
2	7	0.741451	0.036576	0.377026	35	6	-2.901949	0.333068	4.503207
3	6	1.296492	-1.194981	0.251220	36	6	-2.031746	0.682176	2.495120
4	6	1.321584	1.229900	0.267480	37	6	-3.650885	0.984113	2.304419
5	6	0.072387	1.217376	0.334929	38	6	-3.717944	-1.132028	3.689627
6	6	0.096527	-1.156488	0.330754	39	6	-2.045176	0.589188	3.888187
7	1	1.812701	-2.144289	0.186161	40	1	-1.379681	1.392766	2.007036
8	1	1.858063	2.170140	0.264793	41	1	-4.271435	-1.585644	1.653526
9	6	0.963826	2.391979	0.353563	42	1	-4.398678	-1.860037	4.114616
10	6	-2.791035	4.471659	0.339634	43	1	-1.394167	1.230605	4.470233
11	7	-2.317021	2.105455	0.371353	44	1	-2.933747	0.426712	5.583223
12	6	0.503683	3.711234	0.342465	45	6	3.508353	0.004181	0.151268
13	6	-1.421942	4.767670	0.338784	46	6	6.357928	0.031576	0.010689
14	6	-3.200250	3.136436	0.354489	47	6	4.213608	1.030778	0.497797
15	1	0.559760	3.916091	0.334835	48	6	4.254002	-1.053386	0.728298
16	1	-1.075433	5.794665	0.332149	49	6	5.649063	-1.063730	0.662127
17	1	-4.247645	2.868006	0.360972	50	6	5.608286	1.014396	0.569187
18	1	-3.538745	5.255564	0.330295	51	1	3.675076	1.837413	0.986463
19	6	-1.006692	-2.315397	0.383569	52	1	3.750621	-1.850066	-1.268107
20	6	-2.853309	-4.371449	0.563642	53	1	6.191281	-1.868205	-1.149481
21	6	0.565553	-3.641416	0.360945	54	1	6.115226	1.808811	1.108284
22	7	-2.350594	-2.011217	0.485712	55	6	7.839921	0.045533	0.062032
23	6	-3.243047	-3.030544	0.576799	56	6	10.669793	0.071964	0.201258
24	6	-1.493331	-4.685657	0.449090	57	6	8.575417	1.159384	0.072104
25	1	0.491661	-3.861487	0.279240	58	6	8.550257	-1.263954	0.122988
26	1	-4.283140	-2.748772	0.671471	59	6	9.949802	-1.277740	0.192040
27	1	-1.160512	-5.717078	0.432534	60	6	9.974981	1.147018	0.140787
28	1	-3.608196	-5.144541	0.641403	61	1	8.056592	2.111173	0.001135
29	75	-2.808464	0.053360	0.507156	62	1	8.009355	-2.205864	0.141684
30	6	-4.697748	0.086606	0.503626	63	1	10.476195	-2.226196	0.246227
31	8	-5.899167	0.115899	0.493965	64	1	10.521765	2.085429	0.139343
32	6	-2.873165	0.125779	-2.389230	65	1	11.754376	0.082102	0.254595
33	8	-2.945609	0.166529	-3.583228					

Table XI.34. Coordinates of the optimized geometry of **IV-3e**.

Center number	Atomic number	Coordinates (Å)			Center number	Atomic number	Coordinates (Å)		
		X	Y	Z			X	Y	Z
1	6	3.255671	0.061977	0.097788	28	1	-2.474806	-5.022295	-1.119388
2	7	0.498809	0.044614	0.334167	29	75	-1.560348	0.124708	0.537476
3	6	2.502523	-1.244164	0.244092	30	6	-3.447555	0.206406	0.609168
4	6	2.581497	1.175049	0.061000	31	8	-4.646589	0.266315	0.648357
5	6	1.190192	1.202900	0.177784	32	6	-1.543776	0.355142	-2.409012
6	6	1.112541	-1.165458	0.359770	33	8	-1.564482	0.496429	-3.596725
7	1	3.002520	-2.203239	0.291459	34	7	-1.671642	0.197098	1.648348
8	1	3.136938	2.092696	0.085771	35	6	-1.874634	0.669451	4.413879
9	6	0.325892	2.395676	0.122022	36	6	0.884995	0.470977	2.532370
10	6	-1.454634	4.510153	0.014474	37	6	-2.558699	-1.104529	2.141918
11	7	-1.031609	2.144844	0.209250	38	6	-2.687653	-1.363177	3.506255
12	6	0.814485	3.696982	0.019038	39	6	0.958240	0.263513	3.911113
13	6	0.080430	4.771266	0.085774	40	1	0.186927	1.191765	2.130276
14	6	-1.892259	3.191746	0.131223	41	1	-3.175283	-1.623743	1.420181
15	1	1.881251	3.874494	0.077989	42	1	-3.412973	-2.094319	3.842860
16	1	0.287765	5.784936	0.193627	43	1	0.306761	0.826124	4.569150
17	1	-2.944328	2.950867	0.195853	44	1	-1.953638	0.850713	5.480223
18	1	-2.184941	5.308510	0.068311	45	6	4.731562	0.118015	0.019706
19	6	0.179683	-2.292023	0.541786	46	7	7.554596	0.222768	0.244173
20	6	-1.705778	-4.277791	0.952641	47	6	5.544512	0.905890	0.503890
21	6	0.588605	-3.626862	0.606790	48	6	5.374033	-1.196091	0.658618
22	7	-1.151674	-1.945067	0.669437	49	6	6.771053	-1.205800	0.747960
23	6	-2.063371	-2.930052	0.874193	50	6	6.935000	0.812173	0.371448
24	6	0.359325	-4.635989	0.812193	51	1	5.118489	1.753077	-1.030382
25	1	1.635700	-3.881890	0.500507	52	1	4.809056	-2.006657	1.105863
26	1	-3.092132	-2.614796	0.985048	53	1	7.283614	-2.024516	1.242647
27	1	0.051752	-5.674013	0.864160	54	1	7.578109	1.587999	0.774234

Table XI.35. Coordinates of the optimized geometry of **IV-4a**.

Center number	Atomic number	Coordinates (Å)			Center number	Atomic number	Coordinates (Å)		
		X	Y	Z			X	Y	Z
1	6	-1.121222	-3.454584	2.769150	35	15	0.466785	1.217583	0.334856
2	7	0.682175	-1.915147	0.532340	36	6	0.602764	2.754797	0.224715
3	6	-2.146774	-2.636614	2.275338	37	6	-2.234809	5.045364	0.003812
4	6	0.124941	-3.496090	2.129269	38	6	-1.953001	2.710884	0.624291
5	6	0.325179	-2.699313	0.995817	39	6	0.079759	3.953689	0.292856
6	6	-1.901062	-1.866714	1.131854	40	6	0.893531	5.091511	0.404333
7	1	-3.108126	-2.610033	2.772320	41	6	-2.761202	3.851446	0.520298
8	1	0.913202	-4.130287	2.514158	42	1	-2.385117	1.799283	1.023874
9	6	1.557791	-2.607119	0.196958	43	1	0.956792	4.010325	0.608679
10	6	3.775231	-2.346708	-1.438639	44	1	0.476690	6.009850	0.806777
11	7	1.511082	-1.731175	0.870460	45	1	-3.798007	3.802486	0.838936
12	6	2.706700	-3.355297	0.470388	46	1	-2.862287	5.927521	0.080127
13	6	3.832478	-3.226533	0.350690	47	6	2.183836	1.875804	0.038176
14	6	2.604805	-1.619680	-1.666203	48	6	4.725592	2.945600	0.618052
15	1	2.723924	-4.034844	1.313392	49	6	2.952928	2.471716	0.979457
16	1	4.727715	-3.802810	0.147440	50	6	2.690361	1.832706	-1.348299
17	1	2.521367	0.940943	-2.502633	51	6	3.956466	2.364622	-1.637045
18	1	4.617307	-2.218530	-2.107963	52	6	4.218901	3.000339	0.690288
19	6	-2.858976	0.987532	0.444581	53	1	2.571715	2.526637	1.994301
20	6	-4.550363	0.628616	-1.035845	54	1	2.102311	1.402686	-2.150625
21	6	-4.188787	0.830239	0.847736	55	1	4.335611	2.324465	-2.653577
22	7	-2.368111	0.336060	0.671171	56	1	4.803738	3.456174	1.483458
23	6	-3.210952	0.452613	-1.387616	57	1	5.706784	3.354325	0.840210
24	6	-5.049455	0.015182	0.103803	58	6	0.595361	0.826941	2.168552
25	1	-4.553453	-1.345053	1.727926	59	6	0.875056	0.113493	4.882098
26	1	-2.788421	0.943119	-2.253340	60	6	1.597225	0.079778	2.569555
27	1	-6.082864	0.109890	0.405697	61	6	0.257934	1.379541	3.137222
28	1	-5.179106	1.265499	-1.646163	62	6	0.117722	1.022208	4.488178
29	75	0.359612	0.762931	-1.166197	63	6	1.737454	0.432312	3.917771
30	6	0.122496	0.380103	-2.651218	64	1	2.292450	0.487690	1.841297
31	8	0.017087	1.108312	-3.601866	65	1	-1.017685	2.102350	2.861950
32	6	0.890458	-2.097903	-2.386622	66	1	0.780438	1.460890	5.228054
33	8	-1.210266	-2.914447	-3.196286	67	1	2.518768	-1.126610	4.211976
34	1	-1.293788	-4.060049	3.651553	68	1	0.982462	0.159232	5.927614

Table XI.36. Coordinates of the optimized geometry of **IV-4b**.

Center number	Atomic number	Coordinates (Å)			Center number	Atomic number	Coordinates (Å)		
		X	Y	Z			X	Y	Z
1	6	0.090002	-3.939329	1.806917	40	1	-1.289652	3.201979	2.572312
2	7	0.095275	-1.854558	0.027841	41	1	-2.922925	5.047414	2.425999
3	6	-1.117844	-3.420887	1.302514	42	1	-3.366249	4.335164	-1.806322
4	6	1.300199	-3.375408	1.362387	43	1	-3.976931	5.625507	0.239177
5	6	1.279104	-2.321415	0.444562	44	6	1.425559	2.394411	0.941424
6	6	-1.092125	-2.370081	0.381630	45	6	3.620005	4.102307	1.383239
7	1	-2.058679	-3.843549	1.633936	46	6	1.774682	2.772230	2.250134
8	1	2.239517	-3.761252	1.739933	47	6	2.170861	2.887383	0.144032
9	6	2.448482	-1.622548	0.113771	48	6	3.263060	3.739511	0.075350
10	6	4.530441	0.274942	-1.317673	49	6	2.872483	3.617864	2.468170
11	7	2.159995	0.620899	-1.017919	50	1	1.202540	2.417314	3.101675
12	6	3.766543	-1.948088	0.215491	51	1	1.893788	2.624403	-1.160248
13	6	4.845840	-1.272743	0.377378	52	1	3.830072	4.116094	0.770603
14	6	3.200564	0.021927	-1.607380	53	1	3.137217	3.901339	3.482441
15	1	3.960031	-2.736915	0.933113	54	1	4.468003	4.758448	1.555241
16	1	2.946373	0.778949	-2.335799	55	6	0.500304	0.475677	2.158667
17	1	5.313479	0.274980	-1.828018	56	6	-1.135797	-1.000767	4.472832
18	6	-2.258516	-1.735175	0.256095	57	6	0.518229	0.140078	2.910613
19	6	-4.329157	0.509932	-1.604067	58	6	-1.840301	0.328365	2.561396
20	6	-3.575874	-2.127035	0.005912	59	6	-2.154841	0.402908	3.716075
21	7	-1.967447	0.730445	-1.155765	60	6	0.200880	0.869455	4.064822
22	6	-3.000894	0.147938	-1.816040	61	1	1.558775	0.049215	2.611177
23	6	-4.649237	-1.517639	0.675838	62	1	-2.640768	0.785585	1.987073
24	1	-3.773799	-2.915096	0.711249	63	1	-3.192348	0.503603	4.020239
25	1	-2.740544	0.614985	-2.535772	64	1	0.996281	-1.332895	4.640683
26	1	-5.107106	0.003545	-2.164680	65	1	-1.379594	-1.563421	5.369033
27	75	0.101994	0.320464	-1.433194	66	6	-6.069607	-1.943090	0.437427
28	6	0.161589	1.125451	-2.644626	67	1	-6.182669	-2.449000	0.525242
29	8	0.230870	2.034459	-3.431242	68	1	-6.393362	-2.640937	-1.220348
30	6	0.185883	-1.461969	-2.928091	69	1	-6.750038	-1.086401	0.465009
31	8	0.231164	-2.148527	-3.904968	70	6	0.084551	-5.048783	2.819930
32	15	0.093361	1.358009	0.559197	71	1	1.006498	-5.635289	2.777740
33	6	-1.403358	2.701804	0.460755	72	1	0.765322	-5.721389	2.672218
34	6	-3.259471	4.812644	0.300297	73	1	0.002683	-4.633239	3.832794
35	6	-1.991258	3.034506	0.768937	74	6	6.268353	-1.591109	0.016426
36	6	-1.740092	3.439416	1.612733	75	1	6.646672	0.863964	0.713561
37	6	-2.667005	4.486517	1.532183	76	1	6.921006	-1.539655	0.893448
38	6	-2.917741	4.086674	0.849261	77	1	6.358348	-2.585627	0.428879
39	1	-1.724777	2.489151	-1.666512					

1. N. G. Connelly and W. E. Geiger, *Chem. Rev.*, 1996, **96**, 877-910.

2. C. Adamo and V. Barone, *J. Chem. Phys.*, 1999, **110**, 6158-6170.

3. M. J. Frisch, G. W. Trucks, H. B. Schlegel, G. E. Scuseria, M. A. Robb, J. R. Cheeseman, G. Scalmani, V. Barone, G. A. Petersson, H. Nakatsuji, X. Li, M. Caricato, A. V. Marenich, J. Bloino, B. G. Janesko, R. Gomperts, B. Mennucci, H. P. Hratchian, J. V. Ortiz, A. F. Izmaylov, J. L. Sonnenberg, Williams, F. Ding, F. Lipparini, F. Egidi, J. Goings, B. Peng, A. Petrone, T. Henderson, D. Ranasinghe, V. G. Zakrzewski, J. Gao, N. Rega, G. Zheng, W. Liang, M. Hada, M. Ehara, K. Toyota, R. Fukuda, J. Hasegawa, M. Ishida, T. Nakajima, Y. Honda, O. Kitao, H. Nakai, T. Vreven, K. Throssell, J. A. Montgomery Jr., J. E. Peralta, F. Ogliaro, M. J. Bearpark, J. J. Heyd, E. N. Brothers, K. N. Kudin, V. N. Staroverov, T. A. Keith, R. Kobayashi, J. Normand, K. Raghavachari, A. P. Rendell, J. C. Burant, S. S. Iyengar, J. Tomasi, M. Cossi, J. M. Millam, M. Klene, C. Adamo, R. Cammi, J. W. Ochterski, R. L. Martin, K. Morokuma, O. Farkas, J. B. Foresman and D. J. Fox, Gaussian 16 Rev. A.03, 2016, Wallingford, CT

4. T. H. Dunning and P. J. Hay, *Modern Theoretical Chemistry III ed.*, Plenum, New York, 1977.

5. P. J. Hay and W. R. Wadt, *J. Chem. Phys.*, 1985, **82**, 299-310.

6. W. R. Wadt and P. J. Hay, *J. Chem. Phys.*, 1985, **82**, 284-298.

7. M. Cossi, N. Rega, G. Scalmani and V. Barone, *J. Comput. Chem.*, 2003, **24**, 669-681.

8. N. M. O'Boyle, A. L. Tenderholt and K. M. Langner, *J. Comput. Chem.*, 2008, **29**, 839-845.

9. S. Leonid, *V 4.53*, 2005-2017, www.chemissian.com.

10. S. P. Schmidt, W. C. Trogler and F. Basolo, *Inorg. Synth.*, 1990, **28**, 160-165.

11. B. A. Frenzel, J. E. Schumaker, D. R. Black and S. E. Hightower, *Dalton Trans.*, 2013, **42**, 12440-12451.

12. B. Laramee-Milette, N. Zaccheroni, F. Palomba and G. S. Hanan, *Chem. Eur. J.*, 2017, **23**, 6370-6379.

13. E. W. Abel, N. J. Long, K. G. Orrell, A. G. Osborne, H. M. Pain and V. Šik, *J. Chem. Soc., Chem. Commun.*, 1992, 303-304.

Chapitre XII. Matériels supplémentaires au chapitre VI

XII.1 Materials and instrumentation

Solvents and reagents were obtained from commercial sources (VWR, Fisher Scientific or Sigma Aldrich) and used as received, unless stated otherwise. $Re_2(CO)_{10}$ was purchased from Pressure Chemical Corporation. Nuclear magnetic resonance (NMR) spectra were recorded in deuterated solvents at room temperature (RT) on a Bruker AV spectrometer at 400MHz for ^{1}H NMR and 162MHz for ^{31}P NMR. Chemical shifts (δ) are reported in part per million (ppm) relative to residual proton resonance of the solvent (for example, 1.94 ppm for acetonitrile-D_3) and relative to pure phosphoric acid (0.0 ppm) for phosphorous resonance. IR spectra were recorded using an ATR sampler on a Bruker Alpha FT-IR spectrometer, ranging from 375 to 4000 cm^{-1}. Relative intensities are given after the wavenumber as vs = very strong, s= strong, m = medium, w = weak, sh = shoulder, br = broad. The high-resolution mass spectrometry (HR-MS) experiments were performed on a Bruker Daltonics MicroOTOF II in negative (or positive) electrospray mode, using HPLC grade solvents for the injected solutions. Appropriate $[M]^z$ species were used for empirical formula determination; exact masses were calculated and images were produced using mMass.[1] Electrochemical measurements were carried out in dry and nitrogen-purged solvents (freshly CaH_2 distilled acetonitrile or commercial anhydrous N,N-dimethylformamide stored in a glovebox) at RT with a BioLogic-SP50 potentiostat-galvanostat interfaced to a PC on which was installed the EC-lab software. The working electrode was a glassy carbon electrode (3mm diameter) which was polished with 0.05µm alumina paste before each sample. The counter electrode was a Pt wire and the pseudo-reference electrode was a silver wire placed in a vycor frit filled with a 0.1M solution of supporting electrolyte to keep it separated from the analyte. The reference was set using either ferrocenium/ferrocene (450mV vs. SCE in DMF[2]) or acetylferrocenium/ acetylferrocene (710 mV vs. SCE in acetonitrile[3]). The analyte concentration was about 1 mM and tetrabutylammonium hexafluorophosphate ($TBAPF_6$) was used as supporting electrolyte at 0.10 M. Cyclic voltammograms were obtained at scan rates between 50 and 500 mV/s. For irreversible processes, we used the cathodic potential determined by square-wave measurements. Adsorption phenomena of POMs on glassy carbon electrode are known to enlarge signals and a desorption peak was sometimes observed

and is identified on the cyclovoltammogram when observed. UV-visible absorption spectra at RT were acquired on a Cary 5000i UV-vis-NIR spectrophotometer while luminescence spectra were obtained on a Perkin-Elmer LS55 fluorescence spectrometer. For the luminescence lifetimes, an Edinburgh OB 900 single-photon-counting spectrometer was used, employing a Hamamatsu PLP2 laser diode as pulse (wavelength output, 408 nm; pulse width, 59 ps). Spectroscopic grade solvents were used to prepare the solution for the luminescence measurements which were nitrogen purged. The microanalyses were performed at the Elemental Analysis Service of the Université de Montréal.

XII.2 Synthesis and characterization

As a general procedure, POMs were only manipulated with glass or plastic spatula and kept away from light to minimize the formation of partially reduced species.

XII.2.1. Polypyridines with triol function

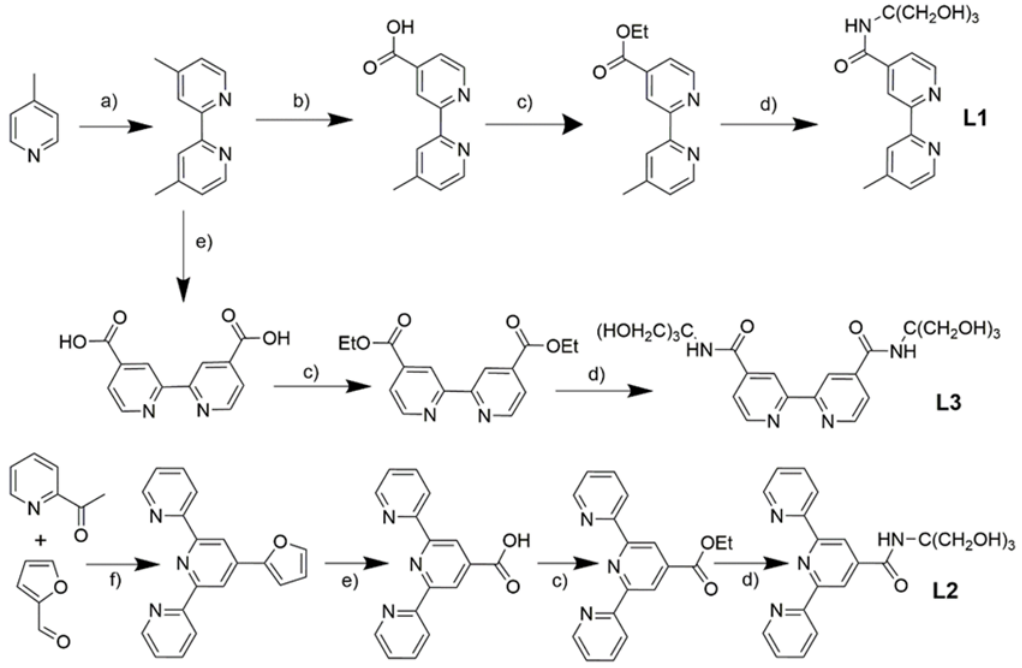

Figure XII.1. Synthetic pathways for **VI-L1**, **VI-L2** and **VI-L3**.

a) Pd/C, MnO_2, neat, 140°C 7d [4] ***b)*** *2 steps : SeO_2 in 1,4-dioxane at reflux 24h – $AgNO_3$, NaOH in EtOH/H_2O at RT overnight*[5] ***c)*** *anhyd. EtOH, conc. H_2SO_4 (cat.) at reflux for 3d*[6] ***d)*** *TRIS and K_2CO_3 in DMSO at RT for 2d*[7-9] ***e)*** *$KMnO_4$ and NaOH in H_2O (pH = 11) for 12h at reflux*[10-11] *and* ***f)*** *KOH and conc. NH_3(aq) in EtOH at RT 24h*[12]

VI-L1 N-(1,3-dihydroxy-2-(hydroxymethyl)propan-2-yl)-4'-methyl-[2,2'-bipyridine]-4-carboxamide

Prepared from the corresponding ethyl ester following a published protocol.[9] 1.2eq of the solid ester were dissolved in dry DMSO, then K_2CO_3 (1.1eq) and TRIS (1eq) were added and the quasi colorless suspension was stirred under N_2 for 2 days. The suspension turned progressively to a limpid yellow solution. A few drops of EtOH were added to ensure that all the salts had precipitated before filtration. The solvents were then removed under vacuum on a rotary evaporator (a strong vacuum with a bath at 80°C max. was used in order to avoid the formation of oxazoline). The residual orange oily material is then dissolved in a minimum of anhydrous EtOH and a few drops of Et_2O were added till a precipitate started to appear. The solution was then poured in excess water and a white suspension was obtained. If precipitation wasn't immediate, partial evaporation on a rotary evaporator was performed to induce the apparition of a solid. The suspension was left for 24h at 4°C to maximize precipitation. The fine white solid was then filtered on a fine glass frit or on a 0.45µm Nylon membrane (centrifugation can be performed before filtration to facilitate it), washed with H_2O then Et_2O and dried under vacuum overnight. If needed, recrystallization using $CHCl_3$ was performed. Yield : 160mg (50% on a 1mmol scale)

^{1}H NMR (D_6-DMSO, 400 MHz, 298 K) : δ 8.78 (dd, 1H), 8.68 (dd, 1H), 8.59 (m, 1H), 8.27 (m, 1H), 7.74 (dd,, 1H), 7.65 (s, 1H, NH), 7.34 (m, 1H), 4.70 (t, 3H), 3.73 (d, 6H), 2.43 (s, 3H). ESI-MS (MeOH): $[M+Na]^+$ calc. for $C_{16}H_{19}N_3O_4Na$ 340.1268; found 340.1267 and $[2M+Na]^+$ calc. 657.2644 for $C_{32}H_{38}N_6O_8Na$; found 657.2699. IR (ATR, cm^{-1}) : 3397 (m), 3272 (s, br), 3078 (m), 1644 (s), 1610 (sh), 1563 (s), 1597 (s), 1545 (s), 1463 (s), 1364 (s), 1335 (m), 1270 (m), 1246 (s), 1149 (w), 1068 (s), 1040 (vs), 992 (m), 923(w), 844 (s), 774 (s), 691 (s), 666 (s), 623 (s), 606 (s), 560 (m), 510 (s), 488 (s) and 408 (s).

VI-L2 N-(1,3-dihydroxy-2-(hydroxymethyl)propan-2-yl)-[2,2':6',2''-terpyridine]-4'-carboxamide

Prepared like **VI-L1** from the corresponding ethyl ester as stated in our previous report.[8] Yield : 250mg (66% on a 1mmol scale)

^{1}H NMR (D_6-DMSO, 400 MHz, 298 K) : δ 8.77 (ddd, 2H), 8.74 (s, 2H), 8.66 (dt, 2H), 8.04 (td, , 2H), 7.81 (s, 1H,NH), 7.54 (ddd, , 2H), 4.73 (t, 3H), 3.76 (d, 6H). ESI-MS (MeOH): $[M+Na]^+$ calc. for $C_{20}H_{20}N_4O_4Na$ 403.1377; found 403.1345 and $[2M+Na]^+$ calc. 783.2861 for $C_{40}H_{40}N_8O_8Na$; found 783.2842. IR (ATR, cm^{-1}) : 3404 (sh), 3292 (s, br), 3059 (m), 1658 (s),

1585 (m), 1539 (vs), 1468 (s), 1395 (s), 1367 (m), 1357 (sh), 1271 (sh), 1265 (s), 1118 (w), 1054 (s), 1041 (s), 1017 (vs), 991 (sh), 888(m), 792 (s), 767 (m), 731 (s), 674 (m), 655 (w), 625 (s), 617(s), 606 (s), 530 (m), 510 (s), 464 (s) and 405 (s).

VI-L3 $N^4,N^{4'}$-bis(1,3-dihydroxy-2-(hydroxymethyl)propan-2-yl)-[2,2'-bipyridine]-4,4'-dicarboxamide

Prepared from the corresponding ethyl ester via the same protocol than **6-L1**, except that the ratios were 1.2:2.2:2 – ester:K_2CO_3:TRIS to account for the presence of two ester group on the precursor. Yield : 245mg (64% on a 0.85mmol scale)

^{1}H NMR (D_6-DMSO, 400 MHz, 298 K) : δ 8.85 (dd, 1H), 8.72 (m, 1H), 7.79 (dd, 1H), 7.69 (s, 1H, NH), 4.70 (t, 6H), 3.73 (d, 12H). ESI-MS (MeOH): $[M+Na]^+$ calc. for $C_{20}H_{26}N_4O_8Na$ 473.1643; found 473.1632 and $[2M+Na]^+$ calc. 923.3393 for $C_{40}H_{52}N_8O_{16}Na$; found 923.3347. IR (ATR, cm^{-1}) : 3404 (sh), 3364 (w), 3231 (s, br), 3092 (m), 1644 (s), 1600 (w), 1541 (s), 1538 (s), 1459 (m), 1405 (w), 1364 (m), 1310 (m), 1242 (m), 1155 (w), 1110 (s), 1040 (vs), 979 (w), 874 (m), 753 (m),714 (sh), 700(m), 631 (m), 574 (m), 560 (sh), 487 (s) and 398 (br).

XII.2.2. Covalently modified POMs

VI-7 ($TBA_5H_4[P_2V_3W_{15}O_{62}]$) was prepared following the rigorous work from Finke *et al.* [13-14]

^{1}H NMR (CD_3CN, 400 MHz, 298 K) : δ 3.14 (m, 40H), 1.64 (m, 40H), 1.40 (m, 40H), 0.99 (t, 60H). (hereafter referred as the TBA resonances). ^{31}P NMR (162 MHz, CD_3CN) δ -7.16 (s), -12.64 (s). IR (ATR, cm^{-1}) : 2959(m), 2931(m), 2871 (m), 1482 (m), 1461 (m), 1379 (m), 1085 (s), 1062 (m), 950(s), 904 (s), 777 (vs), 731 (vs), 599 (m), 561 (w), 526 (s), 467 (w). Elemental analysis calc (%) for $C_{80}H_{184}N_5O_{62}P_2V_3W_{15}$: C 18.55, H 3.58, N 1.35; found: C 19.14, H 3.59, N 1.23.

VI-8 ($TBA_5H[P_2V_3W_{15}O_{62}C_4H_8N]$) was prepared by adapting the reported procedure: a 1:1 mixture of **VI-7** and TRIS in DMAc was heated at 80°C in the dark for 24h. Dropwise addition to excess Et_2O, filtration, redissolution in the minimum of MeCN followed by re-precipitation dropwise in Et_2O yielded the desired compound in 73% yield.

^{1}H NMR (CD_3CN, 400 MHz, 298 K) : δ 5.56 (s, 6H), in addition to the TBA resonances. ^{31}P NMR (162 MHz, CD_3CN) δ -6.70 (s), -12.74 (s). IR (ATR, cm^{-1}) : 2959(m), 2931(m), 2871 (m), 1482 (m), 1461 (m), 1379 (m), 1085 (s), 1062 (m), 950(s), 904 (s), 777 (vs), 731 (vs), 599 (m), 561 (w), 526 (s), 467 (w). Elemental analysis calc (%) for $C_{84}H_{189}N_6O_{62}P_2V_3W_{15}$: C 19.23, H 3.63, N 1.60; found: C 19.63, H 3.72, N 1.68.

VI-1 ($TBA_5H[P_2V_3W_{15}O_{63}C_{16}H_{16}N_3]$)[9] was prepared by combining in a 1:1 molar ratio **7** and **VI-L1** in DMAc (3mL for 520mg/0.1mmol of **7**) under N_2 and heating them in the dark for 8 days at 80°C. After cooling, the desired compound was then obtained through precipitation by dropwise addition to excess Et_2O. The yellow solid was re-dissolved in a minimum of MeCN and re-precipitated twice in Et_2O before being dried at 50°C. Yield : 490mg (90%)

^{1}H NMR (CD_3CN, 400 MHz, 298 K) : δ 8.89 (d,1H), 8.80 (s, 1H), 8.73 (d, 1H), 8.56 (s, 2H), 7.87 (s, 1H), 7.73 (s, 1H), 7.16 (s, 1H), 5.81 (s, 6H), 2.67 (s, 3H) in addition to the TBA resonances. ^{31}P NMR (162 MHz, CD_3CN) δ -6.75 (s), -12.77 (s). IR (ATR, cm^{-1}) : 2960(m), 2931(m), 2871 (m), 1671 (w), 1545 (w), 1482 (m), 1461 (m), 1379 (m), 1328 (w), 1084 (s), 1062 (m), 948 (s), 905 (s), 796 (vs), 722 (vs), 597 (m), 561 (w), 526 (s), 478 (w). Elemental analysis calc (%) for $C_{96}H_{197}N_8O_{63}P_2V_3W_{15}$: C 21.18, H 3.65, N 2.06; found: C 21.56, H 3.77, N 2.20.

VI-2 ($TBA_5H[P_2V_3W_{15}O_{63}C_{20}H_{17}N_4]$) was prepared as **VI-1** using **VI-L2**. Yield : 510mg (93%)

^{1}H NMR (CD_3CN, 400 MHz, 298 K) : δ 8.83 (br s, 2H), 8.75 (s, 2H), 8,71(d, 2H), 8.12 (s, 2H), 7.58 (br s, 2H), 7.10 (s, 2H, NH), 5.86 (s, 6H) in addition to the TBA resonances. ^{31}P NMR (162 MHz, CD_3CN) δ -6.73 (s), -12.78 (s). IR (ATR, cm^{-1}) : 2960(m), 2931(m), 2871 (m), 1678 (w), 1584 (w), 1482 (m), 1466 (m), 1379 (m), 1310 (w), 1083 (s), 1062 (m), 947 (s), 904 (s), 797 (vs), 719 (vs), 597 (m), 561 (w), 524 (s), 477 (w). Elemental analysis calc (%) for $C_{100}H_{198}N_9O_{63}P_2V_3W_{15}$: C 22.78, H 3.62, N 2.26; found: C 22.48, H 3.66, N 2.28.

VI-3 ($TBA_{10}H_2[(P_2V_3W_{15}O_{59})_2C_{20}H_{20}N_4O_8]$) was previously reported by Cronin *et al.*[15]. It was prepared in the same fashion than **VI-1**, except that the ratio was 2:1 **VI-7**:**VI-L3** to account for the bifunctionality of the ligand. Yield : 920mg (86%)

^{1}H NMR (CD_3CN, 400 MHz, 298 K) : δ 8.81 (br s, 2H), 8,73 (br s, 2H), 7.75 (br s, 2H), 6.96 (s, 2H, NH), 5.86 (s, 12H), in addition to the TBA resonances. ^{31}P NMR (162 MHz, CD_3CN) δ -6.73 (s), -12.76 (s). IR (ATR, cm^{-1}) : 2960(m), 2931(m), 2871 (m), 1703 (w), 1666 (w), 1584 (w), 1482 (m), 1465 (m), 1379 (m), 1318 (w), 1084 (s), 1061 (m), 947 (s), 905 (s), 797 (vs), 721 (vs), 597 (m), 525 (s), 477 (w). Elemental analysis calc (%) for $C_{180}H_{382}N_{14}O_{126}P_4V_6W_{30}$: C 20.19, H 3.62, N 1.83; found: C 20.49, H 3.64, N 2.00.

XII.2.3. Re^{I} complexes based on covalently modified POMs

General procedure: In a dried Schlenk cooled under N_2, $Re(CO)_5Br$ and the desired hybrid were combined in stoichiometric amount (typical scale: 20µmol) and dissolved in DMAc (2.5mL). The yellow solution was then heated overnight at 80°C in the dark. Once cooled back to RT, the now orange solution was added dropwise to excess Et_2O, resulting in a really fine yellow solid. The suspension was left in the fridge for 1h to ensure total precipitation. The fine yellow solid was then filtered on a 0.45µm PTFE membrane and washed with THF (5mL), DCM (5mL) and Et_2O (10mL). The solid was re-precipitated by retaking it in MeCN (3mL) before dropwise addition to excess Et_2O followed by filtration, yielding a fine solid that was air dried for 2h.

VI-4 ($TBA_5H[P_2V_3W_{15}O_{66}C_{19}H_{16}N_3ReBr]$) yellow-orange powder Yield : 101mg (87%, 20µmol scale) ^{1}H NMR (400 MHz, CD_3CN) δ 9.11 (t, 1H), 8.87 (t, 1H), 8.74 (s, 1H), 8.50 (s, 1H), 7.93 (m, 2H), 7.50 (m, 1H), 7.16 (s, 1H, NH), 5.97 (s, 6H), 2.60 (s, 3H) in addition to the TBA resonances. ^{31}P NMR (162 MHz, CD_3CN) δ -6.97 (s), -12.43 (s). IR (ATR, cm^{-1}) : 2960(m), 2931(m), 2871 (m), 2019 (s), 1916 (s), 1891 (s), 1672 (w), 1621 (w), 1542 (w), 1482 (m), 1462 (m), 1379 (m), 1318 (w), 1084 (s), 1062 (m), 951 (s), 905 (s), 804 (sh), 794 (vs), 719 (vs), 598 (m), 526 (s), 478 (w).Elemental analysis calc (%) for $C_{99}H_{197}N_8O_{66}P_2V_3W_{15}ReBr$: C 20.52, H 3.43, N 1.93; found: C 20.54, H 3.40, N 1.98.

VI-5 ($TBA_5H[P_2V_3W_{15}O_{66}C_{23}H_{17}N_4ReBr]$) greenish-yellow powder Yield : 110mg (94%, 20µmol scale) ^{1}H NMR (400 MHz, CD_3CN) δ 9.06 (d, 1H), 8.80 (m, 2H), 8.70 (d, 1H), 8.27 (t, 1H), 8.08 (d, 1H), 8.00 (td, 1H), 7.82 (d, 1H), 7.65 (t, 1H), 7.57 (t, 1H), 7.20 (s, 1H, NH), 5.90 (s, 6H), in addition to the TBA resonances. ^{31}P NMR (162 MHz, CD_3CN) δ -6.88 (s), -12.60 (s). IR (ATR, cm^{-1}) : 2960(m), 2931(m), 2871 (m), 2020 (s), 1916 (s), 1894 (s), 1674 (w), 1542 (w), 1482 (m), 1462 (m), 1415 (w), 1379 (m), 1315 (w), 1084 (s), 1065 (m), 949 (s), 904 (s), 800 (vs br), 722 (vs), 598 (m), 526 (s), 478 (w).Elemental analysis calc (%) for $C_{103}H_{198}N_9O_{66}P_2V_3W_{15}ReBr$: C 21.12, H 3.41, N 2.15; found: C 21.21, H 3.38, N 2.19.

VI-6 ($TBA_{10}H_2[(P_2V_3W_{15}O_{59})_2C_{23}H_{20}N_4O_{11}ReBr]$) yellow-orange powder Yield : 90mg (82%, 10µmol scale) ^{1}H NMR (400 MHz, CD_3CN) δ 9.11 (m, 2H), 8.84 (br s, 2H), 8.01 (m, 2H), 7.12 (s, 2H, NH), 5.92 (s, 12H), in addition the TBA resonances. ^{31}P NMR (162 MHz, CD_3CN) δ -6.70 (s), -12.66 (s). IR (ATR, cm^{-1}) : 2960(m), 2931(m), 2872 (m), 2023 (s), 1925 (s), 1899 (s), 1672 (w), 1542 (w), 1482 (m), 1462 (m), 1415 (w), 1379 (m), 1330 (w), 1264 (w), 1084 (s), 1063 (m), 949 (s), 906 (s), 805 (vs br), 723 (vs), 598 (m), 526 (s), 478 (w). Elemental analysis calc (%) for $C_{183}H_{382}N_{14}O_{129}P_4V_6W_{30}ReBr$: C 19.88, H 3.48, N 1.77; found: C 19.98, H 3.49, N 1.91.

VI-9 $[Re(CO)_3Br(dmb)]$ was prepared following literature procedure. Briefly, dmb (4,4'-dimethyl,2,2'-bipyridine) and $Re(CO)_5Br$ were refluxed in cyclohexane for 3h, a yellow precipitate progressively appearing. The solid was filtered and washed with Et_2O. Yield 230mg (86%, 50 µmol scale)

^{1}H NMR (400 MHz, $CDCl_3$) δ 8.89 (d, 2H), 7.98 (s, 2H), 7.32 (dd, 2H), 2.58 (s, 6H). ESI-MS (MeOH): $[M-Br]^+$ calc. for $C_{15}H_{12}N_2O_3Re$ 455.0405; found 455.0408 and $[2M-Br]^+$ calc. 988.9994 for $C_{30}H_{24}N_4O_6Re_2Br$; found 998.9973. IR (ATR, cm^{-1}) : 3030 (w), 2012 (vs), 1882 (vs), 1865 (vs), 1620 (s), 1555 (w), 1484 (m), 1444 (m), 1379 (w), 1300 (m), 1243 (m), 1183 (w), 1077 (w), 1031 (m), 892 (m), 839 (s), 742 (m), 647 (s), 630 (s), 567 (m), 537 (s), 506 (s), 484 (s), 417(s). Elemental analysis calc (%) for $C_{15}H_{12}BrN_2O_3Re$: C 33.71, H 2.26, N 5.24; found: C 33.81, H 2.17, N 5.18.

XII.2.4. FT-IR and UV-visible spectra

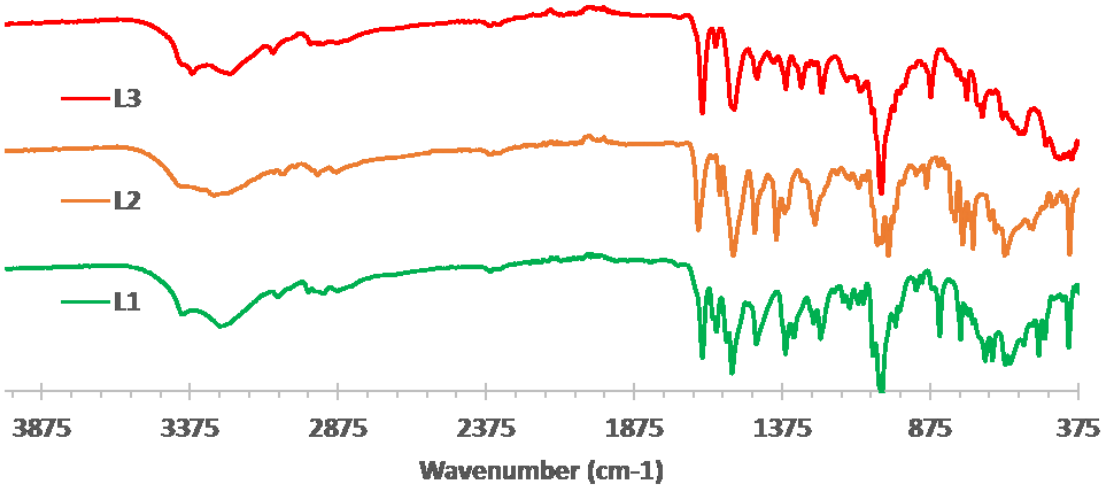

Figure XII.2. FTIR spectra of the three triol decorated polypyridyl ligands **VI-L1**-**VI-L3**

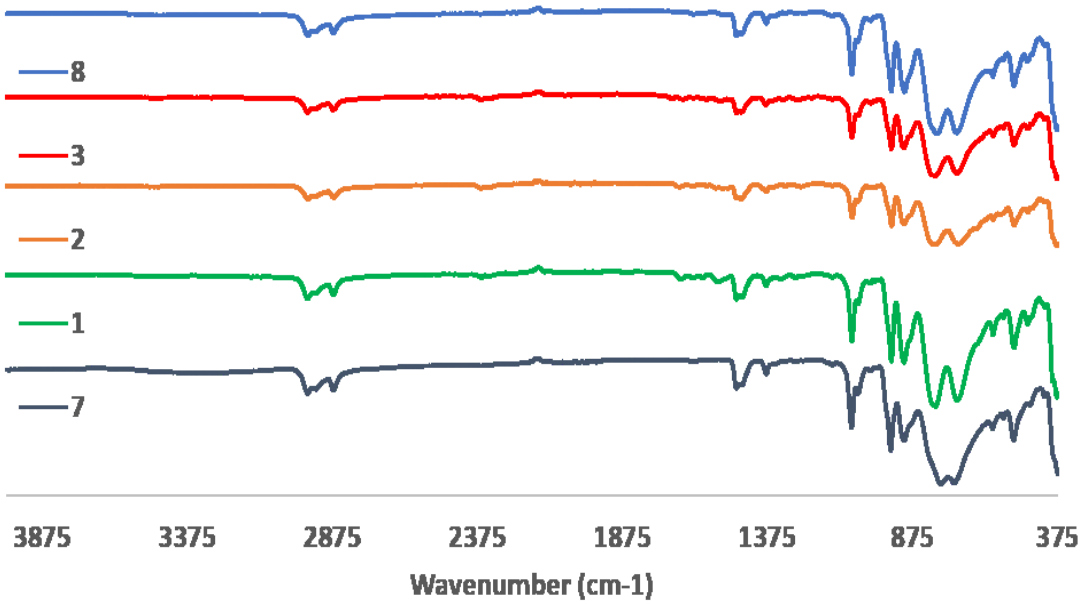

Figure XII.3. Comparison of the FTIR spectra for the starting POM **VI-**7 and functionalized POMs **VI-1**, **VI-2**, **VI-3** and **VI-8**.

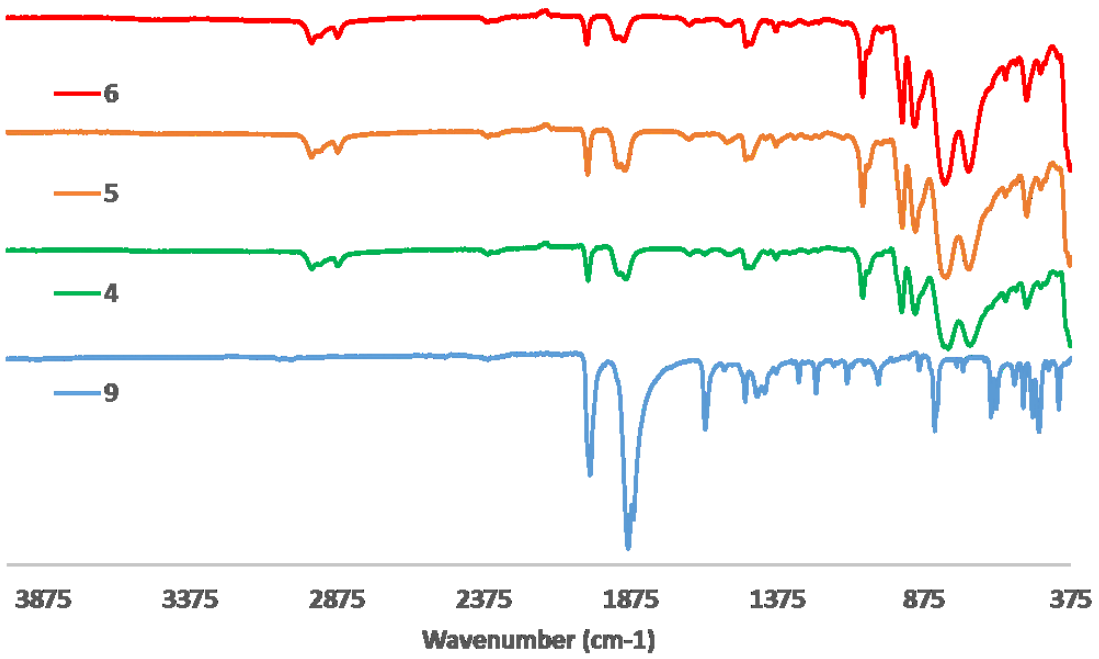

Figure XII.4. Comparison of the FTIR spectra of the Re(I) complexes **VI-4**, **VI-5**, **VI-6** and **VI-9** (as reference).

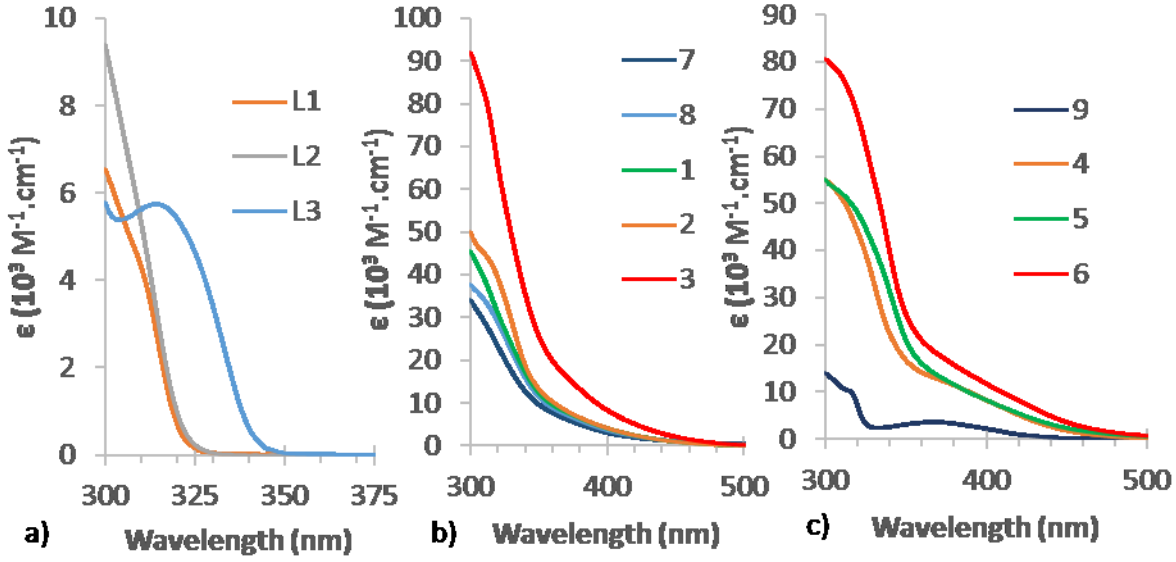

Figure XII.5. Absorption spectra in DMF for a) ligands **VI-L1**-**VI-L3** b) POMs **VI-1**-**VI-3**, **VI-7** and **VI-8** c) complexes **VI-4**-**VI-6** and **VI-9**.

XII.2.5. ESI-MS analysis

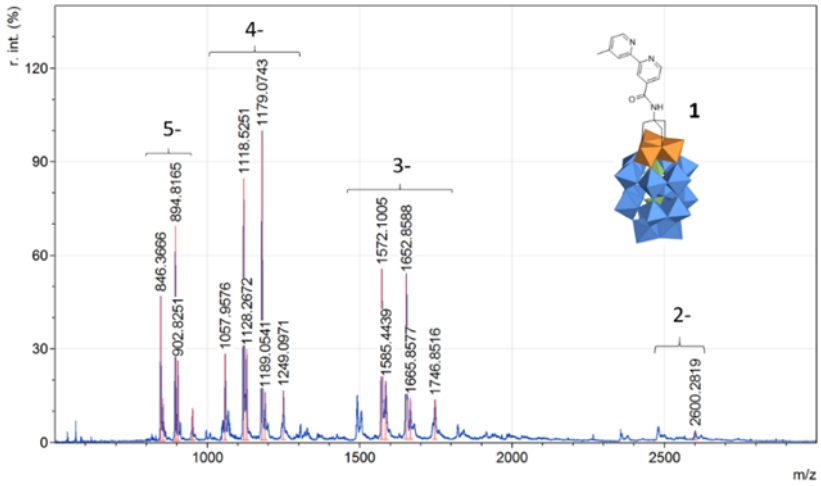

Figure XII.6. ESI-MS full spectrum for **VI-1** (negative mode).

Composition	Formula	Calc.	Observed
[M+H]5-	$C_{16}H_{17}N_3O_{63}P_2V_3W_{15}^{5-}$	846.1740	846.1631
[M+TBA]5-	$C_{32}H_{52}N_4O_{63}P_2V_3W_{15}^{5-}$	894.6298	894.6262
[M+2TBA]4-	$C_{48}H_{88}N_5O_{63}P_2V_3W_{15}^{4-}$	1178.8584	1178.8341
[M+3TBA]3-	$C_{64}H_{124}N_6O_{63}P_2V_3W_{15}^{3-}$	1652.5727	1652.4896
[M+4TBA]2-	$C_{80}H_{160}N_7O_{63}P_2V_3W_{15}^{2-}$	2600.0013	2599.9900

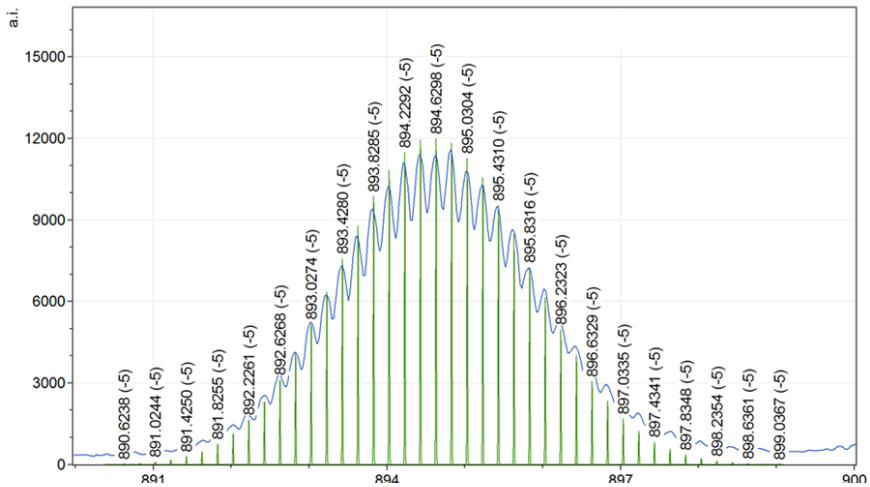

Figure XII.7. Isotopic distribution of the peak for $[M+TBA]^{5-}$ at m/z = 894.6262 (green: calculated, blue: observed) for **VI-1**. Values are for the calculated peaks.

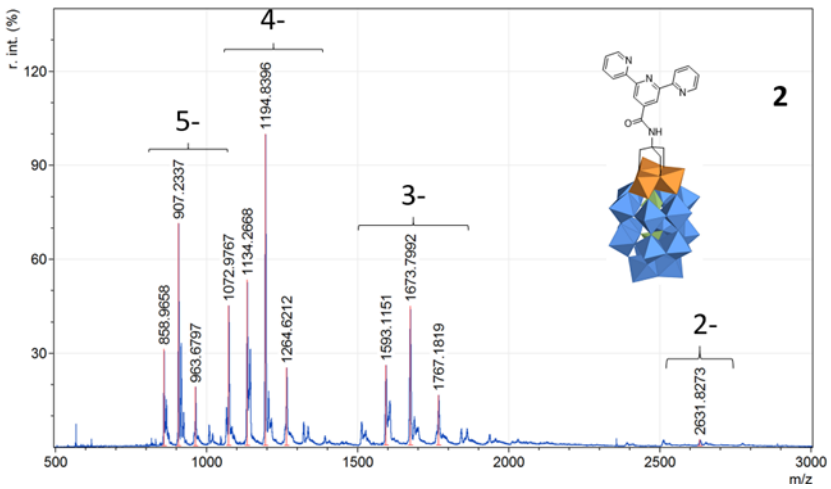

Figure XII.8. ESI-MS full spectrum for **VI-2** (negative mode).

Composition	Formula	Calc.	Observed
[M+TBA]5-	$C_{36}H_{53}N_5O_{63}P_2V_3W_{15}^{5-}$	907.2320	907.2337
[M+2TBA]4-	$C_{52}H_{89}N_6O_{63}P_2V_3W_{15}^{4-}$	1194.6111	1194.5538
[M+3TBA]3-	$C_{68}H_{125}N_7O_{63}P_2V_3W_{15}^{3-}$	1673.5763	1673.4871
[M+4TBA]2-	$C_{84}H_{161}N_8O_{63}P_2V_3W_{15}^{2-}$	2632.0075	2631.8273

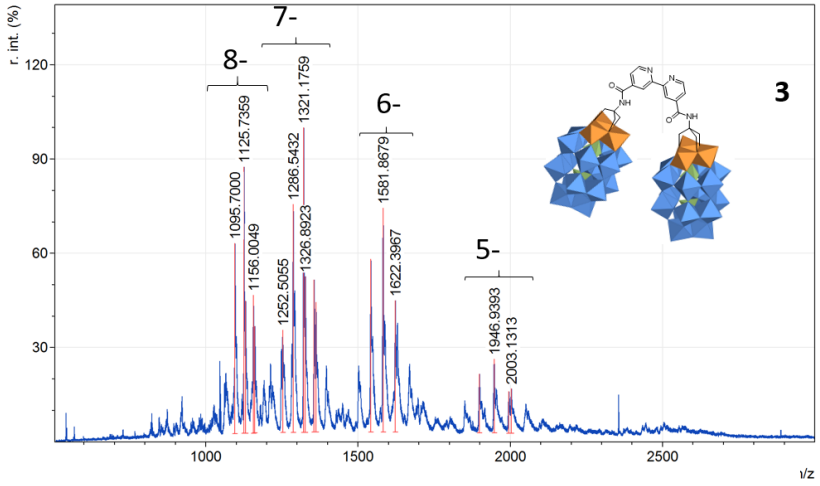

Figure XII.9. ESI-MS full spectrum for **VI-3** (negative mode).

Composition	Formula	Calc.	Observed
[M+4TBA]8-	$C_{84}H_{164}N_8O_{126}P_4V_6W_{30}^{8-}$	1155.8458	1155.7887
[M+5TBA]7-	$C_{100}H_{200}N_9O_{126}P_4V_6W_{30}^{7-}$	1355.5787	1355.6362
[M+6TBA]6-	$C_{116}H_{236}N_{10}O_{126}P_4V_6W_{30}^{8-}$	1621.8893	1621.9612
[M+7TBA]5-	$C_{132}H_{272}N_{11}O_{126}P_4V_6W_{30}^{8-}$	1994.9244	1995.0549

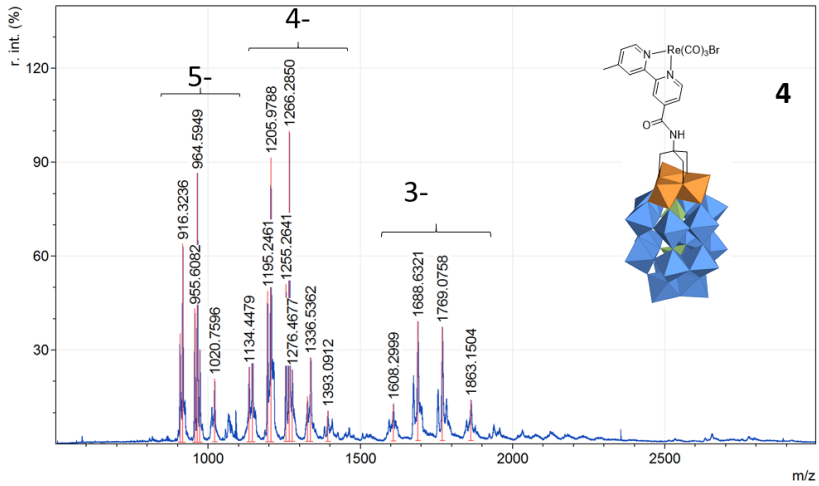

Figure XII.11. ESI-MS full spectrum for **VI-4** (negative mode).

Composition	Formula	Calc.	Observed
[M+TBA]5-	$C_{35}H_{52}N_4O_{66}P_2V_3W_{15}ReBr^{5-}$	964.6011	964.5949
[M+2TBA]4-	$C_{51}H_{88}N_5O_{66}P_2V_3W_{15}ReBr^{4-}$	1266.3225	1266.2825
[M+3TBA]3-	$C_{67}H_{124}N_6O_{66}P_2V_3W_{15}ReBr^{3-}$	1769.5253	1769.4236

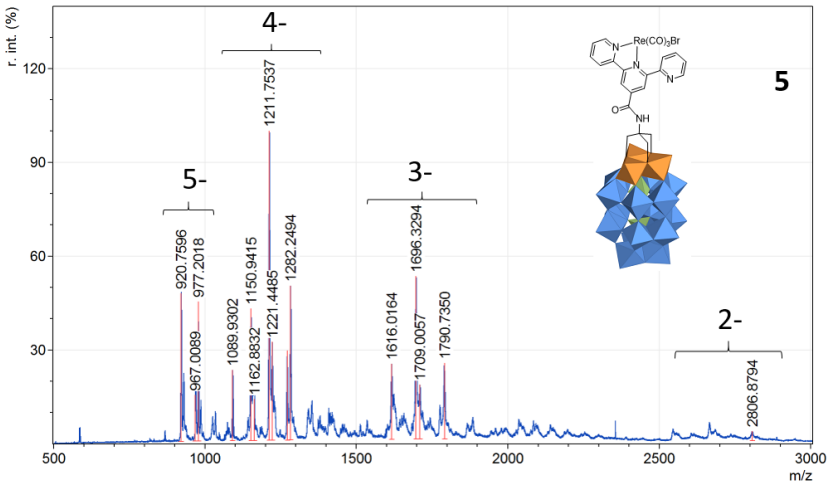

Figure XII.10. ESI-MS full spectrum for **VI-5** (negative mode).

Composition	Formula	Calc.	Observed
[M+TBA]5-	$C_{39}H_{53}N_5O_{66}P_2V_3W_{15}ReBr^{5-}$	977.2033	977.2018
[M+2TBA]4-	$C_{55}H_{89}N_6O_{66}P_2V_3W_{15}ReBr^{4-}$	1282.0752	1282.0217
[M+3TBA]3-	$C_{71}H_{125}N_7O_{66}P_2V_3W_{15}ReBr^{3-}$	1790.5290	1790.4121
[M+4TBA]2-	$C_{87}H_{161}N_8O_{66}P_2V_3W_{15}ReBr^{2-}$	2806.9346	2806.8794

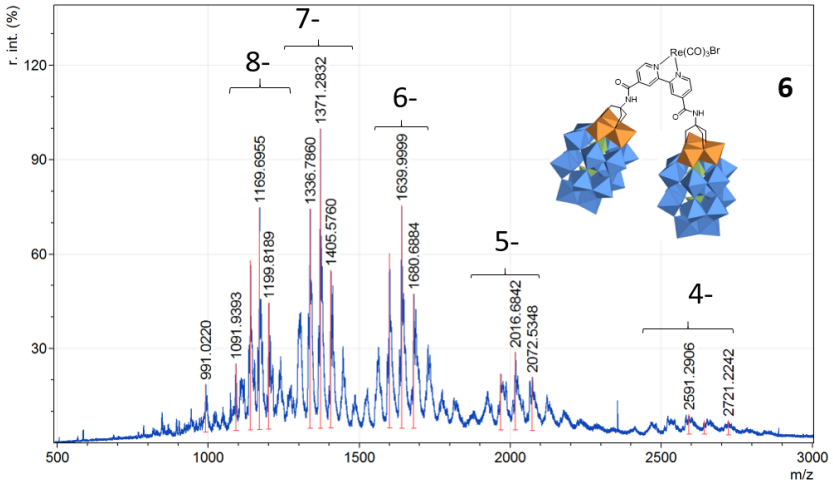

Figure XII.13. ESI-MS full spectrum for **VI-6** (negative mode).

Composition	Formula	Calc.	Observed
[M+4TBA]8-	$C_{87}H_{164}N_8O_{129}P_4V_6W_{30}ReBr^{8-}$	1199.5779	1199.5986
[M+5TBA]7-	$C_{103}H_{200}N_9O_{129}P_4V_6W_{30}ReBr^{7-}$	1405.5582	1405.5760
[M+6TBA]6-	$C_{119}H_{236}N_{10}O_{129}P_4V_6W_{30}ReBr^{6-}$	1680.3656	1680.3234
[M+7TBA]5-	$C_{135}H_{272}N_{11}O_{129}P_4V_6W_{30}ReBr^{5-}$	2064.8957	2064.7819
[M+8TBA]4-	$C_{151}H_{308}N_{12}O_{129}P_4V_6W_{30}ReBr^{4-}$	2641.6894	2641.7580

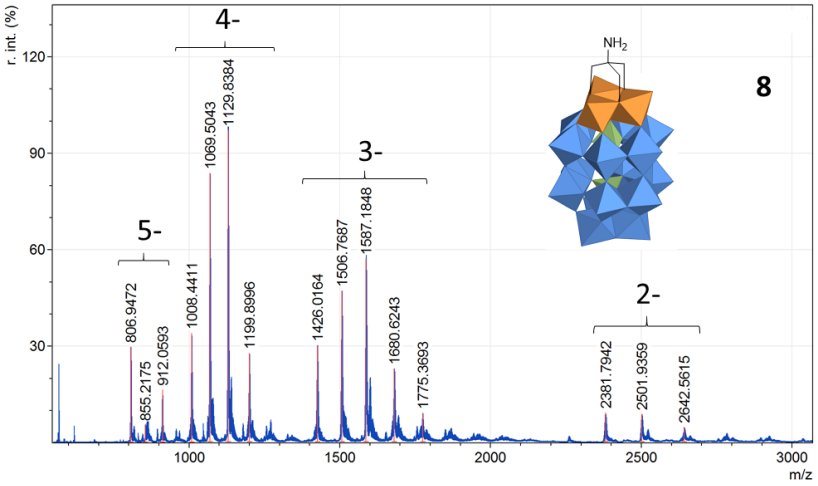

Figure XII.12. ESI-MS full spectrum for **VI-8** (negative mode).

Composition	Formula	Calc.	Observed
[M+TBA]5-	$C_{20}H_{44}N_2O_{62}P_2V_3W_{15}^{5-}$	855.2167	855.2175
[M+2TBA]4-	$C_{36}H_{80}N_3O_{62}P_2V_3W_{15}^{4-}$	1129.8424	1129.8384
[M+3TBA]3-	$C_{52}H_{116}N_4O_{62}P_2V_3W_{15}^{3-}$	1587.2180	1587.1848
[M+4TBA]2-	$C_{68}H_{152}N_5O_{62}P_2V_3W_{15}^{2-}$	2501.9693	2501.9359

XII.2.6. Electrochemistry

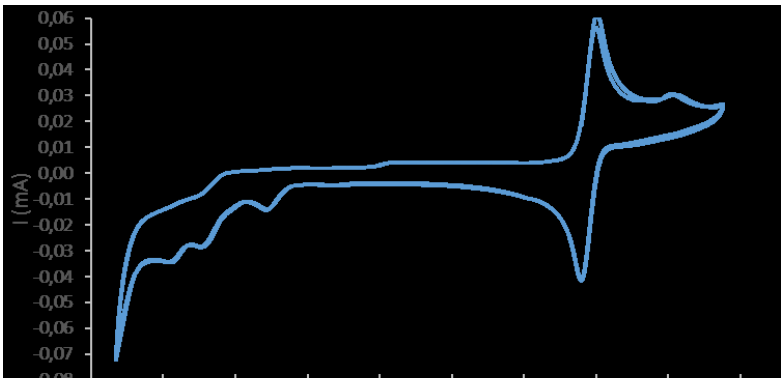

Figure XII.14. Cyclovoltammogram for **VI-L1** in DMF, with Fc as internal ref. (200mV.s-1)

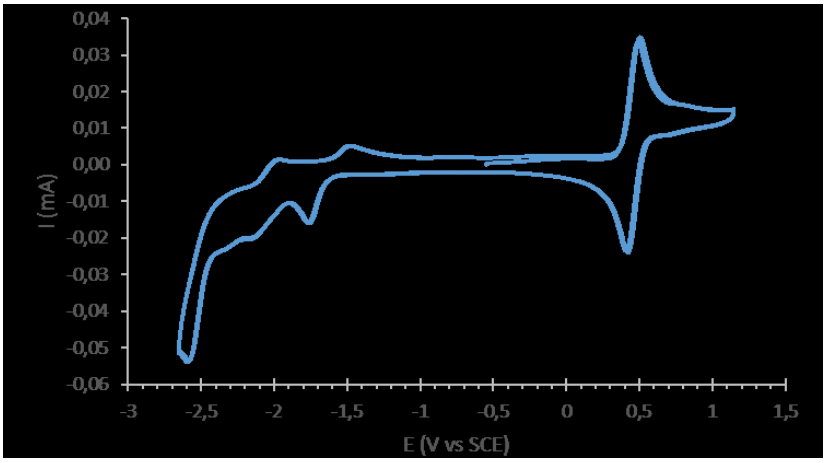

Figure XII.15. Cyclovoltammogram for **VI-L2** in DMF, with Fc as internal ref. (200mV.s-1)

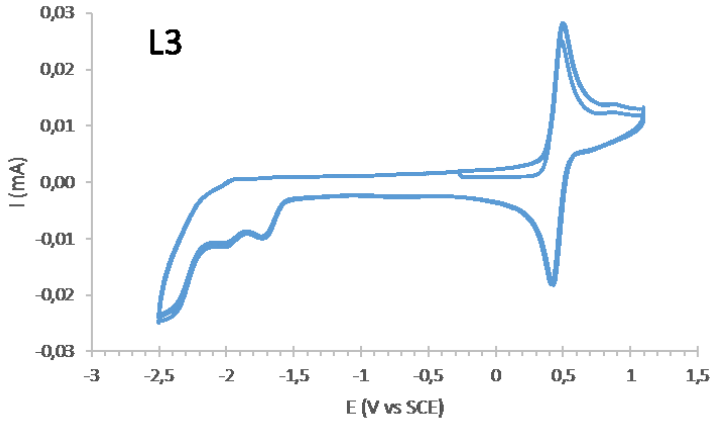

Figure XII.16. Cyclovoltammogram for **VI-L3** in DMF, with Fc as internal ref. (200mV.s-1)

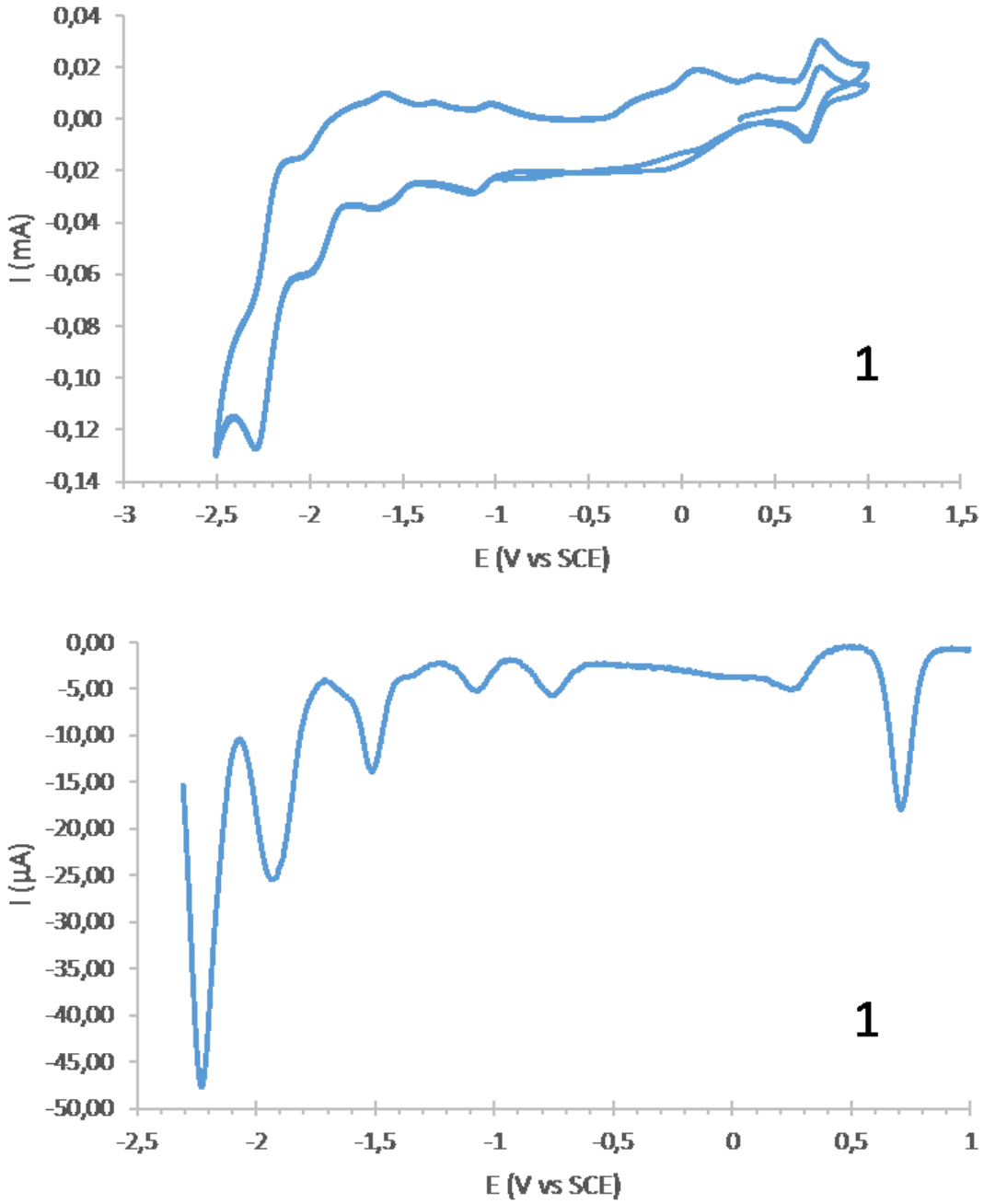

Figure XII.17. Top/ Cyclovoltammogram (200mV.s-1) Bottom/ SW voltammogram of **VI-1** in MeCN (AcFc as reference)

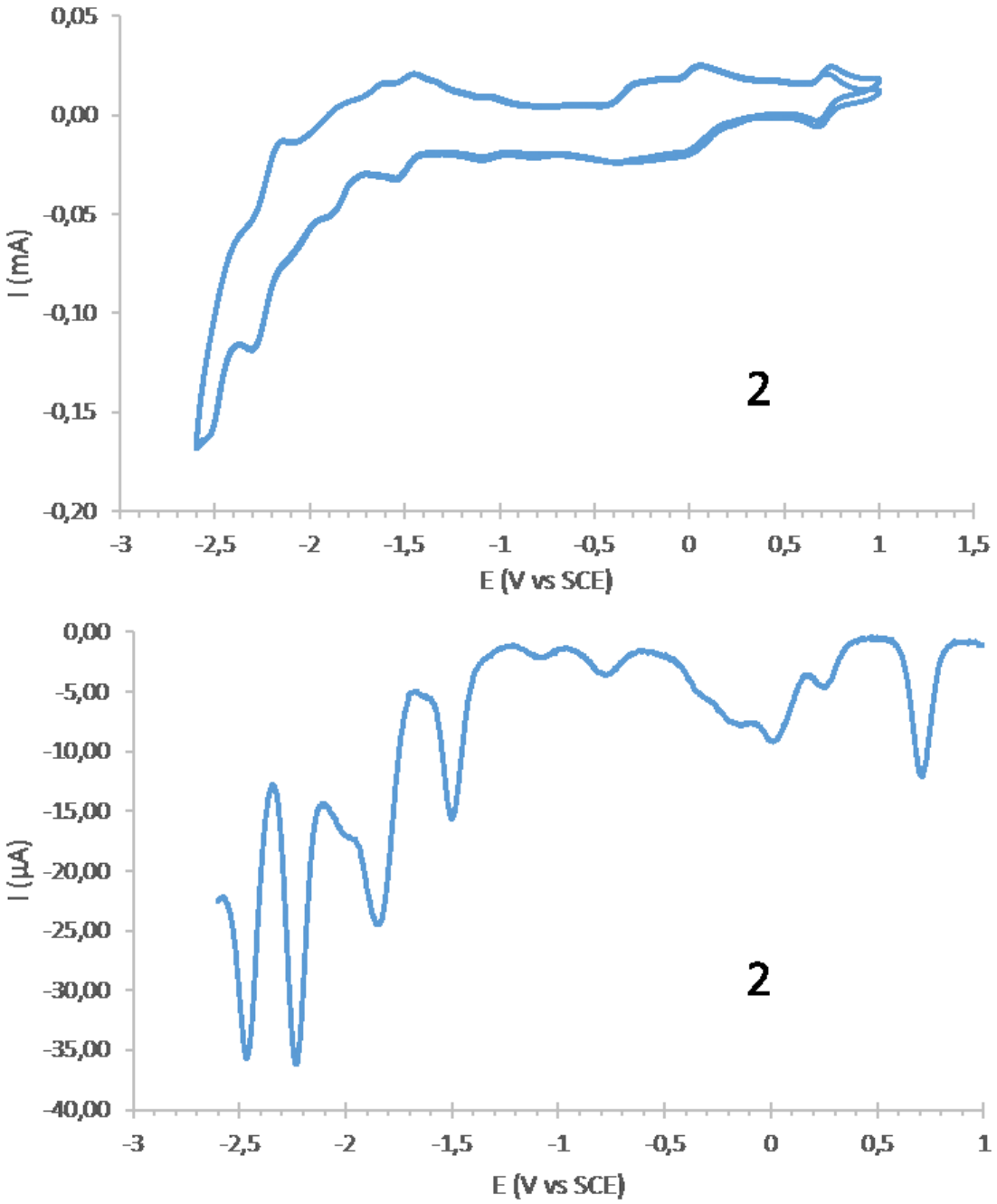

Figure XII.18. Top/ Cyclovoltammogram (200mV.s-1) Bottom/ SW voltammogram of **VI-2** in MeCN (AcFc as reference)

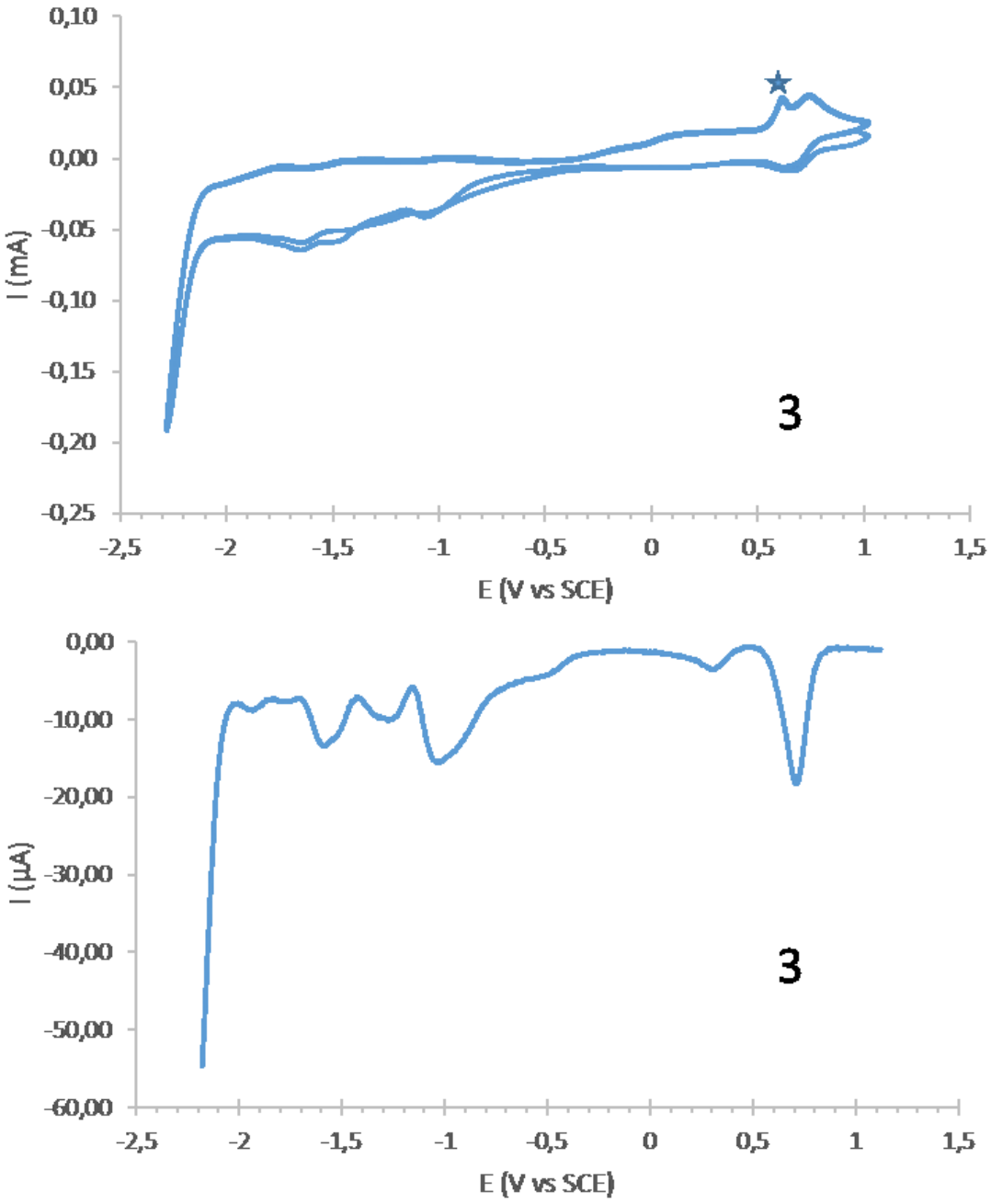

Figure XII.19. Top/ Cyclovoltammogram (200mV.s-1) Bottom/ SW voltammogram of **VI-3** in MeCN (AcFc as reference) - The measurements were highly affected by the adsorption on the electrode as shown by the desorption peak marked with a star on the CV.

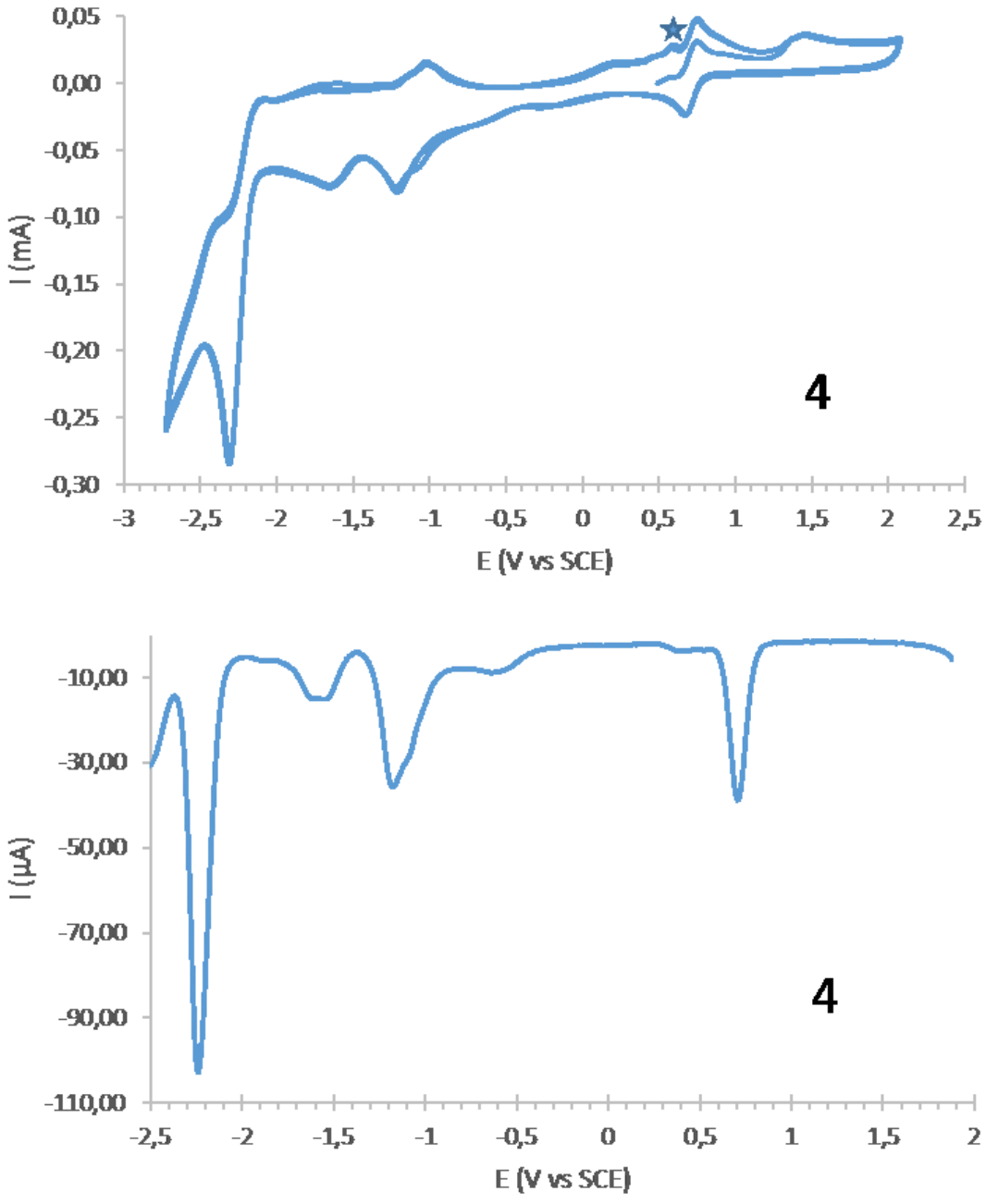

Figure XII.20. Top/ Cyclovoltammogram (200mV.s-1) Bottom/ SW voltammogram of **VI-4** in MeCN (AcFc as reference) - The measurements were highly affected by the adsorption on the electrode as shown by the desorption peak marked with a star on the CV.

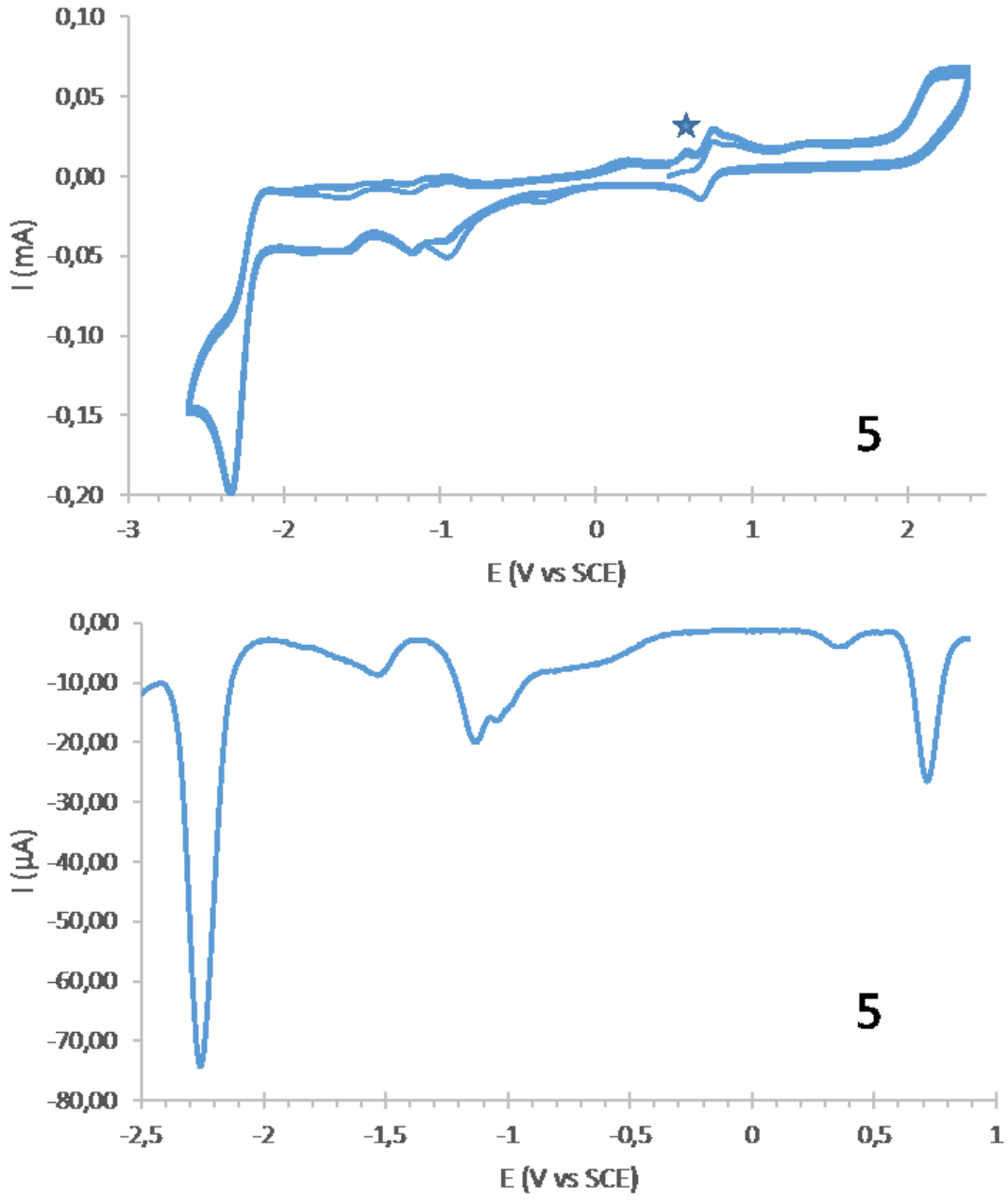

Figure XII.21. Top/ Cyclovoltammogram (200mV.s-1) Bottom/ SW voltammogram of **VI-5** in MeCN (AcFc as reference) - The measurements were highly affected by the adsorption on the electrode as shown by the desorption peak marked with a star on the CV.

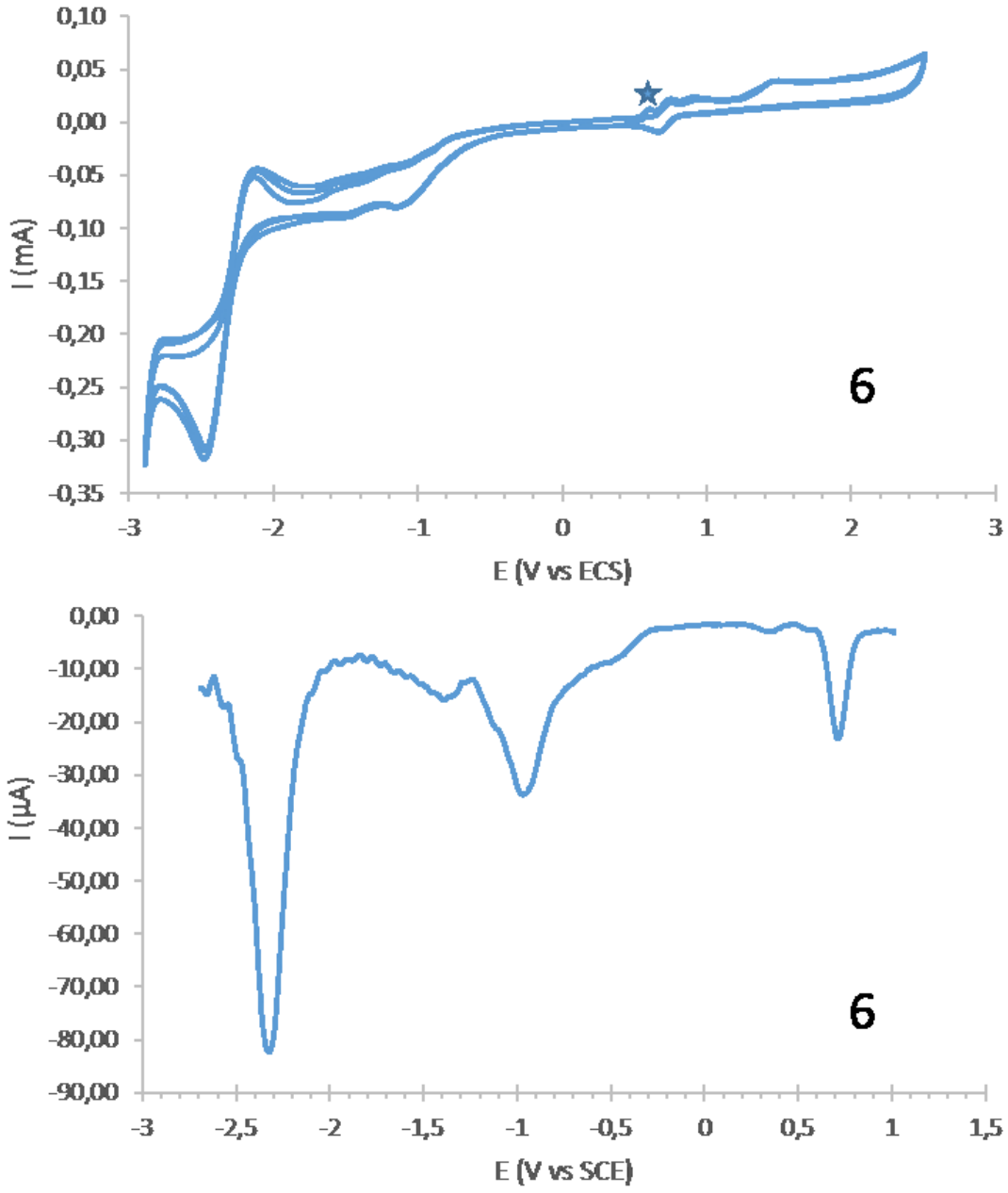

Figure XII.22. Top/ Cyclovoltammogram (200mV.s-1) Bottom/ SW voltammogram of **VI-6** in MeCN (AcFc as reference) - The measurements were highly affected by the adsorption on the electrode as shown by the desorption peak marked with a star on the CV.

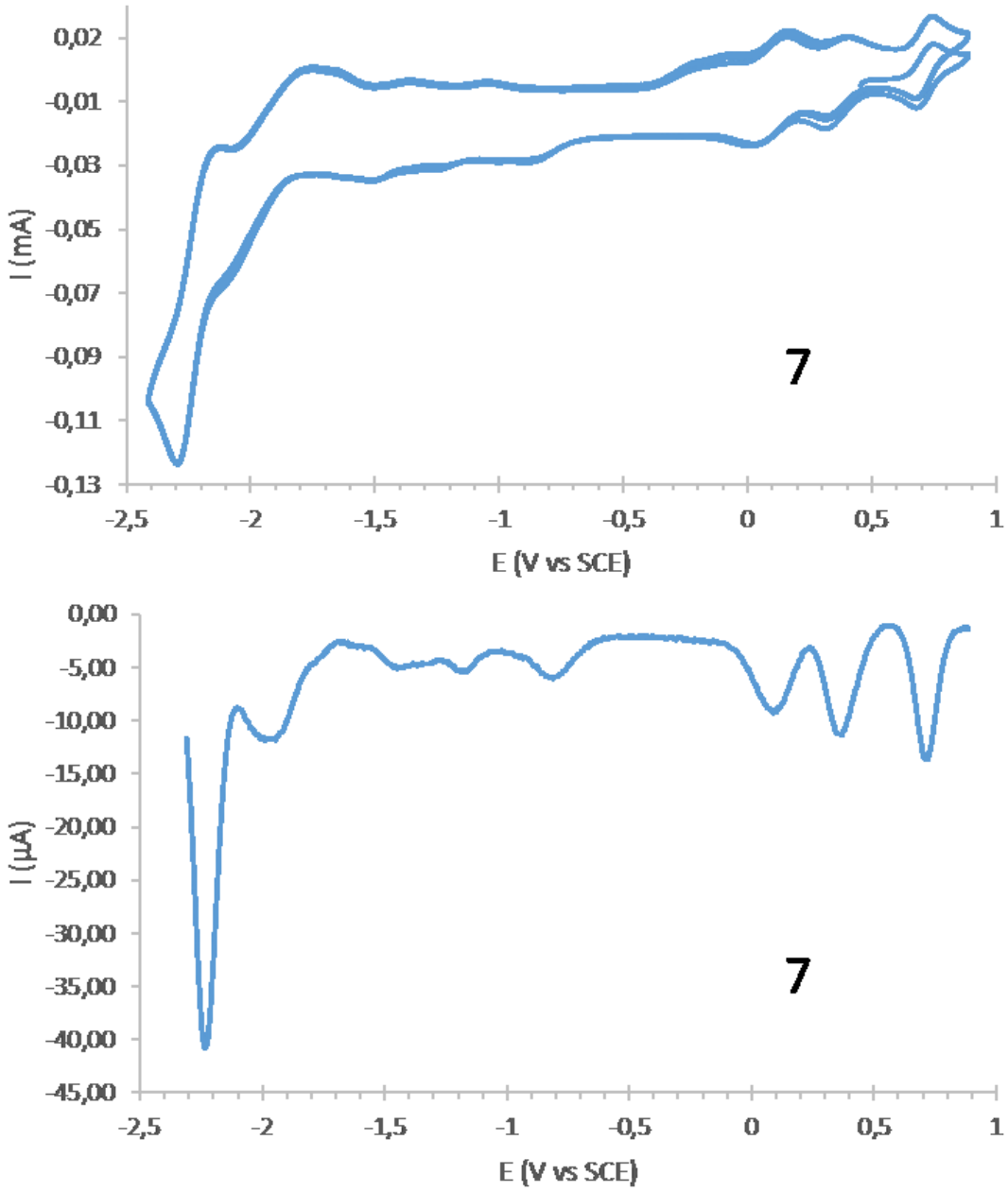

Figure XII.23. Top/ Cyclovoltammogram (200mV.s-1) Bottom/ SW voltammogram of **VI-7** in MeCN (AcFc as reference).

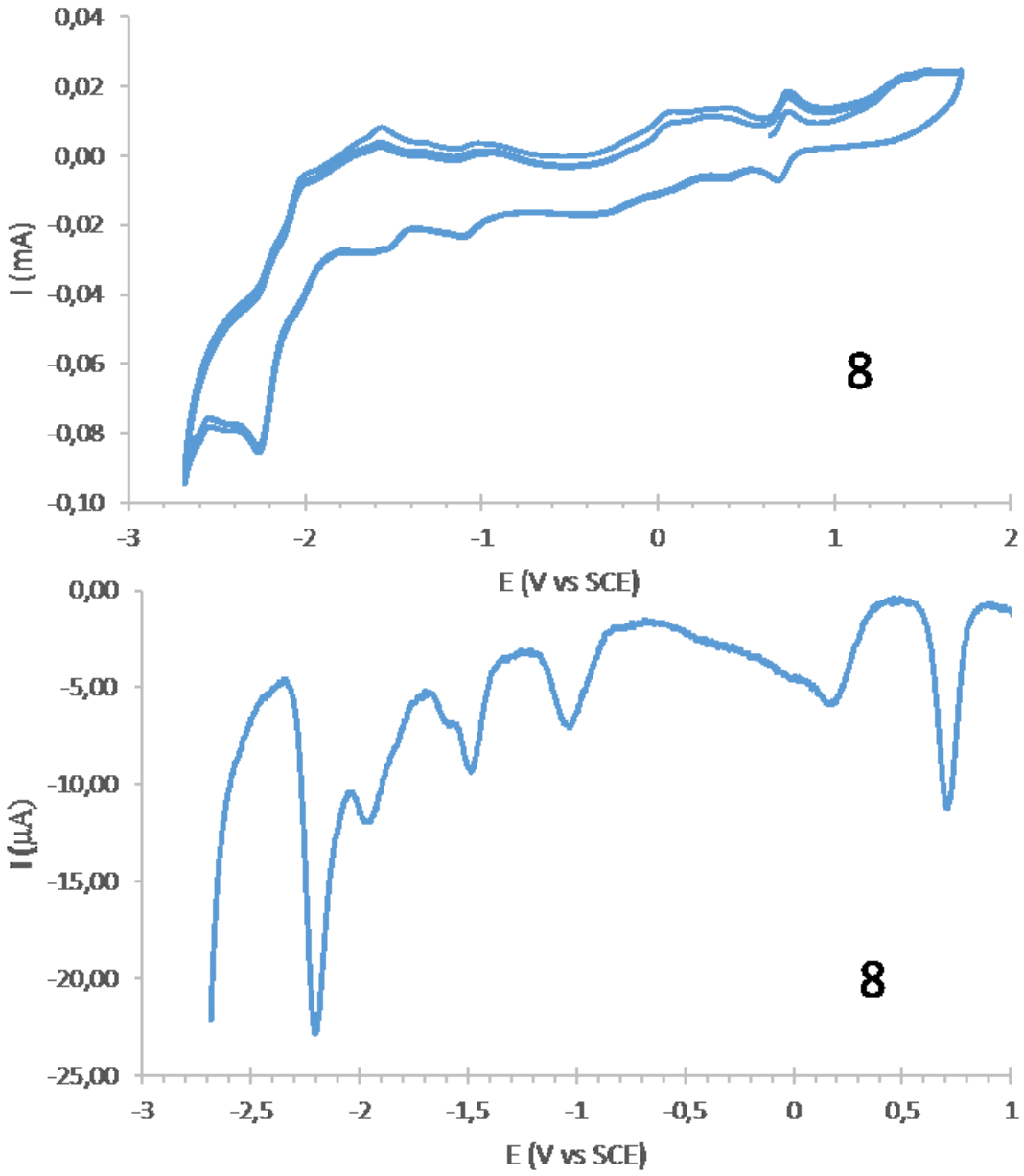

Figure XII.24. Top/ Cyclovoltammogram (200mV.s-1) Bottom/ SW voltammogram of **VI-8** in MeCN (AcFc as reference).

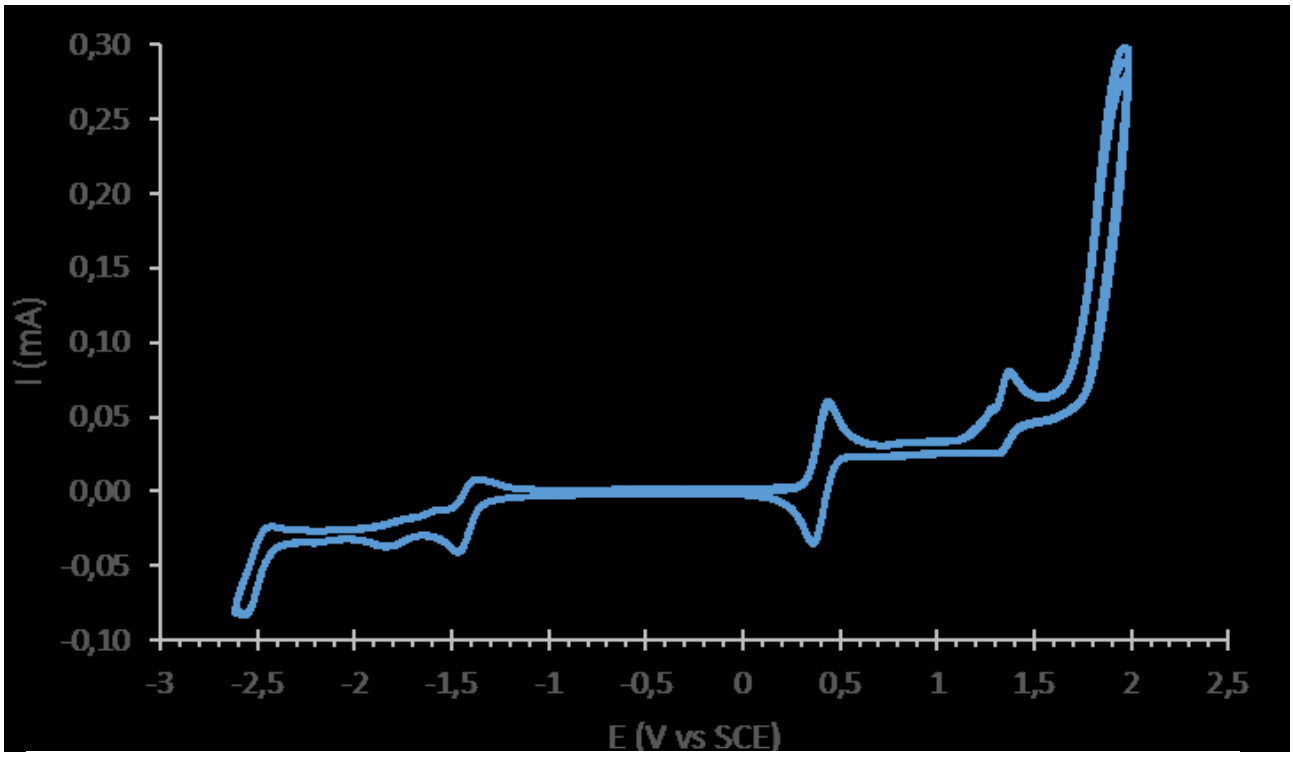

Figure XII.25. Cyclovoltammogram for **VI-9** in MeCN, with Fc as internal ref. (200mV.s-1)

XII.2.7. Quenching study

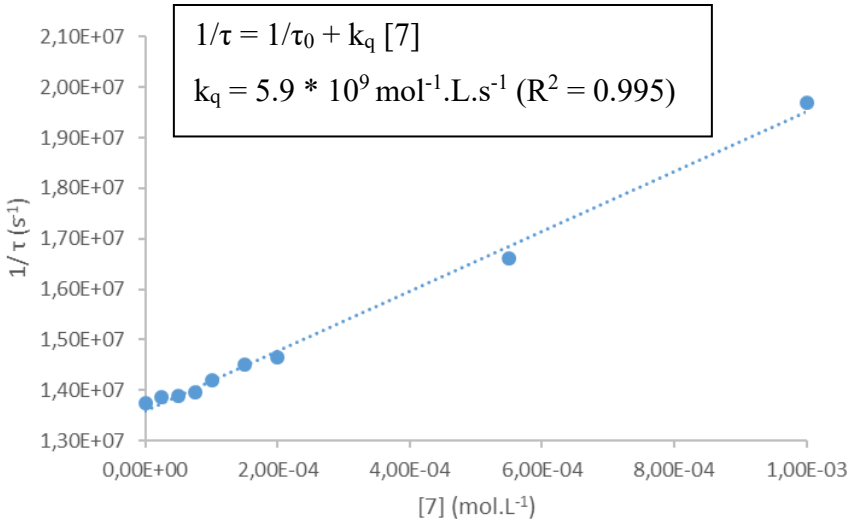

Figure XII.26. Stern-Volmer plot for quenching by **VI-7** $TBA_5H_4[P_2V_3W_{15}O_{62}]$ of **VI-9** *fac*-$[ReBr(CO)_3(dmb)]$ at 0.1mM in a degassed solution of 0.1 M $TBAPF_6$ in CH_3CN at 298 K. Excitation wavelength for the emission is 405 nm.

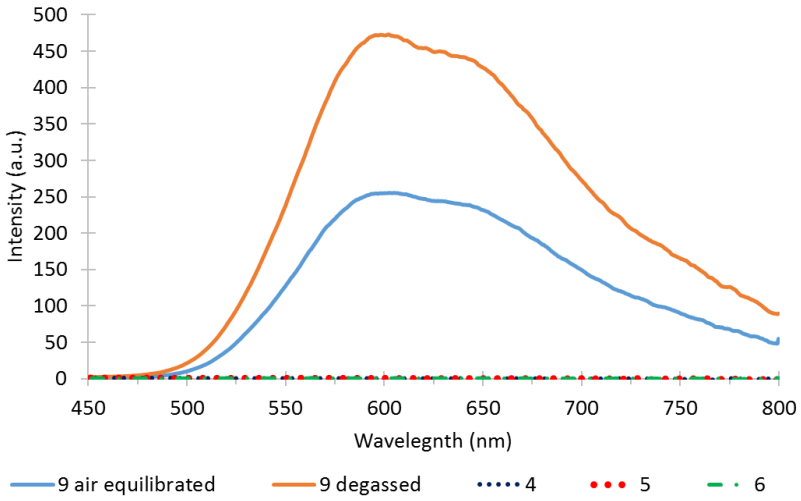

Figure XII.27. Emission spectra in N_2 purged CH_3CN for the hybrid Re complexes **VI-4-VI-6**, and in both air equilibrated or degassed CH_3CN for the reference **VI-9**. Excitation wavelength : 385nm.

XII.3 Computational details

DFT calculations were performed using Gaussian 09 rev E01.[16] The B3LYP method[17-19] was used to carry the DFT[20-23] and TD-DFT[24-26] calculations. The 6-31G** basis set was used for the light atoms (H, C, N, O, P and V)[27-29] while the LanL2DZ basis set was used for heavier atoms (Br, W, Re)[30-31]. Geometry optimizations were conducted without symmetry constraints. Frequency calculations after optimization confirmed that energy minima had been reached in all cases. Energy, oscillator strength, and related MO contributions for the 100 lowest singlet–singlet and 10 lowest singlet–triplet excitations were obtained from the TD-DFT/singlets and the TD-DFT/triplets output files, respectively, for the S_0-optimized geometry. GaussView5.0.9[32], GaussSum 3.0[33] and Chemissian 4.44[34] were used for data analysis, visualization and surface plots. All calculations were performed in CH_3CN solution by use of the polarized continuum (PCM) solvation model as implemented in Gaussian 09.[35-36]

Compound **VI-9** was modeled using the same method to confirm the reliability of the model obtained.

Table XII.1. Predicted and experimental CO stretching vibrations (σ / cm-1) for compounds **VI-4** and reference **VI-9**

Experimental (**VI-4**)	Predicted (**VI-4**)	Experimental (**VI-9**)	Predicted (**VI-9**)
2019	2088	2012	2012
1916	1981	1882	1897
1891	1967	1865	1891

Table XII.2. Predicted luminescence wavelength for reference **VI-**9

Compound	λ_{TDDFT}	$\lambda_{0,0}$	λ_{AE}	λ_{298}	Error
VI-9	436	472	561	584^{ref}	4%

λTDDFT = wavelength of $S_0 \rightarrow T_1$ transition obtained by TDDFT at the S_0 optimized geometry.

$\lambda_{0,0} = 1240/[E(T_1) - E(S_0)]$ at their respective optimized geometries obtained by DFT.

$\lambda_{AE} = 1240/[E(T_1) - E(S_0)]$ at the T_1 optimized geometry (adiabatic electronic emission) obtained by DFT.

Error = $|[\lambda_{em}(298\ K) - \lambda_{AE}]/\lambda_{298}|/100$ in %.

Table XII.3. Extended frontiers orbitals of compound **VI-**4

Orbitals (energy)	*Contributions*	*Orbitals (energy)*	*Contributions*
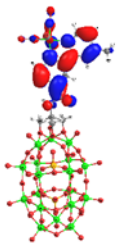 LUMO+6	$Re(CO)_3Br$: 8% POM : 1% Triol : 0% bpyCONH : 91%	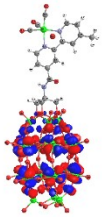 LUMO -3.5eV	$Re(CO)_3Br$: 0% POM : 99% Triol : 1% bpyCONH : 0%
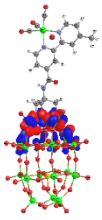 LUMO+5 -2.58eV	$Re(CO)_3Br$: 0% POM : 97% Triol : 6% bpyCONH : 0%	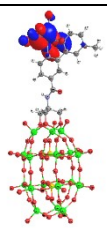 HOMO -6.05eV	$Re(CO)_3Br$: 97% POM : 0% Triol : 0% bpyCONH : 3%
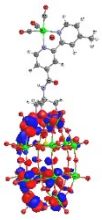 LUMO+4 -2.85eV	$Re(CO)_3Br$:0 % POM : 97% Triol : 3% bpyCONH : 0%	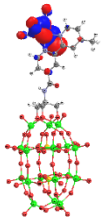 HOMO-1 -6.11eV	$Re(CO)_3Br$: 96% POM : 0% Triol : 0% bpyCONH : 4%
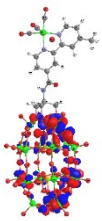 LUMO+3 -2.85eV	$Re(CO)_3Br$: 0% POM : 97% Triol : 3% bpyCONH : 0%	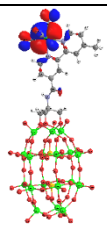 HOMO-2 -6.62eV	$Re(CO)_3Br$: 98% POM : 0% Triol :0 % bpyCONH : 2%
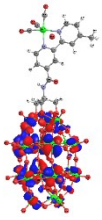 LUMO+2 -3.23eV	$Re(CO)_3Br$: 0% POM : 99% Triol : 1% bpyCONH : 0%	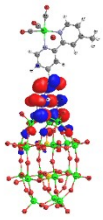 HOMO-3 -6.73eV	$Re(CO)_3Br$: 0% POM : 12% Triol : 62% bpyCONH : 26%
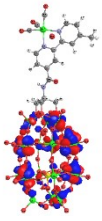 LUMO+1 -3.24eV	$Re(CO)_3Br$: 0% POM : 99% Triol : 1% bpyCONH : 0%	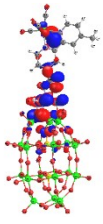 HOMO-4 -6.93eV	$Re(CO)_3Br$: 14% POM : 14% Triol : 54% bpyCONH : 18%

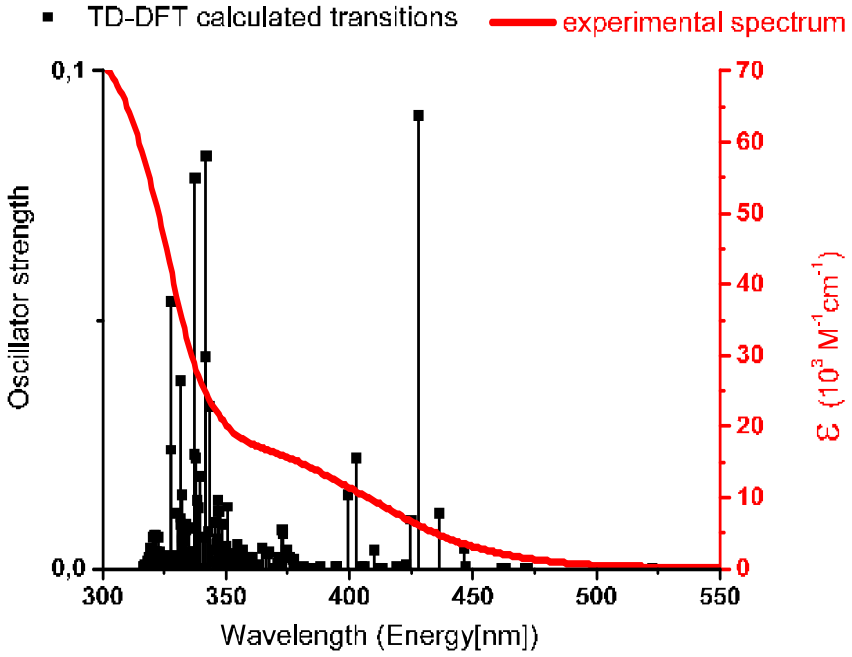

Figure XII.29. Experimental and calculated transitions for **VI-4** in CH_3CN

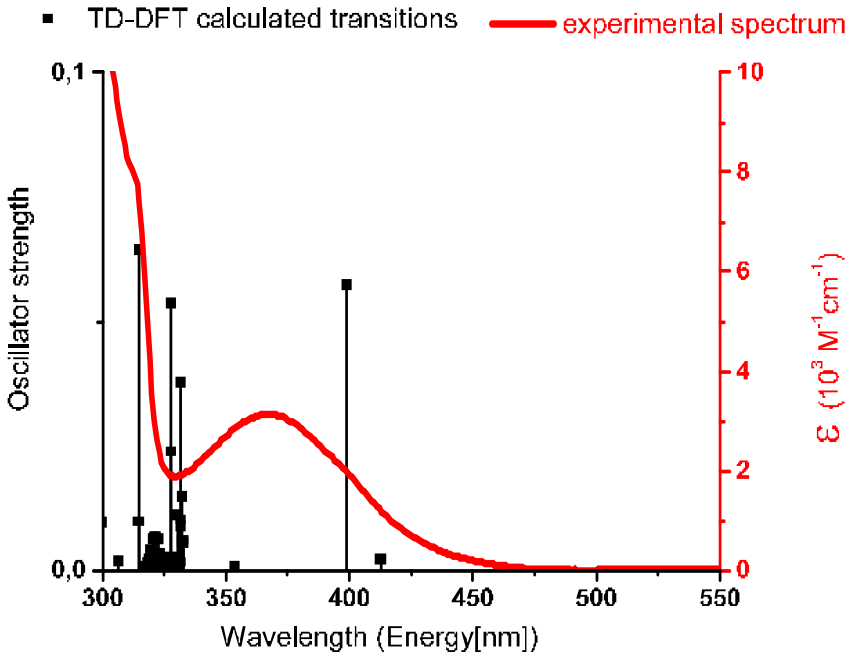

Figure XII.28. Experimental and calculated transitions for **VI-9** in CH_3CN

Table XII.4. The 150 lowest singlet–singlet and 10 lowest singlet–triplet transitions obtained from the TD-DFT/singlets and the TD-DFT/triplets output files for **VI-4** at the S_0-optimized geometry.

S_0 to Sx	λ (nm)	Osc. Strength	Major contributions (above 5%)	triol	POM	$ReCO_3Br$	Bpy-amide
1	522,74	0.0	HOMO->LUMO (100%)	0-->1 (1)	0-->99 (99)	97-->0 (-97)	3-->0 (-3)
2	511,42	0.0	H-1->LUMO (100%)	0-->1 (1)	0-->99 (99)	96-->0 (-96)	4-->0 (-4)
3	472,41	0.0	HOMO->L+1 (98%)	0-->1 (1)	0-->99 (99)	97-->0 (-97)	3-->0 (-3)
4	471,05	0.0001	HOMO->L+2 (98%)	0-->1 (1)	0-->99 (99)	97-->0 (-97)	3-->0 (-3)
5	463,32	0.0001	H-1->L+1 (97%)	0-->1 (1)	0-->99 (99)	95-->0 (-95)	4-->0 (-4)
6	461,90	0.0002	H-1->L+2 (97%)	0-->1 (1)	0-->99 (99)	96-->0 (-96)	4-->0 (-4)
7	446,85	0.0003	H-3->LUMO (95%)	60-->1 (-59)	13-->99 (86)	1-->0 (-1)	26-->0 (-26)
8	446,55	0.0041	HOMO->L+6 (97%)	0-->0 (0)	0-->3 (3)	97-->8 (-89)	3-->89 (86)
9	436,35	0.0111	H-3->L+1 (65%), H-3->L+3 (22%)	59-->2 (-57)	13-->98 (85)	3-->0 (-3)	25-->0 (-25)
10	427,92	0.091	H-1->L+6 (94%)	2-->1 (-1)	0-->6 (6)	93-->7 (-86)	5-->86 (81)
11	424,81	0.0098	H-3->L+2 (60%), H-3->L+4 (14%)	54-->1 (-53)	13-->96 (83)	10-->0 (-10)	23-->2 (-21)
12	423,08	0.0009	H-4->LUMO (23%), H-2->LUMO (61%)	19-->1 (-18)	5-->99 (94)	67-->0 (-67)	9-->0 (-9)
13	419,39	0.0003	H-4->LUMO (51%), H-2->LUMO (35%)	30-->1 (-29)	10-->99 (89)	48-->0 (-48)	12-->0 (-12)
14	413,18	0.0001	HOMO->L+3 (97%)	0-->2 (2)	0-->97 (97)	97-->0 (-97)	3-->0 (-3)
15	412,15	0.0001	HOMO->L+4 (95%)	1-->3 (2)	0-->96 (96)	96-->0 (-96)	3-->1 (-2)
16	410,14	0.0037	H-4->L+2 (49%), H-4->L+4 (17%)	43-->2 (-41)	16-->98 (82)	23-->0 (-23)	18-->0 (-18)
17	406,20	0.0003	H-1->L+3 (96%)	1-->2 (1)	0-->97 (97)	95-->0 (-95)	4-->0 (-4)
18	405,06	0.0003	H-1->L+4 (95%)	0-->3 (3)	0-->96 (96)	95-->0 (-95)	4-->2 (-2)
19	402,59	0.0221	H-4->L+1 (48%), H-4->L+3 (12%)	39-->2 (-37)	25-->98 (73)	21-->0 (-21)	16-->0 (-16)
20	399,47	0.0147	H-10->LUMO (62%)	9-->1 (-8)	84-->99 (15)	4-->0 (-4)	3-->0 (-3)
21	394,92	0.0003	H-9->LUMO (47%), H-8->LUMO (28%)	2-->1 (-1)	96-->99 (3)	1-->0 (-1)	2-->0 (-2)
22	394,64	0.0005	H-9->LUMO (29%), H-8->LUMO (46%)	2-->1 (-1)	96-->99 (3)	0-->0 (0)	2-->0 (-2)
23	388,04	0.0004	H-2->L+1 (97%)	1-->1 (0)	0-->99 (99)	96-->0 (-96)	2-->0 (-2)
24	387,29	0.0	H-2->L+2 (98%)	1-->1 (0)	0-->99 (99)	97-->0 (-97)	2-->0 (-2)
25	383,45	0.0002	H-12->LUMO (39%), H-11->LUMO (28%)	2-->2 (0)	79-->98 (19)	8-->0 (-8)	11-->0 (-11)
26	383,15	0.0	HOMO->L+5 (92%)	0-->6 (6)	6-->94 (88)	90-->0 (-90)	4-->0 (-4)
27	381,51	0.0005	H-13->LUMO (14%), H-12->LUMO (25%), H-11->LUMO (27%)	5-->1 (-4)	78-->99 (21)	4-->0 (-4)	14-->0 (-14)
28	378,30	0.0	H-5->LUMO (87%)	10-->1 (-9)	5-->99 (94)	69-->0 (-69)	15-->0 (-15)
29	377,56	0.0001	H-1->L+5 (90%)	5-->6 (1)	1-->93 (92)	88-->0 (-88)	6-->0 (-6)
30	377,22	0.0018	H-2->L+6 (97%)	0-->0 (0)	0-->3 (3)	98-->8 (-90)	2-->89 (87)
31	375,63	0.0021	H-3->L+1 (13%), H-3->L+3 (32%)	37-->2 (-35)	40-->98 (58)	4-->0 (-4)	19-->0 (-19)
32	374,43	0.0039	H-3->L+3 (24%)	26-->2 (-24)	57-->98 (41)	2-->0 (-2)	15-->0 (-15)
33	373,21	0.0071	H-15->LUMO (15%), H-6->LUMO (22%), H-3->L+4 (23%)	26-->2 (-24)	39-->98 (59)	21-->0 (-21)	14-->0 (-14)
34	372,75	0.0078	H-6->LUMO (40%), H-3->L+4 (30%)	31-->2 (-29)	16-->98 (82)	35-->0 (-35)	18-->0 (-18)
35	372,37	0.0005	H-16->LUMO (38%)	7-->2 (-5)	77-->98 (21)	5-->0 (-5)	10-->0 (-10)
36	371,48	0.0021	H-15->LUMO (45%), H-6->LUMO (12%)	11-->2 (-9)	71-->98 (27)	10-->0 (-10)	7-->0 (-7)
37	371,19	0.001	H-16->LUMO (13%), H-6->LUMO (13%), H-3->L+5 (42%)	32-->4 (-28)	35-->96 (61)	15-->0 (-15)	17-->0 (-17)

38	368,97	0.0002	H-14->L+1 (15%)	5-->2 (-3)	86-->98 (12)	3-->0 (-3)	7-->0 (-7)
39	367,63	0.0033	H-14->LUMO (45%)	7-->2 (-5)	85-->98 (13)	1-->0 (-1)	6-->0 (-6)
40	366,51	0.0028	H-3->L+5 (13%)	12-->2 (-10)	78-->98 (20)	2-->0 (-2)	8-->0 (-8)
41	364,56	0.0041	H-21->LUMO (46%)	2-->1 (-1)	95-->99 (4)	1-->0 (-1)	3-->0 (-3)
42	363,22	0.0009	H-22->LUMO (17%), H-9->L+2 (14%), H-8->L+1 (15%)	2-->1 (-1)	92-->99 (7)	1-->0 (-1)	5-->0 (-5)
43	362,81	0.0004	H-23->LUMO (14%), H-9->L+1 (15%), H-8->L+2 (14%)	3-->1 (-2)	90-->99 (9)	2-->0 (-2)	5-->0 (-5)
44	360,44	0.0021		8-->1 (-7)	70-->99 (29)	6-->0 (-6)	16-->0 (-16)
45	359,57	0.002	H-24->LUMO (20%), H-7->LUMO (14%)	4-->1 (-3)	74-->99 (25)	4-->0 (-4)	18-->0 (-18)
46	358,81	0.0022	H-17->LUMO (23%), H-10->L+2 (16%)	6-->1 (-5)	85-->99 (14)	3-->0 (-3)	6-->0 (-6)
47	358,11	0.0003	H-10->L+1 (11%), H-7->LUMO (51%)	2-->1 (-1)	43-->99 (56)	5-->0 (-5)	50-->0 (-50)
48	357,27	0.0006	H-4->L+2 (13%), H-4->L+4 (31%)	30-->2 (-28)	40-->98 (58)	15-->0 (-15)	16-->0 (-16)
49	356,52	0.0037	H-4->L+3 (24%)	23-->2 (-21)	54-->98 (44)	11-->0 (-11)	12-->0 (-12)
50	355,03	0.0015	H-10->LUMO (14%), H-9->L+1 (19%), H-8->L+2 (19%)	2-->1 (-1)	95-->99 (4)	1-->0 (-1)	2-->0 (-2)
51	354,82	0.0021	H-4->L+5 (46%)	32-->4 (-28)	37-->95 (58)	17-->0 (-17)	14-->0 (-14)
52	354,41	0.0048	H-22->LUMO (16%), H-7->LUMO (10%)	8-->1 (-7)	65-->99 (34)	10-->0 (-10)	17-->0 (-17)
53	354,18	0.0004	HOMO->L+7 (88%)	1-->1 (0)	3-->97 (94)	93-->0 (-93)	3-->1 (-2)
54	353,82	0.003	H-4->L+5 (12%), HOMO->L+8 (43%)	13-->2 (-11)	29-->98 (69)	51-->0 (-51)	8-->0 (-8)
55	353,68	0.0023	HOMO->L+8 (51%)	10-->2 (-8)	23-->98 (75)	60-->0 (-60)	7-->0 (-7)
56	351,65	0.0016	H-5->L+1 (67%)	10-->1 (-9)	16-->99 (83)	58-->0 (-58)	15-->0 (-15)
57	350,93	0.0029	H-5->L+2 (49%)	10-->1 (-9)	32-->99 (67)	45-->0 (-45)	13-->0 (-13)
58	350,60	0.0124	H-5->L+1 (13%)	5-->2 (-3)	70-->98 (28)	16-->0 (-16)	9-->0 (-9)
59	349,88	0.0044	H-5->L+2 (23%)	4-->1 (-3)	62-->99 (37)	23-->0 (-23)	10-->0 (-10)
60	349,55	0.0039		3-->1 (-2)	84-->99 (15)	8-->0 (-8)	6-->0 (-6)
61	349,25	0.0035	H-10->L+2 (10%)	3-->1 (-2)	90-->99 (9)	3-->0 (-3)	5-->0 (-5)
62	349,01	0.0003	H-1->L+7 (92%)	0-->1 (1)	0-->97 (97)	95-->0 (-95)	4-->1 (-3)
63	348,55	0.0001	H-1->L+8 (92%)	0-->1 (1)	0-->99 (99)	95-->0 (-95)	4-->0 (-4)
64	348,28	0.0089	H-17->LUMO (13%), H-10->L+1 (17%)	4-->1 (-3)	80-->99 (19)	10-->0 (-10)	6-->0 (-6)
65	348,09	0.0021	H-14->L+1 (10%), H-12->L+2 (16%)	5-->1 (-4)	74-->99 (25)	13-->0 (-13)	8-->0 (-8)
66	347,27	0.0007	H-6->L+1 (16%), H-2->L+3 (55%)	3-->2 (-1)	21-->98 (77)	71-->0 (-71)	5-->0 (-5)
67	346,96	0.0115	H-26->LUMO (10%), H-6->L+1 (15%), H-2->L+3 (28%)	3-->2 (-1)	44-->98 (54)	46-->0 (-46)	7-->0 (-7)
68	346,88	0.0058	H-26->LUMO (12%), H-11->L+2 (10%), H-2->L+4 (21%)	3-->2 (-1)	52-->98 (46)	38-->0 (-38)	7-->0 (-7)
69	346,63	0.0136	H-26->LUMO (28%), H-2->L+4 (31%)	2-->2 (0)	56-->98 (42)	39-->0 (-39)	3-->0 (-3)
70	346,38	0.0051	H-2->L+4 (34%)	3-->2 (-1)	53-->98 (45)	39-->0 (-39)	6-->0 (-6)
71	346,06	0.0047		5-->2 (-3)	71-->98 (27)	17-->0 (-17)	6-->0 (-6)
72	345,85	0.0092	H-8->L+1 (10%)	4-->1 (-3)	83-->98 (15)	8-->0 (-8)	5-->0 (-5)
73	345,27	0.0015	H-6->L+1 (12%), H-6->L+2 (46%)	6-->1 (-5)	34-->99 (65)	49-->0 (-49)	10-->0 (-10)
74	344,62	0.0036	H-12->L+1 (12%), H-6->L+1 (14%), H-6->L+2 (14%)	5-->1 (-4)	60-->99 (39)	25-->0 (-25)	10-->0 (-10)
75	343,38	0.0325		3-->1 (-2)	89-->99 (10)	3-->0 (-3)	4-->0 (-4)
76	342,84	0.0073		3-->1 (-2)	89-->99 (10)	2-->0 (-2)	6-->0 (-6)
77	341,86	0.0829	H-26->LUMO (10%), H-20->LUMO (10%)	3-->1 (-2)	88-->99 (11)	4-->0 (-4)	5-->0 (-5)
78	341,53	0.0426	H-19->LUMO (14%)	4-->1 (-3)	87-->99 (12)	4-->0 (-4)	5-->0 (-5)
79	340,88	0.0002	HOMO->L+9 (94%)	2-->2 (0)	1-->97 (96)	94-->0 (-94)	4-->1 (-3)

80	340,46	0.0063	H-25->LUMO (13%), H-10->L+1 (12%)	4-->1 (-3)	88-->99 (11)	2-->0 (-2)	5-->0 (-5)
81	339,62	0.0186	H-32->LUMO (15%), H-27->LUMO (10%)	10-->1 (-9)	78-->99 (21)	6-->0 (-6)	7-->0 (-7)
82	338,73	0.0121	H-3->L+11 (17%)	29-->1 (-28)	42-->98 (56)	13-->0 (-13)	16-->1 (-15)
83	338,31	0.0136		7-->1 (-6)	81-->98 (17)	4-->0 (-4)	7-->0 (-7)
84	337,85	0.0221	H-30->LUMO (12%)	3-->1 (-2)	94-->98 (4)	1-->0 (-1)	3-->0 (-3)
85	337,83	0.0083	H-29->LUMO (10%)	3-->2 (-1)	91-->98 (7)	2-->0 (-2)	4-->0 (-4)
86	337,47	0.0022	HOMO->L+10 (60%)	4-->1 (-3)	29-->98 (69)	63-->0 (-63)	5-->0 (-5)
87	337,45	0.0784	H-39->LUMO (10%), H-28->LUMO (18%)	4-->1 (-3)	84-->98 (14)	9-->0 (-9)	3-->1 (-2)
88	337,22	0.023	HOMO->L+10 (17%), HOMO->L+11 (13%)	8-->1 (-7)	50-->98 (48)	35-->0 (-35)	7-->1 (-6)
89	336,86	0.0035	H-1->L+9 (13%), HOMO->L+11 (30%)	6-->2 (-4)	36-->96 (60)	53-->0 (-53)	6-->2 (-4)
90	336,77	0.0011	HOMO->L+11 (25%)	3-->1 (-2)	57-->96 (39)	35-->0 (-35)	5-->2 (-3)
91	336,63	0.0029		3-->1 (-2)	87-->99 (12)	4-->0 (-4)	6-->0 (-6)
92	336,16	0.0013	H-1->L+9 (61%)	10-->2 (-8)	8-->94 (86)	73-->0 (-73)	8-->3 (-5)
93	335,40	0.0034	H-3->L+10 (12%), HOMO->L+20 (14%), HOMO->L+23 (20%)	20-->1 (-19)	10-->67 (57)	58-->1 (-57)	13-->30 (17)
94	335,25	0.0025		10-->1 (-9)	48-->84 (36)	32-->1 (-31)	11-->14 (3)
95	335,17	0.0083	H-34->LUMO (15%)	6-->1 (-5)	67-->93 (26)	14-->0 (-14)	13-->5 (-8)
96	335,07	0.0032	H-33->LUMO (11%), H-7->L+1 (13%)	18-->1 (-17)	38-->94 (56)	16-->0 (-16)	28-->4 (-24)
97	334,31	0.0028	H-7->L+1 (42%), H-7->L+2 (19%)	3-->1 (-2)	32-->98 (66)	4-->0 (-4)	60-->0 (-60)
98	333,70	0.0091	H-7->L+2 (22%)	7-->1 (-6)	52-->96 (44)	6-->0 (-6)	34-->3 (-31)
99	333,50	0.0079	H-33->LUMO (10%)	2-->1 (-1)	87-->99 (12)	1-->0 (-1)	9-->0 (-9)
100	333,00	0.0011	H-3->L+6 (45%), H-3->L+9 (20%)	45-->1 (-44)	18-->51 (33)	13-->4 (-9)	24-->45 (21)
101	332,50	0.0057	H-1->L+10 (38%)	3-->1 (-2)	45-->98 (53)	41-->0 (-41)	11-->0 (-11)
102	332,42	0.0061	H-1->L+10 (36%), H-1->L+11 (12%)	6-->1 (-5)	32-->93 (61)	51-->0 (-51)	11-->6 (-5)
103	332,28	0.0149	H-7->L+2 (10%)	5-->1 (-4)	76-->95 (19)	6-->0 (-6)	13-->4 (-9)
104	331,78	0.0102	H-1->L+11 (41%)	13-->1 (-12)	22-->88 (66)	55-->1 (-54)	11-->10 (-1)
105	331,68	0.0088	H-5->L+6 (16%), H-3->L+9 (16%)	25-->1 (-24)	14-->60 (46)	46-->3 (-43)	15-->37 (22)
106	331,46	0.0377	H-5->L+6 (43%), H-1->L+11 (12%)	10-->1 (-9)	13-->38 (25)	64-->4 (-60)	13-->57 (44)
107	331,25	0.0017		11-->1 (-10)	76-->92 (16)	5-->0 (-5)	7-->6 (-1)
108	331,07	0.0017		9-->1 (-8)	78-->92 (14)	5-->1 (-4)	8-->7 (-1)
109	330,61	0.0025	H-38->LUMO (19%)	6-->1 (-5)	84-->98 (14)	3-->0 (-3)	8-->1 (-7)
110	330,29	0.0112	H-6->L+6 (16%), H-4->L+6 (11%), H-1->L+20 (19%), H-1->L+23 (29%)	9-->1 (-8)	3-->42 (39)	76-->3 (-73)	11-->55 (44)
111	329,68	0.0003	H-41->LUMO (16%)	3-->1 (-2)	92-->99 (7)	2-->0 (-2)	4-->0 (-4)
112	329,50	0.0011	H-40->LUMO (11%), H-16->L+2 (10%)	3-->1 (-2)	89-->99 (10)	2-->0 (-2)	5-->0 (-5)
113	329,32	0.0001	H-16->L+2 (14%), H-15->L+1 (15%), H-15->L+2 (13%)	2-->1 (-1)	92-->99 (7)	2-->0 (-2)	4-->0 (-4)
114	327,81	0.0239	H-39->LUMO (22%)	8-->1 (-7)	74-->81 (7)	13-->1 (-12)	6-->17 (11)
115	327,70	0.0537	H-6->L+6 (10%), H-4->L+6 (28%), H-1->L+23 (11%)	20-->1 (-19)	30-->43 (13)	40-->4 (-36)	10-->53 (43)
116	327,38	0.0009	H-40->LUMO (18%)	5-->1 (-4)	87-->98 (11)	3-->0 (-3)	5-->0 (-5)
117	327,01	0.0011	H-42->LUMO (10%), H-21->L+1 (12%)	3-->1 (-2)	92-->98 (6)	3-->0 (-3)	3-->1 (-2)
118	326,67	0.0026	H-3->L+12 (11%), HOMO->L+12 (52%)	13-->2 (-11)	22-->96 (74)	57-->0 (-57)	8-->2 (-6)
119	326,51	0.0022	HOMO->L+12 (12%)	4-->2 (-2)	78-->98 (20)	14-->0 (-14)	4-->1 (-3)
120	326,01	0.0001	HOMO->L+13 (57%)	2-->2 (0)	35-->98 (63)	59-->0 (-59)	4-->0 (-4)
121	325,99	0.001	HOMO->L+13 (39%)	2-->2 (0)	51-->98 (47)	43-->0 (-43)	4-->0 (-4)

122	325,67	0.0014	H-2->L+5 (63%), HOMO->L+12 (11%)	11-->5 (-6)	5-->94 (89)	78-->0 (-78)	6-->1 (-5)
123	325,61	0.0022	H-3->L+12 (15%), H-2->L+5 (34%), HOMO->L+12 (19%)	21-->4 (-17)	9-->95 (86)	60-->0 (-60)	10-->1 (-9)
124	324,87	0.0013	H-43->LUMO (27%)	3-->1 (-2)	93-->98 (5)	2-->0 (-2)	2-->0 (-2)
125	324,45	0.0012		3-->1 (-2)	93-->98 (5)	1-->0 (-1)	3-->0 (-3)
126	324,34	0.0011	H-36->LUMO (10%)	3-->1 (-2)	94-->99 (5)	1-->0 (-1)	2-->0 (-2)
127	323,62	0.0002	H-23->L+2 (10%)	3-->2 (-1)	89-->98 (9)	2-->0 (-2)	7-->0 (-7)
128	323,01	0.0033	H-25->L+2 (11%)	6-->2 (-4)	84-->98 (14)	4-->0 (-4)	6-->0 (-6)
129	322,39	0.0062	H-6->L+6 (12%), H-1->L+12 (23%), H-1->L+13 (13%)	20-->2 (-18)	14-->76 (62)	54-->2 (-52)	13-->21 (8)
130	322,23	0.0034	H-3->L+13 (10%), H-1->L+12 (16%), H-1->L+13 (37%)	17-->2 (-15)	14-->95 (81)	58-->0 (-58)	10-->3 (-7)
131	321,69	0.003	H-25->L+1 (10%), H-21->L+1 (10%)	3-->2 (-1)	92-->98 (6)	2-->0 (-2)	4-->0 (-4)
132	321,59	0.0068	H-6->L+6 (14%), H-1->L+12 (37%), H-1->L+13 (11%)	11-->2 (-9)	12-->67 (55)	66-->2 (-64)	11-->29 (18)
133	321,27	0.0032	H-1->L+13 (13%)	7-->2 (-5)	64-->87 (23)	20-->1 (-19)	9-->10 (1)
134	321,19	0.0025	H-23->L+1 (12%)	5-->2 (-3)	83-->96 (13)	6-->0 (-6)	6-->2 (-4)
135	320,93	0.0066		4-->2 (-2)	89-->96 (7)	3-->0 (-3)	4-->2 (-2)
136	320,69	0.0031	H-4->L+10 (12%), H-1->L+13 (11%)	26-->2 (-24)	39-->92 (53)	22-->0 (-22)	13-->6 (-7)
137	320,53	0.0064	H-4->L+9 (11%), H-3->L+12 (11%), H-1->L+12 (10%)	27-->2 (-25)	34-->88 (54)	25-->1 (-24)	14-->9 (-5)
138	320,03	0.0021		10-->2 (-8)	75-->94 (19)	8-->0 (-8)	8-->4 (-4)
139	319,80	0.0002	HOMO->L+14 (84%)	4-->2 (-2)	4-->97 (93)	88-->0 (-88)	4-->0 (-4)
140	319,65	0.0016	H-24->L+1 (11%)	4-->2 (-2)	85-->98 (13)	7-->0 (-7)	4-->0 (-4)
141	319,29	0.0041	H-20->L+1 (12%)	7-->2 (-5)	70-->97 (27)	11-->0 (-11)	12-->1 (-11)
142	318,93	0.0021	H-4->L+11 (17%), H-3->L+13 (14%)	38-->2 (-36)	24-->97 (73)	21-->0 (-21)	17-->1 (-16)
143	318,12	0.0015	H-12->L+3 (11%)	5-->2 (-3)	82-->98 (16)	7-->0 (-7)	6-->0 (-6)
144	318,06	0.0001	H-18->LUMO (43%)	3-->1 (-2)	54-->99 (45)	38-->0 (-38)	5-->0 (-5)
145	318,00	0.0004	H-18->LUMO (28%)	4-->1 (-3)	63-->98 (35)	28-->0 (-28)	6-->0 (-6)
146	317,53	0.0005	H-5->L+3 (56%)	9-->2 (-7)	29-->98 (69)	51-->0 (-51)	12-->0 (-12)
147	317,36	0.0006	H-45->LUMO (11%), H-21->L+2 (10%)	5-->2 (-3)	80-->98 (18)	10-->0 (-10)	5-->0 (-5)
148	317,12	0.0006	H-5->L+3 (11%), H-5->L+4 (16%)	9-->2 (-7)	56-->97 (41)	26-->0 (-26)	10-->1 (-9)
149	316,99	0.0009		4-->2 (-2)	83-->98 (15)	7-->0 (-7)	6-->0 (-6)
150	316,61	0.0006	H-5->L+4 (42%)	6-->2 (-4)	47-->97 (50)	36-->0 (-36)	11-->1 (-10)

S_0 to Tx	λ (nm)	Osc. Strength	Major contributions (above 5%)	triol	POM	$ReCO_3Br$	Bpy-amide
1	522,77	0	HOMO->LUMO (100%)	0-->1 (1)	0-->99 (99)	97-->0 (-97)	3-->0 (-3)
2	511,44	0	H-1->LUMO (100%)	0-->1 (1)	0-->99 (99)	96-->0 (-96)	4-->0 (-4)
3	472,48	0	HOMO->L+1 (98%)	0-->1 (1)	0-->98 (98)	97-->0 (-97)	3-->0 (-3)
4	471,15	0	HOMO->L+2 (98%)	0-->1 (1)	0-->98 (98)	97-->0 (-97)	3-->0 (-3)
5	465,34	0	HOMO->L+6 (80%)	0-->0 (0)	0-->5 (5)	91-->8 (-83)	8-->87 (79)
6	463,93	0	H-1->L+1 (82%)	9-->1 (-8)	2-->98 (96)	82-->0 (-82)	7-->1 (-6)
7	462,46	0	H-1->L+2 (87%)	4-->1 (-3)	1-->98 (97)	89-->0 (-89)	6-->0 (-6)
8	458,79	0	H-3->L+1 (32%), H-3->L+3 (12%), H-1->L+1 (12%)	45-->2 (-43)	13-->98 (85)	22-->0 (-22)	20-->0 (-20)
9	454,35	0	H-3->LUMO (60%), H-3->L+2 (13%)	56-->2 (-54)	14-->98 (84)	6-->0 (-6)	24-->0 (-24)
10	453,66	0	H-1->L+6 (88%)	0-->0 (0)	0-->3 (3)	95-->8 (-87)	5-->88 (83)

XII.4 Crystallography

The data collection was carried out on a Bruker Venture Metaljet diffractometer equipped with an Oxford Cryosystem liquid N_2 device set at 150K, using Ga-Kα radiation (λ = 1.34139 Å). The cell parameters were determined from reflections taken from three sets of omega scans (104 frames, 1° per frame) using APEX3 software package[37]. Data reduction was performed with SAINT[38], adsorption correction with SADABS[39]. The structure was solved by dual-space refinement via SHELXT[40] in OLEX2[41]. The non-H atoms were refined anisotropically, using weighted full-matrix least-squares on F^2, the H-atoms were included in calculated positions and treated as riding atoms (SHELXL97[42]).

The absorption correction optimization appeared to be difficult for this dataset containing several highly absorbing heavy atoms of tungsten. Besides, a complex mix of disordered solvent and counter-cations surrounding the functionalized cluster was affecting the model. Some of the counter cations could however be identified and were modeled using the appropriate restraints (DFIX, DANG, RIGU, SIMU and BUMP). The first two TBAs yielded a reasonable model, while the third one required the use of tighter restraints. Albeit the two remaining cations (5 TBA expected according to other analytical results) could be partially identified, we were unable to obtain a reasonable model for them. We thus used the solvent-mask protocol in OLEX2 to remove the remaining densities (void of 6432 $Å^3$ i.e. 40% containing 644 electrons while 2 TBA^+ would correspond to 278 electrons). During the solvent mask procedure, the flack-x parameter value (refined using TWIN/BASF) increased from 0.010(4) to 0.255(19) while the hooft-y remained around 0.02. Similar observations were made using the PLATON/SQUEEZE routine. This systematic observation was treated as an artefact from the solvent-mask procedure. CCDC 1548013 contains the complete crystallographic data for this structure.

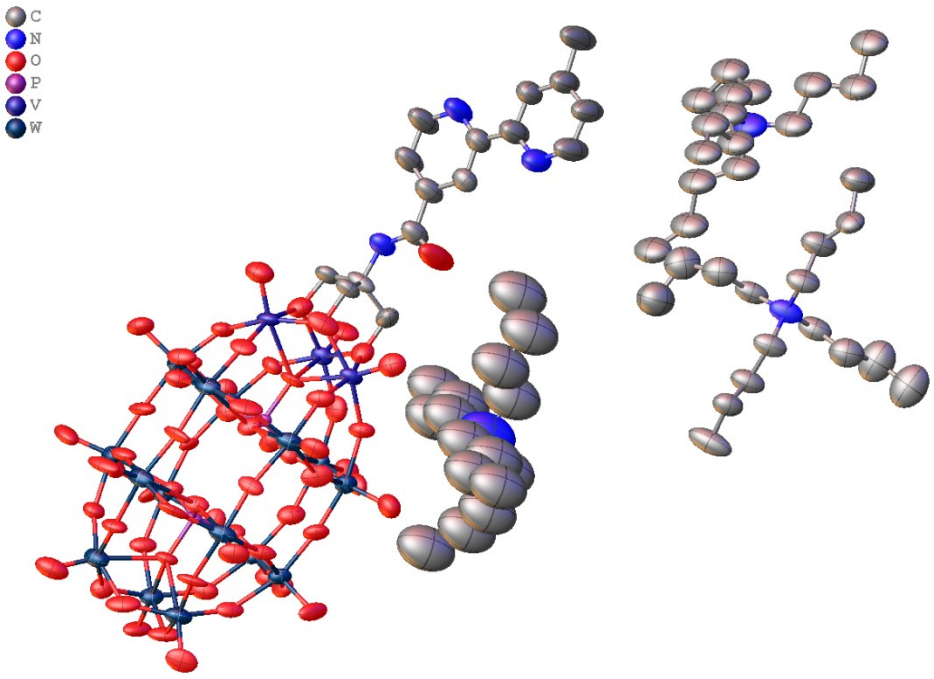

Figure XII.30. X-ray structure of compound **VI-1** (Ellipsoids are at 50% probability, hydrogens are omitted for clarity)

Identification code	auvr28
Empirical formula	$C_{64}H_{124}N_6O_{63}P_2V_3W_{15}$
Formula weight	4958.19
Temperature/K	150.0
Crystal system	orthorhombic
Space group	$P2_12_12_1$
a/Å	28.0308(10)
b/Å	36.9998(13)
c/Å	15.5102(5)
α/°	90
β/°	90
γ/°	90
Volume/Å^3	16086.2(10)
Z	4
ρ_{calc}g/cm^3	2.047
μ/mm^{-1}	15.072
F(000)	9052.0
Crystal size/mm^3	0.19 × 0.19 × 0.04
Radiation	GaKα (λ = 1.34139)
2Θ range for data collection/°	3.44 to 108.51
Index ranges	$-33 \leq h \leq 33$, $-44 \leq k \leq 44$, $-18 \leq l \leq 18$
Reflections collected	413250
Independent reflections	29712 [R_{int} = 0.1004, R_{sigma} = 0.0386]
Data/restraints/parameters	29712/674/1380
Goodness-of-fit on F^2	1.059
Final R indexes [I>=2σ (I)]	R_1 = 0.0652, wR_2 = 0.1782
Final R indexes [all data]	R_1 = 0.0726, wR_2 = 0.1867
Largest diff. peak/hole / e Å^{-3}	3.52/-1.28
Flack parameter	0.255(19)

XII.5 References

1. M. Strohalm, D. Kavan, P. Novak, M. Volny and V. Havlicek, *Anal. Chem.*, 2010, **82**, 4648-4651.

2. N. G. Connelly and W. E. Geiger, *Chem. Rev.*, 1996, **96**, 877-910.

3. J. R. Aranzaes, M. C. Daniel and D. Astruc, *Can. J. Chem.*, 2006, **84**, 288-299.

4. M. T. Robo, M. R. Prinsell and D. J. Weix, *J. Org. Chem.*, 2014, **79**, 10624-10628.

5. D. M. Ryan, M. K. Coggins, J. J. Concepcion, D. L. Ashford, Z. Fang, L. Alibabaei, D. Ma, T. J. Meyer and M. L. Waters, *Inorg. Chem.*, 2014, **53**, 8120-8128.

6. A. Stublla and P. G. Potvin, *Eur. J. Inorg. Chem.*, 2010, **2010**, 3040-3050.

7. G. R. Newkome, G. R. Baker, S. Arai, M. J. Saunders, P. S. Russo, K. J. Theriot, C. N. Moorefield, L. E. Rogers and J. E. Miller, *J. Am. Chem. Soc.*, 1990, **112**, 8458-8465.

8. M. P. Santoni, A. K. Pal, G. S. Hanan, A. Proust and B. Hasenknopf, *Inorg. Chem.*, 2011, **50**, 6737-6745.

9. M. P. Santoni, A. K. Pal, G. S. Hanan, M. C. Tang, A. Furtos and B. Hasenknopf, *Dalton Trans.*, 2014, **43**, 6990-6993.

10. S. Anderson, E. C. Constable, K. R. Seddon, J. E. Turp, J. E. Baggott and M. J. Pilling, *J. Chem. Soc., Dalton Trans.*, 1985, 2247-2261.

11. J. Husson, J. Dehaudt and L. Guyard, *Nat. Protoc.*, 2014, **9**, 21-26.

12. J. H. Wang and G. S. Hanan, *Synlett*, 2005, 1251-1254.

13. R. G. Finke, B. Rapko, R. J. Saxton and P. J. Domaille, *J. Am. Chem. Soc.*, 1986, **108**, 2947-2960.

14. W. W. Laxson, S. Ozkar and R. G. Finke, *Inorg. Chem.*, 2014, **53**, 2666-2676.

15. C. P. Pradeep, F. Y. Li, C. Lydon, H. N. Miras, D. L. Long, L. Xu and L. Cronin, *Chem. Eur. J.*, 2011, **17**, 7472-7479.

16. M. J. Frisch, G. W. Trucks, H. B. Schlegel, G. E. Scuseria, M. A. Robb, J. R. Cheeseman, G. Scalmani, V. Barone, B. Mennucci, G. A. Petersson, H. Nakatsuji, M. Caricato, X. Li, H. P. Hratchian, A. F. Izmaylov, J. Bloino, G. Zheng, J. L. Sonnenberg, M. Hada, M. Ehara, K. Toyota, R. Fukuda, J. Hasegawa, M. Ishida, T. Nakajima, Y. Honda, O. Kitao, H. Nakai, T. Vreven, J. A. Montgomery, J. E. Peralta, F. Ogliaro, M. Bearpark, J. J. Heyd, E. Brothers, K. N. Kudin, V. N. Staroverov, R. Kobayashi, J. Normand, K. Raghavachari, A. Rendell, J. C. Burant,

S. S. Iyengar, J. Tomasi, M. Cossi, N. Rega, J. M. Millam, M. Klene, J. E. Knox, J. B. Cross, V. Bakken, C. Adamo, J. Jaramillo, R. Gomperts, R. E. Stratmann, O. Yazyev, A. J. Austin, R. Cammi, C. Pomelli, J. W. Ochterski, R. L. Martin, K. Morokuma, V. G. Zakrzewski, G. A. Voth, P. Salvador, J. J. Dannenberg, S. Dapprich, A. D. Daniels, Farkas, J. B. Foresman, J. V. Ortiz, J. Cioslowski and D. J. Fox, *Gaussian 09, Revision E.01*, Wallingford CT, 2016.

17. C. Lee, W. Yang and R. G. Parr, *Phys. Rev. B*, 1988, **37**, 785-789.

18. A. D. Becke, *J. Chem. Phys.*, 1993, **98**, 5648-5652.

19. B. Miehlich, A. Savin, H. Stoll and H. Preuss, *Chem. Phys. Lett.*, 1989, **157**, 200-206.

20. P. Hohenberg and W. Kohn, *Phys. Rev.*, 1964, **136**, B864-B871.

21. W. Kohn and L. J. Sham, *Phys. Rev.*, 1965, **140**, A1133-A1138.

22. R. G. Parr and Y. Weitao, *Density-Functional Theory of Atoms and Molecules*, Oxford University Press, 1989.

23. D. R. Salahub and M. C. Zerner, eds., *The Challenge of d and f Electrons*, ACS, Washington DC, 1989.

24. R. Bauernschmitt and R. Ahlrichs, *Chem. Phys. Lett.*, 1996, **256**, 454-464.

25. M. E. Casida, C. Jamorski, K. C. Casida and D. R. Salahub, *J. Chem. Phys.*, 1998, **108**, 4439-4449.

26. R. E. Stratmann, G. E. Scuseria and M. J. Frisch, *J. Chem. Phys.*, 1998, **109**, 8218-8224.

27. P. C. Hariharan and J. A. Pople, *Theor. Chim. Acta*, 1973, **28**, 213-222.

28. M. M. Francl, W. J. Pietro, W. J. Hehre, J. S. Binkley, M. S. Gordon, D. J. DeFrees and J. A. Pople, *J. Chem. Phys.*, 1982, **77**, 3654-3665.

29. V. A. Rassolov, J. A. Pople, M. A. Ratner and T. L. Windus, *J. Chem. Phys.*, 1998, **109**, 1223-1229.

30. P. J. Hay and W. R. Wadt, *J. Chem. Phys.*, 1985, **82**, 299-310.

31. W. R. Wadt and P. J. Hay, *J. Chem. Phys.*, 1985, **82**, 284-298.

32. GaussView, V. 5.09, R. Dennington, T. Keith and J. Millam, *Semichem Inc.*, 2009, Shawnee Mission, KS.

33. N. M. O'Boyle, A. L. Tenderholt and K. M. Langner, *J. Comput. Chem.*, 2008, **29**, 839-845.

34. L. Skripnikov, *Chemissian*, 2005-2016, V. 4.44.

35. S. Miertuš, E. Scrocco and J. Tomasi, *Chem. Phys.*, 1981, **55**, 117-129.

36. J. Tomasi, B. Mennucci and R. Cammi, *Chem. Rev.*, 2005, **105**, 2999-3093.
37. *APEX3*, v2016 ; 9-0, Bruker AXS Inc.: Madison, USA.
38. *SAINT*, Release 7.34A;, Bruker AXS Inc.: Madison, USA.
39. G. M. Sheldrick, *SADABS*, 1996&2004, Bruker AXS Inc.: Madison, USA.
40. G. M. Sheldrick, *Acta Crystallogr., Sect. A*, 2015, **71**, 3.
41. O. V. Dolomanov, L. J. Bourhis, R. J. Gildea, J. A. K. Howard and H. Puschmann, *J. Appl. Cryst.*, 2009, **42**, 339-341.
42. G. M. Sheldrick, *Acta Cryst.*, 2008, **A64**, 112.

Chapitre XIII. Matériels supplémentaires au chapitre VII

XIII.1 Synthesis and structural characterization

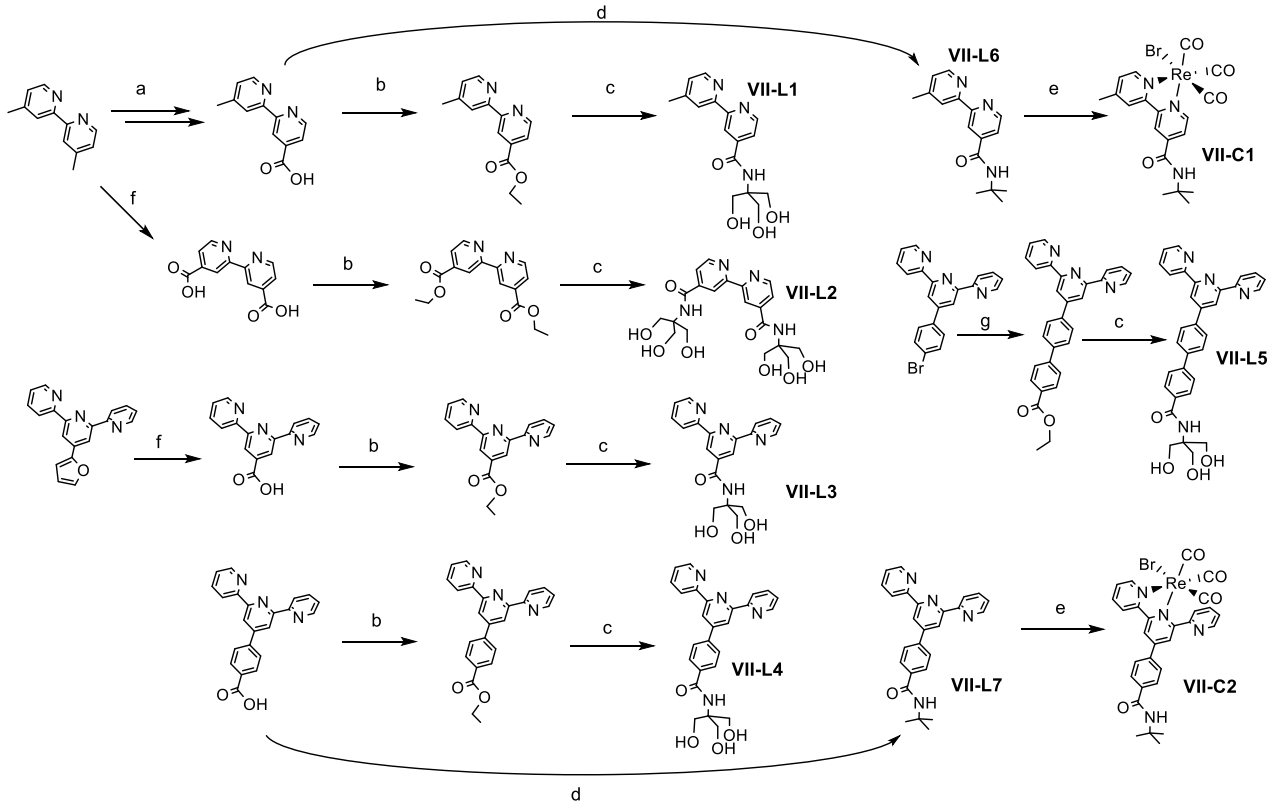

Figure XIII.1. Synthetic pathways for VII-L1-5 and VII-C1-2. a) 1-SeO_2 in 1,4-dioxane 2-$AgNO_3$, NaOH in EtOH/H_2O; b) anhyd. EtOH, conc. H_2SO_4 (cat.); c) TRIS 1 eq. K_2CO_3 1 eq. in DMSO; d) 1-$SOCl_2$ 2- NH_2tert-Bu 10 eq. in DCM; e) $Re(CO)_5Br$ in toluene ; $KMnO_4$ in H_2O pH 11.[1-4]

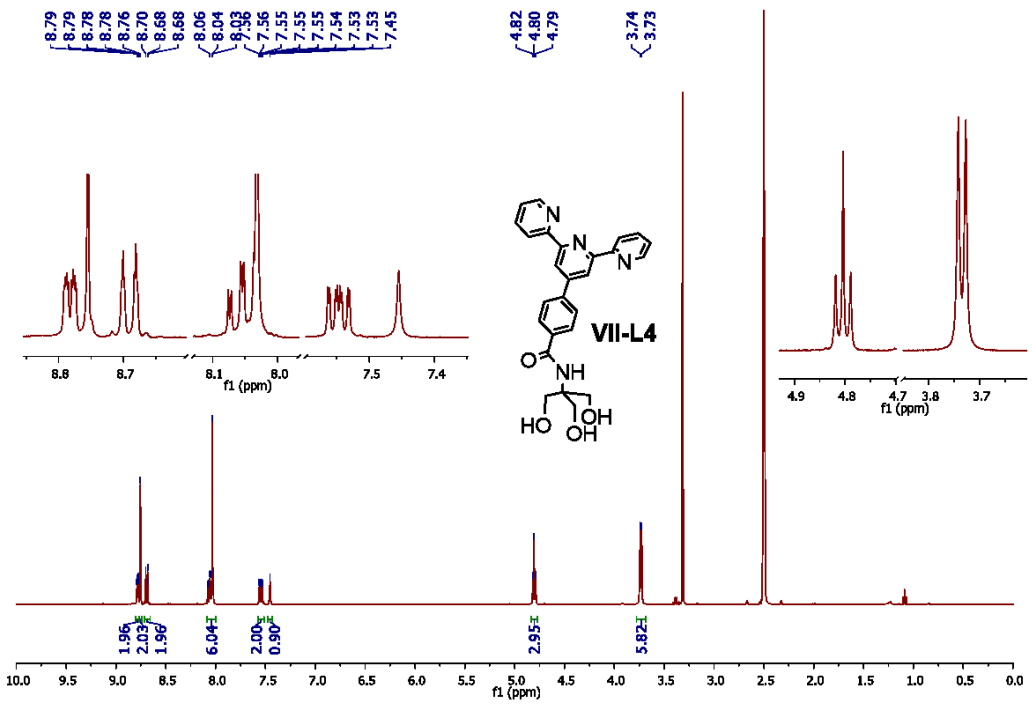

Figure XIII.2. ^{1}NMR spectra of **VII-L4** in DMSO-d^{6}

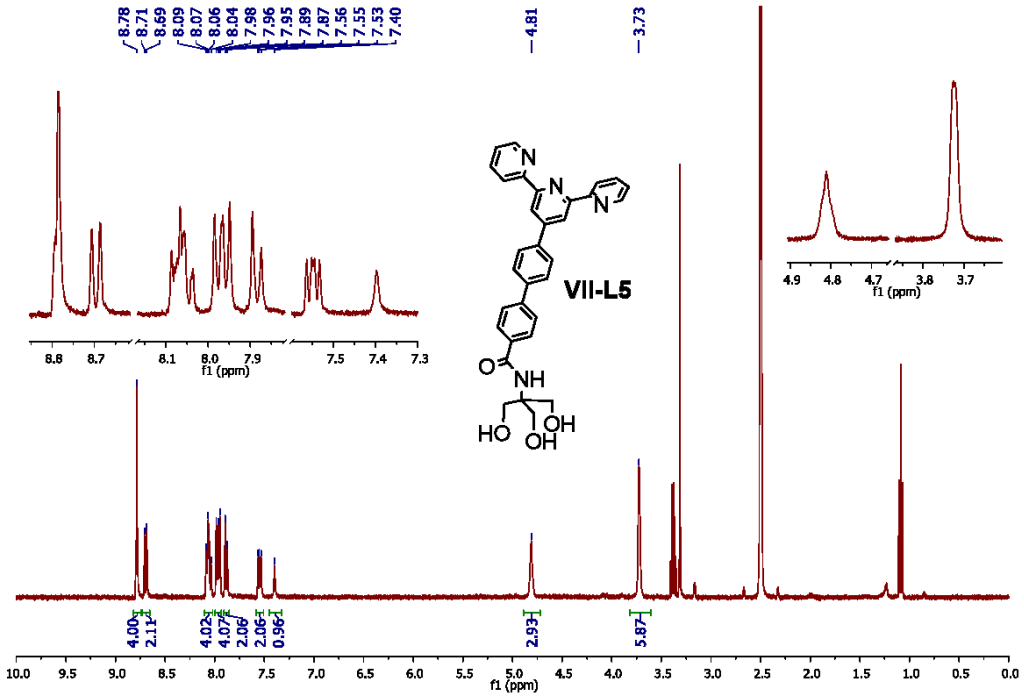

Figure XIII.3. ^{1}NMR spectra of **VII-L5** in DMSO-d^{6}

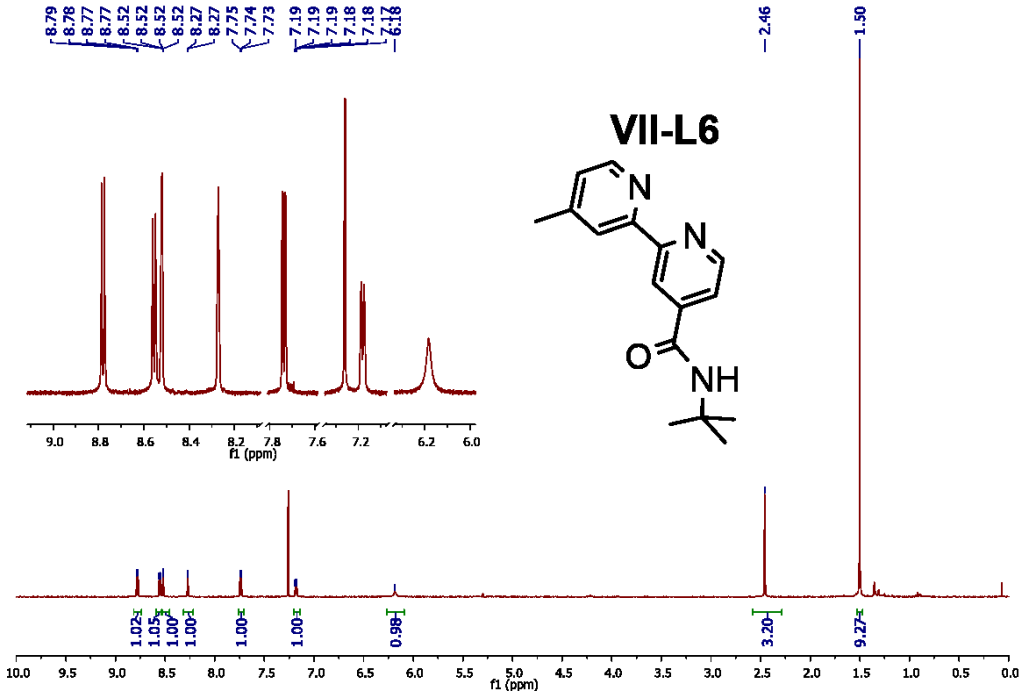

Figure XIII.4. ^{1}NMR spectra of **VII-L6** in $CDCl_3$

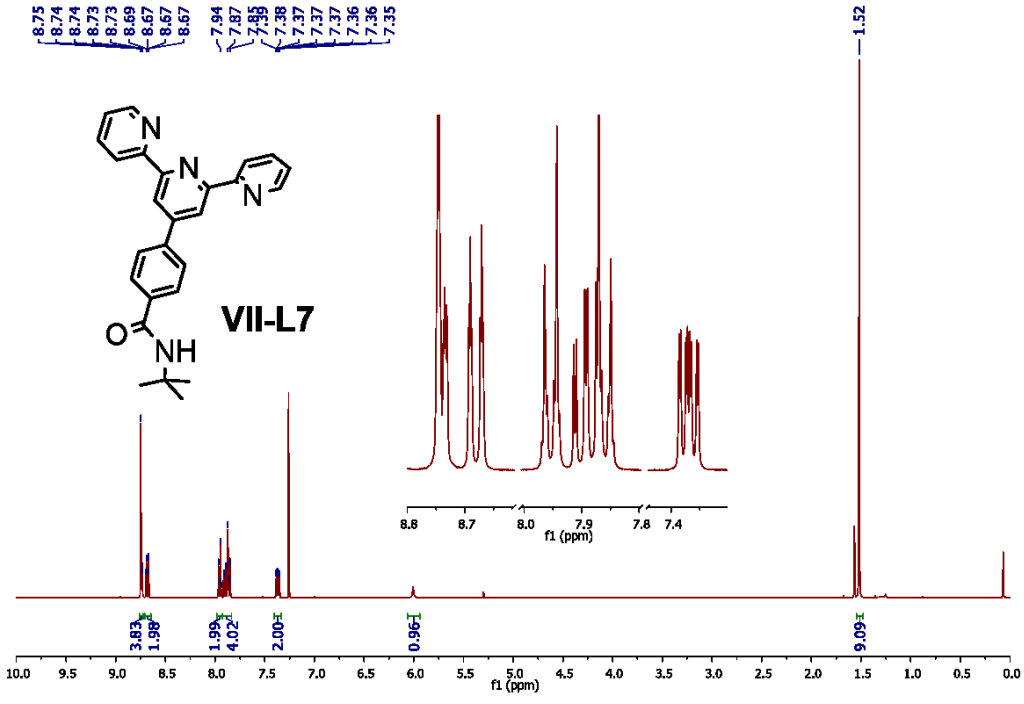

Figure XIII.5. ^{1}NMR spectra of **VII-L7** in $CDCl_3$

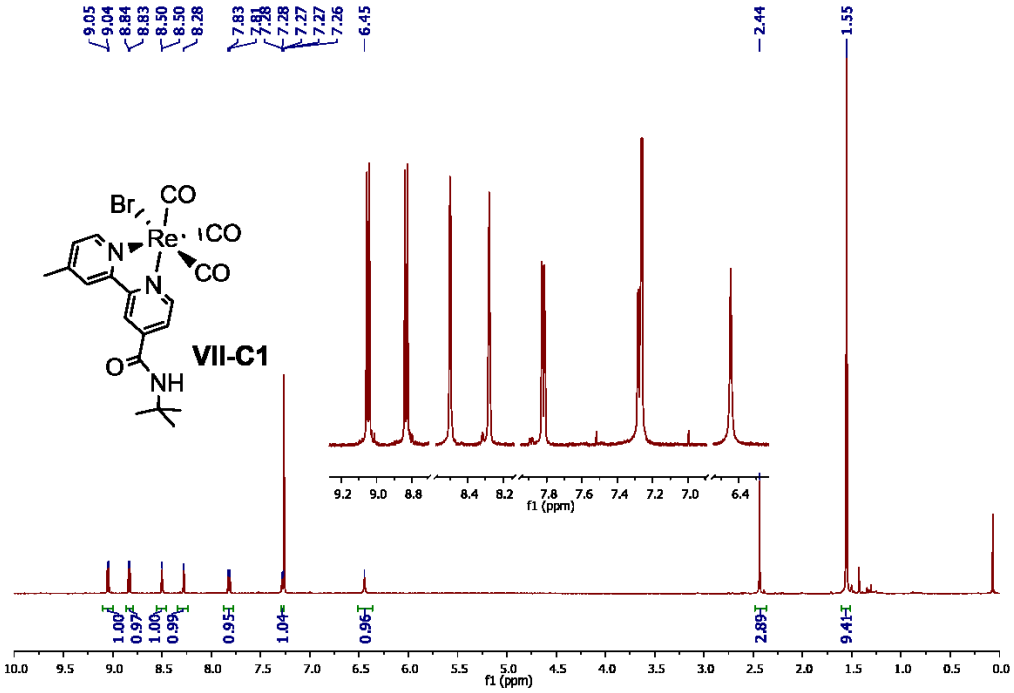

Figure XIII.6. ^{1}NMR spectra of **VII-C1** in $CDCl_3$

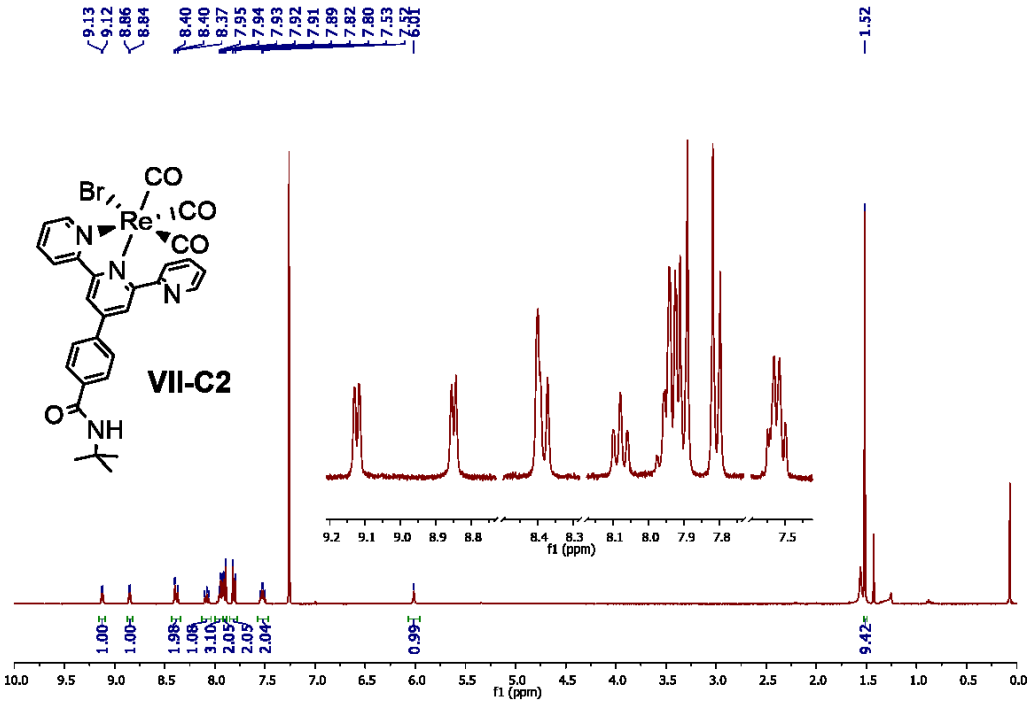

Figure XIII.7. ^{1}NMR spectra of **VII-C2** in $CDCl_3$

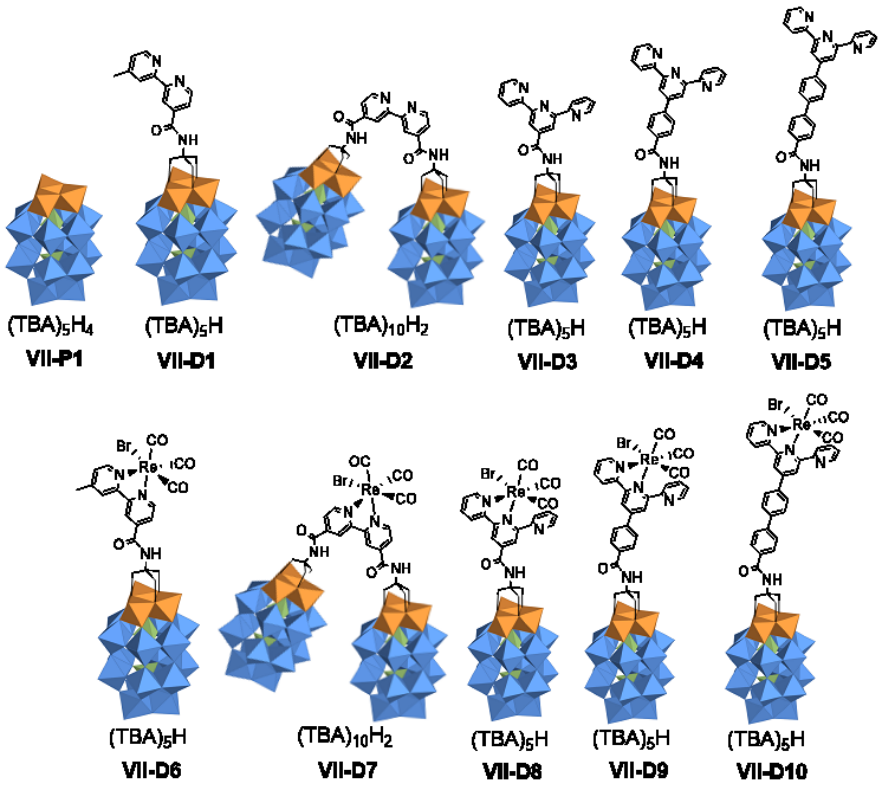

Figure XIII.8. Structures of the polypyridyl functionalized POMs and their Re(I) complexes.

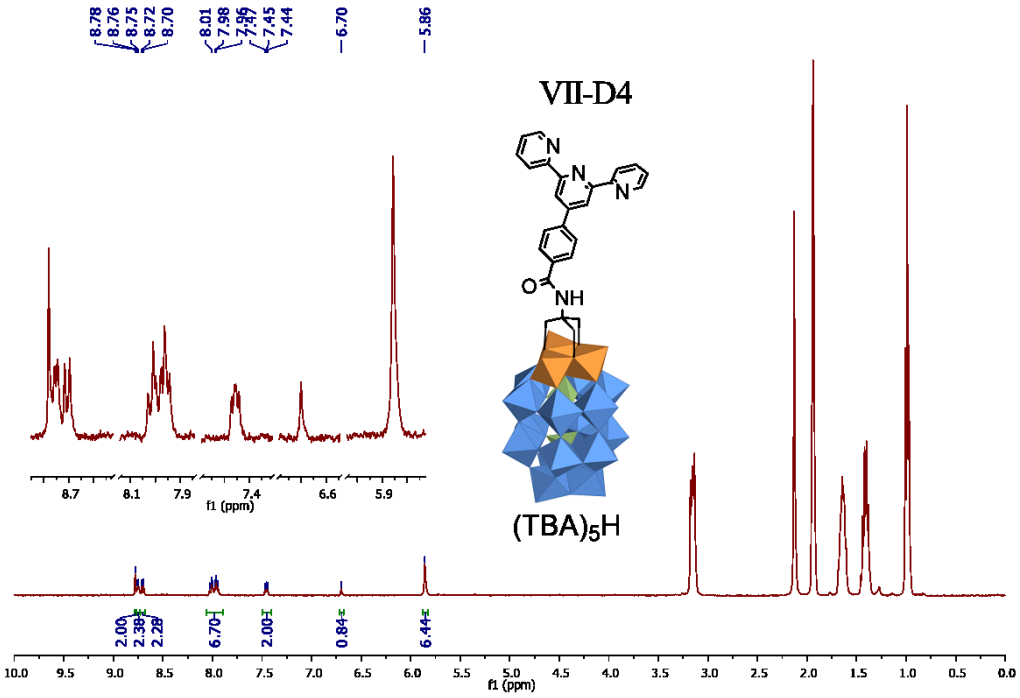

Figure XIII.9. ^{1}NMR spectra of **VII-D4** in CD_3CN

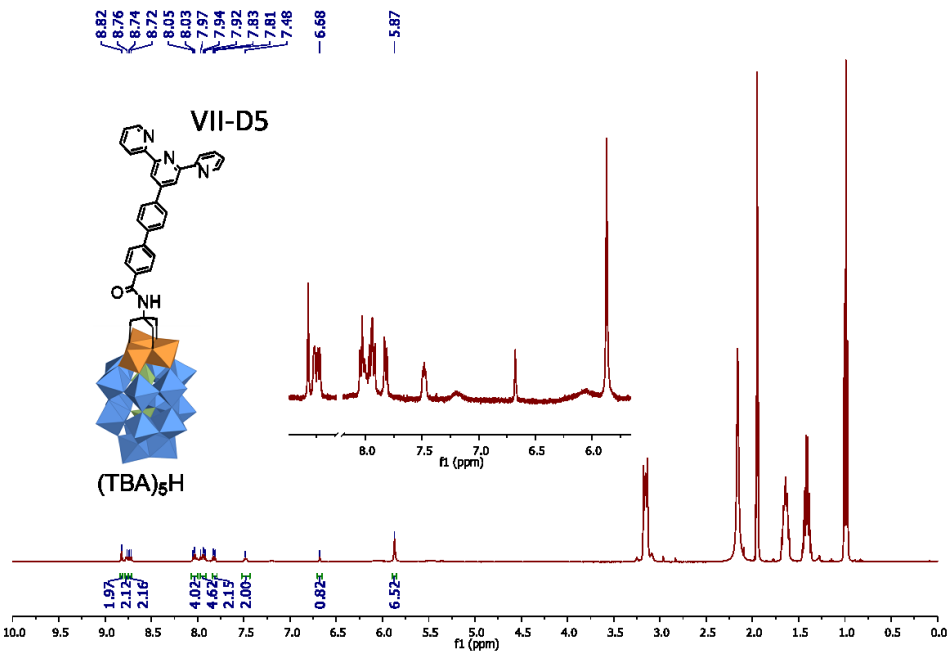

Figure XIII.10. ^{1}NMR spectra of **VII-D5** in CD_3CN

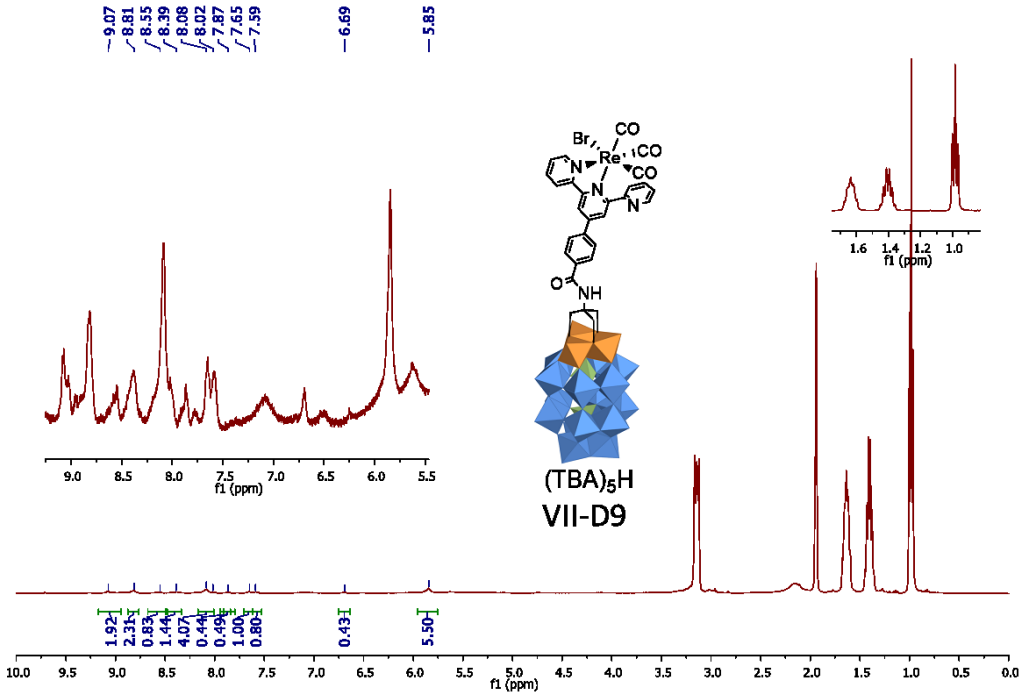

Figure XIII.11. ^{1}NMR spectra of **VII-D9** in CD_3CN (the aromatic signals are broaden by the fluxionality process)

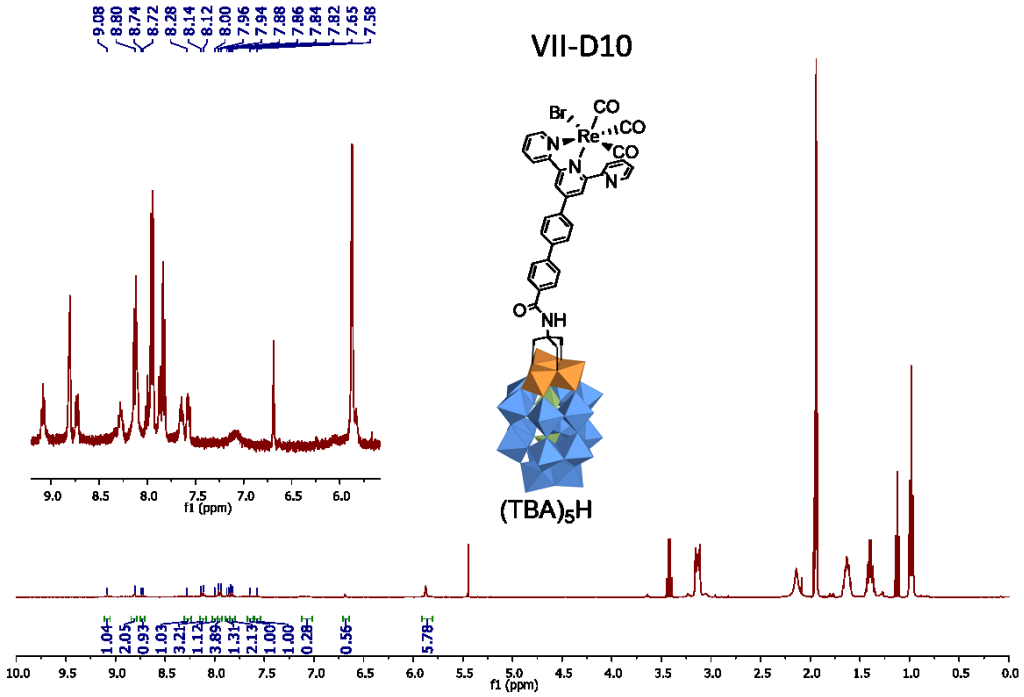

Figure XIII.12 ^{1}NMR spectra of **VII-D10** in CD_3CN

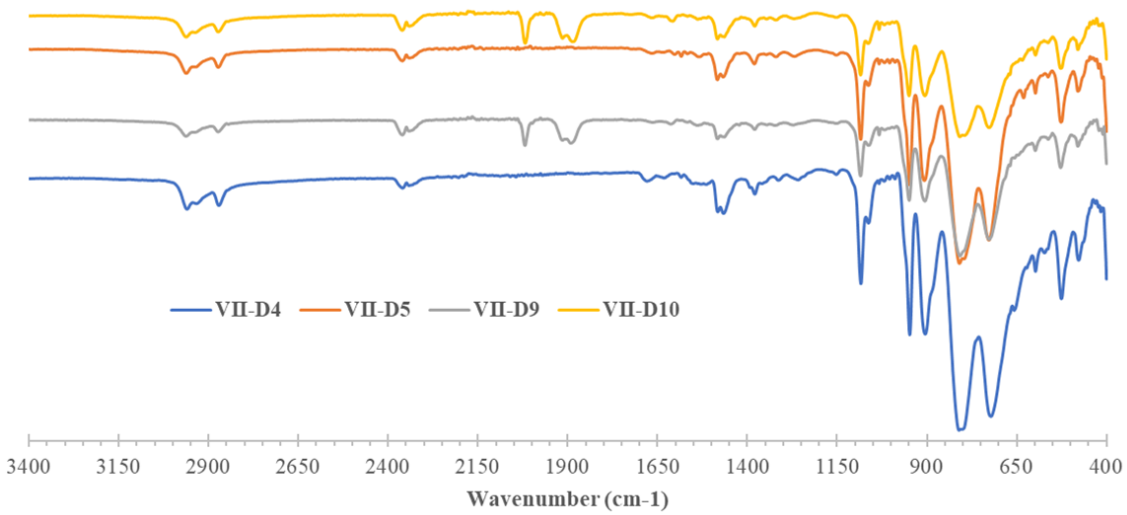

Figure XIII.13. IR spectra of **VII-D4-5** and **VII-D9-10** showing the additional bands corresponding to the carbonyls around 2000 cm-1 after complexation.

XIII.2 Electrochemistry

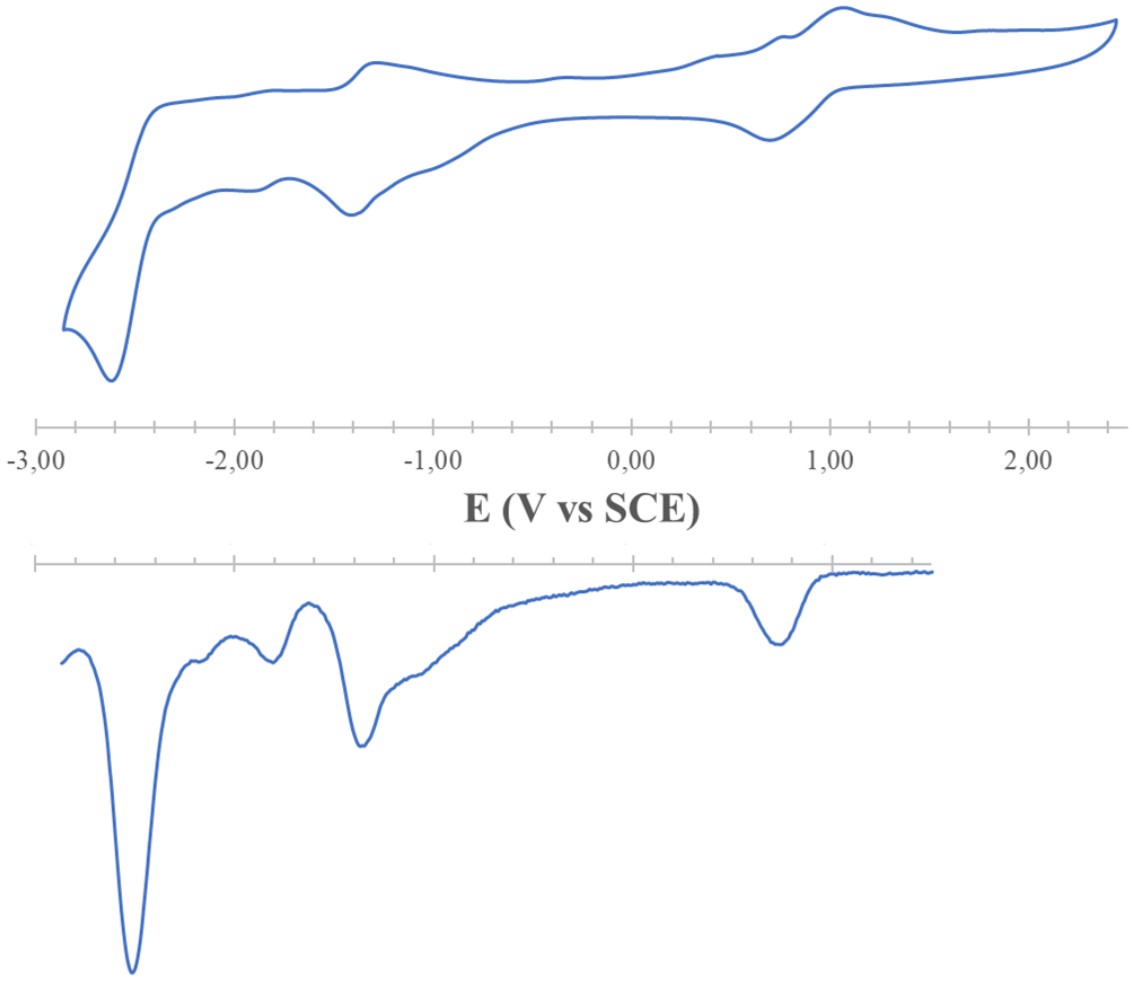

Figure XIII.14 Cyclovoltammogram and square-wave analysis of **VII-D9** in acetonitrile with TBAP 0.1 M (internal ref. acetylferrocene)

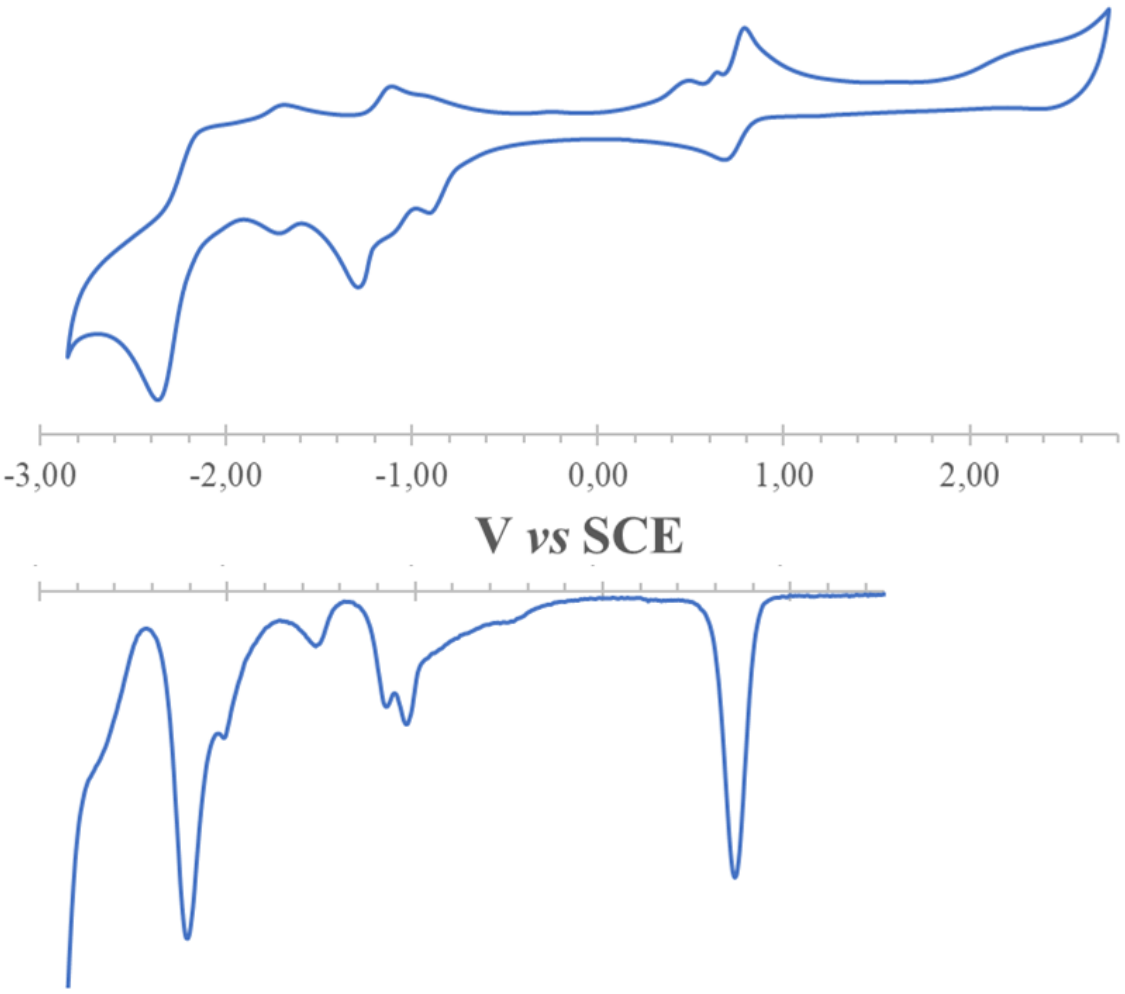

Figure XIII.15. Cyclovoltammogram and square-wave analysis of **VII-D10** in acetonitrile with TBAP 0.1 M (internal ref. acetylferrocene)

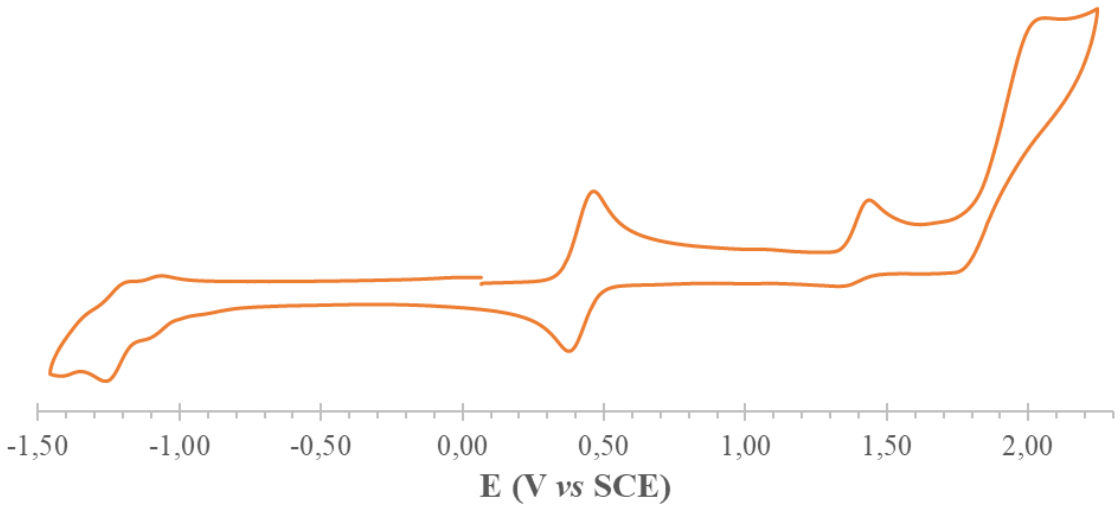

Figure XIII.16 Cyclovoltammogram of **VII-C1** in acetonitrile with TBAP 0.1 M (internal ref. ferrocene)

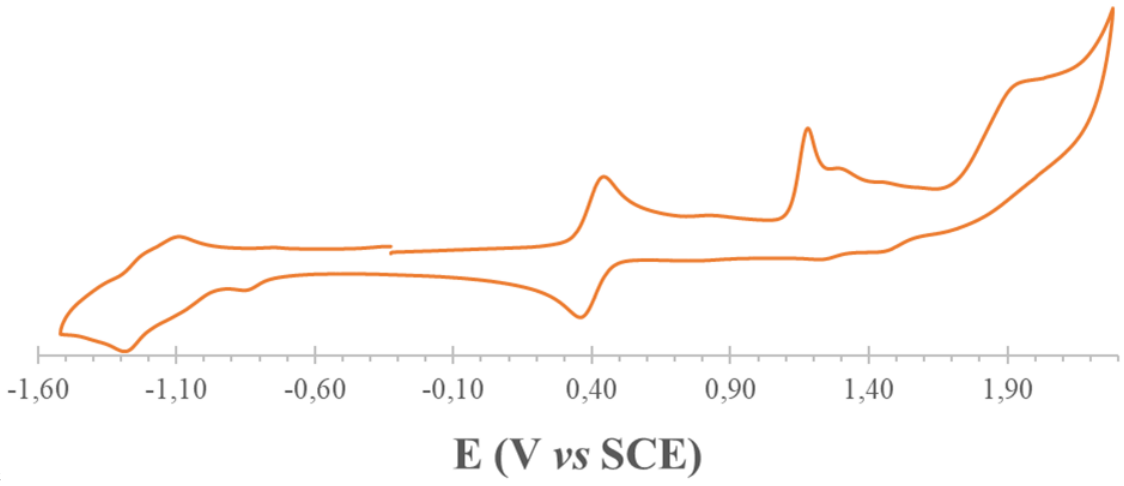

c

Figure XIII.17. Cyclovoltammogram of **VII-C2** in acetonitrile with TBAP 0.1 M (internal ref. ferrocene)

XIII.3 Absorption and emission spectroscopy

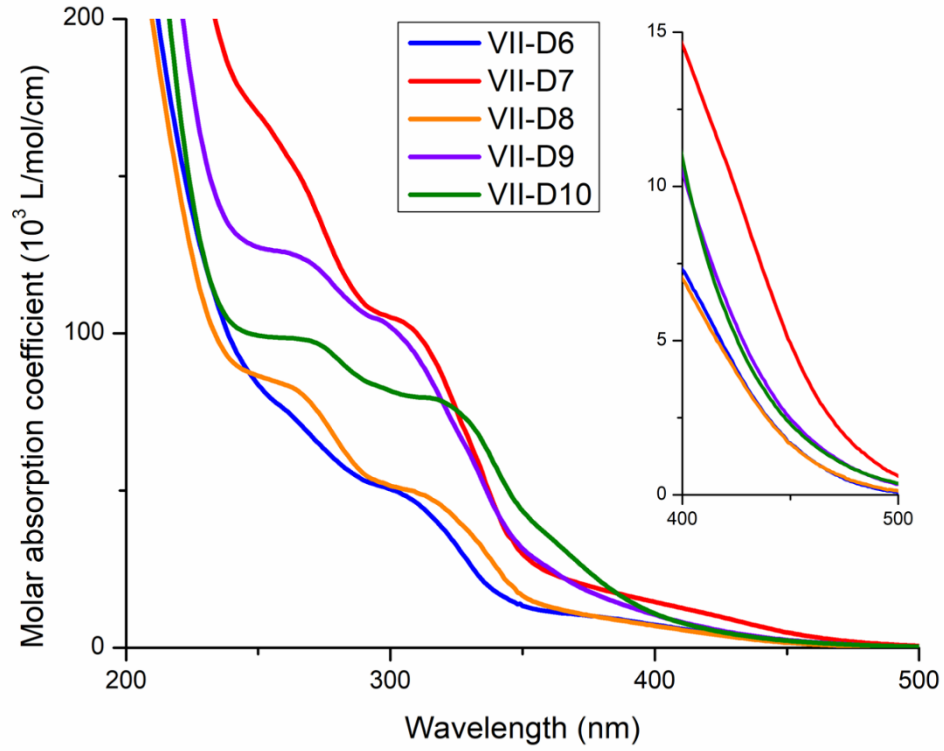

Figure XIII.18. Absorption spectra of the Re-POM dyads **VII-D6-10** in acetonitrile

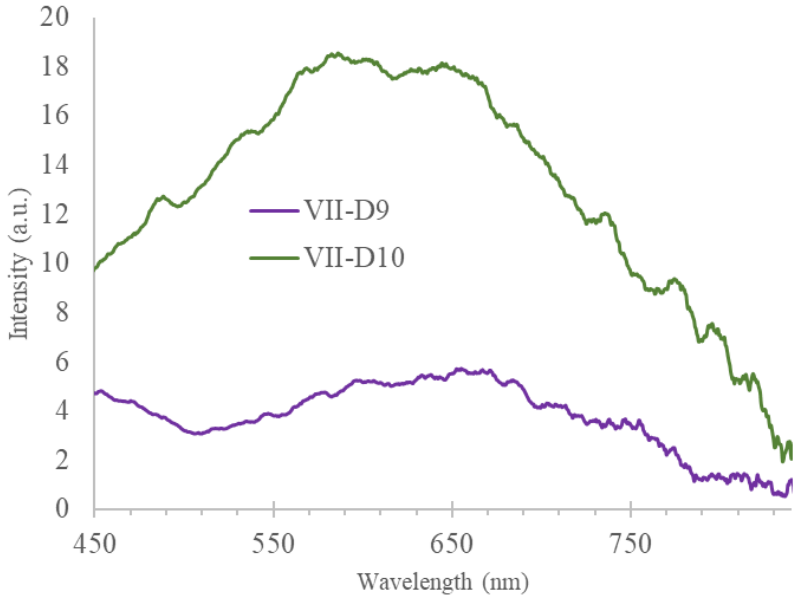

Figure XIII.19. Emission spectra of dyads **VII-D9-10** in degassed acetonitrile (λ_{exc} = 370 nm). The solutions had equal absorbance of ≈ 0.1.

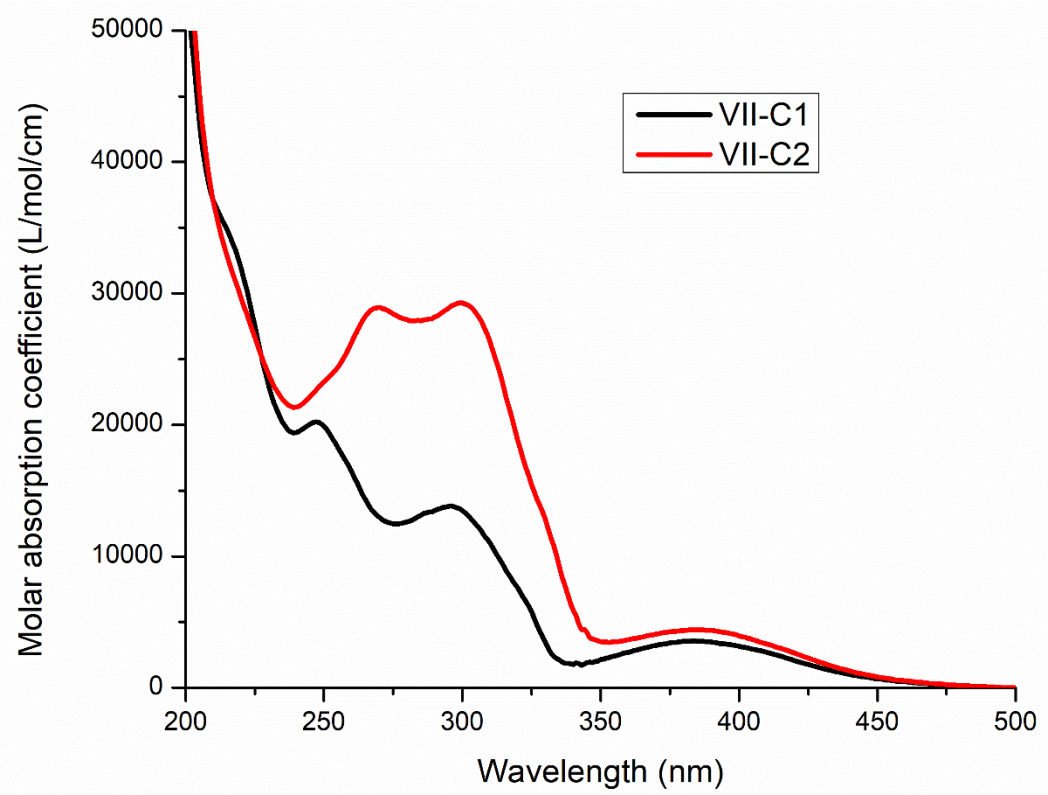

Figure XIII.20. Absorption spectra of the model Re(I) complexes **VII-C1-2** in acetonitrile.

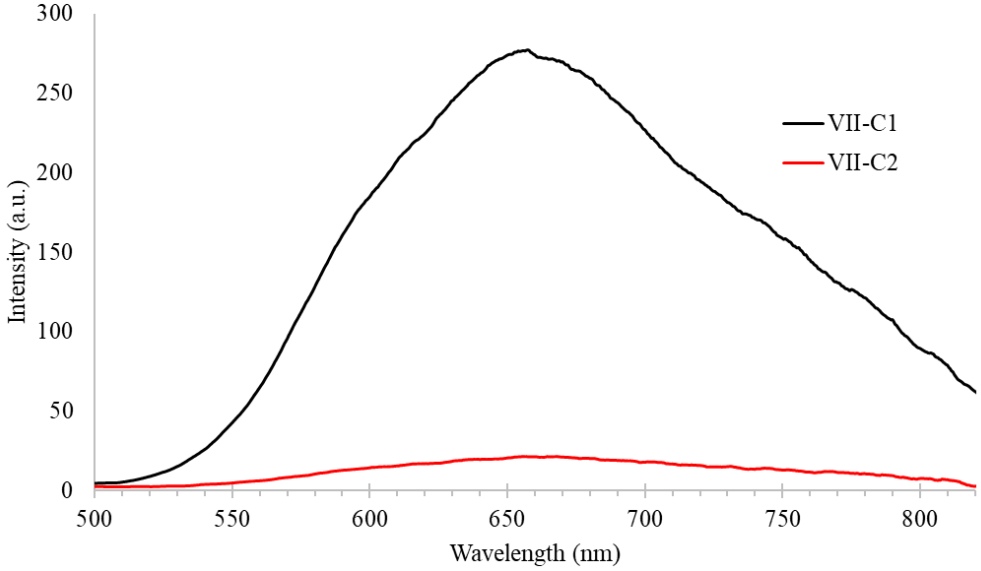

Figure XIII.21. Emission spectra of the model Re(I) complexes **VII-C1-2** in degassed acetonitrile (λ_{exc} = 370 nm). The solution had equal absorbance of ≈ 0.05.

XIII.4 Ultrafast spectroscopy data

All measurements were made in acetonitrile solution, with excitation at 400 nm.

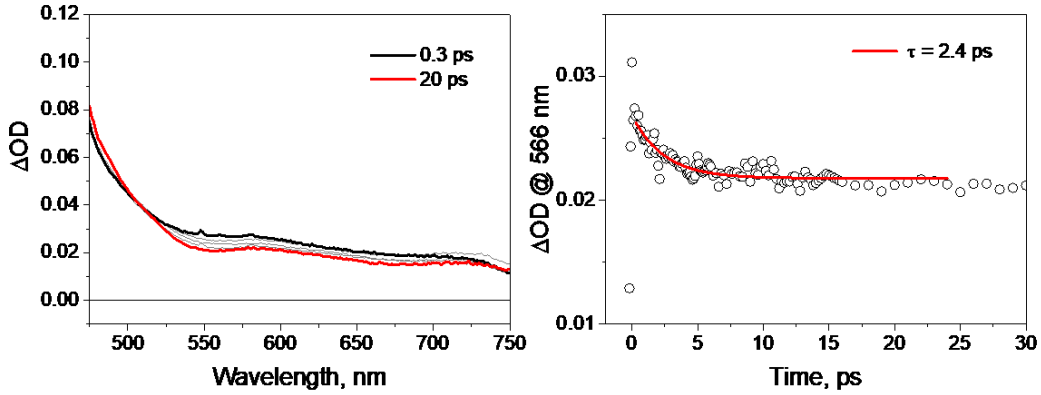

Figure XIII.22. Spectral evolution and kinetic analysis for [Re((4,4'-diMe-2,2'-bpy)$(CO)_3$Br]

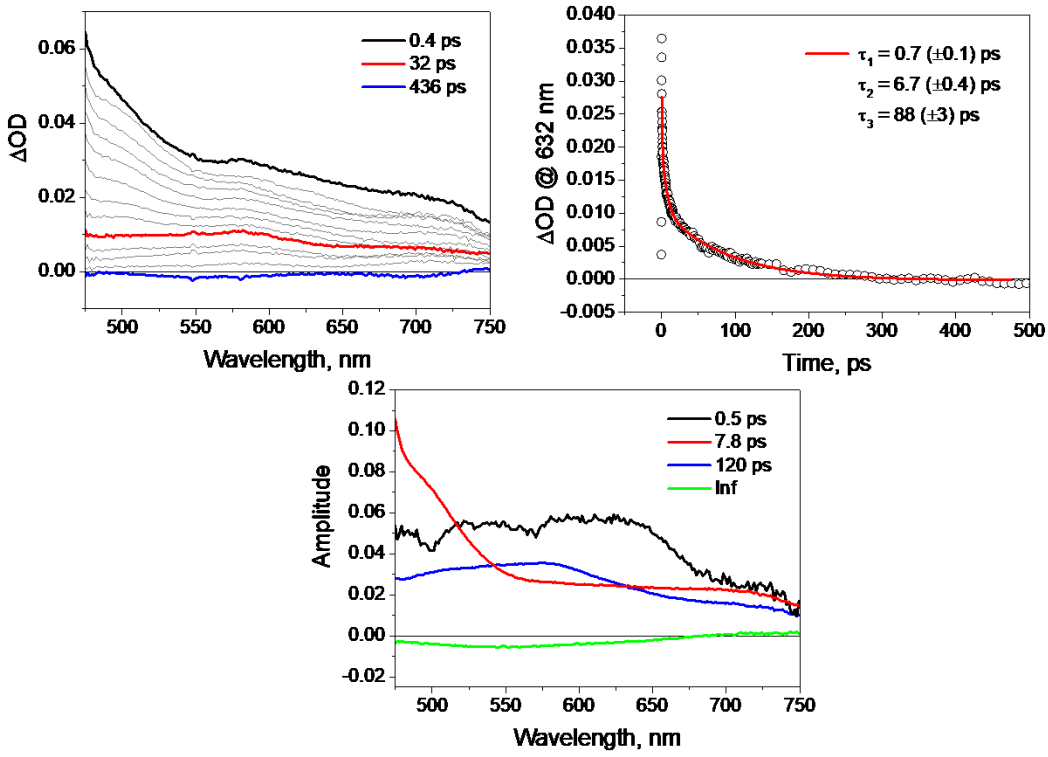

Figure XIII.23. Spectral evolution, kinetic analysis and global fitting for **VII-D6**.

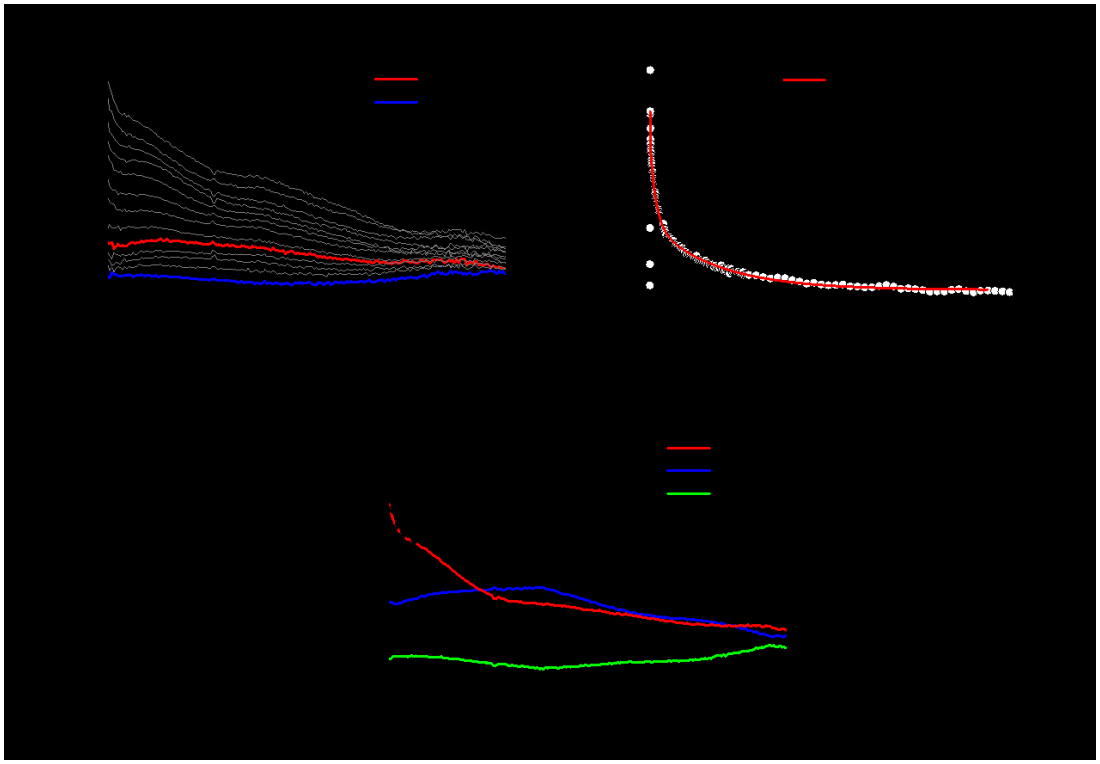

Figure XIII.24. Spectral evolution, kinetic analysis and global fitting for **VII-D7**.

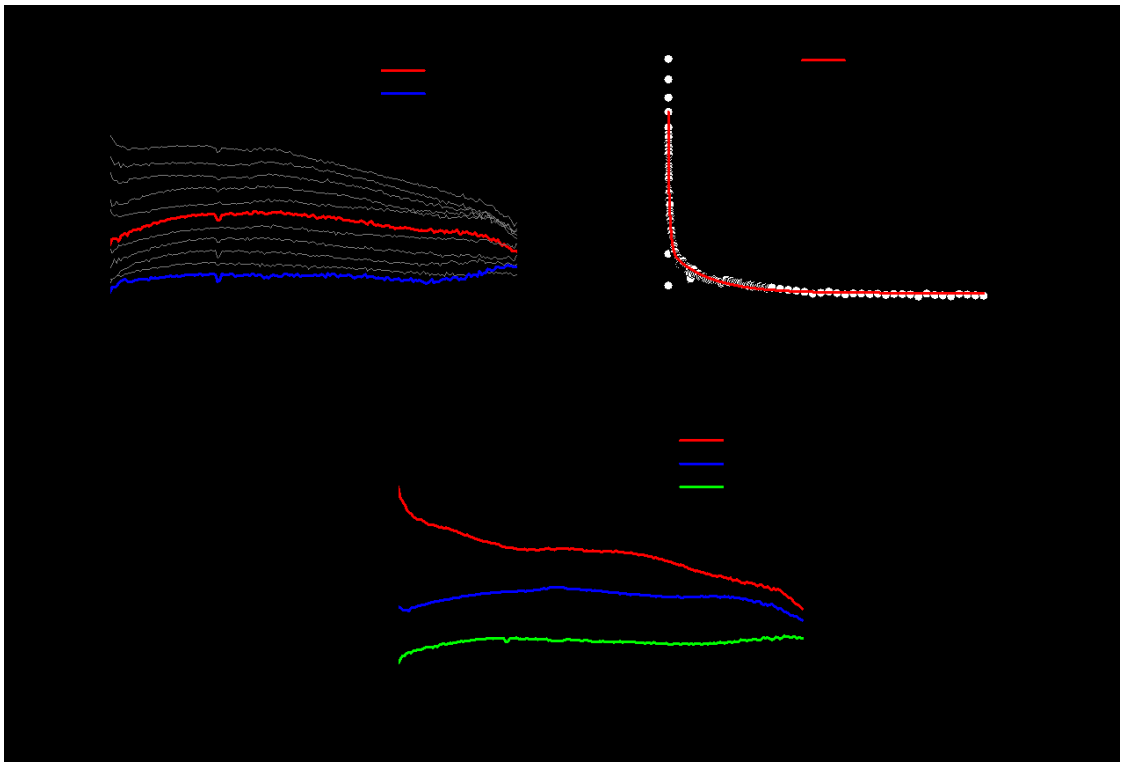

Figure XIII.25. Spectral evolution, kinetic analysis and global fitting for **VII-D8**.

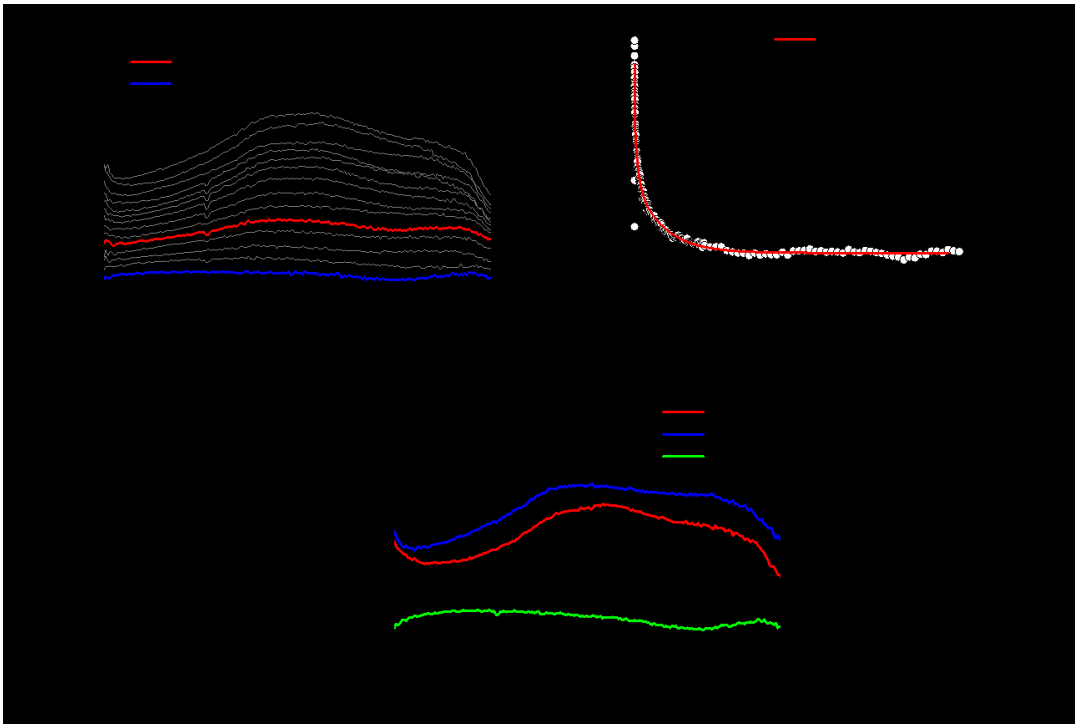

Figure XIII.26. Spectral evolution, kinetic analysis and global fitting for **VII-D9**.

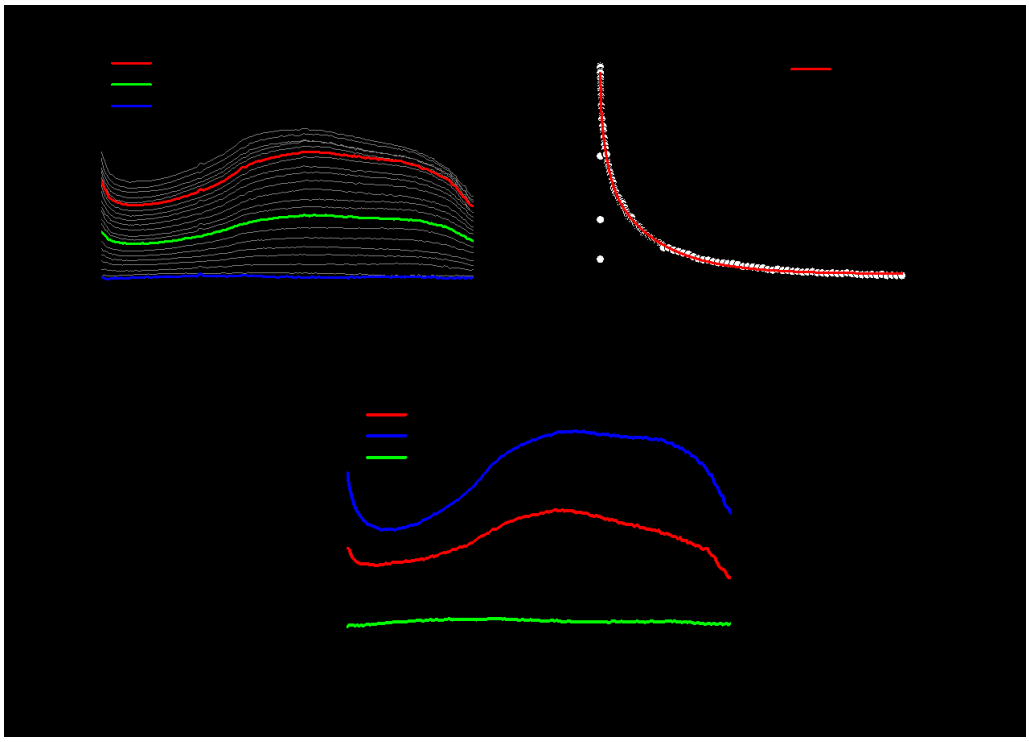

Figure XIII.27. Spectral evolution, kinetic analysis and global fitting for **VII-D10**.

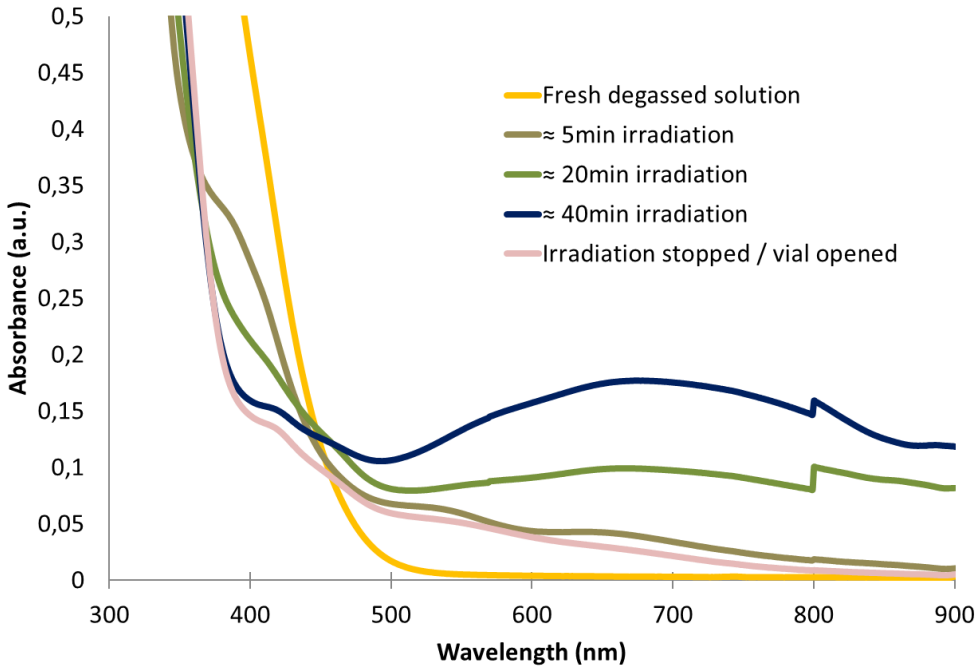

Figure XIII.28. Spectral variation of a solution of **VIII-D6** in DMF with triethanolamine irradiated at 420 nm.

XIII.4 Hydrogen photoproduction

Hydrogen evolution was monitored using a Perkin Elmer Clarus-480 gas chromatograph (GC) with a thermal conductivity detector, argon as carrier and eluent gas, a 7 ft. HayeSep N 60/80 pre-column, a 9 ft. molecular sieve 13 x 45/60 column and a 2 ml injection loop. Three distinct solutions for the sacrificial electron donor and proton source, the photosensitizer and the catalyst were prepared and mixed together to obtain 5 ml of solutions in standard 20 ml headspace vials. Using DMF as a solvent, the resulting molar concentration of photocatalytic medium are: 1 M for triethanolamine (TEOA), 0.1 M for HBF4, 0.56 M for water (*pH*apparent= 8.9). The concentration of active species were: 0.1 mM for the photosensitizer, 1 mM of cobalt pre-catalyst $[Co(H_2O)_6](BF_4)_2$ and 6 mM of dimethylglyoxime.

The vials were placed on top of a LED in an aluminum cast connected to a thermostatic bath set at 20 °C. They were sealed with a rubber septum pierced with two stainless steel tubes. The first tube carried an argon flow pre-bubbled in DMF. The flow was set between at 5 ml/min (adjusted with calibrated mass flow MCseries from Alicat) and referenced with a digital flowmeter

(Perkin Elmer FlowMark). The second tube led the flow to the GC sample loop through a 2 ml overflow protection vial, then through an 8-port stream select valve (VICCI) and finally to GC sample loop. A microprocessor (Arduino Uno) coupled with a custom PC interface allowed for timed injections. For calibration testing, stock cylinders of known concentration of H_2 in argon replaced the argon flow (inserted at the pre-bubbler, to keep the same vapor matrix). The measured results, independent of flow rate (under same pressure) can be easily converted into a rate of hydrogen production following equation 1. The errors associated to the *TON* (TurnOver Number) and *TOF* (TurnOver Frequency) were estimated to be within 10 %. They are calculated using the equations below.

(Eq. 1) H_2 rate (µL/min) = [H_2 standard] (ppm) × Ar flow rate (mL/min)

(Eq. 2) H_2 rate (nmol/min) = H_2 rate (µL/min) / 24.45 × 1000

(Eq. 3) TOF ($mmol_{H2}.mol_{PS}.min^{-1}$) = H_2 rate (nmol/min) / n_{PS} (mol) / 10^6

The amount of hydrogen produced between two injections is calculated using the average rate over that period of time [t_i ; t_j], multiplied by the time between two injections (tj-ti).

(Eq. 4) $n_{H2\ total}$ (nmol) = $\sum_{t0}^{tf} n_{H2}[ti\ ;\ tj] = \sum_{t0}^{tf}$(($H_2$ rate (ti) + H_2 rate (tj)) /2) × (tj-ti))

(Eq. 5) For a chosen length of experiment (t_f) TON(t_f) = $n_{H2(tf)}$ / n_{PS}

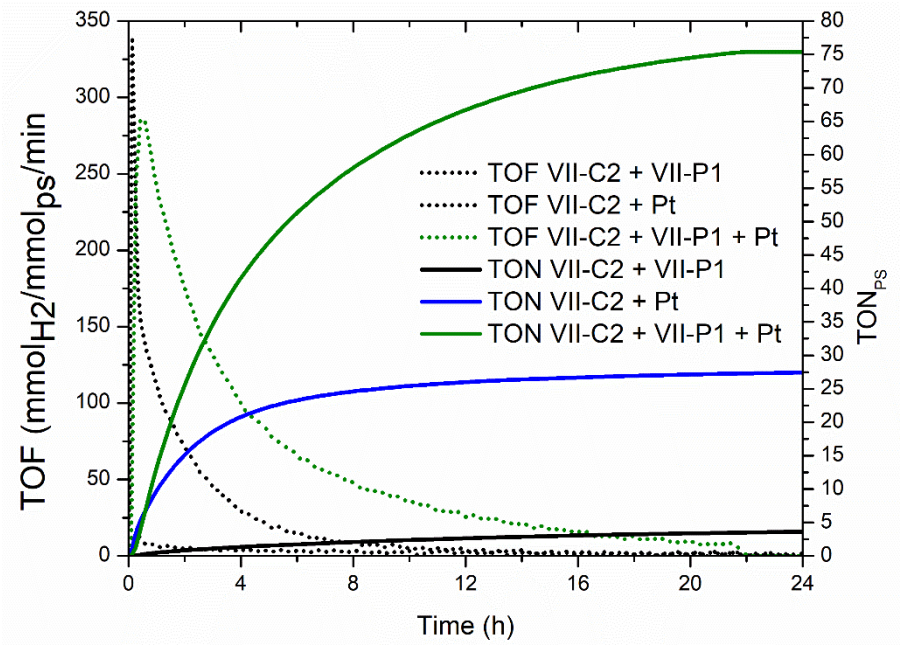

Figure XIII.29. Photocatalytic hydrogen evolution rate of dissociated system based on **VII-C2** and different catalyst (irradiation at 410 nm (50 mW) with 0.1 mM **VII-P1**/**VII-C2**, 0.05 mM K_2PtCl_4 in DMF, TEOA 1 M, HBF_4 0.1 M)

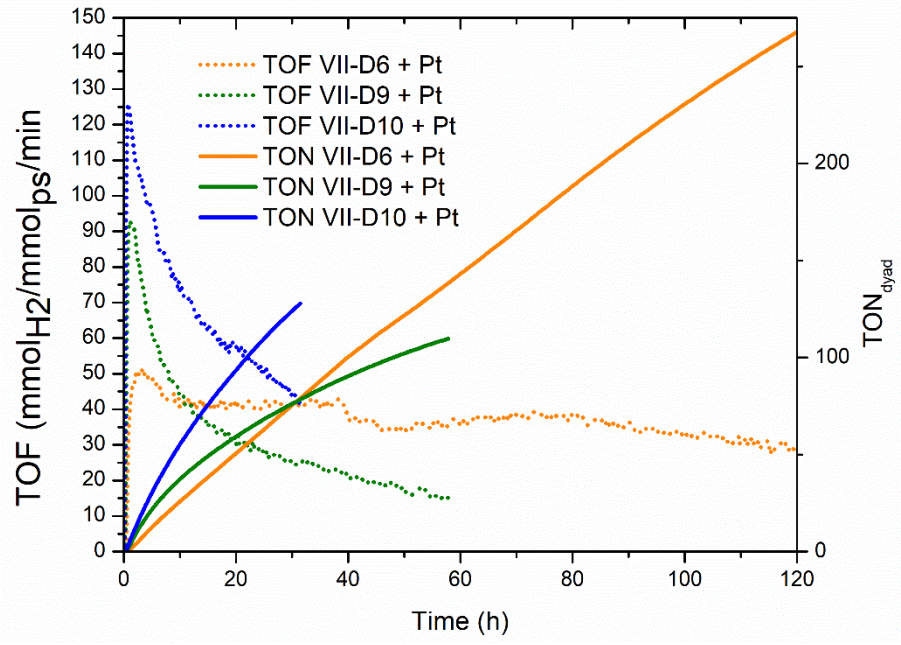

Figure XIII.30. Photocatalytic hydrogen evolution activity of dyads **VII-D6**, **VII-D9** and **VII-D10** with Pt as catalyst (irradiation at 410 nm (50 mW) with 0.1 mM **VII-D**, 0.05 mM K_2PtCl_4 in DMF, TEOA 1 M, HBF_4 0.1 M)

XIII.5 References

1. A. Stublla and P. G. Potvin, *Eur. J. Inorg. Chem.*, 2010, **2010**, 3040-3050.
2. D. M. Ryan, M. K. Coggins, J. J. Concepcion, D. L. Ashford, Z. Fang, L. Alibabaei, D. Ma, T. J. Meyer and M. L. Waters, *Inorg. Chem.*, 2014, **53**, 8120-8128.
3. T. Auvray, M. P. Santoni, B. Hasenknopf and G. S. Hanan, *Dalton Trans.*, 2017, **46**, 10029-10036.
4. Z. Popovic, M. Busby, S. Huber, G. Calzaferri and L. De Cola, *Angew. Chem. Int. Ed.*, 2007, **46**, 8898-8902.